STUDIES ON DESIGN, OPTIMIZATION AND CHARACTERIZATION OF PEROVSKITE SOLAR CELLS

A Thesis Submitted
In Partial Fulfilment of the Requirements
for the Degree of

DOCTOR OF PHILOSOPHY

by

RAHUL KUNDARA

(2K20/PHDAP/10)

Under the Supervision of

Dr. SARITA BAGHEL **Delhi Technological University**



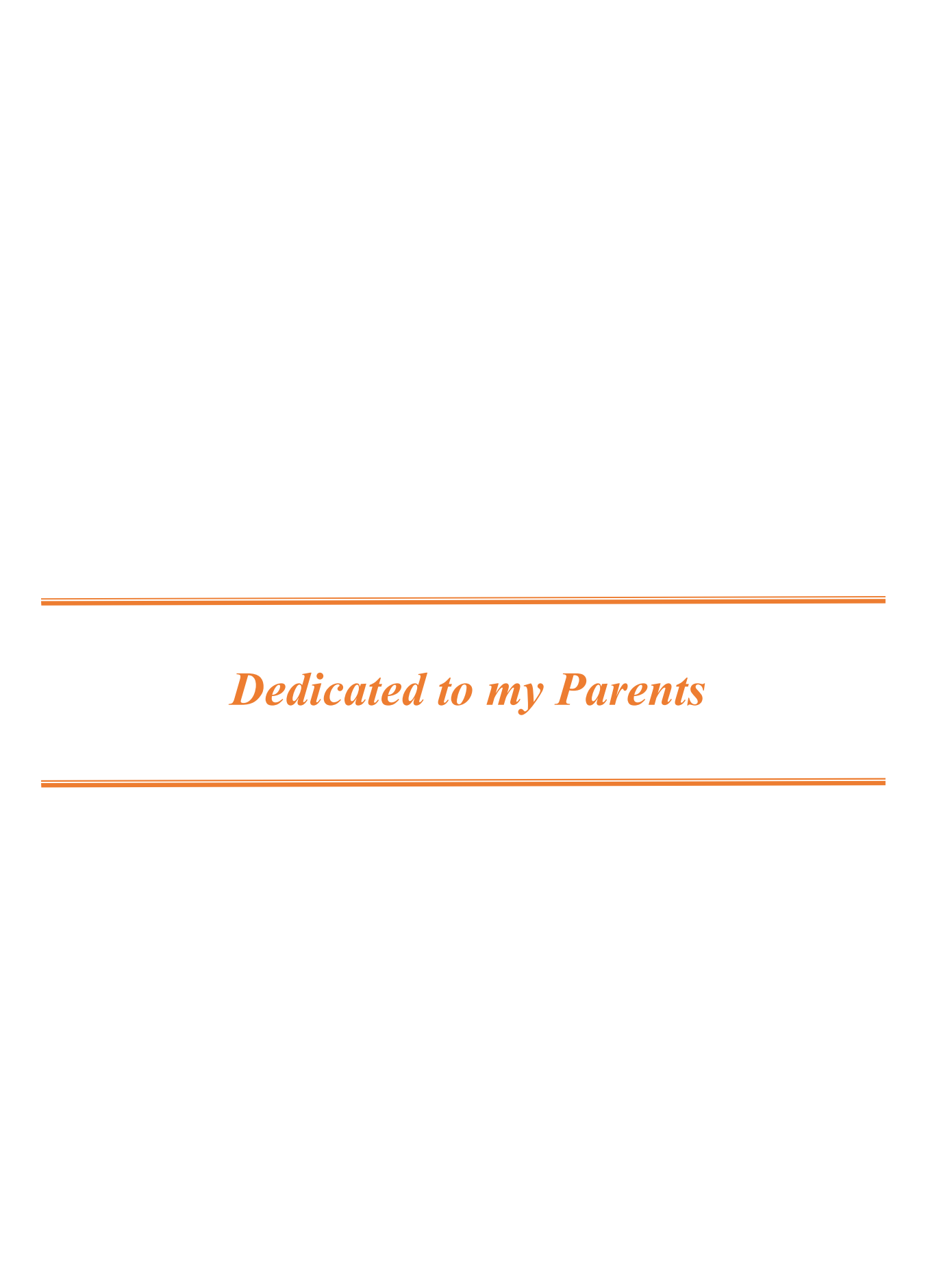
Department of Applied Physics

DELHI TECHNOLOGICAL UNIVERSITY

(Formerly Delhi College of Engineering) Shahbad Daulatpur, Main Bawana Road, Delhi-110042, India

March, 2025

©Delhi Technological University-2025 All rights reserved.





DELHI TECHNOLOGICAL UNIVERSITY

(Formerly Delhi College of Engineering)

Shahbad Daulatpur, Main Bawana Road, Delhi-110042

CANDIDATE'S DECLARATION

I <u>Rahul Kundara</u> hereby certify that the work which is being presented in the thesis entitled "Studies on Design, Optimization and Characterization of Perovskite Solar Cells" in partial fulfilment of the requirements for the award of the Degree of Doctor of Philosophy, submitted in <u>Applied Physics</u>, Delhi Technological University is an authentic record of my own work carried out during the period from <u>November</u>, 2020 to <u>March</u>, 2025 under the supervision of <u>Dr</u>. <u>Sarita Baghel</u>.

The matter presented in the thesis has not been submitted by me for the award of any other degree of this or any other Institute.

Candidate's Signature

This is to certify that the student has incorporated all the corrections suggested by the examiners in the thesis and the statement made by the candidate is correct to the best of our knowledge,

Signature of Supervisor (s)

Signature of External Examiner



DELHI TECHNOLOGICAL UNIVERSITY

(Formerly Delhi College of Engineering)

Shahbad Daulatpur, Main Bawana Road, Delhi-110042

CERTIFICATE BY THE SUPERVISOR(s)

Certified that <u>Rahul Kundara</u> (2K20/PHDAP/10) has carried out their research work presented in this thesis entitled <u>"Studies on Design, Optimization and Characterization of Perovskite Solar Cells"</u> for the award of <u>Doctor of Philosophy</u> from Department of Applied Physics, Delhi Technological University, Delhi, under my supervision. The Thesis embodies results of original work, and studies are carried out by the student himself and the contents of the thesis do not form the basis for the award of any other degree to the candidate or to anybody else from this or any other University/Institution.

Signature

Dr. Sarita Baghel

Assistant Professor

Department of Applied Physics

Delhi Technological University

Date:

ACKNOWLEDGEMENTS

First and foremost, I would like to extend my heartfelt gratitude to my parents and family, whose unwavering support has been the cornerstone of my emotional, physical, and mental well-being throughout my academic journey. In particular, my parents, Mr. Prem Chand and Mrs. Saroj, have played an instrumental role in shaping my values and academic aspirations. Their wisdom, guidance, and encouragement from my earliest years have fostered in me a profound love for learning and a relentless pursuit of academic excellence. I am eternally grateful to them for instilling such invaluable principles in my life, which have been pivotal to my success.

I extend my heartfelt gratitude to the **Almighty**, whose continuous blessings granted me the strength and guidance to complete this work successfully.

Throughout my four years at Department of Applied Physics, especially within the Renewable Energy Research Laboratory, I have been privileged to receive invaluable guidance and support from many generous individuals, to whom I offer my heartfelt thanks. It is with immense gratitude, respect, and a deep sense of indebtedness that I acknowledge my supervisor, Dr. Sarita Baghel, from the Department of Applied Physics at Delhi Technological University. Working under such an enthusiastic, distinguished, and supportive mentor has been a true privilege. Her unwavering encouragement, continuous guidance, meticulous supervision, and insightful feedback have been instrumental in reaching this significant milestone in my academic journey.

I would also like to express my sincere appreciation to **Prof. Vinod Singh**, Head and DRC Chairperson of the Department of Applied Physics, for their assistance and suggestions. My heartfelt thanks also go to **Dr. Amrish K. Panwar**, SRC member, as well as to the SRC and DRC committee members, for their continuous support and constructive recommendations. I am deeply grateful to **Dr. Deshraj Meena** from the Department of Applied Physics for his unwavering support.

I would like to acknowledge the enjoyable company and kind help provided by my dear friends, Ms. Priyanka, Mr. Vishal Deswal, Mr. Jasveer Singh, Ms. Sheetal Kumari, Mr. Naveen, Mr. Sharad Singh Jadaun, and Mr. Vinay Kumar Yadav for their help and support during this tenure. I sincerely acknowledge the financial support provided by Delhi Technological University through the Junior and Senior Research Fellowship during the course of my research. I also extend my heartfelt thanks to the staff in the Administration, Accounts, Store & Purchase, Library, and Computer Centre for their assistance and valuable services. I extend my heartfelt thanks to everyone who contributed to the successful completion of this thesis.

Thank you all!!!

Rahul Kundara

STUDIES ON DESIGN, OPTIMIZATION AND CHARACTERIZATION OF PEROVSKITE SOLAR CELLS

Rahul Kundara

ABSTRACT

Solar energy has become an increasingly important alternative source of power in the quest to mitigate environmental impact of fossil fuels and reduce global carbon footprint. The advancement of solar cell technologies has played a significant role in this transition, with solar cells evolving over the years in efficiency, material use, and fabrication methods. The development of various generations of solar cells has opened new avenues for harnessing solar power more effectively and sustainably. Among the most promising innovations in solar technology are perovskite solar cells (PSCs), which have gained attention due to their high efficiency and potential for low-cost production. Solar cells work by converting sunlight into electricity, a process that depends on the properties and behaviour of the materials used to construct them. The most widely used solar cells today are silicon-based, but these cells have limitations in terms of cost, efficiency, and material availability. As a result, need of exploration of alternative materials and structures to overcome these challenges. Among the newer types of solar cells, perovskite-based cells have shown significant promise due to their ease of fabrication, high absorption coefficient, and relatively low production costs. Perovskite materials, which have a unique crystal structure, offer excellent electrical, optical, and physical properties that make them ideal for use in solar cells. However, the use of lead-based perovskites materials in solar cells has raised significant environmental and health concerns. Lead is a toxic substance, and the potential for environmental contamination during production, use, and disposal of these materials has prompted lead-free alternatives. These lead-free PSCs are not only more eco-friendly but also have the potential to maintain or even surpass the performance of their lead-based counterparts. A wide range of materials, including tin (Sn), germanium (Ge), bismuth (Bi), antimony (Sb), and silver (Ag) have been explored as substitutes for lead. While these materials have shown potential, achieving the same level of efficiency and stability as lead-based PSCs remains a substantial challenge. To optimize the performance of lead-free PSCs, we have employed simulation tool such as SCAPS-1D, a software designed to model the behaviour of solar cells under various conditions. This software has been instrumental in fine-tuning device structures and parameters that affect performance, such as the thickness of absorber layer, operating temperature, defect density, series resistance, radiative recombination rate, shunt resistance, work function of back contact, energy band gap and carrier concentration. By optimizing these factors, we can design solar cells with improved efficiency and stability, even when using alternative perovskite materials such as (CH₃NH₃)₂CuX₄, LaFeO₃, KSnI₃, CsSnI₃ and KGeCl₃ have all been simulated employing SCAPS-1D to assess their potential as lead-free solar cell materials. The design of PSCs also involves optimizing the structure of the layers used in the cell, such as the electron transport layer (ETL) and hole transport layer (HTL), as well as the perovskite absorber layer. The interaction between these layers plays a crucial role in determining the overall efficiency of the solar cell. By carefully selecting and optimizing the materials and thickness of these layers, we can enhance the efficiency of the devices. In addition to material optimization, the development of machine learning techniques has provided new insights into the design and prediction of solar cell performance. By training machine learning modes with experimental data and simulation results, we can predict the performance of different material combinations and device structures, thus reducing the time and effort needed for trial-and-error experimentation. The machine learning model also predicts the effect of distinct parameters on device performance and PCE using SHAP plot, XGB and RF algorithm. XGB model predicts performance with higher accuracy. The machine learning model analysis is helpful for the fabrication of efficient device. This integration of machine learning and simulation tool is accelerating the development of high-performance, lead-free solar cells. The synthesis of novel perovskite materials also plays a key role in advancing solar cell technology. For instance, the sol-gel method has been used to synthesize LaFeO₃ and Cs₂AlBiCl₆ materials for solar cell applications. These materials are characterized using techniques such as XRD, SEM, UV-Vis and FTIR spectroscopy to assess their structural and optical properties. The characterization results provide valuable insights into the suitability of these materials for use in solar cells, guiding the design for more efficient and cost-effective devices. Cs₂AlBiCl₆, a double perovskite material, is a promising lead-free PSC material with excellent structural and optical properties. We synthesized and characterized it, confirming its photovoltaic potential. Developing such lead-free perovskites is vital for sustainable, efficient solar technologies that can advance clean energy solutions and address climate change.

LIST OF PUBLICATIONS

PUBLICATIONS RESULTING FROM THIS THESIS WORK (06)

Article in International Refereed Journals (06):

- 1. "Study on the Various Parameters Affecting the Power Conversion Efficiency of Lead-Free Perovskite Solar Cell by SCAPS-1D"; Rahul Kundara, Sarita Baghel, Journal of Mines, Metals and Fuels, 70 (2022) 24–29.
- 2. "Device modelling of lead free (CH₃NH₃)₂CuX₄ based perovskite solar cells using SCAPS simulation"; Rahul Kundara, Sarita Baghel, Optical and Quantum Electronics, 55 (2023) 968.
- 3. "Performance analysis of LaFeO₃ perovskite solar cells: A theoretical and experimental study"; Rahul Kundara, Sarita Baghel, Solid State Communications, 389 (2024) 115590.
- "Predictive design of KSnI₃-based perovskite solar cells using SCAPS and machine learning model"; Rahul Kundara, Sarita Baghel, Materials Science & Engineering B, 307 (2024) 117536.
- 5. "Performance optimization of lead-free KGeCl₃ based perovskite solar cells using SCAPS-1D"; Rahul Kundara, Sarita Baghel, Solar Energy, 287 (2025) 113253.
- 6. "Performance optimization of CsSnI₃-based perovskite solar cells using SCAPS-1D and machine learning analysis"; Rahul Kundara, Sarita Baghel, Journal of Optics, (2025).

PUBLICATIONS OTHER THAN THIS THESIS WORK (02)

Article in International Refereed Journals (02):

- 1. "Investigating the Efficiency and Optimization of Germanium-based Perovskite Solar Cell using SCAPS 1D"; Anushansha Yadav, Vanshika, Rahul Kundara, Sarita Baghel, Indian Journal of Engineering & Materials Sciences, 30 (2023) 706-712.
- 2. "Numerical simulation of highly efficient Cs₂AgInBr₆-based double perovskite solar cell using SCAPS-1D"; Vishal Deswal, Shubhda Kaushik, Rahul Kundara, Sarita Baghel, Materials Science & Engineering B, 299 (2024) 117041.

International Conferences Presentation (04):

- 1. *International Conference on Design and Materials (ICDM)* Organized by Department of Design, Delhi Technological University (DTU) held on 27th-30th January 2022.
- 2. International Conference on Nanotechnology: Opportunities & Challenges (ICNOC-2022) organized by Department of Applied Science & Humanities, Faculty of Engineering & Technology, Jamia Millia Islamia, on 28th 30th November 2022, at New Delhi, India.
- 3. International Conference on Artificial Intelligence, Advanced Materials, & Mechatronics Systems (AIAMMS-2023) organized by School of Engineering & Technology, JECRC University, on 3rd-4th November 2023, at Jaipur, India.
- 4. International Conference on Atomic, Molecular, Material, Nano & Optical Physics with Applications (ICAMNOP-2023) on 20-22nd Dec 2023, organized by Delhi Technological University (DTU), Delhi.

CONTENTS

Declaration	i
Certificate	iii
Acknowledgments	v
Abstract	vi
List of publications	viii
Table of Contents	xi
List of tables	xviii
List of figures	xx
CHAPTER 1: INTRODUCTION	1-16
1.1 Introduction	2
1.2 Solar cells.	2
1.3 Photovoltaic Technologies	3
1.3.1 Classic Silicon/First Generation Solar Cells	5
1.3.1.1 Monocrystalline/Single crystal Silicon Solar Cell	5
1.3.1.2 Poly/Multicrystalline Silicon Solar Cells	6
1.3.2 Thin Film / Second Generation Solar Cells	6
1.3.2.1 Amorphous Silicon	7
1.3.2.2 Cadmium Telluride (CdTe)	7
1.3.2.3 Copper Indium Gallium Di-Selenide Solar Cell (CIGS)	7
1.3.3 Third Generation Solar Cells	7
1.3.3.1 Dye Sensitized Solar Cells (DSSCs)	7
1.3.3.2 Organic Solar Cells	8
1.3.3.3 Concentrated solar Cells	8

1.3.3.4 Perovskite Solar Cells	8
1.3.3.4.1 Basic structure of perovskite solar cell	9
1.4 Losses in solar cells	11
1.5 Problem Statement and Objectives	12
1.6 References	13
CHAPTER 2: LITERATURE REVIEW	17-27
2.1 Introduction	18
2.2 Literature Review	18
2.2.1 Organic Perovskite Materials	19
2.2.2 Inorganic Perovskite Materials	20
2.2.3 3D Perovskite Materials	20
2.2.4 PIN and NIP Perovskite Structures.	21
2.3 Research Gap	22
2.4 References	23
CHAPTER 3: MATERIALS AND METHODS	28-42
3.1 Perovskite Materials	29
3.1.1 CH ₃ NH ₃ PbI ₃	29
3.1.2 Need of Lead-Free Solar Cells.	29
3.1.3 Potential Alternatives	29
3.1.3.1 CsSnI ₃ and KSnI ₃	29
3.1.3.2 Copper (Cu)-based	30
3.1.3.3 LaFeO ₃	30
3.1.3.4 KGeCl ₃	31
3.1.3.5 Cs ₂ AlBiCl ₆ Double Perovskite Material	31
3.2 Methodology	31

3.2.1 SCAPS-1D Simulation Software	31
3.2.2 Machine Learning Analysis	33
3.2.3 Characterization Methods	34
3.2.3.1 X-ray Diffraction (XRD)	34
3.2.3.2 UV-Visible Spectroscopy	35
3.2.3.3 Scanning Electron Microscopy (SEM)	36
3.2.3.4 Fourier Transform Infrared Spectroscopy (FTIR)	36
3.2.3.5 Current-Voltage Characteristics	37
3.3 References	39
CHAPTER 4: STUDY OF VARIOUS PARAMETERS AFFECTING THE DIFFERENT PHOTOVOLTAIC PARAMETERS OF PEROVSKITE SOLAR CELLS BY SCAPS-1D	43-52
4.1 Introduction	44
4.2 Simulation Procedure and Device Architecture	44
4.3 Result and Discussion.	47
4.3.1 Effect of Change in Thickness	47
4.3.2 Effect of Variation in Operating Temperature	48
4.3.3 Impact of Change in Defect Density	49
4.4 Summary	50
4.5 References	51
CHAPTER 5: DEVICE MODELLING OF LEAD FREE (CH3NH3)2CuX4 BASED PEROVSKITE SOLAR CELLS USING SCAPS SIMULATION	53-71
5.1 Introduction.	54
5.2 Device Architecture and Simulation	54
5.3 Result and Discussion.	57
5.3.1 Modulation of Various ETLs and HTLs to Impact Device Performance	57
5.3.1.1 Comparison with Experimental Results	61

	5.3.2 Impact of Thickness of Absorber Layer on Device Performance	61
	5.3.3 Effect of Operating Temperature on Absorber Layer	63
	5.3.4 Effect of Change in Series Resistance on Performance	64
	5.3.5 Effect of Radiative Recombination Rate on PCE	65
	5.3.6 Effect of Back Contact Work Function on PCE	66
5.4	4 Summary	67
5.5	5 References	68
	HAPTER 6: PERFORMANCE ANALYSIS OF LaFeO ₃ PEROVSKITE SOLAR ELLS: A THEORETICAL AND EXPERIMENTAL STUDY	72-98
6.	1 Introduction	73
6.2	2 Device Architecture	73
6.3	3 Experimental Section	74
	6.3.1 Materials and Method.	74
	6.3.2 Material Characterization Techniques	75
6.4	4 Experimental Result and Discussion	75
	6.4.1 XRD Analysis	75
	6.4.2 SEM Results	76
	6.4.3 EDS Spectrum.	77
	6.4.4 UV-Vis Spectroscopy	77
	6.4.5 FT-IR Analysis	78
	6.4.6 Photoluminescence Spectrum	79
6.5	5 Simulation Result and Discussion	79
	6.5.1 Optimization of Suitable ETL and HTL	79
	6.5.2 Impact of Thickness of Absorber Layer	86
	6.5.3 Effect of Operating Temperature	87
	6.5.4 Effect of Defect Density	88

6.5.5 Effect of Series Resistance	89
6.5.6 Effect of Shunt Resistance	90
6.5.7 Appropriate Back Contact	91
6.6 Comparison of Experimental Results with Previously Reported Results	92
6.6.1 Simulation Results	92
6.6.2 Experimental Results	93
6.7 Summary	94
6.8 References	95
CHAPTER 7: PREDICTIVE DESIGN OF KSnI ₃ -BASED PEROVSKITE SOLAR CELLS USING SCAPS AND MACHINE LEARNING MODEL	99-117
7.1 Introduction	100
7.2 Device Architecture and Methods	100
7.2.1 Machine Learning	102
7.3 Result and Discussion	102
7.3.1 Selection of Appropriate HTL	102
7.3.2 Optimization of HTL	105
7.3.2.1 Impact of Thickness	105
7.3.2.2 Impact of Doping Density	106
7.3.2.3 Impact of Defect Density	107
7.3.3 Optimization of KSnI ₃ Layer	108
7.3.3.1 Impact of Thickness	108
7.3.3.2 Impact of Defect Density	109
7.3.4 Optimized Device	110
7.3.5 Machine Learning Analysis	111
7.4 Summary	113
7.5 References	114

CHAPTER 8: PERFORMANCE OPTIMIZATION OF CsSnI ₃ -BASED PEROVSKITE SOLAR CELLS USING SCAPS-1D AND MACHINE LEARNING	118-135
8.1 Introduction	119
8.2 Simulation Procedure and Device Structure	119
8.2.1 Verification of the Model and Comparison of Experimental Result	121
8.2.2 Appropriate ETLs and HTLs to Improve Performance	122
8.3 Result and Discussion	123
8.3.1 Effect of Change in Thickness	123
8.3.2 Impact of Change in Operating Temperature	125
8.3.3 Impact of Change in Defect Density	126
8.3.4 J-V and QE Plots of Various ETLs and HTLs	127
8.3.5 Effect of Work Function	129
8.3.6 Machine Learning Analysis	129
8.3.7 Effect of Doping Density	131
8.4 Summary	132
8.5 References	133
CHAPTER 9: INVESTIGATION OF LEAD-FREE KGeCl ₃ BASED PEROVSKITE SOLAR CELLS USING SCAPS-1D	136-152
9.1 Introduction	137
9.2 Device Architecture and Simulation Method	137
9.3 Result and Discussion	140
9.3.1 Impact of Distinct Parameters on KGeCl ₃ -based PSC	140
9.3.1.1 Effect of Bandgap with Thickness	140
9.3.1.2 Effect of Donor Carrier Concentration with Thickness	142
9.3.1.3 Effect of Acceptor Carrier Concentration with Thickness	144
9.3.2 Effect of Operating Temperature on PSC	146

9.4 Summary	148
9.5 References	150
CHAPTER 10: SYNTHESIS AND CHARACTERIZATION OF Cs2AlBiCl6 DOUBLE PEROVSKITE MATERIAL FOR PHOTOVOLTAIC APPLICATION	153-160
10.1 Introduction	154
10.2 Material and Method	154
10.2.1 Material Characterization Techniques	156
10.3 Result and Discussion.	156
10.3.1 XRD Analysis	156
10.3.2 SEM Results	157
10.3.3 UV-Vis Spectroscopy	158
10.3.4 Photoluminescence Spectrum	158
10.4 Summary	159
10.5 References	160
CHAPTER 11: CONCLUSION, FUTURE SCOPE AND SOCIAL IMPACT	161-163
11.1 Conclusion	162
11.2 Future Scope of Work and Social Impact	163
11.3 Social Impact	163

List of Tables

Table 2.1 Organic perovskite solar cells efficiency
Table 2.2 Inorganic perovskite solar cells efficiency
Table 4.1 Various parameters employed in simulation of cell 1 and cell 2
Table 4.2 Various parameters employed in simulation of cell 3
Table 4.3 Optimized value of different variable and PV parameters50
Table 4.4 Device output of previous reported theoretical studies and outcome of present simulation for PSCs (at 300 K)
Table 5.1 Various input parameters of perovskite layers employed in simulation55
Table 5.2 Various input parameters employed in simulation of different ETLs56
Table 5.3 Various input parameters employed in simulation of different HTLs56
Table 5.4 PCE of various combinations of Cu-based PSC with different ETL and HTL60
Table 5.5 Optimized PCE of Cu-based PSC with various ETLs and HTLs60
Table 5.6 The previously reported result of different Cu-based PSCs61
Table 6.1 Weight % of the element composition of LaFeO ₃ powder
Table 6.2 Input parameters of PSCs
Table 6.3 Input parameters of different ETLs81
Table 6.4 Input parameters of different HTLs83
Table 6.5 The PSC performance of CBTS with the different ETLs85
Table 6.6 Defect properties of LaFeO ₃ absorber layer88
Table 6.7 Comparison of Experimental, SCAPS-1D and previously reported outcomes94
Table 7.1 Input parameters of simulated PSC
Table 7.2 Input parameters of distinct HTLs101
Table 7.3 Comparison with previously reported results
Table 7.4 The PV parameters of KSnI ₃ -based PSC with distinct HTLs104
Table 8.1 Input parameters of PSCs

Table 8.2 The previously reported experimental and simulation results	121
Table 8.3 Input parameters of various ETLs1	122
Γable 8.4 Input parameters of distinct HTLs	123
Table 8.5 Performance of CsSnI ₃ PSC with various ETLs	127
Table 8.6 Performance of CsSnI ₃ PSC with several HTLs	127
Γable 8.7 Comparison with previous results 1	129
Γable 9.1 Input parameters were used in simulation of distinct ETLs	139
Γable 9.2 Input parameters used in simulation of various HTLs	139
Table 9.3 KGeCl ₃ PSC performance before optimization (at thickness of absorber layer = 3 mm, $E_g = 1.49$ eV, $N_D = N_A = 1 \times 10^{14}$ cm ⁻³ and $N_t = 10^{13}$ cm ⁻³) with different ETLs a HTLs	anc
Γable 9.4 Effect of change in temperature on PV parameters	147

List of Figures

Figure 1.1 A p-n junction solar cell
Figure 1.2 Generation of PV cells
Figure 1.3 NREL efficiency chart for various solar cells
Figure 1.4 Czochralski process
Figure 1.5 (a) Monocrystalline and (b) Polycrystalline solar module
Figure 1.6 Perovskite crystal structure
Figure 1.7 Basic structure of perovskite solar cell
Figure 1.8 Current-voltage characteristics of a solar cell
Figure 2.1 A p-i-n device architecture
Figure 2.2 A n-i-p device architecture
Figure 3.1 SCAPS-1D software simulation procedure
Figure 3.2 SCAPS-1D data used in machine learning analysis
Figure 3.3 Schematic diagram of XRD
Figure 3.4 Schematic diagram of UV-vis spectrometer
Figure 3.5 Schematic diagram of SEM
Figure 3.6 Schematic sketch of FTIR spectrometer
Figure 3.7 Current-voltage characteristics of a solar cell
Figure 3.8 Schematic diagram of a solar simulator
Figure 4.1 Structure of the Simulated model of CH ₃ NH ₃ SnI ₃ , CH ₃ NH ₃ GeI ₃ and CH ₃ NH ₃ PbI ₃ PSC
Figure 4.2 SCAPS-1D software simulation procedure
Figure 4.3 Impact of thickness on PV parameters of CH ₃ NH ₃ SnI ₃ , CH ₃ NH ₃ GeI ₃ and CH ₃ NH ₃ PbI ₃ PSCs
Figure 4.4 Change in the PV parameters of CH ₃ NH ₃ SnI ₃ , CH ₃ NH ₃ GeI ₃ and CH ₃ NH ₃ PbI ₃ PSCs with operating temperature

Figure 4.5 Impact of N _t on the performance of CH ₃ NH ₃ SnI ₃ , CH ₃ NH ₃ GeI ₃ and CH ₃ NH ₃ PbI ₃ PSCs
Figure 5.1 Architecture of the Simulated model of (MA) ₂ CuCl ₄ , (MA) ₂ CuCl ₂ I ₂ and (MA) ₂ CuCl ₂ Br ₂ PSC
Figure 5.2 The energy level alignment between ETL, PAL and HTL materials
Figure 5.3 J-V characteristics of Cu-based PSCs
Figure 5.4 Quantum efficiency (QE) curve for Cu-based PSCs
Figure 5.5 Absorption coefficient of Cu-based PSCs
Figure 5.6 Band alignment diagram of optimized device
Figure 5.7 Change in photovoltaic parameters with the thickness of PAL for different ETL and HTL of Cu-based PSC
Figure 5.8 Change in photovoltaic parameters with the operating temperature for various Cubased PSCs
Figure 5.9 Change in PCE of different PSCs with R _S 65
Figure 5.10 The change in PV parameters with recombination coefficient for Cu-based PSCs
Figure 5.11 Change in PCE of different PSCs with metal work function (eV)
Figure 6.1 Architecture of LaFeO ₃ -based PSC
Figure 6.2 Flow chart of stepwise synthesis of LaFeO ₃
Figure 6.3 Preparation of LaFeO ₃ perovskite
Figure 6.4 XRD pattern of (a) LaFeO ₃ and (b) Calcined LaFeO ₃ 76
Figure 6.5 (a) SEM image of LaFeO ₃ nanoparticles and (b) Particle size distribution76
Figure 6.6 EDS spectrum of LaFeO ₃ nanoparticles
Figure 6.7 UV-Vis spectrum of LaFeO ₃ nanoparticles
Figure 6.8 FT-IR spectrum of LaFeO ₃ nanoparticles
Figure 6.9 PL spectrum of LaFeO ₃ nanoparticles
Figure 6.10 Band alignment diagram of various ETLs with LaFeO ₃ absorber layer80
Figure 6.11 Band alignment diagram of various HTLs with LaFeO ₃ absorber layer82

Figure 6.12 Optimization of LaFeO ₃ PSC PV parameters for various ETLs (TiO ₂ , PCBM, IGZO, In ₂ O ₃ , C ₆₀ , ZnO, SnO ₂ , WS ₂) and HTLs (Cu ₂ O, CuInSe ₂ , Spiro-OMeTAD, P3HT, D-PBTTT-14, V ₂ O ₅ , CFTS, CBTS) with Au as metal back contact
Figure 6.13 J-V and QE with distinct ETLs85
Figure 6.14 Impact of thickness on PV parameters of LaFeO ₃ -based PSCs
Figure 6.15 Change in performance of LaFeO ₃ -based PSCs with operating temperature87
Figure 6.16 Impact of N _t on the performance of LaFeO ₃ -based PSCs89
Figure 6.17 Impact of R_S on the performance of LaFeO ₃ -based PSC at $R_{SH} = 10^5 \ \Omega$ -cm ² 90
Figure 6.18 Impact of R_{sh} on the performance of LaFeO ₃ -based PSC at $R_S = 0.5~\Omega$ -cm ² 91
Figure 6.19 Impact of various work functions on efficiency91
Figure 6.20 Structure and band alignment diagram of optimized device92
Figure 6.21 J-V and QE curve of optimized device
Figure 6.22 Fabricated LaFeO ₃ PSC93
Figure 6.23 J-V curve of fabricated LaFeO ₃ -based PSC93
Figure 7.1 Architecture of simulated PSCs
Figure 7.2 Energy band diagram of various HTLs
Figure 7.3 (a) J-V and (b) QE plots of simulated PSCs with various HTLs104
Figure 7.4 Impact of the thickness of PEDOT: PSS layer on PV parameters of PSC106
Figure 7.5 (a) Efficiency versus N_A of the PEDOT: PSS and (b) J-V curves of HTL depending on its N_A
Figure 7.6 Impact of N _t of the PEDOT: PSS on PV parameters of KSnI ₃ -based PSC108
Figure 7.7 (a) Efficiency vs thickness of the absorber layer. (b) J-V curves with function of absorber layer thickness
Figure 7.8 (a) Efficiency vs N _t of the absorber layer and (b) Effects of N _t on the J-V characteristics of KSnI ₃ -based PSCs
Figure 7.9 Architecture and band alignment diagram of optimized PSC110
Figure 7.10 (a) J-V and (b) QE plot of optimized device
Figure 7.11 Different features with relative importance in the ML model
Figure 7.12 Derived and predicted values of PV parameters
Figure 8.1 Structure of simulated model of PSCs

Figure 8.2 Band alignment diagram of distinct ETLs, perovskite layer and HTLs	21
Figure 8.3 (a) Quantum efficiency and (b) J-V characteristics plots	22
Figure 8.4 Change in PV parameters of CsSnI ₃ -based PSCs with thickness	24
Figure 8.5 (a) QE curve (b) J-V plots of optimized CsSnI ₃ PSC with thickness	25
Figure 8.6 Change in the PV parameters of CsSnI ₃ -based PSCs with operating temperatum	
Figure 8.7 Impact of N _t on the performance of CsSnI ₃ PSCs	27
Figure 8.8 J-V curve for CsSnI ₃ PSC with different (a) ETLs and (b) HTLs1	28
Figure 8.9 Quantum efficiency curve for CsSnI ₃ -based PSC with different (a) ETLs and (HTLs	` ′
Figure 8.10 Energy level diagram of optimized device	28
Figure 8.11 (a) QE curve and (b) J–V characteristics of optimized CsSnI ₃ PSC with various back-contact work functions	
Figure 8.12 Actual and predicted value of PCE using (a) RF model (c) XGB model and SHA plots (b) RF model (d) XGB model	
Figure 8.13 Impact of N _A on the PCE and FF of CsSnI ₃ -based PSC	32
Figure 9.1 Architecture and band alignment diagram for KGeCl ₃ PSC	38
Figure 9.2 Energy band diagram of FTO/WS ₂ /KGeCl ₃ /PEDOT: PSS/Au PSC1	38
Figure 9.3 Change in PV parameters of simulated PSC such as (a) V_{OC} (b) J_{SC} (c) FF and (PCE with thickness of absorber layer and bandgap at doping concentration of 10^{15} c 3	m
Figure 9.4 The JV curves of the PSC with thickness of the absorber layer	42
Figure 9.5 Variation in PV parameters of simulated PSC such as (a) V_{OC} (b) J_{SC} (c) FF and (PCE with thickness of absorber layer and N_D at E_g = 1.40 eV	
Figure 9.6 Variation in PV parameters of simulated PSC such as (a) V_{OC} (b) J_{SC} (c) FF and (PCE with thickness of absorber layer and N_A	
Figure 9.7 The QE curves of the simulated PSC as a function of absorber layer (a) thickne (b) E_g , (c) N_D and (d) N_A	
Figure 9.8 Impact of temperature on PV parameters of KGeCl ₃ PSC	48
Figure 9.9 PCE vs temperature curves of various PSC materials	48
Figure 10.1 Flow chart of Cs ₂ AlBiCl ₆ material synthesis	55
Figure 10.2 Preparation of Cs ₂ AlBiCl ₆ double perovskite material	55

Figure 10.3 XRD pattern of Cs ₂ AlBiCl ₆	156
Figure 10.4 SEM images of Cs ₂ AlBiCl ₆ nanoparticles	157
Figure 10.5 UV-vis spectrum of Cs ₂ AlBiCl ₆ double perovskite material	158
Figure 10.6 PL spectrum of Cs ₂ AlBiCl ₆ double perovskite material	159

CHAPTER 1

INTRODUCTION

This Chapter presents a thorough background of the research work, with a primary emphasis on the importance of solar cells and need of its optimization for sustainable world.

- > The fundamental structure and function of a solar cell is explained.
- ➤ The brief introduction of current-voltage characteristics of a solar cell and various photovoltaic parameters such as short circuit current, open circuit voltage, fill factor and efficiency.
- ➤ Various types of possible losses in solar cells.
- ➤ The evolution of photovoltaic technologies and their pros and cons have been discussed.
- ➤ The photovoltaic effect, basic structure and working of perovskite solar cell discussed.

1.1 Introduction

The limited amount of conventional source of energy is the motivation behind the exploration of alternative source of energy. The main concern is how to conserve fossil fuels for future generation while also harnessing various energy resources to achieve sustained economic growth. Thermal power plants have a severe impact on the surrounding environment. Notably, they emit a substantial amount of carbon dioxide (0.9-0.95 kg/kWh), along with sulphur oxides (SO_X) and nitrogen oxides (NO_X). These emissions contribute to global warming and drive climate change [1]. The renewable energy technologies include biomass, wind, tidal and solar power. Solar power is seen as the most vital renewable energy resource because it is clean, limitless, and cost-effective. The advanced use of solar energy does not result in additional pollution or environmental harm, unlike traditional fossil fuels [2]. In recent decades, numerous technologies have been developed to harness solar energy, including solar heater [3], solar architecture [4], photovoltaics [5], artificial photosynthesis [6], photocatalytic water splitting [7,8]. Among these technologies, photovoltaic (PV), which convert sun light into electricity, have gained significant attention due to their capacity to generate sufficient energy to meet all our power needs while remaining environmentally friendly for the foreseeable future. The phenomenon photovoltaic was given by a French physicist A.E. Becquerel in 1839. Charles Fritts introduced the first solar cell in 1883, using selenium as the primary material. This solar cell based on the principle of photoconductivity and had an efficiency of 1 %. The first actual silicon solar PV cell introduced in 1954 at Bell Laboratory [9]. In a PV cell, electrons travel in one direction while holes move in the opposite direction, resulting in a current that flows along the path of the holes. The number of ejected electrons directly determines the total amount of current. By 2050, the European union (EU) aims to generate 43 % of its total electricity from solar photovoltaic system [10]. Moreover, the USA intends to meets its target before 2050, whereas China aims to reach its goal by 2060 [11]. India aims to reach its netzero emissions target by 2070 by harnessing its wind and solar energy resources [12].

1.2 Solar Cells

Solar cells, also referred to as photovoltaic (PV) cells, are a promising renewable energy technology with the potential to transform the global energy landscape. The fundamental structure and function of solar cells are explained, emphasizing the role of semiconductor materials and their interaction with incoming light to produce electron-hole pairs [13]. A solar cell is a p-n junction device. In n-type semiconductors, donor impurity atoms supply negatively charged electrons, whereas in p-type semiconductors, acceptor impurity atoms create positively charged holes shown in Fig. 1.1 of PV structure. A PV cell is the basic building block of a solar energy system which convert the sunlight directly into electrical energy this phenomenon known as photovoltaic effect [14].

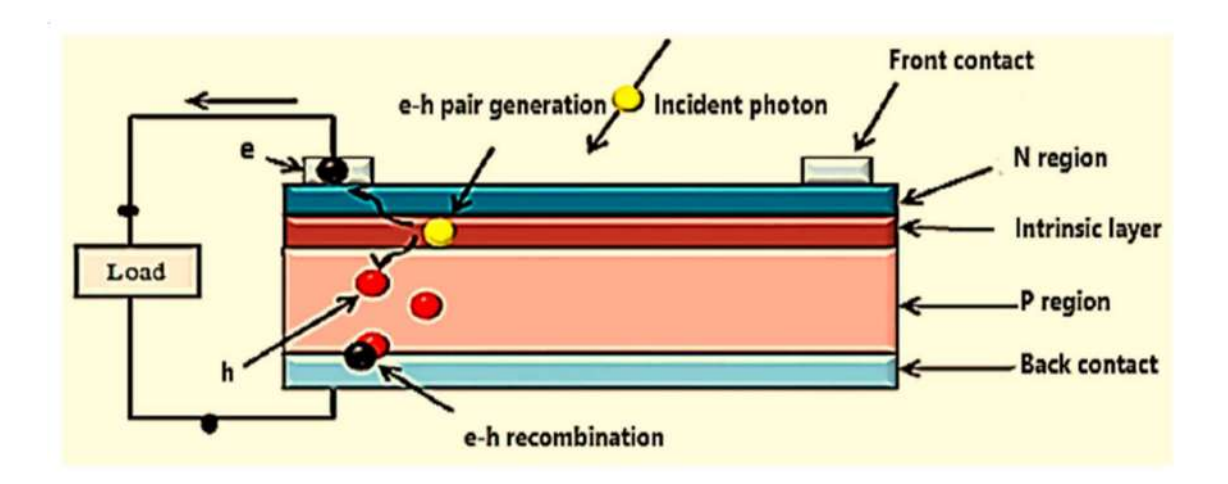


Figure 1.1 A p-n junction solar cell [14].

The functioning of solar cell based on photovoltaic effect. The PV effect consists of three fundamental steps:

- (i) Absorption of light to produce electron-hole pairs.
- (ii) The segregation of electrons and holes.
- (iii) The development of an electric potential difference caused by the movement of electrons and holes at their respective electrodes across the p-n junction.

1.3 Photovoltaic Technologies

An overview of PV production technologies is explained and comparative analysis of different generation such as first, second and third given below in Fig. 1.2 [15]. The evolution of solar cell manufacturing has undergone numerous changes, evolving from wafer-based silicon to the latest third-generation technologies. The efficiency chart of various PV technologies given by NREL demonstrated in Fig. 1.3 [16]. First generation solar cells also known as wafer-based technology, consist monocrystalline and polycrystalline silicon materials which required high temperature and high-vacuum process for the fabrication [17]. Second generation solar cells based on materials like CIGS, CdTe and a-Si have some drawbacks such as expensive materials and efficiency drop in high temperature. Third generation cells are made up of materials such as dye, organic, nanomaterial and perovskite which are abundant and having low-cost fabrication process.

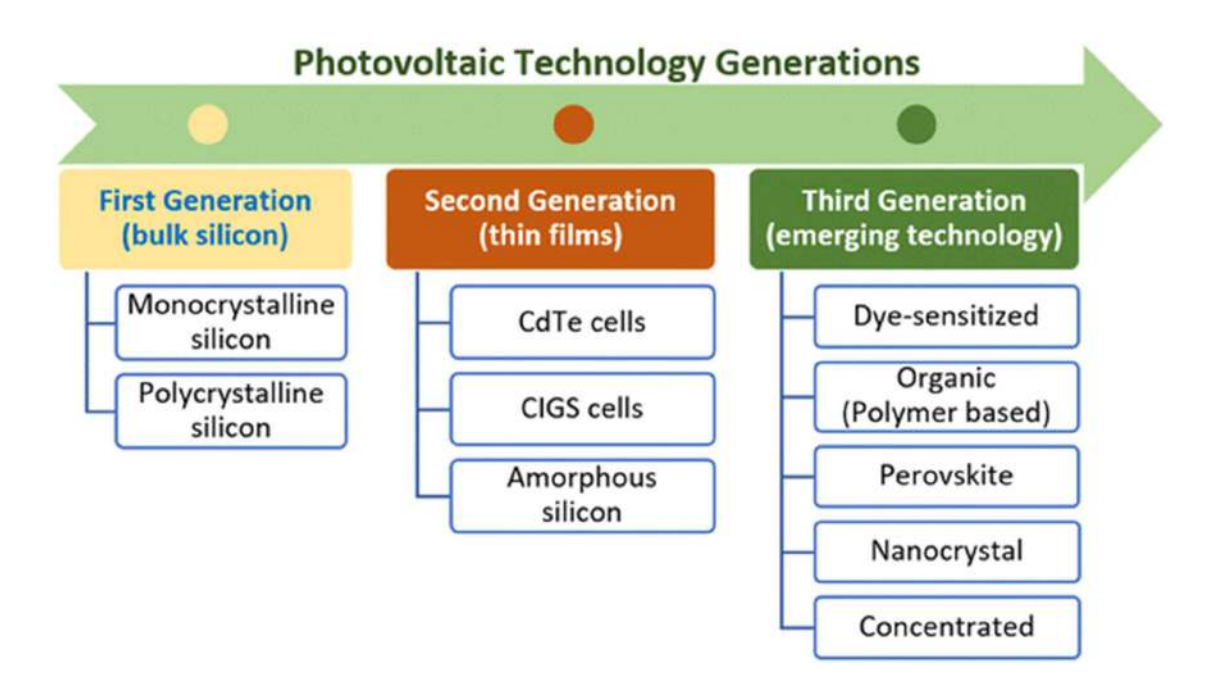


Figure 1.2 Generation of PV cells [15].

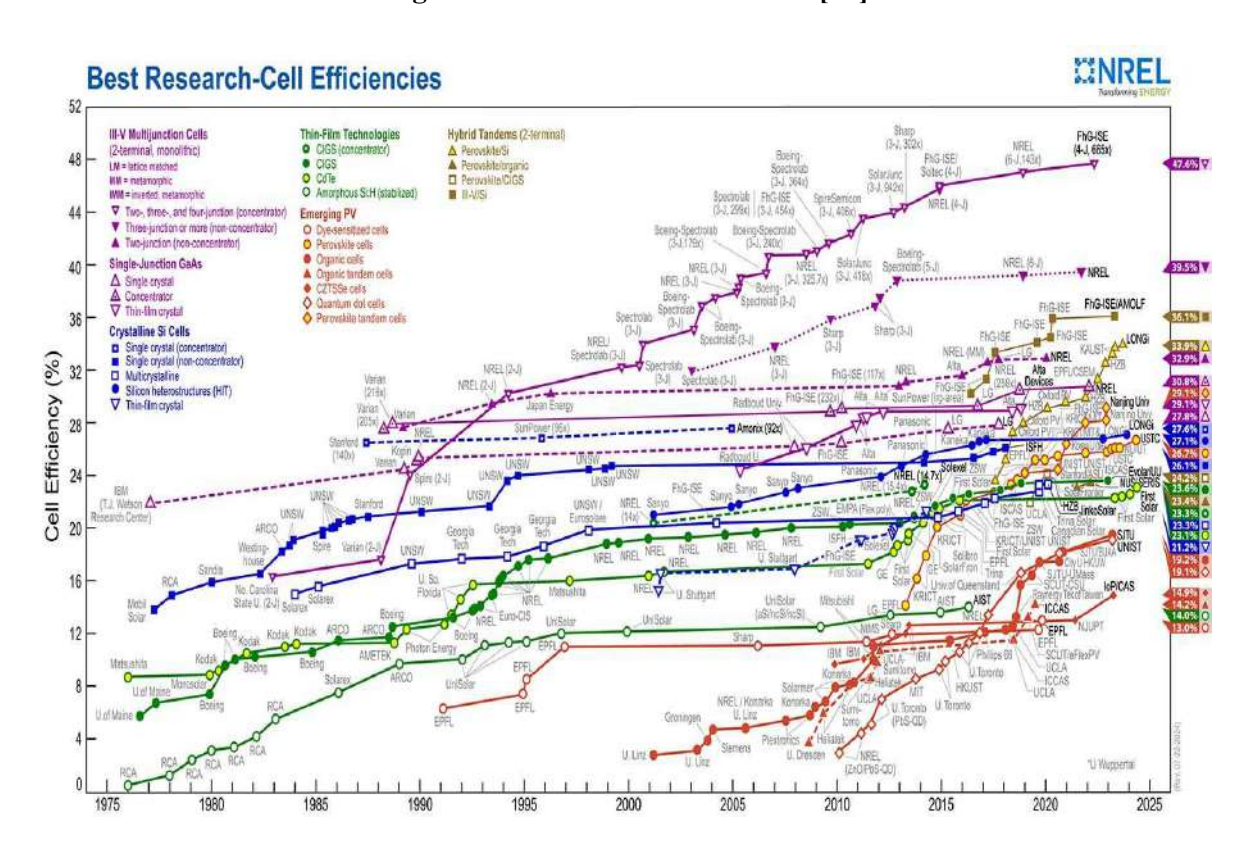


Figure 1.3 NREL efficiency chart for various solar cells [16].

1.3.1 First Generation Solar Cells

1.3.1.1 Monocrystalline/Single Crystal Silicon

Si-wafers are the building blocks for single-crystal Si and bulk polycrystalline Si-wafers are layered to create first-generation solar cells [18]. The first Si solar cell, reported in 1941, had a PCE of less than 1 %. The n-type Si wafer based solar cell has achieved highest PCE of 26.6 % with cell structure of heterojunction integrated back contacts (HBC) by Kaneka research institute [19]. All of the cell's components are single Si crystal. The Czochralski process is used to create single crystals as illustrated in Fig. 1.4 [20]. It is particularly well-suited for the wafers now utilized in IC fabrication. The steps involved in this process are as follows:

- 1. Electronic-grade silicon, melted in the furnace.
- 2. A tiny seed crystal is dipped into the molten silicon and oriented to match the final wafer's intended orientation.
- 3. The seed crystal is spun while being pulled to ensure consistency over the surface. The crystal puller rotates in the opposite direction of the furnace.
- 4. The molten silicon sticks to it and starts to solidify in the same direction, when the seed crystal is removed. Through this technique, single crystal ingot is formed.

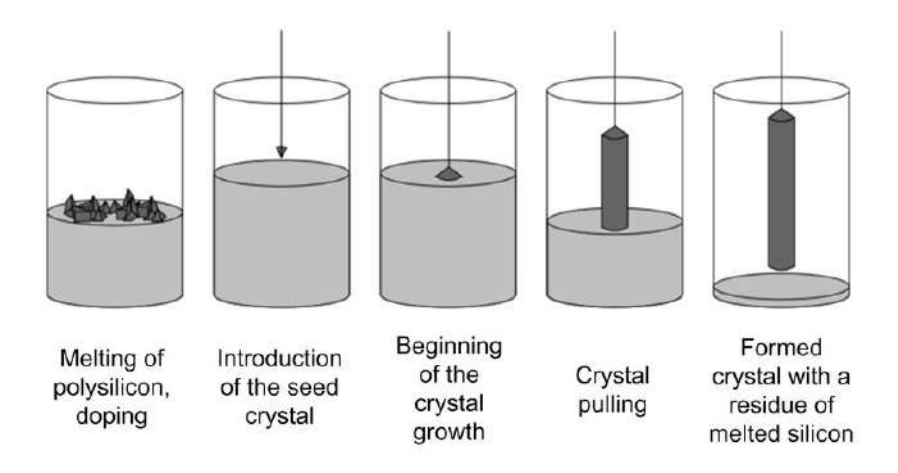


Figure 1.4 Czochralski process [20].

This process is often used to generate large cylindrical single crystals of silicon that have diameters of more than 12.5 cm and lengths of 1-2 meters. After that, the massive single crystal silicon is cut into wafers as thin as feasible. To absorb the majority of the appropriate solar wavelengths, silicon solar cells normally only need to be roughly 300 µm thick. The silicon wafers are sliced with a diamond cutter; during the cutting process, half of the ingot is wasted. The entire process requires meticulous precision. The production of monocrystalline silicon solar cells involves several processes, making them expensive. However, these cells are chemically stable and have minimal defects [21]. The highest efficiency recorded in laboratory for monocrystalline silicon solar cells is 26.7 % [22]. A major drawback these cells are stability, efficiency reduces with increase in temperature above 25°C [23,24] and a complicated manufacturing process, leading to slightly higher costs compared to alternative technologies [25].

1.3.1.2 Poly/Multi-Crystalline Silicon

In an effort to reduce the cost of producing silicon ingots, polycrystalline silicon wafers and ingots were produced in the middle of the 1970s, and research into them has continued ever since. In order to create polycrystalline silicon solar cells are typically developed by heating trichlorosilane, which deposits silicon onto rods at high temperatures. The efficiency of stand ard industrial polycrystalline cells ranges from 15 to 17 %, which is about 1% less than that of monocrystalline cells made on the same manufacturing lines.

In 2008, polycrystalline solar cells constituted around 48 % of the world's total solar cell manufacturing, making them the most extensively produced cells [26]. The most advanced polycrystalline solar cell is a PERL cell manufactured by Fraunhofer ISE, achieves a PCE of 20.3 % [27]. Some of the advantages of Si-based solar cells include their proven high efficiency and reliable operation, as well as their readily available raw materials and long history of remarkable efficiency. These solar cells also have several limitations, including high production and manufacturing cost, restricted flexibility, requires significant energy to produce, vulnerable to temperature fluctuations dirt accumulation and shade [15]. Monocrystalline and polycrystalline solar module are shown below in Fig. 1.5.

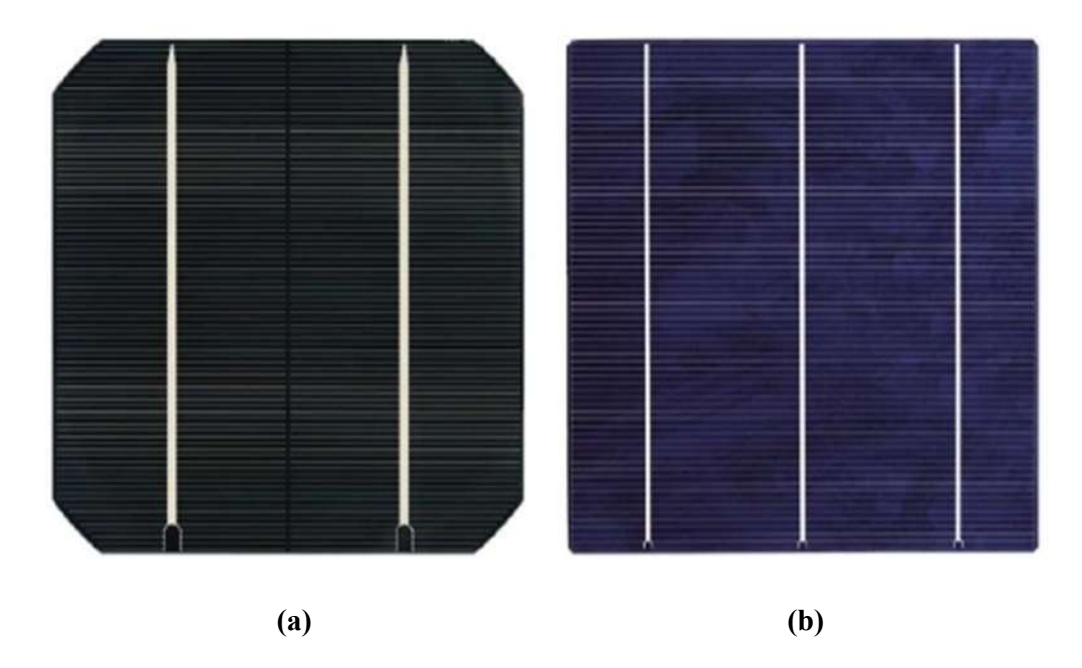


Figure 1.5 (a) Monocrystalline and (b) Polycrystalline solar module [28].

1.3.2 Thin Film/Second Generation Solar Cells

A thin film-based solar cell is manufactured by layering light-absorbing materials in extremely thin layers, about 1 μ m, over a substrate (insulator or metal) can be used to deposit various layers-such as buffer, contact, absorber, and reflector by employing distinct methods, including PVD, CVD, ECD, plasma-based methods, and hybrid approaches. This layer is much thinner than silicon wafers, which have a thickness of about 300 μ m. This versality enables the tailoring and engineering of layers to enhance device performance. For large area devices needed in

practical applications, the fabricating thin-film devices become intricate and demands precise control throughout the whole production sequence.

1.3.2.1 Amorphous Silicon

Amorphous silicon solar cells possess a disordered atomic structure, allowing them to absorb light at a rate 40 times greater than that of mono-Si cells. They are the most commonly used and highly developed thin-film solar cells. Amorphous silicon can be deposited on large, cost-effective substrates (glass) through continuous deposition techniques, resulting in lower manufacturing costs. In the laboratory, the efficiency of single-junction a-Si cells can achieve up to 12.2 % [29]. The primary drawback of amorphous silicon solar cells is the degradation of output power over time (by 15 % to 35 %), after which it stabilizes at a minimum level when exposed to light [30]. To reduce light-induced degradation, multijunction a-Si solar cells have been created with improved conversion efficiency.

1.3.2.2 Cadmium Telluride (CdTe)

Cadmium Telluride thin-film PV solar cells are composed of two key raw materials: cadmium, which is a by-product of zinc mining, and tellurium, a by-product of copper processing. They offer lower production costs and higher cell efficiency (greater than 15 %) compared to a-Si cells [31,32]. Commercially, CdTe cells can reach a conversion efficiency of 20 % thanks to their optimal band gap of 1.45 eV [33]. Recently, CdTe/CdS thin-film solar cells have been reported to achieve a conversion efficiency of 22 % [34]. However, defects in grain boundaries and intra-grain dislocations enhance carrier recombination and shorten the average lifetime of minority carriers, which results in a reduction in efficiency [35]. The toxicity of cadmium represents an environmental hazard, which is a major concern with CdTe thin-film technology.

1.3.2.3 Copper Indium Gallium Di-Selenide Solar Cell (CIGS)

CIGS cells are gaining popularity as one of the fastest-growing thin-film solar technologies. Their high conversion efficiency, with 21 % reported at the laboratory level, makes them competitive with other thin-film cells [29]. CIGS thin-film solar cells degrade by only 10%, in contrast to higher degradation in other thin-film cells [36,37]. The primary challenges with CIGS technology involve a lack of understanding in areas such as junction activation treatment, interfacial and grain boundary properties, and the development of stable back contacts. Another major challenge is the limited availability of indium, which could disrupt the production process [38].

1.3.3 Third Generation Solar Cells

1.3.3.1 Dye Sensitized Solar Cells (DSSCS)

Dye-sensitized solar cells (DSSCs) have gained considerable attention due to their advantages, including reduced production costs, a straightforward manufacturing process, and unique aesthetic features such as vibrant colours and transparency. A dye-sensitized solar cell (DSSC) consists of three key components: the dye-sensitized photoanode, the counter electrode, and the redox electrolyte. Titanium dioxide (TiO₂) nanoparticles are used to anchor the dye molecules. The TiO₂ nanoparticles are submerged in a dye solution overnight to allow the dye

molecules to be absorbed and form a chemical bond with the TiO_2 surface. This process is referred to as sensitization [39]. When sunlight strikes the DSSC, photons from the light energy excite the dye molecules, causing electrons to escape. These electrons are transferred to the TiO_2 , leaving a hole in the dye. The redox electrolyte then acts as a mediator, filling the hole by donating an electron, and the cycle continues [40]. Electrons move through the counter electrode to the external circuit, delivering power to devices. However, the low conversion efficiency of this technology is a major concern. Ongoing research is focused on improving its efficiency. A recent study has reported a conversion efficiency of 11.9 % for this technology [29].

1.3.3.2 Organic Solar Cells

Organic solar cells are an emerging technology gaining popularity as an alternative solar cell material. They offer several advantageous properties, including mechanical flexibility, low material and production costs, lightweight design, disposability, and semi-transparency. These are also called plastic solar cells, consisting of organic materials, typically around 100 nm thick. Common materials include polymers, pentacene, copper phthalocyanine, polyphenylene vinylene, and carbon fullerenes, which are known as small-molecule compounds [38,41]. Organic solar cells are produced without the need for vacuum processing systems, utilizing advanced printing techniques in a continuous process. As a result, they have short energy payback times and a lower environmental impact during both manufacturing and operation [42]. The operation of organic solar cells is based on the formation of electron-hole pairs between the donor and acceptor materials. When exposed to light, photons excite the donor material, providing enough energy to transfer electrons to the acceptor, creating a hole in the donor. This process continues as the electron-hole pairs are transported and collected before recombination can occur. Organic solar cells are especially promising for building-integrated photovoltaics due to their mechanical flexibility and semi-transparency. However, issues such as low conversion efficiency and long-term reliability present major obstacles to their largescale adoption.

1.3.3.3 Concentrated Solar Cells

Concentrated solar power technologies fall into two categories. The first is concentrated solar thermal energy systems, where solar energy is concentrated to generate thermal energy, which is then converted into electrical energy through a thermodynamic cycle [43,44]. The second type is the concentrated solar photovoltaic (SPV) system, where solar energy is concentrated using mirrors and directed onto multijunction solar cells to improve conversion efficiency. Commercial-scale CPV modules deliver a conversion efficiency exceeding 30 % [45].

1.3.3.4 Perovskite Solar Cells

Perovskite was first discovered in the URAL mountains of Russia by Gustav Rose in 1839. Perovskite solar cells are named after the crystal structure of their light-absorbing materials, which is based on the structure of the mineral CaTiO₃. This structure is shared by many compounds with the ABX₃ formula, where A and B are cations with 12- and 8-fold coordination, respectively, and X is the anion shown in Fig. 1.6 [46]. Perovskites usually contain divalent anions, and the strong electrostatic bonding tends to produce high bandgaps,

which are not ideal for solar PV applications. In this discussion, we will focus on halide perovskites that contain one divalent cation (Pb²⁺) and one monovalent cation, typically CH₃NH₃⁺. The most efficient halide perovskite solar absorbers are made up of organic ammonium ions (CH₃NH₃⁺ or NH = CHNH₃⁺), Pb²⁺, and halide ions (I⁻, Br⁻) [46]. CH₃NH₃PbI₃ demonstrates broad and intense light absorption. As an ambipolar semiconductor, it can function as either n-type or p-type, with charge carriers that exhibit long diffusion lengths and lifetimes. These characteristics enable solar cells made from it to achieve high PCE [46,47,48]. A further advantage of perovskite absorbers is their ability to be processed at low temperatures, which contributes to reduced fabrication costs. While lead halide perovskite materials have been used in other optoelectronic devices, such as lasers [49], photodetectors [50], and lightemitting diodes [51], solar cells based on these materials are the most extensively researched. The efficiency of perovskite solar cells has soared from 3.8 % to 26.7 % between 2009 and 2024 [52]. Perovskite layers were prepared through solution-based and vapor deposition processes.

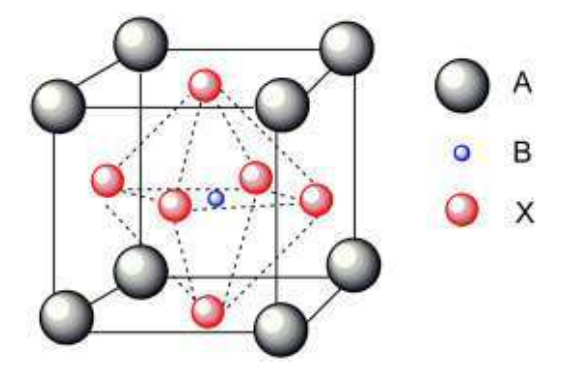


Figure 1.6 Perovskite crystal structure.

1.3.3.4.1 Basic Structure of Perovskite Solar Cell

Most PSCs employ a p-i-n architecture (or its variant, n-i-p), with the p, i, and n layers commonly known as the p-type hole-transport layer (HTL), the intrinsic perovskite layer, and the n-type electron-transport layer (ETL), respectively [53,54]. Similar to the p-n junction architecture, local electric fields in p-i-n devices arise at the HTL/perovskite and ETL/perovskite interfaces due to the formation of depletion zones [52,55]. When the perovskite is illuminated, the photoexcited charge carriers are spatially separated and injected into the ETL and HTL layers, where they are subsequently collected at their respective electrodes. Different layers of PSC device shown below in Fig. 1.7 and their operation as follows:

- 1. In standard device structure perovskite layer is sandwiched between electron transporting layer (ETL), and hole transporting layer (HTL).
- 2. ETL is used to allow transfer of electrons and blocks transfer of holes through it.
- 3. Perovskite layer generates free charge carriers, which are electrons and holes when light fall on it.
- 4. HTL is used to allow flow of holes and blocks transfer of electrons through it.
- 5. The front electrode is a glass coated with FTO, and the back electrode layer deposited through thermal evaporation.

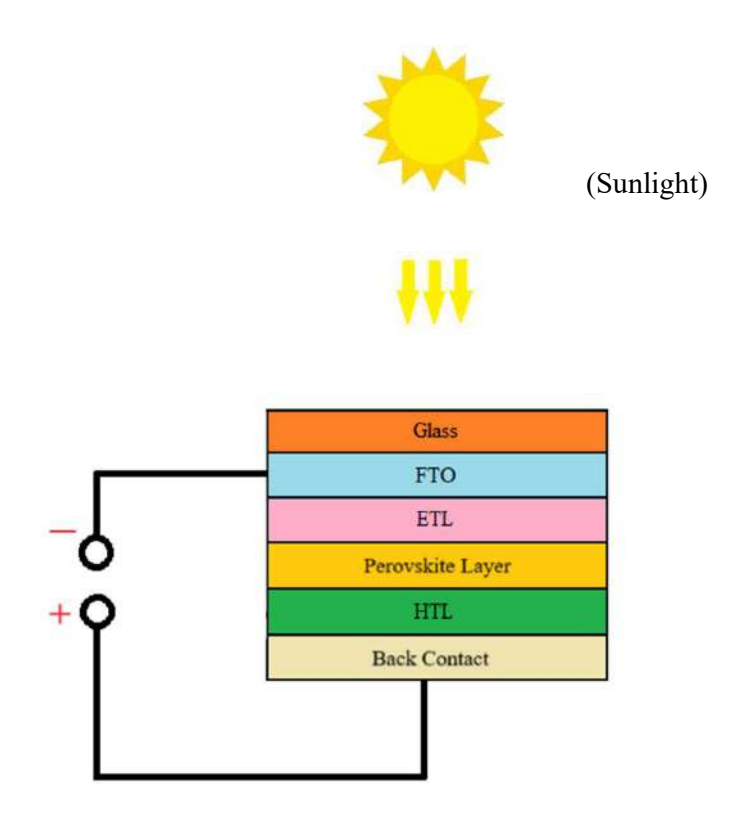


Figure 1.7 Basic structure of perovskite solar cell.

The current-voltage characteristics of a solar cell as shown in Fig. 1.8 and different PV parameters such as I_{SC} , V_{OC} , FF and η as follows:

Short circuit current (Isc)- The short circuit current, is the maximum current produced by a solar cell when its terminals are shorted.

<u>Open circuit voltage (V_{oc})</u>- The open circuit voltage, is the maximum voltage available from a solar cell, when its terminal is left open. The open-circuit voltage corresponds to the amount of forward bias of a P-N junction due to light generated current (at this voltage load current becomes equal and opposite to forward bias diffusion current of a P-N junction diode).

<u>Fill Factor</u>- The Fill Factor (FF) is essentially a measure of quality of solar cell. It is calculated by comparing the maximum power to the theoretical power that would be output at both the open circuit voltage (V_{OC}) and short circuit current (I_{SC}) together.

$$FF = I_m V_m / I_{SC} V_{OC}$$
 (1.1)

Efficiency of solar cell- It is the ratio of output power to the input power.

$$\eta = (P_m / P_{rad}) = (I_m V_m / P_{rad}) = (V_{OC} I_{SC} .FF / P_{rad})$$
(1.4)

According to international standard for characteristics of solar cells.

Where, $I_m = Max$. current & $V_m = Max$. voltage

 $P_{rad} = 100 \text{ mW} / \text{cm}^2 \text{ or } 1000 \text{ W} / \text{m}^2$

 $P_m = Max$. Power of solar cell = $V_{OC} I_{SC} FF$

 η is the efficiency

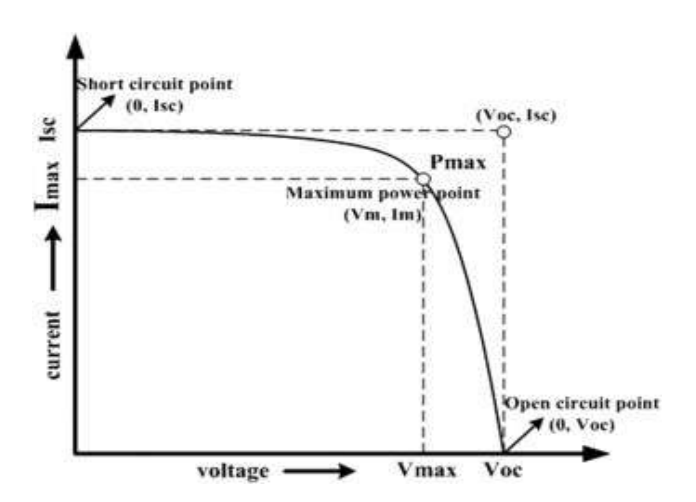


Figure 1.8 Current-voltage characteristics of a solar cell [56].

1.4 Losses in Solar Cells

- 1. <u>Loss of low energy photons</u>: The photon having energy less than the band gap energy do not get absorbed in the material and therefore, do not contribute to generation of e⁻ -hole pairs. This is referred as transmission loss, and is almost equal to 23 % for a single junction solar cell [57].
- 2. Losses due to excess energy of photons: Photon energy is greater than band gap energy.

Excess energy = E- Eg is given off as heat to material. This loss is referred as the thermalization loss [57].

- 3. <u>Voltage loss</u>: The voltage corresponding to band gap of a material is obtained by dividing the band gap by charge ie. E_g/q this referred as band gap voltage. The actual band gap voltage obtained from solar cell is V_{oc} . This is happening due to the unavoidable auger recombination [58].
- 4. <u>Fill Factor loss:</u> I-V curve of ideal solar cell is square (FF=1) but in reality, the solar cell I-V curve is given by exponential behaviour. This type of losses arises from the parasitic resistance of cell [59].

1.5 Problem Statement and Objectives

The present thesis aims to investigate the distinct PSCs and optimize the different factors which affects the device efficiency. The work also includes synthesis, characterization and fabrication of PSC.

- ➤ Optimization and simulation of lead/lead-free perovskite solar cells. This involves finetuning the materials, structure, and fabrication processes of the solar cells to achieve the best possible performance. Optimization techniques include adjusting layer thickness, doping levels or the interface properties of the materials used in the solar cells.
- > The use of mathematical modelling and simulations to better understand and improve the functioning of perovskite solar cells. Mathematical models can describe how charge carriers move through different layers of the cell. It also accounts for factors like charge recombination and charge transport efficiency.
- ➤ Synthesis of the perovskite materials, LaFeO₃ and Cs₂AlBiCl₆ have been done using solution-based spin-coating technique. LaFeO₃ composed of earth-abundant and cost-effective material. It has narrow bandgap of 2.3 eV which enables visible-light absorption, suitable for photoelectrochemical cells. Cs₂AlBiCl₆ offers structural stability, enhances thermal and phase stability. It has wide bandgap of 2.92 eV, suitable for UV detectors or as a top cell in tandem solar cells and inorganic composition improves resistance to moisture.
- ➤ Tin based perovskite materials such as KSnI₃ and CsSnI₃ have optimal bandgap, ideal for single-junction solar cells. They have high charge carrier mobility similar to lead-based perovskites. Inorganic composition offers better thermal stability than organic-inorganic hybrids.
- ➤ KGeCl₃ has potential for high dielectric constant which aids in effective charge separation and moderate availability. Uses Ge instead of toxic lead and stable cubic perovskite structure enhances integrity and durability.
- ➤ (CH₃NH₃)₂CuX₄ has layered 2D perovskite structure enhances moisture stability and allows for bandgap tunability. Useful in optoelectronics due to efficient light absorption and emission. Uses a non-toxic (Cu²⁺), abundant transition metal with interesting magnetic and electronic properties.
- ➤ The application of developed perovskite materials for solar cells refers to the use of perovskite compounds as the light-absorbing layer in photovoltaics devices, specifically in PSCs.

1.6 REFERENCES

- [1] Panwar, V. and Kaur, T., 2014. Overview of renewable energy resources of India. *International Journal of Advanced Research in Electrical, Electronics and Instrumentation Engineering*, 3(2), pp.7118-7125.
- [2] Celik, I., Phillips, A.B., Song, Z., Yan, Y., Ellingson, R.J., Heben, M.J. and Apul, D., 2017. Environmental analysis of perovskites and other relevant solar cell technologies in a tandem configuration. *Energy & Environmental Science*, 10(9), pp.1874-1884.
- [3] Shukla, R., Sumathy, K., Erickson, P. and Gong, J., 2013. Recent advances in the solar water heating systems: A review. *Renewable and Sustainable Energy Reviews*, 19, pp.173-190.
- [4] Ionescu, C., Baracu, T., Vlad, G.E., Necula, H. and Badea, A., 2015. The historical evolution of the energy efficient buildings. *Renewable and Sustainable Energy Reviews*, 49, pp.243-253.
- [5] Hedley, G.J., Ruseckas, A. and Samuel, I.D., 2017. Light harvesting for organic photovoltaics. *Chemical Reviews*, 117(2), pp.796-837.
- [6] Karkas, M.D., Verho, O., Johnston, E.V. and Åkermark, B., 2014. Artificial photosynthesis: molecular systems for catalytic water oxidation. *Chemical reviews*, 114(24), pp.11863-12001.
- [7] Ran, J., Zhang, J., Yu, J., Jaroniec, M. and Qiao, S.Z., 2014. Earth-abundant cocatalysts for semiconductor-based photocatalytic water splitting. *Chemical Society Reviews*, 43(22), pp.7787-7812.
- [8] Sharma, S., Jain, K.K. and Sharma, A., 2015. Solar cells: in research and applications—a review. *Materials Sciences and Applications*, 6(12), pp.1145-1155.
- [9] Shahabuddin, M., Asim, M. and Sarwar, A., 2024. Evolution and Modeling of Solar Photovoltaic Cells: From Early to Modern Concepts. *Photovoltaic Systems Technology*, pp.27-41.
- [10] Potrč, S., Čuček, L., Martin, M. and Kravanja, Z., 2021. Sustainable renewable energy supply networks optimization—The gradual transition to a renewable energy system within the European Union by 2050. *Renewable and Sustainable Energy Reviews*, 146, p.111186.
- [11] Rogelj, J., Geden, O., Cowie, A. and Reisinger, A., 2021. Net-zero emissions targets are vague: three ways to fix. *Nature*, 591(7850), pp.365-368.
- [12] Molla, S., Farrok, O. and Alam, M.J., 2024. Electrical energy and the environment: Prospects and upcoming challenges of the World's top leading countries. *Renewable and Sustainable Energy Reviews*, 191, p.114177.
- [13] Arya, S. and Mahajan, P., 2023. Introduction to Solar Cells. In *Solar Cells: Types and Applications*. Singapore: Springer Nature Singapore.
- [14] Al-Ezzi, A.S. and Ansari, M.N.M., 2022. Photovoltaic solar cells: a review. *Applied System Innovation*, 5(4), p.67.
- [15] Solak, E.K. and Irmak, E., 2023. Advances in organic photovoltaic cells: a comprehensive review of materials, technologies, and performance. *RSC advances*, 13(18), pp.12244-12269.
- [16] https://www.nrel.gov/pv/cell-efficiency.html[accessed 20 October2024].

- [17] Lee, G.H., Rhee, C.K. and Lim, K.S., 2006. A study on the fabrication of polycrystalline Si wafer by direct casting for solar cell substrate. *Solar Energy*, 80(2), pp.220-225.
- [18] Badawy, W.A., 2015. A review on solar cells from Si-single crystals to porous materials and quantum dots. *Journal of advanced research*, 6(2), pp.123-132.
- [19] Yoshikawa, K., Yoshida, W., Irie, T., Kawasaki, H., Konishi, K., Ishibashi, H., Asatani, T., Adachi, D., Kanematsu, M., Uzu, H. and Yamamoto, K., 2017. Exceeding conversion efficiency of 26% by heterojunction interdigitated back contact solar cell with thin film Si technology. *Solar Energy Materials and Solar Cells*, 173, pp.37-42.
- [20] Mesquita, D.D.B., Silva, J.L.D.S., Moreira, H.S., Kitayama, M. and Villalva, M.G., 2019, September. A review and analysis of technologies applied in PV modules. In IEEE PES Innovative Smart Grid Technologies Conference-Latin America (ISGT Latin America)2019, pp. 1-6.
- [21] Di Sabatino, M., Hendawi, R. and Garcia, A.S., 2024. Silicon solar cells: trends, manufacturing challenges, and AI perspectives. *Crystals*, 14(2), p.167.
- [22] Green, M., Dunlop, E., Hohl-Ebinger, J., Yoshita, M., Kopidakis, N., Bothe, K., Hinken, D., Rauer, M., and Hao, X., 2022. Solar cell efficiency tables (version 60). *Progress in photovoltaics: research and applications*, 30(7), pp.687-701.
- [23] Sun, C., Zou, Y., Qin, C., Zhang, B. and Wu, X., 2022. Temperature effect of photovoltaic cells: a review. *Advanced Composites and Hybrid Materials*, 5(4), pp.2675-2699.
- [24] Chander, S., Purohit, A., Sharma, A., Nehra, S.P. and Dhaka, M.S., 2015. A study on photovoltaic parameters of mono-crystalline silicon solar cell with cell temperature. *Energy Reports*, 1, pp.104-109.
- [25] Chikate, B.V., Sadawarte, Y. and Sewagram, B.D.C.O.E., 2015. The factors affecting the performance of solar cell. *International journal of computer applications*, 1(1), pp.0975-8887.
- [26] Photon International, 176 (2009).
- [27] Schultz, O., Glunz, S.W. and Willeke, G.P., 2004. ACCELERATED PUBLICATION: Multicrystalline silicon solar cells exceeding 20% efficiency. *Progress in photovoltaics: Research and Applications*, 12(7), pp.553-558.
- [28] Saga, T., 2010. Advances in crystalline silicon solar cell technology for industrial mass production. *npg asia materials*, 2(3), pp.96-102.
- [29] Green, M.A., Emery, K., Hishikawa, Y., Warta, W., Dunlop, E.D., 2016. Solar cell efficiency tables (version 47). *Progress in photovoltaics: research and applications*, 24(1), pp.3-11.
- [30] McCann, M.J., Catchpole, K.R., Weber, K.J. and Blakers, A.W., 2001. A review of thin-film crystalline silicon for solar cell applications. Part 1: Native substrates. *Solar Energy Materials and Solar Cells*, 68(2), pp.135-171.
- [31] El Chaar, L. and El Zein, N., 2011. Review of photovoltaic technologies. *Renewable and sustainable energy reviews*, 15(5), pp.2165-2175.
- [32] Britt, J. and Ferekides, C., 1993. Thin-film CdS/CdTe solar cell with 15.8% efficiency. *Applied physics letters*, 62(22), pp.2851-2852.

- [33] Gloeckler, M., Sankin, I. and Zhao, Z., 2013. CdTe solar cells at the threshold to 20% efficiency. *IEEE Journal of Photovoltaics*, 3(4), pp.1389-1393.
- [34] Ali, N., Hussain, A., Ahmed, R., Wang, M.K., Zhao, C., Haq, B.U. and Fu, Y.Q., 2016. Advances in nanostructured thin film materials for solar cell applications. *Renewable and Sustainable Energy Reviews*, 59, pp.726-737.
- [35] Fthenakis, V.M. and Kim, H.C., 2007. CdTe photovoltaics: Life cycle environmental profile and comparisons. *Thin Solid Films*, 515(15), pp.5961-5963.
- [36] Akinyele, D.O., Rayudu, R.K. and Nair, N.K.C., 2015. Global progress in photovoltaic technologies and the scenario of development of solar panel plant and module performance estimation— Application in Nigeria. *Renewable and Sustainable Energy Reviews*, 48, pp.112-139.
- [37] Vick, B.D. and Neal, B.A., 2012. Analysis of off-grid hybrid wind turbine/solar PV water pumping systems. *Solar Energy*, 86(5), pp.1197-1207.
- [38] Pandey, A.K., Tyagi, V.V., Jeyraj, A., Selvaraj, L., Rahim, N.A. and Tyagi, S.K., 2016. Recent advances in solar photovoltaic systems for emerging trends and advanced applications. *Renewable and Sustainable Energy Reviews*, 53, pp.859-884.
- [39] Kuzmych, O., 2014. Development and characterization of dye-and semiconductor sensitized solar cells based on structurally organized titanium dioxide. *University of Warsaw*.
- [40] Duncan, W.R. and Prezhdo, O.V., 2007. Theoretical studies of photoinduced electron transfer in dye-sensitized TiO2. *Annu. Rev. Phys. Chem.*, 58(1), pp.143-184.
- [41] Goetzberger, A., Hebling, C. and Schock, H.W., 2003. Photovoltaic materials, history, status and outlook. *Materials science and engineering: R: Reports*, 40(1), pp.1-46.
- [42] Scharber, M.C. and Sariciftci, N.S., 2013. Efficiency of bulk-heterojunction organic solar cells. *Progress in polymer science*, 38(12), pp.1929-1940.
- [43] Khan, J. and Arsalan, M.H., 2016. Solar power technologies for sustainable electricity generation—A review. *Renewable and Sustainable Energy Reviews*, 55, pp.414-425.
- [44] Desideri, U. and Campana, P.E., 2014. Analysis and comparison between a concentrating solar and a photovoltaic power plant. *Applied energy*, 113, pp.422-433.
- [45] Philipps, S.P., Bett, A.W., Horowitz, K. and Kurtz, S., 2015. *Current status of concentrator photovoltaic (CPV) technology* (No. NREL/TP-5J00-65130). National Renewable Energy Lab (NREL), Golden, CO, United States.
- [46] Green, M.A., Ho-Baillie, A. and Snaith, H.J., 2014. The emergence of perovskite solar cells. *Nature photonics*, 8(7), pp.506-514.
- [47] Stranks, S.D., Eperon, G.E., Grancini, G., Menelaou, C., Alcocer, M.J., Leijtens, T., Herz, L.M., Petrozza, A. and Snaith, H.J., 2013. Electron-hole diffusion lengths exceeding 1 micrometer in an organometal trihalide perovskite absorber. *Science*, 342(6156), pp.341-344.
- [48] Mitzi, D.B., Feild, C.A., Harrison, W.T.A. and Guloy, A.M., 1994. Conducting tin halides with a layered organic-based perovskite structure. *Nature*, 369(6480), pp.467-469.
- [49] Deschler, F., Price, M., Pathak, S., Klintberg, L.E., Jarausch, D.D., Higler, R., Hüttner, S., Leijtens, T., Stranks, S.D., Snaith, H.J. and Atatüre, M., 2014. High photoluminescence

- efficiency and optically pumped lasing in solution-processed mixed halide perovskite semiconductors. *The journal of physical chemistry letters*, 5(8), pp.1421-1426.
- [50] Dou, L., Yang, Y., You, J., Hong, Z., Chang, W.H., Li, G. and Yang, Y., 2014. Solution-processed hybrid perovskite photodetectors with high detectivity. *Nature communications*, 5(1), p.5404.
- [51] Tan, Z.K., Moghaddam, R.S., Lai, M.L., Docampo, P., Higler, R., Deschler, F., Price, M., Sadhanala, A., Pazos, L.M., Credgington, D. and Hanusch, F., 2014. Bright light-emitting diodes based on organometal halide perovskite. *Nature nanotechnology*, 9(9), pp.687-692.
- [52] Green, M.A., Dunlop, E.D., Yoshita, M., Kopidakis, N., Bothe, K., Siefer, G., Hinken, D., Rauer, M., Hohl-Ebinger, J. and Hao, X., 2024. Solar cell efficiency tables (Version 64). *Progress in Photovoltaics*, 32(7), pp.425-441.
- [53] Chen, S. and Shi, G., 2017. Two-dimensional materials for halide perovskite-based optoelectronic devices. *Advanced Materials*, 29(24), p.1605448.
- [54] Luo, D., Su, R., Zhang, W., Gong, Q. and Zhu, R., 2020. Minimizing non-radiative recombination losses in perovskite solar cells. *Nature Reviews Materials*, 5(1), pp.44-60.
- [55] Laban, W.A. and Etgar, L., 2013. Depleted hole conductor-free lead halide iodide heterojunction solar cells. *Energy & Environmental Science*, 6(11), pp.3249-3253.
- [56] El-Ahmar, M.H., El-Sayed, A.H.M. and Hemeida, A.M., 2016, December. Mathematical modeling of Photovoltaic module and evalute the effect of varoius parameters on its performance. In *Eighteenth International Middle East Power Systems Conference* (MEPCON)2016, pp. 741-746.
- [57] Lei, Y., Li, Y. and Jin, Z., 2022. Photon energy loss and management in perovskite solar cells. *Energy Reviews*, 1(1), p.100003.
- [58] Wang, J., Yao, H., Xu, Y., Ma, L. and Hou, J., 2021. Recent progress in reducing voltage loss in organic photovoltaic cells. *Materials Chemistry Frontiers*, 5(2), pp.709-722.
- [59] Grabowski, D., Liu, Z., Schöpe, G., Rau, U. and Kirchartz, T., 2022. Fill factor losses and deviations from the superposition principle in lead halide perovskite solar cells. *Solar Rrl*, 6(11), p.220050.

CHAPTER 2

LITERATURE REVIEW AND RESEARCH GAP

- > The Chapter focuses on the extensive literature review of distinct potential perovskite materials for optimizing the performance of solar device.
- > Evaluation and analysis of different type of perovskite solar cells and their performance.
- The toxicity of lead-based PSCs is the reason to explore the lead-free, stable and highly efficient PSC.
- The research gap between the existing research with previous research also discussed.

2.1 Introduction

The development of innovative solar PV technologies is regarded as a vital solution to address the rising global energy demand [1]. Commercial solar cells have been developed using inorganic light absorbers like silicon, copper indium gallium selenide (CIGS), gallium arsenide (GaAs), and cadmium telluride (CdTe). However, the complex fabrication processes increase production costs and limit their broader adoption [2]. Halide PSCs demonstrate immense potential as a key technology for the next generation of renewable energy [3]. The perovskite crystal structure, first discovered in 1839 in calcium titanate (CaTiO₃), refers to any substance with a similar crystal arrangement and the chemical formula ABX₃, where A represents Cs⁺, CH₃NH₃⁺, or NH₂CHNH₂⁺, B stands for Pb²⁺, Sn²⁺, or Ge²⁺, and X is a halide anion. A stable and durable halide perovskite structure must maintain cations with appropriate ionic sizes, as indicated by the geometric constant "t," known as the tolerance factor. This factor serves as a measure of how much the perovskite deviates from its ideal cubic form. The tolerance factor, denoted as t, ranges from 0.8 to 1.0. It is calculated using the equation: $t = (r_A + r_O)/\sqrt{2(r_B + r_O)}$, where r_A , r_B , and r_O represent the ionic radii of A, B, and O, respectively [4]. PSCs have emerged as a promising contender for the next generation of photovoltaic technology, thanks to their rapid improvement in PCE. In 2009, 3D perovskite CH₃NH₃PbX₃ (X = Br, I) was introduced as an inorganic sensitizer in dye-sensitized solar cells. hey achieved a PCE of 3.1 % for X = Br and 3.8 % for X = I [5]. Park et al. reported a PCE of 6.5 % using $CH_3NH_3PbI_3$ [6]. Park et al. were the first to report perovskite solar cells with long-term stability and a PCE of 9.7 % [7]. Sanchez et al. proposed a crystalline inorganic mixed halide perovskite material thin film achieved a PCE of greater than 10 % [8]. Rapid advancements were made over the years, resulting in PCEs exceeding 15 % with organo-lead halide perovskites [9,10]. Organic lead halide perovskite solar cells have reached efficiencies above 25 % [11]. Along with environmental concerns, lead-based perovskite solar cells face stability challenges due to the rapid oxidation of the Pb cation [12]. It is essential to replace lead-based perovskites with alternative materials that are not only less toxic and more environmentally friendly but also have the potential to offer enhanced photovoltaic performance. Researchers have explored various potential candidates in search of a suitable alternative to lead. Lead has been successfully replaced by Sn [13], Ge [14], Bi [15], Sb [16] and Ag [17].

A typical PSC device is composed of three layers: an electron transport layer (ETL), an absorber layer, and a hole transport layer (HTL). The key function of the ETL is to block the motion of holes through it and collect electrons from the absorber layer. The HTL is to block the motion of electrons through it and collect holes from the absorber layer [18]. We have investigated the impact of several ETLs (ZnO, TiO₂, IGZO, WO₃ and CdS) and HTLs (MoS₂, Cu₂O, CuInS₂ QD, CuSbS₂ and V₂O₅) on the performance of PSC. The work optimized and designed Pb, Cu, Ge and Sn-based PSC by exploring different device parameters. The optimization of different parameters such as thickness of absorber layer, operating temperature, defect density (N_t), doping concentration (N_A and N_D), series resistance (R_S), shunt resistance (R_{Sh}) and back contact has been done to obtain the optimum performance of a PSC.

2.2 Literature Review

The performance of a PSC is determined by its PV parameters such as V_{OC}, J_{SC}, FF and PCE. The optical and electrical properties of Pb-based perovskites are nearly ideal for solar cell applications [19]. The most recent efficiency of PSC has reached 26.7 % [20], surpassing the efficiency of Cu (In,Ga)(Se,S)₂, CdTe, and Si-based solar cells. However, Pb-based perovskite solar cells face two major challenges: low stability and high toxicity [21]. Alternative Pb-free absorber layer should possess low toxicity, narrow direct bandgaps, high optical absorption coefficients, high mobilities, low exciton-binding energies, long charge carrier lifetimes, and excellent stability for solar cell application.

2.2.1 Organic Perovskite Materials

In 2012, Park et al. achieved the first long-lasting, high-efficiency perovskite solar cell by substituting liquid electrolytes with a solid hole-transporting material. This configuration obtained a PCE of 9.7 %, utilizing a submicron-thick TiO₂ film and 2 nm-sized CH₃NH₃PbI₃ [7]. Snaith et al. presented a solid-state perovskite material, CH₃NH₃PbI₂Cl that employed the Spiro-OMeTAD as HTL, TiO₂ and Al₂O₃ used as ETL, resulting in a PCE of 10.9 % [22]. The previously reported organic perovskite solar cells outcomes tabulated below in Table 2.1. The efficiency and stability of PSCs are primarily limited by the quality of the light absorber. A MgF_X interlayer, approximately 1 nm thick, is thermally evaporated at the perovskite/C60 interface to optimally adjust the surface energy of the perovskite layer. This enhancement promotes efficient electron extraction and displaces C₆₀ from the perovskite surface, thereby reducing nonradiative recombination. These advancements lead to a champion V_{OC} of 1.92 V, a higher FF of 80.7 %, and a PCE of 29.3 % for a monolithic perovskite-silicon tandem solar cell [39].

Table 2.1 Organic perovskite solar cells efficiency.

Device structure/Materials	Efficiency (%)	Ref.
TO Z O CHANDA Z OM TARA	10.50	F221
ITO/ZnO/CH ₃ NH ₃ PbI ₃ /Spiro-OMeTAD/Ag	13.50	[23]
ITO/PEDOT: PSS/CH ₃ NH ₃ PbI ₃ /PCBM/Ca/Al	18.00	[24]
TiO ₂ /CH ₃ NH ₃ PbI ₃ /Spiro-OMeTAD	20.00	[25]
FTO/TiO ₂ /perovskite/CuSCN/Au	20.40	[26]
FTO/NiO _X /CH ₃ NH ₃ PbI _{3-x} Cl _x /Au	20.50	[27]
FTO/TiO ₂ /FA _{0.15} MA _{0.85} PbI ₃ /Spiro-OMeTAD/Au	21.38	[28]
ITO/SnO ₂ /(FAPbI ₃) _{1-X} (MAPbBr ₃) _x /Spiro-OMeTAD/Au	21.60	[29]
TiO ₂ /CH ₃ NH ₃ PbI ₃	22.10	[30]
FAPbI ₃ polycrystalline film	22.80	[31]
ITO/PTAA/perovskite/C ₆₀ /BCP/Ag	23.37	[32]
FAPbI ₃ film	25.20	[33]
FTO/SnO ₂ / FAPbI ₃ +MAPbBr ₃	25.20	[34]
FTO/SnO ₂ / FAPbI ₃ +MAPbBr ₃	25.40	[35]
FTO/CuI/GA _{0.2} FA _{0.78} SnI ₃ -1% EDAI ₂ /ZnOS/Ag	26.00	[36]
FTO/TiO ₂ /CH ₃ NH ₃ SnI ₃ /Cu ₂ O/Pt	28.39	[37]
AZO/SnO ₂ /MAPbI ₃ /D-PBTTT-14/RGO	28.39	[38]
Al/FTO/WS ₂ /FASnI ₃ /Zn ₃ P ₂ /Ni	29.81	[40]
FTO/CdS/CH ₃ NH ₃ BiI ₃ /MoS ₂ /Pt	26.60	[41]

2.2.2 Inorganic Perovskite Materials

A lead-free perovskite layer, CsSnBr₃ is used as the absorber layer, Cu₂O as the HTL, and TiO₂, PCBM, WS₂, ZnO, SnO₂, and IGZO as ETLs. The optimized structure ITO//TiO₂/CsSnBr₃/Cu₂O/Au has been achieved a PCE of 22.43 % using wxAMPS simulation software [42]. The efficiency of the device architecture, ITO/ZnMgO/CsSnI₃/P3HT/Au is analysed, investigating the impacts of five different HTLs such as P3HT, PEDOT: PSS, PTAA, MoO₃, and CFTS along with ZnMgO as ETL using SCAPS-1D. The maximum PCE, V_{OC}, J_{SC}, and FF are enhanced to 17.04 %, 0.67 V, 35.61 mA/cm², and 71.39 %, respectively [43]. The past Inorganic perovskite solar cells result tabulated below in Table 2.2.

Table 2.2 Inorganic perovskite solar cells efficiency.

Device structure/Materials	Efficiency (%)	Ref.
ITO/PCBM/CsSnI ₃ /CFTS/Se	24.73	[44]
Nb:STO/In ₂ O ₃ /LaFeO ₃ /MoO ₃ /Au	9.11	[45]
ITO/PCBM/CsSnI ₃ /CuI/Au	10.10	[46]
FTO/ZnO/CsSnI ₃ /NiO _X /Au	23.84	[47]
FTO/TiO ₂ /KSnI ₃ /Spiro-OMeTAD/Au	9.77	[48]
FTO/ZnO/KSnI ₃ /CuI/Au	20.99	[49]
FTO/TiO ₂ /KSnI ₃ /Spiro-OMETAD/Au	20.34	[50]
FTO/SnS ₂ /KGeCl ₃ /Cu ₂ O/C	15.83	[51]
SnO ₂ /C ₆₀ /KGeCl ₃ /Me4PACz	19.62	[52]
ITO/IGZO/KGeCl ₃ /V ₂ O ₅ /Au	21.23	[53]
FTO/MoO ₃ /KGeCl ₃ /WS ₂ /Au	29.83	[54]
FTO/ZnOS/KSnI ₃ /Sb ₂ S ₃	18.81	[55]
FTO/SnO ₂ /CsSnI ₃ /Cu ₂ O/Carbon	17.36	[56]
FTO/WS ₂ /CsSnI ₃ /PEDOT: PSS/Au	20.73	[57]

2.2.3 3D Perovskite Materials

Double perovskite materials are often considered as 3D perovskite materials they maintain 3D crystal structure characteristics. Cs₂BiAgI₆, a lead-free material, has recently gained considerable research attention for its potential as an absorber layer in PSC designs, owing to its low cost, strong stability, and high PCE. This research primarily focuses on improving the PV performance of Cs₂BiAgI₆ double perovskite solar cells (DPSCs) by optimizing the optoelectronic properties of the absorber, ETL, HTL, and various interface layers. SCAPS-1D was employed to optimize the performance of Cs₂BiAgI₆ DPSCs, with CBTS as the HTL and TiO₂, PCBM, ZnO, IGZO, SnO₂, and WS₂ as ETLs achieved PCE of 23.14, 23.71, 23.69, 22.97, 23.61, and 21.72 %, respectively [58]. Cs₂AgBiBr₆ has wide bandgap and PCE typically below 4.23 %. The bandgap of Cs₂AgBiBr₆ films is tuneable between 2.18 eV and 1.64 eV. Meanwhile, the PCE of hydrogenated Cs₂AgBiBr₆ DPSCs has been enhanced to 6.37 %, demonstrating excellent environmental stability. The study present effective strategies for developing high-performance PSCs [59]. A new halide DP material, Cs₂AlBiCl₃, showing

notable similarities to lead-based compounds. The device demonstrated a PCE of 1.965 %, which is comparable to that of single PSCs [60].

2.2.4 PIN and NIP Perovskite Structures

In PIN structure, has order of layers P-layer (HTL): P-layer typically placed on top of the device and it felicitates efficient hole extraction when the solar cell generates electricity. I-layer (Intrinsic layer): This is light absorbing layer also known as absorber layer and create e⁻-h⁺ pairs (excitons). N-layer (ETL): N-layer used to transport the electrons and placed at back of solar cell, facilitating efficient e⁻ collection. A p-i-n device structure shown below in Fig. 2.1. The P-I-N structure tends to show better stability and environmental exposure, especially when using stable HTL. A p-i-n PSC with a record PCE of 24.6% over 18 square mm and 23.1% over 1 square cm [61].

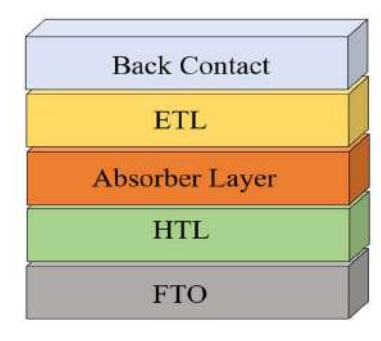


Figure 2.1 A p-i-n device architecture.

In NIP structure, has order of layers N-layer (ETL): N-layer placed in front side of the device and it ensures that e⁻s generated in the absorber layer are quickly and efficiently collected. I-layer (Intrinsic layer): This is light absorbing perovskite layer, which absorb photons and generates e⁻-h⁺ pairs. P-layer (HTL): P-layer is placed at back of the device. Helps in extraction of holes generated in intrinsic layer, eventually direct them to the electrode. The NIP structure offers higher PCEs, particularly when combined with suitable ETL that have high conductivity and low energy barriers shown below in Fig. 2.2. Tetramethylammonium chloride (TMACl) based device achieved highest PCE of 23.08 % with n-i-p structure [62].

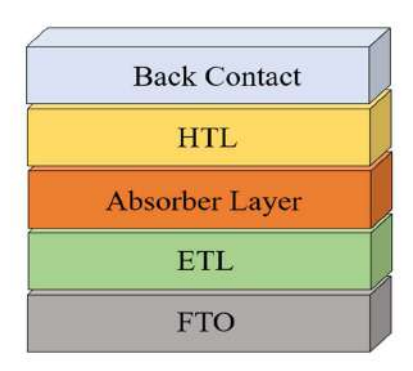


Figure 2.2 A n-i-p device architecture.

2.3 Research Gap

- (i) Optimization of defects in the perovskite layer is vital for producing highly efficient and stable PSCs.
- (ii) Optimization of the composition of perovskite materials, including the selection of metal cations and halide ions.
- (iii) Investigation into alternative designs, their impact on efficiency is needed and optimizing the cell parameters.
- (iv) The environmental impact of lead-free PSCs and their stability enhancement for the commercial application.
- (v) Reducing the cost of materials and processing methods for PSCs is crucial for their commercial viability.
- (vi) The lifecycle analysis and eco-friendly disposal methods for PSCs is necessary for their sustainable deployment.

2.4 REFERENCES

- [1] Kabir, E., Kumar, P., Kumar, S., Adelodun, A.A. and Kim, K.H., 2018. Solar energy: Potential and future prospects. *Renewable and Sustainable Energy Reviews*, 82, pp.894-900.
- [2] Zuo, C. and Ding, L., 2017. Lead-free perovskite materials (NH₄)₃Sb₂I_xBr_{9-x}. *Angewandte Chemie*, 129(23), pp.6628-6632.
- [3] Moiz, S.A., Alahmadi, A.N.M. and Aljohani, A.J., 2021. Design of a novel lead-free perovskite solar cell for 17.83% efficiency. *IEEE Access*, 9, pp.54254-54263.
- [4] Jong, U.G., Yu, C.J., Kye, Y.H., Choe, Y.G., Hao, W. and Li, S., 2019. First-principles study on structural, electronic, and optical properties of inorganic Ge-based halide perovskites. *Inorganic chemistry*, 58(7), pp.4134-4140.
- [5] Kojima, A., Teshima, K., Shirai, Y. and Miyasaka, T., 2009. Organometal halide perovskites as visible-light sensitizers for photovoltaic cells. *Journal of the american chemical society*, 131(17), pp.6050-6051.
- [6] Im, J.H., Lee, C.R., Lee, J.W., Park, S.W. and Park, N.G., 2011. 6.5% efficient perovskite quantum-dot-sensitized solar cell. *Nanoscale*, 3(10), pp.4088-4093.
- [7] Kim, H.S., Lee, C.R., Im, J.H., Lee, K.B., Moehl, T., Marchioro, A., Moon, S.J., Humphry-Baker, R., Yum, J.H., Moser, J.E. and Grätzel, M., 2012. Lead iodide perovskite sensitized all-solid-state submicron thin film mesoscopic solar cell with efficiency exceeding 9%. *Scientific reports*, 2(1), p.591.
- [8] Sanchez, S., Christoph, N., Grobety, B., Phung, N., Steiner, U., Saliba, M. and Abate, A., 2018. Efficient and stable inorganic perovskite solar cells manufactured by pulsed flash infrared annealing. *Advanced Energy Materials*, 8(30), p.1802060.
- [9] Burschka, J., Pellet, N., Moon, S.J., Humphry-Baker, R., Gao, P., Nazeeruddin, M.K. and Grätzel, M., 2013. Sequential deposition as a route to high-performance perovskite-sensitized solar cells. *Nature*, 499(7458), pp.316-319.
- [10] Liu, M., Johnston, M.B. and Snaith, H.J., 2013. Efficient planar heterojunction perovskite solar cells by vapour deposition. *Nature*, 501(7467), pp.395-398.
- [11] National Renewable Energy Laboratory (2020). Best Research-Cell Efficiency Chart. Available online at: https://www.nrel.gov/pv/cell-efficiency.html[accessed 6 April2020].
- [12] Ke, W., Stoumpos, C.C. and Kanatzidis, M.G., 2019. "Unleaded" perovskites: status quo and future prospects of tin-based perovskite solar cells. *Advanced Materials*, 31(47), p.1803230.
- [13] Noel, N.K., Stranks, S.D., Abate, A., Wehrenfennig, C., Guarnera, S., Haghighirad, A.A., Sadhanala, A., Eperon, G.E., Pathak, S.K., Johnston, M.B. and Petrozza, A., 2014. Lead-free organic–inorganic tin halide perovskites for photovoltaic applications. *Energy & Environmental Science*, 7(9), pp.3061-3068.
- [14] Ju, M.G., Chen, M., Zhou, Y., Garces, H.F., Dai, J., Ma, L., Padture, N.P. and Zeng, X.C., 2018. Earth-abundant nontoxic titanium (IV)-based vacancy-ordered double perovskite halides with tunable 1.0 to 1.8 eV bandgaps for photovoltaic applications. *ACS Energy Letters*, 3(2), pp.297-304.

- [15] Zhang, Z., Li, X., Xia, X., Wang, Z., Huang, Z., Lei, B. and Gao, Y., 2017. High-quality (CH₃NH₃)₃Bi₂I₉ film-based solar cells: pushing efficiency up to 1.64%. *The journal of physical chemistry letters*, 8(17), pp.4300-4307.
- [16] Wang, M., Zeng, P., Bai, S., Gu, J., Li, F., Yang, Z. and Liu, M., 2018. High-quality sequential-vapor-deposited Cs₂AgBiBr₆ thin films for lead-free perovskite solar cells. *Solar rrl*, 2(12), p.1800217.
- [17] Zong, Y., Zhou, Y., Zhang, Y., Li, Z., Zhang, L., Ju, M.G., Chen, M., Pang, S., Zeng, X.C. and Padture, N.P., 2018. Continuous grain-boundary functionalization for high-efficiency perovskite solar cells with exceptional stability. *Chem*, 4(6), pp.1404-1415.
- [18] Fatema, K. and Arefin, M.S., 2022. Enhancing the efficiency of Pb-based and Sn-based perovskite solar cell by applying different ETL and HTL using SCAPS-ID. *Optical Materials*, 125, p.112036.
- [19] Stoumpos, C.C. and Kanatzidis, M.G., 2016. Halide Perovskites: poor Man's high-performance semiconductors. *Advanced Materials*, 28(28), pp.5778-5793.
- [20] https://www.nrel.gov/pv/assets/pdfs/best-research-cell-efficiencies.pdf[accessed 17 September2024].
- [21] Ke, W., Stoumpos, C.C. and Kanatzidis, M.G., 2019. "Unleaded" perovskites: status quo and future prospects of tin-based perovskite solar cells. *Advanced Materials*, 31(47), p.1803230.
- [22] Lee, M.M., Teuscher, J., Miyasaka, T., Murakami, T.N. and Snaith, H.J., 2012. Efficient hybrid solar cells based on meso-superstructured organometal halide perovskites. *science*, 338(6107), pp.643-647.
- [23] Liu, D., Yang, J. and Kelly, T.L., 2014. Compact layer free perovskite solar cells with 13.5% efficiency. *Journal of the American Chemical Society*, 136(49), pp.17116-17122.
- [24] Wu, C.G., Chiang, C.H., Tseng, Z.L., Nazeeruddin, M.K., Hagfeldt, A. and Grätzel, M., 2015. High efficiency stable inverted perovskite solar cells without current hysteresis. *Energy & Environmental Science*, 8(9), pp.2725-2733.
- [25] Liu, F., Zhu, J., Wei, J., Li, Y., Lv, M., Yang, S., Zhang, B., Yao, J. and Dai, S., 2014. Numerical simulation: toward the design of high-efficiency planar perovskite solar cells. *Applied Physics Letters*, 104(25).
- [26] Arora, N., Dar, M.I., Hinderhofer, A., Pellet, N., Schreiber, F., Zakeeruddin, S.M. and Grätzel, M., 2017. Perovskite solar cells with CuSCN hole extraction layers yield stabilized efficiencies greater than 20%. *Science*, 358(6364), pp.768-771.
- [27] Yue, S., Liu, K., Xu, R., Li, M., Azam, M., Ren, K., Liu, J., Sun, Y., Wang, Z., Cao, D. and Yan, X., 2017. Efficacious engineering on charge extraction for realizing highly efficient perovskite solar cells. *Energy & Environmental Science*, 10(12), pp.2570-2578.
- [28] Cui, P., Wei, D., Ji, J., Huang, H., Jia, E., Dou, S., Wang, T., Wang, W. and Li, M., 2019. Planar p—n homojunction perovskite solar cells with efficiency exceeding 21.3%. *Nature Energy*, 4(2), pp.150-159.
- [29] Jiang, Q., Chu, Z., Wang, P., Yang, X., Liu, H., Wang, Y., Yin, Z., Wu, J., Zhang, X. and You, J., 2017. Planar-structure perovskite solar cells with efficiency beyond 21%. *Advanced materials*, 29(46), p.1703852.

- [30] Nazeeruddin, M.K., 2016. Twenty-five years of low-cost solar cells. *Nature*, 538(7626), pp.463-464.
- [31] Alsalloum, A.Y., Turedi, B., Almasabi, K., Zheng, X., Naphade, R., Stranks, S.D., Mohammed, O.F. and Bakr, O.M., 2021. 22.8%-Efficient single-crystal mixed-cation inverted perovskite solar cells with a near-optimal bandgap. *Energy & Environmental Science*, 14(4), pp.2263-2268.
- [32] Li, F., Deng, X., Qi, F., Li, Z., Liu, D., Shen, D., Qin, M., Wu, S., Lin, F., Jang, S.H. and Zhang, J., 2020. Regulating surface termination for efficient inverted perovskite solar cells with greater than 23% efficiency. *Journal of the American Chemical Society*, 142(47), pp.20134-20142.
- [33] Lu, H., Liu, Y., Ahlawat, P., Mishra, A., Tress, W.R., Eickemeyer, F.T., Yang, Y., Fu, F., Wang, Z., Avalos, C.E. and Carlsen, B.I., 2020. Vapor-assisted deposition of highly efficient, stable black-phase FAPbI₃ perovskite solar cells. *Science*, 370(6512), p.eabb8985.
- [34] Kim, G.H. and Kim, D.S., 2021. Development of perovskite solar cells with> 25% conversion efficiency. *Joule*, 5(5), pp.1033-1035.
- [35] Yoo, J.J., Seo, G., Chua, M.R., Park, T.G., Lu, Y., Rotermund, F., Kim, Y.K., Moon, C.S., Jeon, N.J., Correa-Baena, J.P. and Bulović, V., 2021. Efficient perovskite solar cells via improved carrier management. *Nature*, 590(7847), pp.587-593.
- [36] Sabbah, H., Arayro, J. and Mezher, R., 2022. Simulation and investigation of 26% efficient and robust inverted planar perovskite solar cells based on GA_{0.2}FA_{0.78}SnI₃₋₁% EDAI₂ films. *Nanomaterials*, 12(21), p.3885.
- [37] Patel, P.K., 2021. Device simulation of highly efficient eco-friendly CH₃NH₃SnI₃ perovskite solar cell. *Scientific reports*, 11(1), p.3082.
- [38] Rabhi, S., Sekar, K., Kalna, K., Bouderbala, Y.I., Bouri, N., Oueldna, N., Belbachir, N., Dadda, K., Aida, M.S. and Attaf, N., 2024. Experimental findings and SCAPS-1D simulations for higherficiency MAPbI₃ perovskite solar cells beyond 31%. *Optical and Quantum Electronics*, 56(8), p.1372.
- [39] Liu, J., De Bastiani, M., Aydin, E., Harrison, G.T., Gao, Y., Pradhan, R.R., Eswaran, M.K., Mandal, M., Yan, W., Seitkhan, A. and Babics, M., 2022. Efficient and stable perovskite-silicon tandem solar cells through contact displacement by MgF x. *Science*, 377(6603), pp.302-306.
- [40] Khan, T.M. and Ahmed, S.R.A., 2024. Investigating the Performance of FASnI₃-Based Perovskite Solar Cells with Various Electron and Hole Transport Layers: Machine Learning Approach and SCAPS-1D Analysis. *Advanced Theory and Simulations*, 7(10), p.2400353.
- [41] Ishraq, M.H., Tarekuzzaman, M., Modak, J.K., Ahmad, S., Rasheduzzaman, M., Arafat, Y. and Hasan, M.Z., 2024. Investigating novel perovskites of lead-free flexible solar cell CH₃NH₃BiI₃ and their photovoltaic performance with efficiency over 26%. *Materials Science and Engineering: B*, 308, p.117622.
- [42] Dar, S.A. and Sengar, B.S., 2024. Optimization and performance analysis of inorganic lead-free CsSnBr₃ perovskite solar cells using diverse electron transport materials. *Energy & Fuels*, 38(9), pp.8229-8248.
- [43] Rahman, M.F., Islam, M.A.I., Chowdhury, M., Farhat, L.B., Ezzine, S. and Islam, A.S., 2024. Efficiency improvement of CsSnI₃ based heterojunction solar cells with P3HT HTL: A numerical simulation approach. *Materials Science and Engineering: B*, 307, p.117524.

- [44] Hossain, M.K., Uddin, M.S., Toki, G.I., Mohammed, M.K., Pandey, R., Madan, J., Rahman, M.F., Islam, M.R., Bhattarai, S., Bencherif, H. and Samajdar, D.P., 2023. Achieving above 24% efficiency with non-toxic CsSnI₃ perovskite solar cells by harnessing the potential of the absorber and charge transport layers. *RSC advances*, 13(34), pp.23514-23537.
- [45] Das, M.K., Panda, S. and Mohapatra, N., 2023. Power conversion efficiency optimization of LaFeO₃ Mott insulator based solar cell with metal oxide transport layers using SCAPS. *Materials Today: Proceedings*, 74, pp.756-762.
- [46] Hossain, M.K., Toki, G.I., Samajdar, D.P., Mushtaq, M., Rubel, M.H.K., Pandey, R., Madan, J., Mohammed, M.K., Islam, M.R., Rahman, M.F. and Bencherif, H., 2023. Deep insights into the coupled optoelectronic and photovoltaic analysis of lead-free CsSnI₃ perovskite-based solar cell using DFT calculations and SCAPS-1D simulations. *ACS omega*, 8(25), pp.22466-22485.
- [47] Park, H.J., Son, H. and Jeong, B.S., 2024. SCAPS-1D simulation for device optimization to improve efficiency in lead-free CsSnI₃ perovskite solar cells. *Inorganics*, 12(4), p.123.
- [48] Pindolia, G., Shinde, S.M. and Jha, P.K., 2023. Non-leaded, KSnI₃ based perovskite solar cell: A DFT study along with SCAPS simulation. *Materials Chemistry and Physics*, 297, p.127426.
- [49] Sumona, F.B., Kashif, M., Danladi, E., Tighezza, A.M., Al-Mahmud, N., Toki, G.F., Pandey, R. and Hossain, M.K., 2023. Optimization of perovskite-KSnI₃ solar cell by using different hole and electron transport layers: a numerical SCAPS-1D simulation. *Energy & Fuels*, 37(23), pp.19207-19219.
- [50] Sumona, F.B., Kashif, M., Madan, J., Metwally, A.S.M. and Danladi, E., 2024. Optimization of lead-free KSnI₃ perovskite solar cell by numerical simulation with enhanced efficiency of 20.34%. *Journal of Optics*, pp.1-15.
- [51] Siddique, M.A.F. and Rahman, A.S.M.S., 2024. The SCAPS-1D simulation of non-toxic KGeCl₃ perovskite from DFT derived properties. *Materials Science and Engineering: B*, 303, p.117268.
- [52] Shrivastav, N., Hamid, M.A., Madan, J. and Pandey, R., 2024. Exploring KGeCl₃ material for perovskite solar cell absorber layer through different machine learning models. *Solar Energy*, 278, p.112784.
- [53] Yasin, S., Waar, Z.A. and Moustafa, M., 2024, October. Eco-Friendly KGeCl₃ Solar Cells: Performance Enhancement Through HTL Engineering. In 2024 International Semiconductor Conference (CAS) 2024, pp. 91-94.
- [54] Rehman, U.U., Sahar, K.U., Hussain, E. and Wang, C.M., 2024. Performance optimization of lead-free potassium germanium halide based perovskite solar cells: A numerical study. *Solar Energy*, 277, p.112752.
- [55] Ullah, S., Al-Rasheidi, M., Khan, F., Rasheed, J.F., Qamar, S. and ul Ain, Q., 2025. Simulation and optimization of KSnI₃/Sb₂S₃-based heterojunction solar cell. Journal of Physics and Chemistry of Solids, p.112598.
- [56] Moone, P.K. and Sharifi, N., 2024. Comparison of Pb-based and Sn-based perovskite solar cells using SCAPS simulation: optimal efficiency of eco-friendly CsSnI₃ devices. *Environmental Science and Pollution Research*, 31(39), pp.51447-51460.
- [57] Danladi, E., Obagboye, L.F., Aisida, S., Ezema, F.I., Okorie, O., Bwamba, J.A., Emmanuel, P.A., Hussaini, A.A., Jubu, P.R. and Ozurumba, A.C., 2025. 20.730% highly efficient lead-free

- CsSnI₃-based perovskite solar cells with various charge transport materials: a SCAPS-1D study. *Multiscale and Multidisciplinary Modeling, Experiments and Design*, 8(1), pp.1-21.
- [58] Hossain, M.K., Samajdar, D.P., Das, R.C., Arnab, A.A., Rahman, M.F., Rubel, M.H.K., Islam, M.R., Bencherif, H., Pandey, R., Madan, J. and Mohammed, M.K., 2023. Design and simulation of Cs₂BiAgI₆ double perovskite solar cells with different electron transport layers for efficiency enhancement. *Energy & Fuels*, 37(5), pp.3957-3979.
- [59] Zhang, Z., Sun, Q., Lu, Y., Lu, F., Mu, X., Wei, S.H. and Sui, M., 2022. Hydrogenated Cs₂AgBiBr₆ for significantly improved efficiency of lead-free inorganic double perovskite solar cell. *Nature communications*, 13(1), p.3397.
- [60] Pandey, N., Neelu, N. and Chakrabarti, S., 2023. Room temperature synthesis of double perovskite Cs₂AlBiCl₆ for photovoltaic applications. *Optical Materials*, 137, p.113570.
- [61] Li, G., Su, Z., Canil, L., Hughes, D., Aldamasy, M.H., Dagar, J., Trofimov, S., Wang, L., Zuo, W., Jerónimo-Rendon, J.J. and Byranvand, M.M., 2023. Highly efficient pin perovskite solar cells that endure temperature variations. *Science*, 379(6630), pp.399-403.
- [62] Chen, P., Pan, W., Zhu, S., Cao, F., Tong, A., He, R., Lan, Z., Sun, W. and Wu, J., 2023. Buried modification with tetramethylammonium chloride to enhance the performance of perovskite solar cells with nip structure. *Chemical Engineering Journal*, 468, p.143652.

CHAPTER 3

MATERIALS AND METHODS

- ➤ This Chapter includes the introduction of potential perovskite and double perovskite materials such as CH₃NH₃PbI₃, CsSnI₃, LaFeO₃, (MA)₂CuX₄, KSnI₃, KGeCl₃ and Cs₂AlBiCl₆.
- > The simulation procedure and employed tool working has been explained.
- > The incorporation of machine learning analysis by using simulation data elaborated for the optimization of high efficiency device.
- The characterization method: XRD, UV-vis, FTIR, SEM analysis and J-V characteristics employed for the optimization of PSC.

3.1 Perovskite Materials

3.1.1 CH₃NH₃PbI₃

Methylammonium Lead Iodide (MAPbI₃), or CH₃NH₃PbI₃ is a potential material in the development of PSCs. Its numerous advantages make it a promising candidate in the field of photovoltaics. MAPbI₃, a type of perovskite material, has gained significant attention in research due to its remarkable advantages, including a tunable band gap, low on—off voltage, long charge diffusion length, and significant dielectric polarization [1-4]. Recently, the efficiency of MAPbI₃-based photovoltaic devices has reached approximately 20 % [5]. It achieves an outstanding theoretical PCE of 28.39 % [6]. In addition, MAPbI₃ has been used in various applications, including photodetectors [7], surface plasmon resonance [3, 8], resonators [9], and resistive random-access memory [4]. The material's exceptional dielectric properties are among the key factors driving its effectiveness in these practical applications. The remarkable dielectric properties of MAPbI₃ play a crucial role in its effectiveness for these practical applications [10]. Simultaneously, the inclusion of lead in MAPbI₃ presents serious environmental and health risks. If the material degrades or is not disposed of properly, it can release toxic lead, which poses a threat to both human health and the environment.

3.1.2 Need of Lead-Free Solar Cells

The effects of both acute and chronic lead (Pb) poisoning are well understood, owing to its extensive use throughout history [11]. Pb compounds can enter the bloodstream via ingestion, inhalation, or absorption through the skin. Pb poisoning primarily affects the Central Nervous System. It can cross the blood-brain barrier, accumulating in the brain and causing damage to genetic material through oxidative stress. Pb poisoning can result in neurological issues, such as decreased intelligence, and anxiety, depression, and aggression. These effects can occur in both children and adults, even with exposure levels as low as 5 μ g/dL or lower [12]. Nonneurological effects of Pb exposure include infertility, cataracts, high blood pressure, and cardiovascular and kidney diseases [12]. So that we need to replace Pb-based PSCs with its alternatives without compromising efficiency and stability of the device.

3.1.3 Potential Alternatives

3.1.3.1 CsSnI₃ and KSnI₃

Unlike traditional Pb-based perovskites, cesium tin iodide (CsSnI₃) reduces toxicity concerns while preserving exceptional optoelectronic properties. Furthermore, numerous studies have shown that replacing the methylammonium cation with cesium, in the PSC structure significantly enhances its thermal stability [13-15]. Additionally, the capability of CsSnI₃ to attain a direct bandgap of approximately 1.3 eV further boosts its potential for high-performance solar cells [13]. It demonstrates a high light-absorption coefficient of about 10⁴ cm⁻¹ in the visible range, which enhances its light-harvesting performance [13]. In recent decades, most reported PCEs for CsSnI₃-based PSCs have ranged from 3 to 6 % [16-17]. The

in-organic CsSnI₃ perovskite combines the benefits of being non-toxic and exhibiting outstanding thermal stability, with a high decomposition temperature of around 450 °C. The pi-n configuration is optimized by analysing the band alignment between the HTL and the absorber, resulting in a PCE of 16.11 % [18]. The simulation study demonstrated that the proposed CsSnI₃-based PSC achieved a maximum PCE of 26.40 % [19]. The optimized configuration: FTO/CdS/CsSnI₃/MoS₂/Pd has been achieved a maximum PCE of 23.45 % at 300 K.

The potential of potassium tin iodide (KSnI₃), a low-toxicity and lead-free material, makes it promising absorber layer in PSCs. The orthorhombic structure of KSnI₃ is thermodynamically stable. It demonstrates strong absorption in the visible light spectrum, making it excellent candidate for light harvesting in PV devices. KSnI₃ has a higher polarizability compared to CsSnI₃ and RbSnI₃ [20]. The KSnI₃ perovskite material exhibits the most optimal properties for fabricating a PSC device [21]. The optimized configuration of KSnI₃-based PSC, FTO/TiO₂/KSnI₃/Spiro-OMeTAD/W obtained a PCE of 9.77 % [22]. By optimizing factors such as thickness, temperature, Nt, Rs, Rsh and back contact, PSCs have achieved remarkable performance with a PCE of 20.34 % [23]. A maximum PCE of 23.08 % has been achieved for KSnI₃-based PSCs with an absorber layer thickness of 550 nm and a N_t of 10¹³ cm⁻³. Potassium doping in KSnI₃ could improve the stability of the material, but like CsSnI₃ it still faces issues with moisture and air degradation. The stability of KSnI₃ might be better than CsSnI₃ in some cases. KSnI₃ has been less explored compared to CsSnI₃, but it is a relatively new candidate with potential for high efficiency, though current efficiency records are lower than those of CsSnI₃. Both CsSnI₃ and KSnI₃ do not contain lead, making them non-toxic alternatives to Pbbased perovskites. This is a significant advantage when considering their use in large-scale solar applications from an environmental and regulatory standpoint.

3.1.3.2 Copper (Cu)-based

Besides environmental concerns, lead-based perovskite solar cells also encounter stability problems due to the rapid oxidation of the Pb cation. There is a need to replace Pb-based perovskites with other perovskite materials that are not only less toxic and more environmentally friendly, but also capable of delivering superior photovoltaic performance. As a result, the exploration of transition metals has gained significant momentum. Many transition metals, such as Fe^{2+} , Cu^{2+} , and Zn^{2+} , are promising alternatives due to their cost-effectiveness, abundance on Earth, and low toxicity. Copper metal has also been explored as a potential replacement for Pb. Cu-based hybrid perovskite materials demonstrate tunable band gaps by varying the halide content ($X = Cl_4$, Cl_2I_2 , Cl_2Br_2). PCE up to 2.41 % have been experimentally reported by Ahmed et al. [24] using Cu-based perovskite materials ((MA)₂CuX₄) for solar cell fabrication. Moreover, the optical absorption within the 300–900 nm wavelength range (covering visible to near-infrared light) can be adjusted by modifying the Cl/I/Br content ratio [24].

3.1.3.3 LaFeO₃

Lanthanum ferrite (LaFeO₃) has a direct, narrow energy band gap. It is chemically stable, non-toxic, and exhibits high electron mobility [25-26]. LaFeO₃ possesses unique characteristics, including catalytic activity, gas sensing capabilities, and mixed ionic and electronic

conductivities [27-29]. LaFeO₃ is a prototypical insulator with a trivalent Fe cation and an energy band gap ranging from 2.1 to 2.6 eV, enabling it to absorb a significant portion of the solar spectrum, from UV to near-IR wavelengths [30]. The LaFeO₃ film was found to effectively absorb visible light and function as a visible light-absorbing semiconductor photocathode. This approach provides a novel design and fabrication method for innovative solar energy conversion devices. All of this information suggests that LaFeO₃ is a highly promising candidate for use in solar cells. The optimized structure such as STO/In₂O₃/LaFeO₃/MoO₃/Au obtained a PCE of 9.11 % using SCAPS-1D simulation software [31]. LaFeO₃ -based PSC experimentally has been achieved a PCE of 0.06 % [32].

3.1.3.4 KGeCl₃

The Potassium Germanium Chloride (KGeCl₃) compounds were exhibited strong structural stability, with lattice constants of 5.269 Å, 7.302 Å, and 7.634 Å for the cubic, tetragonal, and trigonal phases, respectively at the ground state. The direct band gaps were determined to be 2.7 eV, 0.8 eV, and 1.2 eV for the trigonal, cubic, and tetragonal phases, respectively. The tetragonal and cubic phases are mechanically stable and ductile whereas the trigonal phase was unstable and brittle. The ability to absorb photon energy in the UV-Vis range of the electromagnetic spectrum makes it promising material for PV applications. The cubic and tetragonal structures exhibited potential for PV applications [33]. The optimized structure FTO/SnS₂/KGeCl₃/Cu₂O/C exhibits PCE of 15.83 % [34]. The KGeCl₃-based configuration achieved a PCE of 19.62 % with SnO₂ as ETL and Me4PACz as HTL [35].

3.1.3.5 Cs₂AlBiCl₆ Double Perovskite Material

Double perovskite materials have attracted considerable attention from the research community due to their exceptional stability to heat, light, and moisture [36,37]. The basic formula of double perovskites is $A_2BB^{\circ}X_6$, where A is a monovalent cation, B is monovalent cation, B' is trivalent cation, and X is halide such as Cl $^{-}$, Br $^{-}$, or Γ [38-41]. Lead-free perovskites offer environmental benefits, exceptional stability, and tunable optoelectronic properties. Cesium aluminium bismuth chloride (Cs₂AlBiCl₆) exhibits exceptional optical and structural properties, making it highly suitable for PV applications. Cs₂AlBiCl₆-based DPSC achieved a PCE of 1.965 % which is comparable to single PSC [42].

3.2 Methodology

3.2.1 SCAPS-1D Simulation Software

The Solar Cell Capacitance Simulator (SCAPS-1D, version 3.3.10) was used to simulate various PSCs. SCAPS-1D simulation software, developed by Ghent University in Belgium, enables users to simulate up to seven semiconducting layers under both light and dark conditions [43]. This software allows simulations under various input physical conditions. The simulations were run at 300 K, using a "air mass 1.5 global" spectrum and a light intensity of 1000 W/m². SCAPS-1D examines the model's physics, providing insights into recombination profiles, electric field distribution, carrier transport mechanisms, and individual current

densities. The simulator utilizes three key differential equations: Poisson's equation, the transport equation, and the continuity equation [44]:

Poisson's equation:

$$\frac{\partial^2 \psi}{\partial x^2} + \frac{q}{\epsilon} \left[p(x) - n(x) + N_D - N_A + \rho_p - \rho_n = 0 \right] \tag{3.1}$$

where, ψ : electrostatic potential, ϵ : permittivity $\rho_{p,n}$: $e^{-/}$ h^+ current density, q: elementary charge, p: density of free hole, n: density of free electron $N_D \& N_A$: donor and acceptor doping density.

Transport equation:

$$L_{n,p} = \sqrt{\left(\frac{k_B T}{q}\right) \mu_{n,p} \, \tau_{n,p}} \tag{3.2}$$

With, $L_{n,p}$: <u>Diffusion length</u> of e^- and h^+ , K_BT/q : Thermal voltage, $\tau_{n,p}$: e^- and h^+ lifetime.

Continuity equation:

$$V_{OC} = \frac{nk_BT}{q} \left[\ln \left(\frac{I_L}{I_0} + 1 \right) \right] \tag{3.3}$$

$$\frac{1}{q}\frac{dJ_p}{dx} = G_{op}(x) - R(x) \tag{3.4}$$

$$\frac{1}{a}\frac{dJ_n}{dx} = -G_{op}(x) + R(x) \tag{3.5}$$

where, V_{OC} : Open-circuit voltage, n: Ideality factor, I_L : Solar cell light generated current, I_0 : Reverse saturation current, G: optical generation rate and R: recombination rate.

SCAPS-1D computes the above equations assuming steady-state conditions. The performance of the solar cells is reflected in the I–V characteristics, which represent the following PV parameters: J_{SC}, FF, V_{OC}, and PCE. All the input data used in the SCAPS-1D simulations were derived from both experimental and theoretical studies. The simulation procedure is shown below in Fig. 3.1 [45].

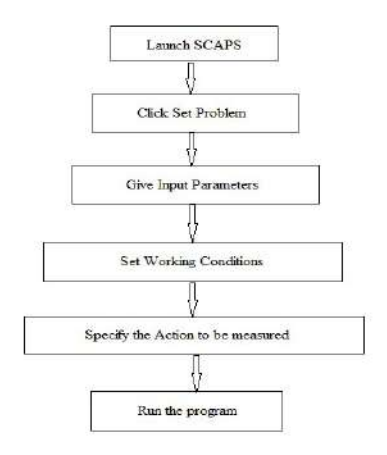


Figure 3.1 SCAPS-1D software simulation procedure.

3.2.2 Machine Learning Analysis

Machine learning (ML) algorithms have been employed in the design of solar cells [46]. The prediction of PCE using advanced ML models is straightforward and easily understandable for solar research. To enhance the prediction of PCE and reduce simulation complexity in forecasting the PCE of different PSCs, ML algorithms such as Random Forest (RF) and XGBoost (XGB) regression were utilized to model the data, accounting for variation in various PV parameters as follows: absorber layer thickness, N_t and operating temperature. The capability of ML models to learn from data allows them to identify patterns and correlations that are difficult to model in traditional simulators. Additionally, these models enhance their PCE predictions for solar cells through ongoing learning from new datasets. A basic RF algorithm from Scikit-Learn was used to assess the importance of each feature in the final model. Two different methods were employed to identify the optimal hyperparameters. The first method involved creating a parameter grid (a python dictionary) that included a range of values for each parameter. The RandomizedSearchCV and GridSearchCV tools from Scikit-Learn were used to identify the best combination of hyperparameters from the grid. RandomizedSearchCV randomly sampled combinations from the grid and assessed their performance through cross-validation, whereas GridSearchCV exhaustively tested all possible combinations of the specified parameters. The test set was then utilized for evaluation. An 80:20 training to testing data ratio was also applied, as it has shown strong performance in model evaluation and validation. The equations for calculating mean square error (MSE) and R^2 [47] are listed below:

$$MSE = \frac{1}{n} \sum_{i=1}^{n} (y_i - \hat{y}_i)^2$$
 (3.6)

$$R^{2} = 1 - \frac{\sum_{i=1}^{n} (y_{i} - \widehat{y}_{i})^{2}}{\sum_{i=1}^{n} (y_{i} - \overline{y}_{i})^{2}}$$
(3.7)

where.

 \hat{y} is the actual value, \bar{y} is the predicted values, is the maean of the actual values and n is the total no. of datasets. XGB boosting approach emerges as the top-performing algorithm for PCE prediction in solar cells, demonstrating its robustness, adaptability, and ability to effectively managing distinct and challenging datasets. Fig. 3.2 depicted that SCAPS-1D data used in machine learning analysis for model selection and model explanation for the optimization final device performance.

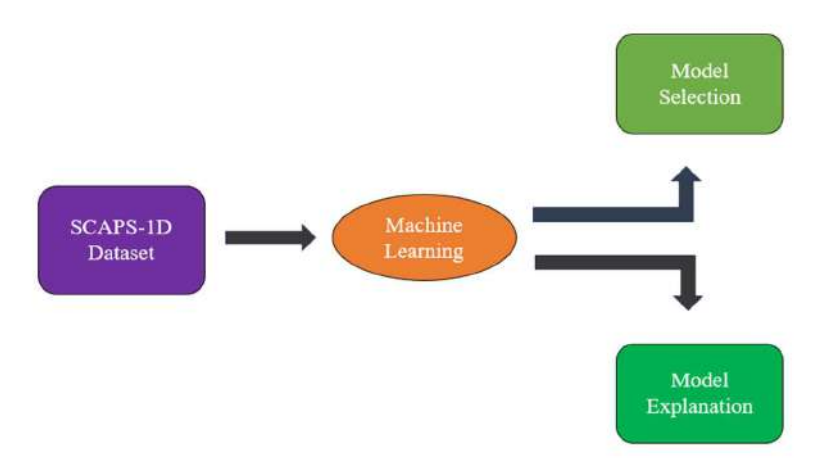


Figure 3.2 SCAPS-1D data used in machine learning analysis.

3.2.3 Characterization Methods

3.2.3.1 X-ray Diffraction (XRD)

XRD is an analytical technique that primarily exploits the dual wave-particle characteristics of X-rays. It is mainly used to identify the structure of crystalline materials and can provide insights into unit cell dimensions, chemical bonds, their disorder, and other related properties. In 1912, Max von Laue discovered that crystalline substances act as 3-D diffraction gratings for X-ray wavelengths, similar to the spacing of planes in a crystal lattice. This systematic diffraction of X-rays by different planes within the crystal makes XRD a highly effective technique for studying crystalline materials. X-ray diffraction by crystals is described by Bragg's Law, $n\lambda = 2d \sin\theta$, which connects the wavelength of electromagnetic radiation (λ) with the diffraction angle (θ) and the lattice spacing (d) in a crystalline material. The diffracted Xrays are subsequently detected, processed, and counted. By scanning the sample across a range of 2θ angles, all potential diffraction directions of the lattice are captured, thanks to the random orientation of the material. The diffraction peaks are then converted to d-spacings, which allows for the identification of the mineral, as each mineral possesses a distinct set of dspacings. This identification is typically performed by comparing the d-spacings with standard reference patterns. The radiation from Cu-Kα with a wavelength of 1.54 Å, was used (Bruker make, model: D-8). The schematic diagram of XRD shown below in Fig. 3.3 [48].

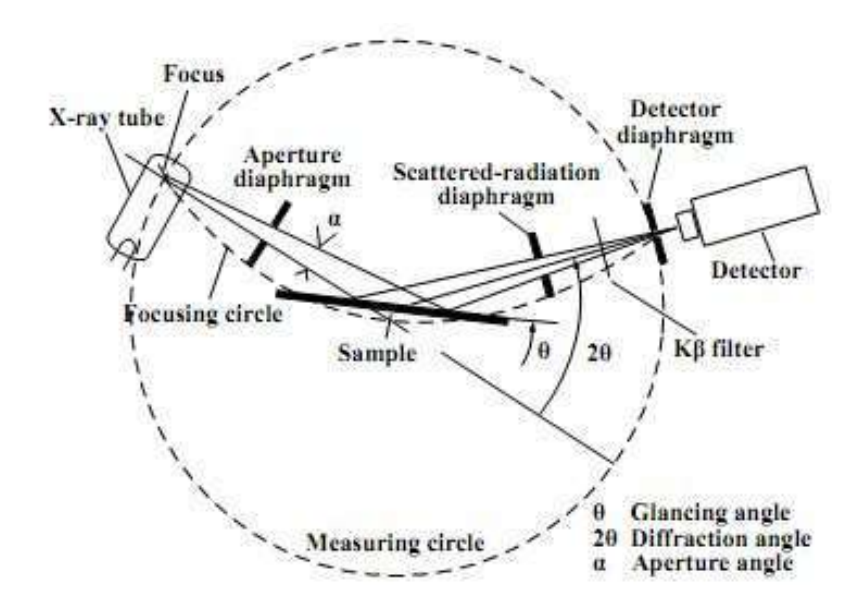


Figure 3.3 Schematic diagram of XRD [Connolly, 2007].

3.2.3.2 UV-Visible Spectroscopy

UV-vis spectroscopy is a technique employed to examine the absorption, reflectance, and transmission spectra of materials within the UV, visible, and NIR region of the electromagnetic spectrum. The Tauc plot method can be used to calculate the optical band gap of a material using its absorption, reflectance, and transmission spectra [49]. The schematic diagram of UV-vis spectrometer depicted in Fig. 3.4. UV-vis spectrometer (Perkin-Elmer 750) was employed to obtain the absorption, reflectance, and transmission spectra of the synthesized perovskite material film with in the wavelength range of 220 to 1100 nm.

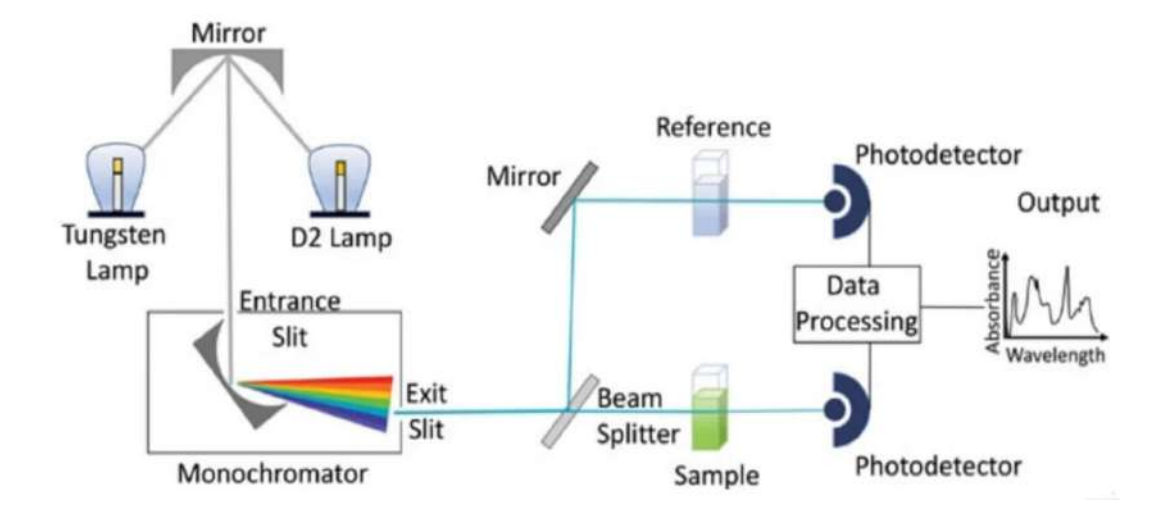


Figure 3.4 Schematic diagram of UV-vis spectrometer [49].

3.2.3.3 Scanning Electron Microscopy (SEM)

It is a type of electron microscope that produces images of a sample by scanning the surface with a focused e⁻ beam. The e⁻s interact with atoms in the sample, producing various signals that contain information about the sample's topography and composition. The SEM is an effective technique for analysing the surface morphology, grain size and shape of the synthesized perovskite material for the fabrication of the device. It also offers insights into the intergranular pores and the grain distribution within the bulk samples. It can provide the crystallographic information about the sample. The defects present in the crystal can be detected also. It produces 3D images of the sample with high resolution and large depth. For non-conducting samples, charging effects are observed, which can be mitigated by coating a thin conducting layer on its surface. The schematic diagram of SEM is shown below in Fig. 3.5. The e⁻s emitted from a filament due to thermionic emission are accelerated by a high voltage, typically between 0-50 KV, and focused into a fine beam using magnetic and electric field. This focused beam irradiates the sample, and the secondary e⁻s emitted from the sample are detected by a detector positioned at a specific angle relative to the sample. Morphological analysis was observed with Nova nano SEM.

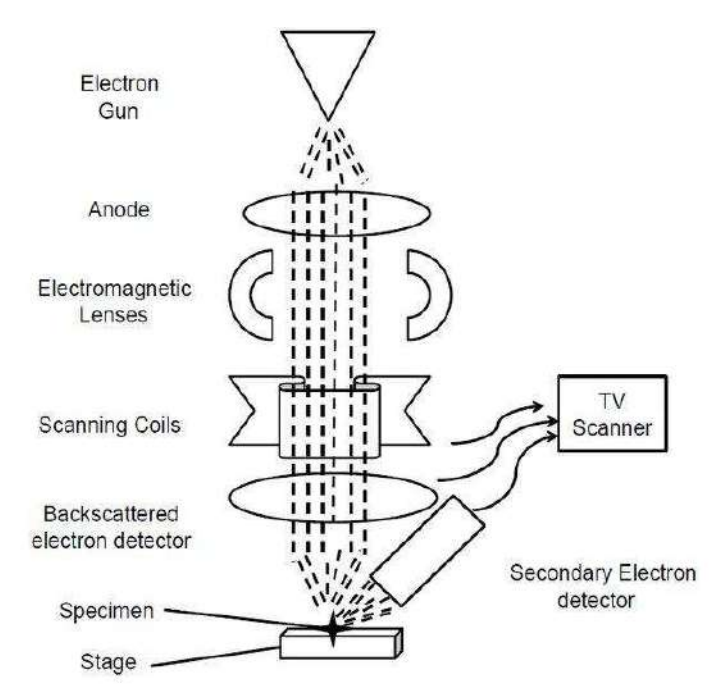


Figure 3.5 Schematic diagram of SEM [50].

3.2.3.4 Fourier Transform Infrared Spectroscopy (FTIR)

FTIR is a fast and cost-effective method for characterizing the chemical properties of cells and identifying the functional groups present in the cell wall. Infrared spectroscopy is a widely used technique for identifying functional groups in organic molecules by analysing their vibration modes at various infrared wavelengths. By analysing the position and intensity of different

infrared absorption bands, it is possible to monitor the presence or absence of functional groups, their protonation states, and any changes due to new interactions [51]. FTIR spectra of the material is obtained by Perkin Elmer Spectrum II spectrometer. Fig. 3.6 shows the different components of the FTIR spectrometer.

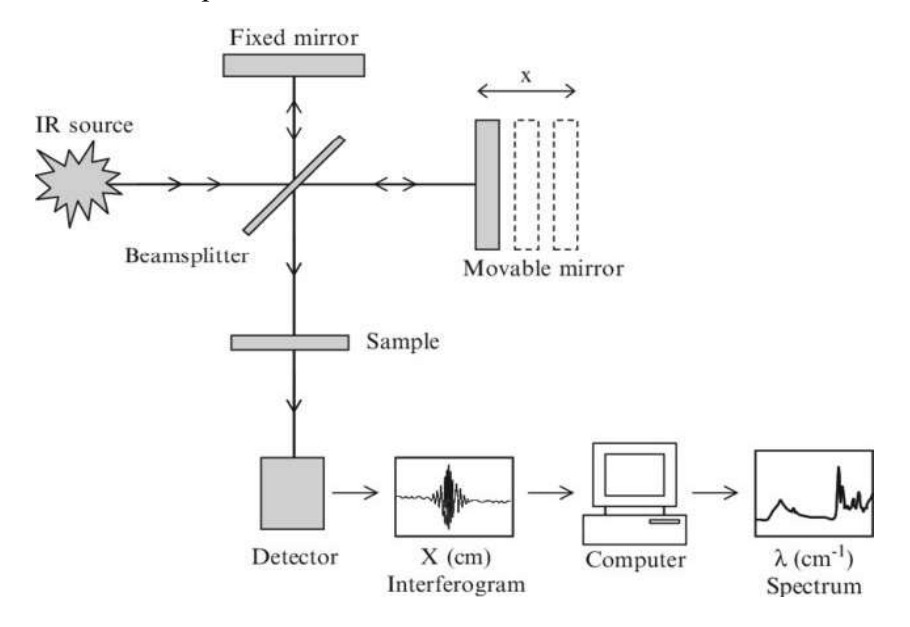


Figure 3.6 Schematic sketch of FTIR spectrometer [51].

3.2.3.5 Current-Voltage Characteristics

The current density-voltage (J-V) characteristics are measured under illumination to assess the performance of the solar cells (FYTRONIX, Class: AAA). This is achieved by applying an external potential bias during the measurement of the J-V characteristics. The fabricated devices were evaluated for photocurrent and voltage measurements under the standard Air Mass 1.5 Global solar spectrum at 25 °C using a solar simulator. The forward current, where the applied potential is termed the forward bias, primarily involves the injection of e⁻ into the from the photoanode. The reverse current, associated with the applied potential called reverse bias, involves the injection of e⁻ from the counter electrode side. The current-voltage characteristics of an ideal solar cell shown below in Fig. 3.7. The schematic diagram of a xenon arc solar simulator depicted below in Fig. 3.8.

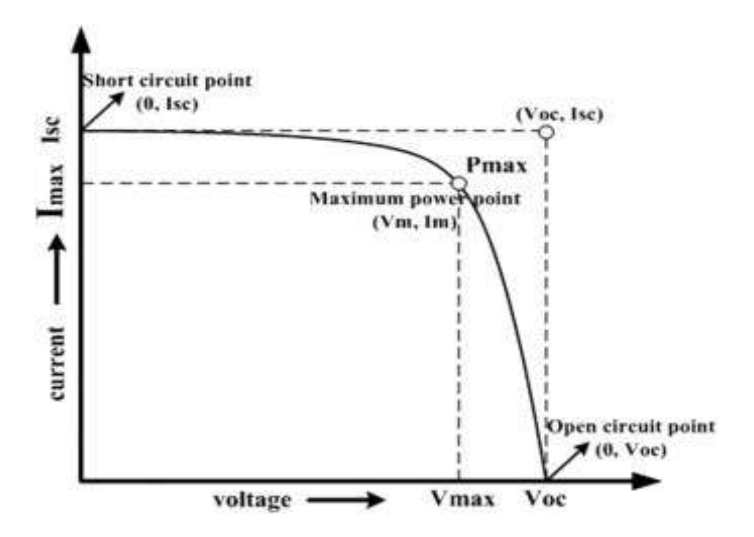


Figure 3.7 Current-voltage characteristics of a solar cell [52].

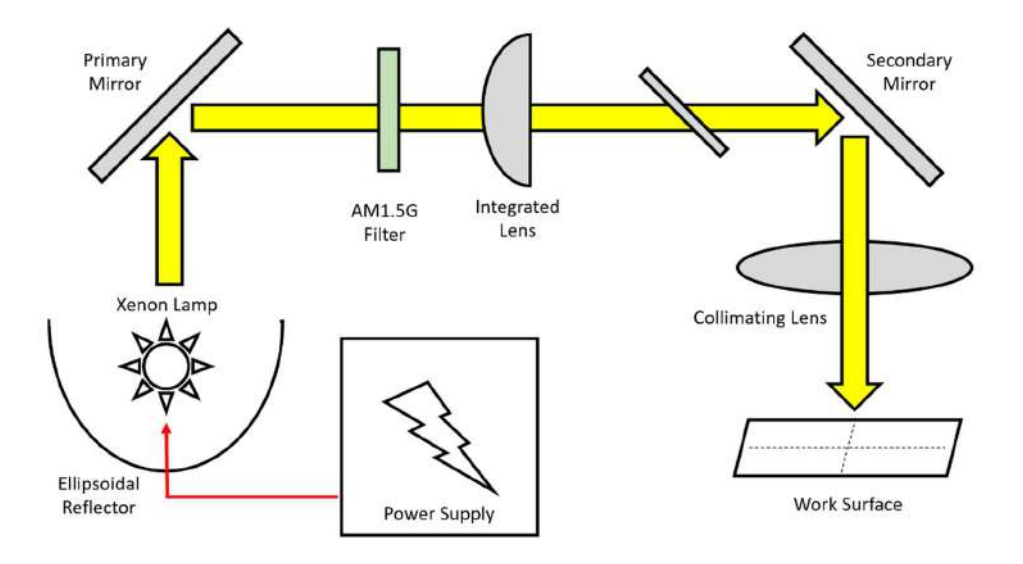


Figure 3.8 Schematic diagram of a solar simulator [53].

3.3 REFERENCES

- [1] Protesescu, L., Yakunin, S., Bodnarchuk, M.I., Krieg, F., Caputo, R., Hendon, C.H., Yang, R.X., Walsh, A. and Kovalenko, M.V., 2015. Nanocrystals of cesium lead halide perovskites (CsPbX₃, X= Cl, Br, and I): novel optoelectronic materials showing bright emission with wide color gamut. *Nano letters*, 15(6), pp.3692-3696.
- [2] Sharada, G., Mahale, P., Kore, B.P., Mukherjee, S., Pavan, M.S., De, C., Ghara, S., Sundaresan, A., Pandey, A., Row, T.G. and Sarma, D.D., 2016. Is CH₃NH₃PbI₃ polar. *J. Phys. Chem. Lett*, 7(13), pp.2412-2419.
- [3] Cui, J., Chen, C., Han, J., Cao, K., Zhang, W., Shen, Y. and Wang, M., 2016. Surface plasmon resonance effect in inverted perovskite solar cells. *Advanced Science*, 3(3), p.1500312.
- [4] Yoo, E.J., Lyu, M., Yun, J.H., Kang, C.J., Choi, Y.J. and Wang, L., 2015. Resistive Switching Behavior in Organic-Inorganic Hybrid CH₃NH₃PbI_{3-x}Cl_x Perovskite for Resistive Random Access Memory Devices. *Advanced Materials (Deerfield Beach, Fla.)*, 27(40), pp.6170-6175.
- [5] Wang, Q., Jiang, J., Wu, X. and Zhang, F., 2024. Improvement of perovskite CH₃NH₃PbI₃ films on crystallization for efficient perovskite solar cells with low-temperature anti-solvent approach. *Journal of Electronic Materials*, 53(1), pp.86-93.
- [6] Rabhi, S., Sekar, K., Kalna, K., Bouderbala, Y.I., Bouri, N., Oueldna, N., Belbachir, N., Dadda, K., Aida, M.S. and Attaf, N., 2024. Experimental findings and SCAPS-1D simulations for higherficiency MAPbI₃ perovskite solar cells beyond 31%. *Optical and Quantum Electronics*, 56(8), p.1372.
- [7] Su, L., Zhao, Z.X., Li, H.Y., Yuan, J., Wang, Z.L., Cao, G.Z. and Zhu, G., 2015. High-performance organolead halide perovskite-based self-powered triboelectric photodetector. *ACS nano*, 9(11), pp.11310-11316.
- [8] Pathak, N.K. and Sharma, R.P., 2016. Study of broadband tunable properties of surface plasmon resonances of noble metal nanoparticles using mie scattering theory: plasmonic perovskite interaction. *Plasmonics*, 11, pp.713-719.
- [9] Jia, Y., Kerner, R.A., Grede, A.J., Brigeman, A.N., Rand, B.P. and Giebink, N.C., 2016. Diodepumped organo-lead halide perovskite lasing in a metal-clad distributed feedback resonator. *Nano letters*, 16(7), pp.4624-4629.
- [10] Zhang, C., Mu, C., Xiang, J., Wang, B., Wen, F., Song, J., Wang, C. and Liu, Z., 2017. Microwave absorption characteristics of CH₃NH₃PbI₃ perovskite/carbon nanotube composites. *Journal of Materials Science*, 52(22), pp.13023-13032.
- [11] Babayigit, A., Boyen, H.G. and Conings, B., 2018. Environment versus sustainable energy: The case of lead halide perovskite-based solar cells. *MRS Energy & Sustainability*, 5, p.E1.
- [12] Sanders, T., Liu, Y., Buchner, V. and Tchounwou, P.B., 2009. Neurotoxic effects and biomarkers of lead exposure: a review. *Reviews on environmental health*, 24(1), pp.15-46.
- [13] Wang, N., Zhou, Y., Ju, M.G., Garces, H.F., Ding, T., Pang, S., Zeng, X.C., Padture, N.P. and Sun, X.W., 2016. Heterojunction-depleted lead-free perovskite solar cells with coarse-grained B-γ-CsSnI₃ thin films. *Advanced Energy Materials*, 6(24), p.1601130.

- [14] Chung, I., Song, J.H., Im, J., Androulakis, J., Malliakas, C.D., Li, H., Freeman, A.J., Kenney, J.T. and Kanatzidis, M.G., 2012. CsSnI₃: semiconductor or metal? High electrical conductivity and strong near-infrared photoluminescence from a single material. High hole mobility and phase-transitions. *Journal of the american chemical society*, 134(20), pp.8579-8587.
- [15] Chung, I., Lee, B., He, J., Chang, R.P. and Kanatzidis, M.G., 2012. All-solid-state dye-sensitized solar cells with high efficiency. *Nature*, 485(7399), pp.486-489.
- [16] Wang, Y., Tu, J., Li, T., Tao, C., Deng, X. and Li, Z., 2019. Convenient preparation of CsSnI₃ quantum dots, excellent stability, and the highest performance of lead-free inorganic perovskite solar cells so far. *Journal of materials chemistry A*, 7(13), pp.7683-7690.
- [17] Ma, S., Gu, X., Kyaw, A.K., Wang, D.H., Priya, S. and Ye, T., 2020. Fully inorganic CsSnI₃-based solar cells with> 6% efficiency and enhanced stability enabled by mixed electron transport layer. *ACS Applied Materials & Interfaces*, 13(1), pp.1345-1352.
- [18] Qaid, S.M., Shaker, A., Jayan, K.D., Alkadi, M., Ahmed, A.A.A. and Zein, W., 2024. Design and numerical simulation of B-γ CsSnI₃-based perovskite solar cells: Conventional versus inverted configurations. *Solar Energy*, 268, p.112275.
- [19] Ravidas, B.K., Roy, M.K. and Samajdar, D.P., 2023. Investigation of photovoltaic performance of lead-free CsSnI₃-based perovskite solar cell with different hole transport layers: First Principle Calculations and SCAPS-1D Analysis. *Solar Energy*, 249, pp.163-173.
- [20] Gul, B., Khan, M.S., Aasim, M., Khan, G., Ahmad, H. and Thounthong, P., 2023. First-principles study of the optoelectronic and thermoelectric properties of lead-free ASnI₃ (A= K, rb, and Cs) novel halide perovskites. *Physica B: Condensed Matter*, 669, p.415316.
- [21] Charlie, D.E., Louis, H., Ogunwale, G.J., Amodu, I.O., Ashishie, P.B., Agwamba, E.C. and Adeyinka, A.S., 2023. Effects of alkali-metals (X= Li, Na, K) doping on the electronic, optoelectronic, thermodynamic, and X-ray spectroscopic properties of X–SnI₃ halide perovskites. *Computational Condensed Matter*, 35, p.e00798.
- [22] Pindolia, G., Shinde, S.M. and Jha, P.K., 2023. Non-leaded, KSnI₃ based perovskite solar cell: A DFT study along with SCAPS simulation. *Materials Chemistry and Physics*, 297, p.127426.
- [23] Sumona, F.B., Kashif, M., Madan, J., Metwally, A.S.M. and Danladi, E., 2024. Optimization of lead-free KSnI₃ perovskite solar cell by numerical simulation with enhanced efficiency of 20.34%. *Journal of Optics*, pp.1-15.
- [24] Elseman, A.M., Shalan, A.E., Sajid, S., Rashad, M.M., Hassan, A.M. and Li, M., 2018. Copper-substituted lead perovskite materials constructed with different halides for working (CH₃NH₃)₂CuX₄-based perovskite solar cells from experimental and theoretical view. *ACS applied materials & interfaces*, 10(14), pp.11699-11707.
- [25] Lotey, G.S. and Verma, N.K., 2013. Gd-doped BiFeO₃ nanoparticles—A novel material for highly efficient dye-sensitized solar cells. *Chemical Physics Letters*, 574, pp.71-77.
- [26] Bai, S., Shi, B., Ma, L., Yang, P., Liu, Z., Li, D. and Chen, A., 2009. Synthesis of LaFeO₃ catalytic materials and their sensing properties. *Science in china Series B: chemistry*, 52(12), pp.2106-2113.
- [27] Idrees, M., Nadeem, M., Siddiqi, S.A., Ahmad, R., Hussnain, A. and Mehmood, M., 2015. The organic residue and synthesis of LaFeO₃ by combustion of citrate and nitrate precursors. *Materials Chemistry and Physics*, 162, pp.652-658.

- [28] Fan, H.T., Xu, X.J., Ma, X.K. and Zhang, T., 2011. Preparation of LaFeO₃ nanofibers by electrospinning for gas sensors with fast response and recovery. *Nanotechnology*, 22(11), p.115502.
- [29] Celorrio, V., Bradley, K., Weber, O.J., Hall, S.R. and Fermín, D.J., 2014. Photoelectrochemical properties of LaFeO₃ nanoparticles. *ChemElectroChem*, 1(10), pp.1667-1671.
- [30] Peng, K., Fu, L., Yang, H. and Ouyang, J., 2016. Perovskite LaFeO₃/montmorillonite nanocomposites: synthesis, interface characteristics and enhanced photocatalytic activity. *Scientific reports*, 6(1), p.19723.
- [31] Das, M.K., Panda, S. and Mohapatra, N., 2023. Power conversion efficiency optimization of LaFeO₃ Mott insulator based solar cell with metal oxide transport layers using SCAPS. *Materials Today: Proceedings*, 74, pp.756-762.
- [32] Moghadam, L.N. and Ranjbar, Z.R., 2019. Cost-efficient solar cells using nanocrystalline perovskite La (Fe and Mn) O₃ and candle soot: theory and experiment. *Journal of Alloys and Compounds*, 785, pp.117-124.
- [33] Namisi, M.M., Musembi, R.J., Mulwa, W.M. and Aduda, B.O., 2023. DFT study of cubic, tetragonal and trigonal structures of KGeCl₃ perovskites for photovoltaic applications. *Computational Condensed Matter*, 34, p.e00772.
- [34] Siddique, M.A.F. and Rahman, A.S.M.S., 2024. The SCAPS-1D simulation of non-toxic KGeCl₃ perovskite from DFT derived properties. *Materials Science and Engineering: B*, 303, p.117268.
- [35] Shrivastav, N., Hamid, M.A., Madan, J. and Pandey, R., 2024. Exploring KGeCl₃ material for perovskite solar cell absorber layer through different machine learning models. *Solar Energy*, 278, p.112784.
- [36] Wu, C., Zhang, Q., Liu, Y., Luo, W., Guo, X., Huang, Z., Ting, H., Sun, W., Zhong, X., Wei, S. and Wang, S., 2018. The dawn of lead-free perovskite solar cell: highly stable double perovskite Cs₂AgBiBr₆ film. *Advanced Science*, 5(3), p.1700759.
- [37] Lei, L.Z., Shi, Z.F., Li, Y., Ma, Z.Z., Zhang, F., Xu, T.T., Tian, Y.T., Wu, D., Li, X.J. and Du, G.T., 2018. High-efficiency and air-stable photodetectors based on lead-free double perovskite Cs₂AgBiBr₆ thin films. *Journal of Materials Chemistry C*, 6(30), pp.7982-7988.
- [38] McClure, E.T., Ball, M.R., Windl, W. and Woodward, P.M., 2016. Cs₂AgBiX₆ (X=Br, Cl): new visible light absorbing, lead-free halide perovskite semiconductors. *Chemistry of Materials*, 28(5), pp.1348-1354.
- [39] Filip, M.R., Hillman, S., Haghighirad, A.A., Snaith, H.J. and Giustino, F., 2016. Band gaps of the lead-free halide double perovskites Cs₂BiAgCl₆ and Cs₂BiAgBr₆ from theory and experiment. *The journal of physical chemistry letters*, 7(13), pp.2579-2585.
- [40] Wei, F., Deng, Z., Sun, S., Zhang, F., Evans, D.M., Kieslich, G., Tominaka, S., Carpenter, M.A., Zhang, J., Bristowe, P.D. and Cheetham, A.K., 2017. Synthesis and properties of a lead-free hybrid double perovskite: (CH₃NH₃)₂AgBiBr₆. *Chemistry of Materials*, 29(3), pp.1089-1094.
- [41] Fan, P., Peng, H.X., Zheng, Z.H., Chen, Z.H., Tan, S.J., Chen, X.Y., Luo, Y.D., Su, Z.H., Luo, J.T. and Liang, G.X., 2019. Single-source vapor-deposited Cs₂AgBiBr₆ thin films for lead-free perovskite solar cells. *Nanomaterials*, 9(12), p.1760.

- [42] Pandey, N., Neelu, N. and Chakrabarti, S., 2023. Room temperature synthesis of double perovskite Cs₂AlBiCl₆ for photovoltaic applications. *Optical Materials*, 137, p.113570.
- [43] Verschraegen, J. and Burgelman, M., 2007. Numerical modeling of intra-band tunneling for heterojunction solar cells in SCAPS. *Thin Solid Films*, 515(15), pp.6276-6279.
- [44] Husainat, A., Ali, W., Cofie, P., Attia, J. and Fuller, J., 2019. Simulation and analysis of methylammonium lead iodide (CH₃NH₃PbI₃) perovskite solar cell with Au contact using SCAPS 1D simulator. *American Journal of Optics and Photonics*, 7(2), p.33.
- [45] Belarbi, M., Zeggai, O. and Louhibi-Fasla, S., 2022. Numerical study of methylammonium lead iodide perovskite solar cells using SCAPS-1D simulation program. *Materials Today: Proceedings*, 51, pp.2115-2119.
- [46] Al-Saban, O., Alkadi, M., Qaid, S.M., Ahmed, A.A.A. and Abdellatif, S.O., 2024. Machine learning algorithms in photovoltaics: evaluating accuracy and computational cost across datasets of different generations, sizes, and complexities. *Journal of Electronic Materials*, 53(3), pp.1530-1538.
- [47] Chicco, D., Warrens, M.J. and Jurman, G., 2021. The coefficient of determination R-squared is more informative than SMAPE, MAE, MAPE, MSE and RMSE in regression analysis evaluation. *Peerj computer science*, 7, p.e623.
- [48] Termtanun, M., 2013. Photocatalytic degradation of pesticides using TiO₂ nanoparticles (Doctoral dissertation, University of Nottingham).
- [49] Rocha, F.S., Gomes, A.J., Lunardi, C.N., Kaliaguine, S. and Patience, G.S., 2018. Experimental methods in chemical engineering: Ultraviolet visible spectroscopy—UV-Vis. *The Canadian Journal of Chemical Engineering*, 96(12), pp.2512-2517.
- [50] Tare, M., Puli, O.R., Oros, S.M. and Singh, A., 2009. Drosophila adult eye model to teach Scanning Electron Microscopy in an undergraduate cell biology laboratory. Drosophila Information Service, 92.
- [51] Ojeda, J.J. and Dittrich, M., 2012. Fourier transform infrared spectroscopy for molecular analysis of microbial cells. *Microbial systems biology: methods and protocols*, pp.187-211.
- [52] El-Ahmar, M.H., El-Sayed, A.H.M. and Hemeida, A.M., 2016, December. Mathematical modeling of Photovoltaic module and evalute the effect of varoius parameters on its performance. In 2016 Eighteenth International Middle East Power Systems Conference (MEPCON)2016, pp. 741-746.
- [53] Leary, G., Switzer, G., Kuntz, G. and Kaiser, T., 2016, June. Comparison of xenon lamp-based and led-based solar simulators. In 2016 IEEE 43rd Photovoltaic Specialists Conference (PVSC)2016, pp. 3062-3067.

CHAPTER 4

STUDY OF VARIOUS PARAMETERS AFFECTING THE DIFFERENT PHOTOVOLTAIC PARAMETERS OF PEROVSKITE SOLAR CELLS BY SCAPS-1D

- \succ The SCAPS-1D simulation tool was used to study the effects of absorber layer thickness, operating temperature, and defect density (N_t) on PSC performance.
- Three PSC architectures were simulated: FTO/TiO₂/CH₃NH₃SnI₃/Cu₂O/Au, FTO/TiO₂/CH₃NH₃GeI₃/Cu₂O/Au, and FTO/TiO₂/CH₃NH₃PbI₃/Cu₂O/Au, with TiO₂ as the ETL and Cu₂O as the HTL.
- ➤ Optimized parameters led to a maximum PCE of 6.15 % for CH₃NH₃SnI₃, 20.90 % for CH₃NH₃GeI₃, and 31.55 % for CH₃NH₃PbI₃ PSCs.
- ➤ Sn and Ge-based PSCs are promising eco-friendly alternatives to toxic Pb-based PSCs, with the Ge-based PSC proposed as a potential replacement for Pb-based devices.

4.1 Introduction

The impact of various parameters on performance of a solar cell were studied like thicknesses of layer, N_t and operating temperature. The solar cell simulation provided that the optimum value of thickness of CH₃NH₃GeI₃ perovskite layer is approximately 600 nm. Ge-based PSCs along Cu₂O and DPBTTT-14 as HTM showed that PCE reached to 21 % [1]. whereas in this simulation the maximum PCE achieved is 20.90 % for CH₃NH₃GeI₃. It has been observed in simulation that efficiency of solar cells can be extended to some limit by changing the doping concentration and electron affinity of the buffer and HTM, whereas the deduction of Nt of the absorber layer increases the solar cell efficiency. By optimizing the N_t of perovskite absorber layer, devices achieve great outcomes such as efficiency of 23.36 % [2]. A strong or enduring halide perovskite architecture must keep cations along suitable ionic size, as reflected through geometrical constant t, is called as the tolerance factor and can be used as a measure of deformation of a perovskite from optimal cubic. The t ranges between 0.8 to 1.0 and the equation for tolerance factor is $t = (r_A + r_O)/\sqrt{2(r_B + r_O)}$, where r_A , r_B , and r_O are ionic radii of A, B, and O, respectively [3]. In planar heterojunction structure of Sn-based PSC, CuSbS₂ employed at first as HTL in combination with MASnI₃ absorber layer in view of this structure because of that implicit characteristic (high V_{OC}) than unstable and expensive Spiro-MeOTAD. By adoption of CuSbS₂ as a HTL in solar cell structure, results are adequate with J_{SC} of 31.7 mA/cm², V_{OC} of 0.936 V, FF of 81.1% and maximum PCE of 24.1 % [4]. The simulation was done and the device achieved results with V_{OC} of 0.58 V, J_{SC} of 28.42 mA/cm², FF of 45.41 %, and maximum efficiency of 7.49 % for CH₃NH₃SnI₃ [5]. Whereas in present simulation maximum PCE of 6.15 % is obtained for CH₃NH₃SnI₃. The simulation was performed for CH₃NH₃PbI₃ the outcomes were V_{OC} of 1.52 V, J_{SC} of 25.60 mA/cm², FF 81.58 %, and PCE was 31.77 % [6]. Whereas in present work maximum PCE of 31.55 % is obtained for CH₃NH₃PbI₃. In this study the simulated PSCs have shown different variation in their PV parameters with temperature, N_t and thickness. In Ge-based PSC the PCE increases with increase of thickness whereas in tin-based PSC the PCE decreases with increase of thickness, the PCE of all PSCs decrease with increase in temperature and PCE of all the PSCs decrease for increase in N_t. This is an excellent piece of work that shows that lead free PSCs can achieve performance levels similar to Pb-based PSC. An analysis of change in thickness of absorber layer, temperature which ranges between 300-480 K and variation in N_t of absorber layer also has been done.

4.2 Simulation Procedure and Device Architecture

The data of different parameters are chosen based on past theoretical [1,2,7] and experimental studies [8-10]. The SCAPS-1D (version 3.3.10) has been employed for simulation [11]. First perovskite solar cell structure is formed with CH₃NH₃SnI₃ perovskite material with layer architecture: glass substrate/TCO/ TiO₂/ CH₃NH₃SnI₃/ Cu₂O/ Au-Metal, second PSC consist of CH₃NH₃GeI₃ absorber material with layer architecture: glass substrate/TCO/ TiO₂/CH₃NH₃GeI₃/ Cu₂O/ Au-Metal and third PSC consist of CH₃NH₃PbI₃ absorber material with layer architecture: glass substrate/TCO/ TiO₂/CH₃NH₃PbI₃/ Cu₂O/ Au-Metal as shown in Fig. 4.1. The TCO layer in the structure is FTO. The simulations were run at 300 K using a "air mass 1.5 global" spectrum and a light power of 1000 W/m². The work is dependent on

alteration in thickness of absorber layer, N_t of absorber layer, and operating temperature at which simulation of the proposed solar cell has been done. The performance outcome of the solar cells has been reflected by the I–V characteristics of the solar cell which represents the following PV parameters: J_{SC} , FF, V_{OC} , and PCE. Procedure of simulation is shown in Fig. 4.2. All the input data used in SCAPS simulation obtained from experimental and theoretical work enclosed is in Table 4.1 for $CH_3NH_3SnI_3$ (cell-1), $CH_3NH_3GeI_3$ (cell-2) and for $CH_3NH_3PbI_3$ (cell-3) in Table 4.2.

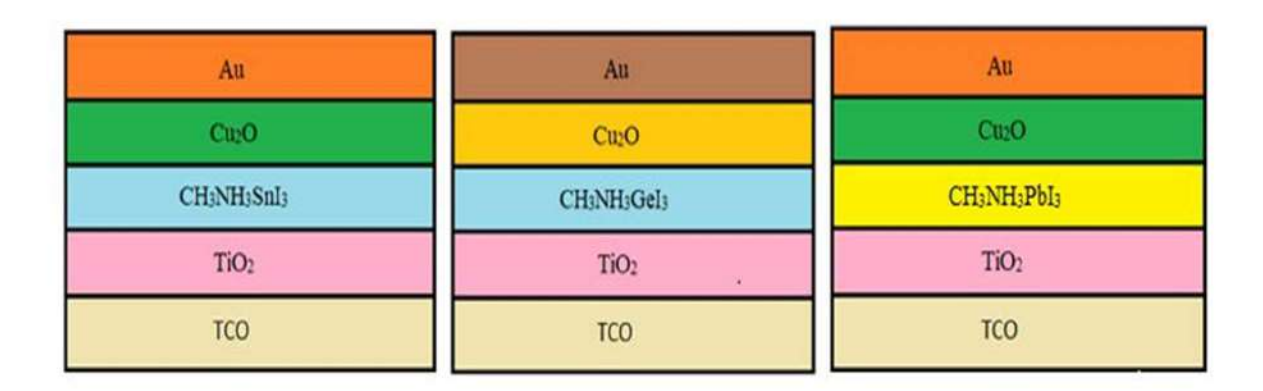


Figure 4.1 Structure of the Simulated model of CH₃NH₃SnI₃, CH₃NH₃GeI₃ and CH₃NH₃PbI₃ PSC.

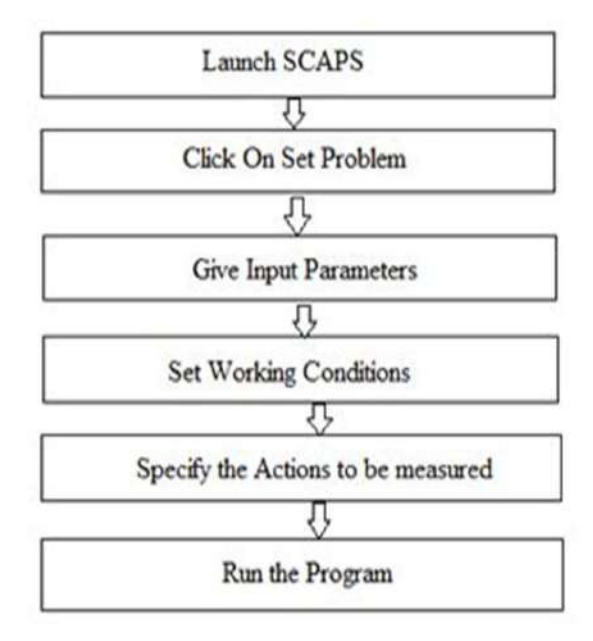


Figure 4.2 SCAPS-1D software simulation procedure.

Table 4.1 Various parameters employed in simulation of cell 1 and cell 2.

Cell 1 Cell 2 FTO [9] CH₃NH₃SnI₃ Cu₂O [10] FTO [14-CH₃NH₃GeI₃ [1] Parameter TiO₂ [2] TiO₂ [7] Cu₂O [10] [8,12-13] 15] Thickness (µm) 0.5 0.03 0.345 0.350 0.400 0.100 0.400 0.350 3.5 3.2 1.3 2.17 3.5 3.26 1.9 2.17 Eg (eV) 3.2 $\chi\left(eV\right)$ 4.0 4.26 [8] 4.1 3.2 4.0 4.2 3.98 9.0 9.0 8.2 7.11 9.0 10 10 7.11 N_C (cm⁻³) 2.2×10^{18} 2.0×10^{18} 10^{18} 2.02×10^{17} 2.2×10^{18} 2.2×10^{18} 10^{16} 2.02×10^{17} 1.8×10^{19} 10^{18} 10^{16} 1.1×10^{19} 1.8×10^{19} 1.1×10^{19} 1.8×10^{18} 1.8×10^{19} Nv (cm⁻³) μ_n (cm²/Vs) 20 20 1.6 200 20 100 162×10^3 200 80 101×10^{3} 80 μ_p (cm²/Vs) 10 10 1.6 10 25 1×10^{18} 1×10^{16} 1×10^{19} 1×10^{19} N_D (cm⁻³) 0 10^{9} 0 1×10^{15} 1×10^{18} 10^{9} 1×10^{18} N_A (cm⁻³) 0 0 10^{14} N_t (cm⁻³) 1×10^{15} 4.5×10^{17} 1×10^{14} 1×10^{14}

Table 4.2 Various parameters employed in simulation of cell 3.

Parameter	FTO [14-15]	TiO ₂ [16]	CH ₃ NH ₃ PbI ₃ [16]	Cu ₂ O [10]
Thickness (μm)	0.400	0.100	0.400	0.350
Eg (eV)	3.5	3.2	1.55	2.17
$\chi \left(eV\right)$	4.0	4.26	3.9	3.2
ε	9.0	50	30	7.11
N_C (cm ⁻³)	2.2×10^{18}	2.0×10^{18}	2.2×10^{18}	2.02×10^{17}
N_V (cm ⁻³)	1.8×10^{18}	1.8×10^{19}	1×10^{18}	1.1×10^{19}
$\mu_n (cm^2/Vs)$	20	2×10^4	2.2	200
$\mu_p (cm^2/Vs)$	10	1×10^3	2.2	80
N_D (cm ⁻³)	1×10^{19}	6×10^{19}	9×10^{20}	0
N_A (cm ⁻³)	0	0	0	1×10^{18}
N_t (cm ⁻³)	-	1×10^{15}	8.5×10^{13}	1×10^{14}

4.3 Result and Discussion

4.3.1 Effect of Change in Thickness

The thickness of the $CH_3NH_3SnI_3$ layer has exhibited a straight relation with the evaluation of the outcomes of PSC through its effect on the charge carrier's diffusion length. It is known to us that as the thickness of the layer decreases, absorption rate also lowers. This results in a decrease in photocurrent and therefore PCE of the solar cell also reduces from 200-1200 nm. Both J_{SC} and PCE parameters decrease exponentially for enlargement in the thickness from 200 to 1200 nm. Optimum thickness value for Ge-based solar cells is 600 nm because FF is maximum at 600 nm and beyond that it falls. Fall in FF beyond 600 nm is 2-3 % [1]. The maximum efficiency of PSC goes up to 15.83 % together with V_{OC} is 0.78 V, J_{SC} is 27.05 mA/cm² and FF is 74.8 % for 200 nm. The FF shows a monotonic decrement with the rise in thickness and also heads for enhancement gradually when thickness becomes greater than 700 nm [17]. The Optimum thickness value for Sn-based PSC is 200 nm and highest efficiency achieved is 7.64 % for ETM= 30 nm and HTM= 350 nm [5]. In this work maximum PCE of 22.57 % is achieved at the thickness of 600 nm for $CH_3NH_3GeI_3$ layer and for the $CH_3NH_3PbI_3$ layer 700 nm is optimized value for thickness at ETM = 100 nm and HTM = 350 nm depicted Fig. 4.3 [18]. The change in other PV parameters is also shown in Fig. 4.3.

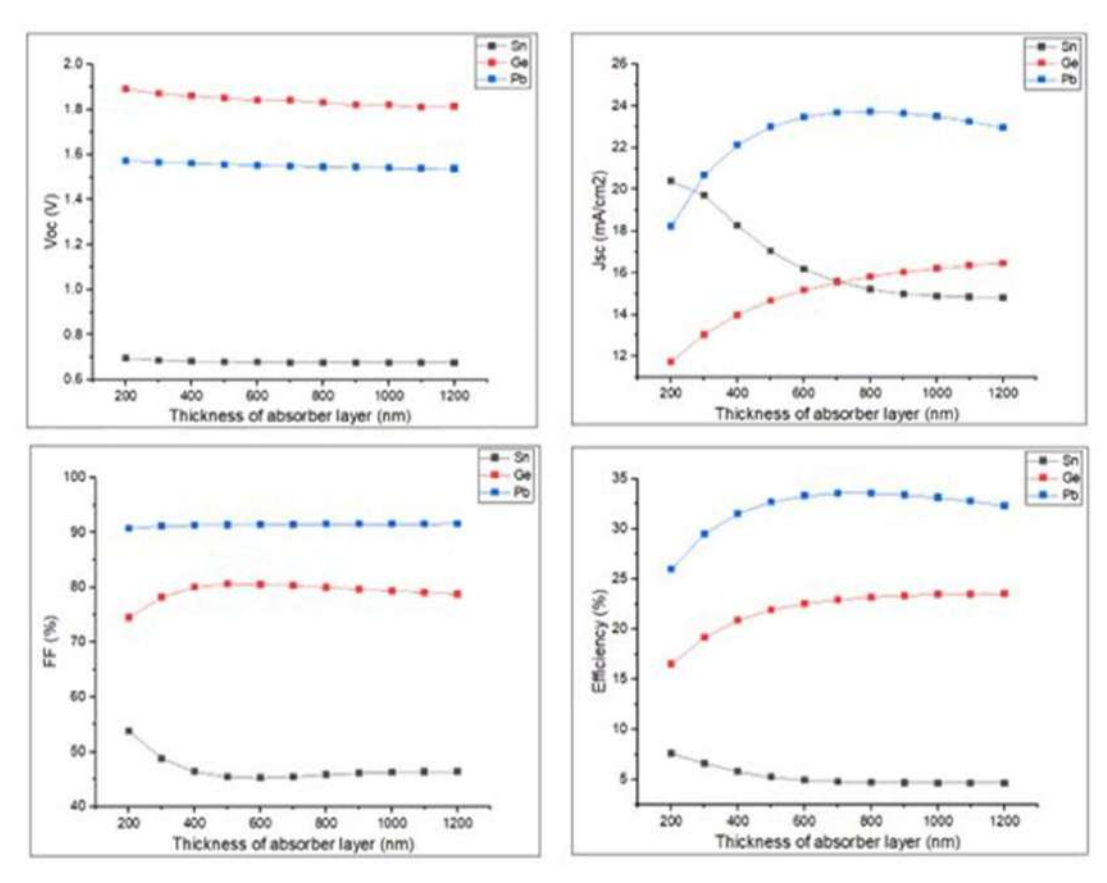


Figure 4.3 Impact of thickness on PV parameters of CH₃NH₃SnI₃, CH₃NH₃GeI₃ and CH₃NH₃PbI₃ PSCs.

4.3.2 Effect of Variation in Operating Temperature

To examine the impact of temperature on the efficiency of solar cells, the working temperature has been varied in the range of 300 to 480 K. Decline in the performance with temperature increase is related to a decrease in diffusion length of charge carriers. Several solar cell architectures show the instability of their overall performance because of deformation among layers at high temperatures. In Ge-based PSC, fall in efficiency with temperature is 1.1 %, while for Pb-based PSC, fall is 4.6 %. Hence Ge-based PSC is more stable against temperature variation though PCE is maximum for ETM= 100 nm and HTM= 350 nm [1]. When the enhancement of temperature occurs, the PCE drops significantly from 24.81 % (at 300 K) to 17.05 % (at 480 K) [17]. We have obtained maximum efficiency of 20.90 % for CH₃NH₃GeI₃ PSC at the operating temperature of 300 K and the maximum PCE is 6.20 % for CH₃NH₃SnI₃ PSC at an operating temperature of 298 K which is shown below in Fig. 4.4 [5]. In simulation of CH₃NH₃PbI₃ PSC the optimized value of temperature is 280 K [18]. V_{OC} is decreasing with an increase in the operating temperature for all PSCs. The impact of operating temperature on other PV parameters together with Voc, Jsc, and FF is shown below in fig 3.4. In Sn-based PSC there is a fall of 45.7 % for efficiency, 36.63 % for V_{OC} and 5.8 % for FF for the temperature ranges between 280 K to 400 K. In Ge-based PSC there is a fall of 0.52 % for efficiency, 8.40 % for V_{OC} for the temperature ranges between 280 K to 400 K. In Pb-based PSC there is a fall of 4.6 % for efficiency, 2.39 % for V_{OC} and 3.21 % for FF for the temperature ranges between 280 K to 400 K. Hence this shows that the Ge-based PSC has better stability as compared to Pb-based PSC.

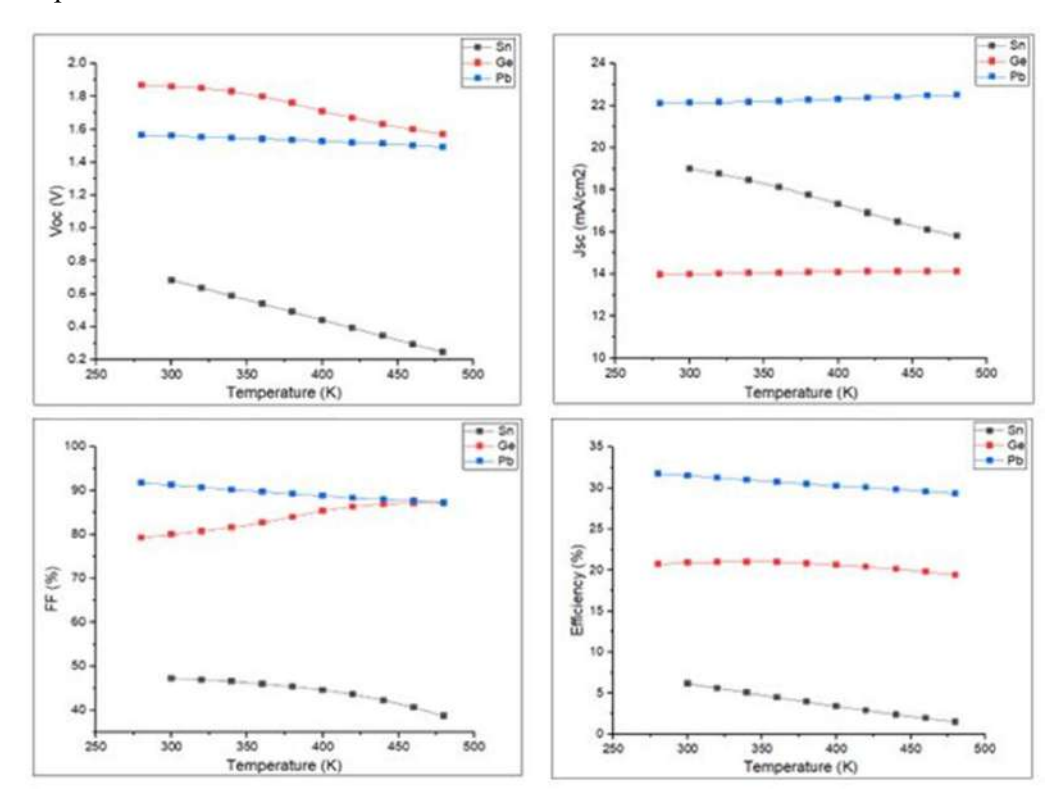


Figure 4.4 Change in the PV parameters of CH₃NH₃SnI₃, CH₃NH₃GeI₃ and CH₃NH₃PbI₃ PSCs with operating temperature.

4.3.3 Impact of Change in Defect Density

The optimized defect density is 4.5×10^{13} cm⁻³ for CH₃NH₃GeI₃ perovskite layer at which it has achieved the maximum PCE of 21.60 % [1], CH₃NH₃SnI₃ perovskite layer has achieved the highest PCE of 23.85 % at which the defect density is 4.5×10^{14} cm⁻³ as demonstrated in Fig. 4.5 [19]. For CH₃NH₃SnI₃ perovskite layer when defect density is increased, the unwanted recombination rate increases as the defects formed the dangling bonds, which behave as the trap state for the photo-generated charge carriers. Because of this short circuit current decreased, which is lastly responsible for decreasing FF of solar devices. The device PCE also decreased from 24.5 % to 16.17 %, when amphoteric N_t was enhanced from 10¹³ to 10¹⁷ cm⁻³. Such an increasing amount of recombination resulted in a sharp fall in solar cell efficiency [19]. The CH₃NH₃PbI₃ layer has obtained the maximum PCE of 32.24 % at defect density of 4.5×10¹³ cm⁻³ [6]. The change in different PV parameters V_{OC}, J_{SC}, and FF with defect density for CH₃NH₃SnI₃, CH₃NH₃GeI₃ and for CH₃NH₃PbI₃ PSC the effect of N_t on PV parameters is demonstrated in Fig. 4.5. In Sn-based PSC 74.56 % fall in the PCE, In Ge-based PSC 26.38 % fall in the PCE and for Pb-based PSC 96.6 % fall in the efficiency with change in the defect density from 4.5×10^{13} to 4.5×10^{17} cm⁻³. This represents that Ge-based PSC has better stability with defect density than Pb-based PSC. This concludes that Ge-based PSC has potential to replace Pb-based PSC. Optimized value of various variable and PV parameters shown below in Table 4.3. Comparison between present and previously reported studies at 300 K demonstrated in Table 4.4.

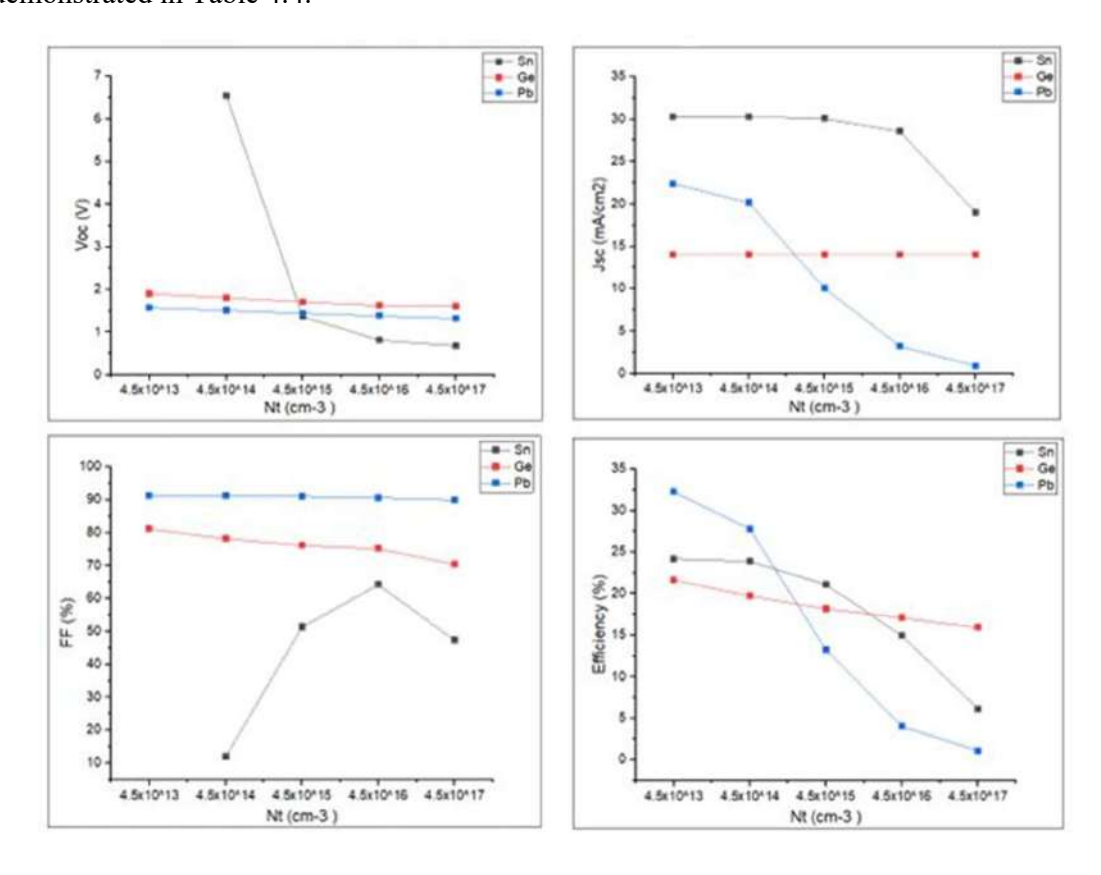


Figure 4.5 Impact of N_t on the performance of CH₃NH₃SnI₃, CH₃NH₃GeI₃ and CH₃NH₃PbI₃ PSCs.

Table 4.3 Optimized value of different variable and PV parameters.

PSC	Thickness (nm)	Temperature (K)	Defect Density (cm ⁻³)	Voc (V)	J _{SC} (mA/cm ²)	FF (%)	PCE (%)
Sn	200	298	4.5 ×10 ¹⁴	2.40	25.43	36.06	22.03
Ge	600	300	4.5×10^{13}	1.88	15.16	81.95	23.43
Pb	700	280	4.5×10^{13}	1.57	24.22	92.00	32.01

Table 4.4 Device output of previous reported theoretical studies and outcome of present simulation for PSCs (at 300 K).

	CH ₃ NH ₃ Snl	[3	CH ₃ NH ₃ Gel ₃	,	CH ₃ NH ₃ PbI ₃	3
Parameter	Simulation Reports [5]	Present Simulation	Simulation Reports [1]	Present Simulation	Simulation Reports [6]	Present Simulation
	Reports [3]	Siliulation	Reports [1]	Simulation	reports [0]	Simulation
Voc (V)	0.58	0.68	1.92	1.86	1.52	1.56
J_{SC} (mA/cm ²)	28.42	19.00	14.20	13.99	25.60	22.13
FF (%)	45.41	47.31	79.28	80.04	81.58	91.33
PCE (%)	7.49	6.15	21.60	20.90	31.77	31.55

4.4 Summary

In this work we have optimized various parameters of PSC using SCAPS-1D software. The performance of these PSCs was found comparable to lead-based PSC. We have examined the impact of operating temperature, thickness, and N_t of all PSCs. The simulation was performed on the cell architecture of FTO/TiO₂/absorber layer/Cu₂O/Au. The optimized value of absorber layer thickness is 200 nm for CH₃NH₃SnI₃, 600 nm for CH₃NHGeI₃ and 700 nm for CH₃NH₃PbI₃ perovskite solar cell. The optimal value of Operating temperature is 298 K for Sn-based PSC, 300 K for Ge-based PSC and for lead-based PSC it is 280 K. The optimized defect density value of Sn-based PSC is 4.5×10^{14} cm⁻¹³, 4.5×10^{13} cm⁻³ for both Ge-based and Pb-based PSC. The optimum value of operating temperature, thickness, and N_t is helpful in the fabrication of high PCE solar cells. It was observed that Ge-based PSC exhibited comparatively high performance. The maximum PCE of 20.90 % was obtained at 300 K with V_{OC} of 1.86 V, FF is 80.04 %, and J_{SC} is 13.99 mA/cm² for Ge-based PSC. Whereas Sn-based perovskite has achieved the PCE of 6.15 % and other PV parameters such as V_{OC} of 0.68 V, FF 47.31%, J_{SC} is 19.00 mA/cm² by employing SCAPS-1D. The simulation outcome of Pb-based PSC is as follows: the maximum PCE of 31.55 %, V_{OC} of 1.56 V, FF is 91.33 % and J_{SC} is 22.13 mA/cm². The simulation results provide the best approach for higher PCE solar cell device fabrication. We have observed that N_t, thickness, and the operating temperature have a deleterious impact on PSCs up to a certain value. The results demonstrate that Sn and Ge-based PSCs are a forthcoming possibility to the PV device with regard to environmental sustainability, as Pbbased PSCs are toxic in nature. We propose an optimized Ge-based PSC as a potential candidate to replace Pb-based PSC. Further research in this direction is needed to harness the full potential of CH₃NH₃GeI₃ as an efficient replacement of CH₃NH₃PbI₃ as a perovskite absorber layer in perovskite solar cells.

4.5 REFERENCES

- [1] Kanoun, A.A., Kanoun, M.B., Merad, A.E. and Goumri-Said, S., 2019. Toward development of high-performance perovskite solar cells based on CH₃NH₃GeI₃ using computational approach. *Solar Energy*, 182, pp.237-244.
- [2] Du, H.J., Wang, W.C. and Zhu, J.Z., 2016. Device simulation of lead-free CH₃NH₃SnI₃ perovskite solar cells with high efficiency. *Chinese Physics B*, 25(10), p.108802.
- [3] Jong, U.G., Yu, C.J., Kye, Y.H., Choe, Y.G., Hao, W. and Li, S., 2019. First-principles study on structural, electronic, and optical properties of inorganic Ge-based halide perovskites. *Inorganic chemistry*, 58(7), pp.4134-4140.
- [4] Devi, C. and Mehra, R., 2019. Device simulation of lead-free MASnI₃ solar cell with CuSbS₂ (copper antimony sulfide). *Journal of materials science*, 54, pp.5615-5624.
- [5] Kumar, M., Kumar, A., Raj, A., Sati, P.C., Sahni, M. and Anshul, A., 2022. Organic-inorganic perovskite-based solar cell designs for high conversion efficiency: A comparative study by SCAPS simulation. *Materials Today: Proceedings*, 49, pp.3081-3087.
- [6] Mandadapu, U., Vedanayakam, S.V. and Thyagarajan, K., 2017. Simulation and analysis of lead based perovskite solar cell using SCAPS-1D. *Indian J. Sci. Technol*, 10(1), pp.1-8.
- [7] Xosrovashvili, G. and Gorji, N.E., 2013. Numerical analysis of TiO₂/Cu₂ZnSnS₄ nanostructured PV using SCAPS-1D. *Journal of Modern Optics*, 60(11), pp.936-940.
- [8] Stoumpos, C.C., Malliakas, C.D. and Kanatzidis, M.G., 2013. Semiconducting tin and lead iodide perovskites with organic cations: phase transitions, high mobilities, and near-infrared photoluminescent properties. *Inorganic chemistry*, 52(15), pp.9019-9038.
- [9] Karimi, E. and Ghorashi, S.M.B., 2017. Investigation of the influence of different hole-transporting materials on the performance of perovskite solar cells. *Optik*, 130, pp.650-658.
- [10] Hossain, M.I., Alharbi, F.H. and Tabet, N., 2015. Copper oxide as inorganic hole transport material for lead halide perovskite based solar cells. Solar energy, 120, pp.370-380.
- [11] Burgelman, M., Nollet, P. and Degrave, S., 2000. Modelling polycrystalline semiconductor solar cells. *Thin solid films*, 361, pp.527-532.
- [12] Noel, N.K., Stranks, S.D., Abate, A., Wehrenfennig, C., Guarnera, S., Haghighirad, A.A., Sadhanala, A., Eperon, G.E., Pathak, S.K., Johnston, M.B. and Petrozza, A., 2014. Lead-free organic—inorganic tin halide perovskites for photovoltaic applications. *Energy & Environmental Science*, 7(9), pp.3061-3068.
- [13] Chen, Q.Y., Huang, Y., Huang, P.R., Ma, T., Cao, C. and He, Y., 2015. Electronegativity explanation on the efficiency-enhancing mechanism of the hybrid inorganic–organic perovskite ABX₃ from first-principles study. *Chinese Physics B*, 25(2), p.027104.
- [14] Sobayel, K., Akhtaruzzaman, M., Rahman, K.S., Ferdaous, M.T., Al-Mutairi, Z.A., Alharbi, H.F., Alharthi, N.H., Karim, M.R., Hasmady, S. and Amin, N., 2019. A comprehensive defect study of tungsten disulfide (WS₂) as electron transport layer in perovskite solar cells by numerical simulation. *Results in physics*, 12, pp.1097-1103.
- [15] Sobayel, K., Shahinuzzaman, M., Amin, N., Karim, M.R., Dar, M.A., Gul, R., Alghoul, M.A., Sopian, K., Hasan, A.K.M. and Akhtaruzzaman, M., 2020. Efficiency enhancement of CIGS solar cell by WS₂ as window layer through numerical modelling tool. *Solar Energy*, 207, pp.479-485.

- [16] Husainat, A., Ali, W., Cofie, P., Attia, J. and Fuller, J., 2019. Simulation and analysis of methylammonium lead iodide (CH₃NH₃PbI₃) perovskite solar cell with Au contact using SCAPS 1D simulator. *American Journal of Optics and Photonics*, 7(2), p.33.
- [17] Yasin, S., Al Zoubi, T. and Moustafa, M., 2021. Design and simulation of high efficiency lead-free heterostructure perovskite solar cell using SCAPS-1D. *Optik*, 229, p.166258.
- [18] Ouslimane, T., Et-Taya, L., Elmaimouni, L. and Benami, A., 2021. Impact of absorber layer thickness, defect density, and operating temperature on the performance of MAPbI₃ solar cells based on ZnO electron transporting material. *Heliyon*, 7(3).
- [19] Samiul Islam, M., Sobayel, K., Al-Kahtani, A., Islam, M.A., Muhammad, G., Amin, N., Shahiduzzaman, M. and Akhtaruzzaman, M., 2021. Defect study and modelling of SnX₃-based perovskite solar cells with SCAPS-1D. *Nanomaterials*, 11(5), p.1218.

CHAPTER 5

DEVICE MODELLING OF LEAD FREE (CH₃NH₃)₂CuX₄ BASED PEROVSKITE SOLAR CELLS USING SCAPS SIMULATION

- The Chapter explores Cu-based perovskite materials like $(CH_3NH_3)_2CuX_4$ or $(MA)_2CuX_4$ with $\int X = Cl_4$, Cl_2I_2 , and Cl_2Br_2 for use in PSCs using SCAPS-1D.
- The optimal absorber layer thicknesses were found to be 400 nm for $(MA)_2CuCl_4$, 500 nm for $(MA)_2CuCl_2I_2$, and 600 nm for $(MA)_2CuCl_2Br_2$, with a defect density of 1×10^{13} cm⁻³ at 300 K operating temperature.
- The optimum operating temperature for most PSCs was 300 K, except for the $C_{60}/(MA)_2CuCl_4/Cu_2O$ PSC, which performed best at 320 K with a 400 nm absorber layer.
- ➤ The highest power conversion efficiency (PCE) of 28.31% was achieved for the PCBM/(MA)₂CuCl₂Br₂/CuI configuration at 300 K.
- The study suggested that PCBM as ETL and CuI and Cu₂O as HTLs are most suitable for Cu-based PSCs.

5.1 Introduction

In the field of solar PV research, organic-inorganic perovskite materials are gaining considerable interest. These materials have a lot of potential as they are abundant and have easy processing techniques. Currently, in comparison with other perovskite materials, lead perovskites of methyl ammonium halide (CH₃NH₃PbX₃) are achieving higher power conversion efficiencies [1,1a]. Some of the factors associated with their superior PV performance are suitable band gap, high absorption coefficients and low N_t [2-5]. However, despite the several advantages, Pb-based PSCs are highly toxic, to entire ecosystem [6], Pbbased PSCs face stability issues [7]. There are many alternatives to Pb-based PSCs [8-12]. Sn²⁺ and Sb²⁺ exhibit low open circuit voltage whereas Ge²⁺ has stability issues due to oxidation. Therefore, exploration of transition metals has now gathered momentum. Many transition metals (e.g Fe²⁺, Cu²⁺, Zn²) are attractive alternatives as they are cost effective, earth abundant and low on toxicity. In this direction, Cu metal has also been investigated as a substitute for Pb. To the best of our knowledge there are only two studies that explored the application of copper as a Pb substitute [14,15]. Recently, PCE efficiencies up to 2.41% has been experimentally reported by Ahmed et. al. [15] by using Cu substituted lead perovskite materials ((MA)₂CuX₄) for solar cell fabrication. This Cu-based hybrid perovskite material also exhibits band gap flexibility with varying content of halides (X=Cl₄, Cl₂I₂, Cl₂Br₂). However, despite optimized Low PCE was attributed to factors such as recombination rate, absorption coefficient, surface roughness and thickness of perovskite films. Also, mismatch between the band levels of ETL and HTL with respect to perovskite absorber layer (PAL) was identified as an important functional parameter for low efficiency. Hence, proper alignment of energy band levels of all three layers is extremely crucial for efficient device performance. So there exists a need to carefully select and optimize ETL and HTL according to the properties of the perovskite absorber layer. (MA)₂CuX₄, TiO₂ and spiro-OMeTAD were used as ETL and HTL materials respectively, which are the traditional choices. However, other suitable alternatives are also available for this role. In this work, we have examined effect of different organic and inorganic ETL and HTL materials on the performance of (MA)₂Cucl₄, (MA)₂Cucl₂I₂, (MA)₂Cucl₂Br₂ based PSCs using SCAPS-1D simulation software. Simulation work also includes analysis and optimization of different device parameters (perovskite layer thickness, recombination rate, device temperature, R_S) for enhanced photovoltaic performance.

5.2 Device Architecture and Simulation

In this structure we have (MA)₂CuX₄ PAL with different halides groups such as Cl₄, Cl₂I₂, and Cl₂Br₂ are utilized in PSC with the thickness of 400 nm shown below in Table 5.1. In modelling of Cu-based PSC, the various ETLs and HTLs are employed for obtaining the maximum PCE with optimum value of absorber layer thickness. The thickness of three different ETLs such as PCBM, TiO₂ and C₆₀ with values of 500 nm, 40 nm and 50 nm respectively employed shown below in table 2. The various HTLs are employed for efficient PSC such as PEDOT: PSS, Cu₂O, CuI, and Spiro-OMeTAD. The thickness of the HTLs varies from 80 nm to 250 nm. In p-i-n devices, electrons are collected at the fluorine doped tin oxide (FTO) and holes at the metal back contact [16]. The SCAPS-1D software is employed for simulation. The software is numerically based on solving semiconductor, Poisson's, and continuity equations for both e⁻s

and h^+s . The basic structure of PSC consists of three different layers such as n-type ETL, PAL and p-type HTL demonstrated in Fig. 5.1. The primarily input data employed in simulation of various layers are enclosed in Table 5.1, 5.2 and 5.3 including thickness, band gap energy (Eg), electron affinity (χ), relative dielectric permittivity (ϵ_r), mobility of electron (μ_n), mobility of hole (μ_p) and N_t . This simulation is based on the change in thickness of absorber layer, operating temperature and N_t of different PSCs [17,18].

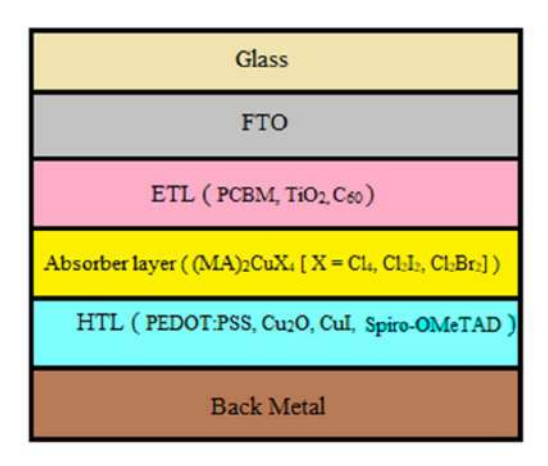


Figure 5.1 Architecture of the Simulated model of (MA)₂CuCl₄, (MA)₂CuCl₂I₂ and (MA)₂CuCl₂Br₂ PSC.

Table 5.1 Various input parameters of perovskite layers employed in simulation.

Parameter	(MA) ₂ CuCl ₄ [15]	$(MA)_2CuCl_2I_2$ [15]	$(MA)_2CuCl_2Br_2$ [15]
Thickness (μm)	0.400	0.400	0.400
Eg (eV)	2.36	1.99	1.04
$\chi \left(eV\right)$	2.92	3.9	3.8
$\epsilon_{ m r}$	25	20	15
N_C (cm ⁻³)	3.5×10^{20}	2.5×10^{20}	3.0×10^{18}
N_V (cm ⁻³)	3.5×10^{20}	2.5×10^{20}	4.0×10^{18}
$\mu_n (cm^2/Vs)$	10	14	15
$\mu_p (cm^2/Vs)$	10	14	15
N_D (cm ⁻³)	7.0×10^{14}	-	1.0×10^{10}
N_A (cm ⁻³)	7.0×10^{14}	6.0×10^{14}	1.0×10^{10}
N_t (cm ⁻³)	1×10^{13}	1×10^{13}	1×10^{13}

Table 5.2 Various input parameters employed in simulation of different ETLs.

Parameter	TiO ₂ [17,21]	PCBM [19,22]	C ₆₀ [20]
Thickness (μm)	0.040	0.500	0.050
Eg (eV)	3.2	2.1	1.7
$\chi \left(eV\right)$	3.9	3.9	3.9
$\epsilon_{ m r}$	9	3.9	4.2
$N_{\rm C}$ (cm ⁻³)	1×10^{21}	2.2×10^{19}	8.0×10^{19}
N_V (cm ⁻³)	2×10^{20}	2.2×10^{19}	8.0×10^{19}
$\mu_n (cm^2/Vs)$	20	0.001	8.0×10^{-2}
$\mu_p (cm^2/Vs)$	10	0.002	3.5×10^{-3}
N_D (cm ⁻³)	1×10^{19}	1×10^{19}	2.6×10^{17}
N_A (cm ⁻³)	-	-	-
N _t (cm ⁻³)	1×10^{15}	$1 \times 10^{9*}$	1×10^{14}

*In this work.

Table 5.3 Various input parameters employed in simulation of different HTLs.

Parameter	FTO [17,18]	CuI [23]	Spiro-OMeTAD [16,24]	Cu ₂ O [17,23]	PEDOT: PSS [19,20]
Thickness (µm)	0.400	0.100	0.213	0.250	0.080
Eg (eV)	3.5	3.1	3	2.17	2.2
$\chi \left(eV\right)$	4.0	2.1	2.2	3.2	2.9
$\epsilon_{ m r}$	9.0	6.5	3	7.11	3.0
N_C (cm ⁻³)	2.02×10^{18}	2.8×10^{19}	1×10^{19}	2.02×10^{17}	2.2×10^{15}
N_V (cm ⁻³)	1.8×10^{19}	1×10^{19}	1×10^{19}	1.1×10^{19}	1.8×10^{18}
$\mu_n (cm^2/Vs)$	20	100	10-4	200	1×10^{-2}
$\mu_p \ (cm^2/Vs)$	10	43.9	10 ⁻⁴	80	2×10^{-4}
N_D (cm ⁻³)	2×10^{19}	-	-	-	-
N_A (cm ⁻³)	0	1×10^{18}	2×10^{19}	1×10^{18}	10 ¹⁹
N_t (cm ⁻³)	1×10^{15}	1×10^{14}	1×10^{14}	1×10^{14}	1×10^{14}

5.3 Result and Discussion

5.3.1 Modulation of Various ETLs and HTLs to Impact Device Performance

In this study we have simulated different ETLs and HTLs, the ETLs are TiO₂, PCBM and C₆₀ with the E_g of 3.2 eV, 2.1 eV and 1.7 eV respectively. Four different HTLs employed in simulation are CuI, Cu2O, inorganic materials and Spiro-OMeTAD and PEDOT: PSS are organic materials. The bandgap energy for CuI is 3.1 eV, Cu₂O is 2.17 eV, Spiro-OMeTAD is 3 eV and for PEDOT: PSS is 2.2 eV shown in Table 5.3. The energy level diagram of ETL, PAL and HTL demonstrated in Fig. 5.2. The optimum thickness of each ETL was first found to be of 500 nm, 40 nm and 50 nm respectively by multiple simulations as depicted in Table 5.2. These values were then kept constant. For a particular PAL, all possible combinations of 3 ETLs and 4 HTLs are studied. Hence for each PAL, there are 12 combinations. Hence, the resulting PCEs are shown in the Table 5.4. Best two configurations for each perovskite are chosen for further evaluation through J-V characteristics. J-V characteristics for the best six configurations have been shown in Fig. 5.3. The variation of quantum efficiency with wavelength for various optimized Cu-based PSCs shown in Fig. 5.4. These Simulation outcomes demonstrated that (MA)₂CuCl₄ based PSC gives the maximum PCE is 18.41 % for PCBM as ETL and PEDOT: PSS as HTL. This can be attributed to high electrical conductivity of PCBM and the highest occupied molecular orbital (HOMO) level properly matching with PAL with their E_g difference of 0.74 eV. Similarly, by using (MA)₂CuCl₂I₂ as absorber layer PSC gives PCE of 17.38 % for Cu₂O with PCBM as ETL due to high hole mobility responsible for high performance of PSC and exact band alignment between HOMO level of PAL and Cu₂O [25-27]. However, the (MA)₂CuCl₂Br₂ based PSC gives the maximum PCE of 28.31 % which is highest among all of three Cu-based PSCs by employing PCBM as ETL and CuI as HTL [28]. The (MA)₂CuCl₂Br₂ PSC has a high absorption coefficient which is responsible for high value of current density (J_{SC}) resulting in high efficiency depicted in Fig. 5.5 [15]. Material with a low absorption coefficient, light is imperfectly absorbed, it should be large for high performance of PSC [29-30]. The absorption coefficient of (MA)₂CuCl₂Br₂ based PSC is greater than other two Cu-based PSCs hence the PCE of (MA)₂CuCl₂Br₂ based PSC is higher than the (MA)₂CuCl₂I₂ based PSC [15]. In addition, (MA)₂CuCl₂Br₂ absorber layer has an appropriate band gap (1.0–1.6 eV) that would maximize efficiency [31]. The band alignment is also a crucial factor for superior performance of (MA)₂CuCl₂Br₂ PSC as shown below in Fig. 5.6. The conduction band of the ETL is always less than the lowest unoccupied molecular orbital (LUMO) of the PAL. The difference between the valence band of ETL and HOMO level of PAL should be always high, which prevents the recombination in the PAL. In this simulation work we have employed various HTLs among which CuI is most suitable for obtaining high performance of Cu-based PSCs. The CuI layer as HTL is more appropriate than spiro-OMeTAD layer because of the high hole mobility and low hysteresis. The HOMO level of CuI and PEDOT: PSS has good band alignment with absorber layer of (MA)₂CuCl₂Br₂ based PSC therefore with CuI it has achieved best PCE but not for PEDOT: PSS because lower value of holes mobility (µ_p) than CuI. Hence, CuI is a more suitable HTL for achieving high efficiency for (MA)₂CuCl₂Br₂ based PSC. Furthermore, the CuI based PSCs exhibit good longterm stability in the ambient atmosphere because of its hydrophobic property [32]. The CuI has outstanding properties such as band matching with the PAL; a wide E_g of 3.1 eV; a high μ_p of 43.9 cm²/Vs, inexpensive; high chemical stability; and non-toxicity make CuI a good choice for HTL in PSCs. This numerical modelling helped in the investigation of the best ETL and

HTL combination with (MA)₂CuCl₂Br₂ based PSC for the high PCE. The optimized result of various ETLs and HTLs with Cu-based PSCs is shown below in Table 5.5.

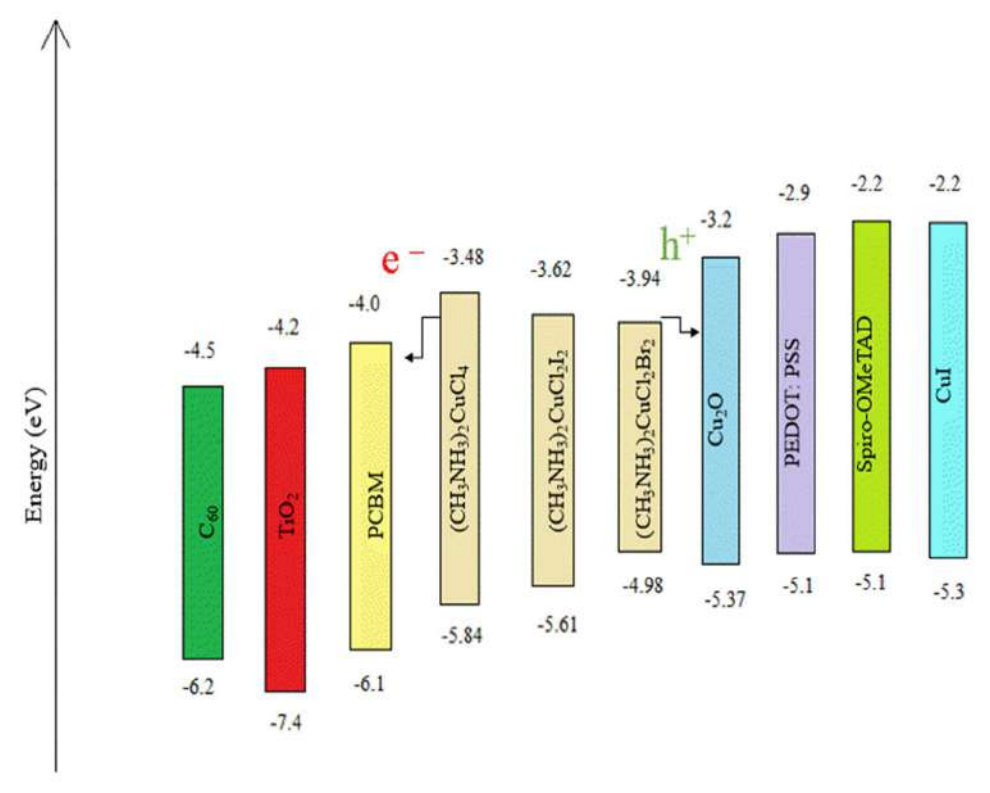


Figure 5.2 The energy level alignment between ETL, PAL and HTL materials.

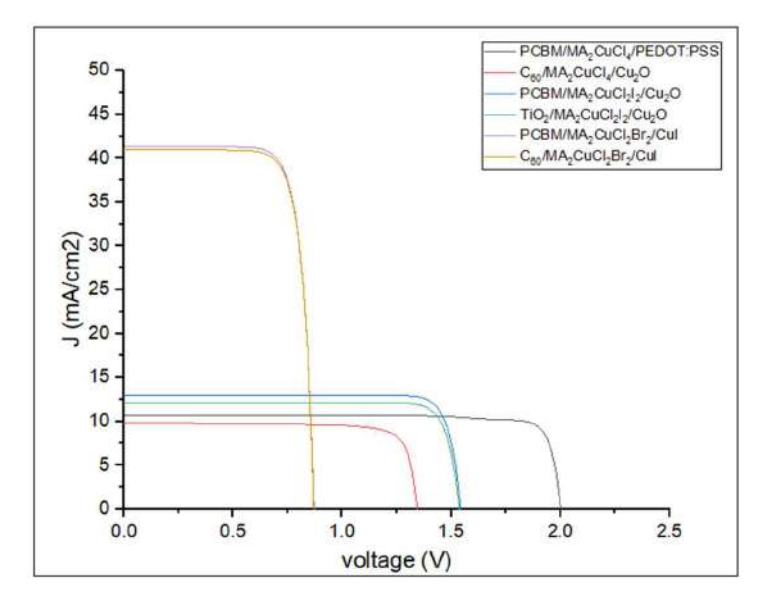


Figure 5.3 J-V characteristics of Cu-based PSCs.

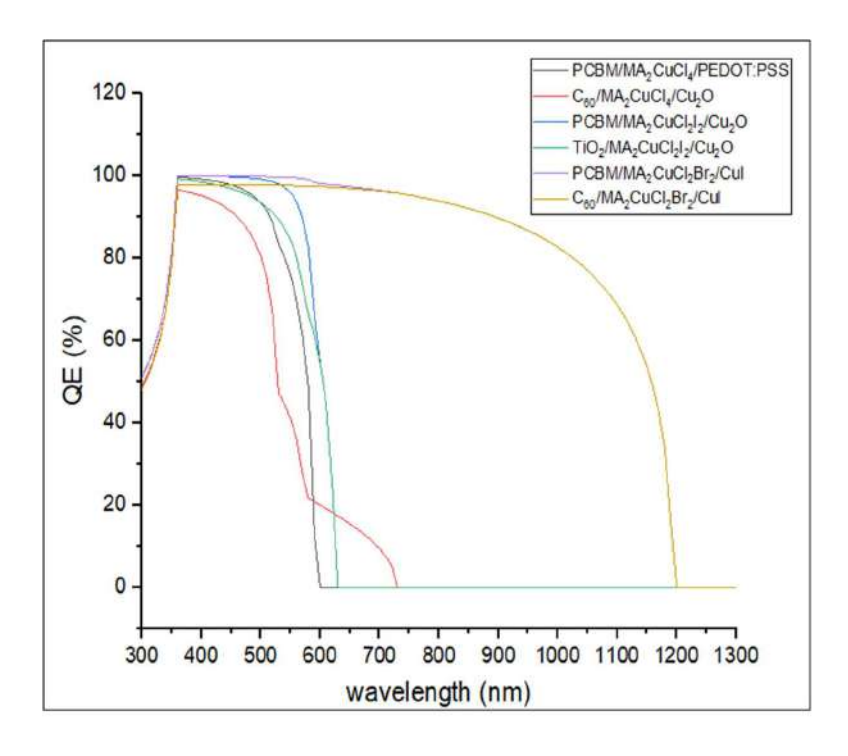


Figure 5.4 Quantum efficiency (QE) curve for Cu-based PSCs.

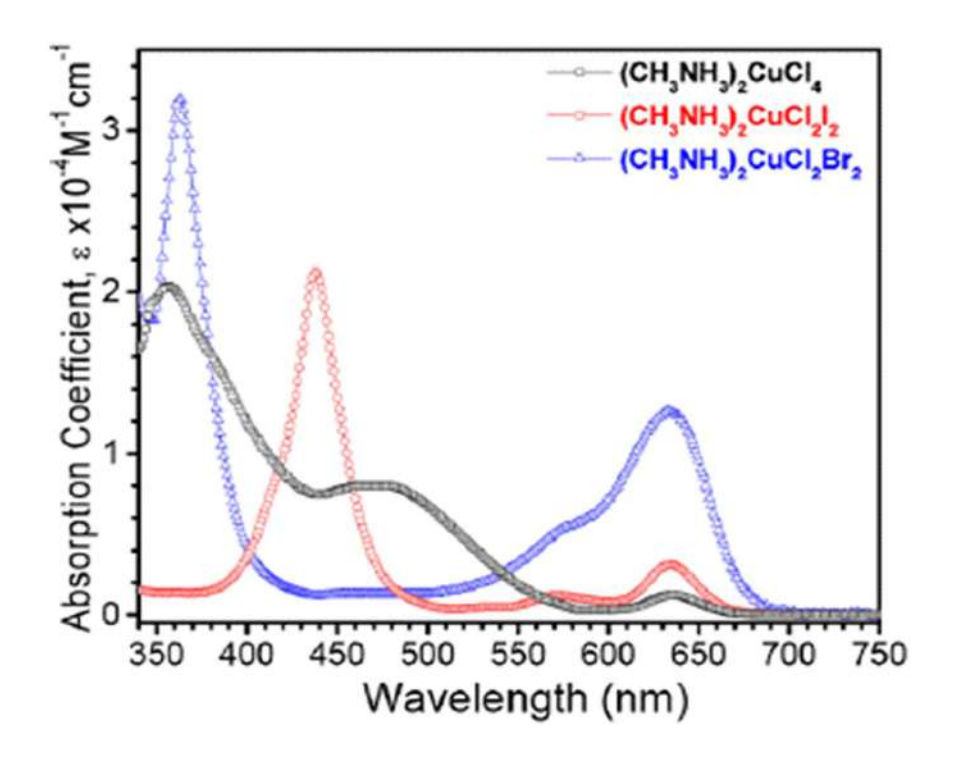


Figure 5.5 Absorption coefficient of Cu-based PSCs [15].

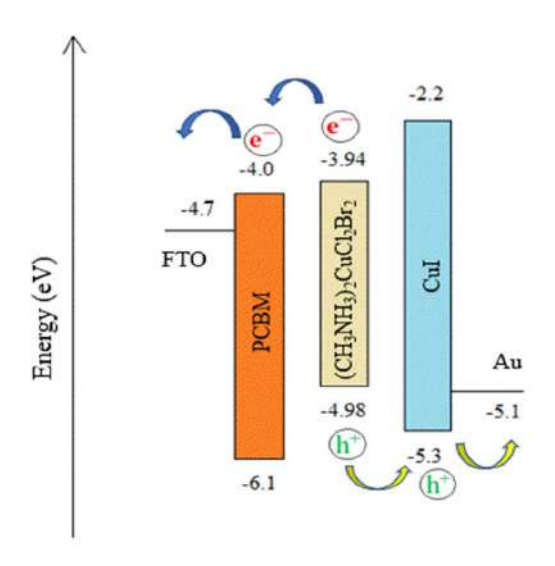


Figure 5.6 Band alignment diagram of optimized device.

Table 5.4 PCE (%) of various combinations of Cu-based PSC with different ETL and HTL.

	(MA)2CuCl4		(MA)2CuCl2I2		(MA)2CuCl2Br2		Br ₂		
HTL		ETL			ETL			ETL	
	TiO_2	C_{60}	PCBM	TiO_2	C_{60}	PCBM	TiO_2	C_{60}	PCBM
PEDOT: PSS	8.42	9.87	18.41	13.44	11.67	14.94	12.20	22.45	22.53
Spiro-OMeTAD	7.81	9.47	18.40	14.69	12.63	16.51	12.49	6.68	6.68
CuI	7.76	9.46	18.40	14.46	11.79	16.26	12.33	28.09	28.31
Cu ₂ O	8.96	10.68	18.39	16.13	14.28	17.38	14.41	13.79	13.78

Table 5.5 Optimized PCE of Cu-based PSC with various ETLs and HTLs.

Perovskite	$V_{OC}(V)$	J_{SC} (mA/cm ²)	FF (%)	PCE (%)
PCBM/ (MA) ₂ CuCl ₄ / PEDOT: PSS	2.00	10.63	86.48	18.41
C ₆₀ / (MA) ₂ CuCl ₄ / Cu ₂ O	1.34	9.83	80.85	10.68
PCBM/ (MA) ₂ CuCl ₂ I ₂ / Cu ₂ O	1.54	12.97	86.82	17.38
TiO ₂ / (MA) ₂ CuCl ₂ I ₂ / Cu ₂ O	1.53	12.14	86.46	16.13
PCBM/ (MA) ₂ CuCl ₂ Br ₂ / CuI	0.87	41.30	78.69	28.31
$C_{60}/(MA)_2CuCl_2Br_2/CuI$	0.87	41.00	78.70	28.09

5.3.1.1 Comparison with Experimental Results

The experimentally obtained efficiency of three PAL: (MA)₂CuCl₄, (MA)₂CuCl₂Br₂ and (MA)₂CuCl₂I₂ PSCs were 2.41 %, 1.75 % and 0.99 % respectively shown below in Table 5.6 using thin film structure of glass/FTO/TiO₂/(MA)₂CuX₄/spiro-OMeTAD/Au. The reason behind the generally low PCE achieved in all reported cells may come from the recombination occurring in perovskite layers. Apart from perovskite absorber layer properties, lower efficiency can be explained by mismatch in the energy bands of ETL, HTL and PAL. For all three perovskites, TiO₂ and Spiro-OMeTAD are employed as ETL and HTL respectively. These can be suitable choices for (MA)₂CuCl₄ but not for (MA)₂CuCl₂Br₂ and (MA)₂CuCl₂I₂ PSCs. This is evident from our simulation results. By using more appropriate HTL such as CuI and Cu₂O (MA)₂CuCl₂Br₂ and (MA)₂CuCl₂I₂ PSCs can give much better results. Cu₂O as HTL is suitable for high efficiency because of its high carrier mobility and a long carrier diffusion length and high charge extraction ability leads to the high J_{SC} [33,34]. It shows high acceptor density because of a suitable band gap of 2.17 eV which may give high PV performance [35]. Also, for CuI, Higher values of J_{SC} are obtained because of a much higher μ_D of CuI relative to spiro-OMeTAD. Optimization of the perovskite/HTL interface is very crucial to reduce recombination as well as for achieving higher V_{OC} and FF for PSCs [36]. It has been found that there is an enhancement in V_{OC} due to two factors: (i) increase in charge carrier mobilities ratio (μ_n/μ_h) of HTL (ii) decrease in the energy gap between HOMO of the HTL and conduction band of PAL [37]. The electron and hole mobility ratio for CuI and Cu₂O is above 2 while for spiro-OMeTAD, this ratio is 1, hence simulation results for CuI and Cu2O as HTL give high V_{OC} leading to higher efficiencies, more so for (MA)₂CuCl₂Br₂ PSC than to experimental results (obtained with spiro-OMeTAD as HTL). Our findings are indicative of the fact that traditional charge transport materials like TiO₂ and spiro-OMeTAD may not be the best choices for new lead-free Cu-based PSCs.

Table 5.6 The previously reported result of different Cu-based PSCs.

Device	$V_{OC}(V)$	J_{SC} (mA/cm ²)	FF (%)	PCE (%)
TiO ₂ /(MA) ₂ CuCl ₄ / Spiro-OMeTAD	0.560	8.12	52	2.41 [15]
TiO ₂ /(MA) ₂ CuCl ₂ I ₂ / Spiro-OMeTAD	0.545	6.78	47	1.75 [15]
TiO ₂ /(MA) ₂ CuCl ₂ Br ₂ / Spiro-OMeTAD	0.581	3.35	50	0.99[15]

5.3.2 Impact of Thickness of Absorber Layer on Device Performance

The thickness of the $(MA)_2CuX_4$ absorber layer has exhibited an apparent impact on the diffusion length of charge carriers. The thickness of PAL varied in the range of 200 to 900 nm at N_t of 1 x 10^{13} cm⁻³ and operating temperature of 300 K. The absorption rate is low for the thin PAL which results in low photocurrent, hence efficiency decreases. As the thickness increases, the charge carriers may not have suitable diffusion length to travel up to the charge collecting layers resulting in a high value of R_s which limits the device performance. Beyond the optimum value of thickness, the device performance stagnates due to the higher recombination of electron-hole pairs. Therefore, there is an increment in the dark saturation current which allows V_{OC} and J_{SC} to fluctuate extremely slowly after a definite value of

thickness. This results in flattening of the PCE curve [38,39]. The n-layer thickness should be optimized for high PCE of a PSC, when the thickness of ETL is near to the surface of PAL, conductance of the device increases towards absorption of radiation [34]. The obtained optimized value of thickness, for PCBM/(MA)₂CuCl₄/PEDOT: PSS is 400 nm, C₆₀/(MA)₂Cu Cl₄/Cu₂O is 600 nm, PCBM/(MA)₂CuCl₂I₂/Cu₂O is 500 nm, TiO₂/(MA)₂CuCl₂I₂/Cu₂O is 600 nm, PCBM/(MA)₂CuCl₂Br₂/CuI is 600 nm and C₆₀/(MA)₂CuCl₂Br₂/CuI is 500 nm for better performance of PSC. The maximum efficiency of PCBM/(MA)₂CuCl₂Br₂/CuI PSC goes up to 29.01 % together with V_{OC} is 0.85 V, J_{SC} is 43.44 mA/cm² and FF is 78.34 % at 600 nm. The change in other PV parameters is also shown in Fig. 5.7. The PCBM/(MA)₂CuCl₄/PEDOT: PSS PSC is most stable towards variation in thickness of PAL because change in the PCE is only 0.43 % for the range of thickness of PAL from 200 to 900 nm. For the TiO₂/(MA)₂CuCl₂I₂/Cu₂O PSC change in PSC is 28.35 % with thickness which varies from 200 to 900 nm, hence it is the most unstable PSC with the variation of thickness of PAL.

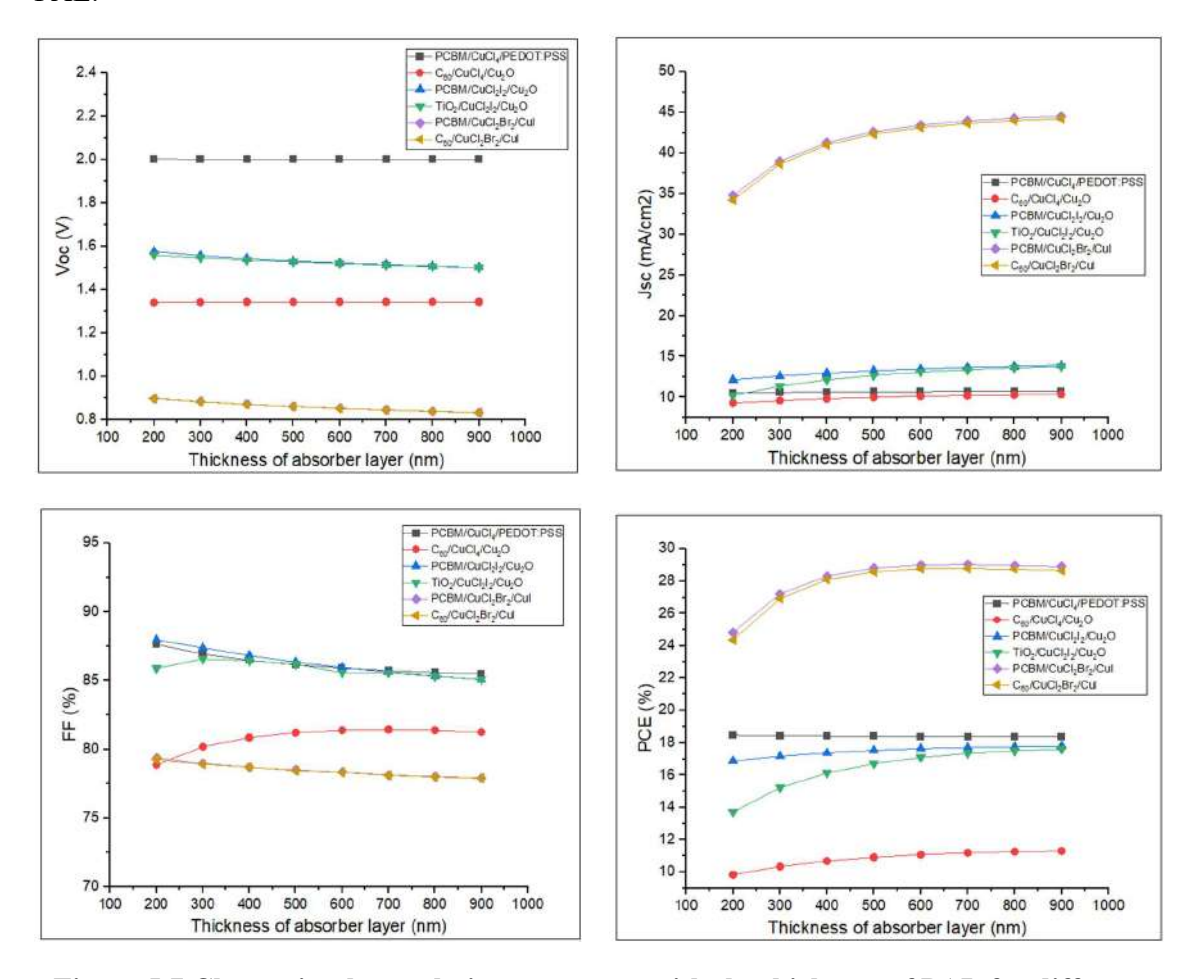


Figure 5.7 Change in photovoltaic parameters with the thickness of PAL for different ETL and HTL of Cu-based PSC.

5.3.3 Effect of Operating Temperature on Absorber Layer

To analyse the impact of temperature on the performance of solar cells, the working temperature has been varied in the range of 260 to 360 K. As a rise in temperature, the PCE drops drastically. Fall in efficiency with temperature is related with decrease in diffusion length of the charge carriers. If the deformation stress on the layers is high, it results in interfacial defects and low interconnectivity among layers. This low interconnectivity alludes to increment of recombination rate in PAL, hence resulting in reducing the diffusion length and increasing R_S, fall in the performance of solar cells [34]. In PCBM/(MA)₂CuCl₄/PEDOT: PSS fall in efficiency with temperature is 17.31 %, for C₆₀/(MA)₂CuCl₄/Cu₂O fall is 0.92 %, for PCBM/(MA)₂CuCl₂I₂/Cu₂O fall is 13.56 %, TiO₂/(MA)₂CuCl₂I₂/Cu₂O is 11.85 %, PCBM/(MA)₂CuCl₂Br₂/CuI is 16.73 %. This shows that the fall in efficiency of C₆₀/(MA)₂CuCl₄/Cu₂O PSC is most stable with increase in operating and for PCBM/(MA)₂CuCl₄/PEDOT: PSS PSC is most unstable. The trend of PV parameters of different Cu-based PSCs as function of operating temperature illustrated in Fig. 5.8.

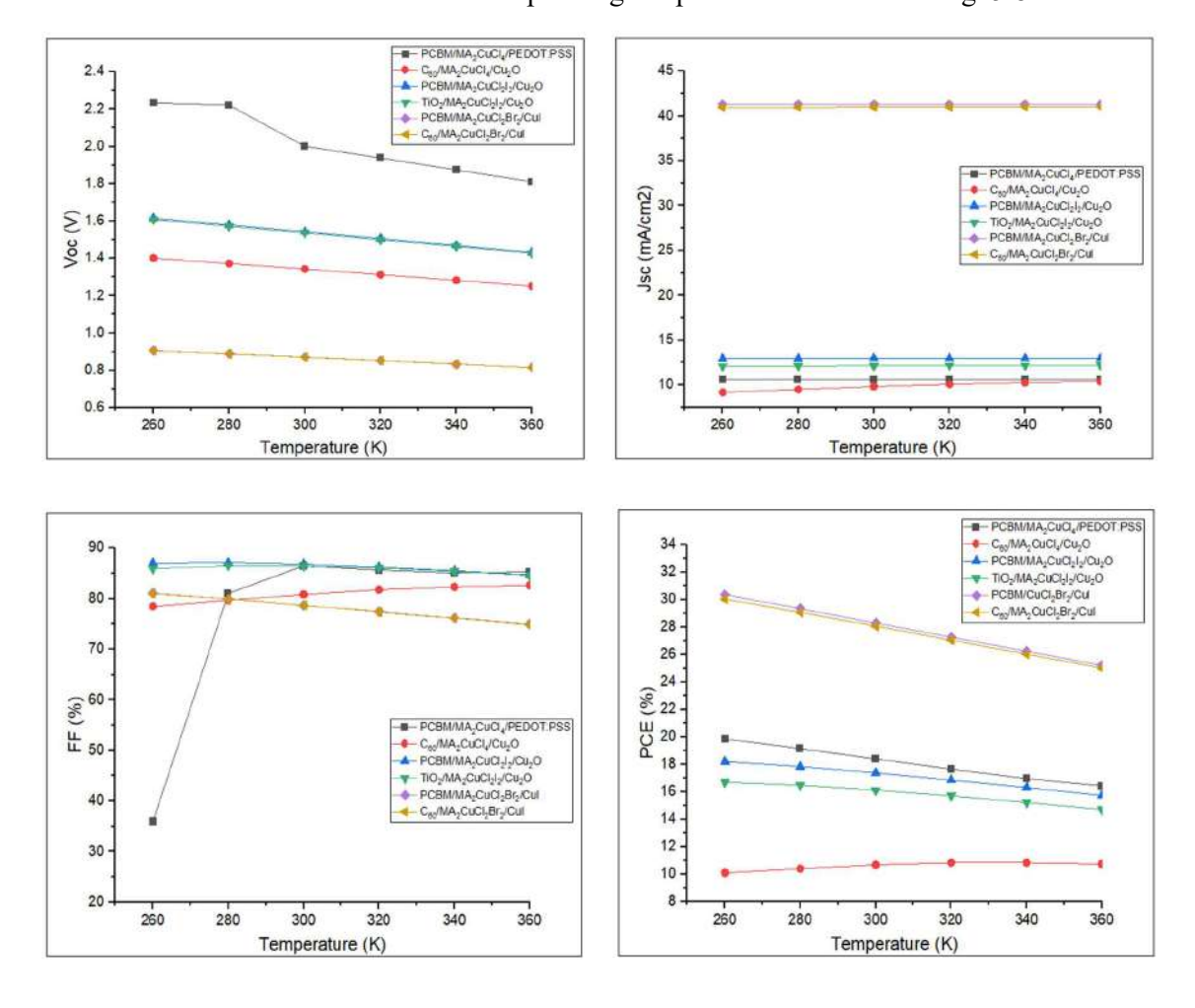
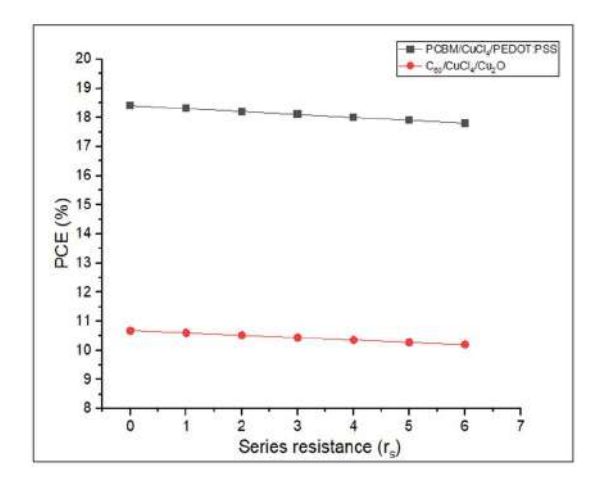
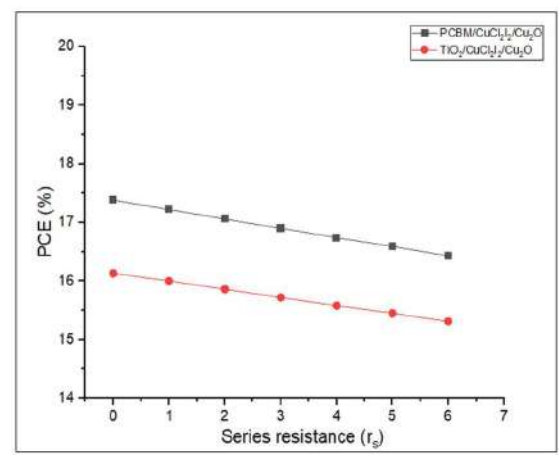


Figure 5.8 Change in photovoltaic parameters with the operating temperature for various Cu-based PSCs.

5.3.4 Effect of Change in Series Resistance on Performance

The impact of variation in the R_S on the performance of Cu-PSC has been examined. It has a significant effect, especially on the FF and J_{SC}. As R_{SC} increases, resulting in a decrease in FF, J_{SC} also starts decreasing for a high value of R_S. Consequently, high values of R_S in a solar device result in poor PCE [40]. In PSC, R_S mainly exists in the interfaces: resistance at the HTL/perovskite interface, ETL/perovskite interface, and at the metal contacts. When solar cells come in contact with the environment, thermomechanical fatigue or cracks evolve in the solder bonds depending on weather circumstances. These cracks result in increment in the value of R_S hence PCE drops [41,42]. The numerical modelling outcomes on the change in R_S on the introduced (MA)₂CuX₄ based PSCs structure is shown below in Fig. 5.9. The PCE of three Cubased PSCs, (MA)₂CuCl₄ (MA)₂CuCl₂I₂, and (MA)₂CuCl₂Br₂, varies with the value of series resistance. In this study, it is analysed that for less value of Rs, the solar cell device is performance high with large FF, resulting in high PCE. As the R_S increases, the performance of active material falls significantly [43]. It has been studied that when the R_S varied from 0 to 6 (Ohm.Cm²), PCE fall nearly 3.25 %, 4.49 %, 5.46 %, 5.08 %, 30.06 % and 29.79 % respectively for PCBM/(MA)₂CuCl₄/PEDOT:PSS, C₆₀/(MA)₂CuCl₄/Cu₂O, PCBM/(MA)2CuCl2I2/Cu2O, TiO2/(MA)2CuCl2I2/Cu2O, PCBM/(MA)2CuCl2Br2/CuI and C60/(MA)2C uCl₂Br₂/CuI at thickness of 400 nm, N_t is 1 x 10¹³ cm⁻³ and operating temperature is 300 K depicted in Fig. 5.9. This shows that the PCBM/(MA)₂CuCl₄/PEDOT: PSS is the most stable and PCBM/(MA)₂CuCl₂Br₂/CuI is the most unstable PSC with increase in R_s.





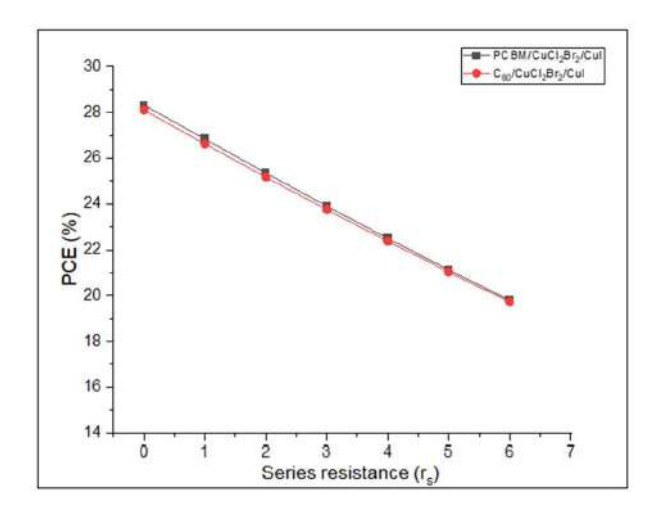


Figure 5.9 Change in PCE of different PSCs with Rs.

5.3.5 Effect of Radiative Recombination Rate on PCE

The effect on performance of solar devices by changing the radiative recombination rate. In this simulation study we varied the radiative recombination rate from 2.3×10^{-8} cm³/sec to 2.3× 10⁻¹² cm³/sec and examined PV parameters trend of PSC devices for different rates with the thickness of PAL which is between 200 to 900 nm. Usually, increment in radiative recombination, carrier lifetime reduces, and PV parameters of device is influenced as shown in Fig. 5.10 for Cu-based PSCs respectively. The Gaussian shape of the curve can be explained by the fact that with an increment in thickness of PAL, large electron-hole pairs are produced [44]. The PCE of (MA)₂CuCl₄ based PSC with PCBM as ETL and PEDOT: PSS as HTL, the maximum PCE has achieved is 18.43 % at PAL thickness of 200 nm and recombination rate of 2.3×10^{-12} cm³/sec whereas when C₆₀ as ETL and Cu₂O as HTL the maximum PCE is 11.29 % at thickness of 900 nm with recombination rate of 2.3×10^{-12} cm³/sec. The obtained PCE is 17.74 % for (MA)₂CuCl₂I₂ based PSC with PCBM as ETL and Cu₂O as HTL and when TiO₂ as ETL and Cu₂O as HTL maximum PCE is 17.55 % at PAL thickness of 900 nm with the value of recombination rate is 2.3×10^{-12} cm³/sec. For the (MA)₂CuCl₂Br₂ based PSC with PCBM as ETL and CuI as HTL, the PCE is 28.61 % whereas C₆₀ as ETL and CuI as HTL obtained maximum PCE is 28.41 % at PAL thickness of 700 nm for the recombination rate of 2.3×10^{-12} cm³/sec illustrated in Fig. 5.10.

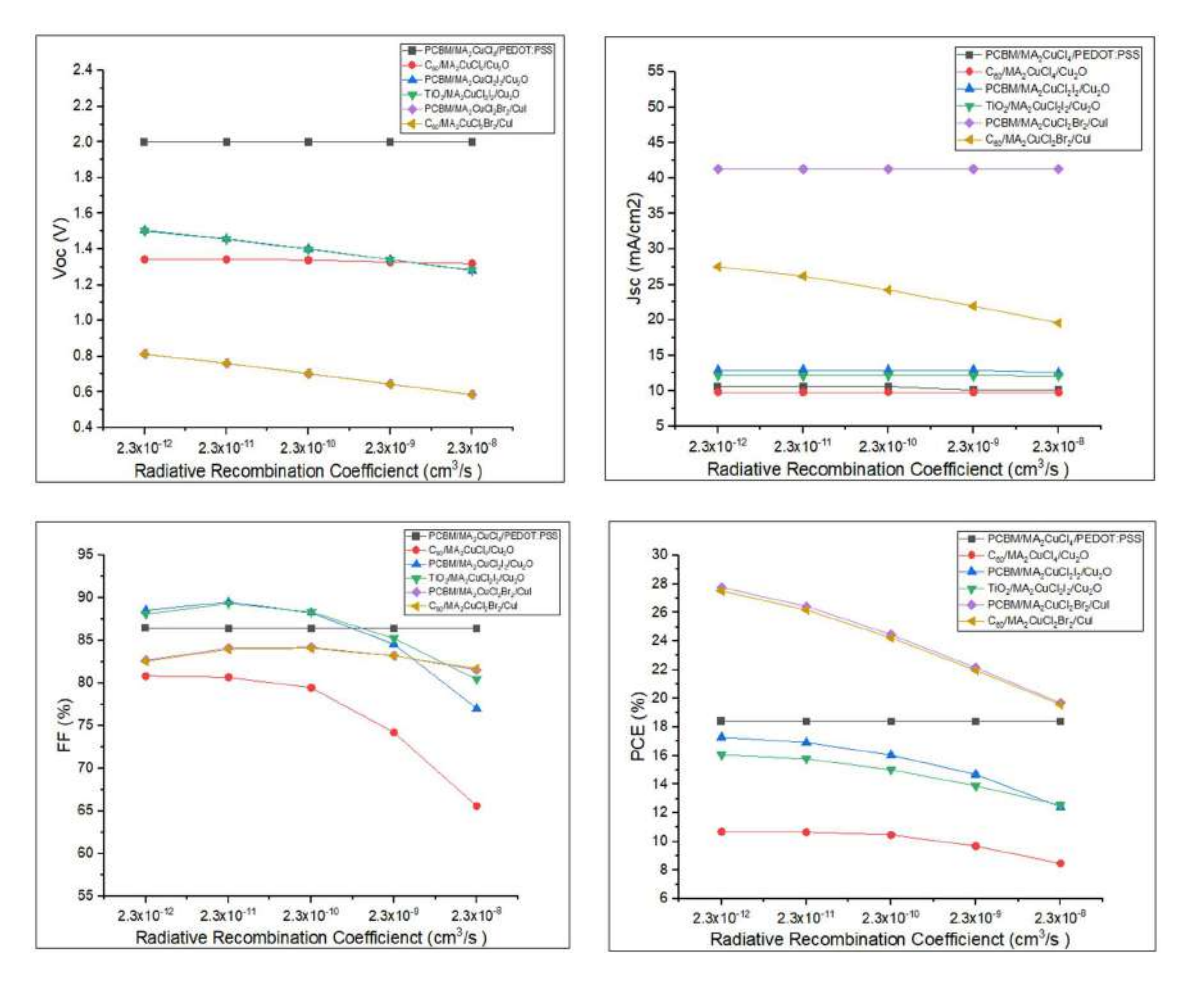


Figure 5.10 The change in PV parameters with recombination coefficient for Cu-based PSCs

5.3.6 Effect of Back Contact Work Function on PCE

The power conversion efficiencies listed in Table 5.5 have been achieved by choosing Gold (Au) as a metal electrode. Au was taken after carefully studying the impact of metal electrode work function on the PCE as shown in Fig. 5.11. The work function was varied from 4.6 to 5.8 eV. This range covers the work function of most of the available metals which are employed as back contact in PSCs. Fig. 5.11 reveals that the photovoltaic performance decreases gradually as the work function of the metal back contact is reduced below 5.1 eV due to formation of Schottky junction at a smaller value of work function [45]. We observed that the maximum PCE of 28.31 % achieved at work function of 5.1 eV (Au) [23].

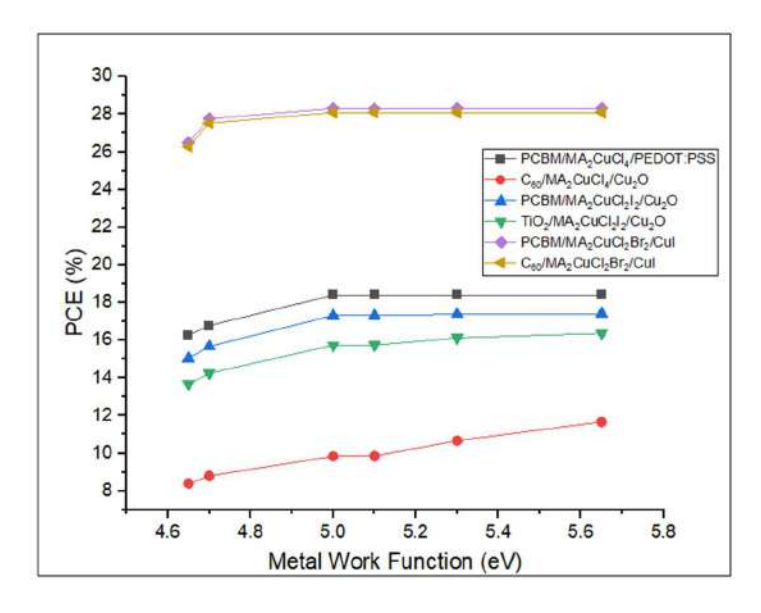


Figure 5.11 Change in PCE of different PSCs with metal work function (eV).

5.4 Summary

We have simulated environment-friendly Cu-based PSCs with optimized ETLs and HTLs for achieving maximum PCE. The PV parameters for first optimized cell FTO/PCBM/(MA)₂Cu Cl₄/PEDOT: PSS PSC are PCE of 18.41 %, V_{OC} is 2.00 V, J_{SC} is 10.63 mA/cm² and FF is 86.48 %. The second optimized cell structure is FTO/PCBM/(MA)₂CuCl₂I₂/Cu₂O with the maximum PCE of 17.38 %, Voc is 1.54 V and FF is 86.82 %. Third optimized cell structure is FTO/PCBM/(MA)₂CuCl₂Br₂/CuI has obtained maximum PCE of 28.31 %, V_{OC} is 0.87 V, J_{SC} is 41.30 mA/cm² and FF is 78.69 % at 400 nm thickness of PAL, operating temperature is 300 K and N_t is 1 x 10¹³ cm⁻³. The maximum PCE of 18.41 %, 17.53 % and 29.01 % have been obtained for all three optimized PSCs with the thickness of PAL as 400 nm, 500 nm and 600 nm respectively for first, second and third cell by using SCAPS-1D. This work also comprises the operating temperature optimization for high performance of PSCs. The optimized value of temperature is 300 K for the PSCs structure. The maximum PCE has obtained of 18.41 %, 17.38 % and 28.31 % for the PSC structure such as FTO/PCBM/(MA)₂CuCl₄/PEDOT: PSS, FTO/PCBM/(MA)₂CuCl₂I₂/Cu₂O and FTO/PCBM/(MA)₂CuCl₂Br₂/CuI respectively at 300 K. Experimentally published results are also compared with simulation results and findings were analysed which highlighted poor ETL and HTL selection as one of the reasons for lower performance of (MA)₂CuX₄ PSCs. R_s effect on PCE is also studied which indicates that (MA)₂CuCl₄ PSC is most stable and (MA)₂CuCl₂Br₂ based PSC is highly unstable with increase in value of R_s . The optimized radiative recombination rate is 2.3×10^{-12} cm³/sec with function of PAL thickness for high PCE of Cu-based PSC with different ETLs and HTLs. Copper based PSC overcome stability and toxicity issue in PSCs. This work helpful in deeply understanding of design, operation mechanism, and in optimization of high efficiency Cubased PSC in near future.

5.5 REFERENCES

- [1] Mahajan, P., Datt, R., Tsoi, W.C., Gupta, V., Tomar, A. and Arya, S., 2021. Recent progress, fabrication challenges and stability issues of lead-free tin-based perovskite thin films in the field of photovoltaics. *Coordination Chemistry Reviews*, 429, p.213633.
- [1a] Sahli, F., Werner, J., Kamino, B.A., Bräuninger, M., Monnard, R., Paviet-Salomon, B., Barraud, L., Ding, L., Diaz Leon, J.J., Sacchetto, D. and Cattaneo, G., 2018. Fully textured monolithic perovskite/silicon tandem solar cells with 25.2% power conversion efficiency. *Nature materials*, 17(9), pp.820-826.
- [2] Momblona, C., Gil-Escrig, L., Bandiello, E., Hutter, E.M., Sessolo, M., Lederer, K., Blochwitz-Nimoth, J. and Bolink, H.J., 2016. Efficient vacuum deposited pin and nip perovskite solar cells employing doped charge transport layers. *Energy & Environmental Science*, 9(11), pp.3456-3463.
- [3] Park, N.G., 2015. Perovskite solar cells: an emerging photovoltaic technology. *Materials today*, 18(2), pp.65-72.
- [4] Cao, Y., Liu, Z., Li, W., Zhao, Z., Xiao, Z., Lei, B., Zi, W., Cheng, N., Liu, J. and Tu, Y., 2021. Efficient and stable MAPbI₃ perovskite solar cells achieved via chlorobenzene/perylene mixed anti-solvent. *Solar Energy*, 220, pp.251-257.
- [5] Kumar, N., Rani, J. and Kurchania, R., 2021. Advancement in CsPbBr₃ inorganic perovskite solar cells: Fabrication, efficiency and stability. *Solar Energy*, 221, pp.197-205.
- [6] Giustino, F. and Snaith, H.J., 2016. Toward lead-free perovskite solar cells. ACS Energy Letters, 1(6), pp.1233-1240.
- [7] Ke, W., Stoumpos, C.C. and Kanatzidis, M.G., 2019. "Unleaded" perovskites: status quo and future prospects of tin-based perovskite solar cells. *Advanced Materials*, 31(47), p.1803230.
- [8] Noel, N.K., Stranks, S.D., Abate, A., Wehrenfennig, C., Guarnera, S., Haghighirad, A.A., Sadhanala, A., Eperon, G.E., Pathak, S.K., Johnston, M.B. and Petrozza, A., 2014. Lead-free organic–inorganic tin halide perovskites for photovoltaic applications. *Energy & Environmental Science*, 7(9), pp.3061-3068.
- [9] Ju, M.G., Chen, M., Zhou, Y., Garces, H.F., Dai, J., Ma, L., Padture, N.P. and Zeng, X.C., 2018. Earth-abundant nontoxic titanium (IV)-based vacancy-ordered double perovskite halides with tunable 1.0 to 1.8 eV bandgaps for photovoltaic applications. *ACS Energy Letters*, 3(2), pp.297-304.
- [10] Zhang, Z., Li, X., Xia, X., Wang, Z., Huang, Z., Lei, B. and Gao, Y., 2017. High-quality (CH₃NH₃)₃Bi₂I₉ film-based solar cells: pushing efficiency up to 1.64%. *The journal of physical chemistry letters*, 8(17), pp.4300-4307.
- [11] Wang, M., Zeng, P., Bai, S., Gu, J., Li, F., Yang, Z. and Liu, M., 2018. High-quality sequential-vapor-deposited Cs₂AgBiBr₆ thin films for lead-free perovskite solar cells. *Solar rrl*, 2(12), p.1800217.
- [12] Zong, Y., Zhou, Y., Zhang, Y., Li, Z., Zhang, L., Ju, M.G., Chen, M., Pang, S., Zeng, X.C. and Padture, N.P., 2018. Continuous grain-boundary functionalization for high-efficiency perovskite solar cells with exceptional stability. *Chem*, 4(6), pp.1404-1415.

- [13] Kour, R., Arya, S., Verma, S., Gupta, J., Bandhoria, P., Bharti, V., Datt, R. and Gupta, V., 2019. Potential substitutes for replacement of lead in perovskite solar cells: a review. *Global Challenges*, 3(11), p.1900050.
- [14] Cortecchia, D., Dewi, H.A., Yin, J., Bruno, A., Chen, S., Baikie, T., Boix, P.P., Grätzel, M., Mhaisalkar, S., Soci, C. and Mathews, N., 2016. Lead-free MA₂CuCl_xBr_{4-x} hybrid perovskites. *Inorganic chemistry*, 55(3), pp.1044-1052.
- [15] Elseman, A.M., Shalan, A.E., Sajid, S., Rashad, M.M., Hassan, A.M. and Li, M., 2018. Copper-substituted lead perovskite materials constructed with different halides for working (CH₃NH₃)₂CuX₄-based perovskite solar cells from experimental and theoretical view. *ACS applied materials & interfaces*, 10(14), pp.11699-11707.
- [16] Bhattarai, S. and Das, T.D., 2021. Optimization of carrier transport materials for the performance enhancement of the MAGeI₃ based perovskite solar cell. *Solar Energy*, 217, pp.200-207.
- [17] Rai, S., Pandey, B.K. and Dwivedi, D.K., 2020. Modeling of highly efficient and low cost CH₃NH₃Pb(I_{1-x}Cl_x)₃ based perovskite solar cell by numerical simulation. *Optical Materials*, 100, p.109631.
- [18] Haider, S.Z., Anwar, H. and Wang, M., 2019. Theoretical device engineering for high-performance perovskite solar cells using CuSCN as hole transport material boost the efficiency above 25%. *physica status solidi (a)*, 216(11), p.1900102.
- [19] Mandadapu, U., Vedanayakam, S.V. and Thyagarajan, K., 2017. Simulation and analysis of lead based perovskite solar cell using SCAPS-1D. *Indian J. Sci. Technol*, 10(1), pp.1-8.
- [20] Jayan, K.D. and Sebastian, V., 2021. Comprehensive device modelling and performance analysis of MASnI₃ based perovskite solar cells with diverse ETM, HTM and back metal contacts. *Solar Energy*, 217, pp.40-48.
- [21] Lakhdar, N. and Hima, A., 2020. Electron transport material effect on performance of perovskite solar cells based on CH₃NH₃GeI₃. *Optical Materials*, 99, p.109517.
- [22] Azri, F., Meftah, A., Sengouga, N. and Meftah, A., 2019. Electron and hole transport layers optimization by numerical simulation of a perovskite solar cell. *Solar energy*, 181, pp.372-378.
- [23] Kanoun, A.A., Kanoun, M.B., Merad, A.E. and Goumri-Said, S., 2019. Toward development of high-performance perovskite solar cells based on CH₃NH₃GeI₃ using computational approach. *Solar Energy*, 182, pp.237-244.
- [24] De Los Santos, I.M., Cortina-Marrero, H.J., Ruíz-Sánchez, M.A., Hechavarría-Difur, L., Sánchez-Rodríguez, F.J., Courel, M. and Hu, H., 2020. Optimization of CH₃NH₃PbI₃ perovskite solar cells: A theoretical and experimental study. *Solar Energy*, 199, pp.198-205.
- [25] Anwar, F., Mahbub, R., Satter, S.S. and Ullah, S.M., 2017. Effect of different HTM layers and electrical parameters on ZnO nanorod-based lead-free perovskite solar cell for high-efficiency performance. *International Journal of Photoenergy*, 2017(1), p.9846310.
- [26] Hossain, M.I. and Alharbi, F.H., 2013. Recent advances in alternative material photovoltaics. *Materials Technology*, 28(1-2), pp.88-97.
- [27] Minami, T., Miyata, T. and Nishi, Y., 2014. Cu₂O-based heterojunction solar cells with an Aldoped ZnO/oxide semiconductor/thermally oxidized Cu₂O sheet structure. *Solar Energy*, 105, pp.206-217.

- [28] Yamada, N., Ino, R. and Ninomiya, Y., 2016. Truly transparent p-type γ-CuI thin films with high hole mobility. *Chemistry of Materials*, 28(14), pp.4971-4981.
- [29] https://www.pveducation.org/pvcdrom/pn-junctions/absorption-coefficient/, (accessed 20 February2022).
- [30] Kalaiselvi, C.R., Muthukumarasamy, N., Velauthapillai, D., Kang, M. and Senthil, T.S., 2018. Importance of halide perovskites for next generation solar cells—a review. *Materials Letters*, 219, pp.198-200.
- [31] Qiu, X., Cao, B., Yuan, S., Chen, X., Qiu, Z., Jiang, Y., Ye, Q., Wang, H., Zeng, H., Liu, J. and Kanatzidis, M.G., 2017. From unstable CsSnI₃ to air-stable Cs₂SnI₆: A lead-free perovskite solar cell light absorber with bandgap of 1.48 eV and high absorption coefficient. *Solar Energy Materials and Solar Cells*, 159, pp.227-234.
- [32] Shi, B., Jia, J., Feng, X., Ma, G., Wu, Y. and Cao, B., 2021. Thermal evaporated CuI film thickness-dependent performance of perovskite solar cells. *Vacuum*, 187, p.110076.
- [33] Chatterjee, S. and Pal, A.J., 2016. Introducing Cu₂O thin films as a hole-transport layer in efficient planar perovskite solar cell structures. *The Journal of Physical Chemistry C*, 120(3), pp.1428-1437.
- [34] Nejand, B.A., Ahmadi, V., Gharibzadeh, S. and Shahverdi, H.R., 2016. Cuprous oxide as a potential low-cost hole-transport material for stable perovskite solar cells. *ChemSusChem*, 9(3), pp.302-313.
- [35] Kale, A.J., Chaurasiya, R. and Dixit, A., 2021. Inorganic lead-Free Cs₂AuBiCl₆ perovskite absorber and Cu₂O hole transport material based single-junction solar cells with 22.18% power conversion efficiency. *Advanced Theory and Simulations*, 4(3), p.2000224.
- [36] Gharibzadeh, S., Nejand, B.A., Moshaii, A., Mohammadian, N., Alizadeh, A.H., Mohammadpour, R., Ahmadi, V. and Alizadeh, A., 2016. Two-step physical deposition of a compact CuI Hole-Transport layer and the formation of an interfacial species in perovskite solar cells. *ChemSusChem*, 9(15), pp.1929-1937.
- [37] Ompong, D. and Singh, J., 2018. High open-circuit voltage in perovskite solar cells: The role of hole transport layer. *Organic Electronics*, 63, pp.104-108.
- [38] Mushtaq, S., Tahir, S., Ashfaq, A., Bonilla, R.S., Haneef, M., Saeed, R., Ahmad, W. and Amin, N., 2023. Performance optimization of lead-free MASnBr₃ based perovskite solar cells by SCAPS-1D device simulation. *Solar Energy*, 249, pp.401-413.
- [39] Hao, L., Li, T., Ma, X., Wu, J., Qiao, L., Wu, X., Hou, G., Pei, H., Wang, X. and Zhang, X., 2021. A tin-based perovskite solar cell with an inverted hole-free transport layer to achieve high energy conversion efficiency by SCAPS device simulation. *Optical and Quantum Electronics*, 53, pp.1-17.
- [40] Chakraborty, K., Choudhury, M.G. and Paul, S., 2019. Numerical study of Cs₂TiX₆ (X= Br-, I-, F- and Cl-) based perovskite solar cell using SCAPS-1D device simulation. *Solar Energy*, 194, pp.886-892.
- [41] Samiul Islam, M., Sobayel, K., Al-Kahtani, A., Islam, M.A., Muhammad, G., Amin, N., Shahiduzzaman, M. and Akhtaruzzaman, M., 2021. Defect study and modelling of SnX₃-based perovskite solar cells with SCAPS-1D. *Nanomaterials*, 11(5), p.1218.

- [42] Poorkazem, K., Liu, D. and Kelly, T.L., 2015. Fatigue resistance of a flexible, efficient, and metal oxide-free perovskite solar cell. *Journal of Materials Chemistry A*, 3(17), pp.9241-9248.
- [43] Jeon, N.J., Noh, J.H., Yang, W.S., Kim, Y.C., Ryu, S., Seo, J. and Seok, S.I., 2015. Compositional engineering of perovskite materials for high-performance solar cells. *Nature*, 517(7535), pp.476-480.
- [44] Islam, M.T., Jani, M.R., Shorowordi, K.M., Hoque, Z., Gokcek, A.M., Vattipally, V., Nishat, S.S. and Ahmed, S., 2021. Numerical simulation studies of Cs₃Bi₂I₉ perovskite solar device with optimal selection of electron and hole transport layers. *Optik*, 231, p.166417.
- [45] Jannat, F., Ahmed, S. and Alim, M.A., 2021. Performance analysis of cesium formamidinium lead mixed halide based perovskite solar cell with MoO_x as hole transport material via SCAPS-1D. *Optik*, 228, p.166202.

CHAPTER 6

PERFORMANCE ANALYSIS OF LaFeO₃ PEROVSKITE SOLAR CELLS: A THEORETICAL AND EXPERIMENTAL STUDY

- Lanthanum ferrite (LaFeO₃) is studied as a potential material for PSCs due to its strong electron-electron correlation, which increases quantum efficiency.
- ➤ Sol-gel method was used to synthesize LaFeO₃ nanoparticles, and the material was characterized using techniques such as XRD, SEM, EDS, UV-Vis, and FTIR.
- > SCAPS-1D simulations were conducted to evaluate LaFeO₃-based PSCs with various ETLs and HTLs, resulting in the analysis of 64 configurations.
- ➤ The simulation study optimized parameters like absorber layer thickness, operating temperature, defect density, series and shunt resistance, and J-V characteristics.
- The theoretical maximum PCE for the configuration of FTO/WS₂/LaFeO₃/CBTS/Au, was 13.03 %, while the experimental efficiency achieved was 0.79 %.
- The results suggest that LaFeO₃ is a promising material for future photovoltaic applications, offering potential for improved PSC performance.

6.1 Introduction

The combustion of fossil fuels leads to pollution in the environment [1]. So, alternative energy technologies are required like biomass, wind, solar and tidal power. Solar energy is a green, accessible and abundant renewable energy [2,3,4]. PSC continues to draw the attention due to high-PCE and simple room temperature fabrication methodology which makes them a cheaper than conventional silicon solar cells [5,6,7]. The researchers have explored numerous candidates to replace Pb, such as Sb [8], La [9,10] and double perovskites etc. LaFeO₃ possesses a tunable energy band-gap which can be altered using suitable dopants [11,12]. The other properties of LaFeO₃ such as chemical stability, low production cost, high electron mobility and its non-toxic nature are already favourable for lead-free PSC application [13,14]. There are very few studies on LaFeO₃ as perovskite material for solar cell application [15]. This work comprises fabrication and characterization of LaFeO₃-based PSCs. LaFeO₃ nanoparticles were first synthesized by using the sol-gel method and then they were used for solar cell application. Prior to fabrication of LaFeO₃-based PSC, we have simulated and optimized the structure of solar cells using SCAPS-1D simulation software. So, we have got eight optimized structures of LaFeO₃-based PSC through simulation with a maximum PCE of 13.03 % for the most efficient configuration which is approximately 30 % greater than the past reported work [14]. The experimental validation was conducted for the optimized PSC. We achieved an PCE of 0.79 % experimentally, which is approximately thirteen times higher than the previously reported result [15]. The spin coating method is employed to obtain PCE of 0.79 % which is the highest achieved efficiency for the LaFeO₃-based PSC till now. This efficiency enhancement is attributed to proper selection of HTL and ETL. To obtain the maximum PCE of a PSC, the energy level alignment of all these layers becomes a very important factor. The selection and optimization of the ETL and HTL is very crucial to maximize the performance of a PSC. In this simulation we have simulated sixty-four configurations with different ETLs (TiO₂, PCBM, IGZO, In₂O₃, C₆₀, ZnO, SnO₂, WS₂) and HTLs (Cu₂O, CuInSe₂, Spiro-OMeTAD, P3HT, D-PBTTT-14, V₂O₅, CFTS, CBTS). The outcomes showed that CBTS is the most suitable HTL for LaFeO₃ PSC and in addition it is abundantly available [16]. The study also includes optimization of the parameters which influences performance of the PSC, thickness, operating temperature, N_t, back contact, R_S and R_{SH}.

6.2 Device Architecture

The LaFeO₃ is employed as an absorber layer in PSC having thickness of 400 nm. In this simulation, we have employed several ETLs (TiO₂, PCBM, IGZO, In₂O₃, C₆₀, ZnO, SnO₂, WS₂) and HTLs (Cu₂O, CuInSe₂, Spiro-OMeTAD, P3HT, D-PBTTT-14, V₂O₅, CFTS, CBTS) to achieve the maximum efficiency. The PSC structure depicted in Fig. 6.1. The thickness of employed ETL = 100 nm and HTL = 50 nm. In p-i-n devices, the e^{-s} and h^{+s} generated within the absorber layer when sunlight falls on it.

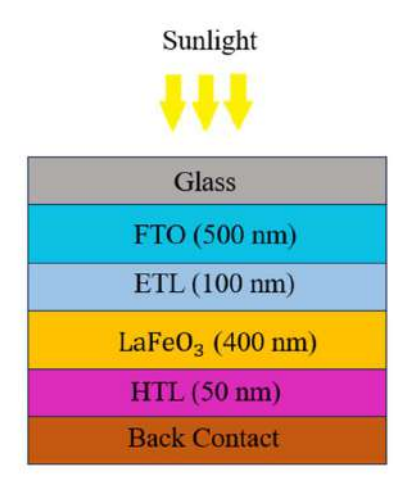


Figure 6.1 Architecture of LaFeO₃-based PSC.

6.3 Experimental Section

6.3.1 Materials and Method

All the precursors employed in synthesis of perovskite are La(NO₃)₃, Fe(NO₃)₃, citric acid and ammonium hydroxide. The light sensitizer LaFeO₃ was prepared by employing a sol-gel method. The flow chart for stepwise preparation of perovskite material is shown below in Fig. 6.2. The lanthanum and iron-based solution were prepared for synthesis of LaFeO₃. Deionized (DI) water chosen as a solvent to dissolve both solutes. At first,1M aqueous solution of La(NO₃)₃ mixed with 1M aqueous solution of Fe(NO₃)₃. The mixture was stirred for 2 days at 300 rpm and 60 °C. Citric acid was added dropwise in the solution. After that, ammonium hydroxide aqueous solution was added dropwise under magnetic stirring to make pH = 7. The sample was stirred at 300 rpm for 72 h and dried in a vacuum oven at 180 °C for 12 h. After that sample was moved into a muffle furnace for calcination in air at 600 °C for 4 h. The synthesized sample shown in Fig. 6.3.

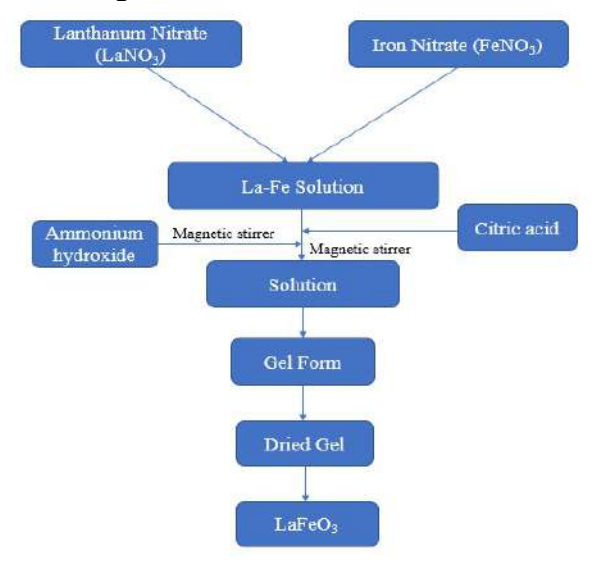


Figure 6.2 Flow chart of stepwise synthesis of LaFeO₃.

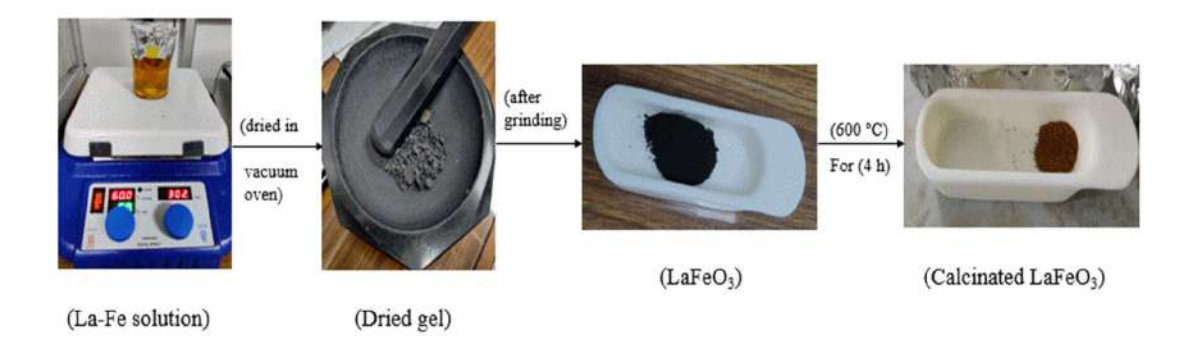


Figure 6.3 Preparation of LaFeO₃ perovskite.

6.3.2 Material Characterization Techniques

XRD pattern of perovskite material was recognized utilizing a diffractometer (Bruker, model: D-8). The size and morphologies of synthesized perovskite by SEM. UV–vis spectrum of the LaFeO₃ sample is observed by employing a Perkin-Elmer, Lamda-750 dual-beam spectrometer. The prepared sample IR transmission spectra was analysed by employing an FTIR spectrometer.

6.4 Experimental Result and Discussion

6.4.1 XRD Analysis

It is primarily used for phase identification and crystallinity of the material. The observed range of XRD data is from 10° to 90° over 2θ with scan rate of 2°/min. The peaks of LaFeO₃ before and after calcination are demonstrated in Fig. 6.4 (a) and (b), respectively. The XRD peaks with 2θ of 32.30°, 39.91°, 46.42°, 57.60°, 67.83°, 76.68° and 81.19° corresponding to (110), (111), (200), (211), (220), (310) and (311) planes of the synthesized LaFeO₃ perovskite nanoparticles having cubic structure (JCPDS#75-0541). Bragg's equation (6.1) was used to calculate the material grain size and display angles.

$$2d\sin\theta = n\lambda \tag{6.1}$$

Crystallite Size =
$$\frac{0.94 \times \lambda}{\beta \cos \theta}$$
 (6.2)

Where, λ = wavelength of X-ray, β = FWHM, θ = Bragg's angle.

The calculated average crystallite size is 18.4 nm by using Debye Scherrer's Eq. (6.2). It is observed that the peak intensities increase after the calcination (600 °C for 4 h) of the LaFeO₃, which confirms the uniform crystal growth of perovskite phase [15].

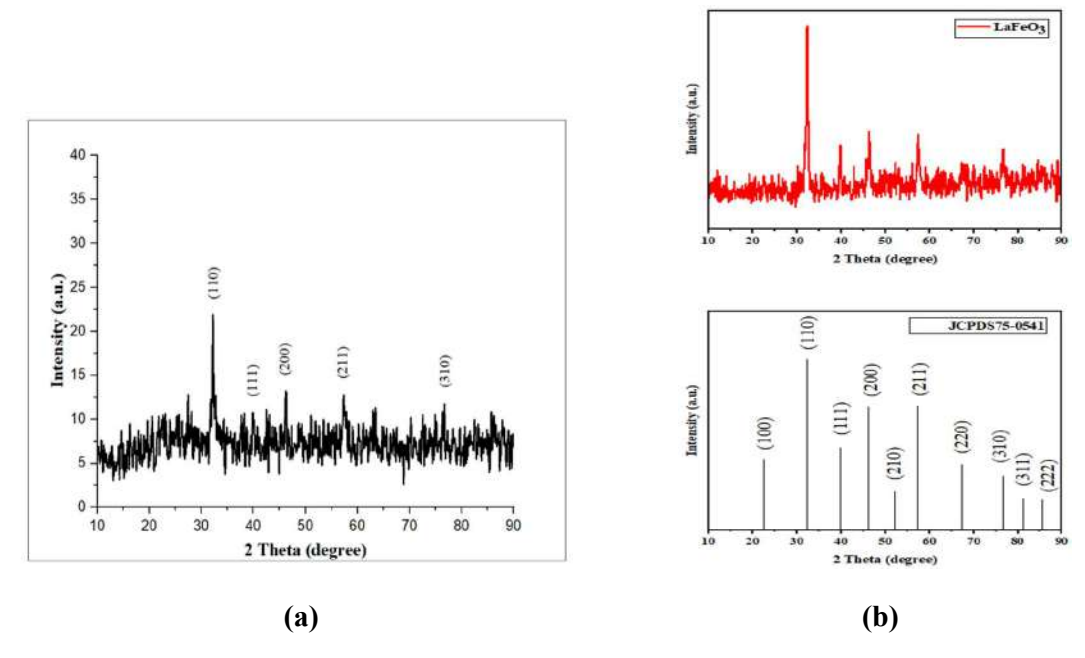


Figure 6.4 XRD pattern of (a) LaFeO₃ and (b) Calcined LaFeO₃.

6.4.2 SEM Results

The SEM is employed to inspect topography and superficial characteristics of LaFeO₃ perovskite material. The nanoparticles of LaFeO₃ did not aggregate and have small size depicted in Fig. 6.5 (a). The nanoparticles are discrete with an average size of ~ 80 nm shown below in Fig 6.5 (b). The SEM investigation showed that film is not uniform due to there are no surface-protecting layers which lead to agglomeration of the particles. The particle shapes are ambiguous, numerous large and small pores exist in the entire material [9].

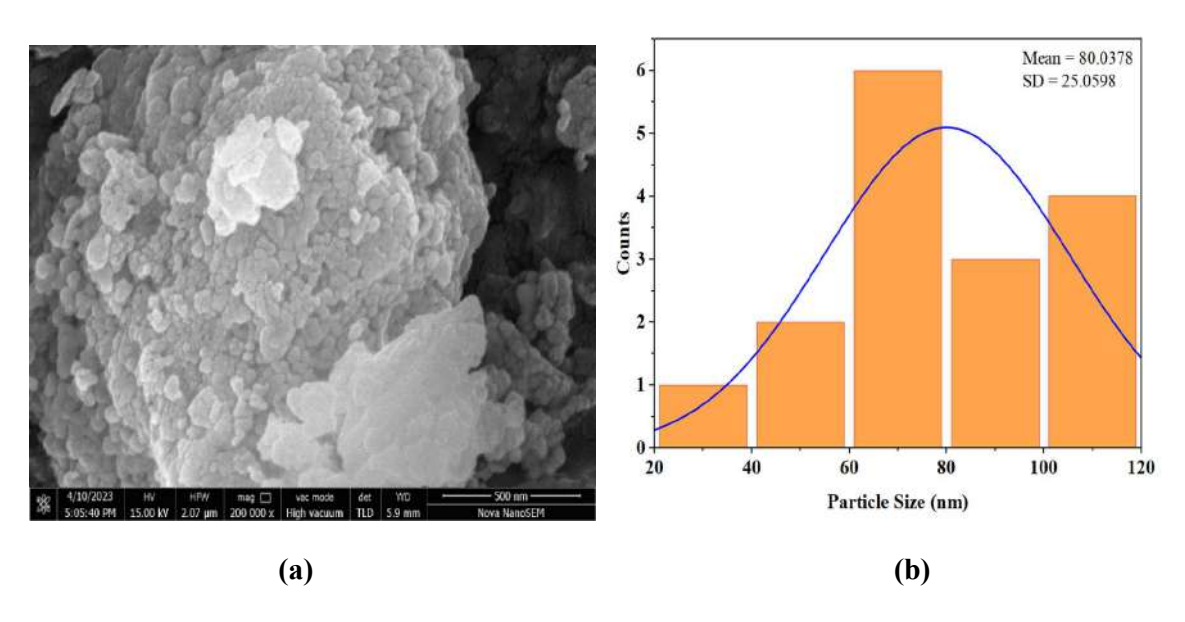


Figure 6.5 (a) SEM image of LaFeO₃ nanoparticles and (b) Particle size distribution.

6.4.3 EDS Spectrum

The composition and chemical purity of elements are investigated using EDS. Fig. 6.6 demonstrates EDS spectroscopy of LaFeO₃. The diagram shows that La, Fe, C and O are observed without no peaks of impurities. The presence of these elements can validate the formation of pure phases. The weight percent of all elements presented in LaFeO₃ perovskite were depicted in Table 6.1.

Element	Series	Weight %	Atomic %
	V Carian	(70	22.42
C	K-Series	6.70	22.42
O	K-Series	17.18	43.16
La	L-Series	47.37	13.71
Fe	K-Series	28.75	20.70

Table 6.1 Weight % of the element composition of LaFeO₃ powder.

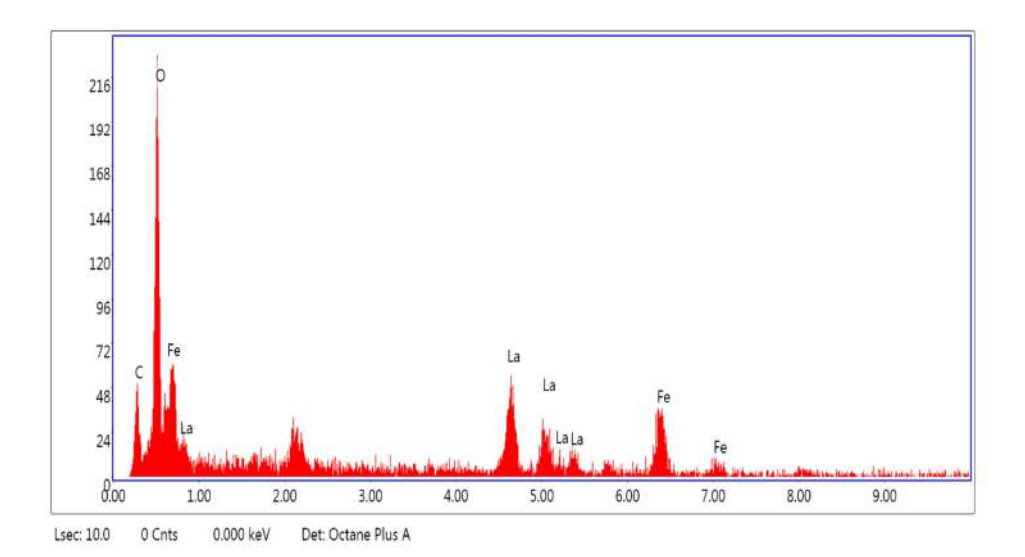


Figure 6.6 EDS spectrum of LaFeO₃ nanoparticles.

6.4.4 UV-Vis Spectroscopy

UV-Vis spectrum of LaFeO₃ perovskite material carried out in order to calculate optical E_g illustrated in Fig. 6.7. The highest absorption peak of the LaFeO₃ sample is observed at 330 nm. The E_g is calculated by the equation (6.3).

$$E_{g} = \frac{hc}{\lambda m}$$
 (6.3)

Where, E_g is the band gap energy of the sample, h = Planck's constant, c = speed of light. λ_{max} is the extreme absorption wavelength of the sample. The calculated value of E_g for LaFeO₃ perovskite is approximately 2.3 eV and is in range as reported by Azozi et al. [17].

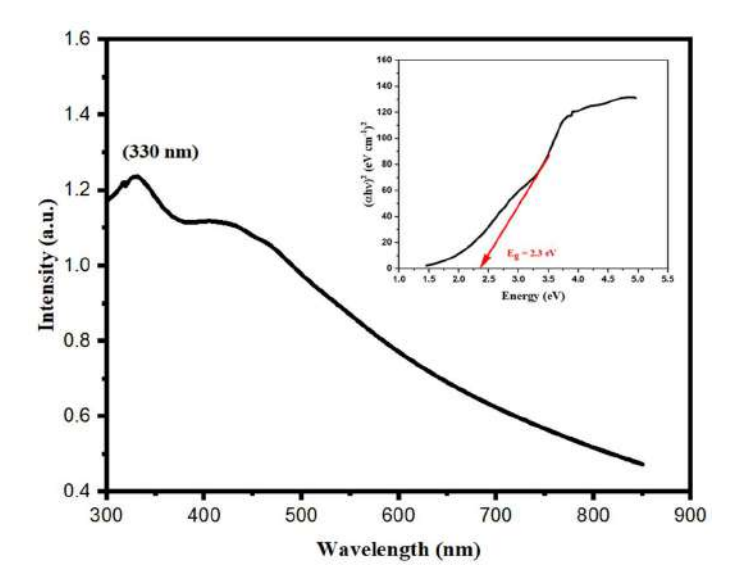


Figure 6.7 UV-vis spectrum of LaFeO₃ nanoparticles.

6.4.5 FT-IR Analysis

FT-IR is employed to distinguish the vibrational modes of LaFeO₃ perovskite material and confirmation of existent functional groups. The FT-IR spectrum of a LaFeO₃ perovskite in the range of 400 to 4000 cm⁻¹ presented in Fig. 6.8. The peaks of the LaFeO₃ nanoparticles are near to 552, 838, 1061, 1404, 1480, 2912 and 3359 cm⁻¹. The absorption band is observed at 552 cm⁻¹ which is attributed to Fe-O stretching vibration mode [18,19]. This peak confirms the formation of perovskite phase which commonly exists between 500 to 700 cm⁻¹ [20]. The IR broad peak at 3359 cm⁻¹ arises from H-O bending mode and 2109 cm⁻¹ due to symmetric stretching of the carboxyl group [21].

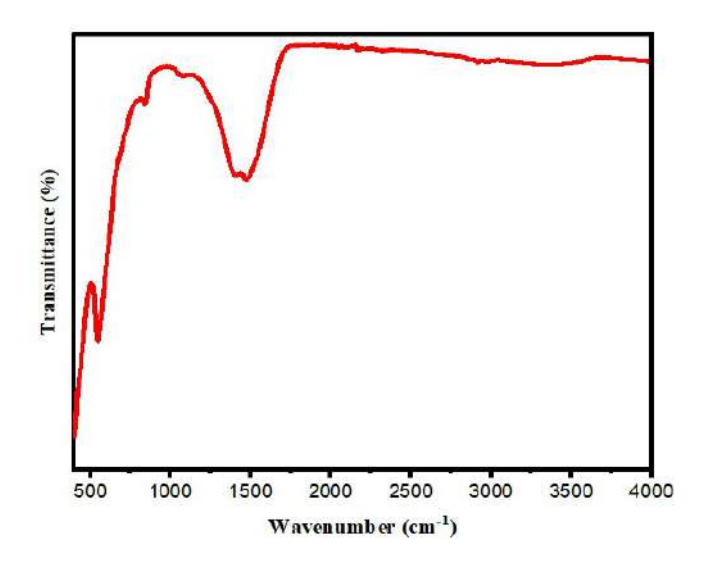


Figure 6.8 FT-IR spectrum of LaFeO₃ nanoparticles.

6.4.6 Photoluminescence Spectrum

To delve deeper into the electronic properties, we conducted room temperature Photoluminescence spectrum (PL) analysis on the synthesized powder. In this investigation, LaFeO₃ exhibited a prominent emission peaking around 450 nm, aligning with the band-edge emission observed with excitation wavelength of 330 nm shown below in Fig. 6.9. The visible emission bands might be associated with oxygen vacancies serving as luminescent sites. These vacancies naturally occur in oxygen- deficient environments and manifest as defects on the surface or within the lattice structures. In this scenario, these oxygen vacancies serve as luminescent centres, capturing both a h⁺ and an e⁻ on the nanostructures surface. The recombination of this e⁻- h⁺ pair results in nonradiative emission. The oxygen vacancies found in synthesized perovskites prompt further investigation into their electrical and optical characteristics.

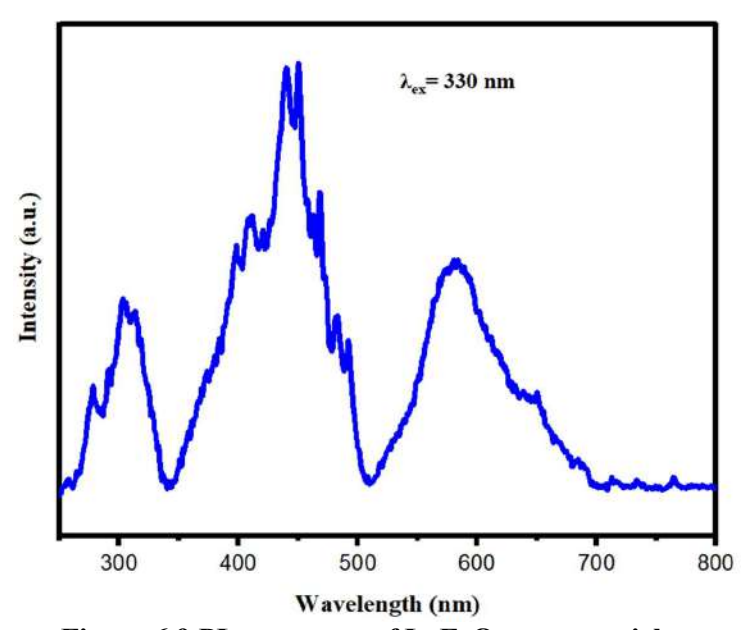


Figure 6.9 PL spectrum of LaFeO₃ nanoparticles.

6.5 Simulation Result and Discussion

6.5.1 Optimization of Suitable ETL and HTL

The input parameters employed in simulation of several layers are enclosed in Table 6.2, 6.3 and 6.4. The various ETLs such as TiO₂, PCBM, IGZO, In₂O₃, C₆₀, ZnO, SnO₂ and WS₂ were inserted into the heterostructure to achieve the optimum performance. The band alignment of various ETLs demonstrated in Fig. 6.10. The input parameters of employed ETLs are demonstrated in Table 6.3. We have done the simulation by varying the thickness of all ETLs from 50 to 250 nm. We found that the optimized value of ETL thickness is 100 nm for all ETLs. It has been analysed that there is a negligible change in efficiency of the LaFeO₃-based PSC for values greater or less than the optimized value. The different configurations of eight ETLs and eight HTLs are studied to achieve the maximum performance. The band matching is

a vital factor. One of the critical issues confronting the PSCs community involves the alignment of energy level between the ETLs and the absorber layer. To tackle this issue, a thorough examination of the ETL/perovskite interface is imperative. Defects arising from lattice mismatching at the ETL/perovskite interface play a vital role in trapping the charge carriers and greatly influence the device efficiency. The conduction band of the WS₂ layer is well aligned to the lowest unoccupied molecular orbital (LUMO) of the absorber layer. This can facilitate smooth charge carrier transport, minimizing the impact of defects that may otherwise trap or recombine charges. This band alignment ensures that e-s can easily move from the absorber layer to the WS₂ layer and eventually to the contact, contributing to higher overall device efficiency [22]. The conduction band of the ETL is always less than the LUMO of the absorber layer. The gap amid the valence band of ETL and HOMO level of the absorber layer must always maintain substantial distance, which inhibits the recombination in the absorber layer. The results illustrate that TiO₂, SnO₂ and ZnO have wide E_g, so that they have exhibited low PCE of around 8 %. ETLs like IGZO, and C₆₀ suffering from mismatch in band alignment hence, exhibited low efficiency relatively. In this work WS₂ is most suitable ETL to achieve maximum PCE for LaFeO₃-based PSC. The WS₂ has advantages such as band matching, photoelectrochromic, toughness, high melting point and corrosion resistance. Due to these properties, WS₂ is the promising candidate for optoelectronic application. The maximum 13.03 % efficiency of has been obtained with the heterostructure FTO/WS₂/LaFeO₃/CBTS/Au.

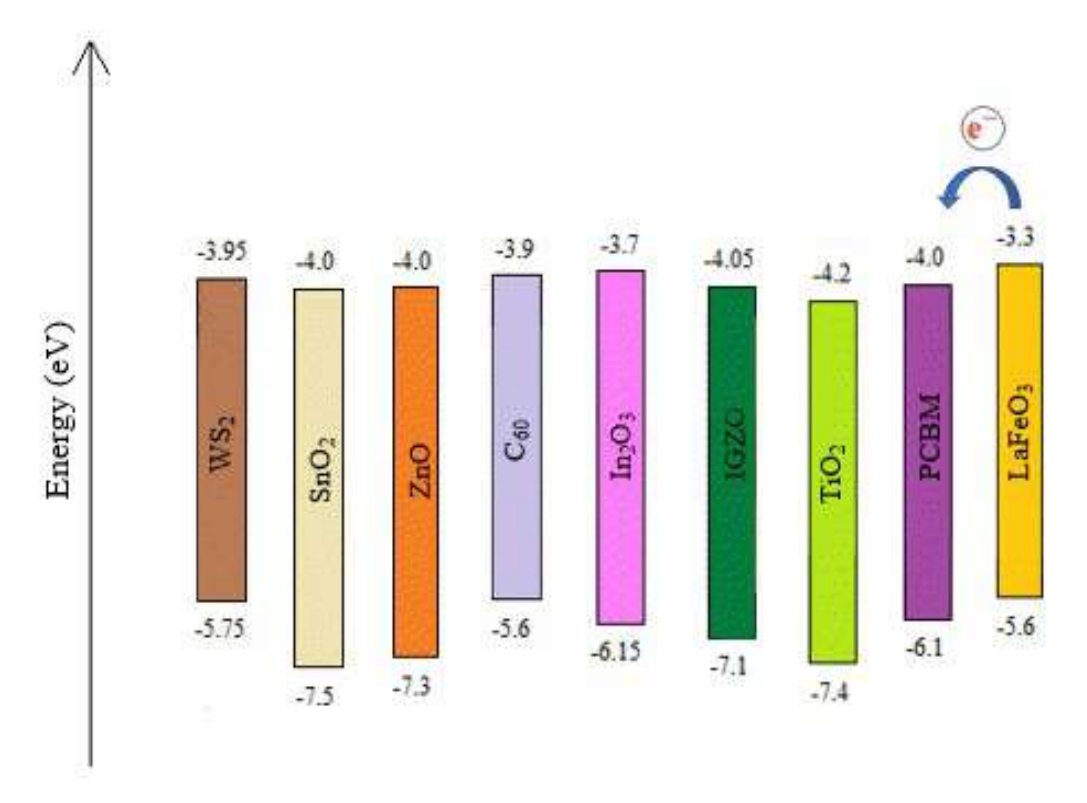


Figure 6.10 Band alignment diagram of various ETLs with LaFeO₃ absorber layer.

Table 6.2 Input parameters of PSCs.

Parameter	FTO [23,24]	TiO ₂ [25,26]	LaFeO ₃ [14,27]	Cu ₂ O [23,27]
Thickness (nm)	500	100	400	50
Eg (eV)	3.5	3.2	2.3	2.17
$\chi \left(eV\right)$	4.0	3.9	3.3	3.2
ε	9.0	32	30	7.11
$N_{\rm C}$ (cm ⁻³)	2.2×10^{18}	1×10^{19}	4×10^{18}	2.02×10^{17}
N_V (cm ⁻³)	1.8×10^{19}	1×10^{19}	1×10^{19}	1.1×10^{19}
$\mu_n \left(cm^2/Vs \right)$	20	20	1.1×10^{-1}	2×10^2
$\mu_p \; (cm^2/Vs)$	10	10	1.1×10^{-3}	80
N_D (cm ⁻³)	1×10^{15}	1×10^{17}	1×10^{15}	0
N_A (cm ⁻³)	0	0	1×10^{15}	1×10^{18}
N _t (cm ⁻³)	1×10^{15}	1×10^{13}	$1 \times 10^{13*}$	1×10^{14}

^{*}In this work

Table 6.3 Input parameters of different ETLs.

Parameter	PCBM [28]	IGZO [14,29]	In ₂ O ₃ [14]	C ₆₀ [24]	ZnO [30]	SnO ₂ [30,25]	WS ₂ [31]
Thickness (μm)	100*	100*	100*	100*	100*	100	100
Eg (eV)	2.1	3.05	2.8	1.7	3.3	3.3	1.8
$\chi \left(eV\right)$	3.9	4.16	3.7	3.9	4.1	4.0	3.95
3	3.9	10	8.9	4.2	9.0	9.0	13.6
$N_{\rm C}$ (cm ⁻³)	2.2×10^{19}	5×10^{18}	1×10^{19}	8×10^{19}	2.2×10^{18}	2.2×10^{17}	1×10^{18}
N_V (cm ⁻³)	2.2×10^{19}	5×10^{18}	1×10^{19}	8×10^{19}	1.9×10^{19}	2.2×10^{16}	2.4×10^{19}
$\mu_n (cm^2\!/Vs)$	1×10^{-3}	15	3.4	8×10^{-2}	100	200	100
$\mu_p (cm^2\!/Vs)$	2×10^{-3}	0.1	3.4	3.5×10^{-3}	25	80	100
N_D (cm ⁻³)	1×10^{18}	1×10^{18}	1×10^{18}	2.6×10^{17}	1×10^{17}	1×10^{17}	1×10^{18}
N_A (cm ⁻³)	0	0	0	0	0	0	0
N_t (cm ⁻³)	$1 \times 10^{13*}$	$1\times10^{13*}$	$1 \times 10^{13*}$	$1 \times 10^{13*}$	$1\times10^{13^*}$	$1\times10^{13^*}$	$1\times10^{13^*}$

^{*}In this work

Impact of distinct HTLs such as Cu₂O, CuInSe₂, Spiro-OMeTAD, P3HT, D-PBTTT-14, V₂O₅, CFTS and CBTS with eight different combinations were studied. In contrast, the V₂O₅, and CFTS achieved less efficiency than other HTLs. The remarkable enhancement in efficiency of a PSC with the inorganic HTL. The inorganic HTL materials are more stable, transparent, and band-aligned, over organic HTL. CBTS is most suitable HTL for LaFeO₃-based PSC due to its diverse properties such as crystalline structure, light absorption, atomic size and an earth-abundant material [16]. The CBTS as HTL offered most suitable band matching as compared to other HTLs shown in Fig. 6.11, so that it exhibited the highest PCE of 13.03 % for LaFeO₃-based PSCs. The performance of CBTS with distinct ETLs shown below in Table 6.5. The total sixty-four different heterostructures have been simulated to explore appropriate combinations of ETL and HTL for LaFeO₃-based PSC to achieve maximum performance depicted in Fig. 6.12. The J-V and QE plots of the best eight configurations are illustrated in Fig. 6.13.

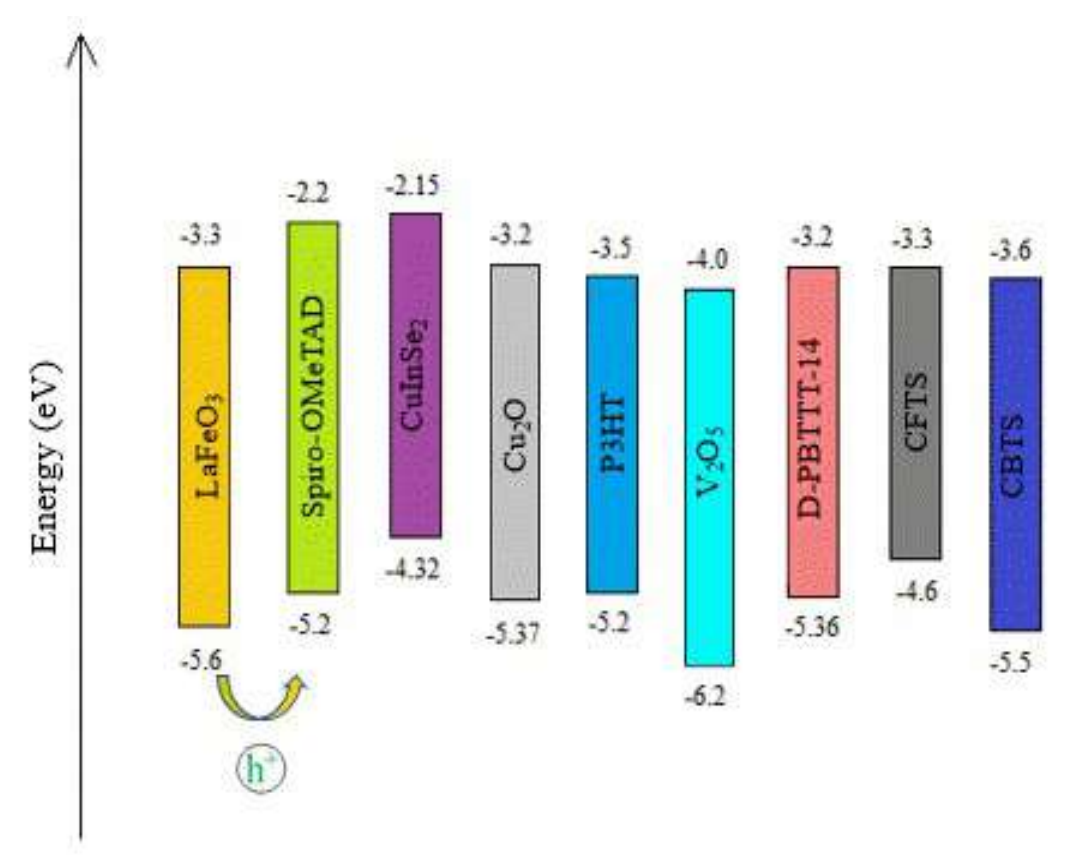
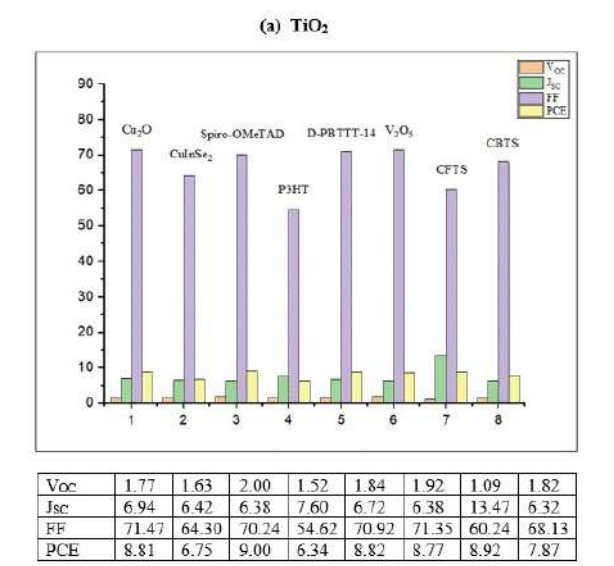


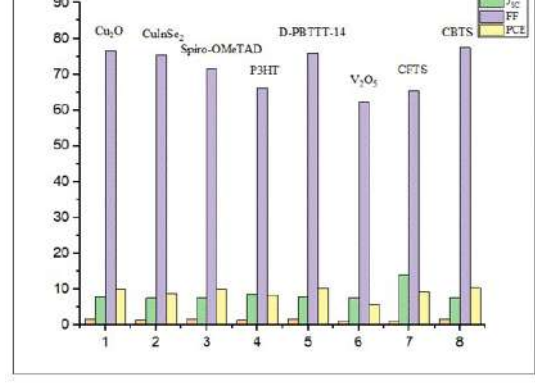
Figure 6.11 Band alignment diagram of various HTLs with LaFeO₃ absorber layer.

Table 6.4 Input parameters of different HTLs.

Parameter	CuInSe ₂ [32,33]	Spiro- OMeTAD [23,27,32,34]	P3HT [24,35]	D-PBTTT-14 [23]	V ₂ O ₅ [32,36]	CFTS [37]	CBTS [37]
Thickness (nm)	50*	50*	50	50	50*	50*	50*
Eg (eV)	2.17	3.0	1.7	2.16	2.2	1.3	1.9
$\chi \left(eV\right)$	3.2	2.45	3.5	3.2	4.0	3.3	3.6
ε	6.6	3.0	3.0	10	10	9.0	5.4
N_C (cm ⁻³)	2.5×10^{20}	1×10^{19}	2×10^{18}	2.8×10^{19}	9.2×10^{17}	2.2×10^{18}	2.2×10^{18}
N_V (cm ⁻³)	2.5×10^{20}	1×10^{19}	2×10^{19}	1×10^{19}	5×10^{18}	1.8×10^{19}	1.8×10^{19}
$\mu_n \left(cm^2/Vs\right)$	80	1×10^{-4}	1.8×10^{-3}	2.83×10^{-3}	3.2×10^{2}	21.98	30
μ_p (cm ² /Vs)	80	1×10^{-4}	1.8×10^{-2}	2.83×10^{-3}	40	21.98	10
N_D (cm ⁻³)	0	0	0	0	0	0	0
N_A (cm ⁻³)	1×10^{18}	2×10^{18}	1×10^{18}	1×10^{18}	1×10^{18}	1×10^{18}	1×10^{18}
N_t (cm ⁻³)	$1\times10^{14*}$	1×10^{14}	1×10^{14}	1×10^{14}	1×10^{14}	$1 \times 10^{14*}$	$1 \times 10^{14*}$

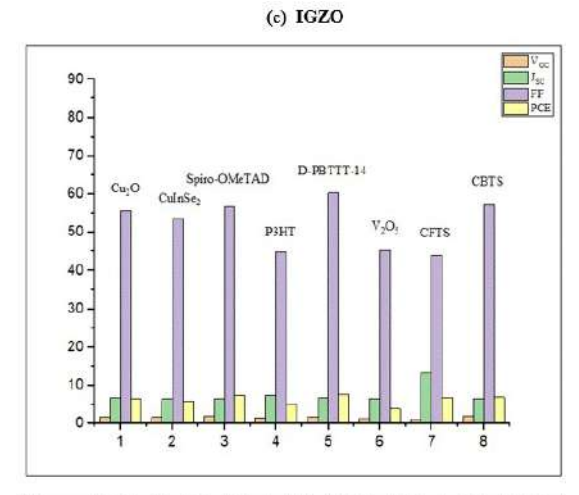
*In this work





(b) PCBM

Voc	1.66	1.58	1.86	1.47	1.74	1.20	1.00	1.76
Jsc	7.72	7.53	7.56	8.67	7.74	7.54	14.10	7.53
FF	76.71	75.32	71.60	66.11	75.81	62.33	65.50	77.49
PCE	9.89	8.98	10.07	8.47	10.23	5.65	9.33	10.32



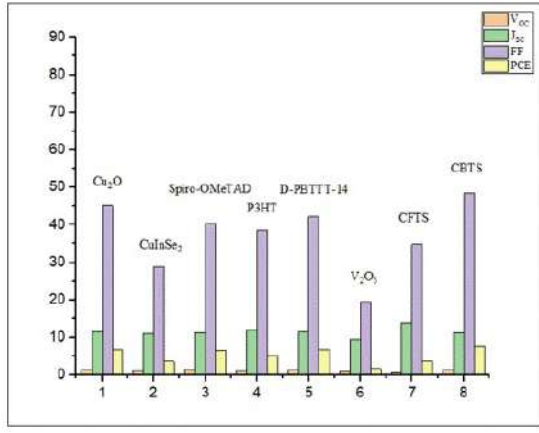
Voc	1.77	1.69	2.01	1.57	1.86	1.30	1.11	1.87
Jsc	6.70	6.41	6.47	7.48	6.74	6.46	13.54	6.41
FF	55.74	53.41	56.66	44.91	60.31	45.32	43.95	57.19
PCE	6.63	5.82	7.40	5.29	7.58	3.81	6.67	6.88

(d) In₂O₃ CBTS FF PCE Ci₂O CuInSe₂ D-PBTTT-14 CFTS 80 -Spiro-OMeTAD V2O3 P3HT 70 -60 -50 -40 -30 -20 -10-

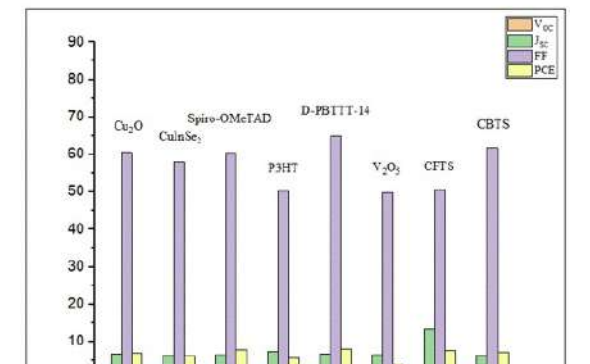
Voc	1.72	1.62	2.00	1.52	1.83	1.22	1.09	1.82
Jsc	6.57	6.39	6.41	7.86	6.68	6.41	13.49	6.37
FF	80.63	79.72	76.51	66.21	82.34	72.83	76.24	81.49
PCE	9.28	8.30	9.84	7.93	10.12	5.73	11.30	9.46

(f) ZnO





Voc	1.29	1.13	1.44	1.10	1.37	0.89	0.67	1.37
Jsc	11.49	11.10	11.36	12.03	11.50	9.58	13.93	11.36
FF	45.21	28.84	40.29	38.62	42.18	19.61	34.82	48.59
PCE	6.72	3.64	6.61	5.13	6.69	1.68	3.26	7.62



Voc	1.72	1.62	2.00	1.52	1.83	1.22	1.09	1.82
Jsc	6.67	6.38	6.45	7.34	6.71	6.43	13.53	6.38
FF	60.58	58.06	60.44	50.18	64.88	49.82	50.71	61.61
PCE	6.97	6.04	7.81	5.62	8.01	3 03	7.53	7.17

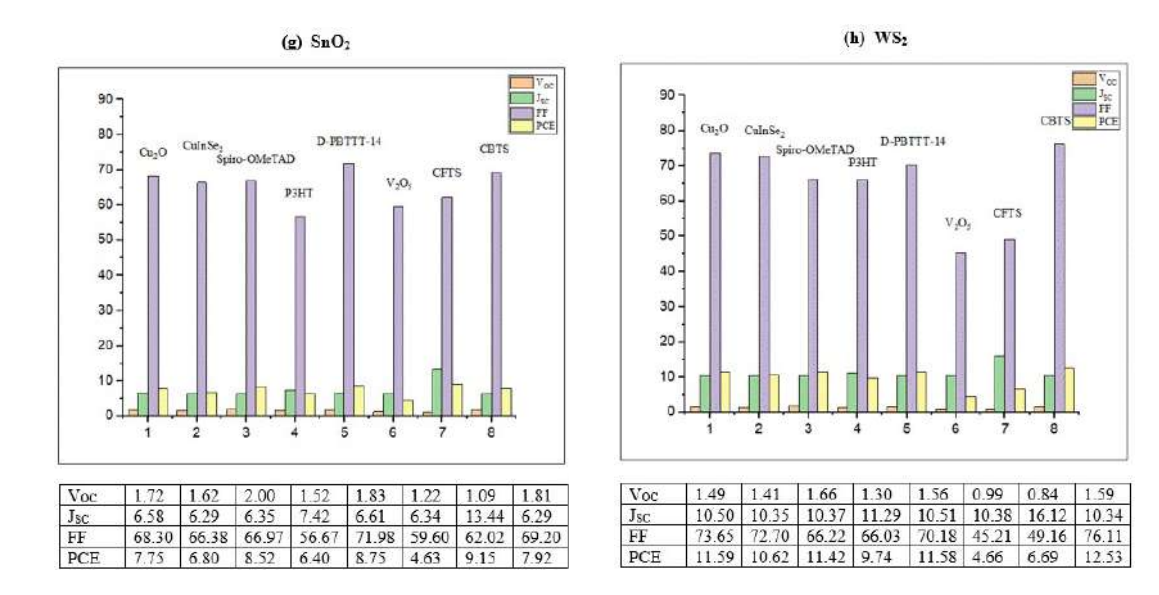


Figure 6.12 Optimization of LaFeO₃ PSC PV parameters for various ETLs (TiO₂, PCBM, IGZO, In₂O₃, C₆₀, ZnO, SnO₂, WS₂) and HTLs (Cu₂O, CuInSe₂, Spiro-OMeTAD, P3HT, D-PBTTT-14, V₂O₅, CFTS, CBTS) with Au as metal back contact.

Table 6.5 The PSC performance of CBTS with the different ETLs.

Device architecture	Voc (V)	J _{SC} (mA/cm ²)	FF (%)	PCE (%)
FTO/TiO ₂ /LaFeO ₃ /CBTS/Au	1.82	6.32	68.13	7.87
FTO/PCBM/LaFeO3/CBTS/Au	1.76	7.53	77.49	10.32
FTO/IGZO/LaFeO3/CBTS/Au	1.87	6.41	57.19	6.88
FTO/In ₂ O ₃ /LaFeO ₃ /CBTS/Au	1.82	6.37	81.49	9.46
FTO/C60/LaFeO3/CBTS/Au	1.37	11.36	48.59	7.62
FTO/ZnO/LaFeO ₃ /CBTS/Au	1.82	6.38	61.62	7.17
FTO/SnO ₂ /LaFeO ₃ /CBTS/Au	1.81	6.29	69.20	7.92
FTO/WS ₂ /LaFeO ₃ /CBTS/Au	1.59	10.34	76.11	12.53

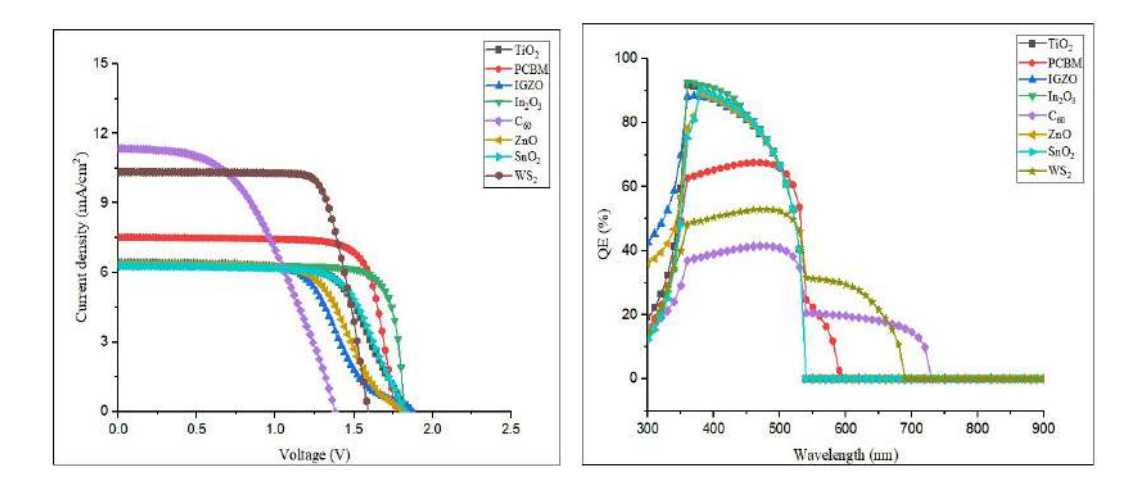


Figure 6.13 J-V and QE with distinct ETLs.

6.5.2 Impact of Thickness of Absorber Layer

The thickness altered from 200 to 1000 nm at N_t of 1×10^{13} cm⁻³ and temperature of 300 K. It is known to us that as thickness of the layer decreases, absorption rate also lowers. This results in a decrease in photocurrent and therefore PCE of the solar cell also reduces after 300 nm. As an increase in thickness, large numbers of photons are absorbed but simultaneously recombination rate increases and high-rate results in V_{OC} [23,27]. Both V_{OC} and PCE parameters decrease exponentially for increase in thickness from 300 to 1000 nm. It can be seen that WS_2 PCE is highest at around 300 nm. Whereas for C_{60} there is a rapid fall in PCE due to very low value of electron mobility as compared to other ETLs. Hence it can be deduced that the Optimum value of thickness is 300 nm for LaFeO₃-based PSC and beyond that PCE falls and decrease in FF is 68.61 %. The maximum efficiency of PSC goes up to 13.03 % together with V_{OC} is 1.61 V, J_{SC} is 9.952 mA/cm² and FF is 81.17 % for the thickness of 300 nm at ETL = 100 nm and HTL = 50 nm. The FF shows a monotonic decrement with the rise in thickness when thickness becomes greater than 300 nm. The change in different PV parameters with thickness of LaFeO₃ layer with CBTS as HTL depicted in Fig. 6.14.

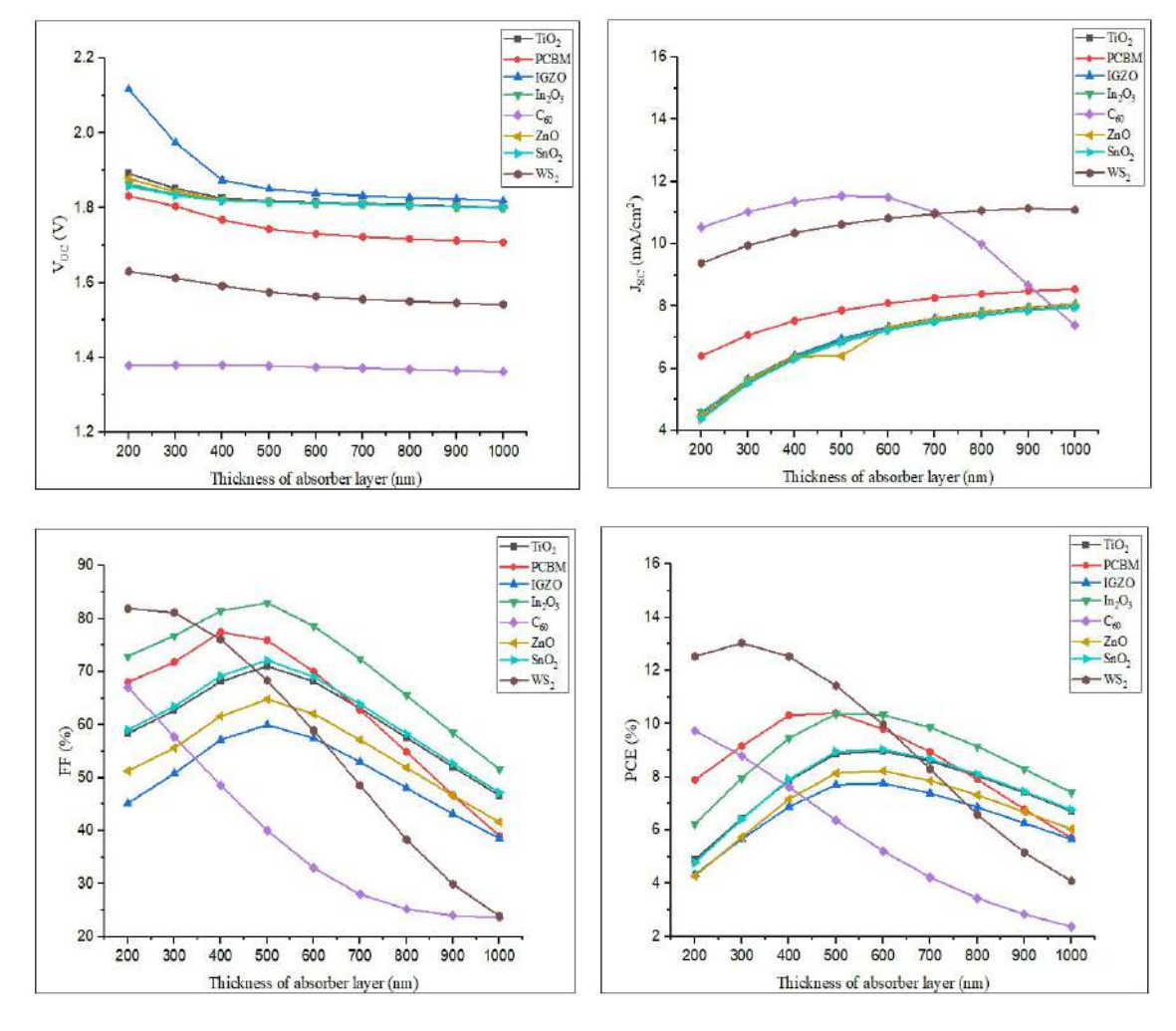


Figure 6.14 Impact of thickness on PV parameters of LaFeO₃-based PSCs.

6.5.3 Effect of Operating Temperature

The working temperature range is between 250 to 550 K. Fall in the performance with temperature increase is related to a reduction in diffusion length of charge carriers. Several solar cell architectures show the instability of their overall performance due to deformation among layers at high temperatures. In LaFeO₃-based PSC, fall in efficiency with temperature is 18.11~% for FTO/WS₂/LaFeO₃/CBTS/Au configuration. When the enhancement of temperature occurs, the PCE drops significantly from 12.70 to 10.40 % for the given range of temperature. The optimized temperature is 250 K for LaFeO₃-based PSC. The value of V_{OC} is decreasing with rise in temperature for all ETLs. The increment in temperature results in reduced the performance of PSC owing to the saturation current and therefore the recombination rate increases [38]. The impact of operating temperature with CBTS as HTL and various ETLs on the PV parameters are shown below in Fig. 6.15.

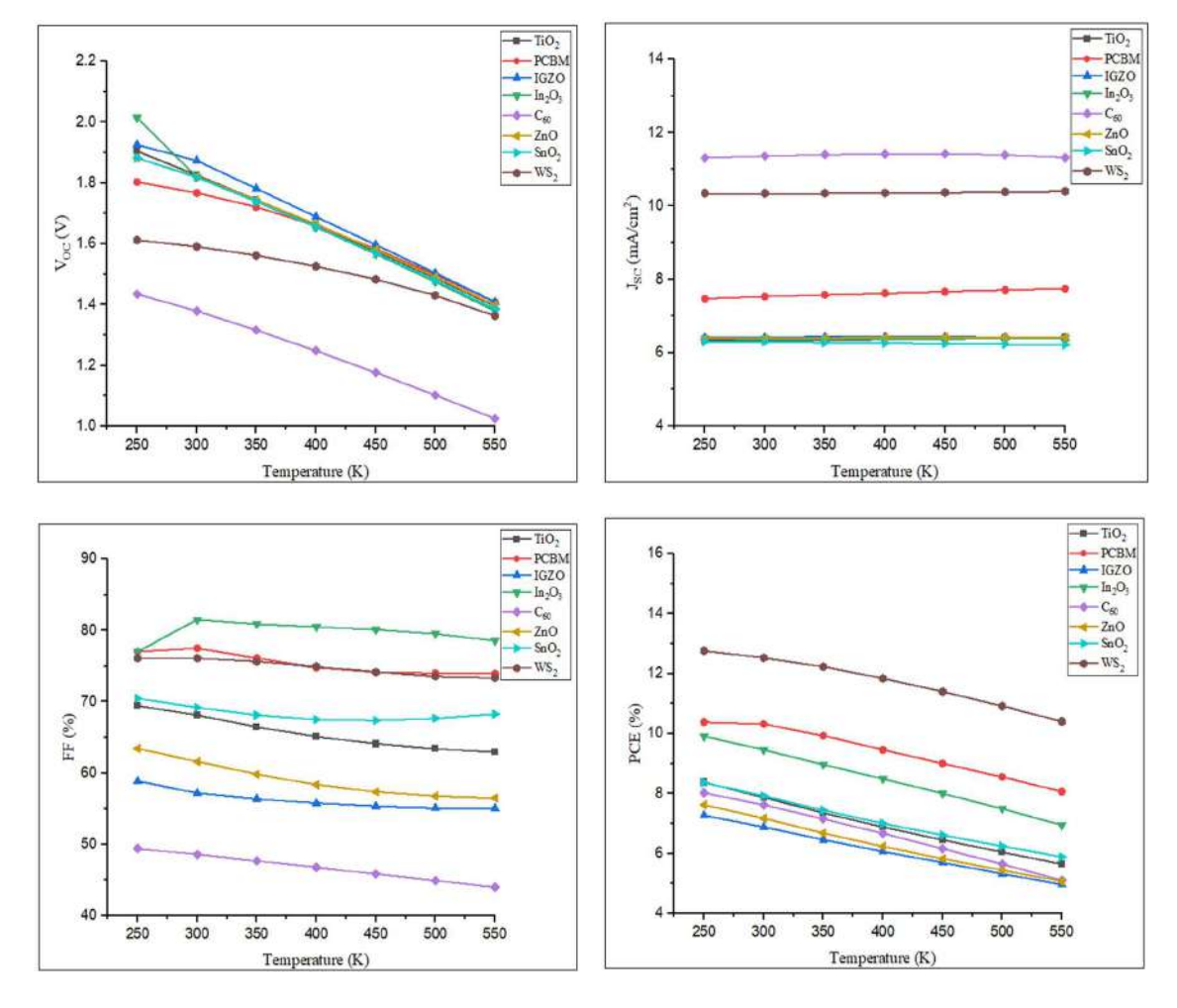


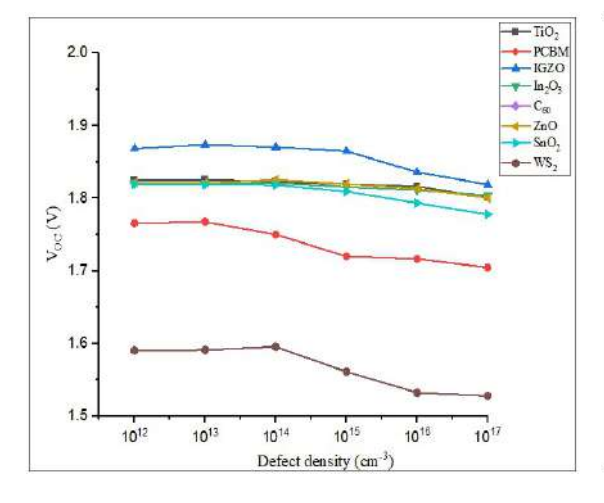
Figure 6.15 Change in performance of LaFeO₃-based PSCs with operating temperature.

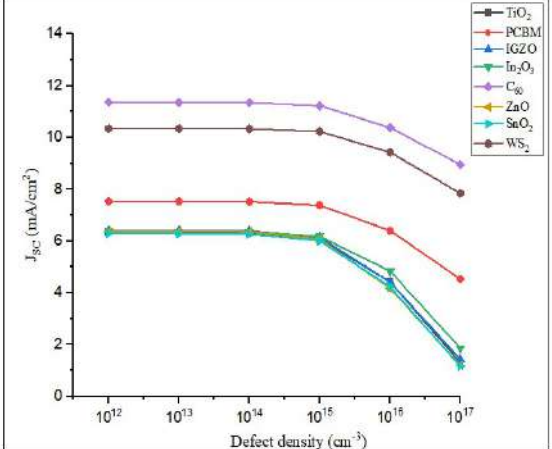
6.5.4 Impact of Defect Density

The PSC performance and stability is expressively reduced at a large number of defects [39]. We have analysed the PV parameters by varying N_t of the absorber layer from 10^{12} to 10^{17} cm⁻³. The optimized value of N_t is 1×10^{13} cm⁻³ for LaFeO₃-based PSC at which it has achieved the maximum PCE of 12.53 %, as illustrated in Fig. 6.16. The PCE and J_{SC} fall sharply after 10^{15} cm⁻³ due to increase in defects hence number of traps of recombination enhances [40,41]. Increase in N_t , results in decrease in short circuit current, which is lastly responsible for fall in FF of the solar devices. The device PCE decreased from 12.53 % to 9.30 % for FTO/WS₂/LaFeO₃/CBTS/Au heterostructure, when N_t was enhanced from 10^{12} to 10^{17} cm⁻³. Such an increasing amount of recombination resulted in a sharp decrease in PCE. The change in different PV parameters with N_t for LaFeO₃ with CBTS as HTL and different ETLs is depicted in Fig. 6.16. The fall in PCE is 25.89 % with an increase in value of N_t for optimized structure of LaFeO₃-based PSC. Some defect parameters of LaFeO₃ absorber layer shown below in Table 6.6.

Table 6.6 Defect properties of LaFeO₃ absorber layer.

Parameters	Values
Density of defect, N _t (cm ⁻³)	10 ¹² -10 ¹⁷
Capture cross section electron σ_n (cm ²)	1×10^{-15}
Capture cross section hole σ_h (cm ²)	1×10^{-15}
Energetic distribution	Single
Туре	Neutral
Energy level	Midgap





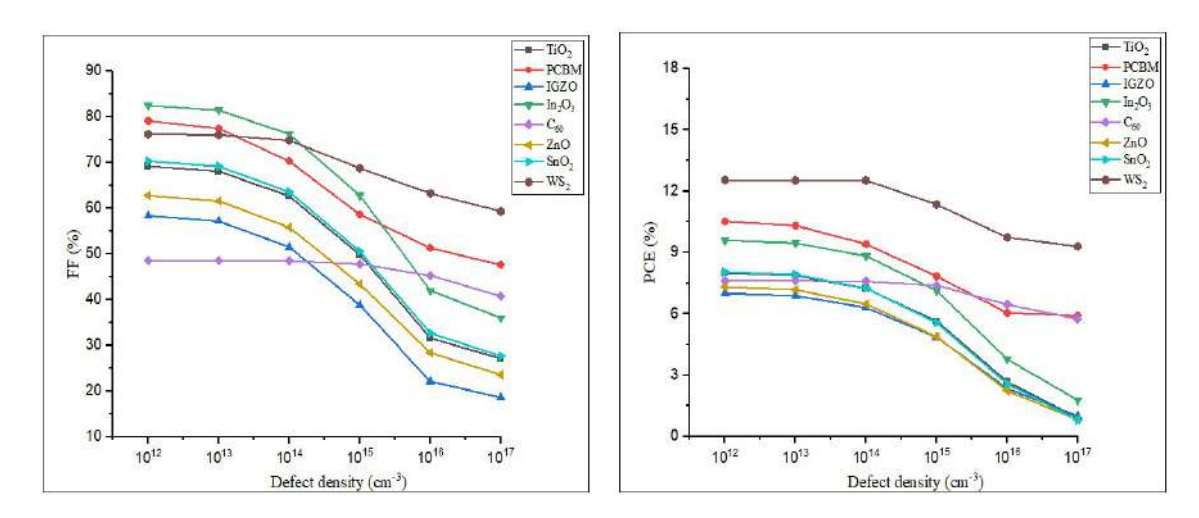
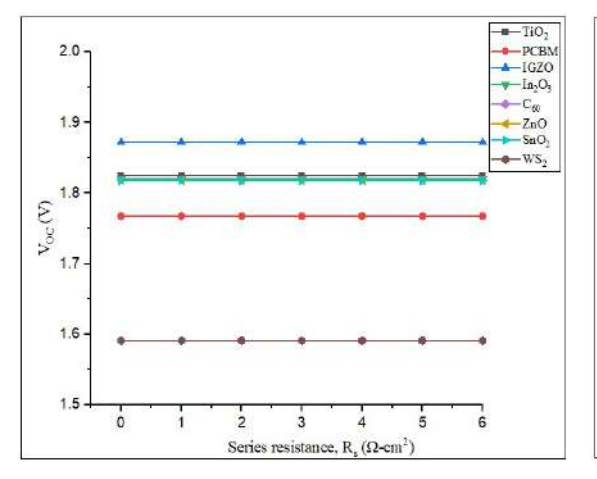
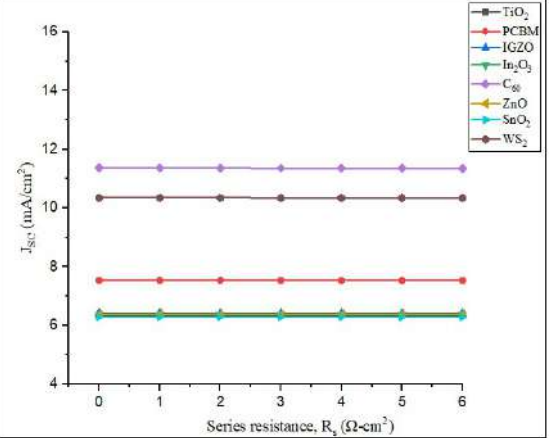


Figure 6.16 Impact of N_t on the performance of LaFeO₃-based PSCs.

6.5.5 Effect of Series Resistance

The R_S has a significant impact on the PCE of the device specially on the FF and short circuit current (I_{SC}). With the increment in R_S , FF reduces which results in decrement in I_{SC} . Hence, devices exhibit poor performance due to large values of R_S . When solar cells are exposed to the environment, thermomechanical fatigue or cracks develop in the solder bonds depending on weather conditions. These cracks lead to an increase in the value of R_S which in turn causes a decline in the PCE [42,43]. The value of R_S varied from 0 to 6 Ω -cm², at R_{SH} of $10^5 \Omega$ -cm². The simulation results of change in value of R_S with PV parameters of PSC shown below in Fig. 6.17. The FF reduced from 76 to 72 % with an increase in value of R_S while the PCE, V_{OC} and J_{SC} were not affected in every device. The results shown in fig. 18 are consistent with the previously reported studies [44,45]. The IGZO/LaFeO₃/CBTS and C_{60} /LaFeO₃/CBTS PSC configuration showed the highest V_{OC} and J_{SC} respectively whereas IGZO/LaFeO₃/CBTS PSC configuration showed relatively poor performance [46].





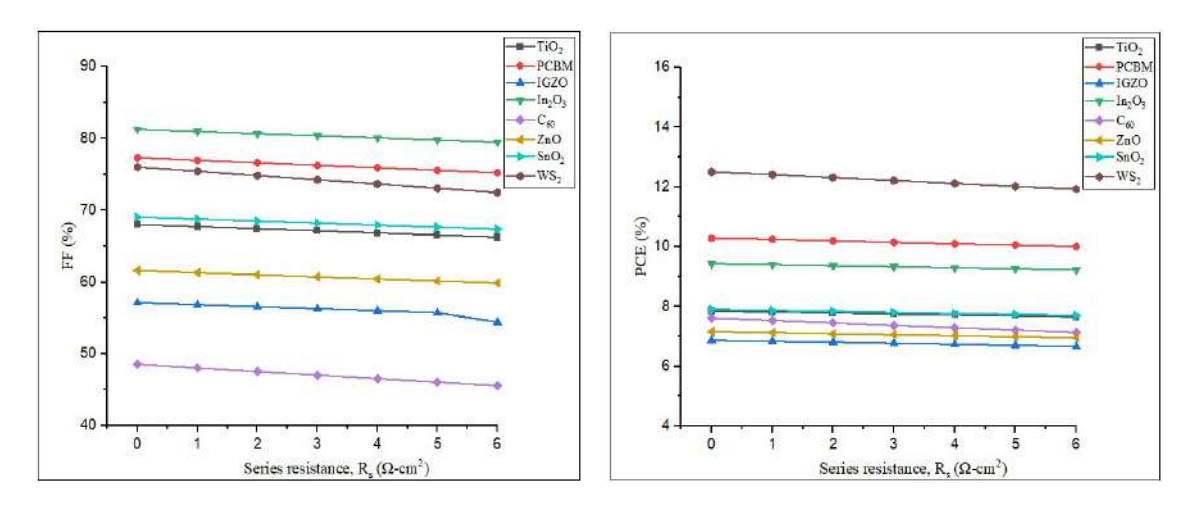
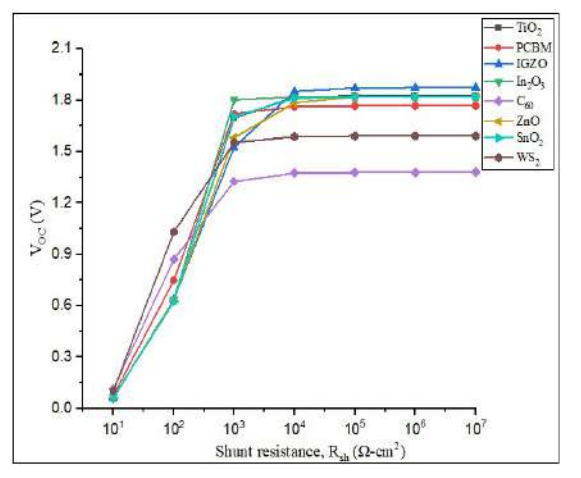
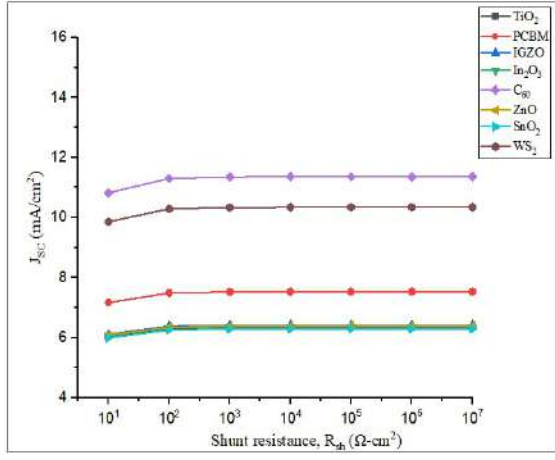


Figure 6.17 Impact of R_S on the performance of LaFeO₃-based PSC at R_{SH} = $10^5 \ \Omega$ -cm².

6.5.6 Effect of Shunt Resistance

The R_{SH} varied from 10^1 to $10^7~\Omega\text{-cm}^2$ at constant value of R_S of 0.5 $\Omega\text{-cm}^2$ for FTO/ETL/LaFeO₃/CBTS/Au configuration. The simulated outcome of different PV parameters shown below in Fig. 6.18. The J_{SC} varied from 10.82 to 11.36 mA/cm² for FTO/C₆₀/LaFeO₃/CBTS/Au structure whereas V_{OC} and PCE show a significant increment from 0.103 to 1.591 V and 0.25 to 12.48 % respectively for FTO/WS₂/LaFeO₃/CBTS/Au configuration. The small increase in J_{SC} with R_{SH} is due to decreased currents in the shunt-resisted path. The increment in V_{OC} is due to enhanced value of R_{SH} developing more voltage across the PSC [47]. The relation of the PCE with R_{SH} reported in the literature [48].





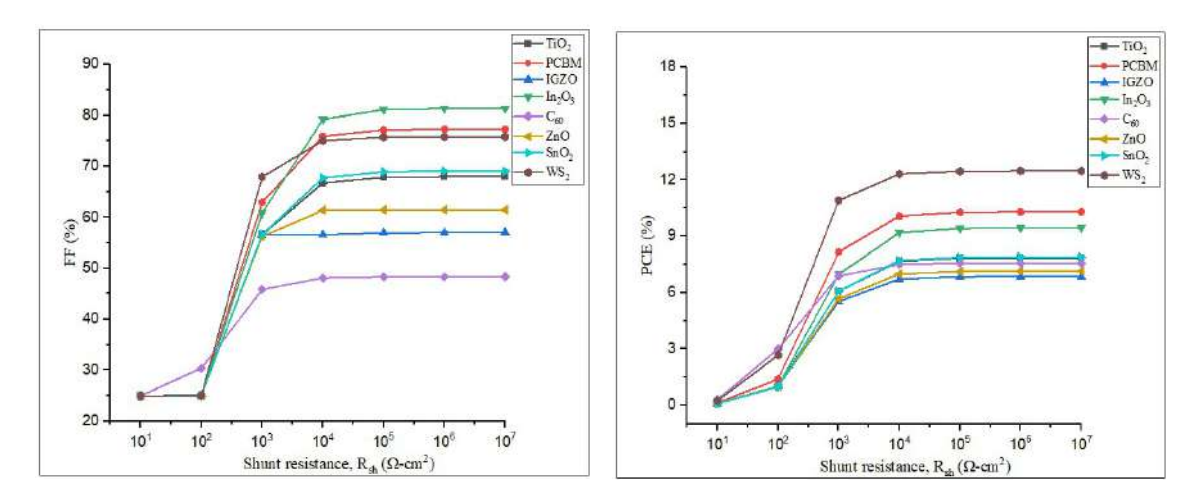


Figure 6.18 Impact of R_{sh} on the performance of LaFeO₃-based PSC at R_S = 0.5 Ω -cm².

6.5.7 Appropriate Back Contact

The impact of back contact on PCE of a PSC is studied. We have simulated the different back contacts with a work function (Φ) of 4.3 to 5.9 eV [49], the range covering the most of the available back contacts. The effect of Φ on the PCE of various PSCs depicted in Figu. 6.19. For the smaller value of work function, performance decreases gradually due to formation of Schottky junction. The enhancement in the PCE with Φ equal to 5.1 eV (Au) was observed. For the large value of work function, PCE remains constant, there is no chemical reaction amid the absorber layer and metal back contacts. The maximum efficiency of 13.03 % achieved at Φ of 5.1 eV (Au).

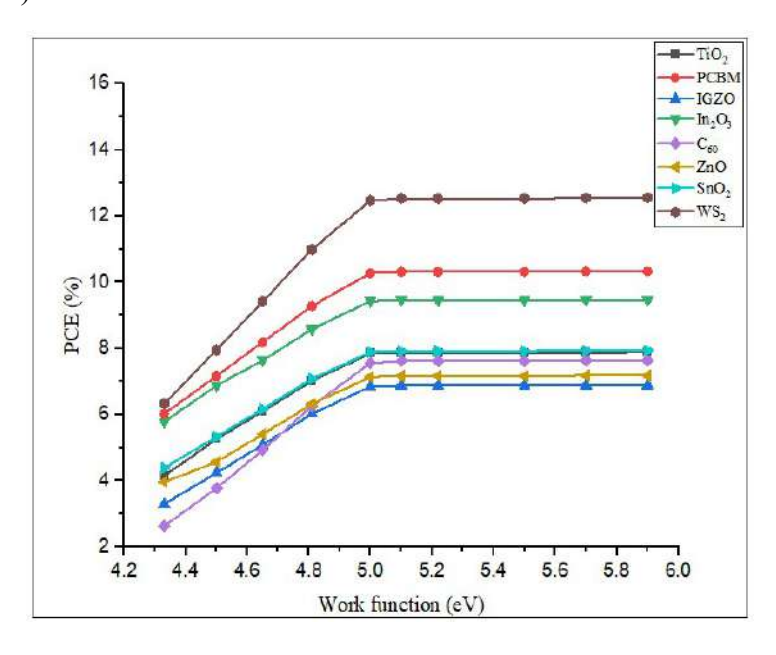


Figure 6.19 Impact of various work functions on efficiency.

6.6 Comparison of Experimental Results with Previously Reported Results

6.6.1 Simulation Results

The PSC structure and energy band diagram of the optimized device demonstrated below in Fig. 6.20. The optimum efficiency of 13.03 % with $V_{\rm OC}$ = 1.61 V, $J_{\rm SC}$ = 9.952 mA/cm², and FF of 81.17 % has been obtained. The optimized ETL and HTL are WS₂ and CBTS respectively with the Au (gold) as metal back contact. The comparison with the previously reported results illustrated in Table 6.7. The JV and QE curves of optimized PSC are illustrated in Fig. 6.21.

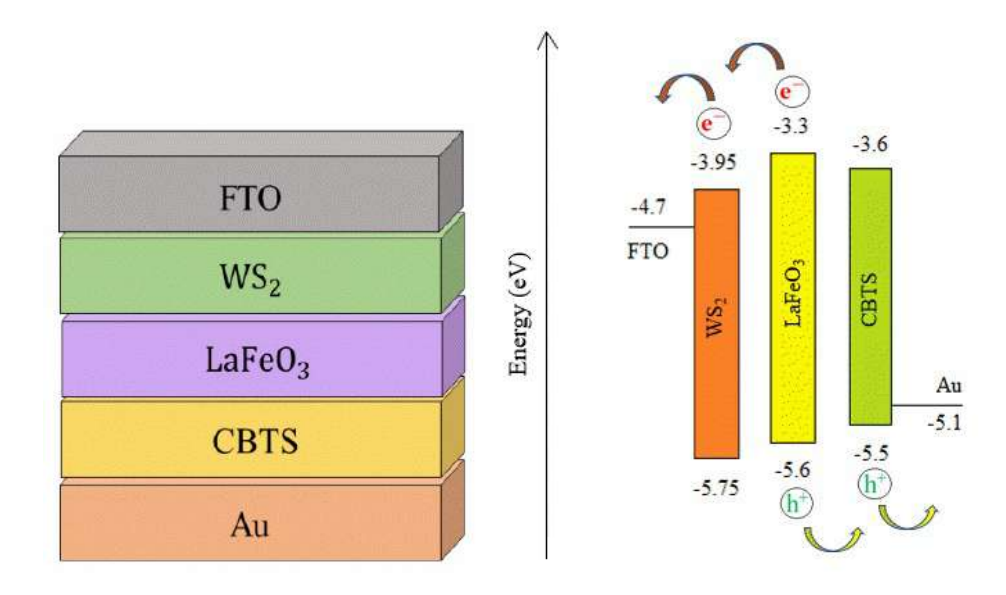


Figure 6.20 Structure and band alignment diagram of optimized device.

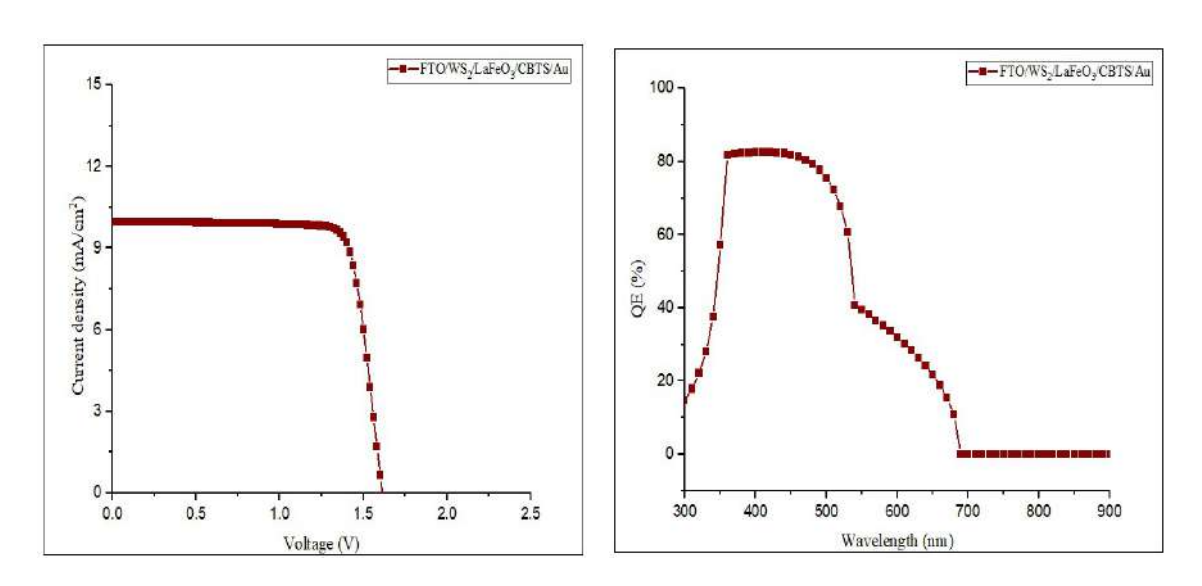


Figure 6.21 J-V and QE curve of optimized device.

6.6.2 Experimental Results

The fabricated LaFeO₃ PSC and its J-V characteristics are shown below in Fig. 6.22 and Fig. 6.23 respectively. The PV parameters of fabricated PSC is tabulated below in Table 6.7. One of the possible reasons for low PCE is the spin-coating process which has certain limitations. That is especially low thermal stability of the film, difficulty in fabricating an ideal multilayer structure, substrate size and shape. Typically, less than 5 % of the initial solution effectively deposits onto the substrate to create the thin film, with the remainder lost due to spinner rotation [50]. The LaFeO₃ possesses a bandgap of approximately 2.3 eV [17], which might not be sufficiently wide to prevent rapid recombination of its photogenerated electron-hole pairs which causes low performance of the device. To address this limitation, the preferred approach involves enhancing the E_g through size variation. Decreasing particle size is anticipated to elevate the bandgap, consequently restraining recombination rates. Additionally, optimizing photocatalytic performance involves creating a porous structure to enhance reaction sites. Therefore, augmenting pore density within the particles becomes crucial for maximizing efficiency [17]. LaFeO₃-based PSC still cannot be commercialized due to its weak photocatalytic performance, including issues like larger particle size and smaller surface area, reduced crystallinity from low temperature treatment and rapid charge recombination rate [51]. A 10 % doping of transition metal such as Mn, Co and Cu has potential to enhance the photocurrent of LaFeO₃ which results in increase in PCE [52].

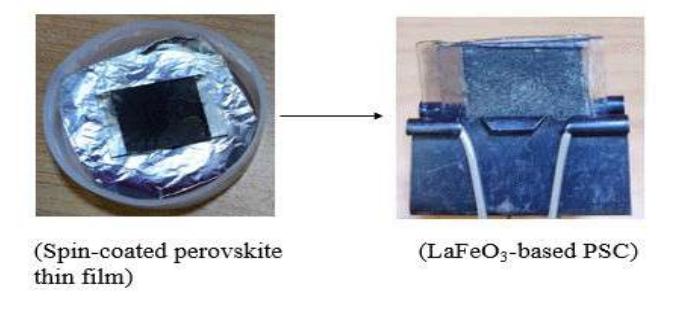


Figure 6.22 Fabricated LaFeO₃ PSC.

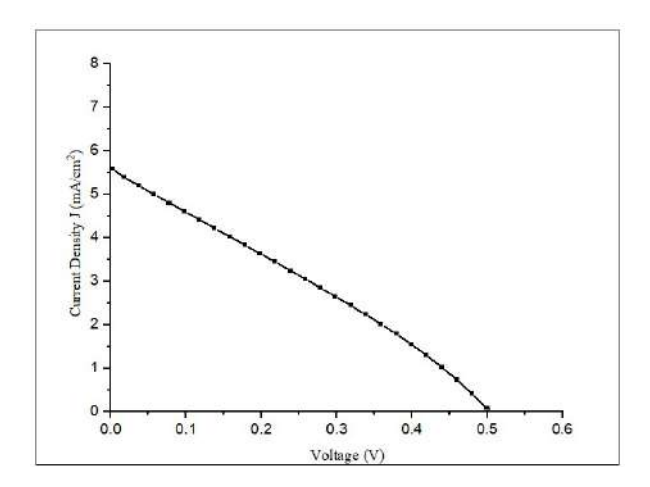


Figure 6.23 J-V curve of fabricated LaFeO₃-based PSC.

Table 6.7 Comparison of Experimental, SCAPS-1D and previously reported outcomes.

Parameters	SCAPS-1D	Experimental	Experimental [15]	Simulation [15]	Simulation [14]
Voc (V)	1.61	0.504	0.56	0.90	1.99
J_{SC} (mA/cm ²)	9.95	5.56	0.30	0.097	6.75
FF (%)	81.17	28.31	22	8.55	67.55
PCE (%)	13.03	0.79	0.06	0.01	9.11

6.7 Summary

This work comprises synthesis of LaFeO₃ perovskite material and simulation of LaFeO₃-based PSC followed by experimental validation. The sol-gel method is employed to synthesize LaFeO₃ perovskite material. The optimization of ETL and HTL has been done to achieve the maximum PCE. The work deduced that WS₂ as ETL and CBTS as HTL is most appropriate for LaFeO₃ PSC. The simulated and experimentally achieved maximum PCE were 13.03 % (with $V_{OC} = 1.61 \text{ V}$, $J_{SC} = 9.952 \text{ mA/cm}^2$, and FF = 81.17 %) and 0.79 % (with $V_{OC} = 0.504 \text{ V}$, $J_{SC} = 5.56 \text{ mA/cm}^2$, and FF = 28.31 %) respectively for the configuration of FTO/WS₂/LaFeO₃/CBTS/Au. This study also includes the optimization of various factors such as thickness of perovskite layer, operating temperature, N_t , metal back contact, series and shunt resistance. The optimized thickness of LaFeO₃ layer is 300 nm and at operating temperature of 300 K. The FTO/WS₂/LaFeO₃/CBTS/Au is the most stable structure. The optimized metal back contact is Gold (Au). These outcomes allude that the study is useful to fabricate the high performance LaFeO₃-based PSC.

6.8 REFERENCES

- [1] Abdulrahim, S.M., Ahmad, Z., Mehmood, M.Q., Paek, S., Bhadra, J., Al-Thani, N.J., Nazeeruddin, M.K., Belaidi, A. and Amani, M., 2021. Effect of illumination and applied potential on the electrochemical impedance spectra in triple cation (FA/MA/Cs) 3D and 2D/3D perovskite solar cells. *Journal of Electroanalytical Chemistry*, 902, p.115800.
- [2] Ahmad, Z., Mishra, A., Abdulrahim, S.M. and Touati, F., 2020. Electrical equivalent circuit (EEC) based impedance spectroscopy analysis of HTM free perovskite solar cells. *Journal of Electroanalytical Chemistry*, 871, p.114294.
- [3] Fu, K., He, Y., Zhang, B., Gao, X. and Zou, G., 2020. Enhanced aqueous stability and radiative-charge-transfer of CsPbBr₃/Ag₂S perovskite nanocrystal hybrids. *Journal of Electroanalytical Chemistry*, 858, p.113835.
- [4] Alizadeh, A. and Shariatinia, Z., 2022. Unveiling the influence of SmFeO₃-TiO₂ nanocomposites as high performance photoanodes of dye-sensitized solar cells. *Journal of Molecular Liquids*, 348, p.118070.
- [5] Rai, N., Rai, S., Singh, P.K., Lohia, P. and Dwivedi, D.K., 2020. Analysis of various ETL materials for an efficient perovskite solar cell by numerical simulation. *Journal of Materials Science: Materials in Electronics*, 31, pp.16269-16280.
- [6] Moradi, F., Shariatinia, Z., Safari, N. and Mohajerani, E., 2022. Boosted performances of mesoscopic perovskite solar cells using LaFeO₃ inorganic perovskite nanomaterial. *Journal of Electroanalytical Chemistry*, 916, p.116376.
- [7] Fan, X., 2023. Advanced progress in metal halide perovskite solar cells: A review. *Materials Today Sustainability*, 24, p.100603.
- [8] Wang, M., Zeng, P., Bai, S., Gu, J., Li, F., Yang, Z. and Liu, M., 2018. High-quality sequential-vapor-deposited Cs₂AgBiBr₆ thin films for lead-free perovskite solar cells. *Solar rrl*, 2(12), p.1800217.
- [9] Çoban Özkan, D., Türk, A. and Celik, E., 2020. Synthesis and characterizations of sol–gel derived LaFeO₃ perovskite powders. *Journal of Materials Science: Materials in Electronics*, 31, pp.22789-22809.
- [10] Nagavenkatesh, K.R., Sambathkumar, C., Murugesan, M., Devendran, P., Nallamuthu, N., Lakshmanan, P. and Shameem, A., 2024. Review on the recent improvements in lanthanum ferrite perovskites for visible light driven textile dyes degradation and its various heterojunctions catalysis mechanism. *Journal of Industrial and Engineering Chemistry*.
- [11] Yu, L., Wang, M., Ye, E., Lei, S., Liu, J., Liu, G. and Qiao, G., 2024. Synergistic enhancement of optical properties in Ca/Ni co-doped LaFeO₃ perovskite coatings enabling high-temperature photothermal conversion. *Applied Surface Science*, 642, p.158595.
- [12] Sabir, M., AlMasoud, N., Ramzan, M., Aamir, M., Ejaz, S.R., Alomar, T.S., El-Bahy, Z.M., Salam, M.A., Albukhari, S.M. and Baamer, D.F., 2023. Rare earth and transition metal co-doped LaFeO₃ perovskite and its CNTs reinforced nanohybrid for environmental remediation application. *Ceramics International*, 49(12), pp.20939-20950.

- [13] Bai, S., Shi, B., Ma, L., Yang, P., Liu, Z., Li, D. and Chen, A., 2009. Synthesis of LaFeO₃ catalytic materials and their sensing properties. *Science in china Series B: chemistry*, 52(12), pp.2106-2113.
- [14] Das, M.K., Panda, S. and Mohapatra, N., 2023. Power conversion efficiency optimization of LaFeO₃ Mott insulator based solar cell with metal oxide transport layers using SCAPS. *Materials Today: Proceedings*, 74, pp.756-762.
- [15] Moghadam, L.N. and Ranjbar, Z.R., 2019. Cost-efficient solar cells using nanocrystalline perovskite La (Fe and Mn) O₃ and candle soot: theory and experiment. *Journal of Alloys and Compounds*, 785, pp.117-124.
- [16] Chakraborty, R., Sim, K.M., Shrivastava, M., Adarsh, K.V., Chung, D.S. and Nag, A., 2019. Colloidal synthesis, optical properties, and hole transport layer applications of Cu₂BaSnS₄ (CBTS) nanocrystals. *ACS Applied Energy Materials*, 2(5), pp.3049-3055.
- [17] Azouzi, W., Sigle, W., Labrim, H. and Benaissa, M., 2019. Sol-gel synthesis of nanoporous LaFeO₃ powders for solar applications. *Materials Science in Semiconductor Processing*, 104, p.104682.
- [18] Zheng, W., Liu, R., Peng, D. and Meng, G., 2000. Hydrothermal synthesis of LaFeO₃ under carbonate-containing medium. *Materials Letters*, 43(1-2), pp.19-22.
- [19] Romero, M., Gómez, R.W., Marquina, V., Pérez-Mazariego, J.L. and Escamilla, R., 2014. Synthesis by molten salt method of the AFeO₃ system (A= La, Gd) and its structural, vibrational and internal hyperfine magnetic field characterization. *Physica B: Condensed Matter*, 443, pp.90-94.
- [20] Sharma, N., Kushwaha, H.S., Sharma, S.K. and Sachdev, K., 2020. Fabrication of LaFeO₃ and rGO-LaFeO₃ microspheres based gas sensors for detection of NO₂ and CO. *RSC advances*, 10(3), pp.1297-1308.
- [21] Ren, X., Yang, H., Gen, S., Zhou, J., Yang, T., Zhang, X., Cheng, Z. and Sun, S., 2016. Controlled growth of LaFeO₃ nanoparticles on reduced graphene oxide for highly efficient photocatalysis. *Nanoscale*, 8(2), pp.752-756.
- [22] Bencherif, H. and Hossain, M.K., 2022. Design and numerical investigation of efficient (FAPbI₃)_{1-x}(CsSnI₃)_x perovskite solar cell with optimized performances. *Solar Energy*, 248, pp.137-148.
- [23] Kanoun, A.A., Kanoun, M.B., Merad, A.E. and Goumri-Said, S., 2019. Toward development of high-performance perovskite solar cells based on CH₃NH₃GeI₃ using computational approach. *Solar Energy*, 182, pp.237-244.
- [24] Jayan, K.D. and Sebastian, V., 2021. Comprehensive device modelling and performance analysis of MASnI₃ based perovskite solar cells with diverse ETM, HTM and back metal contacts. *Solar Energy*, 217, pp.40-48.
- [25] Raj, A., Kumar, M., Bherwani, H., Gupta, A. and Anshul, A., 2021. Evidence of improved power conversion efficiency in lead-free CsGeI₃ based perovskite solar cell heterostructure via scaps simulation. *Journal of Vacuum Science & Technology B*, 39(1).
- [26] Husainat, A., Ali, W., Cofie, P., Attia, J. and Fuller, J., 2019. Simulation and analysis of methylammonium lead iodide (CH₃NH₃PbI₃) perovskite solar cell with Au contact using SCAPS 1D simulator. *American Journal of Optics and Photonics*, 7(2), p.33.

- [27] Bhattarai, S. and Das, T.D., 2021. Optimization of carrier transport materials for the performance enhancement of the MAGeI₃ based perovskite solar cell. *Solar Energy*, 217, pp.200-207.
- [28] Mandadapu, U., Vedanayakam, S.V. and Thyagarajan, K., 2017. Simulation and analysis of lead based perovskite solar cell using SCAPS-1D. *Indian J. Sci. Technol*, 10(1), pp.1-8.
- [29] Azri, F., Meftah, A., Sengouga, N. and Meftah, A., 2019. Electron and hole transport layers optimization by numerical simulation of a perovskite solar cell. *Solar energy*, 181, pp.372-378.
- [30] Mushtaq, S., Tahir, S., Ashfaq, A., Bonilla, R.S., Haneef, M., Saeed, R., Ahmad, W. and Amin, N., 2023. Performance optimization of lead-free MASnBr₃ based perovskite solar cells by SCAPS-1D device simulation. *Solar Energy*, 249, pp.401-413.
- [31] Hossain, M.K., Toki, G.I., Kuddus, A., Rubel, M.H., Hossain, M.M., Bencherif, H., Rahman, M.F., Islam, M.R. and Mushtaq, M., 2023. An extensive study on multiple ETL and HTL layers to design and simulation of high-performance lead-free CsSnCl₃-based perovskite solar cells. *Scientific Reports*, 13(1), p.2521.
- [32] Lakhdar, N. and Hima, A., 2020. Electron transport material effect on performance of perovskite solar cells based on CH₃NH₃GeI₃. *Optical Materials*, 99, p.109517.
- [33] Singh, M., Kumar, R. and Singh, V., 2021. Investigation of CH₃NH₃PbI₃ and CH₃NH₃SnI₃ based perovskite solar cells with CuInSe₂ nanocrystals. *Optik*, 246, p.167839.
- [34] De Los Santos, I.M., Cortina-Marrero, H.J., Ruíz-Sánchez, M.A., Hechavarría-Difur, L., Sánchez-Rodríguez, F.J., Courel, M. and Hu, H., 2020. Optimization of CH₃NH₃PbI₃ perovskite solar cells: A theoretical and experimental study. *Solar Energy*, 199, pp.198-205.
- [35] Bencherif, H., Meddour, F., Elshorbagy, M.H., Hossain, M.K., Cuadrado, A., Abdi, M.A., Bendib, T., Kouda, S. and Alda, J., 2022. Performance enhancement of (FAPbI₃)_{1-x}(MAPbBr₃)_x perovskite solar cell with an optimized design. *Micro and Nanostructures*, 171, p.207403.
- [36] Kuddus, A., Rahman, M.F., Ahmmed, S., Hossain, J. and Ismail, A.B.M., 2019. Role of facile synthesized V₂O₅ as hole transport layer for CdS/CdTe heterojunction solar cell: validation of simulation using experimental data. *Superlattices and Microstructures*, 132, p.106168.
- [37] Hossain, M.K., Arnab, A.A., Das, R.C., Hossain, K.M., Rubel, M.H.K., Rahman, M.F., Bencherif, H., Emetere, M.E., Mohammed, M.K. and Pandey, R., 2022. Combined DFT, SCAPS-1D, and wxAMPS frameworks for design optimization of efficient Cs₂BiAgI₆-based perovskite solar cells with different charge transport layers. *RSC advances*, 12(54), pp.35002-35025.
- [38] Ahmed, S., Jannat, F., Khan, M.A.K. and Alim, M.A., 2021. Numerical development of ecofriendly Cs₂TiBr₆ based perovskite solar cell with all-inorganic charge transport materials via SCAPS-1D. *Optik*, 225, p.165765.
- [39] Rai, S., Pandey, B.K. and Dwivedi, D.K., 2020. Modeling of highly efficient and low cost CH₃NH₃Pb(I_{1-x}Cl_x)₃ based perovskite solar cell by numerical simulation. *Optical Materials*, 100, p.109631.
- [40] Johnston, M.B. and Herz, L.M., 2016. Hybrid perovskites for photovoltaics: charge-carrier recombination, diffusion, and radiative efficiencies. *Accounts of chemical research*, 49(1), pp.146-154.

- [41] Bencherif, H., 2022. Towards a high efficient Cd-free double CZTS layers kesterite solar cell using an optimized interface band alignment. *Solar Energy*, 238, pp.114-125.
- [42] Samiul Islam, M., Sobayel, K., Al-Kahtani, A., Islam, M.A., Muhammad, G., Amin, N., Shahiduzzaman, M. and Akhtaruzzaman, M., 2021. Defect study and modelling of SnX₃-based perovskite solar cells with SCAPS-1D. *Nanomaterials*, 11(5), p.1218.
- [43] Poorkazem, K., Liu, D. and Kelly, T.L., 2015. Fatigue resistance of a flexible, efficient, and metal oxide-free perovskite solar cell. *Journal of Materials Chemistry A*, 3(17), pp.9241-9248.
- [44] Danladi, E., Egbugha, A.C., Obasi, R.C., Tasie, N.N., Achem, C.U., Haruna, I.S. and Ezeh, L.O., 2023. Defect and doping concentration study with series and shunt resistance influence on graphene modified perovskite solar cell: a numerical investigation in SCAPS-1D framework. *Journal of the Indian Chemical Society*, 100(5), p.101001.
- [45] Karthick, S., Velumani, S. and Bouclé, J., 2020. Experimental and SCAPS simulated formamidinium perovskite solar cells: A comparison of device performance. *Solar Energy*, 205, pp.349-357.
- [46] Heriche, H., Rouabah, Z. and Bouarissa, N., 2017. New ultra thin CIGS structure solar cells using SCAPS simulation program. *International Journal of Hydrogen Energy*, 42(15), pp.9524-9532.
- [47] Sharma, A.K., Chourasia, N.K., Jha, P.K., Kumar, R., Kumar, M. and Chourasia, R.K., 2023. Characteristic features and performance investigations of a PTB7: PC71BM/PFN: Br pure organic solar cell using SCAPS-1D. *Journal of Electronic Materials*, 52(7), pp.4302-4311.
- [48] Jha, P.K., Chourasia, N.K., Sharma, A.K. and Chourasia, R.K., 2022. Optimization of electrical properties for performance analysis of p-Si/n-CdS/ITO heterojunction photovoltaic cell. *Materials Today: Proceedings*, 67, pp.620-624.
- [49] Pindolia, G., Shinde, S.M. and Jha, P.K., 2023. Non-leaded, KSnI₃ based perovskite solar cell: A DFT study along with SCAPS simulation. *Materials Chemistry and Physics*, 297, p.127426.
- [50] Nisticò, R., Scalarone, D. and Magnacca, G., 2017. Sol-gel chemistry, templating and spin-coating deposition: A combined approach to control in a simple way the porosity of inorganic thin films/coatings. *Microporous and Mesoporous Materials*, 248, pp.18-29.
- [51] Humayun, M., Ullah, H., Usman, M., Habibi-Yangjeh, A., Tahir, A.A., Wang, C. and Luo, W., 2022. Perovskite-type lanthanum ferrite based photocatalysts: Preparation, properties, and applications. *Journal of Energy Chemistry*, 66, pp.314-338.
- [52] Peng, Q., Shan, B., Wen, Y. and Chen, R., 2015. Enhanced charge transport of LaFeO₃ via transition metal (Mn, Co, Cu) doping for visible light photoelectrochemical water oxidation. *international journal of hydrogen energy*, 40(45), pp.15423-15431.

CHAPTER 7

PREDICTIVE DESIGN OF KSnI₃-BASED PEROVSKITE SOLAR CELLS USING SCAPS AND MACHINE LEARNING MODEL

- ➤ The Chapter includes SCAPS-1D simulation to evaluate the impact of various HTLs on the performance of Potassium Tin Iodide (KSnI₃)-based PSCs, including materials like Spiro-OMeTAD, CuI, and PEDOT: PSS.
- ➤ A maximum efficiency of 23.08 % is achieved for KSnI₃-based PSCs with an absorber layer thickness of 550 nm and a defect density of 10¹³ cm⁻³.
- ➤ A machine learning model is trained to predict the performance of PSCs, achieving an accuracy of approximately 89% in forecasting the performance metrics.
- The FTO/WS₂/KSnI₃/PEDOT: PSS/Au device configuration is identified as the most suitable for manufacturing highly efficient photovoltaic devices.

7.1 Introduction

In 2009, PSC was reported with an efficiency of 3.8 % and has achieved maximum PCE of greater than 26 % till now [1]. The study comprises investigation of KSnI₃ as a perovskite material which is used as an absorber in a PSC. In past reported investigations there is very limited study on KSnI₃ PSC. Grishma et al. (2023) have reported efficiency of 9.77 % [2]. So there needs to be proper optimization to enhance the efficiency of PSC. Whereas, in this work we have obtained a maximum PCE of 23.08 %. The SCAPS enabled machine learning model is used to optimize and predict the best efficiency [3]. It has been exhibited that ML is helpful in forecasting the design and performance of PSCs [4]. Firstly, we have simulated KSnI₃-based PSC with several HTLs (Spiro-OMeTAD, CuI, CuSCN, Cu₂O, PEDOT: PSS, CdTe, MASnBr₃ and CFTS) and KSnI₃ is employed as a perovskite absorber layer. Secondly, we have optimized the effect of distinct performance parameters of PSCs such as absorber layer thickness, N_t and doping density (NA). Ultimately, we trained an ML model to predict the performance parameters of the PSCs with an accuracy of approximately 89 %. The present method serves as a sturdy foundation for subsequent research and investigations driven by artificial intelligence (AI). The efficient PSCs can be designed with application of ML modelling and SCAPS-1D assisted by previous studies.

7.2 Device Architecture and Methods

The PSC consists of KSnI₃ absorber material with layer architecture: FTO/ETL/Perovskite layer/HTL/Back-contact depicted in Fig. 7.1. All the input data used in SCAPS simulation obtained from experimental and theoretical work enclosed is in Table 7.1 for FTO/TiO₂/KSnI₃/Spiro-OMeTAD/Au-Metal and HTLs in Table 7.2. The SCAPS-1D (version 3.3.10) has been employed for simulation. The work is based on change in thickness, N_t, and N_A at which simulation of the proposed PSC has been done.

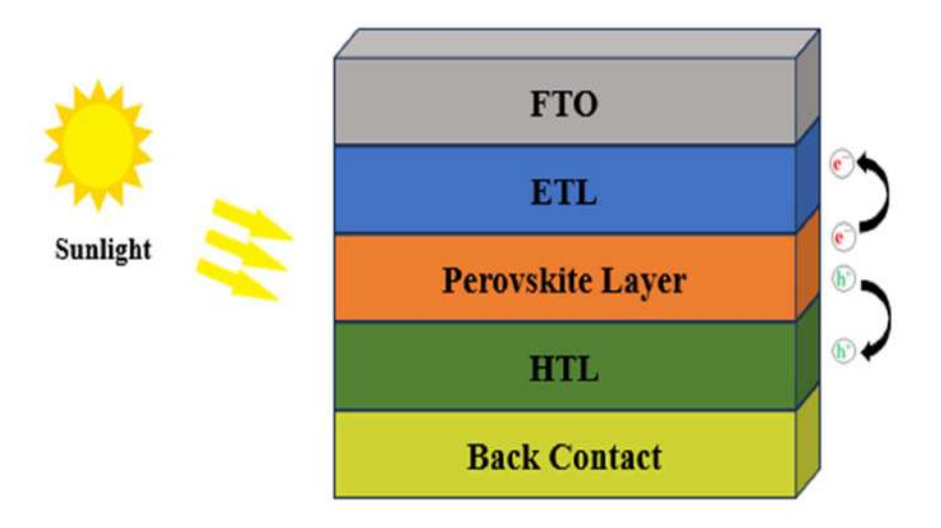


Figure 7.1 Architecture of simulated PSCs.

Table 7.1 Input parameters of simulated PSC.

Parameter	FTO [5,6]	WS ₂ [7]	KSnI ₃ [2]	Spiro-OMeTAD [8,9]
Thickness (nm)	400	100*	300	50
Eg (eV)	3.5	1.8	1.84	3.0
$\chi \left(eV\right)$	4.0	3.95	3.44	2.45
ε	9.0	13.6	10.4	3.0
$N_{\rm C}$ (cm ⁻³)	2.02×10^{18}	1×10^{18}	2.2×10^{18}	1×10^{19}
N_V (cm ⁻³)	1.8×10^{19}	2.4×10^{19}	1.8×10^{19}	1×10^{19}
μ_n (cm ² /Vs)	20	100	21.28	1×10^{-4}
μ_p (cm ² /Vs)	10	100	19.46	1×10^{-4}
N_D (cm ⁻³)	2×10^{19}	1×10^{18}	1×10^{15}	0
N_A (cm ⁻³)	0	0	1×10^{15}	2×10^{18}
N _t (cm ⁻³)	1×10^{15}	$1 \times 10^{13*}$	1×10^{13}	1×10^{14}

Table 7.2 Input parameters of distinct HTLs.

Parameter	CuI [8,9]	CuSCN [9,10]	Cu ₂ O [5,9,11]	PEDOT: PSS [9,12,13]	CdTe [9,14]	MASnBr ₃ [15,9,16]	CFTS [9,17]
Thickness (nm)	50	50	50	50	50	50	50
Eg (eV)	3.1	3.4	2.17	2.2	1.5	2.15	1.3
$\chi\left(eV\right)$	2.1	1.9	3.2	2.9	3.9	3.39	3.3
3	6.5	10	7.11	3.0	9.4	8.2	9.0
N_C (cm ⁻³)	2.8×10^{19}	2.2×10^{19}	2.02×10^{17}	2.2×10^{15}	8.0×10^{17}	1×10^{18}	2.2×10^{18}
N_V (cm ⁻³)	1×10^{19}	1.8×10^{18}	1.1×10^{19}	1.8×10^{18}	1.8×10^{19}	1×10^{18}	1.8×10^{19}
$\mu_n (cm^2/Vs)$	100	1×10^{-4}	200	1×10^{-2}	3.2×10^2	1.6	21.98
$\mu_p (cm^2/Vs)$	80	1×10^{-2}	80	2×10^{-4}	40	1.6	21.98
N_D (cm ⁻³)	0	0	0	0	0	0	0
N_A (cm ⁻³)	1×10^{18}	1×10^{16}	1×10^{18}	1×10^{19}	2×10^{14}	1×10^{18}	1×10^{18}
N_t (cm ⁻³)	1×10^{14}	$1 \times 10^{14*}$	1×10^{14}	1×10^{14}	$1 \times 10^{14*}$	$1\times10^{14^*}$	$1\times10^{14^*}$

*In this work

7.2.1 Machine Learning

Python was chosen as the programming language for implementing ML due to its widespread use in AI applications [18-20]. To work with the dataset, Numpy and Pandas libraries were utilized. The dataset pertains to solar cell features and was thoroughly cleaned and preprocessed to make it compatible with ML algorithms. Initially, a simple Random Forest algorithm from Scikit-Learn (Sklearn) was employed to determine the significance of each feature for the final model. As a result of this phase, eleven features were selected for further analysis. For feature extraction related to composition of perovskites, Pymatgen and Matminer packages were utilized. The data was then split into training and testing sets for model training. To find the best hyperparameters, two distinct approaches were taken. First a parameter grid (a Python dictionary) inclusive various values for each parameter was prepared. The RandomizedSearchCV and GridSearchCV tools from Scikit-Learn were employed to assess the optimal combination of hyperparameters from this grid. The RandomizedSearchCV randomly selected combinations from the grid and evaluated their performance using crossvalidation, while the GridSearchCV evaluated every possible combination of the provided parameters. To ensure the model's performance and consistency, five-fold cross-validation was performed on the final model. Subsequently, a separate test set was used to assess the model's accuracy and overall performance. Random Forest's ability to aggregate the results of individual decision trees helped mitigate overfitting issues and improved the model's predictive performance [21]. Overfitting occurs when a model becomes too tailored to the training data, resulting in high variance and poor predictive performance on the test set. To mitigate overfitting, various techniques can be applied, such as comparing the prediction results between the training and test sets. Several approaches can be used, including increasing the number of decision trees and reducing their maximum depth. The prediction's coefficient of determination acted as the evaluation metric. According to the Sklearn, this metric exhibited as is defined as:

$$R^2 = \left(1 - \frac{u}{v}\right) \tag{7.1}$$

u represent the residual sum of squares $((y_{pred} - y_{true})^2)$. Meanwhile, v stands for the total sum of squares = $((y_{pred} - mean (y_{true}))^2$. It's worth noting that a constant model that solely predicts the anticipated y, irrespective of input, could obtain a score of R² equal to 0.0. The significance of a node j within a single decision tree, the calculation involved as follows [21]:

$$ni_{j} = w_{j}C_{j} - w_{left(j)}Cleft(j) - w_{right(j)}C_{right(j)}$$

$$(7.2)$$

where w_j denotes the weighted number of samples in node j as a fraction of the total weighted number of samples. C_i represents the impurity in node j and left (j) and right (j) corresponds to the child nodes associated with it. The following calculation is used to determine feature's importance [21]:

$$fi_i = \frac{\sum_{j:nodejsplitsonfeaturei} ni_j}{\sum_{j \in allnodes} ni_j}$$
Ultimately, the feature values were calculated as the mean of every particular decision tree.

7.3 Results and Discussion

7.3.1 Selection of Appropriate HTL

The HTL exhibits an important role in optimization of PSC performance via two ways such as it transports the light generated holes towards the back contact and HTL hampers the interaction between absorber layer and back contact. Despite the comprehensive application of Spiro-OMeTAD into PSC to increase PCE, low hole mobility (μ_p) , and environment instability confined its commercial application. Consequently, various kinds of HTLs like CuI, CuSCN, Cu₂O, PEDOT: PSS, CdTe, MASnBr₃ and CFTS have been analysed shown in Table 7.2. To begin the simulation, a PSC architecture of FTO/TiO2/KSnI3/Spiro-OMeTAD/Au was simulated to validate with previously reported results [22]. WS₂ opted as ETL due to its high electron mobility (μ_n), wide range of E_g, and high conductivity of $10^{-3} \Omega^{-1} \text{ cm}^{-1}$ [23]. The validation of the simulated result shown below in Table 7.3. The highest occupied molecular orbital (HOMO) of HTL should be appropriately aligned with that of the perovskite layer. The proper optimization is required to select appropriate ETL and HTL to maximize the performance of the PSC. The energy bandgap diagram of ETL, absorber layer and various HTLs illustrated below in Fig. 7.2. The J-V and QE plots of PSC with various HTLs are shown below in Fig. 7.3. The plotted curve from simulations is well-fitted with the previously reported outcomes, which validates numerical simulations.

Cell structure	V _{OC} (V)	J _{SC} (mA/cm ²)	FF (%)	PCE (%)
FTO/TiO ₂ /KSnI ₃ /Spiro-OMeTAD/W	1.70	15.85	36.13	9.77 [22]
FTO/C ₆₀ /KSnI ₃ /PTAA/C	0.76	17.44	80.80	10.83 [24]
FTO/TiO ₂ /KSnI ₃ /Spiro-OMeTAD/Au	1.48	13.20	79.07	15.55 [This work]

Table 7.3 Comparison with previously reported results.

To examine the impact of the several HTLs like Spiro-OMeTAD, CuI, CuSCN, Cu₂O, PEDOT: PSS, CdTe, MASnBr₃ and CFTS on the PV parameters of PSC. The thickness of HTLs was 50 nm throughout the simulation. The simulated results are demonstrated in Fig. 7.3. The PV parameters with several HTLs are presented below in Table 7.4.

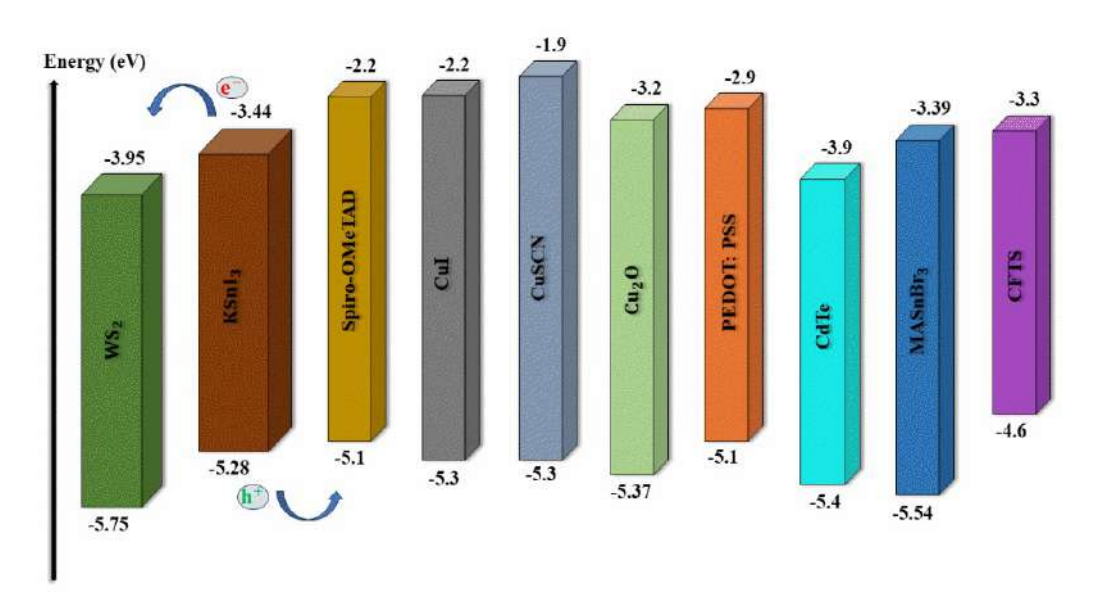


Figure 7.2 Energy band diagram of various HTLs.

Cell structure	V _{OC} (V)	J _{SC} (mA/cm ²)	FF (%)	PCE (%)
			. ,	
FTO/WS ₂ /KSnI ₃ /CuI/Au	1.59	15.01	87.40	20.98
FTO/WS ₂ /KSnI ₃ /CuSCN/Au	1.59	15.01	84.48	20.27
FTO/WS ₂ /KSnI ₃ /Cu ₂ O/Au	1.59	14.96	87.63	20.96
FTO/WS ₂ /KSnI ₃ /Spiro-OMeTAD/Au	1.59	14.89	79.18	18.85
FTO/WS ₂ /KSnI ₃ /PEDOT: PSS/Au	1.59	15.08	87.43	21.08
FTO/WS ₂ /KSnI ₃ /CdTe/Au	1.33	14.93	71.06	14.18
FTO/WS ₂ /KSnI ₃ /MASnBr ₃ /Au	1.59	15.09	85.14	20.56
FTO/WS2/KSnI2/CFTS/A11	1 13	19 32	81.26	17.85

Table 7.4 The PV parameters of KSnI₃-based PSC with distinct HTLs.

The Spiro-OMeTAD and PEDOT: PSS both are organic materials. The Eg for Spiro-OMeTAD is 3 eV and for PEDOT: PSS is 2.2 eV depicted in Table 7.1 and 7.2. The PEDOT: PSS has excellent properties such as high electrical conductivity, mechanical flexibility and suitable for thin film formation [25]. The simulation results demonstrated that KSnI₃-based PSC exhibited maximum PCE of 21.08 % (with V_{OC} of 1.59 V, J_{SC} of 15.08 mA/cm² and FF of 87.43 %) for WS₂ as ETL and PEDOT: PSS employed as HTL. The HOMO level of Spiro-OMeTAD and PEDOT: PSS has good band alignment with KSnI₃ therefore with PEDOT: PSS it has achieved maximum PCE but not for Spiro-OMeTAD. This can be attributed to lower hole mobility (μ_p) than PEDOT: PSS [26,27]. Hence, PEDOT: PSS is an appropriate HTL for achieving high PCE. Furthermore, the PEDOT: PSS exhibits good stability in air over Spiro-OMeTAD so that it has wide application in PSCs. Zuo et al. (2017) doped PEDOT: PSS with polymer electrolyte PSS-Na which results in high work function and good band alignment of modified PEDOT: PSS with the absorber layer. Hence, enhanced PCE has been obtained from 12.35 to 15.56 % [28]. The small amount of 2,3,5,6-tetrafluoro-7,7,8,8-tetracyanoquinodimethane (F4-TCNQ) added to PEDOT: PSS could improve the electrical conductivity and better band matching with the absorber layer. Therefore, the PCE enhanced from 13.30 to 17.22 % [29,30].

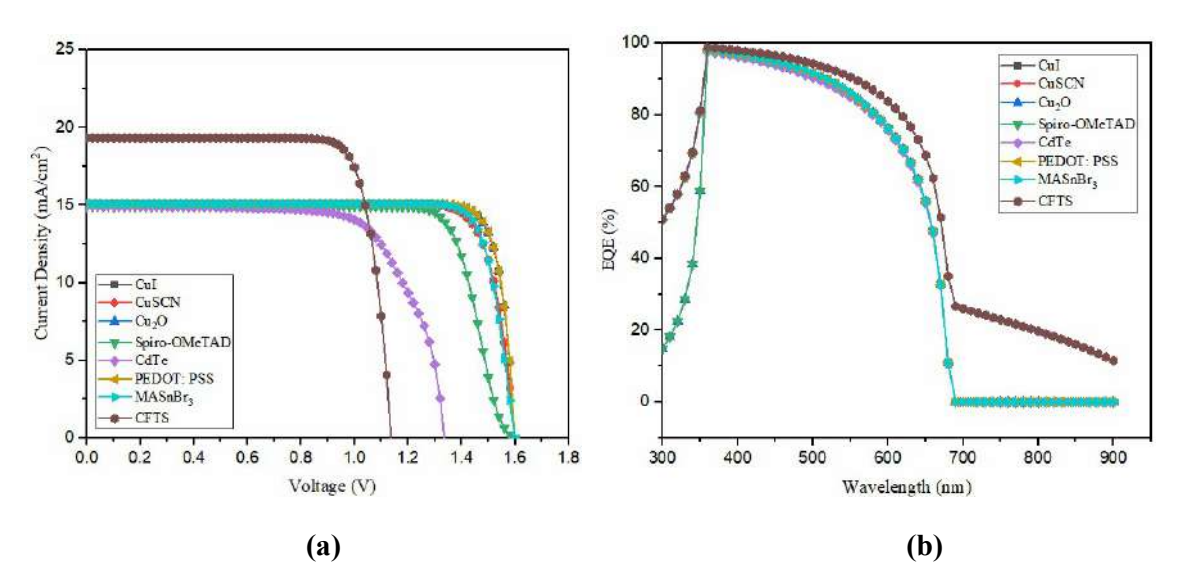
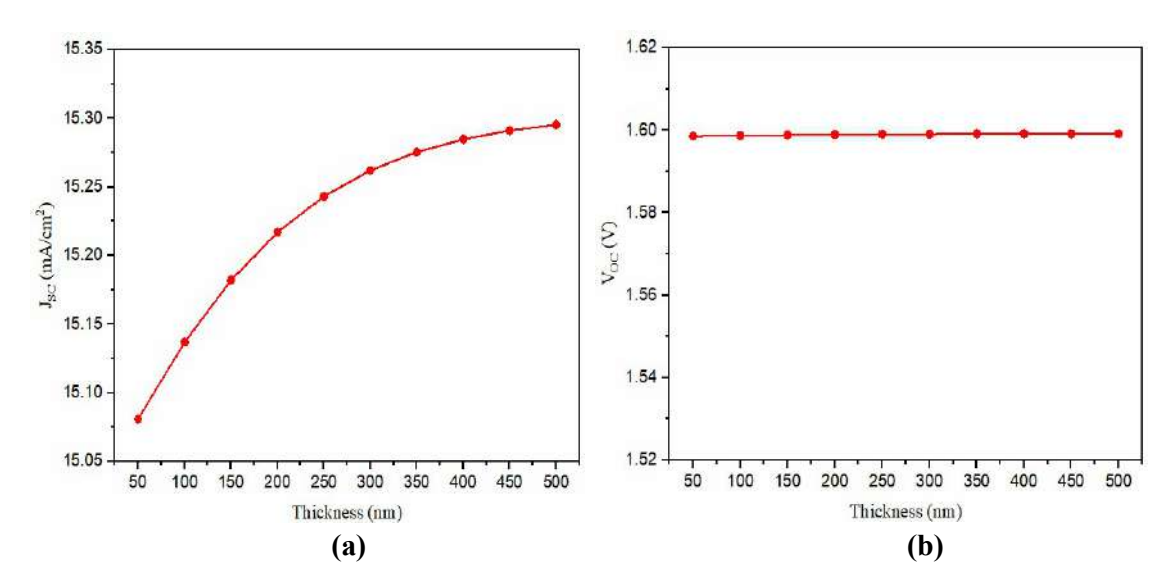


Figure 7.3 (a) J-V and (b) QE plots of simulated PSCs with various HTLs.

7.3.2 Optimization of HTL

7.3.2.1 Impact of Thickness

In the preceding section, Table 7.4 highlighted that PEDOT: PSS emerges as the most promising HTL for KSnI₃-based PSC. As the attributes of HTL, such as thickness, doping density (N_A), and N_t, exert a substantial influence on PSC performance and these parameters must be optimized. Notably, HTL thickness exhibits a vital role in facilitating efficacious carrier transport and controlling the recombination rate [31]. Consequently, the thickness of an HTL is optimized to get high PCE. Fig. 7.4a, b demonstrates the impact of PEDOT: PSS thickness on the J_{SC} and V_{OC} of PSCs. The findings reveal that increasing PEDOT: PSS thickness up to 250 nm enhances both J_{SC} and V_{OC}, beyond which they become constant. According to experimental surveys, thicker HTLs yields smoother film surfaces, reducing interfacial recombination and thus enhancing Voc. The suitable HTL thickness is required to avoid R_S for thicker layers [32,33]. Firstly, a thinner HTL might not accumulate a sufficient number of holes. Secondly, the region among the absorber layer and a thin HTL might not be as potent as in thicker layers, leading to inadequate driving force for carrier partition. The study also indicates that when HTL thickness exceeds 250 nm both $V_{\rm OC}$ and $J_{\rm SC}$ tend to be constant. This is primarily due to carrier travel distance to reach the interface. Consequently, traps promote non-radiative Shockley-Read-Hall (SRH) recombination and enhanced trap-assisted recombination rate [34]. The influence of thickness on PV parameters is depicted in Fig. 7.4. The initial fall in the curve is a result of an increase in R_S. The optimized thickness of HTL is 250 nm, yielding a PCE of 21.30 % demonstrated in Fig. 7.4d.



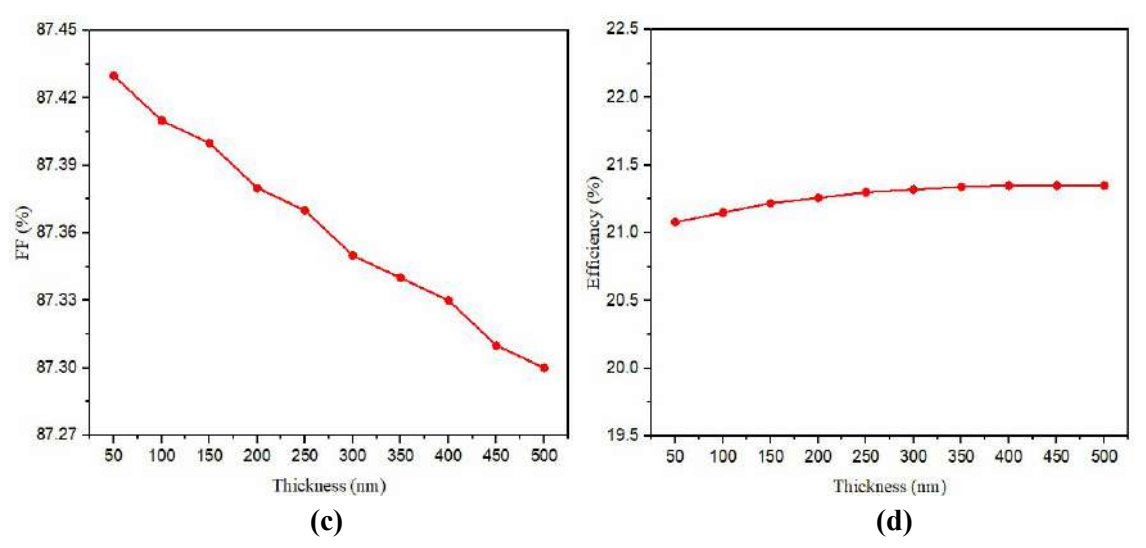


Figure 7.4 Impact of the thickness of PEDOT: PSS layer on PV parameters of PSC.

7.3.2.2 Impact of Doping Density

The findings from previous studies have shown the significant impact of doping density (N_A) in the HTL vastly affects the PV parameters of PSCs, including conductivity, recombination rate and V_{OC} [15]. Hence, the solar cell parameters were simulated in the range of N_A values from 10^{14} to 10^{22} cm⁻³ at a thickness of 250 nm of HTL. As depicted in Fig. 7.5a, an enhancement in N_A leads to an increase in V_{OC} . In layered semiconductor architectures, the alignment of the fermi level at the same value results in an equilibrium state, causing band bending and built-in voltage (V_{bi}) [35]. This internal electric field drifts segregated photogenerated e^{-s} and h^{+s} towards the n and p regions respectively, where they gather. Under illumination and open-circuit conditions, the excited carriers induce the separation of quasi-Fermi-levels (EFn and EFp) for e^{-s} and h^{+s}, respectively, within the photoactive semiconductor material. This effectively nullifies V_{bi} , and forms a photo-voltage referred to as V_{OC} [36].

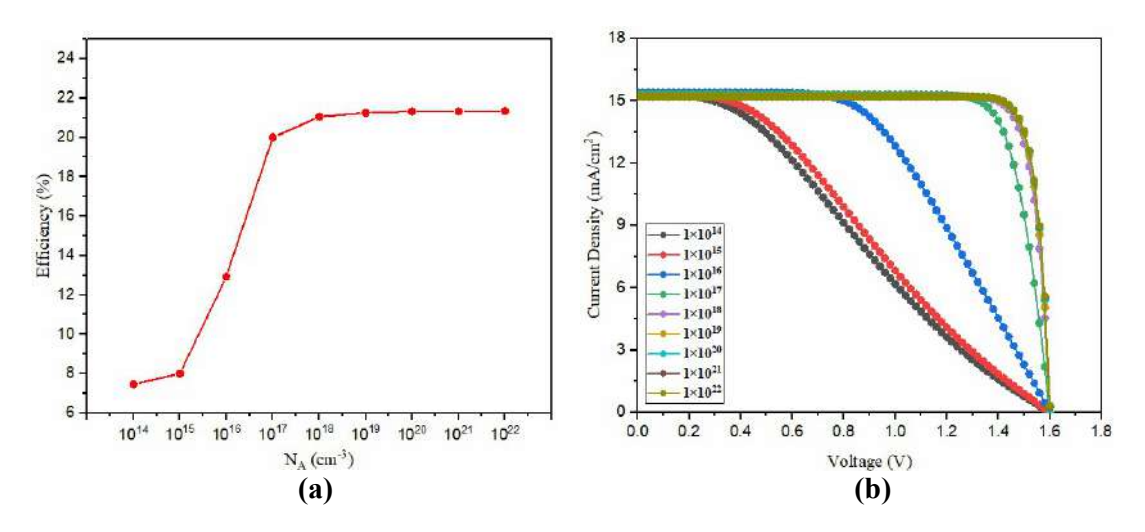
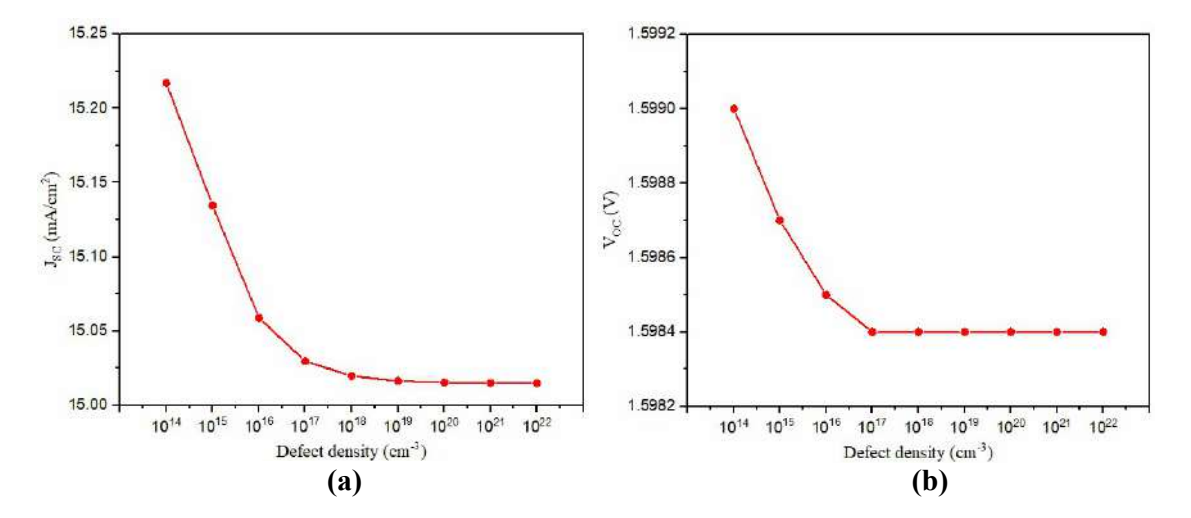


Figure 7.5 (a) Efficiency versus N_A of the PEDOT: PSS and (b) J-V curves of HTL depending on its N_A

Raising the dopant concentration leads to reduction in the recombination rate, owing to an enhanced internal electric field and accelerated carrier segregation. Simultaneously, there's a slight decrease in J_{SC} within the N_A range of 10^{14} to 10^{18} cm $^{-3}$ depicted in Fig. 7.5b. Notably, a pronounced fall in the J_{SC} is observed at 10^{19} cm $^{-3}$ due to generation of numerous deep Coulomb traps that reduce the μ_p [37]. The Fig. 7.5a show that the maximum PCE of 21.32 % is obtained at N_A of 10^{20} cm $^{-3}$.

7.3.2.3 Impact of Defect Density

In addition to the N_A , HTL defect density (N_t) affects the performance of PSCs. The impact on the PSC characteristics demonstrated in Fig. 7.6. The N_t of 10^{17} to 10^{22} cm⁻³, Fig. 7.6a, b, c and d reveal no significant changes in PV parameters. However, a pronounced decline in V_{OC} , J_{SC} and PCE surface for change in N_t from 10^{14} to 10^{17} cm⁻³. This precipitous shift is primarily attributed to the rapid emergence of numerous recombination sites in the HTL and at interfaces [38]. A high value of N_t in HTL, arising from diverse sources like undesirable foreign atoms, and native defects, give rise to shallow or deep traps. These traps adversely impact cell performance. Fig. 7.6d shows that an increase in interface defects leads to reduced efficiency. Beyond a certain N_t , it becomes constant. These interface defects, primarily stemming from the lattice mismatch between absorber layer (AL) and HTL, yield deep traps at the interface. These traps function as SRH recombination centers. Consequently, PCE experiences a decline, reaching about 20.97 % at $N_t = 10^{22}$ cm⁻³. In the beginning FF decline is attributed to the abundance of recombination centers and R_S resulting from a significant number of traps (Fig. 7.6c). Despite the superior outcomes at lower N_t , simulation results diverge from experimental findings. Hence, a value of 1×10^{14} cm⁻³ was selected.



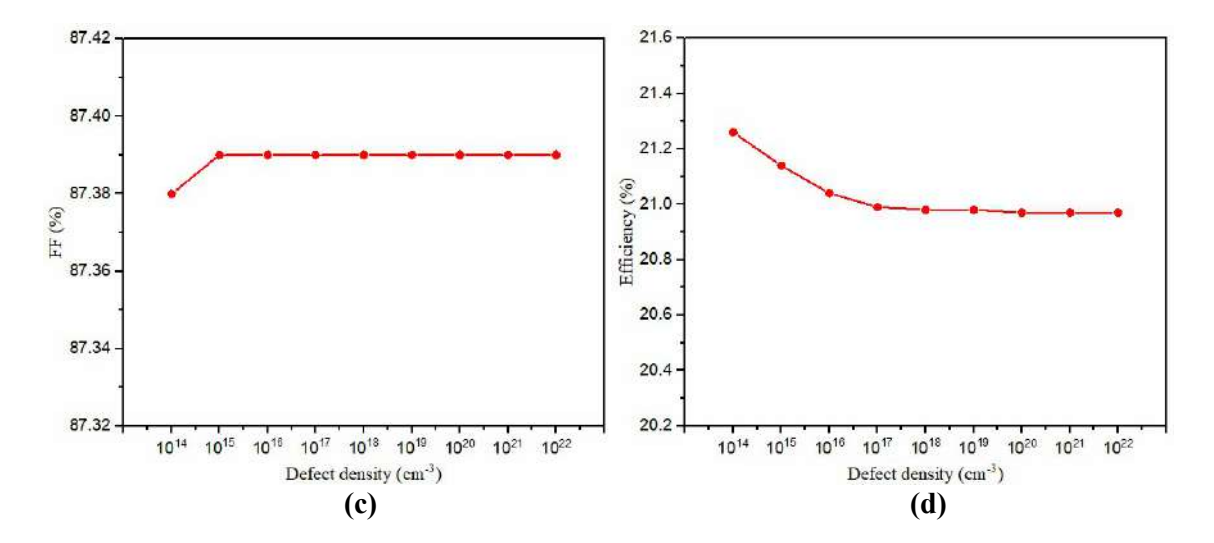


Figure 7.6 Impact of N_t of the PEDOT: PSS on PV parameters of KSnI₃-based PSC.

7.3.3 Optimization of KSnI₃ Layer

The above outcomes have shown that PEDOT: PSS is the most suitable HTL for KSnI₃-based PSC. The maximum PCE of beyond 21 % has been obtained at 250 nm of thickness of HTL, N_A of 10^{20} cm⁻³ and at N_t of 1^{\times} 10¹⁴ cm⁻³. Therefore, we have opted for this optimized value of thickness, N_A and N_t for the further simulation study to optimize the performance of KSnI₃-based PSC.

7.3.3.1 Impact of Thickness

The characteristics parameters like J_{SC} , V_{OC} , FF and PCE of PSCs are significantly influenced by the thickness of the perovskite absorber layer. In our investigation, we explored the impact of thickness of the absorber layer on the performance of the architecture: FTO/WS₂(100nm)/KSnI₃/PEDOT: PSS (250 nm)/Au. The thickness of the KSnI₃ layer has exhibited a straight relation with the evaluation of the outcomes of PSC through its effect on the charge carrier's diffusion length. It is known to us that as the thickness of the layer decreases, the absorption rate also lowers. This results in a decrement in photocurrent and therefore PCE of the PSC also reduces from 200-1000 nm. The change in PCE is depicted below in Fig. 7.7a. However, with the thickness increasing up to 550 nm, PCE gradually rises. This phenomenon can be attributed to the generation of large amounts of charge carriers by absorbed photons, leading to higher EQE, J_{SC} , and overall improved performance [39]. This enhancement is also evident in the J-V curves (Fig. 7.7b). As the absorber layer thickness exceeds 550 nm, both V_{OC} and FF parameters decrease. Optimum thickness value for KSnI₃-based PSC is 550 nm. The maximum efficiency goes up to 23.08 % together with V_{OC} is 1.57 V, J_{SC} is 16.90 mA/cm² and FF is 86.59 % at a thickness of 550 nm.

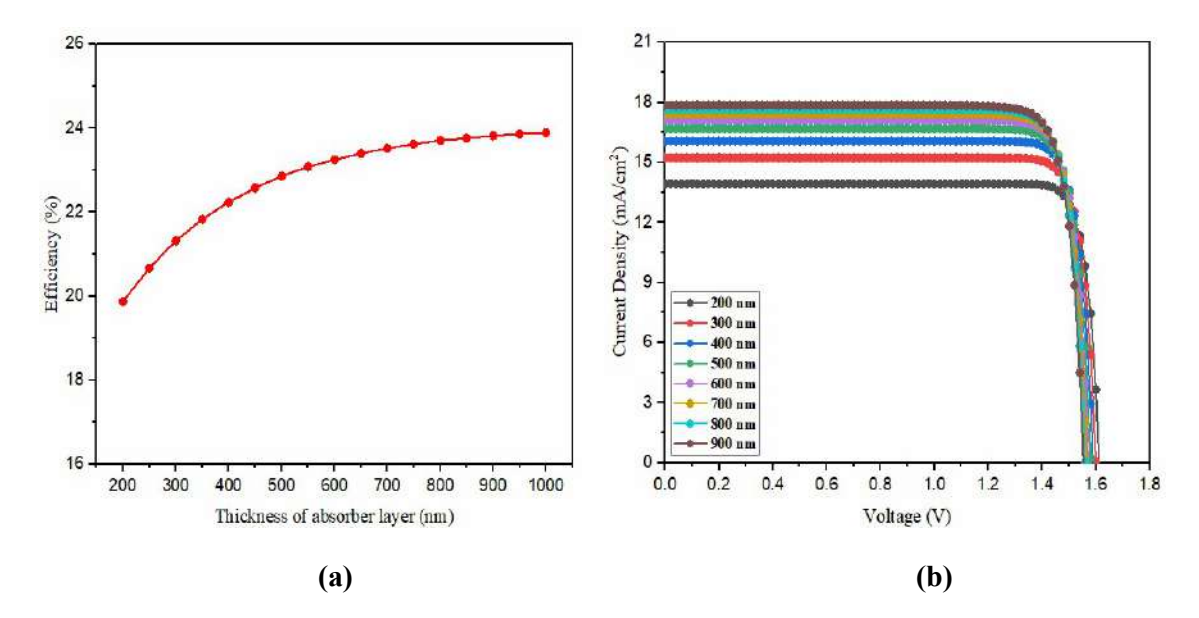


Figure 7.7 (a) Efficiency vs thickness of the absorber layer. (b) J-V curves with function of absorber layer thickness.

7.3.3.2 Impact of Defect Density

Similarly, with the HTL influence, there is a lack of substantial change in the PV parameters until an N_t value of 10¹³ cm⁻³ is reached. These PV parameters exhibit a decline when a high defect concentration is present. A heightened defect concentration within a low-quality perovskite layer results in an increased number of non-radiative recombination centers, consequently deteriorating PV parameters of PSC. This degradation can be attributed to alterations in the diffusion length of charge carriers and their lifetime. While a low N_t value might contribute to high PCE in simulated PSCs, the elevated fabrication cost is a deterrent. Moreover, a low N_t value does not accurately reflect real-world conditions due to the instability of such perovskites under humid conditions, leading to partial degradation. Therefore, we propose N_t values ranging from 10¹³ to 10¹⁵ cm⁻³ for the building of high-performance PSCs with reasonable stability. The optimized N_t is 1×10^{13} cm⁻³ for KSnI₃ perovskite layer at which it has achieved the maximum PCE of 23.08 %, as demonstrated in Fig. 7.8a. The J-V plot of KSnI₃ PSCs based on the N_t of the absorber layer is simulated and demonstrated in Fig. 7.8b. For perovskite layers when N_t is increased, the undesirable recombination rate also rises, attributed to the formation of defects that act as dangling bonds, serving as trap state for the charge carriers. This enhancement in recombination leads to fall in J_{SC}, which is subsequently responsible for the decrement in FF of solar devices. The device PCE also decreased from 23.08 % to 7.85 %, when N_t was increased from 10¹³ to 10²⁰ cm⁻³. Such an increasing amount of recombination resulted in a sharp fall in PCE of PSC.

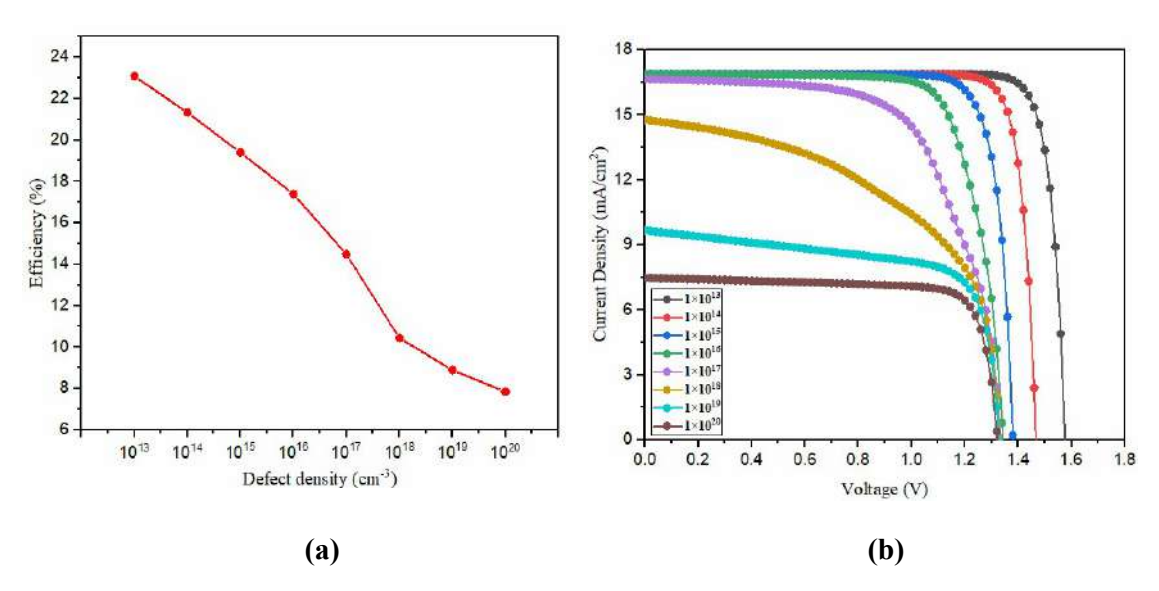


Figure 7.8 (a) Efficiency vs N_t of the absorber layer and (b) Effects of N_t on the J-V characteristics of KSnI₃-based PSCs.

7.3.4 Optimized Device

The optimized ETL and HTL are WS₂ and PEDOT: PSS respectively with the Au (gold) as metal back contact. The optimized parameters such as 1) Thickness: PEDOT: PSS (250 nm), KSnI₃ (550 nm), WS₂ (100 nm) and FTO (400 nm); 2) N_A: PEDOT: PSS (10^{20} cm⁻³) and 3) N_t: PEDOT: PSS (1×10^{14} cm⁻³), KSnI₃ (1×10^{13} cm⁻³) and WS₂ (1×10^{13} cm⁻³). The PSC structure and energy band diagram of the optimized device demonstrated in Fig. 7.9. The optimized PCE of 23.08 % with V_{OC} = 1.57 V, J_{SC} = 16.90 mA/cm², and FF of 86.59 % has been obtained. The JV and QE curves of optimized PSC are illustrated in Fig. 7.10(a-b).

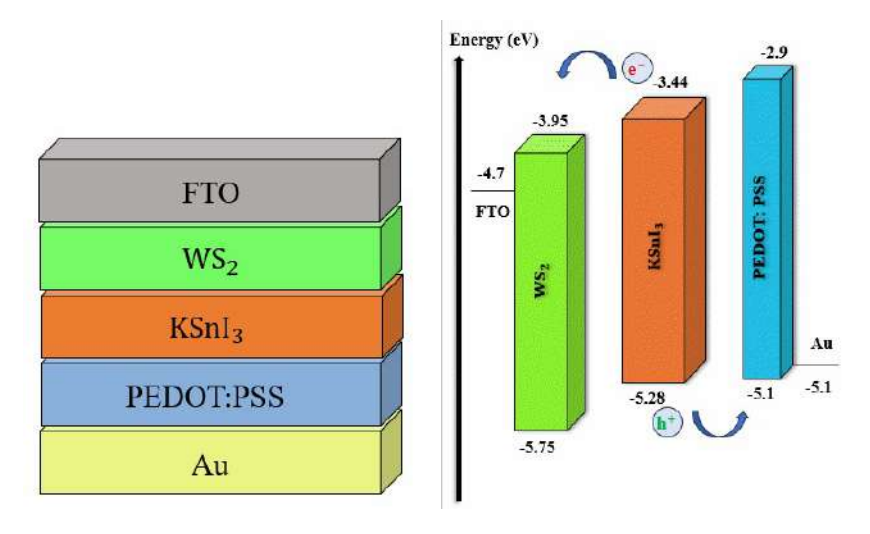


Figure 7.9 Architecture and band alignment diagram of optimized PSC.

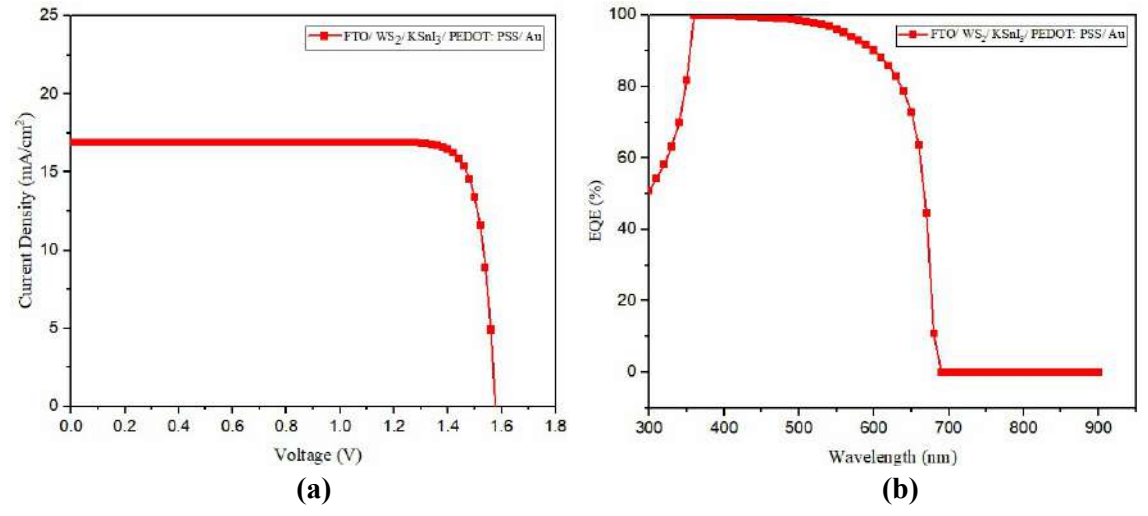


Figure 7.10 (a) J-V and (b) QE plot of optimized device.

7.3.5 Machine Learning Analysis

In this work, python is employed for the prediction of factors affecting the performance of the PSC. Due to its robustness to overfitting and optimal complexity, the Random Forest algorithm was used for the training and testing [40]. The researchers noted that more powerful rivals, like neural networks and deep neural networks, acquire needless complexity, leading to overfitting and reduced performance [41,42]. Considering the relatively small size of the dataset and its high complexity, compiling a larger set of records would be beneficial. The research focused on reducing the dataset's complexity to improve the model's accuracy. By employing Scikit-Learn, influence of every feature on the entire predictive performance of the ML model was observed. The eleven most important features were identified, and their relative importance was shown in Fig. 7.11. It has shown that the features such as thickness, N_t, N_A, of the HTL were found to be the most responsible in differentiating between the performance of two distinct PSCs. The outcomes guide for the design of new solar cells. Subsequently, a new model was built using the selected important features aiming to achieve a similar level of performance while reducing the model's size due to the fewer features used. The model results were measured and illustrated in Fig. 7.12 (a-d). Ideally, the slope of plots is near to 1, indicating accurate predictions. The ML model achieved a mean accuracy of 0.89 % and mean R² of 0.8921 between actual and predicted values for each target feature. While the accuracy might not be extremely high, the results are encouraging for further investigation and bridging the gap between artificial intelligence and materials science. The model trained for large input data which leads to highly efficient and realistic results.

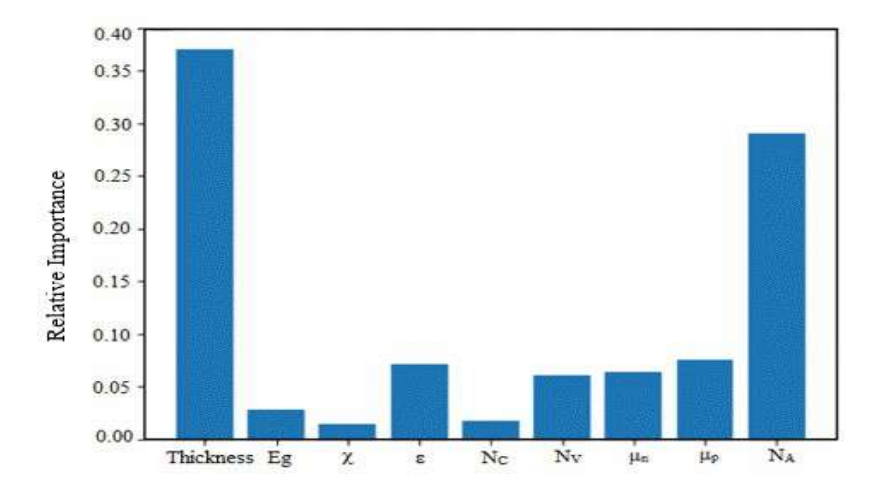


Figure 7.11 Different features with relative importance in the ML model.

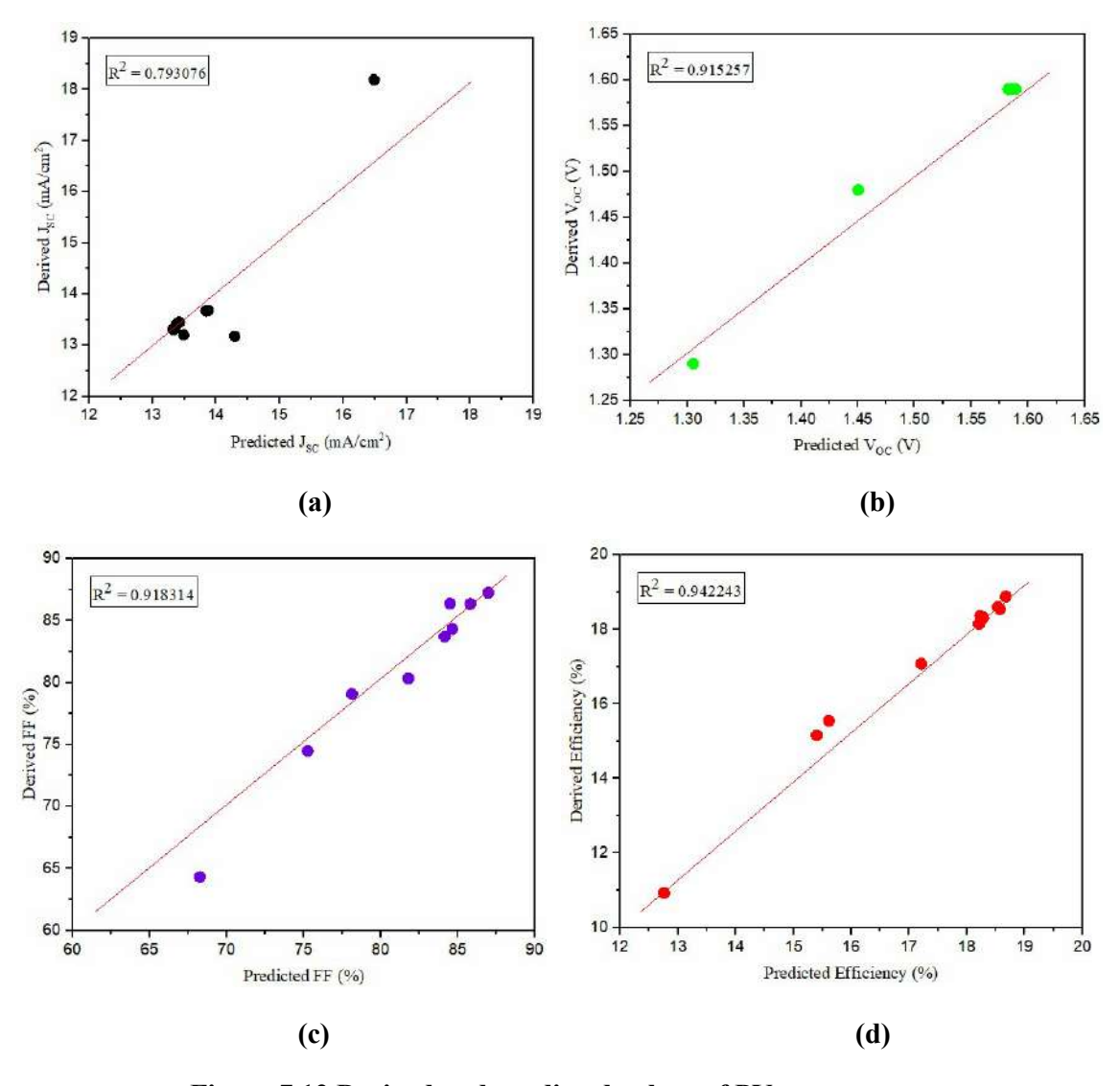


Figure 7.12 Derived and predicted values of PV parameters.

7.4 Summary

This work comprises analysis of KSnI₃-based PSC with the various HTLs. The effect of distinct parameters, including thickness of perovskite absorber layer and HTL, as well as N_A and N_t have been examined using SCAPS-1D. The ML model was used to predict the performance of the PSCs. The study demonstrated PEDOT: PSS as a promising HTL that could replace the expensive and less-conductive Spiro-OMeTAD. The maximum PCE of 23.08 % was obtained for the configuration of FTO/WS2/KSnI3/PEDOT: PSS/Au. The SCAPS-1D outcomes, deduced that the optimized thickness of HTL was 200 nm, with N_t of 1×10^{14} cm⁻³ and a N_A of 1×10^{20} cm⁻³ results in maximum PCE. The optimized thickness of the KSnI₃ layer is 550 nm and at N_t of 1×10^{13} cm⁻³ for an efficient PSC. The incorporation of the ML approach provided enhanced insight into the critical factors involved in designing and fabricating solar cells. The ML model demonstrated an accuracy score of 89 % in predicting the performance metrics of PSCs. The device PCE improved beyond 23 % by optimizing parameters such as thickness of absorber layer and HTL, N_t and N_A. The study focused on proper optimization of perovskite absorber layer and HTL for advanced and efficient architecture of KSnI₃-based PSC. A precise and powerful model can be trained by providing a large number of inputs to ML. With the series of this study, we can study the lead free and other potential material to optimize the performance of PSCs using the ML model.

7.5 REFERENCES

- [1] Singha, A., Paul, A., Koul, S., Sharma, V., Mallick, S., Balasubramaniam, K.R. and Kabra, D., 2023. Stable and Efficient Large-Area 4T Si/perovskite Tandem Photovoltaics with Sputtered Transparent Contact. *Solar RRL*, 7(12), p.2300117.
- [2] Pindolia, G., Shinde, S.M. and Jha, P.K., 2023. Non-leaded, KSnI₃ based perovskite solar cell: A DFT study along with SCAPS simulation. *Materials Chemistry and Physics*, 297, p.127426.
- [3] Tara, A., Bharti, V., Sharma, S. and Gupta, R., 2021. Device simulation of FASnI₃ based perovskite solar cell with Zn (O0. 3, S0. 7) as electron transport layer using SCAPS-1D. *Optical Materials*, 119, p.111362.
- [4] Yan, W., Liu, Y., Zang, Y., Cheng, J., Wang, Y., Chu, L., Tan, X., Liu, L., Zhou, P., Li, W. and Zhong, Z., 2022. Machine learning enabled development of unexplored perovskite solar cells with high efficiency. *Nano Energy*, 99, p.107394.
- [5] Rai, S., Pandey, B.K. and Dwivedi, D.K., 2020. Modeling of highly efficient and low cost CH₃NH₃Pb(I_{1-x}Cl_x)₃ based perovskite solar cell by numerical simulation. *Optical Materials*, 100, p.109631.
- [6] Kumar, M., Raj, A., Kumar, A. and Anshul, A., 2020. An optimized lead-free formamidinium Sn-based perovskite solar cell design for high power conversion efficiency by SCAPS simulation. *Optical Materials*, 108, p.110213.
- [7] Hossain, M.K., Toki, G.I., Kuddus, A., Rubel, M.H., Hossain, M.M., Bencherif, H., Rahman, M.F., Islam, M.R. and Mushtaq, M., 2023. An extensive study on multiple ETL and HTL layers to design and simulation of high-performance lead-free CsSnCl₃-based perovskite solar cells. *Scientific Reports*, 13(1), p.2521.
- [8] Kanoun, A.A., Kanoun, M.B., Merad, A.E. and Goumri-Said, S., 2019. Toward development of high-performance perovskite solar cells based on CH₃NH₃GeI₃ using computational approach. *Solar Energy*, 182, pp.237-244.
- [9] Bhattarai, S. and Das, T.D., 2021. Optimization of carrier transport materials for the performance enhancement of the MAGeI₃ based perovskite solar cell. *Solar Energy*, 217, pp.200-207.
- [10] Haider, S.Z., Anwar, H. and Wang, M., 2019. Theoretical device engineering for high-performance perovskite solar cells using CuSCN as hole transport material boost the efficiency above 25%. *physica status solidi (a)*, 216(11), p.1900102.
- [11] Li, B., Di, H., Chang, B., Yin, R., Fu, L., Zhang, Y.N. and Yin, L., 2021. Efficient passivation strategy on Sn related defects for high performance all-inorganic CsSnI₃ perovskite solar cells. *Advanced Functional Materials*, 31(11), p.2007447.
- [12] Mandadapu, U., Vedanayakam, S.V. and Thyagarajan, K., 2017. Simulation and analysis of lead based perovskite solar cell using SCAPS-1D. *Indian J. Sci. Technol*, 10(1), pp.1-8.
- [13] Jayan, K.D. and Sebastian, V., 2021. Comprehensive device modelling and performance analysis of MASnI₃ based perovskite solar cells with diverse ETM, HTM and back metal contacts. *Solar Energy*, 217, pp.40-48.

- [14] Ahmad, O., Rashid, A., Ahmed, M.W., Nasir, M.F. and Qasim, I., 2021. Performance evaluation of Au/p-CdTe/Cs₂TiI₆/n-TiO2/ITO solar cell using SCAPS-1D. *Optical Materials*, 117, p.111105.
- [15] Mushtaq, S., Tahir, S., Ashfaq, A., Bonilla, R.S., Haneef, M., Saeed, R., Ahmad, W. and Amin, N., 2023. Performance optimization of lead-free MASnBr₃ based perovskite solar cells by SCAPS-1D device simulation. *Solar Energy*, 249, pp.401-413.
- [16] Gan, Y., Bi, X., Liu, Y., Qin, B., Li, Q., Jiang, Q. and Mo, P., 2020. Numerical investigation energy conversion performance of tin-based perovskite solar cells using cell capacitance simulator. *Energies*, 13(22), p.5907.
- [17] Hossain, M.K., Arnab, A.A., Das, R.C., Hossain, K.M., Rubel, M.H.K., Rahman, M.F., Bencherif, H., Emetere, M.E., Mohammed, M.K. and Pandey, R., 2022. Combined DFT, SCAPS-1D, and wxAMPS frameworks for design optimization of efficient Cs₂BiAgI₆-based perovskite solar cells with different charge transport layers. *RSC advances*, 12(54), pp.35002-35025.
- [18] Ong, S.P., Richards, W.D., Jain, A., Hautier, G., Kocher, M., Cholia, S., Gunter, D., Chevrier, V.L., Persson, K.A. and Ceder, G., 2013. Python Materials Genomics (pymatgen): A robust, open-source python library for materials analysis. *Computational Materials Science*, 68, pp.314-319.
- [19] Ward, L., Dunn, A., Faghaninia, A., Zimmermann, N.E., Bajaj, S., Wang, Q., Montoya, J., Chen, J., Bystrom, K., Dylla, M. and Chard, K., 2018. Matminer: An open source toolkit for materials data mining. *Computational Materials Science*, 152, pp.60-69.
- [20] Yarlagadda, R.T., 2018. Python engineering automation to advance artificial intelligence and machine learning systems. *International Journal of Innovations in Engineering Research and Technology*, 5(6), pp.87-97.
- [21] Jin, Z., Shang, J., Zhu, Q., Ling, C., Xie, W. and Qiang, B., 2020. RFRSF: Employee turnover prediction based on random forests and survival analysis. In *Web Information Systems Engineering–WISE 2020: 21st International Conference, Amsterdam, The Netherlands, October 20–24, 2020, Proceedings, Part II 21*, pp. 503-515.
- [22] Ju, M.G., Chen, M., Zhou, Y., Garces, H.F., Dai, J., Ma, L., Padture, N.P. and Zeng, X.C., 2018. Earth-abundant nontoxic titanium (IV)-based vacancy-ordered double perovskite halides with tunable 1.0 to 1.8 eV bandgaps for photovoltaic applications. *ACS Energy Letters*, 3(2), pp.297-304.
- [23] Sobayel, K., Akhtaruzzaman, M., Rahman, K.S., Ferdaous, M.T., Al-Mutairi, Z.A., Alharbi, H.F., Alharthi, N.H., Karim, M.R., Hasmady, S. and Amin, N., 2019. A comprehensive defect study of tungsten disulfide (WS₂) as electron transport layer in perovskite solar cells by numerical simulation. *Results in physics*, 12, pp.1097-1103.
- [24] Pindolia, G. and Shinde, S.M., 2023. Effect of organic charge transport layers on unleaded KSnI₃ based perovskite solar cell. *Results in Optics*, 12, p.100469.
- [25] Xia, Y. and Dai, S., 2021. Review on applications of PEDOTs and PEDOT: PSS in perovskite solar cells. *Journal of materials science: materials in electronics*, 32(10), pp.12746-12757.
- [26] Zhao, L., Mou, J., Zhu, L. and Song, J., 2021. Synergistic effect of NiO and Spiro-OMeTAD for hole transfer in perovskite solar cells. *Journal of Electronic Materials*, 50, pp.6512-6517.

- [27] Du, Q., Shen, Z., Chen, C., Li, F., Jin, M., Li, H., Dong, C., Zheng, J., Ji, M. and Wang, M., 2021. Spiro-OMeTAD: Sb₂S₃ Hole Transport Layer with Triple Functions of Overcoming Lithium Salt Aggregation, Long-Term High Conductivity, and Defect Passivation for Perovskite Solar Cells. *Solar RRL*, 5(11), p.2100622.
- [28] Zuo, C. and Ding, L., 2017. Modified PEDOT layer makes a 1.52 V Voc for perovskite/PCBM solar cells. *Advanced Energy Materials*, 7(2), p.1601193.
- [29] Liu, D., Li, Y., Yuan, J., Hong, Q., Shi, G., Yuan, D., Wei, J., Huang, C., Tang, J. and Fung, M.K., 2017. Improved performance of inverted planar perovskite solar cells with F4-TCNQ doped PEDOT: PSS hole transport layers. *Journal of Materials Chemistry A*, 5(12), pp.5701-5708.
- [30] Li, S., Cao, Y.L., Li, W.H. and Bo, Z.S., 2021. A brief review of hole transporting materials commonly used in perovskite solar cells. *Rare Metals*, 40(10), pp.2712-2729.
- [31] Sharma, H., Verma, V.K., Singh, R.C., Singh, P.K. and Basak, A., 2023. Numerical analysis of high-efficiency CH₃NH₃PbI₃ perovskite solar cell with PEDOT: PSS hole transport material using SCAPS 1D simulator. *Journal of Electronic Materials*, 52(7), pp.4338-4350.
- [32] Nalianya, M.A., Awino, C., Barasa, H., Odari, V., Gaitho, F., Omogo, B. and Mageto, M., 2021. Numerical study of lead free CsSn_{0.5}Ge_{0.5}I₃ perovskite solar cell by SCAPS-1D. *Optik*, 248, p.168060.
- [33] Marinova, N., Tress, W., Humphry-Baker, R., Dar, M.I., Bojinov, V., Zakeeruddin, S.M., Nazeeruddin, M.K. and Grätzel, M., 2015. Light harvesting and charge recombination in CH₃NH₃PbI₃ perovskite solar cells studied by hole transport layer thickness variation. *ACS nano*, 9(4), pp.4200-4209.
- [34] Azri, F., Meftah, A., Sengouga, N. and Meftah, A., 2019. Electron and hole transport layers optimization by numerical simulation of a perovskite solar cell. *Solar energy*, 181, pp.372-378.
- [35] Williams, B.L., Zardetto, V., Kniknie, B., Verheijen, M.A., Kessels, W.M. and Creatore, M., 2016. The competing roles of i-ZnO in Cu (In, Ga) Se₂ solar cells. *Solar Energy Materials and Solar Cells*, 157, pp.798-807.
- [36] Paquin, F., Rivnay, J., Salleo, A., Stingelin, N. and Silva-Acuña, C., 2015. Multi-phase microstructures drive exciton dissociation in neat semicrystalline polymeric semiconductors. *Journal of Materials Chemistry C*, 3(41), pp.10715-10722.
- [37] Yoo, S.J., Lee, J.H., Lee, J.H. and Kim, J.J., 2013. Doping-concentration-dependent hole mobility in a ReO₃ doped organic semiconductor of 4, 4', 4 "-tris (N-(2-naphthyl)-N-phenylamino)-triphenylamine. *Applied Physics Letters*, 102(18).
- [38] Anwar, F., Mahbub, R., Satter, S.S. and Ullah, S.M., 2017. Effect of different HTM layers and electrical parameters on ZnO nanorod-based lead-free perovskite solar cell for high-efficiency performance. *International Journal of Photoenergy*, 2017(1), p.9846310.
- [39] Hao, L., Li, T., Ma, X., Wu, J., Qiao, L., Wu, X., Hou, G., Pei, H., Wang, X. and Zhang, X., 2021. A tin-based perovskite solar cell with an inverted hole-free transport layer to achieve high energy conversion efficiency by SCAPS device simulation. *Optical and Quantum Electronics*, 53, pp.1-17.
- [40] McKinney, W., 2010. Data structures for statistical computing in Python. *SciPy*, 445(1), pp.51-56.

- [41] Schmidhuber, J., 2015. Deep learning in neural networks: An overview. *Neural networks*, 61, pp.85-117.
- [42] Hasanzadeh Azar, M., Aynehband, S., Abdollahi, H., Alimohammadi, H., Rajabi, N., Angizi, S., Kamraninejad, V., Teimouri, R., Mohammadpour, R. and Simchi, A., 2023, SCAPS empowered machine learning modelling of perovskite solar cells: predictive design of active layer and hole transport materials. In *Photonics*, 10(3) p.271.

CHAPTER 8

PERFORMANCE OPTIMIZATION OF CsSnI₃-BASED PEROVSKITE SOLAR CELLS USING SCAPS-1D AND MACHINE LEARNING

- ➤ The study utilizes SCAPS-1D software to simulate the performance of Cesium Tin Iodide (CsSnI₃)-based PSCs, analysing the effect of various electron transport layers (ETLs) like ZnO, TiO₂, and CdS.
- The optimized device configuration of FTO/CdS/CsSnI₃/MoS₂/Pd achieved a maximum efficiency of 23.45 % at 300 K with a N_t of 1×10^{13} cm⁻³, using a 400 nm absorber layer thickness.
- ➤ A ML model, utilizing SHAP plot, XGB, and RF algorithms, accurately predicts the effects of various parameters on the device performance and PCE, with the XGB model achieving 99.93 % accuracy.
- ➤ The ML model serves as a valuable tool for predicting and optimizing parameters, aiding in the fabrication of highly efficient CsSnI₃-based PSCs.

8.1 Introduction

In recent years, the PCE of Sn-based devices has enhanced up to 22 % [1]. Elements such as Sn, Bi and Ge are alternatives to Pb in PSCs [2]. A CsSnI₃-based PSC has achieved the highest efficiency of 3.83 % [3]. Lead-free inorganic tin-based PSC such as CsSnI₃ has congenial narrow direct bandgap of 1.3 eV with structural stability, long charge-carrier life-time, excellent hole μ_p of 585 cm²/V-¹s⁻¹, and high absorption coefficient of 10^4 cm⁻¹. All these properties are analogous to that of methylammonium lead triiodide (CH₃NH₃PbI₃) [4,5]. Therefore, it is the widely explored tin-based semiconductor material for PV applications. For a suitable HTL in perovskite device, it must have high hole mobility, the band matching with the other layers and electrodes [6]. The PSC efficiency is improved by the use of an appropriate ETL and HTL which extracts the photoelectrons and the holes respectively introduced by the perovskite layer. To achieve the maximum efficiency, the proper band matching of the device layers is essential. To choose the best ETL and HTL to increase PSC performance, the suitable bandgap optimization is needed. Till date, the CsSnI₃-based PSC has achieved the maximum efficiency of 12.96 % with conventional device structure of ITO/TiO₂/CsSnI₃/Spiro-OMeTAD/Au [7].

We have investigated the impact of several ETLs (ZnO, TiO₂, IGZO, WO₃ and CdS) and HTLs (MoS₂, Cu₂O, CuInS₂ QD, CuSbS₂ and V₂O₅) on the performance of PSC. The optimization of thickness of absorber layer, operating temperature, N_t and back contact has been done to obtain the optimum performance. Back contact's work function was changed from 4.6 to 5.3 eV. The simulated device structure is FTO/ETL/CsSnI₃/HTL/Pd and achieved a maximum PCE of 23.45 % for the CsSnI₃-based PSC. The outcome demonstrates that through proper optimization for suitable selection of ETL and HTL, leads to enhanced the performance of PSC. Alongside its substantial influence in multiple fields, ML has become a powerful tool for analyzing and optimizing complex systems. In this work, ML is employed to eliminate the lengthy and tedious calculations usually necessary in simulations. SCAPS-1D produces an extensive dataset by varying the thickness, N_t and operating temperature. We have employed XGBoost (XGB) and random forest (RF) algorithms to predict PCE of the PSCs. The XGB outperforms RF with high R² and low mean square error (MSE). The trained XGB model predicts the PCE of PSC with an accuracy of above 99 %. The integration of ML with SCAPS data holds the potential to transform the optimization process and fabrication of the efficient PSCs.

8.2 Simulation Procedure and Device Structure

The data for various parameters have been selected from past studies enclosed is in Table 8.1, ETLs in Table 8.2 and HTLs in Table 8.3, and the simulation was performed through SCAPS-1D. The PSC consists of layer structure: glass substrate/FTO/ETL /CsSnI₃/HTL/Back contact as depicted in Fig. 8.1.

Sunlight

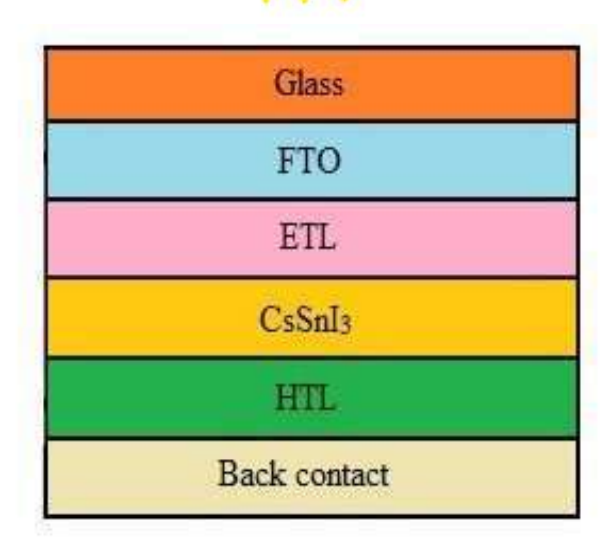


Figure 8.1 Structure of simulated model of PSCs.

Table 8.1 Input parameters of PSCs.

Parameter	FTO [8,9]	TiO ₂ [10,11]	CsSnI ₃ [12]	Spiro-OMeTAD [12,13,14]
Thickness (μm)	0.400	0.050	0.100	0.200
Eg (eV)	3.5	3.2	1.27	3.0
$\chi \left(eV\right)$	4.0	4.0	4.47	2.45
ε	9.0	9	18	3.0
N_C (cm ⁻³)	2.02×10^{18}	1×10^{21}	1×10^{19}	1×10^{19}
N_V (cm ⁻³)	1.8×10^{19}	2×10^{20}	1×10^{19}	1×10^{19}
μ_n (cm ² /Vs)	20	20	4.37	1×10^{-4}
μ_p (cm ² /Vs)	10	10	4.37	1×10^{-4}
N_D (cm ⁻³)	2×10^{19}	1×10^{19}	0	0
N_A (cm ⁻³)	0	4×10^{15}	1×10^{13}	2×10^{18}
N _t (cm ⁻³)	1×10^{15}	1×10^{15}	$1\times10^{15^*}$	1×10^{14}

8.2.1 Verification of the Model and Comparison of Experimental Result

The simulated result of PSC shown in Table 8.2 using previously reported data in Table 8.1. The thickness of the employed absorber layer, ETL and HTL are 100, 50 and 200 nm respectively. The device obtained PCE of 13.28 %, $V_{\rm OC} = 0.90$ V, $J_{\rm SC} = 17.37$ mA/cm² and FF = 84.10 %. The low value of $V_{\rm OC}$ due to direct charge recombination which results in low PCE. The device with TiO₂ as ETL has low PCE by virtue of small $V_{\rm OC}$ due to the lowest value of electron affinity. The improper band matching of various ETLs, perovskite absorber layer and HTLs is also a reason for low efficiency shown below in Fig. 8.2. The simulated device PCE is comparable to both the experimental and simulated outcomes demonstrated in Table 8.2. The QE and J-V plots of PSC are shown in Fig. 8.3(a) and (b) respectively. The obtained PCE is low so there is a need to explore more ETLs and HTLs to improve the performance of PSC.

Parameters Before optimization Experimental Result [7] Simulation [12] $V_{OC}(V)$ 0.90 0.86 0.86 J_{SC} (mA/cm²) 23.2 23.34 17.37 FF (%) 84.10 65 64.73 PCE (%) 13.28 12.96 12.96

Table 8.2 The previously reported experimental and simulation results.

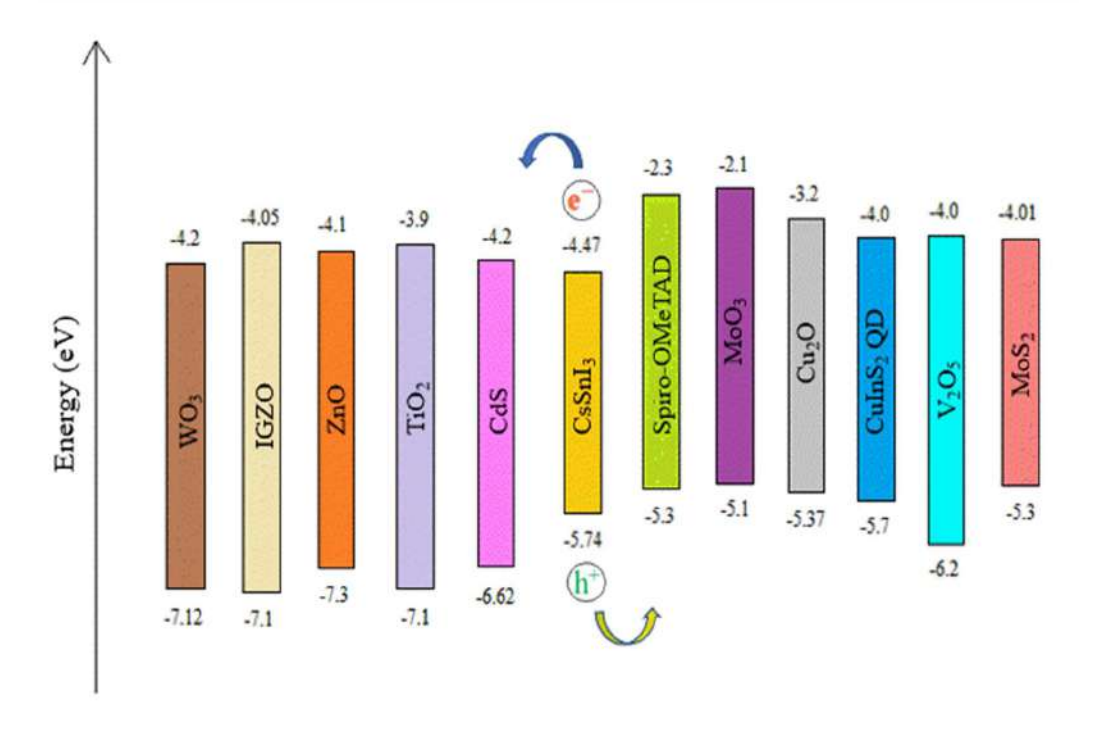


Figure 8.2 Band alignment diagram of distinct ETLs, perovskite layer and HTLs.

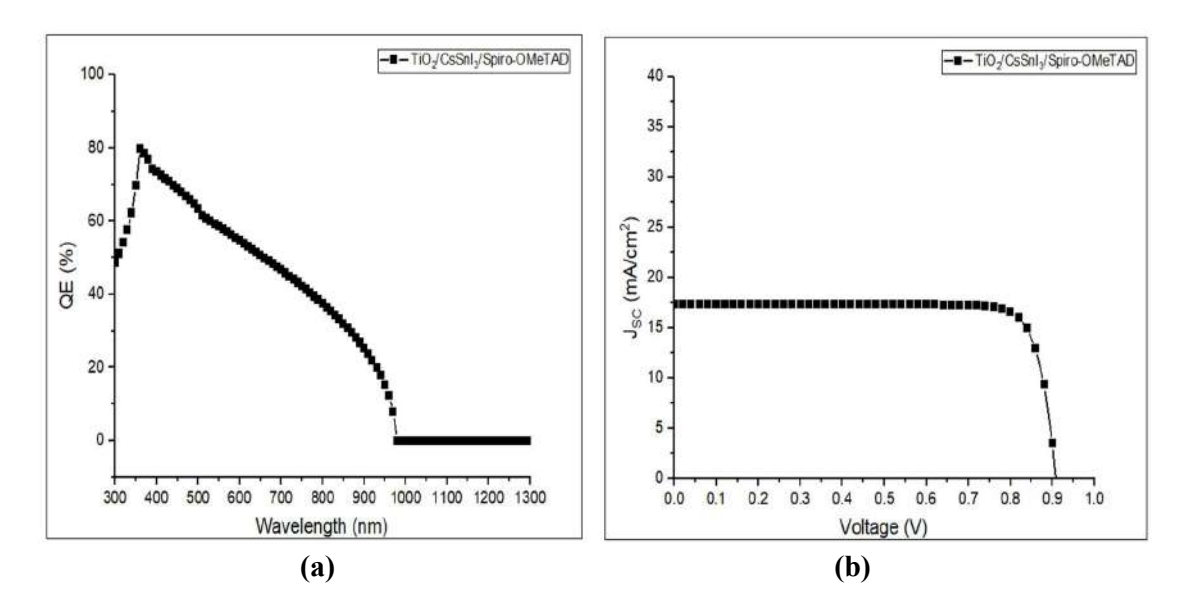


Figure 8.3 (a) Quantum efficiency and (b) J-V characteristics plots.

8.2.2 Appropriate ETLs and HTLs to Improve Performance

To choose a suitable layer, the various ETLs and HTLs simulated for optimization of the PSC performance. The input parameters of simulated different ETLs such as ZnO, TiO₂, IGZO, WO₃ and CdS shown below in Table 8.3. The employed HTLs in simulation are MoS₂, CuSbS₂, Cu₂O, V₂O₅ and CuInS₂ QD demonstrated in Table 8.4. The value of J_{SC} for the IGZO and TiO₂ offer much nearer value with the congenial mobility of the carriers [13]. The E_g of n-type CdS is 2.4 eV which is an appropriate window material that permits a major portion of the solar spectrum to reach the perovskite layer. CdS has high transmittance and low resistivity due to its wide E_g ; it is appropriate for the fabrication of solar devices [15,16]. When the MoS₂ is employed as HTL, it gives the highest PCE of 18.82 % due to its properties such as profound light-matter interactions, significant carrier mobility and exceptional absorption capacity in visible light wavelengths therefore it has applications in fabrication of PV devices. It has the thermal stability in between the temperature from 300 K to 400 K which is efficient for outside installation [17].

Table 8.3 Input parameters of various ETLs.

Parameter	ZnO [13,18]	IGZO [10]	WO ₃ [12,13]	CdS [15]
Thickness (μm)	0.050	0.050	0.050	0.050
Eg (eV)	3.2	3.05	2.92	2.42
$\chi \left(eV\right)$	4.26	4.16	4.5	4.3
ε	9.0	10	5.76	9.35

$N_{\rm C}$ (cm ⁻³)	2.0×10^{18}	5×10^{18}	1.96×10^{19}	2.2×10^{18}
N_V (cm ⁻³)	5.0×10^{18}	5×10^{18}	1.96×10^{19}	1.8×10^{19}
$\mu_n (cm^2/Vs)$	200	15	10	100
$\mu_p \ (cm^2/Vs)$	5	0.1	10	25
N_D (cm ⁻³)	1.5×10^{17}	1×10^{18}	3.68×10^{19}	1.15×10^{17}
N_A (cm ⁻³)	0	0	0	0
N_t (cm ⁻³)	1×10^{15}	1×10^{15}	$1 \times 10^{15*}$	$1\times10^{15*}$

Table 8.4 Input parameters of distinct HTLs.

Parameter	MoO ₃ [19]	Cu ₂ O [8,12,5]	CuInS ₂ QD [20]	V ₂ O ₅ [15]	MoS ₂ [21]
Thickness (μm)	0.200	0.200	0.200*	0.200*	0.200*
Eg (eV)	3.0	2.17	1.7	2.2	1.29
$\chi \left(eV\right)$	2.3	3.2	4.1	4.0	4.2
ε	5.7	7.11	9.76	10.0	3.0
N_C (cm ⁻³)	4.386×10^{19}	2.02×10^{17}	2×10^{18}	9.2×10^{17}	2.2×10^{18}
N_V (cm ⁻³)	4.343×10^{19}	1.1×10^{19}	2×10^{19}	5×10^{18}	1.8×10^{19}
$\mu_n \; (cm^2/V_S)$	1×10^{-4}	200	100	3.2×10^{2}	100
$\mu_p \; (cm^2/Vs)$	1×10^{-4}	80	25	4×10^{1}	150
N_D (cm ⁻³)	0	0	0	0	1×10^{15}
N_A (cm ⁻³)	1×10^{18}	1×10^{18}	2×10^{16}	1×10^{18}	1×10^{17}
N_t (cm ⁻³)	1.5×10^{17}	1×10^{14}	1×10^{14}	$1\times10^{14*}$	1×10^{14}

^{*}In this study

8.3 Result and Discussion

8.3.1 Effect of Change in Thickness

The thickness of the $CsSnI_3$ layer has a direct impact on PSC performance, influencing the charge carrier's diffusion length. It is well-established that a reduction in thickness leads to a lower absorption rate. This leads to reduction in photocurrent, which consequently lowers the solar cell PCE across the 200-1000 nm range. Both V_{OC} and PCE decline exponentially as the

thickness expands from 200 to 1000 nm. Optimum thickness for CsSnI₃-based PSC is 400 nm and beyond that it falls. Fall in FF beyond 400 nm is 17.03 %. PCE of the PSC goes up to 21.86 % together with V_{OC} is 0.79 V, J_{SC} is 33.62 mA/cm² and FF is 81.60 % for 400 nm. The FF decreases consistently as the thickness exceeds 400 nm. The Optimum thickness for CsSnI₃ PSC is 400 nm and highest efficiency achieved is 21.86 % for ETL = 50 nm and HTL = 200 nm. The variation in various PV parameters with the thickness of the absorber layer, with CdS as ETL, are illustrated in Fig. 8.4.

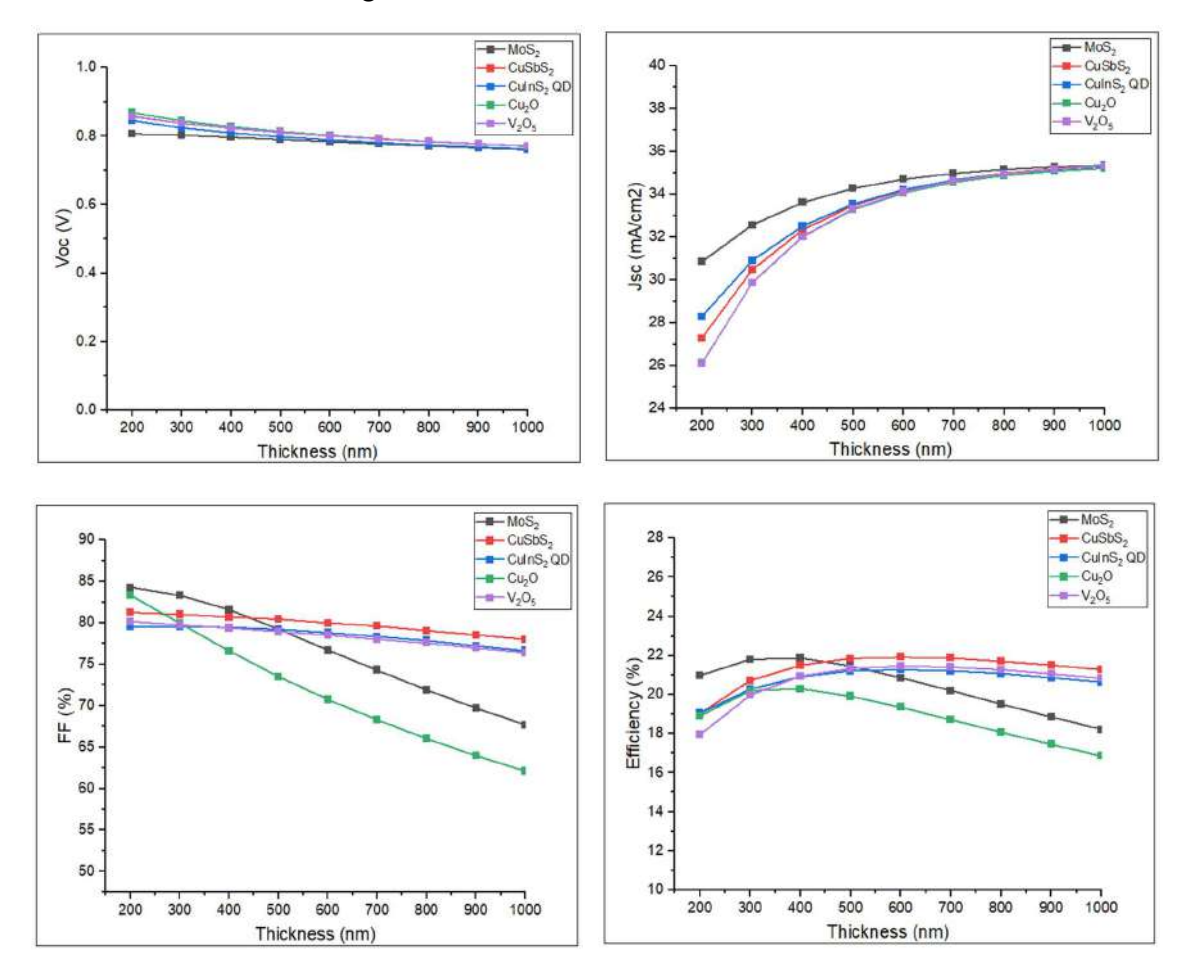


Figure 8.4 Change in PV parameters of CsSnI₃-based PSCs with thickness.

The calculated QE illustrates the increment in area of the absorption spectrum with the thickness of CsSnI₃ layer, demonstrated in Fig. 8.5(a). This results in high concentration of photo-generated carriers due to the improved light absorption. Hence the performance of solar cells increases. The effect of absorber layer thickness on J-V curves within a range of 100–800 nm is displayed in Fig. 8.5(b). J_{SC} is significantly enhanced from 27.93 mA/cm² to 34.35 mA/cm² for increment in thickness of the CsSnI₃ from 100 to 500 nm. For the layer greater than 500 nm, gradual enhancement in J_{SC} attains saturation due to thick layer which could result in increment in the charge carrier recombination rate.

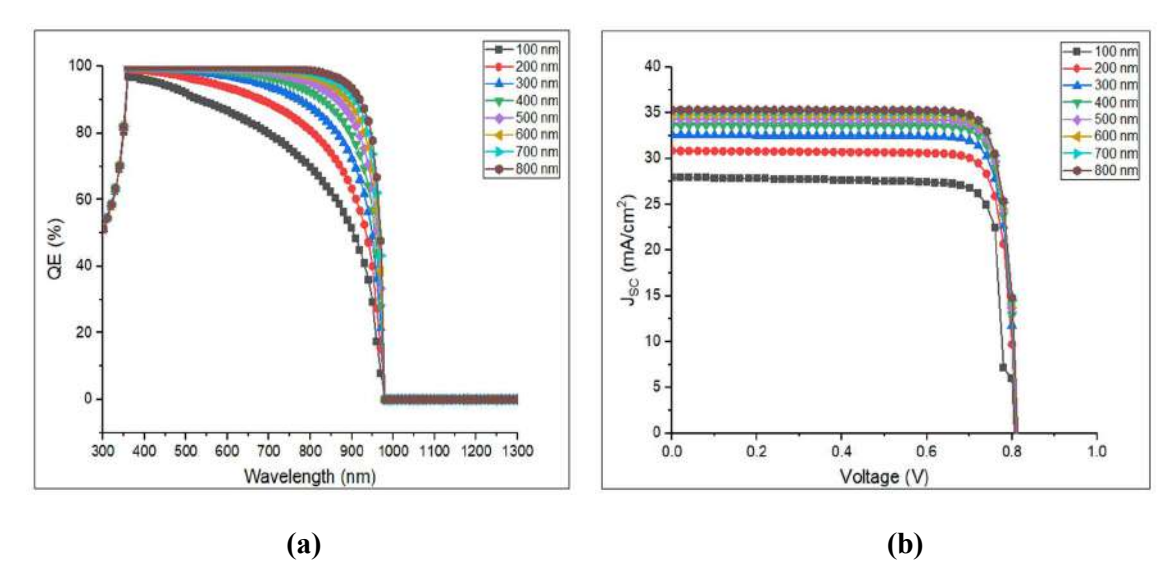
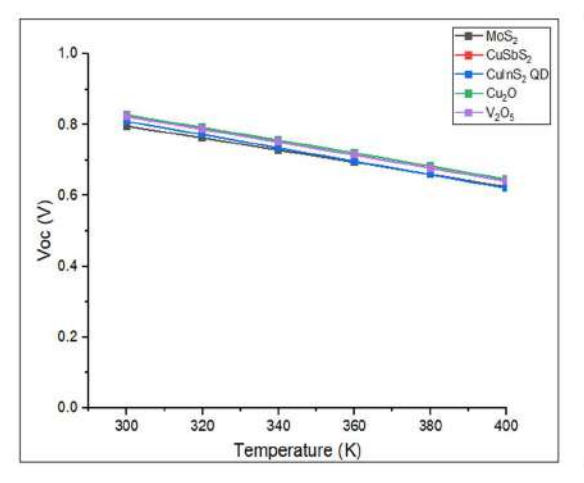
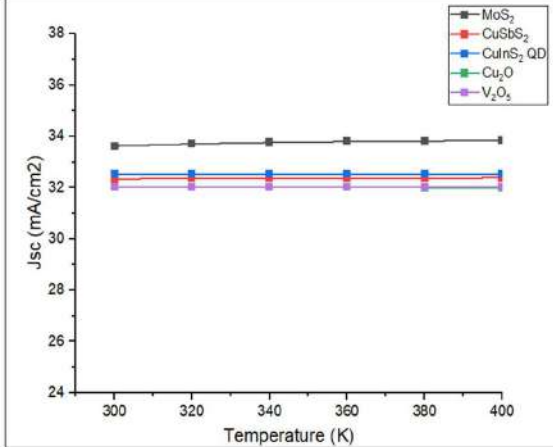


Figure 8.5 (a) QE curve (b) J-V plots of optimized CsSnI₃ PSC with thickness.

8.3.2 Impact of Change in Operating Temperature

To evaluate the impact of the temperature on the PCE of PSC devices, the operating temperature was changed from 300 to 400 K. Decline in performance with rising temperature is associated with a shorter diffusion length of charge carriers. Many PSCs structures exhibit instability in thorough performance due to layer deformation at high temperatures. For CsSnI $_3$ PSC, the efficiency drops by 27.90 % as the temperature rises, for ETL = 50 nm and HTL = 200 nm. With rising temperature, the PCE drops substantially, from 21.86 % at 300 K to 15.76 % at 400 K. In simulation of CsSnI $_3$ PSC the optimized value of temperature is 300 K. V_{OC} is reduced with an increase in the operating temperature for all HTLs. The rise in temperature results in decreased performance of PSCs due to an increment in saturation current, which subsequently raises the recombination rate [22]. The effect of temperature with CdS as ETL and different HTLs on other PV parameters together with V_{OC} , J_{SC} , and FF is shown below in Fig. 8.6.





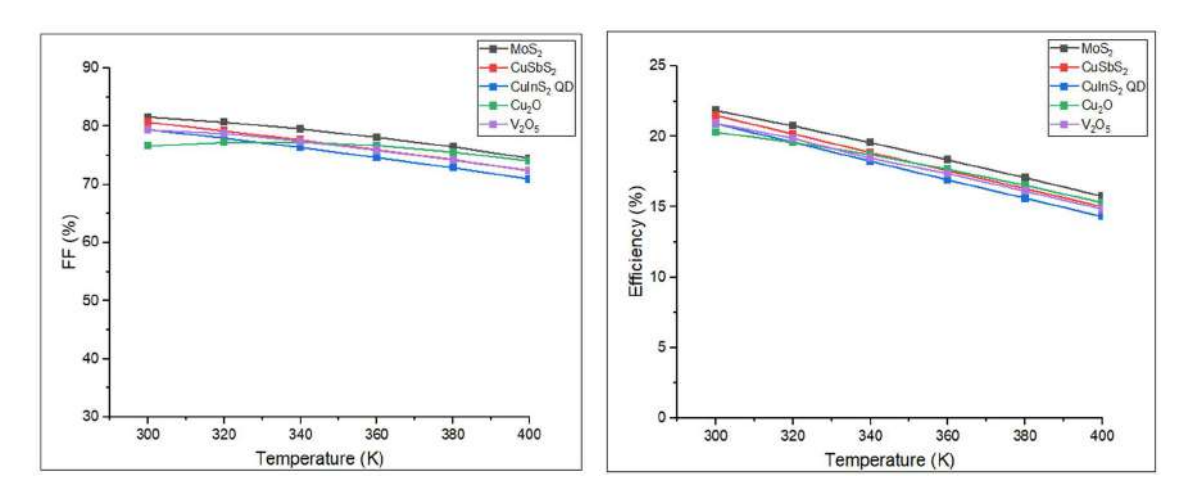
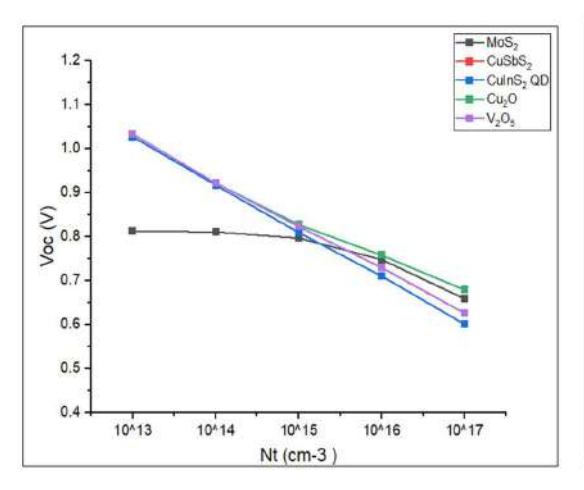
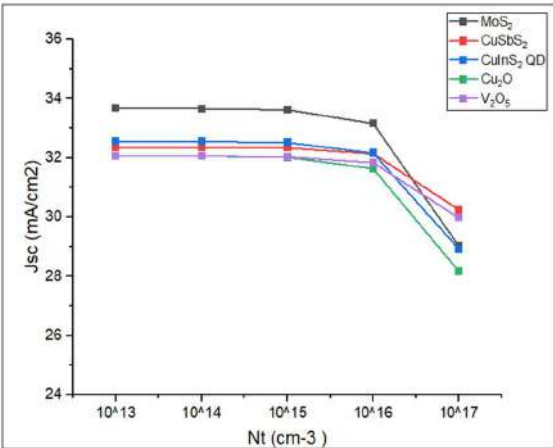


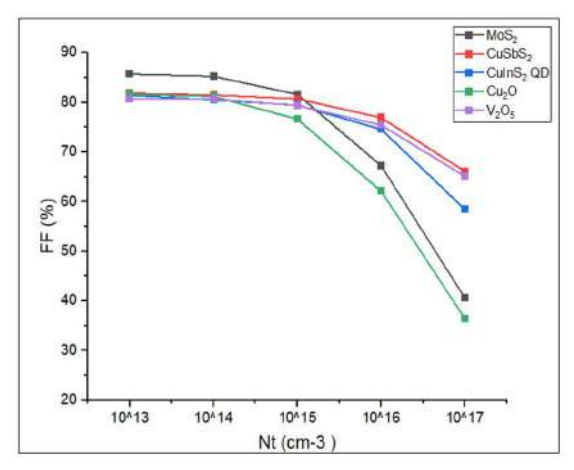
Figure 8.6 Change in the PV parameters of CsSnI₃-based PSCs with operating temperature.

8.3.3 Impact of Change in Defect Density

The CsSnI₃ layer achieves a maximum PCE of 23.45 % at an optimized N_t of 1×10^{13} cm⁻³, as illustrated in Fig. 8.7. For perovskite layers when N_t is increased, the unwanted recombination rate rises as defects create dangling bonds, which function as the trap states for the photogenerated charge carriers. As a result, the J_{SC} decreased, ultimately leading to a reduction in the FF of the PSCs. The device's PCE dropped from 23.45 to 7.76 % as N_t was enhanced from 10^{13} to 10^{17} cm⁻³. This significant rise in recombination led to a steep decline in solar cell efficiency. The change in different PV parameters V_{OC} , J_{SC} , and FF with defect density for CsSnI₃ with CdS as ETL and different HTLs is demonstrated in Fig. 8.7. CsSnI₃-based PSC, 66.90 % fall in the PCE with increase in N_t . The simulated results are comparable to jiang et al. and chen et al. reported outcomes displayed in Table 8.2.







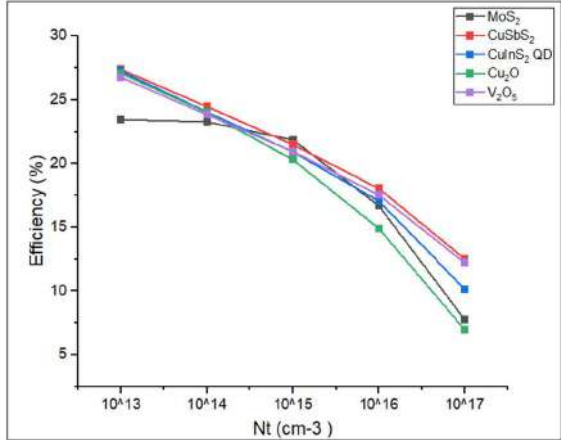


Figure 8.7 Impact of N_t on the performance of CsSnI₃ PSCs.

8.3.4 J-V and QE Plots of Various ETLs and HTLs

The J-V curves of distinct ETLs and HTLs shown below in Fig. 8.8 and QE curve demonstrated in Fig. 8.9. The highest occupied QE is illustrated in Fig. 8.9(a) for the CdS layer and in Fig. 8.9(b) for the MoS₂ layer. The device performance with various ETLs and spiro-OMeTAD as HTL in Table 8.5. The device performance with different HTLs and CdS as ETL tabulated in Table 8.6. The MoS₂ HTL has highest hole mobility among the other layers, higher charge mobility is directly proportional to high value J_{SC} [23]. We can observe that all ETLs exhibit nearly the same PCE. The cell performance is affected by the band alignment and conductivity of ETLs and HTLs in PSCs [24]. High conductivity decreases ohmic losses of the cell [25]. Result shows that CdS as ETL and MoS₂ as HTL suitable to achieve high efficiency of PSCs. The energy level diagram of the optimized device shown below in Fig. 8.10.

Table 8.5 Performance of CsSnI₃ PSC with various ETLs.

ETLs	V _{oc} (V)	J_{SC} (mA/cm ²)	FF (%)	PCE (%)
TiO ₂	0.90	17.37	84.10	13.28
IGZO	0.90	17.38	84.11	13.27
ZnO	0.90	17.36	84.04	13.18
WO_3	0.90	17.41	83.98	13.26
CdS	0.90	17.69	84.02	13.41

Table 8.6 Performance of CsSnI₃ PSC with several HTLs.

HTLs	Voc (V)	J _{SC} (mA/cm ²)	FF (%)	PCE (%)
MoS_2	0.80	27.93	83.63	18.82
Cu_2O	0.90	19.18	85.94	14.97
CuInS ₂ QD	0.88	23.90	80.71	17.08
$CuSbS_2$	0.88	21.55	81.25	15.54
V_2O_5	0.88	19.14	80.59	13.65

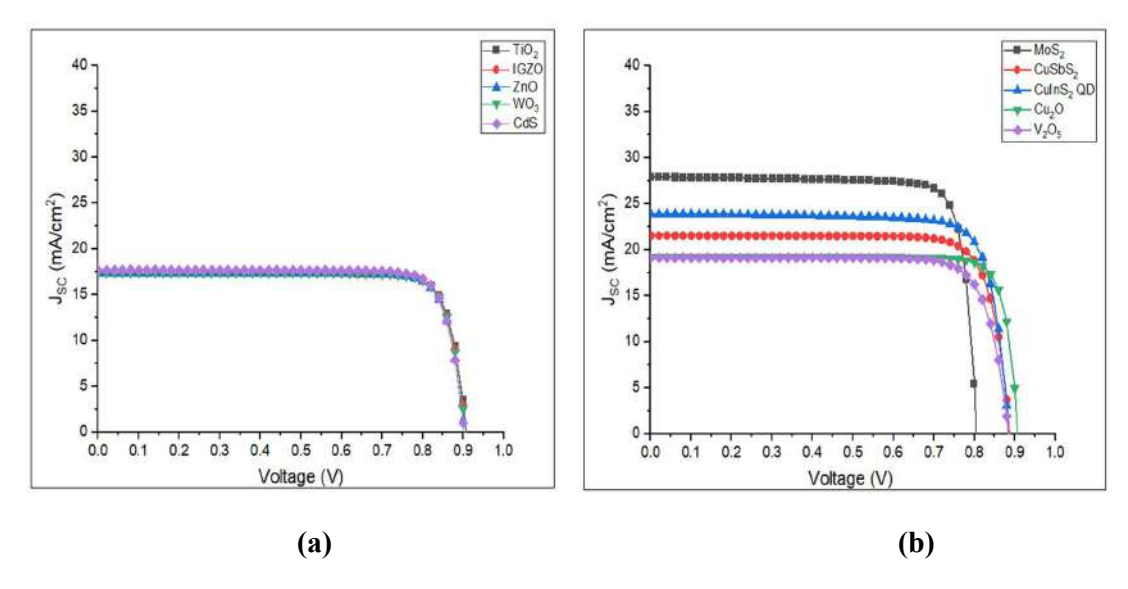


Figure 8.8 J-V curve for CsSnI₃ PSC with different (a) ETLs and (b) HTLs.

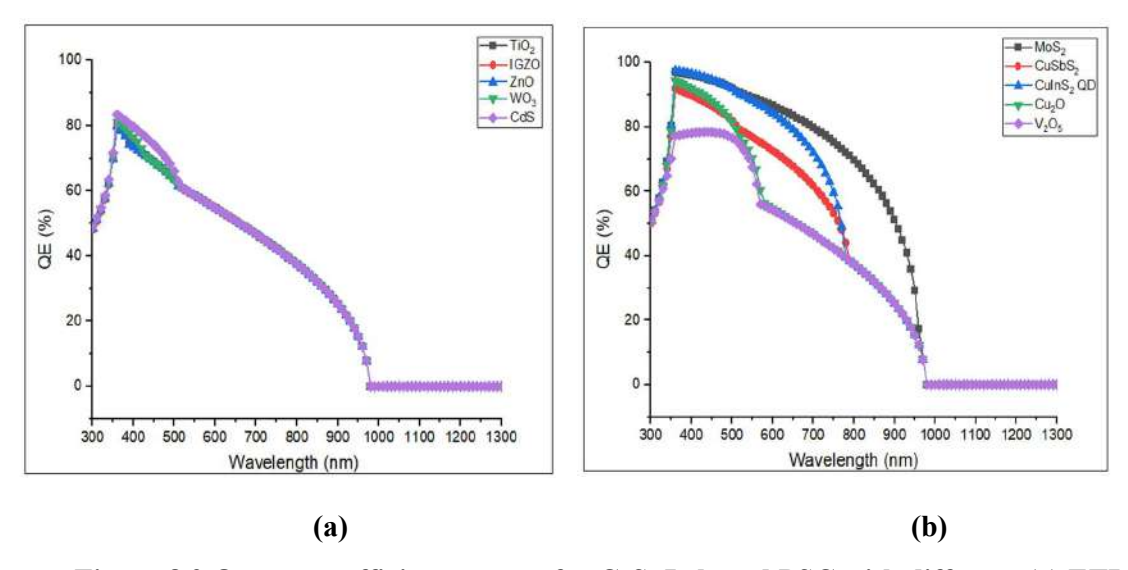


Figure 8.9 Quantum efficiency curve for CsSnI₃-based PSC with different (a) ETLs and (b) HTLs.

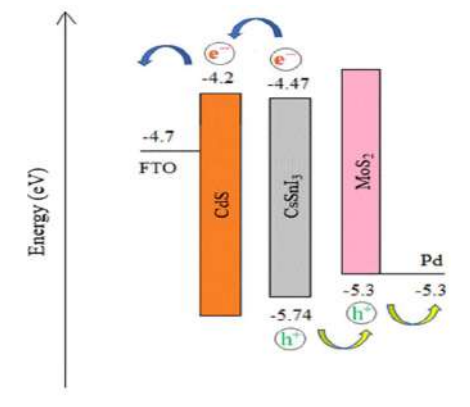


Figure 8.10 Energy level diagram of optimized device.

8.3.5 Effect of Work Function

The change in quantum efficiency with the work function of back contact demonstrated in Fig. 8.11(a) and (b) shows the change in J-V characteristics with the back contact work function. It is varied from 4.6 to 5.3 eV to examine its impact on the device performance. The V_{OC} increases from 0.42 to 0.78 V and J_{SC} slightly elevated from 32.87 to 33.62 mA/cm² for the given range of work function shown in Fig. 8.11(b). For the small value of work function (4.6-4.9 eV), a Schottky junction forms hence we witness poor performance of the device [26]. Comparison of present work with past results shown below in Table 8.7.

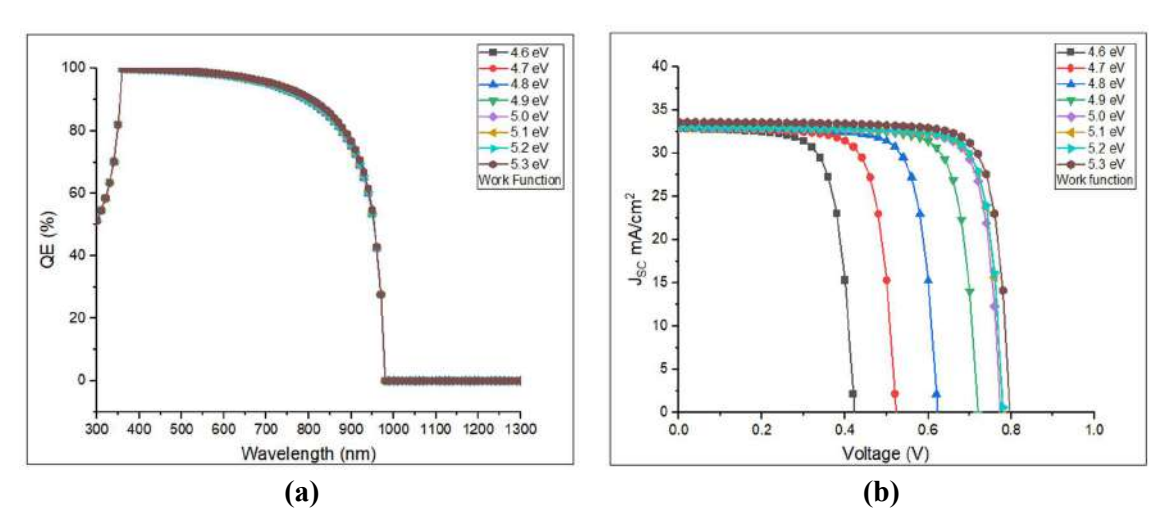


Figure 8.11 (a) QE curve and (b) J–V characteristics of optimized CsSnI₃ PSC with various back-contact work functions.

Cell structure	$V_{OC}(V)$	J_{SC} (mA/cm ²)	FF (%)	PCE (%)
FTO/CdS/CsSnI ₃ /MoS ₂ /Pd	0.81	33.67	85.71	23.45 [This work]
ITO/ZnMgO/CsSnI ₃ /P3HT/Au	0.67	35.61	71.39	17.04 [27]
ITO/PEDOT: PSS/CsSnI ₃ /ICBA/BCP/Ag	0.77	22.68	69.00	12.05 [28]
ITO/c-TiO ₂ /mp-TiO ₂ /CsSnI ₃ -	0.45	24.85	67.00	7.50 [29]
MBAA/P3HT/Au				
ITO/NiO _x /CsSnI ₃ : CBZ/PCBM/Ag	0.73	21.38	71.99	11.21 [30]
ITO/PCBM/CsSnI ₃ /CuI/Au	0.91	14.24	78.11	10.10 [31]

Table 8.7 Comparison with previous results.

8.3.6 Machine Learning Analysis

To improve the prediction PCE and minimize simulation complexity in forecasting the PCE of $CsSnI_3$ PSCs, ML algorithms (RF and XGB) were applied to simulate the data, incorporating variations in thickness of absorber layer, N_t and operating temperature. The optimization of

CsSnI₃-based PSC includes change in the thickness of from 200 to 2100 nm, with varying N_t of 10^{13} , 10^{16} and 10^{17} cm⁻³ with operating temperature ranging from 300 to 400 K. Python code is utilized to predict PCE using XGB and RF algorithms. Both the algorithms were used for the training and testing [32]. In comparing the XGB and RF models, XGB demonstrated superior performance. The model accuracy metrics showed that RF was less adequate, with a high MSE of 0.272 and a lower R² of 99.53 %. In contrast, XGB achieved a much lower MSE of 0.040 and a higher R² of 99.93 %. The equations used for computing R² and MSE are shown below [33]:

$$MSE = \frac{1}{n} \sum_{i=1}^{n} (y_i - \hat{y}_i)^2$$
 (8.1)

$$R^{2} = 1 - \frac{\sum_{i=1}^{n} (y_{i} - \hat{y}_{i})^{2}}{\sum_{i=1}^{n} (y_{i} - \bar{y}_{i})^{2}}$$
(8.2)

Where, y_i = actual value, y = predicted values, y = mean of the actual values and n = total no. of datasets.

The SHAP and actual vs predicted PCE plots for both models are presented in Fig 8.12. In Fig. 8.12(b) RF model's SHAP plot demonstrated that the SHAP values for defect density are mostly negative. This suggests that higher values of defect density tend to decrease the model's output. The SHAP values for thickness are mostly positive, indicating that higher values of thickness generally lead to an increase in the model's output. The SHAP values for the temperature have a wider distribution, with some values being positive and others negative. This implies that the effect of temperature on the model's output is more complex and depends on its specific value. The model is likely sensitive to changes in defect density and thickness. The Fig. 8.12(d) XGB model's SHAP plot shows that defect density seems to have a strong negative impact on the model's output. The red dots (indicating high feature values) are mostly clustered on the left side of the plot, suggesting that higher defect density leads to lower predictions. Thickness appears to have a mixed impact. The are both red and blue dots scattered across the plot, indicating that the effect of thickness on the model's output might not be as straightforward. Temperature also shows a mixed impact, similar to thickness. The red and blue dots are intermingled, suggesting that temperature's influence on the model's output might not be solely positive or negative. This SHAP plot provides insights into how the features contribute to the model's predictions. By understanding the impact of each feature, we can potentially improve the model's performance. The Fig. 8.12 demonstrated that the XGB method exceeds the performance of RF algorithm, it is clear that the XGB algorithm provides the most accurate PCE anticipation [34]. The models, trained on extensive input data, deliver highly efficient and realistic outcomes. The results provide guidance for designing new PSCs.

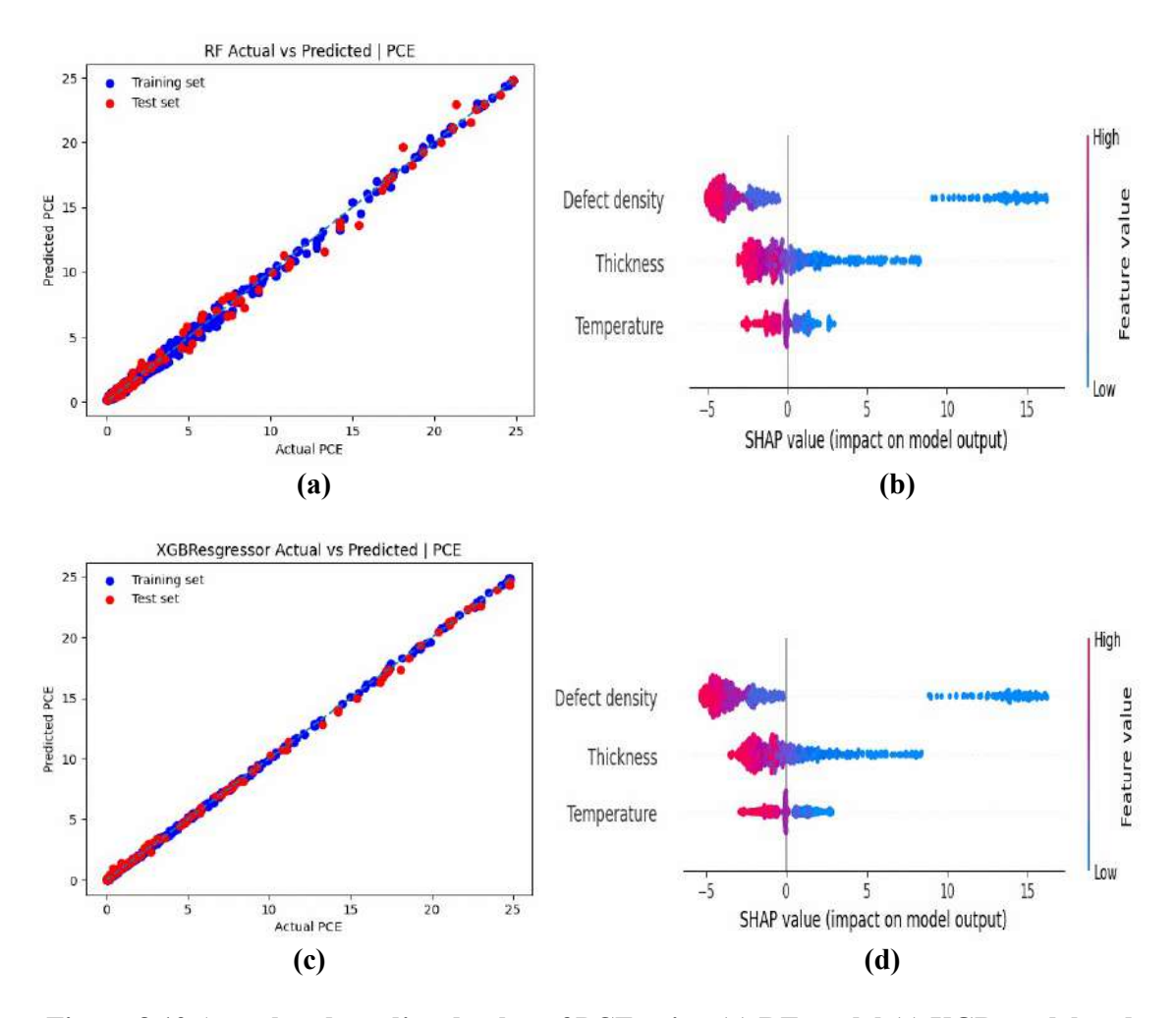


Figure 8.12 Actual and predicted value of PCE using (a) RF model (c) XGB model and SHAP plots (b) RF model (d) XGB model.

8.3.7 Effect of Doping Density

The absorber layer was doped with p-type, depicted that the N_A was there only, and $N_D = 0$ cm⁻³. Fig. 8.13 illustrated that change in the PV parameters such as PCE and FF with absorber layer N_A ranging from 1×10^{13} to 1×10^{19} cm⁻³ at thickness of 400 nm, temperature of 300 K and N_t of 10^{13} cm⁻³. As N_A increases, the FF and PCE of absorber layer increases [35]. For further increase in N_A , the electric field at the CsSnI₃ interface strengthens, resulting is more efficient charge separation. However, this enhanced electric field also leads to increased recombination, which negatively affects performance [25]. The maximum values for FF and PCE are obtained at a N_A is 1×10^{15} cm⁻³, reaching a highest value of 85.73 % and 23.46 % respectively [36]. These simulation results conclude that the optimized value of N_A is 1×10^{15} cm⁻³ for CsSnI₃-based PSC.

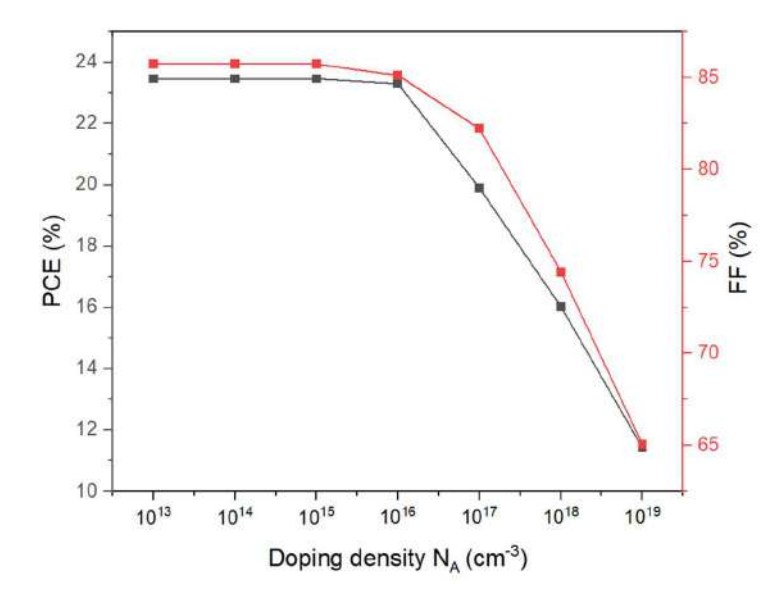


Figure 8.13 Impact of NA on the PCE and FF of CsSnI₃-based PSC.

8.4 Summary

The work incorporates comprehensive study of tin-based PSC with the several ETLs and HTLs. The impact of thickness of absorber layer, operating temperature and N_t on CsSnI₃ PSC were analysed using SCAPS-1D. The device with maximum efficiency of 23.45 % was obtained for the configuration of FTO/CdS/CsSnI₃/MoS₂/Pd. Whereas, suitable HTL must have balanced hole mobility to prepare high PCE devices. The optimized thickness of the CsSnI₃ layer is 400 nm for an efficient PSC. The highest efficiency achieved at a temperature of 300 K and N_t of 10¹³ cm⁻³. The simulation trend demonstrated that photovoltaic performance of a PSC falls with increment in operating temperature and defect density. The device's PCE increased over 23 % by optimizing parameters like thickness, work function of back contact, N_t and operating temperature. The proper optimization of suitable ETL and HTL has been completed for CsSnI₃based PSC. The ML approach is employed to predict the PCE and the parameters which affect the performance of the PSC. Outcomes demonstrated that the XGB algorithm outperforms the RF algorithm with higher R² of 99.93 % with low MSE of 0.040. A highly accurate and effective model can be created by providing a substantial amount of data into ML algorithms. Hence, we can optimize the performance of PSCs with the assistance of outcomes of this numerical modelling and ML model.

8.5 REFERENCES

- [1] Liu, Y., Li, T., Shi, M., Zhu, J., Ma, X., Wu, M., Wu, J., Zhang, C., Zhang, T. and Qi, Y., 2022. Hole-transport layer-free tin-based perovskite solar cells: improving their performance from a simulation perspective. *ECS Journal of Solid State Science and Technology*, 11(10), p.103001.
- [2] Wu, B., Zhou, Y., Xing, G., Xu, Q., Garces, H.F., Solanki, A., Goh, T.W., Padture, N.P. and Sum, T.C., 2017. Long minority-carrier diffusion length and low surface-recombination velocity in inorganic lead-free CsSnI₃ perovskite crystal for solar cells. *Advanced Functional Materials*, 27(7), p.1604818.
- [3] Song, T.B., Yokoyama, T., Logsdon, J., Wasielewski, M.R., Aramaki, S. and Kanatzidis, M.G., 2018. Piperazine suppresses self-doping in CsSnI₃ perovskite solar cells. *ACS Applied Energy Materials*, 1(8), pp.4221-4226.
- [4] Duan, Q., Ji, J., Hong, X., Fu, Y., Wang, C., Zhou, K., Liu, X., Yang, H. and Wang, Z.Y., 2020. Design of hole-transport-material free CH₃NH₃PbI₃/CsSnI₃ all-perovskite heterojunction efficient solar cells by device simulation. *Solar Energy*, 201, pp.555-560.
- [5] Li, B., Di, H., Chang, B., Yin, R., Fu, L., Zhang, Y.N. and Yin, L., 2021. Efficient passivation strategy on Sn related defects for high performance all-inorganic CsSnI₃ perovskite solar cells. *Advanced Functional Materials*, 31(11), p.2007447.
- [6] Elango, I., Selvamani, M., Ramamurthy, P.C. and Kesavan, A.V., 2022. Studying VOC in lead free inorganic perovskite photovoltaics by tuning energy bandgap and defect density. *Ceramics International*, 48(19), pp.29414-29420.
- [7] Chen, L.J., Lee, C.R., Chuang, Y.J., Wu, Z.H. and Chen, C., 2016. Synthesis and optical properties of lead-free cesium tin halide perovskite quantum rods with high-performance solar cell application. *The journal of physical chemistry letters*, 7(24), pp.5028-5035.
- [8] Rai, S., Pandey, B.K. and Dwivedi, D.K., 2020. Modeling of highly efficient and low cost CH₃NH₃Pb(I_{1-x}Cl_x)₃ based perovskite solar cell by numerical simulation. *Optical Materials*, 100, p.109631.
- [9] Haider, S.Z., Anwar, H. and Wang, M., 2019. Theoretical device engineering for high-performance perovskite solar cells using CuSCN as hole transport material boost the efficiency above 25%. *physica status solidi (a)*, 216(11), p.1900102.
- [10] Lakhdar, N. and Hima, A., 2020. Electron transport material effect on performance of perovskite solar cells based on CH₃NH₃GeI₃. *Optical Materials*, 99, p.109517.
- [11] Xu, X., Wang, J., Cao, D., Zhou, Y. and Jiao, Z., 2022. Design of all-inorganic hole-transport-material-free CsPbI₃/CsSnI₃ heterojunction solar cells by device simulation. *Materials Research Express*, 9(2), p.025509.
- [12] Jiang, M. and Tang, J., 2021. Simulated development and optimized performance of narrow-bandgap CsSnI₃-based all-inorganic perovskite solar cells. *Journal of Physics D: Applied Physics*, 54(46), p.465104.
- [13] Bhattarai, S. and Das, T.D., 2021. Optimization of carrier transport materials for the performance enhancement of the MAGeI₃ based perovskite solar cell. *Solar Energy*, 217, pp.200-207.

- [14] De Los Santos, I.M., Cortina-Marrero, H.J., Ruíz-Sánchez, M.A., Hechavarría-Difur, L., Sánchez-Rodríguez, F.J., Courel, M. and Hu, H., 2020. Optimization of CH₃NH₃PbI₃ perovskite solar cells: A theoretical and experimental study. *Solar Energy*, 199, pp.198-205.
- [15] Kuddus, A., Rahman, M.F., Ahmmed, S., Hossain, J. and Ismail, A.B.M., 2019. Role of facile synthesized V₂O₅ as hole transport layer for CdS/CdTe heterojunction solar cell: validation of simulation using experimental data. *Superlattices and Microstructures*, 132, p.106168.
- [16] Chopra, K.L. and Das, S.R., 1983. Thin film solar cells Springer US.
- [17] Patel, A.K., Mishra, R. and Soni, S.K., 2022. Performance enhancement of CIGS solar cell with two dimensional MoS₂ hole transport layer. *Micro and Nanostructures*, 165, p.207195.
- [18] Jayan, K.D. and Sebastian, V., 2021. Comprehensive device modelling and performance analysis of MASnI₃ based perovskite solar cells with diverse ETM, HTM and back metal contacts. *Solar Energy*, 217, pp.40-48.
- [19] Maram, D.K., Haghighi, M., Shekoofa, O., Habibiyan, H. and Ghafoorifard, H., 2021. A modeling study on utilizing ultra-thin inorganic HTLs in inverted p—n homojunction perovskite solar cells. *Solar Energy*, 213, pp.1-12.
- [20] Singh, M., Kumar, R., Singh, V. and Srivastava, S., 2021. Theoretical study of highly efficient CH₃NH₃SnI₃ based perovskite solar cell with CuInS₂ quantum dot. *Semiconductor Science and Technology*, 37(2), p.025010.
- [21] Kohnehpoushi, S., Nazari, P., Nejand, B.A. and Eskandari, M., 2018. MoS₂: a two-dimensional hole-transporting material for high-efficiency, low-cost perovskite solar cells. *Nanotechnology*, 29(20), p.205201.
- [22] Ahmed, S., Jannat, F., Khan, M.A.K. and Alim, M.A., 2021. Numerical development of ecofriendly Cs₂TiBr₆ based perovskite solar cell with all-inorganic charge transport materials via SCAPS-1D. *Optik*, 225, p.165765.
- [23] Gu, Y.F., Du, H.J., Li, N.N., Yang, L. and Zhou, C.Y., 2019. Effect of carrier mobility on performance of perovskite solar cells. *Chinese Physics B*, 28(4), p.048802.
- [24] Nalianya, M.A., Awino, C., Barasa, H., Odari, V., Gaitho, F., Omogo, B. and Mageto, M., 2021. Numerical study of lead free CsSn_{0.5}Ge_{0.5}I₃ perovskite solar cell by SCAPS-1D. *Optik*, 248, p.168060.
- [25] Abdelaziz, S., Zekry, A., Shaker, A. and Abouelatta, M.J.O.M., 2020. Investigating the performance of formamidinium tin-based perovskite solar cell by SCAPS device simulation. *Optical materials*, 101, p.109738.
- [26] Fang, G., Tian, H., Chang, W., Wang, Z., He, Q. and Gao, X., 2020. Optimized analysis of back-contact perovskite solar cells architectures. *Optik*, 207, p.164362.
- [27] Rahman, M.F., Islam, M.A.I., Chowdhury, M., Farhat, L.B., Ezzine, S. and Islam, A.S., 2024. Efficiency improvement of CsSnI₃ based heterojunction solar cells with P3HT HTL: A numerical simulation approach. *Materials Science and Engineering: B*, 307, p.117524.
- [28] Zhang, Z., Yu, H., Huang, J., Liu, Z., Sun, Q., Li, X., Dai, L., Shen, Y. and Wang, M., 2024. Over 12% efficient CsSnI₃ perovskite solar cells enabled by surface post-treatment with bifunctional polar molecules. *Chemical Engineering Journal*, 490, p.151561.

- [29] Ye, T., Wang, K., Hou, Y., Yang, D., Smith, N., Magill, B., Yoon, J., Mudiyanselage, R.R., Khodaparast, G.A., Wang, K. and Priya, S., 2021. Ambient-air-stable lead-free CsSnI₃ solar cells with greater than 7.5% efficiency. *Journal of the American Chemical Society*, 143(11), pp.4319-4328.
- [30] Duan, C., Zou, F., Wen, Q., Qin, M., Li, J., Chen, C., Lu, X., Ding, L. and Yan, K., 2023. A bifunctional carbazide additive for durable CsSnI₃ perovskite solar cells. *Advanced Materials*, 35(26), p.2300503.
- [31] Hossain, M.K., Toki, G.I., Samajdar, D.P., Mushtaq, M., Rubel, M.H.K., Pandey, R., Madan, J., Mohammed, M.K., Islam, M.R., Rahman, M.F. and Bencherif, H., 2023. Deep insights into the coupled optoelectronic and photovoltaic analysis of lead-free CsSnI₃ perovskite-based solar cell using DFT calculations and SCAPS-1D simulations. *ACS omega*, 8(25), pp.22466-22485.
- [32] Shrivastav, N., Madan, J. and Pandey, R., 2024. Maximizing performance in Cs₂CuBiCl₆ perovskite cells through machine learning-driven absorber layer parameter analysis. *Materials Letters*, 359, p.135929.
- [33] Chicco, D., Warrens, M.J. and Jurman, G., 2021. The coefficient of determination R-squared is more informative than SMAPE, MAE, MAPE, MSE and RMSE in regression analysis evaluation. *Peerj computer science*, 7, p.e623.
- [34] Shrivastav, N., Madan, J. and Pandey, R., 2024. Predicting photovoltaic efficiency in Cs-based perovskite solar cells: A comprehensive study integrating SCAPS simulation and machine learning models. *Solid State Communications*, 380, p.115437.
- [35] Bencherif, H., Dehimi, L., Mahsar, N., Kouriche, E. and Pezzimenti, F., 2022. Modeling and optimization of CZTS kesterite solar cells using TiO₂ as efficient electron transport layer. *Materials Science and Engineering: B*, 276, p.115574.
- [36] Chabri, I., Benhouria, Y., Oubelkacem, A., Kaiba, A., Essaoudi, I. and Ainane, A., 2023. SCAPS device simulation study of formamidinium Tin-Based perovskite solar Cells: Investigating the influence of absorber parameters and transport layers on device performance. *Solar Energy*, 262, p.111846.

CHAPTER 9

INVESTIGATION OF LEAD-FREE KGeCl₃ BASED PEROVSKITE SOLAR CELLS USING SCAPS-1D

- The SCAPS-1D software is used to examine the impact of various HTLs, ETLs, and absorber layer parameters, aiming to maximize the performance of Potassium Germanium Chloride (KGeCl_{3s})-based PSCs.
- ➤ The optimized configuration of FTO/WS₂/KGeCl₃/PEDOT: PSS/Au achieves a maximum efficiency of 29.82 %, with a V_{OC} of 1.19 V, J_{SC} of 30.08 mA/cm², and an FF of 82.74 %.
- The study identifies the optimal absorber layer thickness of 600 nm, along with a radiative recombination coefficient of 10^{-12} cm³/sec, an operating temperature of 300 K, and a defect density of 10^{15} cm⁻³ for maximum device performance.
- The research suggests that the combination of WS₂ as the ETL and PEDOT: PSS as the HTL is most suitable for fabricating highly efficient Ge-based PSC devices.

9.1 Introduction

Recently various hybrid organic-inorganic perovskite materials have been reported which possess high charge carrier mobilities and also offer low temperature solution-based fabrication techniques [1-3]. They possess some challenges related to stability, toxicity and scalability [4]. The inorganic PSCs, particularly those employing materials like cesium lead halides have advantages over hybrid PSCs as follows: improved stability, scalability and non-toxic alternatives [5,6] but they have phase stability issues and complexity in fabrication [7]. Recently reported DFT study shows that KGeCl₃ is a promising perovskite material for PV application [Namisi et al. 2023]. There are very few experimental or theoretical investigations on KGeCl₃ for solar cell application so far. The study comprises the application of KGeCl₃ as a perovskite material and simulated the PSC using SCAPS-1D. Previously germanium-based double PSC has been simulated and obtained a maximum PCE of 22.5 % [8] whereas MAGeI₃based PSC has achieved a theoretical PCE of 25.34 % [9]. SnGe-based PSC has been theoretically obtained at an efficiency of 24.20 % [10]. We have simulated the various ETLs (CdS, PCBM, C₆₀ and WS₂) and HTLs (CuI, Spiro-OMeTAD, Cu₂O, PEDOT: PSS and MoS₂) and analysed the effects on the PV parameters of PSC. The optimization of thickness of absorber layer, operating temperature, Eg and carrier concentration (ND, NA) have been done to achieve the maximum PCE. The simulated KGeCl₃ device achieved a highest PCE of 29.82 % (with $V_{OC} = 1.19 \text{ V}$, $J_{SC} = 30.08 \text{ mA/cm}^2$, and FF = 82.74 %) at 300 K with WS₂ as ETL and PEDOT: PSS as HTL. These photovoltaic outcomes showed that KGeCl₃ is promising material to fabricate lead-free low cost and efficient PSCs.

9.2 Device Architecture and Simulation Method

The Fig. 9.1 depicts the device architecture and band alignment of the KGeCl₃-based PSC. The PSC structure typically includes distinct layers, an absorber layer situated between ETL and HTL. The gold (Au) is chosen as a back contact electrode with a work function of 5.1 eV. During the simulation of the Ge-based PSC, different ETLs and HTLs are simulated to determine the optimal combination that yields the maximum PCE while also optimizing the thickness of the absorber layer. The thickness of various ETLs (CdS, PCBM, C₆₀ and WS₂) varies from 50 nm to 500 nm and the employed KGeCl₃ absorber layer with thickness of 300 nm shown below in Table 9.1. Various HTLs are used to enhance the PCE of the PSC, including CuI, Spiro-OMeTAD, Cu₂O, PEDOT: PSS and MoS₂ with thickness varying from 80 nm to 250 nm shown below in Table 9.2. The band alignment diagram of the optimized device shown in Fig. 9.2 illustrates the transport of charge carriers, specifically the movement of photogenerated e's and h's across the device. Electrons have propensity to migrate from higher to lower energy levels, transitioning from PEDOT: PSS (E_C ~ 2.2 eV) to KGeCl₃ (with E_C ranging from 0.05 to 1.50 eV), then WS₂ ($E_C \sim 1.2$ eV), and ultimately to FTO ($E_C \sim 1.1$ eV). Likewise, hole transport is facilitated by the configuration of valence levels. Holes have ability to migrate freely from FTO ($E_V \sim -2.36 \text{ eV}$) to WS₂ ($E_V \sim -0.60 \text{ eV}$), then to KGeCl₃ ($E_V \sim 0 \text{ eV}$), and finally to PEDOT: PSS ($E_V \sim 0.04 \text{ eV}$). At the interface of WS₂/KGeCl₃, a moderate upward cleavage is observed. Instead of being detrimental, this phenomenon acts as a barrier, preventing excessive photo-generated e's and h's from flowing through the conduction and valence bands, respectively. Such regulation is crucial as it helps prevent rapid current

saturation. The simulated performance data of KGeCl₃ PSC before optimization with distinct ETLs and HTLs demonstrated in Table 9.3. The SCAPS-1D (version 3.3.10) has been employed for simulation. The work is dependent on change in thickness, E_g , N_D , and N_A at which simulation of the proposed PSC has been done.

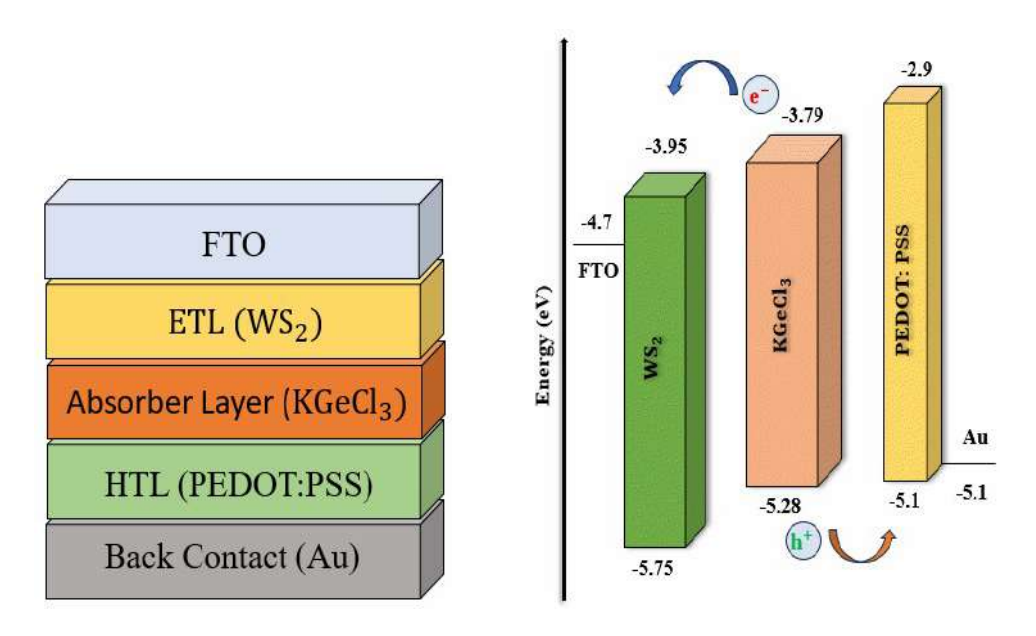


Figure 9.1 Architecture and band alignment diagram for KGeCl₃ PSC.

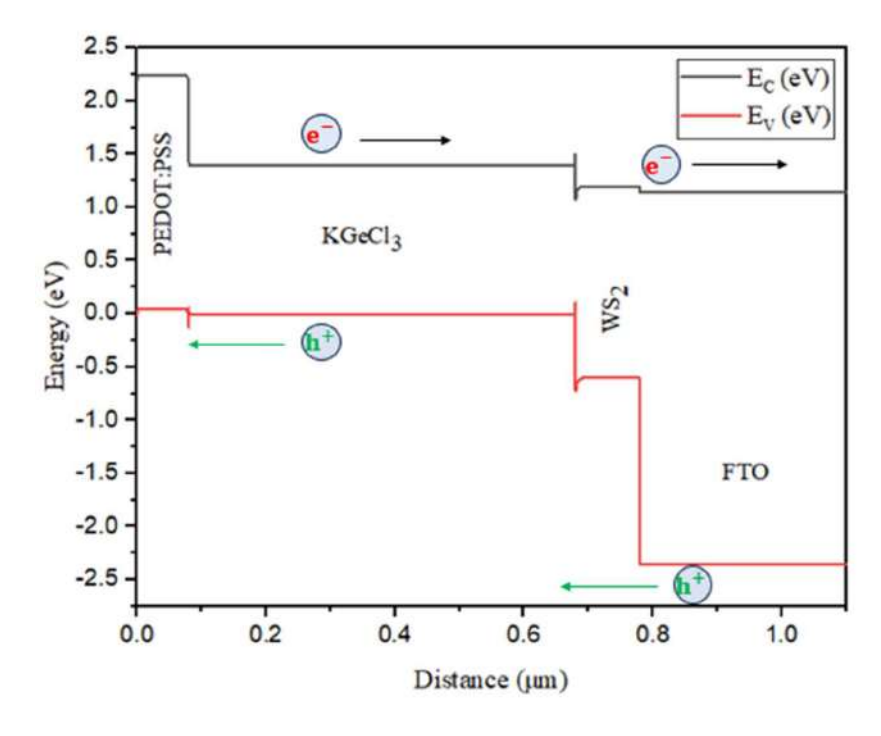


Figure 9.2 Energy band diagram of FTO/WS2/KGeCl3/PEDOT: PSS/Au PSC.

Table 9.1 Input parameters were used in simulation of distinct ETLs.

Parameter	CdS [11]	PCBM [12,13]	C ₆₀ [14]	WS ₂ [15]	KGeCl ₃ [16]
Thickness (μm)	0.050	0.500	0.050	0.100*	0.300
Eg (eV)	2.42	2.1	1.7	1.8	1.49
$\chi \left(eV\right)$	4.3	3.9	3.9	3.95	3.52
ϵ_{r}	9.35	3.9	4.2	13.6	3.52
$N_{\rm C}$ (cm ⁻³)	2.2×10^{18}	2.2×10^{19}	8.0×10^{19}	1×10^{18}	1×10^{18}
N_V (cm ⁻³)	1.8×10^{19}	2.2×10^{19}	8.0×10^{19}	2.4×10^{19}	1×10^{19}
$\mu_n (cm^2/Vs)$	100	0.001	8.0×10^{-2}	100	20
$\mu_p (cm^2/Vs)$	25	0.002	3.5×10^{-3}	100	20
N_D (cm ⁻³)	1.15×10^{17}	1×10^{19}	2.6×10^{17}	1×10^{18}	1×10^{15}
N_A (cm ⁻³)	0	-	-	0	1×10^{15}
N _t (cm ⁻³)	$1 \times 10^{15*}$	$1 \times 10^{9*}$	1×10^{14}	$1 \times 10^{13*}$	1×10^{13}

^{*}In this work.

Table 9.2 Input parameters used in simulation of various HTLs.

Parameter	FTO [17,18]	CuI [19]	Spiro-OMeTAD [20,21]	Cu ₂ O [17,19]	PEDOT: PSS [12,14]	MoS ₂ [22]
Thickness (µm)	0.400	0.100	0.213	0.250	0.080	0.200
Eg (eV)	3.5	3.1	3	2.17	2.2	1.29
$\chi \left(eV\right)$	4.0	2.1	2.2	3.2	2.9	4.2
$\epsilon_{ m r}$	9.0	6.5	3	7.11	3.0	3.0
$N_{\rm C}$ (cm ⁻³)	2.02×10^{18}	2.8×10^{19}	1×10^{19}	2.02×10^{17}	2.2×10^{15}	2.2×10^{18}
N_V (cm ⁻³)	1.8×10^{19}	1×10^{19}	1×10^{19}	1.1×10^{19}	1.8×10^{18}	1.8×10^{19}
$\mu_n (cm^2/Vs)$	20	100	10 ⁻⁴	200	1×10^{-2}	100
$\mu_p \; (cm^2/Vs)$	10	43.9	10-4	80	2×10^{-4}	150
N_D (cm ⁻³)	2×10^{19}	-	-	-	-	1×10^{15}
N_A (cm ⁻³)	0	1×10^{18}	2×10^{19}	1×10^{18}	10^{19}	1×10^{17}
N_t (cm ⁻³)	1×10^{15}	1×10^{14}	1×10^{14}	1×10^{14}	1×10^{14}	1×10^{14}

Table 9.3 KGeCl₃ PSC performance before optimization (at thickness of absorber layer = 300 nm, E_g = 1.49 eV, N_D = N_A = 1 × 10¹⁴ cm⁻³ and N_t = 10¹³ cm⁻³) with different ETLs and HTLs.

Device architecture	$V_{OC}(V)$	J_{SC} (mA/cm ²)	FF (%)	PCE (%)
FTO/C ₆₀ /KGeCl ₃ / Spiro-OMeTAD/Au	1.30	22.60	80.39	23.63
FTO/C ₆₀ /KGeCl ₃ / PEDOT: PSS/Au	1.30	22.67	80.49	23.74
FTO/C ₆₀ /KGeCl ₃ / Cu ₂ O/Au	1.30	22.80	80.56	23.90
FTO/WS ₂ /KGeCl ₃ /MoS ₂ /Au	1.02	23.04	81.11	19.09
FTO/WS ₂ /KGeCl ₃ /CuI/Au	1.31	23.10	84.41	25.57
FTO/WS ₂ /KGeCl ₃ /Spiro-OMeTAD/Au	1.31	23.10	84.22	25.51
FTO/WS ₂ /KGeCl ₃ /PEDOT: PSS/Au	1.31	23.15	84.36	25.61
FTO/WS ₂ /KGeCl ₃ /CuI/Au	1.31	23.10	84.41	25.57
FTO/CdS/KGeCl ₃ / PEDOT: PSS/Au	1.30	22.50	74.98	22.05
FTO/WS ₂ /KGeCl ₃ /CBTS/Au	1.31	23.20	83.92	25.52
FTO/WS2/KGeCl3/CFTS/Au	1.12	25.34	87.86	25.01
FTO/PCBM/KGeCl ₃ /Cu ₂ O/Au	1.28	13.61	84.24	14.73

9.3 Result and Discussion

9.3.1 Impact of Distinct Parameters on KGeCl₃-based PSC

9.3.1.1 Effect of Bandgap with Thickness

This section includes effect of the absorber layer thickness, Eg, donor and acceptor carrier concentration (N_D and N_A) on PV parameters (V_{OC}, J_{SC}, FF and PCE) of KGeCl₃-based PSC where thickness of absorber layer, bandgap, N_D and N_A are fixed at 0.3 μ m, 1.49 eV and 10^{15} cm⁻³ respectively. The contour plot shown below in Fig. 9.3 demonstrates that change in PV parameters of simulated PSC as a function of thickness of KGeCl₃ and its E_g change from 100 to 800 nm and from 1.25 to 1.55 eV respectively. Fig. 9.3(a) shows that V_{OC} increases from 1.041 V at E_g of 1.25 eV to about 1.408 V at E_g of 1.55 eV while the change in V_{OC} with thickness rises from 100 to 800 nm. For Fig. 9.3(a), a higher Eg leads to a higher V_{OC}, it allows a larger separation between the quasi-fermi levels of electrons and holes. It reduces thermal carrier generation and intrinsic recombination rates. The decrease in V_{OC} with increasing temperature can be attributed to the creation of more interfacial defects, an increase in series resistance, and a reduction in carrier diffusion length [23,24]. The value of J_{SC} falls from 34.30 to 15.09 mA/cm² with an increment in value of 1.25 to 1.55 eV depicted in Fig. 9.3(b). For Fig. 9.3(b), J_{SC} has low values as E_g increases for the thickness between 100 to 300 nm. This is perhaps due to low charge carrier generation due to very small value of thickness. High value of J_{SC} obtained for thickness between 600 to 700 nm and at E_g of 1.30 eV. For the as E_g greater than 1.30 eV causes decreasing the absorption within the layer and hence J_{SC} decreases [25]. The value of J_{SC} increases for each thickness of KGeCl₃, ranging from 100 to 800 nm.

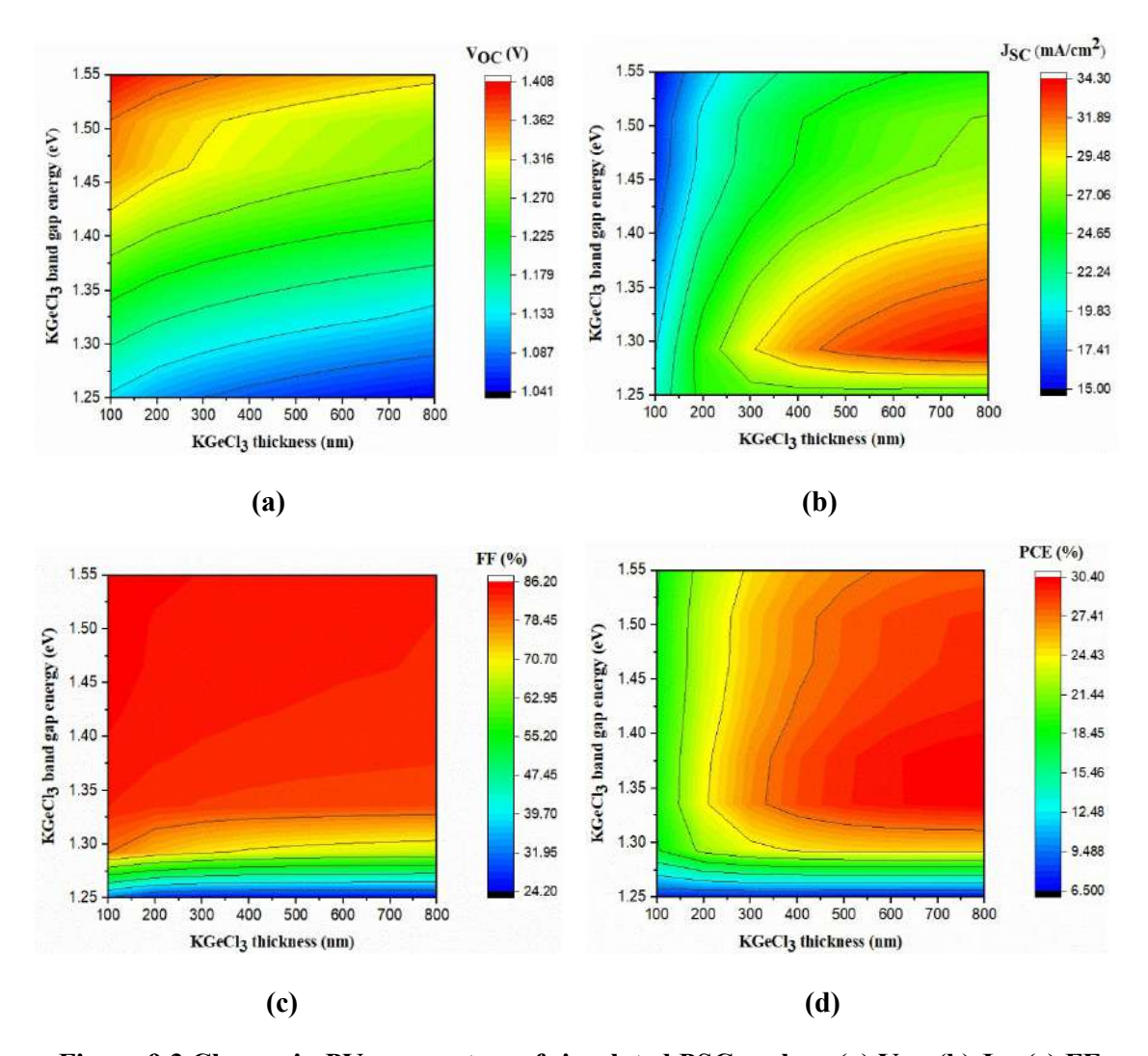


Figure 9.3 Change in PV parameters of simulated PSC such as (a) V_{OC} (b) J_{SC} (c) FF and (d) PCE with thickness of absorber layer and bandgap at doping concentration of 10^{15} cm⁻³.

The Fig. 9.3(c) indicate that the FF was increased from 31.69 to 86.02 % with increment in the value of E_g from 1.25 to 1.55 eV and this with simultaneous increment in KGeCl₃ thickness from 100-800 nm with approximate decrement of 2.59 % in value of FF. The Fig. 9.3(d) depicted that the value of PCE was 6.89 % at E_g of 1.25 eV with increment in thickness of KGeCl₃ from 100-800 nm at various regions. An average PCE of approximately 23.30 % is attained across variations of E_g ranging from 1.25 to 1.55 eV. Additionally, within a thickness range of 500 to 800 nm, a higher performance level of about 28.85 % is achieved. These findings can be elucidated as follows: with an increase in the E_g , there is a concurrent rise in the local collection of light absorption within the KGeCl₃ thin film. These outcomes can be clarified by observing that as the E_g increases, the local collection efficiency of light absorption within the absorber layer increases. This enhancement augments the carrier generation rate, consequently leading to a dramatic increase in the V_{OC} , as indicated by the equation 9.1 [26].

$$V_{oc} = \frac{K_B T}{q} \ln \left(1 + I_{Ph} I_0 \right) \tag{9.1}$$

Where V_{OC} is open circuit voltage, K_B is Boltzmann constant, T is temperature in K, q is electronic charge, I_{Ph} is Photogenerated current and I_0 is reverse saturation current. The outcomes suggest that to maximize the PCE in PSC, it is optimal to have a KGeCl₃ E_g of 1.40 eV and a thickness ranging from 500 to 800 nm. JV plots were simulated for PSCs varying KGeCl₃ thickness ranging from 300 to 800 nm while maintaining a fixed E_g of 1.40 eV, as depicted in Fig. 9.4. It is suggested that the E_g should be tuned using suitable dopants to get this optimal value of band gap. These results reveal the following trends: V_{OC} ranges between 1.18 V and 1.20 V, the J_{SC} changes from 26.05 to 30.60 mA/cm², FF remains constant at 89 % and PCE ranges from 28.06 to 29.82 % with increase in thickness of KGeCl₃ thickness. Notably, the PCE trend closely follows the variations in V_{OC} and FF values.

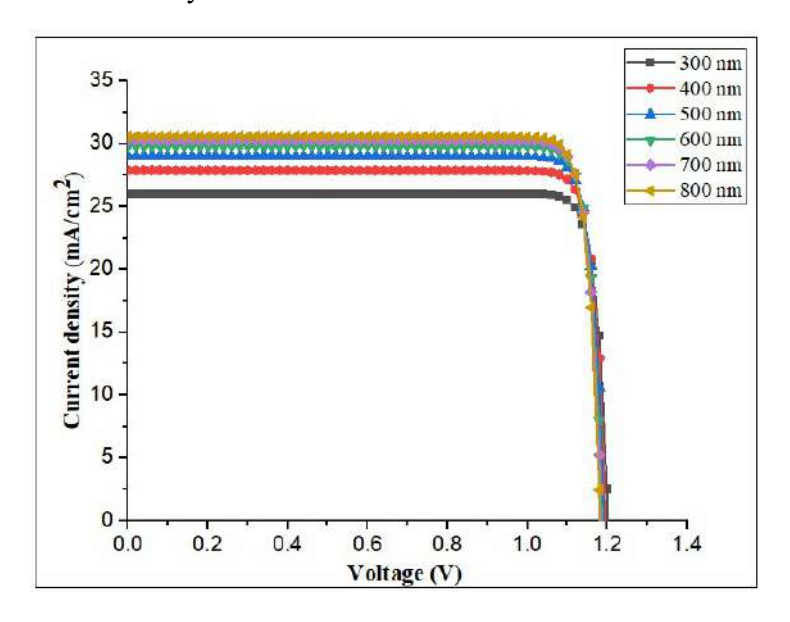


Figure 9.4 The JV curves of the PSC with thickness of the absorber layer.

9.3.1.2 Effect of Donor Carrier Concentration with Thickness

The Fig. 9.5 demonstrates the contour plot depicting the PV parameters as functions of the KGeCl₃ layer thickness varies 100 to 800 nm (x-axis) and N_D ranging between 1 × 10¹⁴ to 1 × 10^{21} cm⁻³ (y-axis) respectively. From Fig. 9.5(a), it is revealed that the V_{OC} increases from approximately 0.96 to 1.41 V as the N_D rises from 1 × 10^{14} to 1 × 10^{21} cm⁻³, with major fluctuations in the V_{OC} values observed with increasing KGeCl₃ thickness. According to Fig. 9.5(b), the J_{SC} value increases approximately 17.72 to 31.06 mA/cm² as N_D rises from 1 × 10^{14} to 1 × 10^{19} cm⁻³ and J_{SC} remain constant at about 28.48 mA/cm² for KGeCl₃ thickness exceeding 400 nm. Conversely, for KGeCl₃ thickness below 400 nm, J_{SC} maintains around 21.90 mA/cm² below N_D of 1 × 10^{20} cm⁻³. Above N_D of 1 × 10^{21} cm⁻³, the value of J_{SC} falls to 0.37 mA/cm² irrespective of the KGeCl₃ thickness. Fig. 9.5(c) suggests that the FF maintains a relatively steady value of approximately 82.44 % across various N_D and thickness, except for N_D ranging from 1 × 10^{19} to 1 × 10^{20} cm⁻³. Within a thickness range of 100 to 800 nm, first FF decreases approximately 13.46 % for the range of N_D of 1 × 10^{14} to 1 × 10^{16} cm⁻³. The FF shows a slight increase by around 3.27 % for the range of N_D of 1 × 10^{17} to 1 × 10^{19} cm⁻³ and further decrease for higher value of N_D. Fig. 9.5(d) depicts a correlation between N_D and PCE

with KGeCl₃ thickness. As N_D increases from 1×10^{14} to 1×10^{19} cm⁻³, PCE increases whereas for N_D greater than the 1×10^{19} cm⁻³ which results in decrease in PCE. Hence, the optimized value of N_D is 1×10^{18} cm⁻³ for KGeCl₃-based PSC. Specifically, it rises from approximately 16.07 to 28.18 % with initial increment in N_D and thickness of the KGeCl₃ layer. The PCE decreased to 0.01 % with a high value of N_D. The high value of doping results in formation of coulomb traps, which decreases the mobility of charge carriers. So, we need to take the optimal value of N_D for simulation [27]. This pattern suggests a direct relationship between N_D and PCE, with a more pronounced effect at higher concentrations. It is evident that increasing N_D of KGeCl₃ absorber layer has no discernible impact on the V_{OC} value, particularly when the concentrations are below 1×10^{20} cm⁻³, across each individual thickness. This could be attributed to the complete formation of the depletion width, impacting the generation rate of charge carriers and the diffusion length of minority carrier's holes in ETL and electrons in HTL. Conversely, the V_{OC} value increases with the thickness of KGeCl₃ for each value of N_A. This phenomenon can be ascribed to the prolonged lifetime and enhanced length of charge collection, resulting in greater photogenerated current. Consequently, leakage current and recombination rate decreases as the KGeCl₃ thickness grows [28]. The PCE values encapsulate the overall performance of V_{OC}, J_{SC} and FF, with its value primarily influenced by V_{OC} and FF.

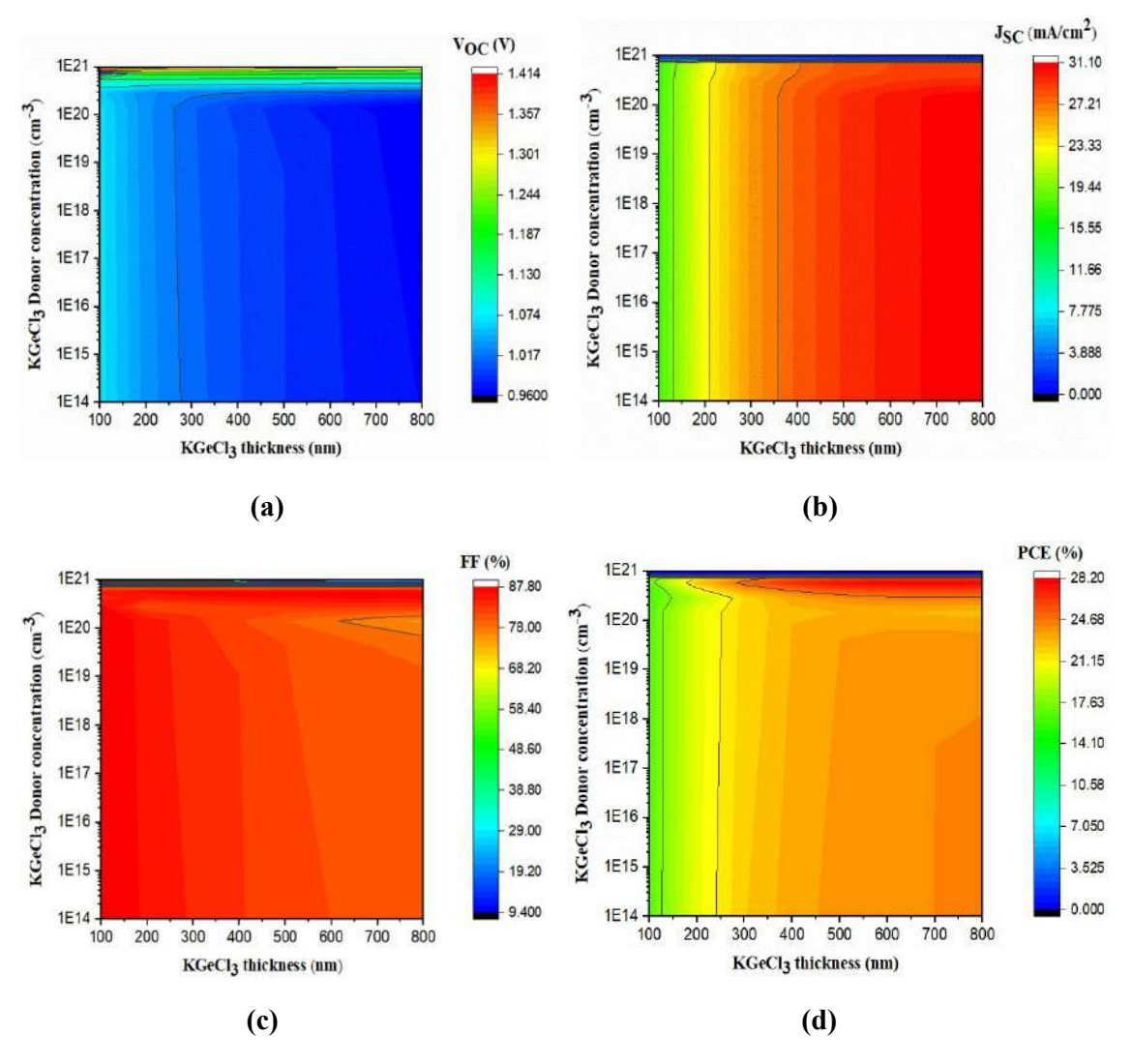
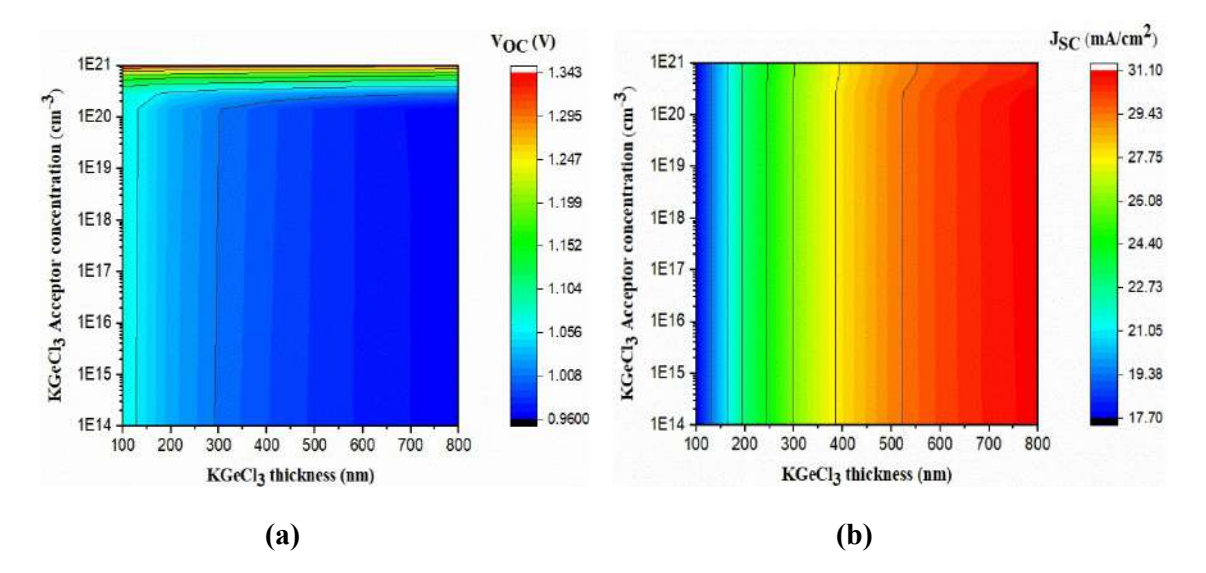


Figure 9.5 Variation in PV parameters of simulated PSC such as (a) V_{OC} (b) J_{SC} (c) FF and (d) PCE with thickness of absorber layer and N_D at $E_g = 1.40$ eV.

9.3.1.3 Effect of Acceptor Carrier Concentration with Thickness

Fig. 9.6 illustrates a contour plot showcasing the change in the photovoltaic parameters with respect to two key factors: thickness of KGeCl₃ ranging from 100 to 800 nm and N_A ranging from 1×10^{14} to 1×10^{21} cm⁻³. From Fig. 9.6(a), it is evident that the V_{OC} shows improvement, increasing from 0.96 to 1.34 V as N_A enhances from 1×10^{14} to 1×10^{21} cm⁻³. Meanwhile, there is only a minor change in the V_{OC} values with increase in KGeCl₃ thickness. In Fig. 9.6(b), it is analysed that the value of J_{SC} increases from approximately 17.71 to 30.60 mA/cm² as N_A rises from 1×10^{14} to 1×10^{21} cm⁻³ for increase in thickness of KGeCl₃. However, the value of J_{SC} remains constant around 17.71 mA/cm² for N_A ranging from 1×10^{14} to 1×10^{21} cm⁻³ at constant thickness of KGeCl₃. From Fig. 9.6(c), it can be inferred that the FF values generally remain constant at around 88 % across various NA and thicknesses. However, there is an exception: for N_A ranging from 1×10^{14} to 1×10^{21} cm⁻³ and thickness of the absorber layer between 100 to 500 nm, the FF increases from approximately 76.48 to 90.58 %. Additionally, a higher FF value of about 91 % is achieved for N_A of 1×10^{21} cm⁻³ and for various thickness ranging from 100 to 800 nm. In Figure 9.6 (d), it is evident that the PCE increases from 16.56 to 28.63 % as N_A rises from 1×10^{14} to 1×10^{17} cm⁻³, accompanied by an increase in thickness. Subsequently, as N_A further increases from 1×10^{17} to 1×10^{21} cm⁻³, the value of PCE rises from 17.50 to 31.10 %. These findings may be rationalized by the increase in carrier concentration leading to heightened electron diffusion from the KGeCl₃ layer to ETL. This elevated electron diffusion subsequently augments the device's built-in voltage (V_{bi}), predominantly formed by the depletion width, consequently resulting in a significant rise in V_{OC} [26,29]. However, the J_{SC} values improve with increasing N_A due to enhancement of photogenerated charge carriers and the reduction of both leakage current and recombination current, particularly noticeable for KGeCl₃ thickness exceeding 300 nm. These simulation results conclude that the optimized value of N_A is 1×10^{19} cm⁻³ for KGeCl₃-based PSC.



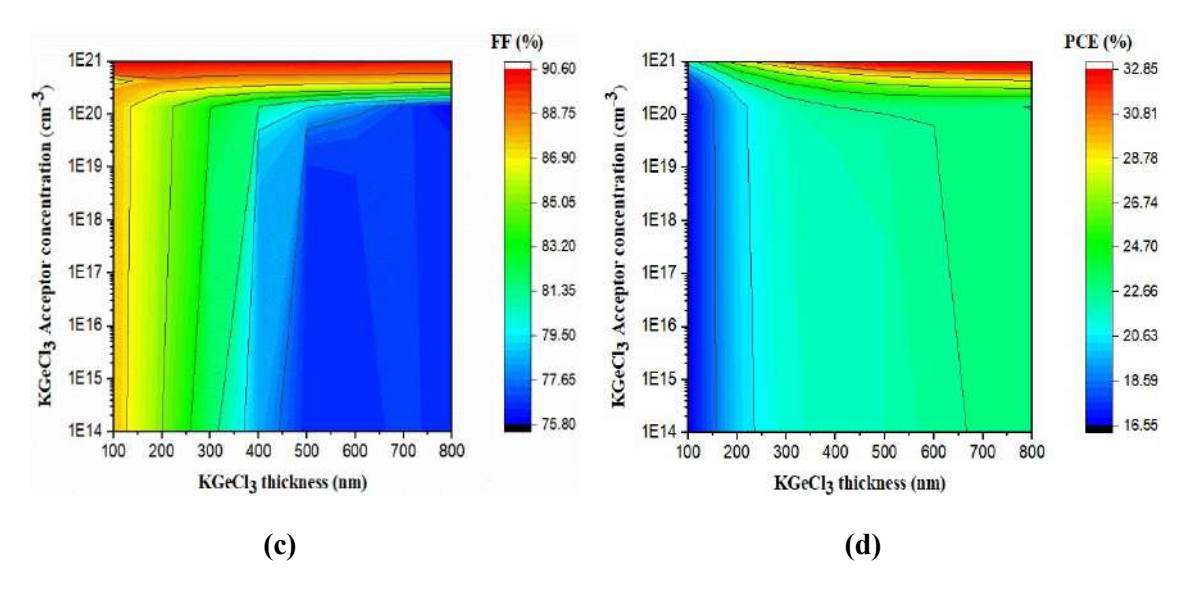


Figure 9.6 Variation in PV parameters of simulated PSC such as (a) Voc (b) Jsc (c) FF and (d) PCE with thickness of absorber layer and Na.

In this instance, the shape of PCE closely mirrors J_{SC}, as the N_A predominantly affects the photogenerated current. Consequently, the QE is measured as a function of thickness of absorber layer, Eg and carrier concentration, as illustrated in Fig. 9.7. It's apparent that QE exhibits a different shape for the different values of thickness, reaching 50 % at 300 nm and 100 % at 800 nm. As the Eg increases from 1.30 to 1.55 eV, the region under the curve representing higher QE shifts downward from 1000 to 800 nm depicted in Fig. 9.7(b). The Fig. 9.7(c) showed that the N_D is raised from 1×10^{14} to 1×10^{20} cm⁻³, the QE value enhances from approximately 50 to 98 % across wavelengths from 300 to 640 nm. Conversely, the QE value declines from 98 to 34 % for longer wavelengths from 640 to 880 nm. The QE value falls from 99 to 4 % for all further wavelengths at N_D of 1×10^{21} cm⁻³. Regardless of the N_A value, the QE maintains consistent values and shapes demonstrated in Fig. 9.7(d). The findings suggest that the photogenerated current increases with high-energy photons but decreases for lowerenergy ones, indicating differing rates of charge generation and recombination that influence J_{SC} . These results confirm and support the notion that PCE is primarily affected by J_{SC} [30]. Based on the simulations, it can be inferred that the KGeCl₃ E_g, thickness, N_D and N_A should fall within the ranges of 1.40 eV, 600 nm, 1×10^{18} cm⁻³ and 1×10^{19} cm⁻³, respectively to attain higher PCE.

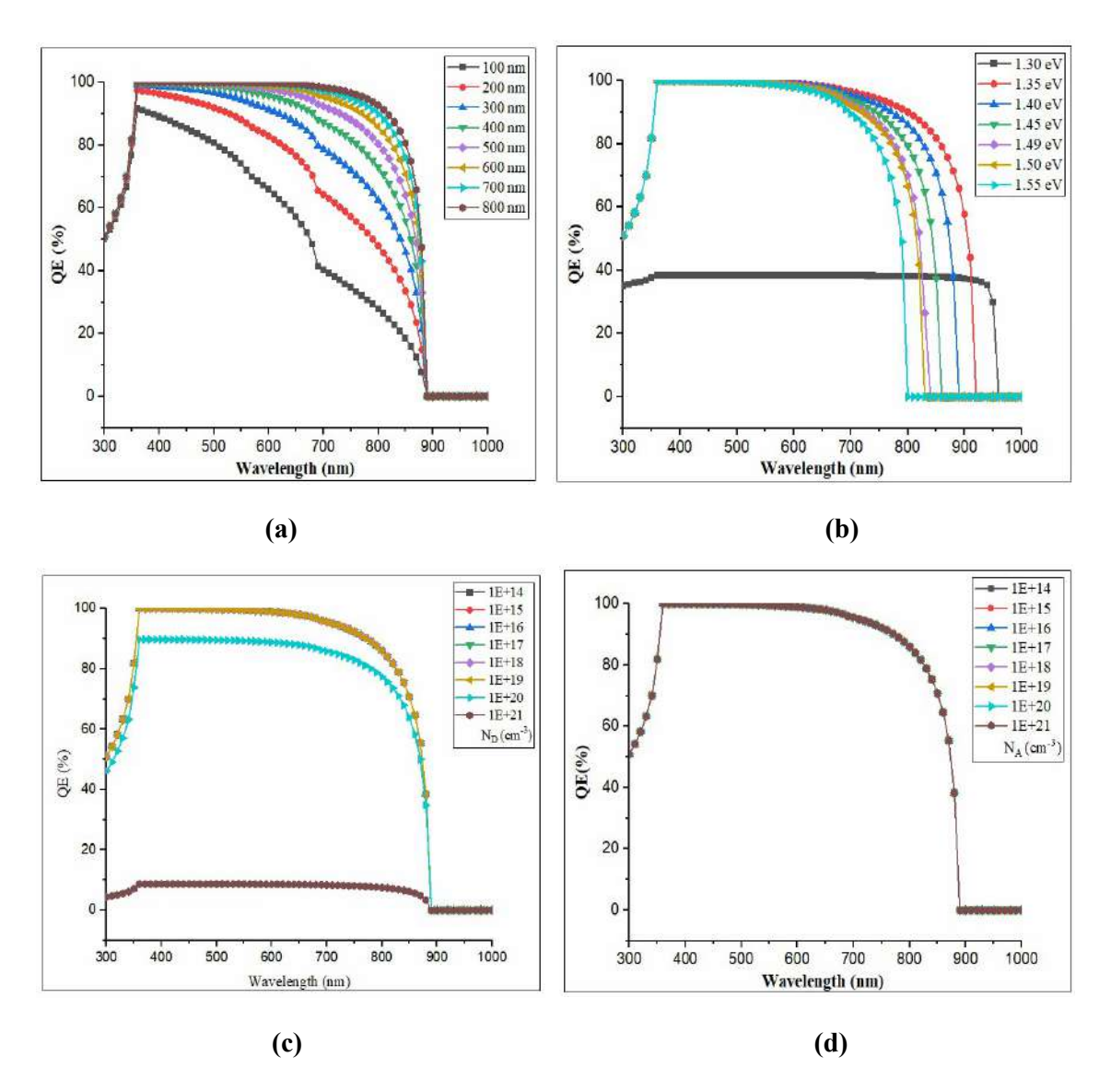


Figure 9.7 The QE curves of the simulated PSC as a function of absorber layer (a) thickness, (b) E_g, (c) N_D and (d) N_A.

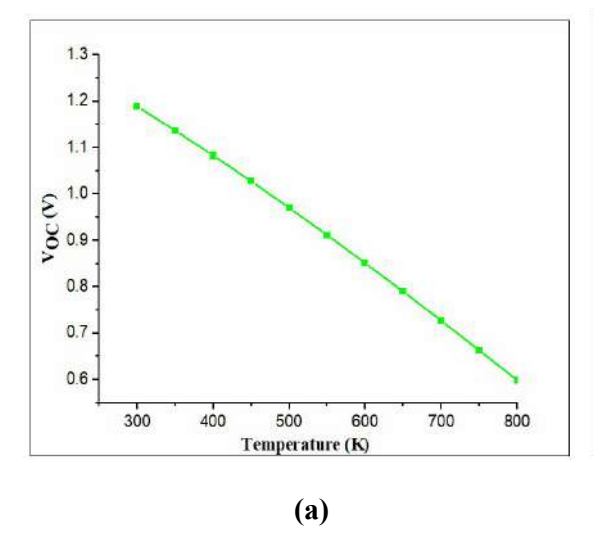
9.3.2 Effect of Operating Temperature on PSC

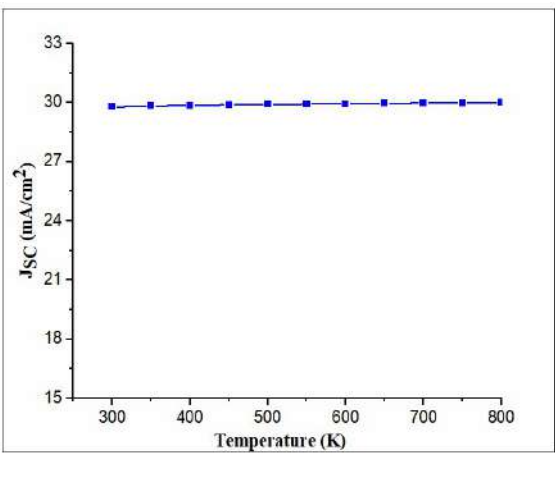
To examine the impact of operating temperature on the PV parameters, WS₂ is used as ETL and PEDOT: PSS as HTL as illustrated in Fig. 9.8. The operating temperature at which the PSC operates has been varied between 300 K and 800 K depicted in Table 9.4. Fall in the performance with temperature increase is related to a decrease in diffusion length of charge carriers [31]. Several solar cell architectures show the instability of their overall performance due to deformation among layers at high temperatures. In KGeCl₃-based PSC, fall in efficiency with temperature is about 63 %, for thickness of ETL and HTL is 100 nm and 80 nm respectively. When the enhancement of temperature occurs, the PCE drops significantly from 31.64 % at 300 K to 11.93 % at 800 K. The sharp fall in PCE shows that the optimized device

is highly unstable towards higher values of temperature. The minor rise in J_{SC} with increasing temperature results in reduced E_g and creation of additional e^-h^+ pairs [32]. The value of V_{OC} is decreasing with an increase in the operating temperature with increasing interfacial defects and series resistance. The decrease in diffusion length with increase in temperature, leading to a rise in series resistance, which in turn impacts the FF and overall PCE of the device [33,34]. The increment in temperature results in enhancement in reverse saturation current and recombination rate of charge carriers, therefore the V_{OC} , FF and PCE decreased [35,36]. The simulation outcomes showed that the optimized value of temperature is 300 K. Comparison of observed temperature dependence with PCE of different PSC materials is shown below in Fig. 9.9.

Table 9.4 Effect of change in temperature on PV parameters.

Temperature	V _{OC} (V)	J_{SC} (mA/cm ²)	FF (%)	PCE (%)
300 K	1.188	29.78	89.39	31.64
350 K	1.136	29.83	87.78	29.78
400 K	1.083	29.86	86.05	27.84
450 K	1.027	29.89	84.23	25.87
500 K	0.970	29.91	82.27	23.88
550 K	0.911	29.93	80.17	21.87
600 K	0.851	29.95	77.91	19.86
650 K	0.789	29.96	75.39	17.84
700 K	0.727	29.98	72.70	15.85
750 K	0.663	29.99	69.74	13.88
800 K	0.598	30.00	66.44	11.93





(b)

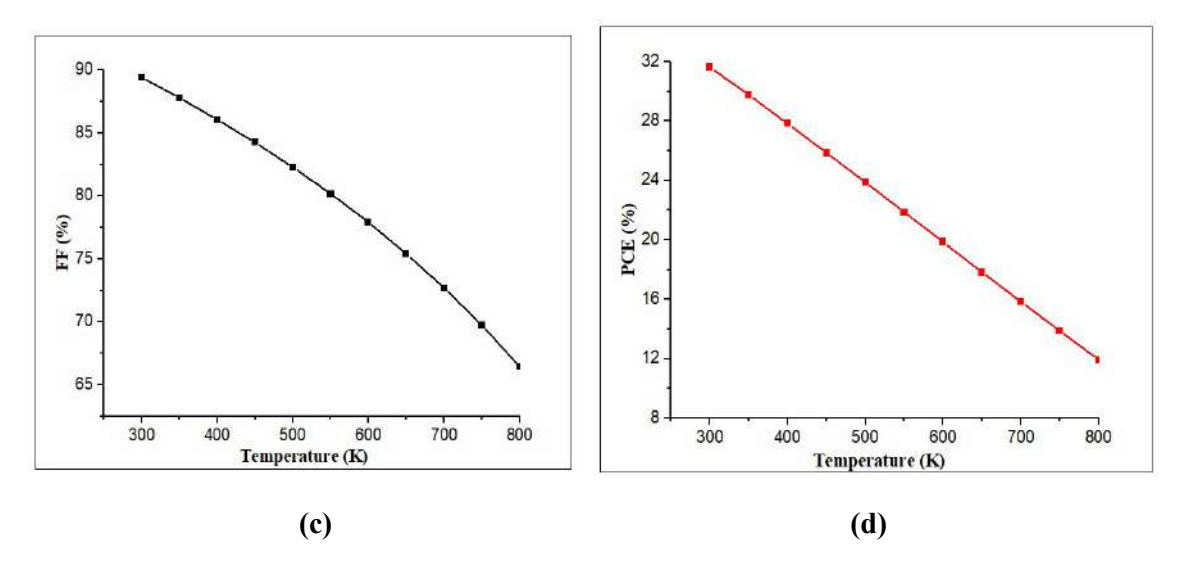


Figure 9.8 Impact of temperature on PV parameters of KGeCl₃ PSC.

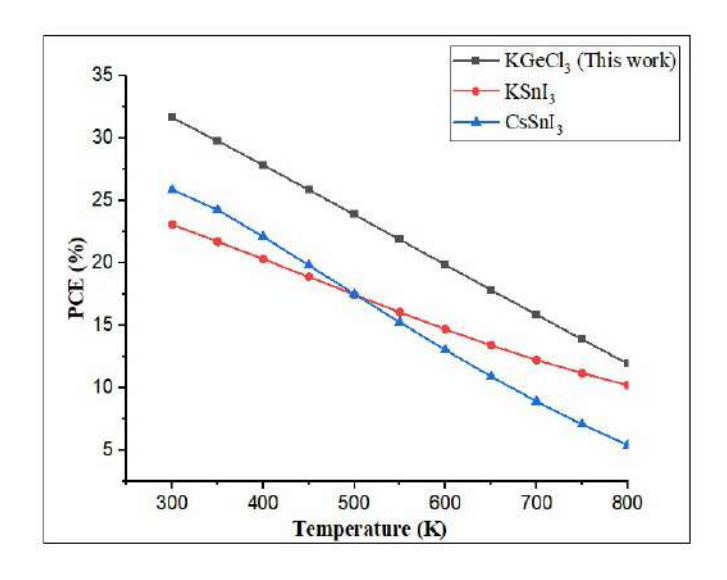


Figure 9.9 PCE vs temperature curves of various PSC materials [37,38].

9.4 Summary

This work comprises simulation study of KGeCl₃-based PSC. The effect of distinct parameters, including thickness of absorber layer, ETLs and HTLs, $E_g\ N_D,\ N_A$ and operating temperature have been examined using SCAPS-1D. The study demonstrated PEDOT: PSS as a promising HTL that could replace the expensive and less-conductive Spiro-OMeTAD. The maximum PCE of 29.82 % was obtained for the configuration of FTO/WS $_2$ /KGeCl $_3$ /PEDOT: PSS/Au. The SCAPS-1D outcomes, deduced that the optimized thickness of the absorber layer was 600 nm, with N_D of $1\times10^{18}\ cm^{-3}$ and a N_A of $1\times10^{19}\ cm^{-3}$ results in maximum PCE at E_g of 1.40 eV. The optimized PSC is simulated at N_t of $1\times10^{15}\ cm^{-3}$. The simulation trend demonstrated

that photovoltaic performance of a PSC falls with increment in operating temperature hence 300 K is optimized temperature. The device PCE improved beyond 29 % by optimizing thickness, operating temperature, E_g , N_D and N_A . The proper optimization of suitable ETL and HTL has been done for KGeCl₃-based PSC hence, this can be an alternative to Pb-based PSC for the preparation of efficient, low-cost and eco-friendly PSCs.

9.5 REFERENCES

- [1] Liu, Y., Liu, Y. and Guo, Y., 2023. Organic–inorganic hybrid perovskite materials and their application in transistors. *Materials Chemistry Frontiers*, 7(21), pp.5215-5246.
- [2] Kojima, A., Teshima, K., Shirai, Y. and Miyasaka, T., 2009. Organometal halide perovskites as visible-light sensitizers for photovoltaic cells. *Journal of the american chemical society*, 131(17), pp.6050-6051.
- [3] Park, N.G., 2015. Perovskite solar cells: an emerging photovoltaic technology. *Materials today*, 18(2), pp.65-72.
- [4] Zhao, Y. and Zhu, K., 2016. Organic–inorganic hybrid lead halide perovskites for optoelectronic and electronic applications. *Chemical Society Reviews*, 45(3), pp.655-689.
- [5] Kulbak, M., Cahen, D. and Hodes, G., 2015. How important is the organic part of lead halide perovskite photovoltaic cells? Efficient CsPbBr₃ cells. *The journal of physical chemistry letters*, 6(13), pp.2452-2456.
- [6] Eperon, G.E., Stranks, S.D., Menelaou, C., Johnston, M.B., Herz, L.M. and Snaith, H.J., 2014. Formamidinium lead trihalide: a broadly tunable perovskite for efficient planar heterojunction solar cells. *Energy & environmental science*, 7(3), pp.982-988.
- [7] Ouedraogo, N.A.N., Chen, Y., Xiao, Y.Y., Meng, Q., Han, C.B., Yan, H. and Zhang, Y., 2020. Stability of all-inorganic perovskite solar cells. *Nano energy*, 67, p.104249.
- [8] Sekar, K., Marasamy, L., Mayarambakam, S., Hawashin, H., Nour, M. and Bouclé, J., 2023. Lead-free, formamidinium germanium-antimony halide (FA₄GeSbCl₁₂) double perovskite solar cells: the effects of band offsets. *RSC advances*, 13(36), pp.25483-25496.
- [9] Kumar, V., Kumar, R. and Chand, F., 2024. Performance analysis of ecofriendly Ge based perovskite solar cell using computational approach. *Materials Letters*, 361, p.136145.
- [10] Azizman, M.S.A., Azhari, A.W., Halin, D.S.C., Ibrahim, N., Sepeai, S., Ludin, N.A., Nor, M.N.M. and Ho, L.N., 2023. Progress in tin-germanium perovskite solar cells: a review. *Synthetic Metals*, 299, p.117475.
- [11] Kuddus, A., Rahman, M.F., Ahmmed, S., Hossain, J. and Ismail, A.B.M., 2019. Role of facile synthesized V₂O₅ as hole transport layer for CdS/CdTe heterojunction solar cell: validation of simulation using experimental data. Superlattices and Microstructures, 132, p.106168.
- [12] Mandadapu, U., Vedanayakam, S.V. and Thyagarajan, K., 2017. Simulation and analysis of lead based perovskite solar cell using SCAPS-1D. *Indian J. Sci. Technol*, 10(1), pp.1-8.
- [13] Azri, F., Meftah, A., Sengouga, N. and Meftah, A., 2019. Electron and hole transport layers optimization by numerical simulation of a perovskite solar cell. *Solar energy*, 181, pp.372-378.
- [14] Jayan, K.D. and Sebastian, V., 2021. Comprehensive device modelling and performance analysis of MASnI₃ based perovskite solar cells with diverse ETM, HTM and back metal contacts. *Solar Energy*, 217, pp.40-48.
- [15] Hossain, M.K., Toki, G.I., Kuddus, A., Rubel, M.H., Hossain, M.M., Bencherif, H., Rahman, M.F., Islam, M.R. and Mushtaq, M., 2023. An extensive study on multiple ETL and HTL layers to design and simulation of high-performance lead-free CsSnCl₃-based perovskite solar cells. *Scientific Reports*, 13(1), p.2521.

- [16] Wei, H., Qiu, P., Li, Y., He, Y., Peng, M., Zheng, X. and Liu, X., 2022. Challenges and strategies of all-inorganic lead-free halide perovskite solar cells. *Ceramics International*, 48(5), pp.5876-5891.
- [17] Rai, S., Pandey, B.K. and Dwivedi, D.K., 2020. Modeling of highly efficient and low cost CH₃NH₃Pb(I_{1-x}Cl_x)₃ based perovskite solar cell by numerical simulation. *Optical Materials*, 100, p.109631.
- [18] Haider, S.Z., Anwar, H. and Wang, M., 2019. Theoretical device engineering for high-performance perovskite solar cells using CuSCN as hole transport material boost the efficiency above 25%. *physica status solidi (a)*, 216(11), p.1900102.
- [19] Kanoun, A.A., Kanoun, M.B., Merad, A.E. and Goumri-Said, S., 2019. Toward development of high-performance perovskite solar cells based on CH₃NH₃GeI₃ using computational approach. *Solar Energy*, 182, pp.237-244.
- [20] Bhattarai, S. and Das, T.D., 2021. Optimization of carrier transport materials for the performance enhancement of the MAGeI₃ based perovskite solar cell. *Solar Energy*, 217, pp.200-207.
- [21] De Los Santos, I.M., Cortina-Marrero, H.J., Ruíz-Sánchez, M.A., Hechavarría-Difur, L., Sánchez-Rodríguez, F.J., Courel, M. and Hu, H., 2020. Optimization of CH₃NH₃PbI₃ perovskite solar cells: A theoretical and experimental study. *Solar Energy*, 199, pp.198-205.
- [22] Kohnehpoushi, S., Nazari, P., Nejand, B.A. and Eskandari, M., 2018. MoS₂: a two-dimensional hole-transporting material for high-efficiency, low-cost perovskite solar cells. *Nanotechnology*, 29(20), p.205201.
- [23] Ompong, D. and Singh, J., 2018. High open-circuit voltage in perovskite solar cells: The role of hole transport layer. *Organic Electronics*, 63, pp.104-108.
- [24] Ouslimane, T., Et-Taya, L., Elmaimouni, L. and Benami, A., 2021. Impact of absorber layer thickness, defect density, and operating temperature on the performance of MAPbI₃ solar cells based on ZnO electron transporting material. *Heliyon*, 7(3).
- [25] Asaduzzaman, M., Hasan, M. and Bahar, A.N., 2016. An investigation into the effects of band gap and doping concentration on Cu (In, Ga) Se₂ solar cell efficiency. *SpringerPlus*, 5(1), p.578.
- [26] Abdelfatah, M., Ledig, J., El-Shaer, A., Wagner, A., Marin-Borras, V., Sharafeev, A., Lemmens, P., Mosaad, M.M., Waag, A. and Bakin, A., 2016. Fabrication and characterization of low cost Cu₂O/ZnO: Al solar cells for sustainable photovoltaics with earth abundant materials. *Solar Energy Materials and Solar Cells*, 145, pp.454-461.
- [27] Shang, Z., Heumueller, T., Prasanna, R., Burkhard, G.F., Naab, B.D., Bao, Z., McGehee, M.D. and Salleo, A., 2016. Trade-off between trap filling, trap creation, and charge recombination results in performance increase at ultralow doping levels in bulk heterojunction solar cells. *Advanced Energy Materials*, 6(24), p.1601149.
- [28] Musselman, K.P., Marin, A., Schmidt-Mende, L. and MacManus-Driscoll, J.L., 2012. Incompatible length scales in nanostructured Cu₂O solar cells. *Advanced Functional Materials*, 22(10), pp.2202-2208.
- [29] Lin, W.M., Yazdani, N., Yarema, O., Volk, S., Yarema, M., Kirchartz, T. and Wood, V., 2019. Simulating nanocrystal-based solar cells: A lead sulfide case study. *The journal of chemical physics*, 151(24).

- [30] Abdelfatah, M., El Sayed, A.M., Ismail, W., Ulrich, S., Sittinger, V. and El-Shaer, A., 2023. SCAPS simulation of novel inorganic ZrS₂/CuO heterojunction solar cells. *Scientific Reports*, 13(1), p.4553.
- [31] Pindolia, G., Shinde, S.M. and Jha, P.K., 2022. Optimization of an inorganic lead free RbGeI₃ based perovskite solar cell by SCAPS-1D simulation. *Solar Energy*, 236, pp.802-821.
- [32] Deswal, V., Kaushik, S., Kundara, R. and Baghel, S., 2024. Numerical simulation of highly efficient Cs₂AgInBr₆-based double perovskite solar cell using SCAPS 1-D. *Materials Science and Engineering: B*, 299, p.117041.
- [33] Hossain, M.K., Rubel, M.H.K., Toki, G.I., Alam, I., Rahman, M.F. and Bencherif, H., 2022. Effect of various electron and hole transport layers on the performance of CsPbI₃-based perovskite solar cells: a numerical investigation in DFT, SCAPS-1D, and wxAMPS frameworks. *ACS omega*, 7(47), pp.43210-43230.
- [34] Kundara, R. and Baghel, S., 2023. Device modelling of lead free (CH₃NH₃)₂CuX₄ based perovskite solar cells using SCAPS simulation. *Optical and Quantum Electronics*, 55(11), p.968.
- [35] Ahmed, S., Jannat, F., Khan, M.A.K. and Alim, M.A., 2021. Numerical development of ecofriendly Cs₂TiBr₆ based perovskite solar cell with all-inorganic charge transport materials via SCAPS-1D. *Optik*, 225, p.165765.
- [36] Chen, A. and Zhu, K., 2012. Computer simulation of a-Si/c-Si heterojunction solar cell with high conversion efficiency. *Solar Energy*, 86(1), pp.393-397.
- [37] Pindolia, G., Shinde, S.M. and Jha, P.K., 2023. Non-leaded, KSnI₃ based perovskite solar cell: A DFT study along with SCAPS simulation. *Materials Chemistry and Physics*, 297, p.127426.
- [38] Jiang, M. and Tang, J., 2021. Simulated development and optimized performance of narrow-bandgap CsSnI₃-based all-inorganic perovskite solar cells. *Journal of Physics D: Applied Physics*, 54(46), p.465104.

CHAPTER 10

SYNTHESIS AND CHARACTERIZATION OF C₈₂AlBiCl₆ DOUBLE PEROVSKITE MATERIAL FOR PHOTOVOLTAIC APPLICATION

- This chapter provides a summary of synthesis and characterization of new Cesium aluminium bismuth chloride (Cs₂AlBiCl₆) double perovskite material.
- ➤ We have synthesized the Cs₂AlBiCl₆ double perovskite material using solution-based method.
- The characterizations such as UV-vis spectroscopy, photoluminescence, SEM and X-ray diffraction have been done to analyse the synthesized material.
- The application of synthesized material in solar cells.

10.1 Introduction

Promising alternatives to lead-based perovskites, which address health and environmental concerns, include lead-free perovskite solar cells based on heavy metal cations such as bismuth (Bi). The newly developed double perovskite materials such as Cs₂AlBiCl₆ possess a stable pair of valence e's typically show greater tolerance factor to defects [1]. The double perovskite structure has a chemical formula of A₂BB X₆. Recently, Bi-based double perovskites, with the formula Cs₂AlBiCl₆ have gained attention as promising alternatives to lead [2]. These perovskites feature a three-dimensional (3D) cubic structure [3]. Bismuth, being a stable cation with large polarizability, demonstrates a high effective charge, leading to a high dielectric constant. This property is essential for better screening of charged defects [2]. In particular, Cs₂AlBiCl₆ has attractive optical characteristics and a stable crystal structure, which makes it a promising option for photovoltaic applications. In contrast to lead-based perovskites, double perovskites typically encounter difficulties with reduced efficiency and charge transport constraints. We have synthesized the Cs₂AlBiCl₆ double perovskite material using solutionbased method. The characterizations such as UV-vis spectroscopy, photoluminescence and Xray diffraction etc. to study the properties of synthesized material. We have calculated a direct bandgap of 2.92 eV using Tauc plot which can be tune up to 2.6 eV with suitable doping. The photoluminescence spectra of the synthesized material are validated with previously reported result. The XRD peaks shows that the synthesized material is crystalline in nature. These properties of Cs₂AlBiCl₆ double perovskite material clearly shows that it is suitable for photovoltaic applications. The combination of Al, Bi, and double perovskites such as Cs₂AlBiCl₆ offers a route toward safer and more sustainable perovskite solar cells, even though research on these lead-free alternatives is still in its early stages.

10.2 Materials and Method

All the precursors used in synthesis of double perovskite material are cesium chloride (CsCl), aluminium chloride (AlCl₃), hydrochloric acid (HCL), bismuth chloride (BiCl₃) and deionized water (DI). The double perovskite material Cs₂AlBiCl₆ was synthesized by employing a solgel method. The flow chart for stepwise preparation of double perovskite material is depicted in Fig. 10.1. DI water chosen as a solvent to dissolve both solutes. At first,1M aqueous solution of CsCl mixed with 1M aqueous solution of BiCl₃ and AlCl₃. After that HCL is dropwise poured in the solution of both precursors. The mixture was stirred for 2 days at 343 rpm and 60 °C. The precipitate of the synthesized material is filter out by using filter paper. The sample was dried in a vacuum oven at 80 °C for 12 h. The sample was grinded with the help of mortar pistol to obtain Cs₂AlBiCl₆ double perovskite powder. The synthesized sample shown in Fig. 10.2.

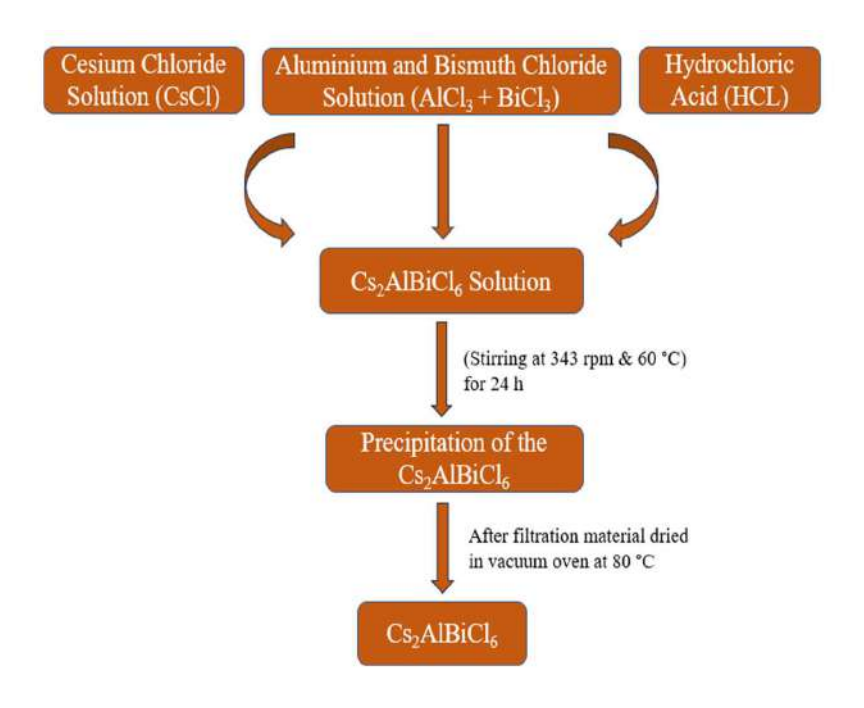


Figure 10.1 Flow chart of Cs₂AlBiCl₆ material synthesis.

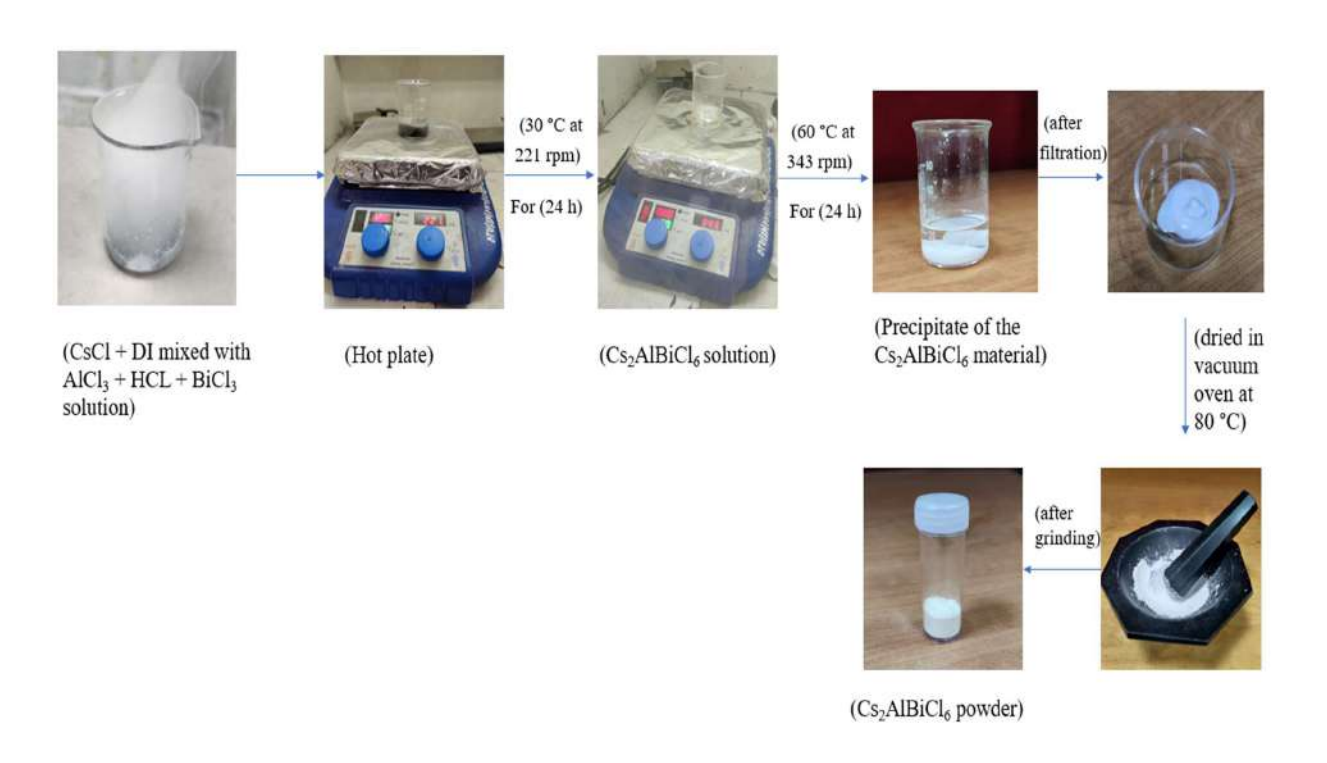


Figure 10.2 Preparation of Cs2AlBiCl6 double perovskite material.

10.2.1 Material Characterization Techniques

XRD pattern of Cs₂AlBiCl₆ double perovskite material was obtained by using a diffractometer (Bruker Model: D-8). The size and morphologies of synthesized double perovskite material is analysed by SEM. UV–vis spectrum of the Cs₂AlBiCl₆ double perovskite material is observed by employing a Perkin-Elmer, Lamda-750 dual-beam spectrometer.

10.3 Result and Discussion

10.3.1 XRD Analysis

It is primarily used for phase identification and crystallinity of the material. The observed range of XRD data is from 10° to 80° over 2θ with scan rate of 2°/min. The XRD peaks of Cs₂AlBiCl₆ double perovskite material are depicted in Fig. 10.3. The XRD peaks with 2θ of 15.78°, 23.38°, 27.48°, 28.72°, 30.64°, 33.26°, 36.34°, 40.92°, 41.04°, 43.62°, 47.72° and 50.06° corresponding to (200), (220), (311), (222), (400), (331), (420), (422), (511), (440), (531) and (442) planes of the synthesized Cs₂AlBiCl₆ double perovskite material which is in good agreement and well-aligned with previously reported data (ISCD#239874) [4,5]. The XRD peaks observed suggest that the synthesized double perovskite material is highly crystalline and forms the desired phase. Extra peaks represent unexpected phases of the AlCl₃ and BiCl₃. Bragg's eq. (10.1) was used to calculate the material grain size and display angles.

$$2d\sin\theta = n\lambda \tag{10.1}$$

Crystallite Size =
$$\frac{0.94 \times \lambda}{\beta \cos \theta}$$
 (10.2)

Where, λ = wavelength of X-ray, β = FWHM, θ = Bragg's angle.

The calculated average crystallite size is 53.85 nm by using Debye Scherrer's eq. (10.2).

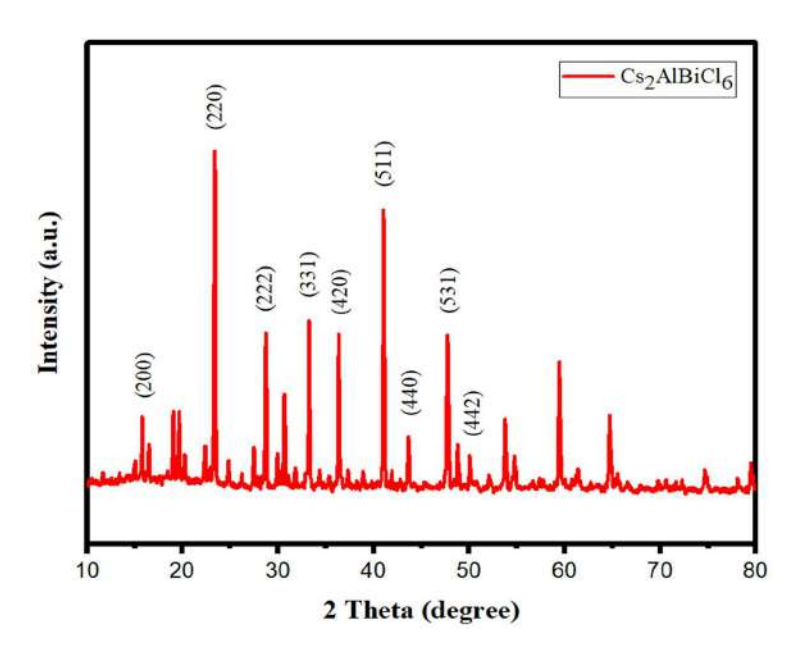


Figure 10.3 XRD pattern of Cs₂AlBiCl₆.

10.3.2 SEM Results

The $Cs_2AlBiCl_6$ double perovskite material topography and superficial characteristics was investigated by using SEM. The SEM images of $Cs_2AlBiCl_6$ material obtained at different resolutions depicted in Fig. 10.4. The average size of synthesized crystals are ~ 763 nm [6]. The SEM images deduced that the synthesized material is composed of multifaced nanoparticles with high crystallinity. There are no surface-protecting layers which lead to agglomeration of the particles. It indicates a face-centered cubic double perovskite structure. The particle shapes are ambiguous, and material contains numerous large and small pores throughout material [7].

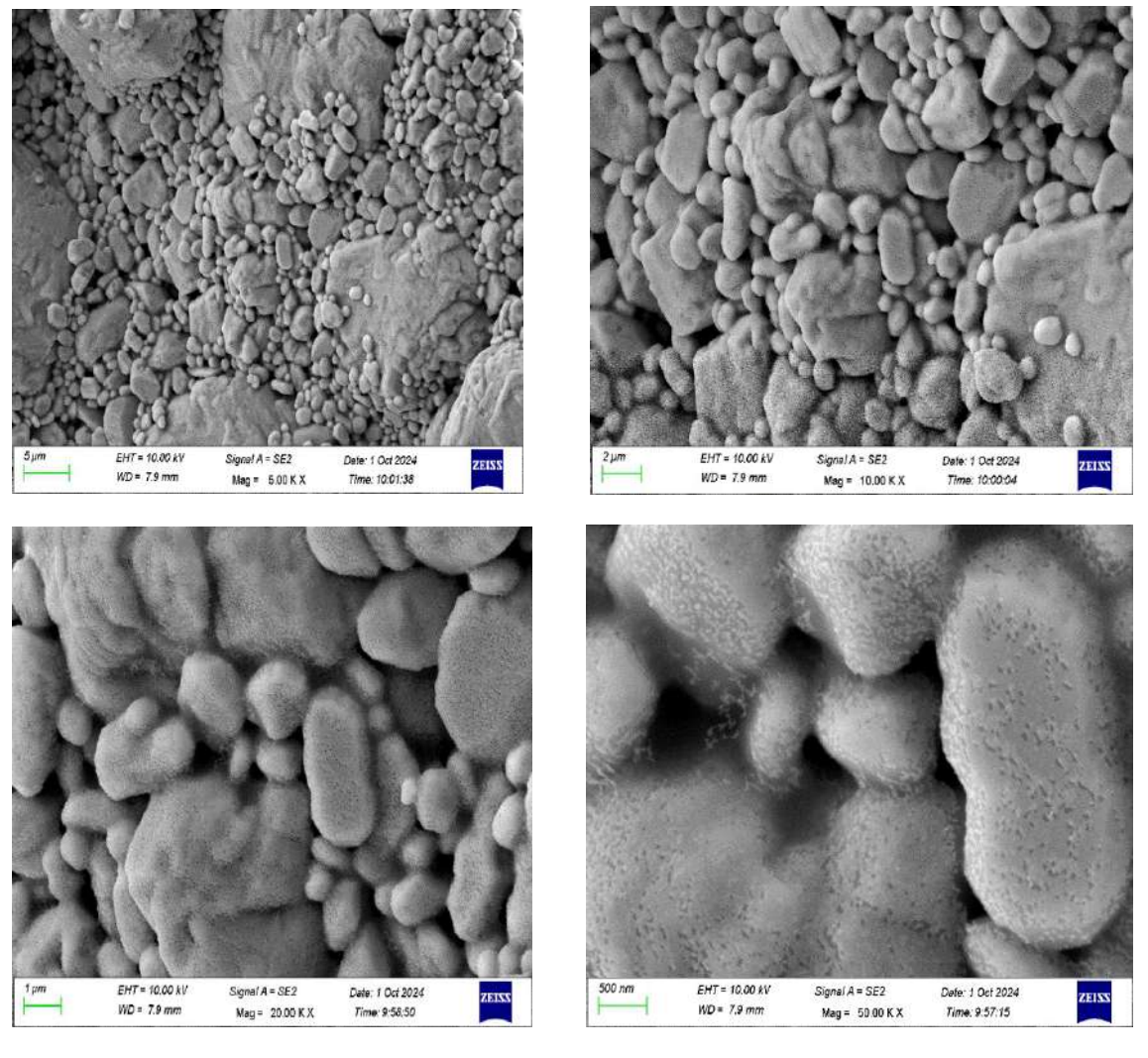


Figure 10.4 SEM images of Cs2AlBiCl6 nanoparticles.

10.3.3 UV-Vis Spectroscopy

UV-vis spectrum of $Cs_2AlBiCl_6$ perovskite material carried out in order to calculate optical E_g depicted in Fig. 10.5. The absorption spectra of the $Cs_2AlBiCl_6$ material are observed from 300 to 800 nm. The E_g is calculated by the equation (10.3).

$$E_{g} = \frac{hc}{\lambda \max}$$
 (10.3)

Where, E_g is the band gap energy of the sample, h = Planck's constant, c = speed of light and λ_{max} is the extreme absorption wavelength of the sample. The calculated value of direct band gap for $Cs_2AlBiCl_6$ double perovskite is approximately 2.92 eV and is in range as reported by Pandey et al. [8]. The synthesized material features a wide band gap demonstrates behaviour as lead halide perovskite material, indicating its potential as a substitute for lead halide perovskites in optoelectronics applications.

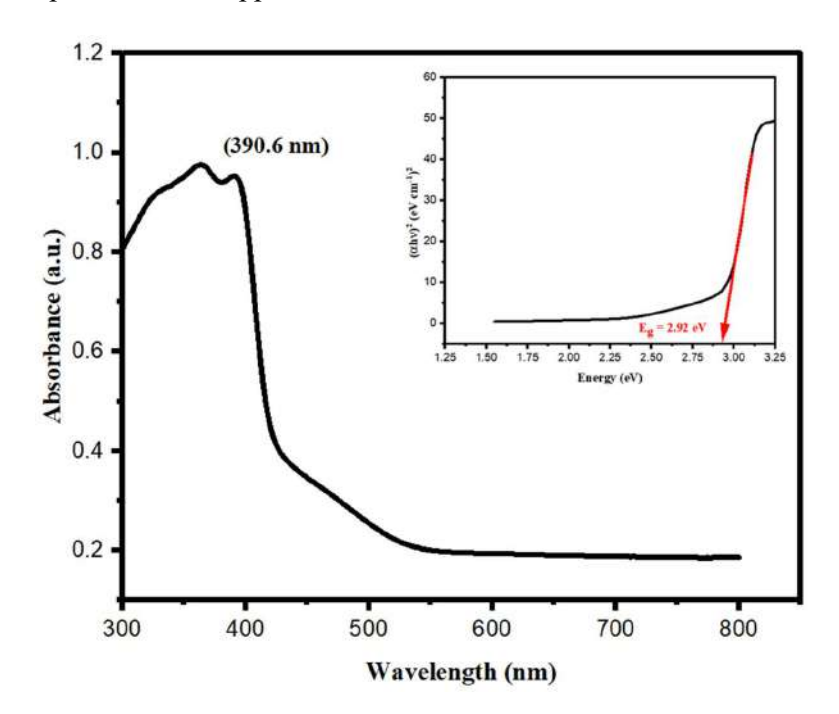


Figure 10.5 UV-vis spectrum of Cs₂AlBiCl₆ double perovskite material.

10.3.4 Photoluminescence Spectrum

To study the optical properties of the synthesized material, Photoluminescence spectrum (PL) has been obtained at room temperature. The Cs₂AlBiCl₆ material observed a prominent emission peak around at 423 nm with excitation wavelength of 308 nm illustrated in Fig. 10.6. The sharp peak is due to band-to-band transition and the broad peak corresponds to trap state transition. The broad PL emission peak results from phonon-assisted carrier recombination due to exciton trapping, resembling behaviour seen in related halide perovskites, as indicated in past studies [5,9,10]. The PL spectra of this material point to its potential for PV applications.

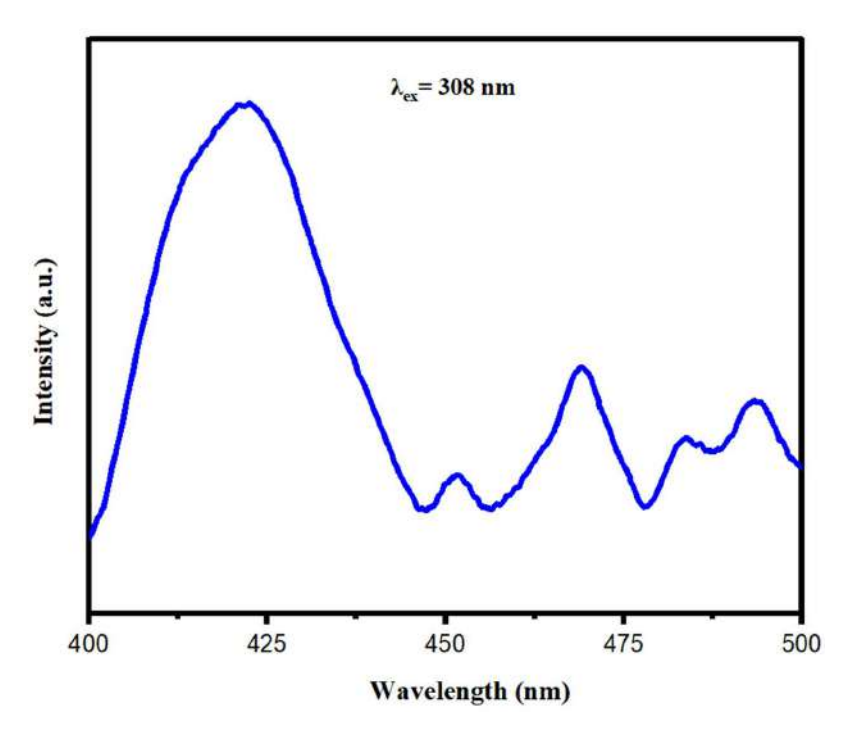


Figure 10.6 PL spectrum of Cs2AlBiCl6 double perovskite material.

10.4 Summary

The work comprises synthesis of $Cs_2AlBiCl_6$ double perovskite material by employing sol-gel method. The XRD pattern of the material deduced that the synthesized material is crystalline in nature and having the average crystallite size of 53.85 nm. The SEM images has been used for the morphological analysis. The synthesized crystals having cubic structure material with average crystal size of \sim 763 nm. The main absorption spectra exist between 300 to 550 nm. The direct band gap of material is approximately 2.92 eV measured by Tauc plot. The main broad peak of $Cs_2AlBiCl_6$ material observed around at 423 nm for the excitation wavelength of 308 nm. The synthesized material structural and optical properties deduced that $Cs_2AlBiCl_6$ is a potential candidate for the solar cell applications.

10.5 REFERENCES

- [1] Brandt, R.E., Stevanović, V., Ginley, D.S. and Buonassisi, T., 2015. Identifying defect-tolerant semiconductors with high minority-carrier lifetimes: beyond hybrid lead halide perovskites. *Mrs Communications*, 5(2), pp.265-275.
- [2] Rahane, S.N., Rahane, G.K., Mandal, A., Jadhav, Y., Godha, A., Rokade, A., Shah, S., Hase, Y., Waghmare, A., Saykar, N.G. and Roy, A., 2024. Lead-free Cs₂AgBiCl₆ double perovskite: experimental and theoretical insights into the self-trapping for Optoelectronic Applications. *ACS Physical Chemistry Au*, 4(5), pp.476-489.
- [3] Chen, M., Ju, M.G., Garces, H.F., Carl, A.D., Ono, L.K., Hawash, Z., Zhang, Y., Shen, T., Qi, Y., Grimm, R.L. and Pacifici, D., 2019. Highly stable and efficient all-inorganic lead-free perovskite solar cells with native-oxide passivation. *Nature communications*, 10(1), p.16.
- [4] Fan, P., Peng, H.X., Zheng, Z.H., Chen, Z.H., Tan, S.J., Chen, X.Y., Luo, Y.D., Su, Z.H., Luo, J.T. and Liang, G.X., 2019. Single-source vapor-deposited Cs₂AgBiBr₆ thin films for lead-free perovskite solar cells. *Nanomaterials*, 9(12), p.1760.
- [5] Liu, Z., Yang, H., Wang, J., Yuan, Y., Hills-Kimball, K., Cai, T., Wang, P., Tang, A. and Chen, O., 2021. Synthesis of lead-free Cs₂AgBiX₆ (X= Cl, Br, I) double perovskite nanoplatelets and their application in CO₂ photocatalytic reduction. *Nano Letters*, 21(4), pp.1620-1627.
- [6] Thawarkar, S., Rondiya, S.R., Dzade, N.Y., Khupse, N. and Jadkar, S., 2021. Experimental and theoretical investigation of the structural and opto-electronic properties of Fe-doped lead-free Cs₂AgBiCl₆ double perovskite. *Chemistry–A European Journal*, 27(26), pp.7408-7417.
- [7] Jeevaraj, M., Devendran, P., Nallamuthu, N., Sudhahar, S. and Kumar, M.K., 2023. Influence of Mn²⁺ doping on the optical properties of Cs₂AgBiCl₆ double perovskite luminescent phosphors. *Journal of Materials Science: Materials in Electronics*, 34(1), p.65.
- [8] Pandey, N., Neelu, N. and Chakrabarti, S., 2023. Room temperature synthesis of double perovskite Cs₂AlBiCl₆ for photovoltaic applications. *Optical Materials*, 137, p.113570.
- [9] Yangui, A., Garrot, D., Lauret, J.S., Lusson, A., Bouchez, G., Deleporte, E., Pillet, S., Bendeif, E.E., Castro, M., Triki, S. and Abid, Y., 2015. Optical investigation of broadband white-light emission in self-assembled organic–inorganic perovskite (C₆H₁₁NH₃)₂PbBr₄. *The Journal of Physical Chemistry C*, 119(41), pp.23638-23647.
- [10] McCall, K.M., Stoumpos, C.C., Kostina, S.S., Kanatzidis, M.G. and Wessels, B.W., 2017. Strong electron–phonon coupling and self-trapped excitons in the defect halide perovskites A₃M₂I₉ (A= Cs, Rb; M= Bi, Sb). *Chemistry of Materials*, 29(9), pp.4129-4145.

CHAPTER 11

CONCLUSION, FUTURE SCOPE AND SOCIAL IMPACT

- > This Chapter conclude the research conducted in this thesis.
- Additionally, it briefly discusses the key conclusions drawn from the results.
- Finally, the chapter highlights the potential future directions for research and the societal impact that could be explored to build on this study.

11.1 Conclusion

The present thesis aims to investigate the distinct PSCs and optimize the different factors which affects the device efficiency. It includes synthesis, characterization and fabrication of the PSCs. The work begins with an overview of solar energy, the history of solar cells, and the photovoltaic phenomenon, explaining how solar cells operate and detailing the evolution of different generations. It also introduces important photovoltaic parameters and structure of perovskite material, along with the working principles and potential losses in PSCs. The literature review highlights the efficiency of lead-based PSCs and the growing interest in leadfree alternatives due to health and environmental concerns. Novel materials like copper (Cu), Tin (Sn), germanium (Ge), bismuth (Bi), antimony (Sb), and silver (Ag), and others are explored as non-toxic substitutes for lead, with a focus on achieving similar performance and stability. This includes using machine learning and simulation techniques to optimize device efficiency. The study also evaluates the performance of various perovskite materials, such as CH₃NH₃SnI₃, CH₃NH₃GeI₃, and CH₃NH₃PbI₃, and identifies key factors like thickness of absorber layer, operating temperature, and defect density that influence PCE. A maximum PCE of 20.90 % was achieved with Ge-based PSC at 300 K, suggesting that Sn and Ge-based PSCs could replace Pb-based devices. Further simulations on (CH₃NH₃)₂CuX₄ perovskite material with $[X = Cl_4, Cl_2I_2, and Cl_2Br_2]$ aimed at improving the device performance by optimizing the combination of ETL, HTL, and other parameters. The study contributes to enhancing performance of Cu-based PSCs. LaFeO₃, a potential candidate for PSCs, is synthesized and simulated, with the material showing promise due to its strong electron-electron correlation properties. The study of various ETLs and HTLs optimized LaFeO₃-based PSC performance, revealing the potential for high-efficiency devices. KSnI₃-based PSCs were simulated with different HTLs, and a maximum PCE of 23.08 % was achieved. The study incorporated machine learning and simulations to predict high-performance outcomes. Simulation of CsSnI₃-based PSCs explored the impact of different ETLs and HTLs, optimizing parameters such as thickness of absorber layer, operating temperature, N_t and back contact. The best configuration achieved a PCE of 23.45 %. KGeCl₃, a lead-free perovskite material, was also examined, showing a maximum PCE of 29.82 % after optimizing the ETL and HTL combination. This work further highlights the potential of KGeCl₃ for lead-free PSC applications. The synthesis of Cs₂AlBiCl₆ double perovskite material was carried out using solgel method. The material showed promising structural and optical properties, suggesting its potential for solar cell applications. The main objective of this dissertation is to optimize the performance of lead-based or lead-free PSCs through mathematical modeling, material synthesis, and characterization. Various factors affecting PSC performance, such as layer thickness, operating temperature, defect density, energy bandgap, work function of back contact, doping concentration, radiative recombination rate, series and shunt resistance, are analysed to guide future experimental and theoretical studies in the field.

11.2 Future Scope of the Work

- ➤ Simulation study of new lead-free perovskite material for high performance device fabrication.
- > Synthesis and characterization of double perovskite material for the application in device manufacturing.
- > Stability analysis of perovskite solar cells towards environment and high temperature.
- Life cycle assessment of different perovskite solar cells for sustainable device fabrication.
- ➤ Incorporation of SCAPS-1D data for machine learning analysis to study various factors which affects the device performance.

11.3 Social Impact

The research on different lead-free perovskite material, as presented in the thesis, holds the potential for substantial social impact on existing solar material and technology. Below are key areas where the social benefits of this work can be emphasized:

- 1. **Application in Optoelectronic Devices**: Beyond solar energy, lead-free perovskites could potentially be used in electronics and display technology, offering safer alternatives to current materials and spurring innovation in more sustainable consumer products.
- 2. **Environmental Benefits**: Traditional perovskite materials often contain lead, which is toxic to both human and the environment. Lead-free perovskite can contribute to reducing air pollution and mitigating climate change. Perovskite solar cells are highly efficient and relatively inexpensive to produce compared to silicon-based cells.
- 3. **Health Benefits**: The use of lead-free alternatives eliminates the risks of lead poisoning from manufacturing processes, waste, and leaks from old solar panels, contributing to safer work conditions and reducing public health risks.
- 4. **Economic Impacts**: Lead-free perovskites could reduce the cost of solar cells, making renewable energy more affordable and accessible for a larger portion of the population, especially in developing countries.
- 5. Global Accessibility: By making solar energy affordable, lead-free perovskite materials can help address energy poverty in underserved regions, allowing access to clean, renewable power even in remote or economically disadvantaged areas.

In summary, the social impact of lead-free perovskite materials is far-reaching, offering benefits in public health, environmental protection, economic growth, and accessibility to clean energy, while simultaneously fostering global sustainability and equity.



Print ISSN: 0022-2755

Journal of Mines, Metals and Fuels

Contents available at: www.informaticsjournals.com/index.php/jmmf



Study on the Various Parameters Affecting the Power Conversion Efficiency of Lead-Free Perovskite Solar Cell by SCAPS-1D

Rahul Kundara^{1*} and Sarita Baghel¹

¹ Department of Applied Physics, Delhi Technological University, Bawana Road, Delhi-110042

Abstract

Perovskite solar cells are becoming an alternative for conventional solar cells, attaining a performance of 29% approximately in eleven years (2009-2020). The SCAPS-1D was employed to take a look at the impact of various parameters inclusive of the thickness of the absorber layer, operating temperature, and defect density (Nt) on the performance of a perovskite solar cell (PSC). Two PSCs architectures are designed and simulated by adopting the SCAPS-1D. It is also employed to analyze the thin-film photovoltaic architecture. One model configuration is FTO/TiO₂/CH₃NH₃SnI₃/Cu₂O/Au and FTO/TiO₂/CH₃NH₃GeI₃/Cu₂O/Au is the configuration of the second one. TiO₂ layer as electron transport layer (ETL) and Cu₂O layer used as hole transport layer (HTL) for both tin (Sn)-based and germanium (Ge)-based PSCs. The simulated result of both PSCs has been compared. In this study, careful theoretical optimization of photovoltaic (PV) parameters has also been done. This study examines the tolerance of Nt in the absorber layer. Optimized value of operating temperature, Nt, and thickness of perovskite layer for both the perovskite solar cells has been obtained using a simulation approach which leads to high PCE of a solar cell. By considering all optimized parameters CH₃NH₃SnI₃ PSC has achieved the maximum efficiency of 6.15 % and CH₃NH₃GeI₃ PSC has exhibited the highest PCE of 20.90 %. The results demonstrate that Sn and Ge-based PSCs are a future possibility to the PV device in terms of eco-friendly nature. This simulation works useful in the design of low-cost and high-efficiency lead-free PSC. These results will give the nontoxic and high-efficiency perovskite solar cell.

Keywords: Parameters, power conversion efficiency, Perovskite solar cell, photovoltaic, SCAPS-1D, Renewable Simulation procedure, tolerance factor

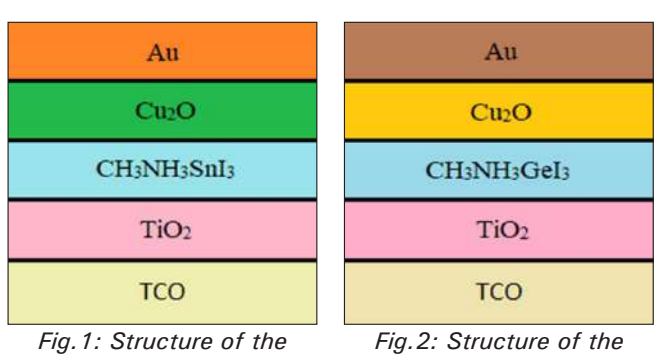
1. Introduction

The finite availability of nonrenewable resources and its severe effect on the environment is one of the causes of development of green and renewable energy resources. Biomass energy, solar energy and geothermal energy are examples of renewable energy sources. Solar energy has shown to be the best option for clean and sustainable energy resources. Due to its low cost and ecologically friendly production, perovskite solar cells are becoming a popular topic in thin-film photovoltaic research. A stable halide perovskite structure must have cations with suitable ionic size, as represented by geometrical constant t, is called as the tolerance factor and can be

used as a measure of distortion of a perovskite from ideal cubic. The t ranges between 0.8 to 1.0 and the equation for tolerance factor is $t = (r_A + r_O) / 2(r_B + r_O)$, where r_A , r_B , and r_O are ionic radii of A, B, and O, respectively [14]. Impact of various parameters on performance of a solar cell were studied such as thicknesses of perovskite, N_t and operating temperature. The solar cell simulation provided that the optimum value of thickness of $CH_3NH_3GeI_3$ absorber layer is approximately 600 nm. Ge-based PSCs with Cu_2O and DPBTTT-14 as HTM showed that overall PCE reached 21% [5]. It has been observed in simulation that performance of solar cells can be enhanced to some limit by changing the doping concentration and electron affinity of the buffer and HTM, whereas the deduction of

^{*}Author for correspondence

N of the absorber layer increases the solar cell efficiency. By optimizing the N₁ of perovskite absorber layer, devices achieve great outcomes such as efficiency of 23.36% [7]. In planar heterojunction structure of Sn-based PSC, CuSbS, employed for the first time as HTL in combination with MASnI, absorber layer in this design because of its implicit features (high V_{OC}) than unstable and expensive Spiro-MeOTAD. By adoption of CuSbS, as a HTL in solar cell design, results are adequate with J_{SC} of 31.7 mA/cm², V_{OC} of 0.936 V, FF of 81.1% and maximum PCE of 24.1% [16]. The simulation was done and the device achieved results with V_{OC} of 0.5803 V, J_{SC} of 28.42 mA/cm², FF 45.41%, and maximum efficiency of 7.49% for CH3NH3SnI3 [19]. Germanium based PSC with Cu₂O as HTM achieved a remarkable overall PCE of 21% [5]. In this study the simulated PSCs have shown different variation in their PV parameters with temperature, Nt and thickness. In Ge-based PSC the PCE increases with increase of thickness whereas in tin-based PSC the PCE decreases with increase of thickness, the PCE of both PSCs decrease with increase in temperature and PCE of both the PSCs decrease for increase in N. This is an excellent piece of work that shows that lead free PSCs can achieve performance levels similar to Pb-based PSC. An analysis of impact of variation in thickness of absorber layer, temperature which ranges between 300-480 K and variation in N. of absorber layer also has been done.



Simulated model of

CH,NH,Gel, PSC

2. Simulation Procedure and Device Architecture

Simulated model of

CH,NH,SnI, PSC

In this investigation, the 1D solar cell capacitance simulator SCAPS (version 3.3.10) has been employed for simulation. Gent University of Belgium developed SCAPS simulation software, which allows users to simulate up to seven semiconducting layers in both light and dark conditions [13]. This software can be used for simulations at different input physical conditions. This perovskite solar cell structure is formed with CH,NH,SnI, perovskite material with layer architecture as shown in Fig. 1: glass substrate/TCO/TiO₂/CH₂NH₂SnI₂/Cu₂O/Au-Metal and other PSC consist of CH,NH,GeI, absorber material with layer architecture as shown in Fig. 2: glass substrate/ TCO/TiO₂/CH₃NH₃GeI₃/Cu₂O/Au-Metal. The TCO layer in the structure is FTO. The input parameters employed in simulation of all layers are enclosed in Tables 1 and 2. The data of different parameters are chosen based on past experimental and theoretical studies [1-12]. The simulations were run at 300 K using a "air mass 1.5 global" spectrum and a light power of 1000 W/m². The work is dependent or related to variation in thickness of absorber layer, N, of absorber layer, and operating temperature at which simulation of the proposed solar cell has been done. The performance of the solar cell has been absorbed via I-V characteristics of the solar cell which represents the following PV parameters: J_{SC}, FF, V_{OC}, and PCE. Procedure of simulation shown in Fig.3. All the input data used in SCAPS simulation obtained from experimental and theoretical work enclosed in Tables 1 and 2 for CH₂NH₂SnI₂ (cell-1) and CH₃NH₃GeI₃ (cell-2) respectively.

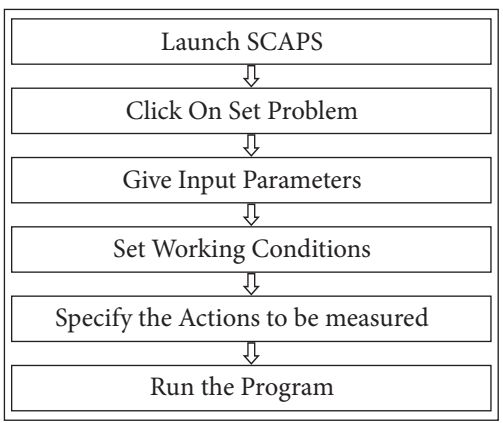


Fig. 3: SCAPS-1D software simulation procedure

Table 1. Various parameters employed in simulation (cell 1)

Parameter	FTO [11]	TiO ₂ [7]	CH ₃ NH ₃ SnI ₃ [8,9,10]	Cu ₂ O [12]
Thickness (µm)	0.5	0.03	0.345	0.350
Eg (eV)	3.5	3.2	1.3	2.17
χ (eV)	4.0	4.26 [8]	4.1	3.2
ε	9.0	9.0	8.2	7.11
N _C (cm ⁻³)	2.2 ×10 ¹⁸	2.0 ×10 ¹⁸	1018	2.02 ×10 ¹⁷
N _v (cm ⁻³)	1.8 ×10 ¹⁹	1.8 ×10 ¹⁹	1018	1.1 ×10 ¹⁹
$\mu_{\rm n}$ (cm ² /Vs)	20	20	1.6	200
μ_{p} (cm ² /Vs)	10	10	1.6	80
N _D (cm ⁻³)	1×10 ¹⁸	1×10 ¹⁶	-	0
N _A (cm ⁻³)	0	0	1×10 ¹⁵	1×10 ¹⁸
N _t (cm ⁻³)	-	1×10 ¹⁵	4.5×10 ¹⁷	1×10 ¹⁴

Table 2. Various parameters used for simulation (cell 2)

Parameter	FTO [1,2]	TiO ₂ [6]	CH ₃ NH ₃ GeI ₃ [5]	Cu ₂ O [12]
Thickness (μ_m)	0.400	0.100	0.400	0.350
E _g (eV)	3.5	3.26	1.9	2.17
χ (eV)	4.0	4.2	3.98	3.2
ε	9.0	10	10	7.11
N _C (cm ⁻³)	2.2 ×10 ¹⁸	2.2 ×10 ¹⁸	10^{16}	2.02 ×10 ¹⁷
N _v (cm ⁻³)	1.8 ×10 ¹⁸	1.8 ×10 ¹⁹	1016	1.1 ×1019
$\mu_{\rm n}$ (cm ² /Vs)	20	100	162 ×10 ³	200
μ_{p} (cm ² /Vs)	10	25	101 ×10 ³	80
N_{D} (cm ⁻³)	1×10 ¹⁹	1×10 ¹⁹	109	0
N _A (cm ⁻³)	0	-	109	1×10 ¹⁸
N _t (cm ⁻³)	-	-	10^{14}	1×10 ¹⁴

3. Result and Discussion

3.1 Effect of change in thickness

The thickness of CH₃NH₃SnI₃ layer has exhibited a straight relation with evaluation of performance of PSC through its effect on charge carrier's diffusion length. It is known to us that as the thickness of the layer decreases, the absorption rate also decreases. This results in a decrease in photocurrent and therefore PCE of the solar cell also reduces from 200-1200 nm. Both J_{SC} and PCE parameters decrease exponentially for enlargement in the thickness from 200 to 1200 nm. The maximum efficiency of PSC goes up to 15.83% together with V_{OC} is 0.78 V, J_{SC} is 27.05 mA/ cm² and FF is 74.8% for 200nm. The FF shows a monotonic decrease with the rise in thickness and also heads for enhancement gradually when thickness greater than 700nm [17]. In this work maximum efficiency of 7.64% has been achieved at 200 nm thickness of CH₂NH₂SnI₃ layer and 23.55% of PCE at the thickness of 1200nm for CH, NH, GeI, layer shown in Fig.4. The change in other PV parameters shown in Fig.4 with the help of Tables 3 and 4.

Table 3. Change in PV parameters with thickness of $CH_3NH_3SnI_3$ layer at 300 K and $N_4 = 4.5 \times 10^{17}$ cm⁻³.

Thickness (nm)	V _{oc} (V)	J_{sc} (mA/cm ²)	FF (%)	PCE (%)
200	0.6968	20.38	53.82	7.64
300	0.6869	19.72	48.73	6.60
400	0.6817	18.27	46.37	5.78
500	0.6789	17.04	45.39	5.25
600	0.6775	16.16	45.20	4.95
700	0.6769	15.58	45.43	4.79
800	0.6766	15.21	45.77	4.71
900	0.6765	15.00	46.07	4.68
1000	0.6765	14.89	46.25	4.66
1100	0.6765	14.83	46.34	4.65
1200	0.6765	14.80	46.37	4.64

Table 4. Variation in PV parameters with thickness of $CH_{3}NH_{3}GeI_{3}$ layer at 300 K and $Nt = 10^{14} \text{ cm}^{-3}$.

Thickness (nm)	V _{oc} (V)	J _{sc} (mA/cm ²)	FF (%)	PCE (%)
200	1.8913	11.72	74.49	16.51
300	1.8769	13.05	78.16	19.16
400	1.8654	13.99	80.04	20.90
500	1.8559	14.67	80.56	21.94
600	1.8477	15.16	80.53	22.57
700	1.8406	15.53	80.28	22.96
800	1.8342	15.82	79.97	23.21
900	1.8284	16.04	79.65	23.36
1000	1.8232	16.21	79.33	23.46
1100	1.8185	16.36	79.05	23.52
1200	1.8140	16.47	78.80	23.55

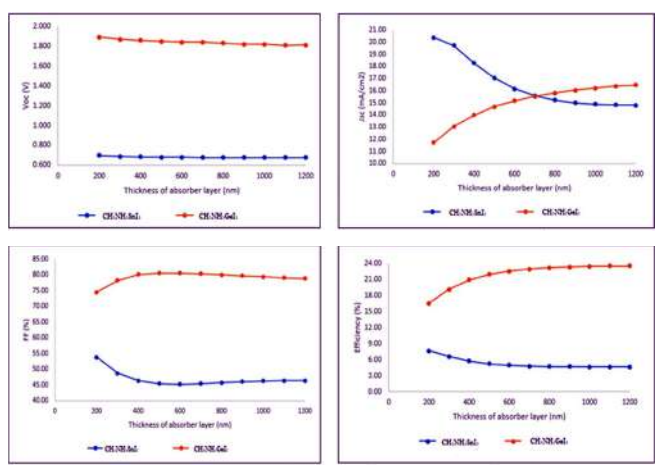


Fig.4: Impact of thickness on PV parameters of CH,NH,Snl, and CH,NH,Gel, PSCs

3.2 Effect of variation in operating temperature

To examine the effect of temperature at the efficiency of solar cells, operating temperature has been changed in the range of 300 to 480 K. Decline in the performance with temperature increase is related to decrease in diffusion length of charge carriers. Several solar cell architectures show instability of their overall performance because of deformation among layers at high temperature. When the temperature increases, the PCE drops significantly from 24.81% (at 300 K) to 17.05% (at 480 K) [17]. We have obtained maximum efficiency of 21.04% for CH₂NH₂GeI₂ PSC at the operating temperature of 340 K and the maximum PCE is 6.15% for CH, NH, SnI, PSC at operating temperature of 300 K shown below in Fig.5. VOC is decreasing with increase in the operating temperature for both PSCs. The impact of operating temperature on other PV parameters together with V_{oc} , J_{sc} and FF shown below in Fig.5 using Tables 5 and 6.

Table 5. Change in PV parameters with temperature of a CH₂NH₂SnI₂ PSC at 350 nm thickness and Nt = 4.5×10^{17} cm⁻³.

3 3 3				
Temperature (K)	$V_{oc}(V)$	J_{sc} (mA/cm ²)	FF (%)	PCE (%)
300	0.6839	19.00	47.31	6.15
320	0.6360	18.75	47.01	5.61
340	0.5876	18.46	46.59	5.06
360	0.5390	18.13	46.06	4.50
380	0.4900	17.75	45.43	3.95
400	0.4409	17.33	44.62	3.41
420	0.3916	16.89	43.62	2.89
440	0.3425	16.48	42.31	2.39
460	0.2939	16.11	40.66	1.93
480	0.2464	15.80	38.73	1.51

Table 6. Change in PV parameters with temperature of a CH₂NH₂GeI₂ PSC at 400 nm thickness and Nt = 10¹⁴ cm⁻³.

Temperature (K)	V _{oc} (V)	J_{sc} (mA/cm ²)	FF (%)	PCE (%)
280	1.8752	13.96	79.34	20.78
300	1.8654	13.99	80.04	20.90
320	1.8527	14.02	80.80	21.00
340	1.8336	14.04	81.66	21.04
360	1.8040	14.06	82.70	20.99
380	1.7630	14.08	84.03	20.87
400	1.7175	14.09	85.37	20.67
420	1.6752	14.11	86.43	20.43
440	1.6386	14.11	87.04	20.14
460	1.6062	14.12	87.22	19.79
480	1.5766	14.13	87.16	19.42

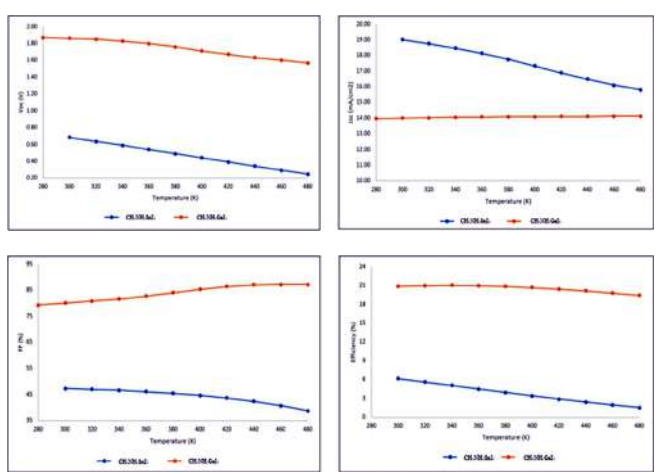


Fig. 5: Change in the PV parameters of CH,NH,Snl, and CH,NH,Gel, PSCs with operating temperature

3.3 Impact of change in defect density

For CH₂NH₂SnI₂ perovskite layer when defect density increased, the unwanted recombination rate increased as the defects formed the dangling bonds, which behave as the trap state for the photo-generated charge carriers.

Because of this short circuit current decreased, which is lastly responsible for decreasing FF of solar devices. The device PCE also decreased from 24.5% to 16.17%, when amphoteric Nt was enhanced from 1013 to 1017 cm-3. Such an increasing amount of recombination resulted in a sharp fall in solar cell efficiency [18]. The optimized defect density is 4.5×1013 cm-3 for CH2NH2SnI2 perovskite layer at which it has achieved the maximum efficiency of 24.18% shown in Fig. 6 and CH3NH3GeI3 perovskite layer has achieved the highest PCE of 22.91% at which the defect density is 1013 cm-3 demonstrated in Fig. 7. The change in different PV parameters V_{oc}, J_{sc} and FF with defect density for CH, NH, SnI, PSC shown in Fig. 6 by using Table 7. For CH3NH3GeI3 PSC the effect of Nt on PV parameters is demonstrated in Fig. 7 with the help of Table 8.

Table 7. Change in PV parameters with Nt of a CH, NH, SnI, PSC at 300 K and 350 nm thickness.

N _t (cm ⁻³)	V _{oc} (V)	J_{sc} (mA/cm ²)	FF (%)	PCE (%)
4.5×1013	-	30.27	-	24.18
4.5×1014	6.5471	30.25	12.04	23.85
4.5×1015	1.3627	30.09	51.36	21.06
4.5×1016	0.8149	28.53	64.22	14.93
4.5×1017	0.6839	19.00	47.31	6.15

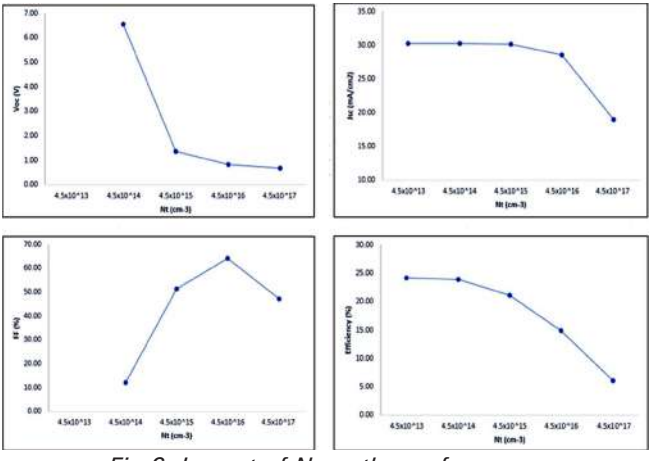


Fig. 6: Impact of N, on the performance of CH,NH,SnI, PSC

Table 8. Change in PV parameters with Nt of a CH₂NH₂GeI₂ PSC at 300 K and 400 nm thickness.

N _t (cm ⁻³)	V _{oc} (V)	J _{sc} (mA/cm ²)	FF (%)	PCE (%)
1013	1.9617	13.999174	83.42	22.91
1014	1.8654	13.999174	80.04	20.90
1015	1.7674	13.999173	77.11	19.08
1016	1.6659	13.999170	76.14	17.76
1017	1.6154	13.999140	73.87	16.71

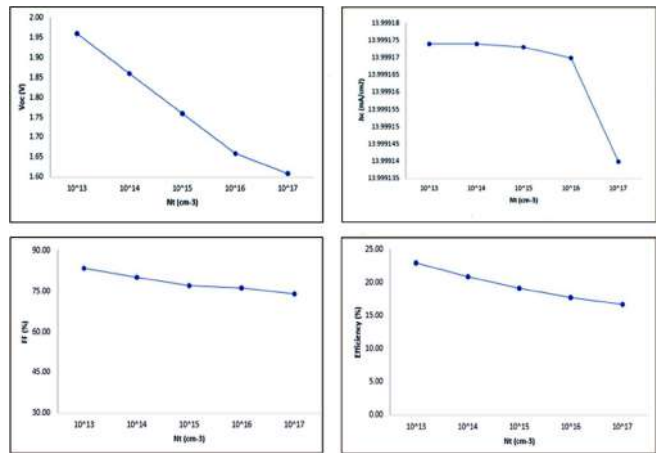


Fig. 7: Impact of N, on the performance of CH,NH,Gel, PSC

Table 9. Device output of previous reported theoretical studies and outcome of present simulation for both PSCs.

CH ₃ NH ₃ SnI ₃		
Parameter	Simulation Reports [19]	Present Simulation
V _{oc} (V)	0.58	0.68
J _{SC} (mA/cm ²)	28.42	19.00
FF (%)	45.41	47.31
PCE (%)	7.49	6.15

CH ₃ NH ₃ GeI ₃					
Parameter	Simulation Reports [5]	Present Simulation			
V _{oc} (V)	1.92	1.86			
J _{SC} (mA/cm ²)	14.20	13.99			
FF (%)	79.28	80.04			
PCE (%)	21.60	20.90			

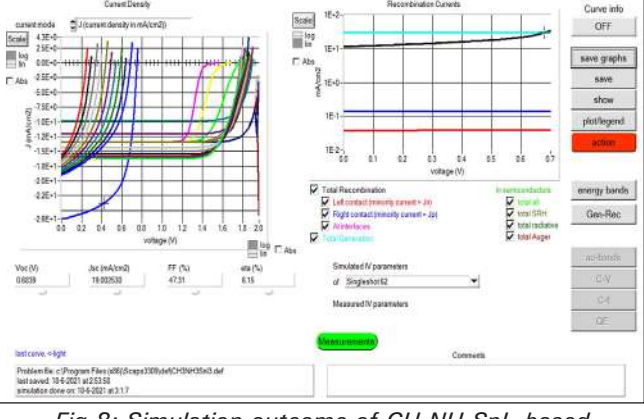


Fig.8: Simulation outcome of CH,NH,Snl, based perovskite solar cell

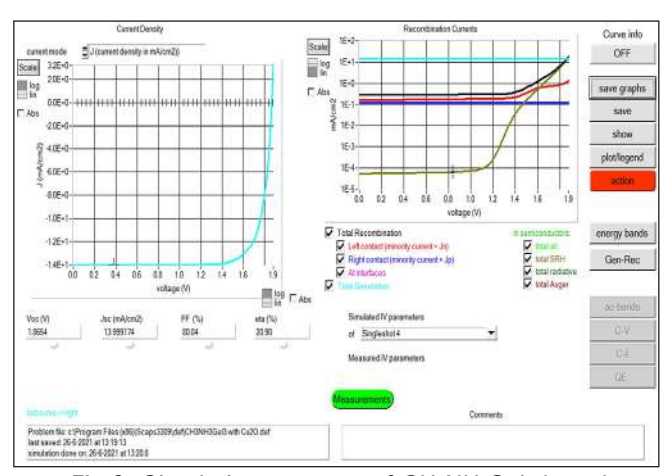


Fig.9: Simulation outcome of CH₂NH₂Gel₂ based perovskite solar cell

4. Conclusions

This study optimized various parameters of PSC using SCAPS-1D software. The performance of these PSCs was found comparable to lead-based PSC. We have examined the impact of operating temperature, thickness, and N. of both PSCs. The simulation was performed on the cell architecture of FTO/TiO₂/absorber layer/Cu₂O/Au. The optimized value of absorber layer thickness is 200 nm for CH2NH2SnI2 and 1200 nm for CH2NH2GeI2 perovskite solar cell. The optimal value of operating temperature is 300 K for Sn-based PSC and 340 K for Ge-based PSC. The optimized defect density value of Sn-based PSC is 4.5×1013 cm-13 and 1013 cm-3 for Ge-based PSC. The optimum value of operating temperature, thickness, and N, is helpful in the fabrication of high PCE solar cells. It was observed that Ge-based PSC exhibited comparatively high performance. The maximum PCE of 20.90% was obtained at 300 K with $V_{\rm oc}$ of 1.8654 V, FF is 80.04%, and J_{sc} is 13.9991 mA/cm² for Ge-based PSC. Whereas Sn-based perovskite has achieved the PCE 6.15% and other PV parameters such as V_{OC} of 0.6839 V, FF 47.31%, J_{sc} is 19.0025 mA/cm² by employing SCAPS-1D. The simulation results provide the best approach for higher PCE solar cell device fabrication. We have observed that N, thickness, and the operating temperature have a deleterious impact on PSCs up to a certain value. This work might provide vital guidance for solar cell device design and optimization of different PV parameters for PSCs.

5. References

- Sobayel, K.; Akhtaruzzaman, M.; Rahman, K.S.; Ferdaous, M.T.; Al-Mutairi, Z.A.; Alharbi, H.F.; Alharthi, N.H.; Karim, M.R.; Hasmady, S.; Amin, N. A comprehensive defect study of tungsten disulfide (WS2) as electron transport layer in perovskite solar cells by numerical simulation. Results Phys. 2019, 12, 1097-1103. [CrossRef]
- Sobayel, K.; Shahinuzzaman, M.; Amin, N.; Karim, M.R.; Dar, M.A.; Gul, R.; Alghoul, M.A.; Sopian, K.; Hasan, A.K.M.; Akhtaruzzaman, M. Efficiency enhancement of CIGS solar cell by WS2 as window layer through numerical modelling tool. Sol. Energy 2020, 207, 479–485. [CrossRef]
- Baktash, A.; Amiri, O.; Sasani, A. Improve efficiency of perovskite solar cells by using magnesium doped ZnO and TiO, compact layers. Superlattices Microstruct. 2016, 93, 128–137. [CrossRef]
- Mahjabin, S.; Haque, M.M.; Sobayel, K.; Jamal, M.S.; Islam, M.A.; Selvanathan, V.; Abdulaziz, A.K.; Alharbi, H.F.; Sopian, K.; Amin, N.; et al. Perceiving of Defect Tolerance in Perovskite Absorber Layer for Efficient Perovskite Solar Cell. IEEE Access 2020,8, 106346-106353. [CrossRef]
- Kanoun AA, Kanoun MB, Merad AE, Goumri-Said S. Toward development of high-performance perovskite solar cells based on CH3NH3GeI3 using computational approach. Solar Energy. 2019 Apr 1;182:237-44.
- G.Xosrovashvili, N.E.Gorji," Numerical analysis of TiO₂/ Cu₂ZnSnS₄ nanostructured PV using SCAPS-1D", Journal of Modern Optics, DOI:Org/10.1080/09500340.2013.827252, Vol.60, No.11, pp.936-940.
- Du H-J, Wang W-C, Zhu J-Z (2016) Device simulation of lead-free CH2NH2SnI2 perovskite solar cells with high efficiency. J Chin Phys B 25:108802
- Noel NK, Stranks SD, Abate A, Wehrenfennig C, Guarnera S, Haghighirad A-A, Sadhanala A, Eperon GE, Pathak SK, Johnston MB, Petrozza A, Herz LM, Snaith HJ (2014) Leadfree organic-inorganic tin halide perovskites for photovoltaic applications. Energy Environ Sci 7:3061-3068
- Stoumpos CC, Malliakas CD, Kanatzidis MG (2013) Semiconducting tin and lead iodide perovskites with organic cations: phase transitions, high mobilities, and near-infrared photoluminescent properties. Inorg Chem 52:9019-9038

- 10. Chen QY, Huang Y, Huang PR, Ma T, Cao C, He Y (2016) Electronegativity explanation on the efficiency-enhancing mechanism of the hybrid inorganic-organic perovskite ABX3 from first-principles study. Chin Phys B 25:27104
- 11. E. Karimi, S.M.B. Ghorashi, Investigation of the influence of different hole-transporting materials on the performance of perovskite solar cells, Optik (Stuttg). (2017), https://doi. org/10.1016/j.ijleo.2016.10.122.
- 12. M.I. Hossain, F.H. Alharbi, N. Tabet, Copper oxide as inorganic hole transport material for lead halide perovskite based solar cells, Sol. Energy. 120 (2015) 370-380. https:// doi.org/10.1016/j.solener.2015.07.040.
- 13. M. Burgelman, P. Nollet, S. Degrave, Modelling polycrystalline semiconductor solar cells, Thin Solid Films 361-362 (2000)527-532, https://doi.org/10.1016/ S0040-6090(99)00825-1.
- 14. Jong UG, Yu CJ, Kve YH, Choe YG, Hao W, Li S. Firstprinciples study on structural, electronic, and optical properties of inorganic Ge-based halide perovskites. Inorganic chemistry. 2019 Mar 13;58(7):4134-40.
- 15. Ke W, Stoumpos CC, Kanatzidis MG. "Unleaded" perovskites: status quo and future prospects of tin-based perovskite solar cells. Advanced Materials. 2019 Nov;31(47):1803230.
- 16. Devi C, Mehra R. Device simulation of lead-free MASnI, solar cell with CuSbS₂ (copper antimony sulfide). Journal of materials science. 2019 Apr 15;54(7):5615-24.
- 17. Yasin S, Al Zoubi T, Moustafa M. Design and simulation of high efficiency lead-free heterostructure perovskite solar cell using SCAPS-1D. Optik. 2021 Mar 1;229:166258.
- 18. Islam S, Sobayel K, Al-Kahtani A, Islam MA, Muhammad G, Amin N, Shahiduzzaman M, Akhtaruzzaman M. Defect Study and Modelling of SnX3-Based Perovskite Solar Cells with SCAPS-1D. Nanomaterials. 2021 May;11(5):1218.
- 19. Kumar M, Kumar A, Raj A, Sati PC, Sahni M, Anshul A. Organic-inorganic perovskite-based solar cell designs for high conversion efficiency: A comparative study by SCAPS simulation. Materials Today: Proceedings. 2020 Dec 15.
- 20. Toshniwal A, Jariwala A, Kheraj V, Opanasyuk AS, Panchal CJ. Numerical simulation of tin based perovskite solar cell: effects of absorber parameters and hole transport materials. Journal of Nano and Electronic Physics. 2017 Jul 1; 9(3).



Device modelling of lead free (CH₃NH₃)₂CuX₄ based perovskite solar cells using SCAPS simulation

Rahul Kundara¹ · Sarita Baghel¹

Received: 21 August 2022 / Accepted: 28 July 2023 © The Author(s), under exclusive licence to Springer Science+Business Media, LLC, part of Springer Nature 2023

Abstract

The Copper (Cu)-based perovskite materials, (CH₃NH₃)₂CuX₄ or (MA)₂CuX₄ with $[X = Cl_4, Cl_2I_2, and Cl_2Br_2]$ are explored for use in perovskite solar cells (PSCs). The foremost objectives of this investigation are the optimization and finding the combination of Electron Transport Layer [ETL], Perovskite Absorber Layer (PAL) and the different organic and inorganic Hole Transport Layers [HTLs] for better device performance. The impact of other important functional parameters on the performance of PSCs are also studied. These parameters are, thicknesses of PAL, operating temperature (T), series resistance (R_S) , and radiative recombination rate under the illuminance of AM1.5. This SCAPS-1D simulation study deduced the optimized value of the thickness for (MA)₂CuCl₄, (MA)₂CuCl₂I₂ and (MA)₂CuCl₂Br₂ based absorber layer to be 400 nm, 500 nm and 600 nm, respectively at defect density (N_t) of 1×10^{13} cm⁻³ and 300 K operating temperature. The optimum value of operating temperature is 300 K for all PSCs but for C₆₀/(MA)₂CuCl₄/Cu₂O PSC, optimum value is 320 K at 400 nm of absorber layer. With considerations of all these optimum values, the highest power conversion efficiency of 28.31% has been obtained for the PCBM/(MA)₂CuCl₂Br₂/CuI configuration at operating temperature of 300 K. Thus, the study reveals that PCBM as ETL, while CuI and Cu2O as HTLs are most suitable for the Cu-based PSC. Based upon the comparison with experimental results, our findings are indicative of the fact that traditional charge transport materials like TiO₂ and spiro-OMeTAD may not be the best choices for new lead-free Cu-based PSCs.

 $\textbf{Keywords} \ \ SCAPS-1D \cdot Cu-based \ perovskite \ solar \ cell \cdot Hole \ transport \ layer \cdot Electron \ transport \ layer$

1 Introduction

In the field of solar photovoltaic research, organic-inorganic perovskite materials are gaining considerable interest. These materials have a lot of potential as they are inexpensive, abundant and have easy processing techniques. Currently, in

Published online: 02 September 2023

Department of Applied Physics, Delhi Technological University, Bawana Road, Delhi 110042, India



 [⊠] Rahul Kundara rahul_2k20phdap10@dtu.ac.in

968 Page 2 of 18 R. Kundara, S. Baghel

comparison with other perovskite materials, lead perovskites of methyl ammonium halide (CH₃NH₃PbX₃) are achieving higher power conversion efficiencies (Mahajan et al. 2021; Sahli et al. 2018). Some of the factors associated with their superior photovoltaic performance are suitable band gap, long electron and hole diffusion lengths, high absorption coefficients, low defect density (N_t) (Momblona et al. 2016; Park 2015; Cao et al. 2021; Kumar et al. 2021). However, despite the several advantages, lead based perovskites cannot be regarded as a sustainable class of photovoltaics as lead is highly toxic, not only to living beings but to the entire earth ecosystem (Giustino and Snaith 2016). In addition to the environmental concern, lead based perovskite solar cells also face stability issues due to rapid oxidation of Pb cation (Ke et al. 2019).

There is a need to replace lead-based perovskites with some other perovskite materials which are not only less toxic and environment friendly, but also, have potential to deliver superior photovoltaic performance. In order to find a suitable substitute for lead, researchers have investigated many potential candidates. Lead has been successfully replaced by Sn (Noel et al. 2014), Ge (Ju et al. 2018), Bi (Zhang et al. 2017), Sb (Wang et al. 2018), Ag (Zong et al. 2018) and subsequent experiments have demonstrated device power conversion efficiency up to 9% (Kour et al. 2019). However, there remain many challenges that need to be addressed. Sn²⁺ and Sb²⁺ exhibit low open circuit voltage whereas Ge²⁺ has stability issues due to oxidation.

Therefore, exploration of transition metals has now gathered momentum. Many transition metals (e.g. Fe²⁺, Cu²⁺, Zn²) are attractive alternatives as they are cost effective, earth abundant and low on toxicity. In this direction, Cu metal has also been investigated as a substitute for lead. To the best of our knowledge there are only two studies that explored the application of copper as a lead substitute (Cortecchia et al. 2016; Elseman et al. 2018). Recently, PCE efficiencies up to 2.41% has been experimentally reported by Elseman et al. (2018) by using Cu substituted lead perovskite materials ((MA)₂CuX₄) for solar cell fabrication. This Cu based hybrid perovskite material also exhibits band gap tunability with varying content of halides $(X = Cl_4, Cl_2I_2, Cl_2Br_2)$. However, despite optimized Low efficiency was attributed to factors such as recombination rate, absorption coefficient, surface roughness and thickness of perovskite films. Also, mismatch between the band levels of electron transport layer (ETL) and hole transfer layer (HTL) with respect to perovskite absorber layer (PAL) was identified as an important functional parameter for low efficiency. A general perovskite solar cell structure contains a PAL sandwiched between ETL and HTL. A photocurrent is generated when photoelectrons (e⁻) are injected into ETL and holes (h⁺) are transferred to HTL from the perovskite layer. Hence, proper alignment of energy band levels of all three layers is extremely crucial for efficient device performance, so there exists a need to carefully select and optimize ETL and HTL according to the properties of the perovskite absorber layer. (MA)₂CuX₄, TiO₂ and spiro-OMeTAD were used as ETL and HTL materials respectively, which are the traditional choices. However, other suitable alternatives are also available for this role. In this work, we have examined effect of different organic and inorganic ETL and HTL materials on the performance of (MA)₂Cucl₄, (MA)₂Cucl₂I₂, (MA)₂Cucl₂Br₂ based PSCs using SCAPS-1D simulation software. Simulation work also includes analysis and optimization of different device parameters (perovskite layer thickness, recombination rate, device temperature, series resistance) for enhanced photovoltaic performance.



Fig. 1 Architecture of the simulated model of (MA)₂CuCl₄, (MA)₂CuCl₂I₂ and (MA)₂CuCl₂Br₂ PSC

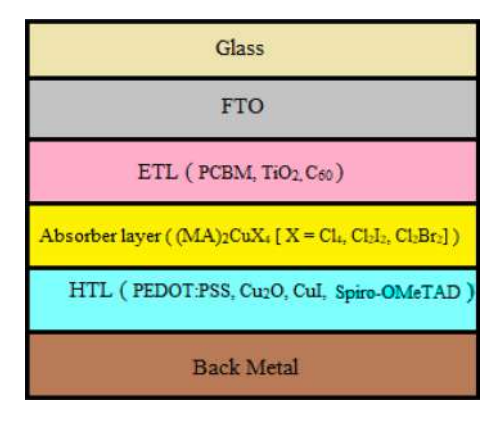


Table 1 Various input parameters of perovskite layers employed in simulation

Parameter	(MA) ₂ CuCl ₄ (Elseman et al. 2018)	(MA) ₂ CuCl ₂ I ₂ (Elseman et al. 2018)	(MA) ₂ CuCl ₂ Br ₂ (Elseman et al. 2018)
Thickness (μm)	0.400	0.400	0.400
Eg (eV)	2.36	1.99	1.04
χ (eV)	2.92	3.9	3.8
$\epsilon_{ m r}$	25	20	15
$N_C (cm^{-3})$	3.5×10^{20}	2.5×10^{20}	3.0×10^{18}
$N_V (cm^{-3})$	3.5×10^{20}	2.5×10^{20}	4.0×10^{18}
$\mu_n (cm^2/Vs)$	10	14	15
$\mu_p (cm^2/Vs)$	10	14	15
$N_D (cm^{-3})$	7.0×10^{14}	_	1.0×10^{10}
$N_A (cm^{-3})$	7.0×10^{14}	6.0×10^{14}	1.0×10^{10}
$N_t (cm^{-3})$	1×10^{13}	1×10^{13}	1×10^{13}

2 Material and methods

2.1 Device architecture

The device architecture for the simulation of PSCs is shown below in Fig. 1. The primary architecture of PSC basically consists of following different layers, a PAL is placed in the middle of the ETL and HTL. In this structure we have (MA)₂CuX₄ PAL with different halides groups such as Cl₄, Cl₂I₂, and Cl₂Br₂ are utilized in PSC with the thickness of 400 nm shown below in Table 1. In modelling of Cu-based PSC, the various ETLs and HTLs are employed for obtaining the maximum PCE with optimum value of absorber layer thickness. The thickness of three different ETLs such as PCBM, TiO₂ and C₆₀ with values of 500 nm, 40 nm and 50 nm respectively employed shown below in Table 2. The various HTLs are employed for efficient PSC such as PEDOT: PSS, Cu₂O, CuI, and Spiro-OMeTAD. The thickness of the HTLs varies from 80 to 250 nm. In p-i-n devices, electrons are collected at the fluorine doped tin oxide (FTO) and holes at the metal back contact (Bhattarai and Das 2021).



968 Page 4 of 18 R. Kundara, S. Baghel

Table 2 Various input parameters employed in simulation of different ETLs

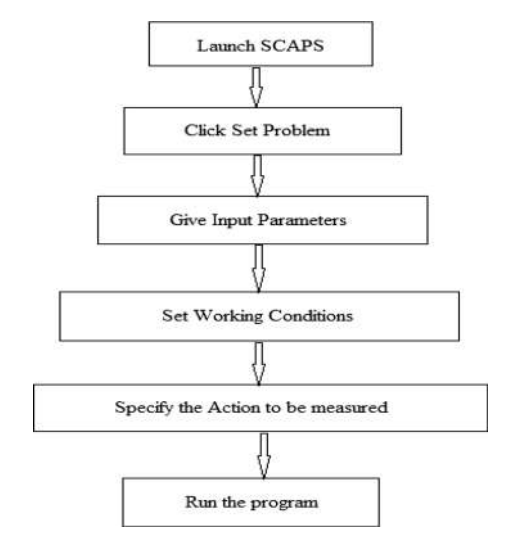
Parameter	TiO ₂ (Rai et al. 2020; Lakhdar and Hima 2020)	PCBM (Mandadapu et al. 2017; Azri et al. 2019)	C ₆₀ (Jayan and Sebastian 2021)
Thickness (µm)	0.040	0.500	0.050
Eg (eV)	3.2	2.1	1.7
χ (eV)	3.9	3.9	3.9
$\epsilon_{ m r}$	9	3.9	4.2
$N_C (cm^{-3})$	1×10^{21}	2.2×10^{19}	8.0×10^{19}
$N_V (cm^{-3})$	2×10^{20}	2.2×10^{19}	8.0×10^{19}
$\mu_n (cm^2/Vs)$	20	0.001	8.0×10^{-2}
$\mu_p (cm^2/Vs)$	10	0.002	3.5×10^{-3}
$N_D (cm^{-3})$	1×10^{19}	1×10^{19}	2.6×10^{17}
$N_A (cm^{-3})$	_	_	_
$N_t (cm^{-3})$	1×10^{15}	$1 \times 10^{9*}$	1×10^{14}

^{*}In this work

2.2 Simulation parameters

In this work, the SCAPS-1D software is employed in simulation. The Gent University of Belgium developed SCAPS simulation software, which allows users to simulate a maximum of seven semiconducting layers in both light and dark conditions. The stepwise procedure of SCAPS-1D simulation is demonstrated in Fig. 2. The Photovoltaic (PV) parameters such as open circuit voltage ($V_{\rm OC}$), short circuit current density ($J_{\rm SC}$), fill factor (FF) and PCE can be calculated at different temperatures and illuminations. The software is numerically based on solving semiconductor, Poisson's, and continuity equations for both electrons and holes under steady-state conditions given below.

Fig. 2 SCAPS-1D software simulation procedure





$$\frac{\partial^2 \psi}{\partial x^2} + \frac{q}{\epsilon} [p(x) - n(x) + N_D - N_A + \rho_p - \rho_n = 0$$
 (1)

$$\frac{1}{q}\frac{dJ_p}{dx} = G_{op}(x) - R(x) \tag{2}$$

$$\frac{1}{q}\frac{dJ_n}{dx} = -G_{op}(x) + R(x) \tag{3}$$

The basic structure of PSC consists of three different layers such as TiO_2 (n-type ETL), PAL and p-type HTL demonstrated in Fig. 1. The primarily input data employed in simulation of various layers are enclosed in Tables 1, 2 and 3 including thickness, band gap energy (Eg), electron affinity (χ), relative dielectric permittivity (ϵ_r), mobility of electron (μ_n), mobility of hole (μ_p) and N_t . This simulation is based on the change in thickness of absorber layer, operating temperature and N_t of different PSCs (Rai et al. 2020; Haider et al. 2019).

3 Result and discussion

3.1 Modulation of various ETLs and HTLs to impact device performance

In this study we have simulated different ETLs and HTLs, the ETLs are TiO2, PCBM and C_{60} with the E_g of 3.2 eV, 2.1 eV and 1.7 eV respectively. Four different HTLs employed in simulation are CuI, Cu2O, inorganic materials and Spiro-OMeTAD and PEDOT: PSS are organic materials. The bandgap energy for CuI is 3.1 eV, Cu₂O is 2.17 eV, Spiro-OMeTAD is 3 eV and for PEDOT: PSS is 2.2 eV shown in Table 3. The energy level diagram of ETL, PAL and HTL demonstrated in Fig. 3. The optimum thickness of each ETL was first found to be of 500 nm, 40 nm and 50 nm respectively by multiple simulations as shown below in Table 2. These values were then kept constant. For a particular PAL, all possible combinations of 3 ETLs and 4 HTLs are studied. Hence for each PAL, there are 12 combinations. Hence, the resulting PCEs are shown in the Table 4. Best two configurations for each perovskite are chosen for further evaluation through J-V characteristics. J-V characteristics for the best six configurations have been shown in Fig. 4. The variation of quantum efficiency with wavelength for various optimized Cu-based PSCs shown in Fig. 5. These Simulation outcomes demonstrated that (MA)₂CuCl₄ based PSC gives the maximum PCE is 18.41% for PCBM as ETL and PEDOT: PSS as HTL. This can be attributed to high electrical conductivity of PCBM and the highest occupied molecular orbital (HOMO) level properly matching with PAL with their E_g difference of 0.74 eV. Similarly, by using (MA)₂CuCl₂I₂ as absorber layer PSC gives PCE of 17.38% for Cu₂O with PCBM as ETL due to high hole mobility responsible for high performance of PSC and exact band alignment between HOMO level of PAL and Cu₂O (Anwar et al. 2017; Hossain and Alharbi 2013; Minami et al. 2014). However, the (MA)₂CuCl₂Br₂ based PSC gives the maximum PCE of 28.31% which is highest among all of three Cu-based PSCs by employing PCBM as ETL and CuI as HTL (Yamada et al. 2016). The (MA)₂CuCl₂Br₂ PSC has a high absorption coefficient which is responsible for high value of current density (J_{SC}) resulting in high efficiency shown in Fig. 6 (Elseman et al. 2018). Material with a low absorption coefficient,



Table 3 Various input parameters employed in simulation of different HTLs

Parameter	FTO (Rai et al. 2020; Haider et al. 2019)	Cul (Kanoun et al. 2019)	Spiro-OMeTAD (Bhattarai and Das Cu ₂ O (Rai et al. 2020; 2021; Los Santos et al. 2020) Kanoun et al. 2019)	Cu ₂ O (Rai et al. 2020; Kanoun et al. 2019)	PEDOT: PSS (Mandadapu et al. 2017; Jayan and Sebastian 2021)
Thickness (µm)	0.400	0.100	0.213	0.250	0.080
Eg (eV)	3.5	3.1	3	2.17	2.2
χ (eV)	4.0	2.1	2.2	3.2	2.9
$\epsilon_{ m L}$	9.0	6.5	3	7.11	3.0
$N_{\rm C} ({ m cm}^{-3})$	2.02×10^{18}	2.8×10^{19}	1×10^{19}	2.02×10^{17}	2.2×10^{15}
$N_{\rm V}~({ m cm}^{-3})$	1.8×10^{19}	1×10^{19}	1×10^{19}	1.1×10^{19}	1.8×10^{18}
$\mu_{\rm n} ({\rm cm}^2/{\rm Vs})$	20	100	10^{-4}	200	1×10^{-2}
$\mu_{\rm p} ({\rm cm}^2/{\rm Vs})$	10	43.9	10^{-4}	80	2×10^{-4}
$N_{\rm D} ({\rm cm}^{-3})$	2×10^{19}	ı	ı	ı	1
$N_A (cm^{-3})$	0	1×10^{18}	2×10^{19}	1×10^{18}	10 ¹⁹
$N_t (cm^{-3})$	1×10^{15}	1×10^{14}	1×10^{14}	1×10^{14}	1×10^{14}



Fig. 3 The energy level alignment between ETL, PAL and HTL materials

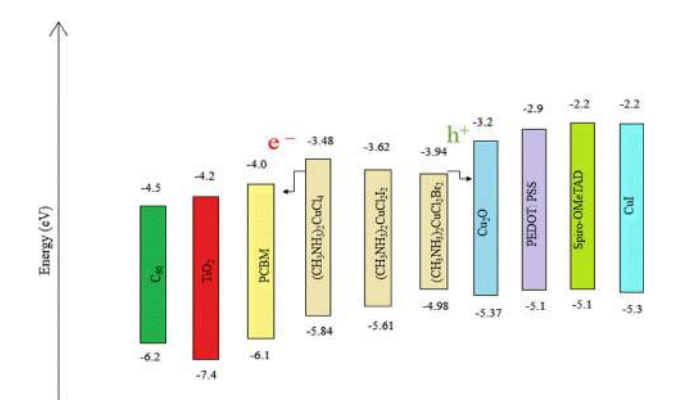
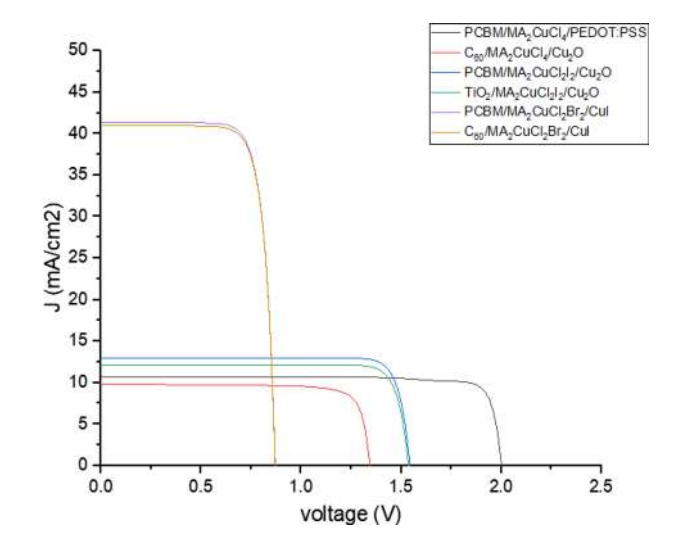


Table 4 PCE (%) of various combinations of Cu-based PSC with different ETL and HTL

HTL	(MA) ₂ CuCl ₄			(MA) ₂ CuCl ₂ I ₂ ETL			(MA) ₂ CuCl ₂ Br ₂ ETL		
	ETL								
	TiO ₂	C ₆₀	PCBM	TiO ₂	C ₆₀	PCBM	TiO ₂	C ₆₀	PCBM
PEDOT: PSS	8.42	9.87	18.41	13.44	11.67	14.94	12.20	22.45	22.53
Spiro-OMeTAD	7.81	9.47	18.40	14.69	12.63	16.51	12.49	6.68	6.68
CuI	7.76	9.46	18.40	14.46	11.79	16.26	12.33	28.09	28.31
Cu_2O	8.96	10.68	18.39	16.13	14.28	17.38	14.41	13.79	13.78

Fig. 4 J-V characteristics of Cubased PSCs



light is imperfectly absorbed, it should be large for high performance of PSC (https://www.pveducation.org/pvcdrom/pn-junctions/absorption-coefficient/; Kalaiselvi et al. 2018). The absorption coefficient of (MA)₂CuCl₂Br₂ based PSC is greater than other two Cu-based PSCs hence the PCE of (MA)₂CuCl₂Br₂ based PSC is higher than the (MA)₂CuCl₂I₂ based



968 Page 8 of 18 R. Kundara, S. Baghel

Fig. 5 Quantum efficiency (QE) curve for Cu-based PSCs

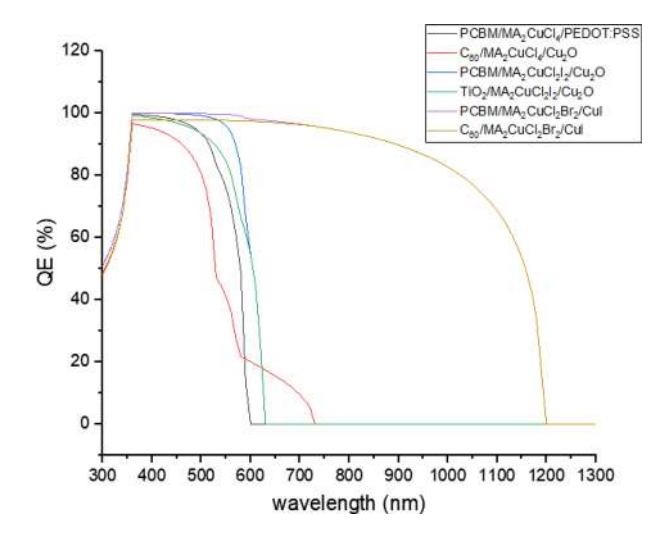
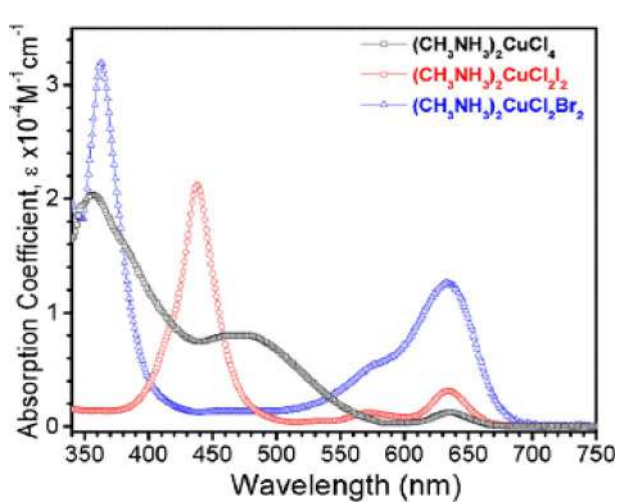


Fig. 6 Absorption coefficient of Cu-based PSCs (Elseman et al. 2018)

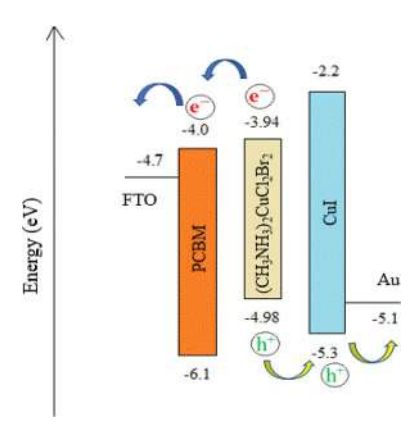


PSC (Elseman et al. 2018). In addition, (MA)₂CuCl₂Br₂ absorber layer has an appropriate band gap (1.0–1.6 eV) that would maximize efficiency (Qiu et al. 2017).

The band alignment is also a crucial factor for superior performance of $(MA)_2CuCl_2Br_2$ PSC as shown in Fig. 7. The conduction band of the ETL is always less than the lowest unoccupied molecular orbital (LUMO) of the PAL. The difference between the valence band of ETL and HOMO level of PAL should be always high, which prevents the recombination in the PAL. In this simulation work we have employed various HTLs among which CuI is most suitable for obtaining high performance of Cu-based PSCs. The CuI layer as HTL is more appropriate than spiro-OMeTAD layer because of the high hole mobility and low hysteresis. The HOMO level of CuI and PEDOT: PSS has good band alignment with absorber layer of $(MA)_2CuCl_2Br_2$ based PSC therefore with CuI it has achieved best PCE but not for PEDOT: PSS because lower value of holes mobility (μ_p) than CuI. Hence, CuI is a more suitable HTL for achieving high efficiency for $(MA)_2CuCl_2Br_2$ based PSC. Furthermore, the CuI based PSCs exhibit good long-term stability in the ambient atmosphere



Fig. 7 Band alignment diagram of optimized device



because of its hydrophobic property (Shi et al. 2021). The CuI has outstanding properties such as band matching with the PAL; a wide E_g of 3.1 eV; a high μ_p of 43.9 cm²/Vs, inexpensive; high chemical stability; and non-toxicity make CuI a good choice for HTL in PSCs. This numerical modelling helped in the investigation of the best ETL and HTL combination with $(MA)_2CuCl_2Br_2$ based PSC for the high PCE. The optimized result of various ETLs and HTLs with Cu-based PSCs is shown below in Table 5.

3.1.1 Comparison with experimental results

The experimentally obtained efficiency of three PAL: (MA)₂CuCl₄, (MA)₂CuCl₂Br₂ and (MA)₂CuCl₂I₂ PSCs were 2.41%, 1.75% and 0.99% respectively shown below in Table 6 using thin film structure of glass/FTO/TiO₂/(MA)₂CuX₄/spiro-OMeTAD/Au. The reason behind the generally low PCE achieved in all reported cells may come from the recombination occurring in perovskite layers. Apart from perovskite absorber layer properties, lower

Table 5 Optimized PCE of Cu-based PSC with various ETLs and HTLs

Perovskite	V _{OC} (V)	J_{SC} (mA/cm ²)	FF (%)	PCE (%)
PCBM/(MA) ₂ CuCl ₄ /PEDOT: PSS	2.00	10.63	86.48	18.41
C ₆₀ /(MA) ₂ CuCl ₄ /Cu ₂ O	1.34	9.83	80.85	10.68
PCBM/(MA) ₂ CuCl ₂ I ₂ /Cu ₂ O	1.54	12.97	86.82	17.38
TiO ₂ /(MA) ₂ CuCl ₂ I ₂ /Cu ₂ O	1.53	12.14	86.46	16.13
PCBM/(MA) ₂ CuCl ₂ Br ₂ /CuI	0.87	41.30	78.69	28.31
C ₆₀ /(MA) ₂ CuCl ₂ Br ₂ /CuI	0.87	41.00	78.70	28.09

Table 6 The previously reported result of different Cu-based PSCs

Device	V _{OC} (V)	J _{SC} (mA/cm ²)	FF (%)	PCE (%)
TiO ₂ /(MA) ₂ CuCl ₄ /Spiro-OMeTAD	0.560	8.12	52	2.41 (Elseman et al. 2018)
TiO ₂ /(MA) ₂ CuCl ₂ I ₂ /Spiro-OMeTAD	0.545	6.78	47	1.75 (Elseman et al. 2018)
TiO ₂ /(MA) ₂ CuCl ₂ Br ₂ /Spiro-OMeTAD	0.581	3.35	50	0.99 (Elseman et al. 2018)



968 Page 10 of 18 R. Kundara, S. Baghel

efficiency can be explained by mismatch in the energy bands of ETL, HTL and PAL. For all three perovskites, TiO2 and Spiro-OMeTAD are employed as ETL and HTL respectively. These can be suitable choices for (MA)₂CuCl₄ but not for (MA)₂CuCl₂Br₂ and (MA)₂CuCl₂I₂ PSCs. This is evident from our simulation results. By using more appropriate HTL such as CuI and Cu₂O (MA)₂CuCl₂Br₂ and (MA)₂CuCl₂I₂ PSCs can give much better results. Cu₂O as HTL is suitable for high efficiency because of its high carrier mobility and a long carrier diffusion length and high charge extraction ability leads to the high J_{SC} (Chatterjee and Pal 2016; Nejand et al. 2016). It shows high acceptor density because of a suitable band gap of 2.17 eV which may give high PV performance (Kale et al. 2021). Also, for CuI, Higher values of J_{SC} are obtained because of a much higher μ_p of CuI relative to spiro-OMeTAD. Optimization of the perovskite/HTL interface is very crucial to reduce recombination as well as for achieving higher V_{OC} and FF for PSCs (Gharibzadeh et al. 2016). It has been found that there is an enhancement in V_{OC} due to two factors: (i) increase in charge carrier mobilities ratio (μ_p/μ_h) of HTL (ii) decrease in the energy gap between HOMO of the HTL and conduction band of PAL (Ompong and Singh 2018). The electron and hole mobility ratio for CuI and Cu₂O is above 2 while for spiro-OMeTAD, this ratio is 1, hence simulation results for CuI and Cu₂O as HTL give high V_{OC} leading to higher efficiencies, more so for (MA)₂CuCl₂Br₂ PSC than to experimental results (obtained with spiro-OMeTAD as HTL). Our findings are indicative of the fact that traditional charge transport materials like TiO₂ and spiro-OMeTAD may not be the best choices for new leadfree Cu-based PSCs.

3.2 Impact of thickness of absorber layer on device performance

The thickness of the (MA)₂CuX₄ absorber layer has exhibited an apparent impact on the diffusion length of charge carriers. The thickness of PAL varied in the range of 200-900 nm at defect density (N_t) of 1×10^{13} cm⁻³ and operating temperature of 300 K. The absorption rate is low for the thin PAL which results in low photocurrent, hence efficiency decreases. As the thickness increases, the charge carriers may not have suitable diffusion length to travel up to the charge collecting layers resulting in a high value of R_s which limits the device performance. Beyond the optimum value of thickness, the device performance stagnates due to the higher recombination of electron-hole pairs. Therefore, there is an increment in the dark saturation current which allows V_{OC} and J_{SC} to fluctuate extremely slowly after a definite value of thickness. This results in flattening of the PCE curve (Mushtaq et al. 2023; Hao et al. 2021). The n-layer thickness should be optimized for high PCE of a PSC, when the thickness of ETL is near to the surface of PAL, conductance of the device increases towards absorption of radiation (Nejand et al. 2016). The obtained optimized value of thickness, for PCBM/(MA)₂CuCl₄/PEDOT: PSS is 400 nm, C₆₀/(MA)₂CuCl₄/ Cu_2O is 600 nm, $PCBM/(MA)_2CuCl_2I_2/Cu_2O$ is 500 nm, $TiO_2/(MA)_2CuCl_2I_2/Cu_2O$ is 600 nm, PCBM/(MA)₂CuCl₂Br₂/CuI is 600 nm and C₆₀/(MA)₂CuCl₂Br₂/CuI is 500 nm shown below in Fig. 8 for better performance of PSC. The maximum efficiency of PCBM/ (MA)₂CuCl₂Br₂/CuI PSC goes up to 29.01% together with V_{OC} is 0.85 V, J_{SC} is 43.44 mA/ cm² and FF is 78.34% at 600 nm. The change in other PV parameters is also shown in Fig. 8. The PCBM/(MA)₂CuCl₄/PEDOT: PSS PSC is most stable towards variation in thickness of PAL because change in the PCE is only 0.43% for the range of thickness of PAL from 200 to 900 nm. For the TiO₂/(MA)₂CuCl₂I₂/Cu₂O PSC change in PSC is 28.35% with thickness which varies from 200 to 900 nm, hence it is the most unstable PSC with the variation of thickness of PAL.



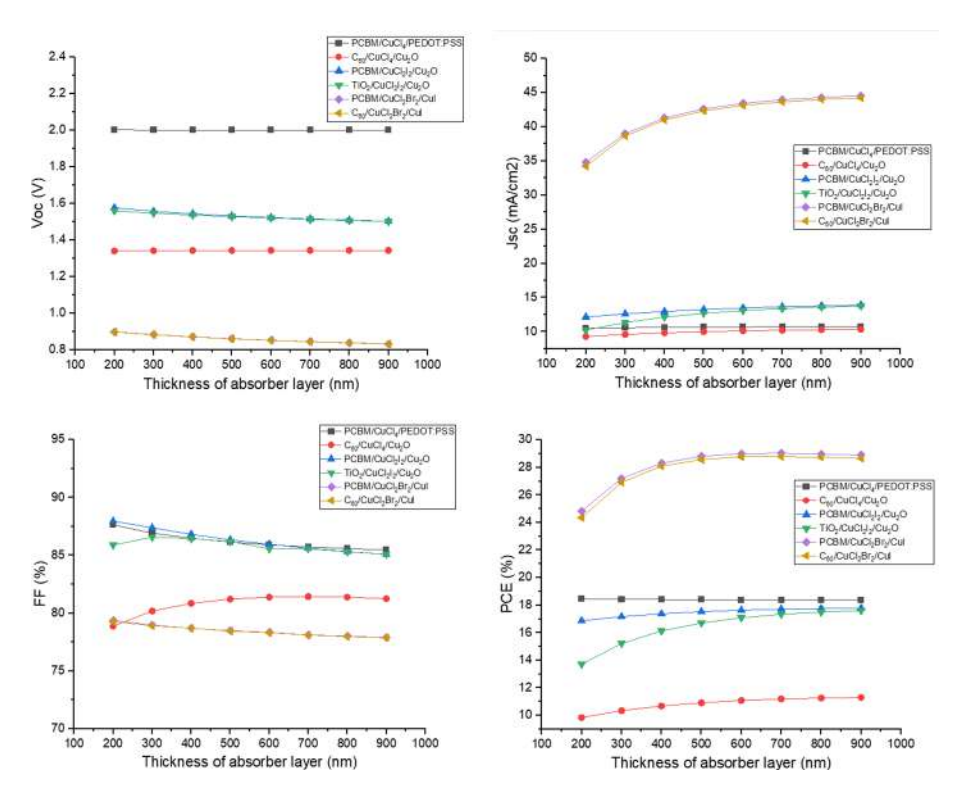


Fig. 8 Change in photovoltaic parameters with the thickness of PAL for different ETL and HTL of Cubased PSC

3.3 Effect of operating temperature on absorber layer

To analyze the impact of temperature on the performance of solar cells, the working temperature has been varied in the range of 260–360 K. As a rise in temperature, the PCE drops drastically. Fall in efficiency with temperature is related with decrease in diffusion length of the charge carriers. If the deformation stress on the layers is high, it results in interfacial defects and low interconnectivity among layers. This low interconnectivity alludes to increment of recombination rate in PAL, hence resulting in reducing the diffusion length and increasing R_S, fall in the performance of solar cells (Nejand et al. 2016). In PCBM/(MA)₂CuCl₄/PEDOT: PSS fall in efficiency with temperature is 17.31%, for C₆₀/(MA)₂CuCl₄/Cu₂O fall is 0.92%, for PCBM/(MA)₂CuCl₂I₂/Cu₂O fall is 13.56%, TiO₂/(MA)₂CuCl₂I₂/Cu₂O is 11.85%, PCBM/(MA)₂CuCl₂Br₂/CuI is 16.95% and for C₆₀/(MA)₂CuCl₂Br₂/CuI is 16.73%. This shows that the fall in efficiency of C₆₀/(MA)₂CuCl₄/Cu₂O PSC is most stable with increase in operating and for PCBM/(MA)₂CuCl₄/PEDOT: PSS PSC is most unstable. The trend of PV parameters of different Cu-based PSCs as function of operating temperature shown in Fig. 9.



968 Page 12 of 18 R. Kundara, S. Baghel

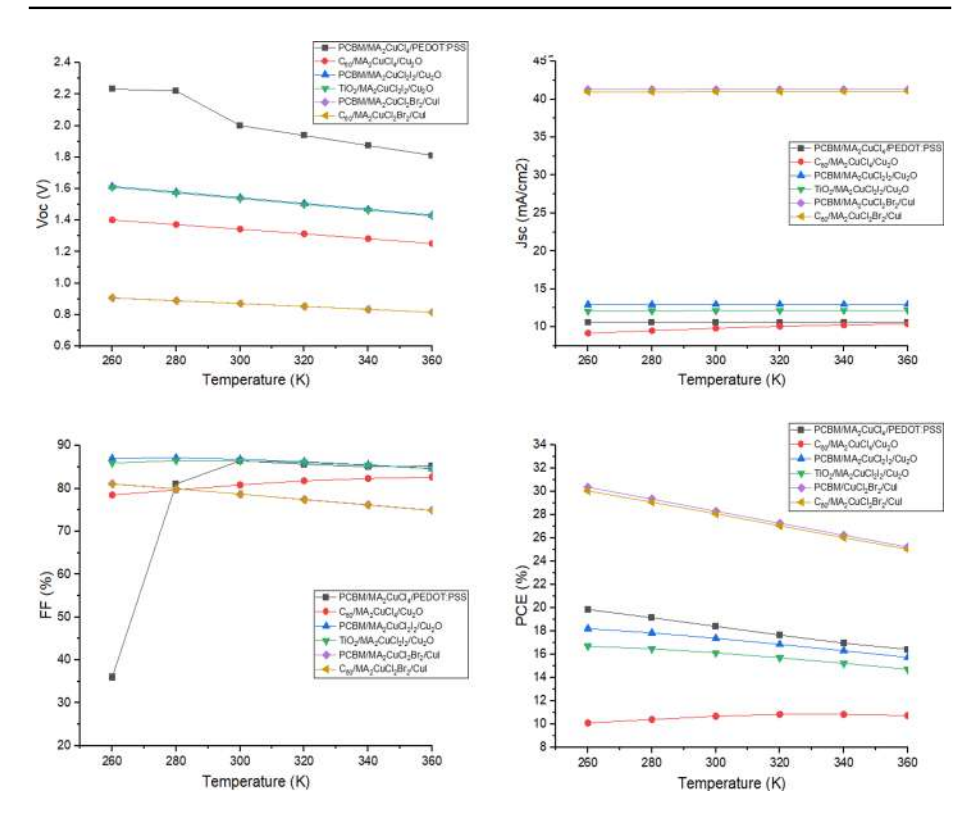


Fig. 9 Change in photovoltaic parameters with the operating temperature for various Cu-based PSCs

3.4 Effect of change in series resistance on performance

The impact of variation in the series resistance (R_s) on the performance of Cu-PSC has been examined. It has a significant effect, especially on the FF and J_{SC}. As R_{SC} increases, resulting in a decrease in FF, J_{SC} also starts decreasing for a high value of R_S. Consequently, high values of R_S in a solar device result in poor PCE (Chakraborty et al. 2019). In PSC, R_s mainly exists in the interfaces: resistance at the HTL/perovskite interface, ETL/perovskite interface, and at the metal contacts. When solar cells come in contact with the environment, thermomechanical fatigue or cracks evolve in the solder bonds depending on weather circumstances. These cracks result in increment in the value of R_S hence PCE drops (Islam et al. 2021a; Poorkazem et al. 2015). The numerical modelling outcomes on the change in R_S on the introduced (MA)₂CuX₄ based PSCs structure is shown below in Fig. 10. The PCE of three Cu-based PSCs, (MA)₂CuCl₄ (MA)₂CuCl₂I₂, and (MA)₂CuCl₂Br₂, varies with the value of series resistance. In this study, it is analyzed that for less value of R_s, the solar cell device is performance high with large FF, resulting in high PCE. As the R_S increases, the performance of active material falls significantly (Jeon et al. 2015). It has been studied that when the R_s varied from 0 to 6 (Ohm Cm²), PCE fall nearly 3.25%, 4.49%, 5.46%, 5.08%, 30.06% and 29.79% respectively for PCBM/(MA)₂CuCl₄/PEDOT:PSS, C₆₀/(MA)₂CuCl₄/ Cu₂O, PCBM/(MA)₂CuCl₂I₂/Cu₂O, TiO₂/(MA)₂CuCl₂I₂/Cu₂O, PCBM/(MA)₂CuCl₂Br₂/ CuI and $C_{60}/(MA)_2CuCl_2Br_2/CuI$ at thickness of 400 nm, defect density is 1×10^{13} cm⁻³





20 - C.,/CuCl/Cu.O ■ Tioyoucijiyćujó 19 18 19 17 18 (%) 15 14 13 PCE (%) 13 12 16 11 10 15 9 ò 3 4 Series resistance (r_e) - PCBM/CuCl.Br./Cul 30 Coo/CuCl₂Br₂/Cul 28 26 PCE (%) 20 18 16 ò 3 6 Series resistance (r.)

Fig. 10 Change in PCE of different PSCs with R_s

and operating temperature is 300 K shown below in Fig. 10. This shows that the PCBM/ (MA)₂CuCl₄/PEDOT: PSS is the most stable and PCBM/(MA)₂CuCl₂Br₂/CuI is the most unstable PSC with increase in series resistance.

3.5 Radiative recombination rate effect on PCE

The effect on performance of solar devices by changing the radiative recombination rate. In this simulation study we varied the radiative recombination rate from 2.3×10^{-8} to 2.3×10^{-12} cm³/sec and examined PV parameters trend of PSC devices for different rates with the thickness of PAL which is between 200 and 900 nm. Usually, increment in radiative recombination, carrier lifetime reduces, and PV parameters of device is influenced as shown in Fig. 11 for Cu-based PSCs respectively. The Gaussian shape of the curve can be explained by the fact that with an increment in thickness of PAL, large electron–hole pairs are produced (Islam et al. 2021b). The PCE of (MA)₂CuCl₄ based PSC with PCBM as ETL and PEDOT: PSS as HTL, the maximum PCE has achieved is 18.43% at PAL thickness of 200 nm and recombination rate of 2.3×10^{-12} cm³/sec whereas when C_{60} as ETL and Cu_2O as HTL the maximum PCE is 11.29% at thickness of 900 nm with recombination rate of 2.3×10^{-12} cm³/sec. The obtained PCE is 17.74% for (MA)₂CuCl₂I₂ based PSC with PCBM as ETL and Cu_2O as HTL and when C_{60} as ETL and Cu_{60} as ETL and Cu_{60}



968 Page 14 of 18 R. Kundara, S. Baghel

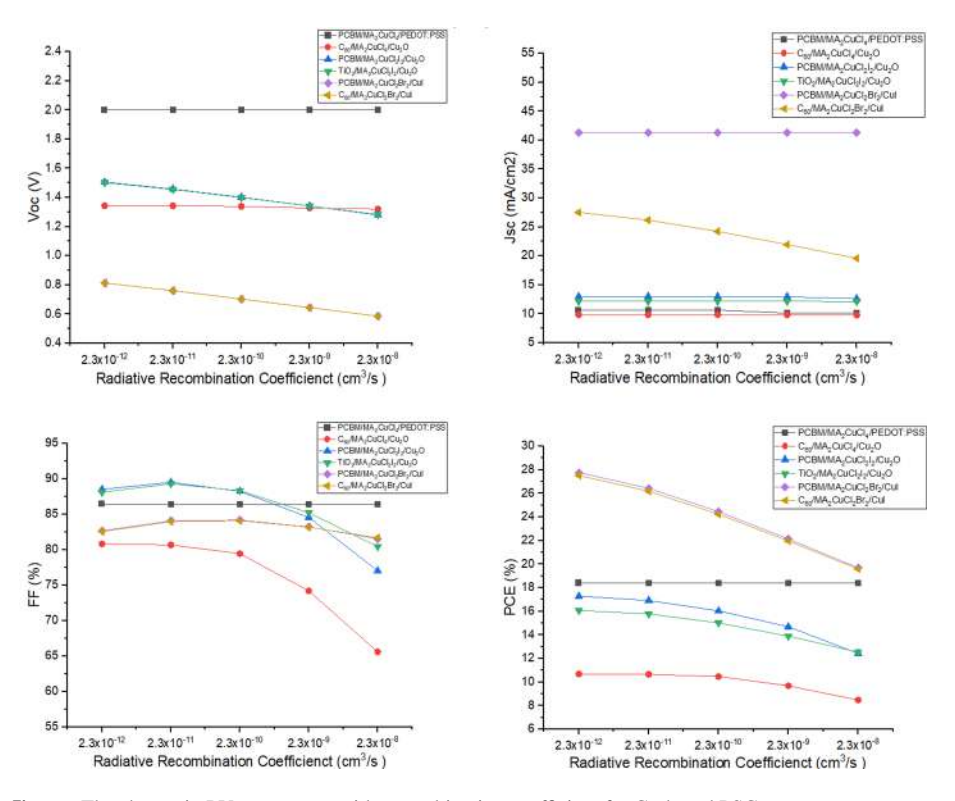


Fig. 11 The change in PV parameters with recombination coefficient for Cu-based PSCs

CuI as HTL obtained maximum PCE is 28.41% at PAL thickness of 700 nm for the recombination rate of 2.3×10^{-12} cm³/sec shown below in Fig. 11.

3.6 Effect of metal back contact work function on PCE

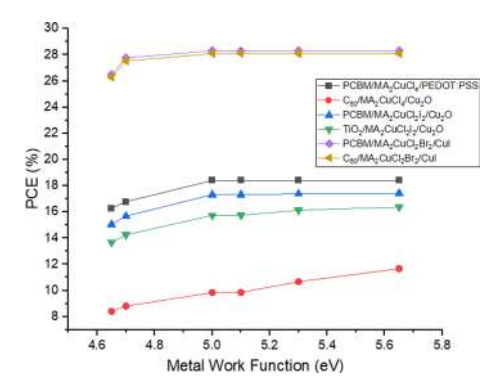
The power conversion efficiencies listed in Table 5 have been achieved by choosing Gold (Au) as a metal electrode. Gold was taken after carefully studying the impact of metal electrode work function on the PCE as shown in Fig. 12. The work function was varied from 4.6 to 5.8 eV. This range covers the work function of most of the available metals which are employed as back contact in PSCs. Figure 12 reveals that the photovoltaic performance decreases gradually as the work function of the metal back contact is reduced below 5.1 eV due to formation of Schottky junction at a smaller value of work function (Jannat et al. 2021). We observed that the maximum PCE of 28.31% achieved at work function of 5.1 eV (Au) (Kanoun et al. 2019).

4 Conclusions

We have simulated environment-friendly Cu-based PSCs with optimized ETLs and HTLs for achieving maximum PCE. The PV parameters for first optimized cell FTO/PCBM/(MA)₂CuCl₄/PEDOT: PSS PSC are PCE of 18.41%, V_{OC} is 2.00 V, J_{SC} is



Fig. 12 Change in PCE of different PSCs with metal work function (eV)



10.63 mA/cm² and FF is 86.48%. The second optimized cell structure is FTO/PCBM/ (MA)₂CuCl₂I₂/Cu₂O with the maximum PCE of 17.38%, V_{OC} is 1.54 V and FF is 86.82%. Third optimized cell structure is FTO/PCBM/(MA)₂CuCl₂Br₂/CuI has obtained maximum PCE of 28.31%, V_{OC} is 0.87 V, J_{SC} is 41.30 mA/cm² and FF is 78.69% at 400 nm thickness of PAL, operating temperature is 300 K and N_t is 1×10^{13} cm⁻³. The maximum PCE of 18.41%, 17.53% and 29.01% have been obtained for all three optimized PSCs with the thickness of PAL as 400 nm, 500 nm and 600 nm respectively for first, second and third cell by using SCAPS-1D. This work also comprises the operating temperature optimization for high performance of PSCs. The optimized value of temperature is 300 K for the PSCs structure. The maximum PCE has obtained of 18.41%, 17.38% and 28.31% for the PSC structure such as FTO/PCBM/(MA)₂CuCl₄/ PEDOT: PSS, FTO/PCBM/(MA)₂CuCl₂I₂/Cu₂O and FTO/PCBM/(MA)₂CuCl₂Br₂/CuI respectively at 300 K. Experimentally published results are also compared with simulation results and findings were analyzed which highlighted poor ETL and HTL selection as one of the reasons for lower performance of (MA)₂CuX₄ PSCs. The series resistance (R_s) effect on PCE is also studied which indicates that (MA)₂CuCl₄ PSC is most stable and (MA)₂CuCl₂Br₂ based PSC is highly unstable with increase in value of R_s. The optimized radiative recombination rate is 2.3×10^{-12} cm³/sec with function of PAL thickness for high PCE of Cu-based PSC with different ETLs and HTLs. Copper based PSC overcome stability and toxicity issue in PSCs. This work helpful in deeply understanding of design, operation mechanism, and in optimization of high efficiency Cubased PSC in near future.

Acknowledgements The author, Rahul Kundara is thankful to Delhi Technological University, New Delhi for providing junior research fellowship. We are also very grateful to Professor Marc Burgelman (University of Gent, Belgium) for providing us with SCAPS-1D software.

Author contributions RK—Conceptualization, Formal analysis, Data curation, Investigation, Methodology, Writing—original draft, Visualization and Software. SB—Supervision, Project administration, critical review and commentary or revision.

Funding This declaration is "not applicable".

Data availability This declaration is "not applicable".

Declarations

Conflict of interest The authors declare that they have no known competing financial interests or personal relationships that could have appeared to influence the work reported in this paper.



968 Page 16 of 18 R. Kundara, S. Baghel

Ethical approval This declaration is "not applicable".

References

- Anwar, F., Mahbub, R., Satter, S.S., Ullah, S.M.: Effect of different HTM layers and electrical parameters on ZnO nanorod-based lead-free perovskite solar cell for high-efficiency performance. Int. J. Photoenergy 2017, 9846310 (2017). https://doi.org/10.1155/2017/9846310
- Azri, F., Meftah, A., Sengouga, N., Meftah, A.: Electron and hole transport layers optimization by numerical simulation of a perovskite solar cell. Sol. Energy 181, 372–378 (2019). https://doi.org/10.1016/j.solener.2019.02.017
- Bhattarai, S., Das, T.D.: Optimization of carrier transport materials for the performance enhancement of the MAGeI₃ based perovskite solar cell. Sol. Energy 217, 200–207 (2021). https://doi.org/10.1016/j.solen er.2021.02.002
- Cao, Y., Liu, Z., Li, W., Zhao, Z., Xiao, Z., Lei, B., Zi, W., Cheng, N., Liu, J., Tu, Y.: Efficient and stable MAPbI₃ perovskite solar cells achieved via chlorobenzene/perylene mixed anti-solvent. Sol. Energy 220, 51–257 (2021). https://doi.org/10.1016/j.solener.2021.03.055
- Chakraborty, K., Choudhury, M.G., Paul, S.: Numerical study of Cs₂TiX₆ (X=Br⁻, I⁻, F⁻ and Cl⁻) based perovskite solar cell using SCAPS-1D device simulation. Sol. Energy 194, 886–892 (2019). https://doi.org/10.1016/j.solener.2019.11.005
- Chatterjee, S., Pal, A.J.: Introducing Cu₂O thin films as a hole-transport layer in efficient planar perovskite solar cell structures. J. Phys. Chem. C 120(3), 1428–1437 (2016). https://doi.org/10.1021/acs.jpcc. 5b11540
- Cortecchia, D., Dewi, H.A., Yin, J., Bruno, A., Chen, S., Baikie, T., Boix, P.P., Grätzel, M., Mhaisalkar, S., Soci, C., Mathews, N.: Lead-free MA₂CuCl_xBr_{4-x} hybrid perovskites. Inorg. Chem. 55(3), 1044–1052 (2016). https://doi.org/10.1021/acs.inorgchem.5b01896
- De Los Santos, I.M., Cortina-Marrero, H.J., Ruíz-Sánchez, M.A., Hechavarría-Difur, L., Sánchez-Rodríguez, F.J., Courel, M., Hu, H.: Optimization of CH₃NH₃PbI₃ perovskite solar cells: a theoretical and experimental study. Sol. Energy 199, 198–205 (2020). https://doi.org/10.1016/j.solener.2020.02.026
- Elseman, A.M., Shalan, A.E., Sajid, S., Rashad, M.M., Hassan, A.M., Li, M.: Copper-substituted lead perovskite materials constructed with different halides for working (CH₃NH₃)₂CuX₄-based perovskite solar cells from experimental and theoretical view. ACS Appl. Mater. Interfaces 10(14), 11699–11707 (2018). https://doi.org/10.1021/acsami.8b00495
- Gharibzadeh, S., Nejand, B.A., Moshaii, A., Mohammadian, N., Alizadeh, A.H., Mohammadpour, R., Ahmadi, V., Alizadeh, A.: Two-step physical deposition of a compact CuI Hole-Transport layer and the formation of an interfacial species in perovskite solar cells. Chemsuschem 9(15), 1929–1937 (2016). https://doi.org/10.1002/cssc.201600132
- Giustino, F., Snaith, H.J.: Toward lead-free perovskite solar cells. ACS Energy Lett. 1(6), 1233–1240 (2016). https://doi.org/10.1021/acsenergylett.6b00499
- Haider, S.Z., Anwar, H., Wang, M.: Theoretical device engineering for high-performance perovskite solar cells using CuSCN as hole transport material boost the efficiency above 25%. Phys. Status Solidi (a) 216(11), 1900102 (2019). https://doi.org/10.1002/pssa.201900102
- Hao, L., Li, T., Ma, X., Wu, J., Qiao, L., Wu, X., Hou, G., Pei, H., Wang, X., Zhang, X.: A tin-based perovskite solar cell with an inverted hole-free transport layer to achieve high energy conversion efficiency by SCAPS device simulation. Opt. Quantum Electron. 53, 1–17 (2021). https://doi.org/10.1007/s11082-021-03175-5
- Hossain, M.I., Alharbi, F.H.: Recent advances in alternative material photovoltaics. Mater. Technol. 8(1–2), 88–97 (2013)
- https://www.pveducation.org/pvcdrom/pn-junctions/absorption-coefficient/ (2022). Accessed 20 February 2022
- Islam, S., Sobayel, K., Al-Kahtani, A., Islam, M.A., Muhammad, G., Amin, N., Shahiduzzaman, M., Akhtaruzzaman, M.: Defect study and modelling of SnX3-based perovskite solar cells with SCAPS-1D. Nanomaterials 11(5), 1218 (2021). https://doi.org/10.3390/nano11051218
- Islam, M.T., Jani, M.R., Shorowordi, K.M., Hoque, Z., Gokcek, A.M., Vattipally, V., Nishat, S.S., Ahmed, S.: Numerical simulation studies of Cs₃Bi₂I₉ perovskite solar device with optimal selection of electron and hole transport layers. Optik 231, 166417 (2021). https://doi.org/10.1016/j.ijleo.2021.166417



- Jannat, F., Ahmed, S., Alim, M.A.: Performance analysis of cesium formamidinium lead mixed halide based perovskite solar cell with MoOx as hole transport material via SCAPS-1D. Optik 228, 166202 (2021). https://doi.org/10.1016/j.ijleo.2020.166202
- Jayan, K.D., Sebastian, V.: Comprehensive device modelling and performance analysis of MASnI₃ based perovskite solar cells with diverse ETM, HTM and back metal contacts. Sol. Energy 217, 40–48 (2021). https://doi.org/10.1016/j.solener.2021.01.058
- Jeon, N.J., Noh, J.H., Yang, W.S., Kim, Y.C., Ryu, S., Seo, J., Seok, S.I.: Compositional engineering of perovskite materials for high-performance solar cells. Nature 517, 476–480 (2015). https://doi.org/ 10.1038/nature14133
- Ju, M.G., Chen, M., Zhou, Y., Garces, H.F., Dai, J., Ma, L., Padture, N.P., Zeng, X.C.: Earth-abundant nontoxic titanium (IV)-based vacancy-ordered double perovskite halides with tunable 1.0 to 1.8 eV bandgaps for photovoltaic applications. ACS Energy Lett. 3(2), 297–304 (2018). https://doi.org/10. 1021/acsenergylett.7b01167
- Kalaiselvi, C.R., Muthukumarasamy, N., Velauthapillai, D., Kang, M., Senthil, T.S.: Importance of halide perovskites for next generation solar cells: a review. Mater. Lett. 219, 198–200 (2018). https://doi.org/10.1016/j.matlet.2018.02.089
- Kale, A.J., Chaurasiya, R., Dixit, A.: Inorganic lead-free Cs₂AuBiCl₆ perovskite absorber and Cu₂O hole transport material based single-junction solar cells with 22.18% power conversion efficiency. Adv. Theory Simul. 4(3), 2000224 (2021). https://doi.org/10.1002/adts.202000224
- Kanoun, A.A., Kanoun, M.B., Merad, A.E., Goumri-Said, S.: Toward development of high-performance perovskite solar cells based on CH₃NH₃GeI₃ using computational approach. Sol. Energy 182, 237–244 (2019). https://doi.org/10.1016/j.solener.2019.02.041
- Ke, W., Stoumpos, C.C., Kanatzidis, M.G.: "Unleaded" perovskites: status quo and future prospects of tin-based perovskite solar cells. Adv. Mater. 31(47), 1803230 (2019). https://doi.org/10.1002/adma. 201803230
- Kour, R., Arya, S., Verma, S., Gupta, J., Bandhoria, P., Bharti, V., Datt, R., Gupta, V.: Potential substitutes for replacement of lead in perovskite solar cells: a review. Glob. Chall. 3(11), 1900050 (2019). https://doi.org/10.1002/gch2.201900050
- Kumar, N., Rani, J., Kurchania, R.: Advancement in CsPbBr₃ inorganic perovskite solar cells: fabrication, efficiency and stability. Sol. Energy 221, 197–205 (2021). https://doi.org/10.1016/j.solener. 2021.04.042
- Lakhdar, N., Hima, A.: Electron transport material effect on performance of perovskite solar cells based on CH₃NH₃GeI₃. Opt. Mater. 99, 109517 (2020). https://doi.org/10.1016/j.optmat.2019.109517
- Mahajan, P., Datt, R., Tsoi, W.C., Gupta, V., Tomar, A., Arya, S.: Recent progress, fabrication challenges and stability issues of lead-free tin-based perovskite thin films in the field of photovoltaics. Coord. Chem. Rev. 429, 213633 (2021). https://doi.org/10.1016/j.ccr.2020.213633
- Mandadapu, U., Vedanayakam, S.V., Thyagarajan, K.: Simulation and analysis of lead based perovskite solar cell using SCAPS-1D. Indian J. Sci. Technol. 10(11), 65–72 (2017). https://doi.org/10.17485/ ijst/2017/v11i10/110721
- Minami, T., Miyata, T., Nishi, Y.: Cu₂O-based heterojunction solar cells with an Al-doped ZnO/oxide semiconductor/thermally oxidized Cu₂O sheet structure. Sol. Energy 105, 206–217 (2014). https:// doi.org/10.1016/j.solener.2014.03.036
- Momblona, C., Gil-Escrig, L., Bandiello, E., Hutter, E.M., Sessolo, M., Lederer, K., Blochwitz-Nimoth, J., Bolink, H.J.: Efficient vacuum deposited pin and nip perovskite solar cells employing doped charge transport layers. Energy Environ. Sci. 9(11), 3456–3463 (2016). https://doi.org/10.1039/C6EE02100J
- Mushtaq, S., Tahir, S., Ashfaq, A., Bonilla, R.S., Haneef, M., Saeed, R., Ahmad, W., Amin, N.: Performance optimization of lead-free MASnBr₃ based perovskite solar cells by SCAPS-1D device simulation. Sol. Energy 249, 401–413 (2023). https://doi.org/10.1016/j.solener.2022.11.050
- Nejand, B.A., Ahmadi, V., Gharibzadeh, S., Shahverdi, H.R.: Cuprous oxide as a potential low-cost hole-transport material for stable perovskite solar cells. Chemsuschem 9(3), 302–313 (2016). https://doi.org/10.1002/cssc.201501273
- Noel, N.K., Stranks, S.D., Abate, A., Wehrenfennig, C., Guarnera, S., Haghighirad, A.A., Sadhanala, A., Eperon, G.E., Pathak, S.K., Johnston, M.B., Petrozza, A.: Lead-free organic–inorganic tin halide perovskites for photovoltaic applications. Energy Environ. Sci. 7(9), 3061–3068 (2014). https://doi. org/10.1039/C4EE01076K
- Ompong, D., Singh, J.: High open-circuit voltage in perovskite solar cells: the role of hole transport layer. Org. Electron. 63, 104–108 (2018). https://doi.org/10.1016/j.orgel.2018.09.006
- Park, N.G.: Perovskite solar cells: an emerging photovoltaic technology. Mater. Today 18(2), 65–72 (2015). https://doi.org/10.1016/j.mattod.2014.07.007



968 Page 18 of 18 R. Kundara, S. Baghel

Poorkazem, K., Liu, D., Kelly, T.L.: Fatigue resistance of a flexible, efficient, and metal oxide-free perovskite solar cell. J. Mater. Chem. A 3(17), 9241–9248 (2015). https://doi.org/10.1039/C5TA0 0084J

- Qiu, X., Cao, B., Yuan, S., Chen, X., Qiu, Z., Jiang, Y., Ye, Q., Wang, H., Zeng, H., Liu, J., Kanatzidis, M.G.: From unstable CsSnI₃ to air-stable Cs₂SnI₆: a lead-free perovskite solar cell light absorber with bandgap of 1.48 eV and high absorption coefficient. Sol. Energy Mater. Sol. Cells 159, 227–234 (2017). https://doi.org/10.1016/j.solmat.2016.09.022
- Rai, S., Pandey, B.K., Dwivedi, D.K.: Modeling of highly efficient and low cost CH₃NH₃Pb(I_{1-x}Cl_x)₃ based perovskite solar cell by numerical simulation. Opt. Mater. 100, 109631 (2020). https://doi.org/10.1016/j.optmat.2019.109631
- Sahli, F., Werner, J., Kamino, B.A., Bräuninger, M., Monnard, R., Paviet-Salomon, B., Barraud, L., Ding, L., Diaz Leon, J.J., Sacchetto, D., Cattaneo, G.: Fully textured monolithic perovskite/silicon tandem solar cells with 25.2% power conversion efficiency. Nat. Mater. 17(9), 820–826 (2018). https://doi.org/10.1038/s41563-018-0115-4
- Shi, B., Jia, J., Feng, X., Ma, G., Wu, Y., Cao, B.: Thermal evaporated CuI film thickness-dependent performance of perovskite solar cells. Vacuum 187, 110076 (2021). https://doi.org/10.1016/j.vacuum.2021. 110076
- Wang, M., Zeng, P., Bai, S., Gu, J., Li, F., Yang, Z., Liu, M.: High-quality sequential-vapor-deposited Cs₂AgBiBr₆ thin films for lead-free perovskite solar cells. Sol. Rrl 2(12), 1800217 (2018). https://doi.org/10.1002/solr.201800217
- Yamada, N., Ino, R., Ninomiya, Y.: Truly transparent p-type γ-CuI thin films with high hole mobility. Chem. Mater. 28(14), 4971–4981 (2016), https://doi.org/10.1021/acs.chemmater.6b01358
- Zhang, Z., Li, X., Xia, X., Wang, Z., Huang, Z., Lei, B., Gao, Y.: High-quality (CH₃NH₃)₃Bi₂I₉ film-based solar cells: pushing efficiency up to 1.64%. J. Phys. Chem. Lett. 8(17), 4300–4307 (2017). https://doi.org/10.1021/acs.jpclett.7b01952
- Zong, Y., Zhou, Y., Zhang, Y., Li, Z., Zhang, L., Ju, M.G., Chen, M., Pang, S., Zeng, X.C., Padture, N.P.: Continuous grain-boundary functionalization for high-efficiency perovskite solar cells with exceptional stability. Chem 4(6), 1404–1415 (2018). https://doi.org/10.1016/j.chempr.2018.03.005

Publisher's Note Springer Nature remains neutral with regard to jurisdictional claims in published maps and institutional affiliations.

Springer Nature or its licensor (e.g. a society or other partner) holds exclusive rights to this article under a publishing agreement with the author(s) or other rightsholder(s); author self-archiving of the accepted manuscript version of this article is solely governed by the terms of such publishing agreement and applicable law.



ELSEVIER

Contents lists available at ScienceDirect

Solid State Communications

journal homepage: www.elsevier.com/locate/ssc



Performance analysis of LaFeO₃ perovskite solar cells: A theoretical and experimental study

Rahul Kundara*, Sarita Baghel

Department of Applied Physics, Delhi Technological University, Delhi, India

ARTICLE INFO

Communicated by: Francois Peeters

Keywords: LaFeO₃ perovskite material Sol-gel method SCAPS-1D ETLs and HTLs

ABSTRACT

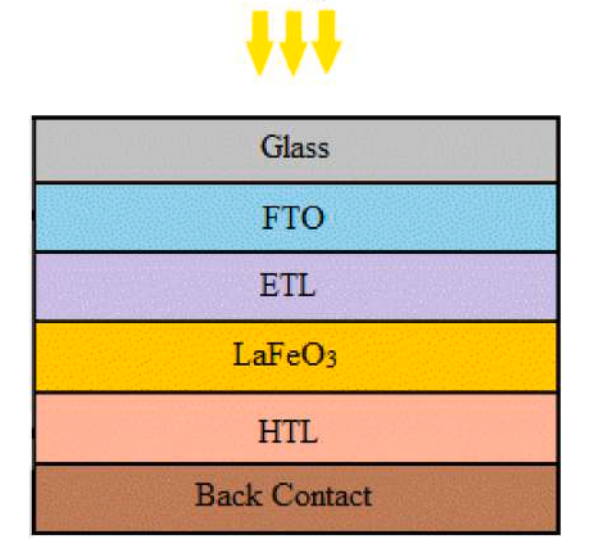
Lanthanum ferrite (LaFeO₃) is a potential candidate for Perovskite Solar Cell (PSC) application. The transition metal oxide has strong electron-electron correlation which results in an increase in quantum efficiency (QE) of PSC. In this investigation, we reported synthesis of LaFeO₃ perovskite material, simulation of LaFeO₃-based PSC followed by experimental validation. The sol-gel method was employed to prepare nanoparticles of LaFeO₃ for PSC application. The prepared perovskite material is analyzed by XRD, SEM, EDS, UV–Vis and FTIR. The photovoltaic (PV) application of synthesized LaFeO₃ material is studied by SCAPS-1D. The LaFeO₃-based PSC is simulated with various ETLs such as TiO₂, PCBM, IGZO, In₂O₃, C₆₀, ZnO, SnO₂, WS₂ and HTLs of Cu₂O, CuInSe₂, Spiro-OMeTAD, P3HT, D-PBTTT-14, V₂O₅, CFTS, CBTS. The simulation outcomes of 64 distinct configurations deduced the eight-best performing PSCs. For these eight PSCs, impact of thickness of perovskite absorber layer, operating temperature, defect density, series and shunt resistance, work function of back contact, J-V characteristics and QE curve has been studied. We have achieved theoretical maximum efficiency of 13.03 % for the configuration of FTO/WS₂/LaFeO₃/CBTS/Au. The optimized structure has experimentally obtained maximum efficiency of 0.79 %. This shows that it is promising material for future PV application.

1. Introduction

The limited amount of fossil fuels and their combustion, leads to pollution in the environment [1]. So, alternative energy technologies are required like biomass, wind, solar and tidal power. Solar energy is a green, accessible and abundant renewable energy [2-4]. Perovskite solar cell (PSC) continues to draw the attention of researchers by virtue of characteristics like high-power conversion efficiency (PCE) and simple room temperature fabrication methodology which makes them a cheaper alternative to conventional silicon solar cells [5-7]. A perovskite has basically ABX3 type structure (where A: alkyl group, B: metal and X: halogen) [8,9]. Pb-based PSCs present sustainability challenges due to high toxicity of lead, posing risks to both living organisms and the ecosystem. Moreover, Pb-based PSCs suffer from stability issues stemming from the rapid oxidation of Pb cation. In the quest for a suitable Pb substitute [10], researchers have explored numerous candidates to replace Pb, such as Sn [11], Ge [12], Bi [13], Sb [14], La [15,16] and double perovskites etc. LaFeO3 possesses a tunable energy band-gap which can be altered using suitable dopants [17,18]. The other properties of LaFeO3 such as chemical stability, low production cost, high electron mobility and its non-toxic nature are already favorable for lead-free PSC application [19,20]. There are very few studies on LaFeO₃ as perovskite material for solar cell application [21]. This work comprises fabrication and characterization of LaFeO₃-based PSCs. LaFeO₃ nanoparticles were first synthesized by using the sol-gel method and then they were used for solar cell application. Prior to fabrication of LaFeO₃-based PSC, we have simulated and optimized the structure of solar cells using SCAPS-1D simulation software. So, we have got eight optimized structures of LaFeO3-based PSC through simulation with a maximum PCE of 13.03 % for the most efficient configuration which is approximately 30 % greater than the past reported work [20]. The experimental validation was conducted for the optimized PSC. We achieved an PCE of 0.79 % experimentally, which is approximately thirteen times higher than the previously reported result [21]. The spin coating method is employed to obtain PCE of 0.79 % which is the highest achieved efficiency for the LaFeO3-based PSC till now. This efficiency enhancement is attributed to proper selection of hole transport layer (HTL) and electron transport layer (ETL). A conventional PSC structure contains a perovskite absorber layer sandwiched amid ETL and HTL. A current is developed when electrons (e-) are traveled through ETL and

E-mail address: rahul_2k20phdap10@dtu.ac.in (R. Kundara).

^{*} Corresponding author.



Sunlight

Fig. 1. Architecture of LaFeO3-based PSC.

holes (h^+) are transferred to HTL from the absorber layer. To obtain the maximum PCE of a PSC, the energy level alignment of all these layers becomes a very important factor. The selection and optimization of the ETL and HTL is very crucial to maximize the performance of a PSC. In this simulation we have simulated sixty-four configurations with different ETLs (TiO₂, PCBM, IGZO, In_2O_3 , C_{60} , ZnO, SnO_2 , WS_2) and

HTLs (Cu_2O , $CuInSe_2$, Spiro-OMeTAD, P3HT, D-PBTTT-14, V_2O_5 , CFTS, CBTS). The outcomes showed that CBTS is the most suitable HTL for LaFeO₃ PSC and in addition it is abundantly available [22]. The study also includes optimization of the parameters which influences performance of the PSC, thickness, operating temperature, defect density (N_t), back contact, series (R_S) and shunt resistance (R_{SH}).

2. Device architecture

The PSC structure consists of ETL, absorber layer and HTL shown below in Fig. 1. The LaFeO $_3$ is employed as an absorber layer in PSC having thickness of 400 nm. In this simulation, we have employed several ETLs (TiO $_2$, PCBM, IGZO, In $_2$ O $_3$, C $_6$ 0, ZnO, SnO $_2$, WS $_2$) and HTLs (Cu $_2$ O, CuInSe $_2$, Spiro-OMeTAD, P3HT, D-PBTTT-14, V $_2$ O $_5$, CFTS, CBTS) to achieve the maximum efficiency. The thickness of employed ETL = 100 nm and HTL = 50 nm. In p-i-n devices, the electrons and holes generated within the absorber layer when sunlight falls on it. The generated e $^-$ and h $^+$ is traveled through ETL and HTL, e $^-$ s are collected at the fluorine doped tin oxide (FTO) and h $^+$ s at the back contact.

3. Experimental section

3.1. Materials and method

All the precursors employed in synthesis of perovskite are $La(NO_3)_3$, $Fe(NO_3)_3$, citric acid and ammonium hydroxide. The light sensitizer $LaFeO_3$ was prepared by employing a sol-gel method. The flow chart for stepwise preparation of perovskite material is shown below in Fig. 2. The lanthanum and iron-based solution were prepared for synthesis of $LaFeO_3$. Deionized (DI) water chosen as a solvent to dissolve both

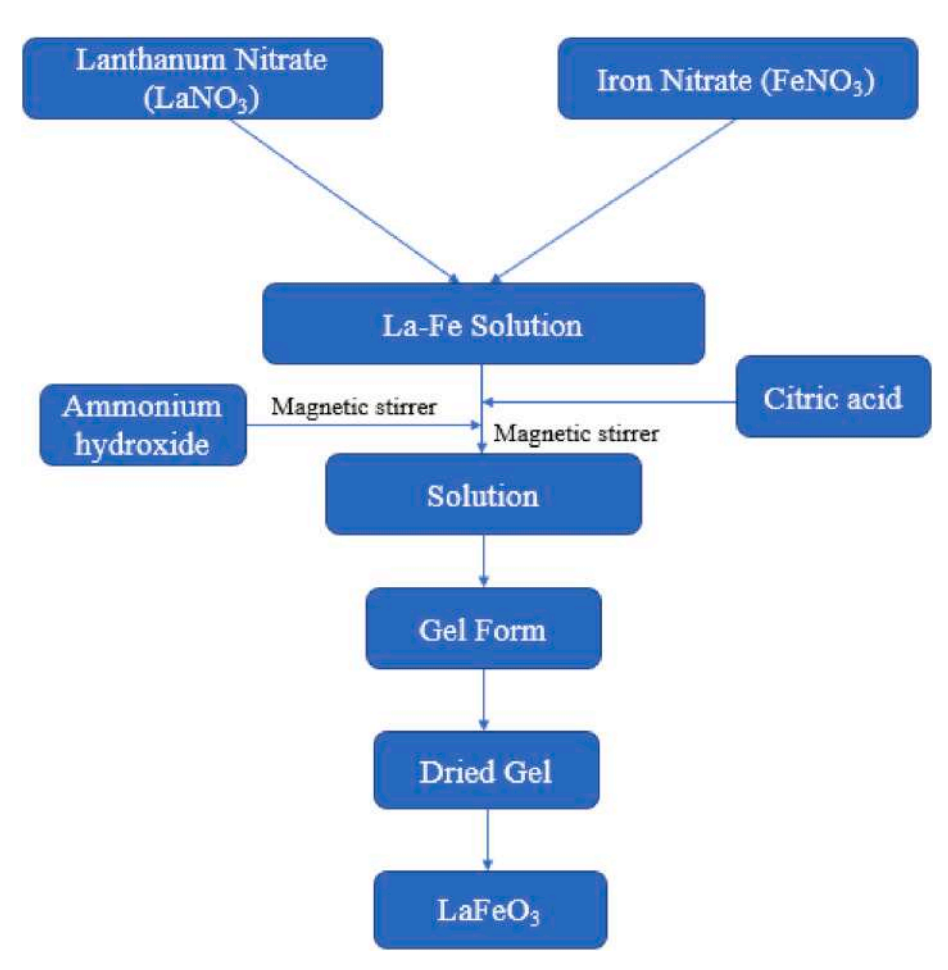


Fig. 2. Flow chart of stepwise synthesis of LaFeO₃.

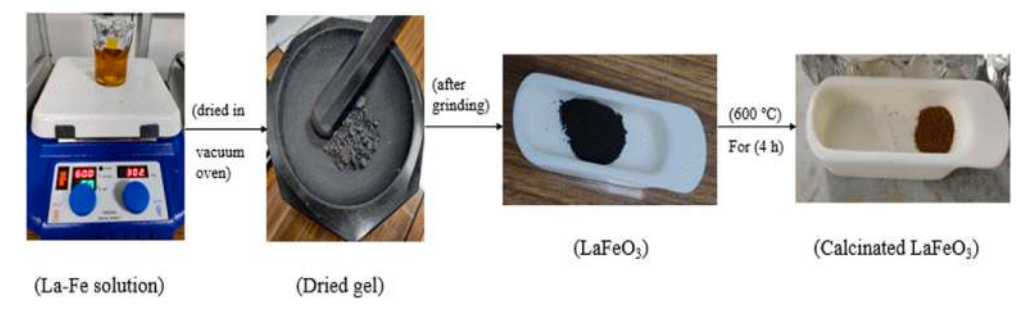
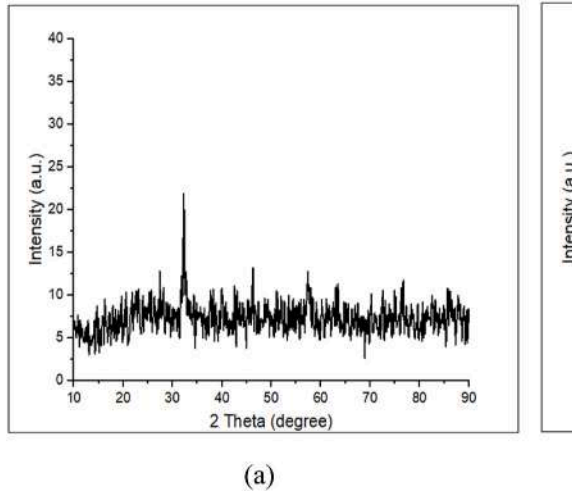


Fig. 3. Preparation of LaFeO₃ perovskite.



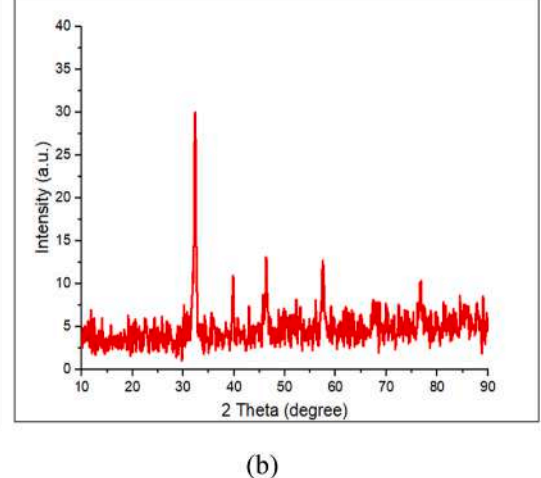


Fig. 4. XRD pattern of (a) LaFeO $_3$ and (b) Calcined LaFeO $_3$.

solutes. At first,1 M aqueous solution of La(NO₃)₃ mixed with 1 M aqueous solution of Fe(NO₃)₃. The mixture was stirred for 2 days at 300 rpm and 60 °C. Citric acid was added dropwise in the solution. After that, ammonium hydroxide aqueous solution was added dropwise under magnetic stirring to make pH = 7. The sample was stirred at 300 rpm for 72 h and dried in a vacuum oven at 180 °C for 12 h. After that sample was moved into a muffle furnace for calcination in air at 600 °C for 4 h. The synthesized sample shown in Fig. 3.

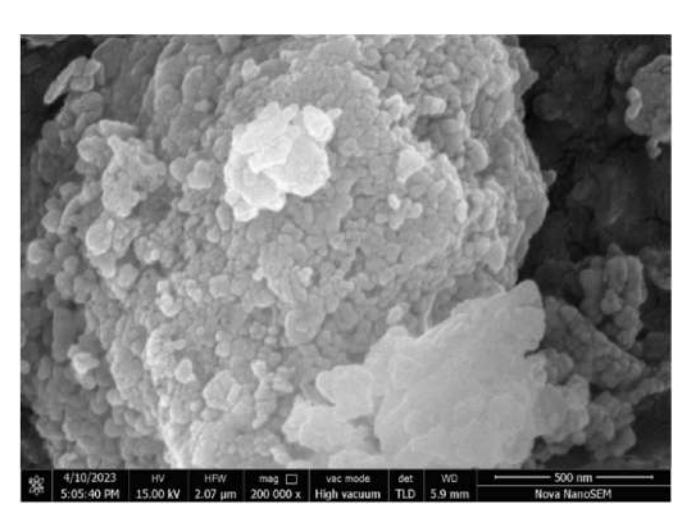


Fig. 5. SEM images of LaFeO₃ nanoparticles.

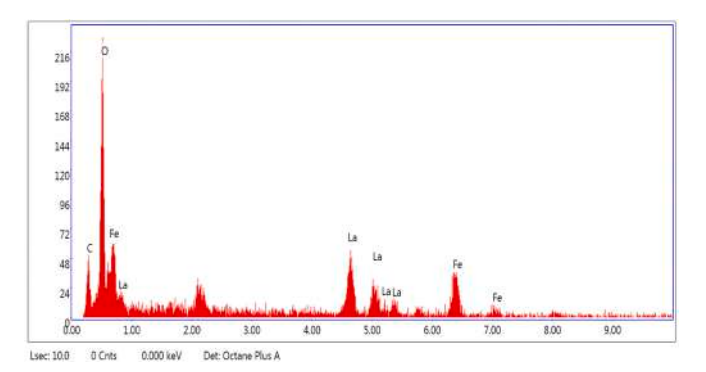


Fig. 6. EDS spectrum of LaFeO₃ nanoparticles.

3.2. Characterizations

XRD pattern of perovskite material was recognized utilizing a diffractometer (Bruker D8 advance). The size and morphologies of synthesized perovskite by SEM. UV–vis spectrum of the LaFeO $_3$ sample is observed by employing a PerkinElmer, Lamda-750 dual-beam spectrometer. The prepared sample IR transmission spectra was analyzed by employing an FTI-R spectrometer.

Table 1 Weight % of the element composition of LaFeO₃ powder.

Element	Series	Weight %	Atomic %	
С	K-Series	6.70	22.42	
0	K-Series	17.18	43.16	
La	L-Series	47.37	13.71	
Fe	K-Series	28.75	20.70	

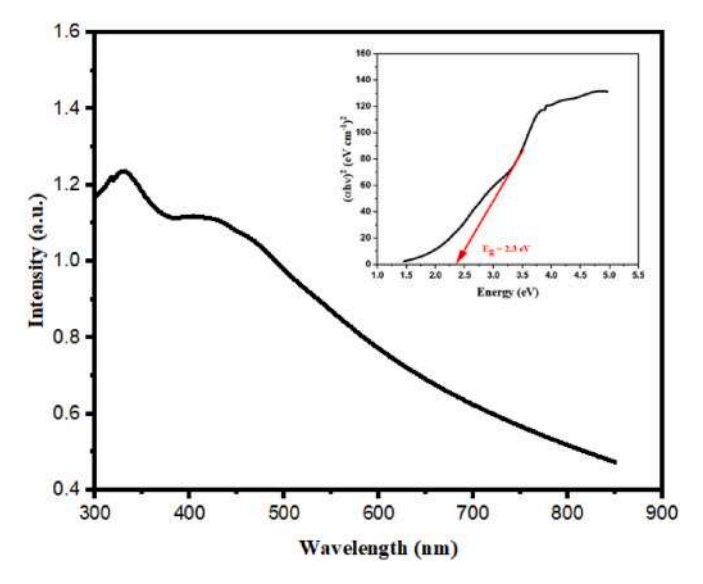


Fig. 7. UV-Vis spectrum of LaFeO₃ nanoparticles.

4. Experimental results and discussion

4.1. XRD analysis

It is primarily used for phase identification and crystallinity of the material. The observed range of XRD data is from 10° to 90° over 2θ with scan rate of 2° /min. The peaks of LaFeO $_3$ before and after calcination are demonstrated in Fig. 4 (a) and (b), respectively. The XRD peaks with 2θ of $32.30^\circ,~39.91^\circ,~46.42^\circ,~57.60^\circ,~67.83^\circ$ and 76.68° correspond to LaFeO $_3$ perovskite nanoparticles of cubic structure (75–0541). Bragg's equation (1) was used to calculate the material grain size and display angles.

$$2dsin\theta = n\lambda \tag{1}$$

Crystallite Size =
$$(0.94 \times \lambda)/\beta \cos\theta$$
 (2)

Where, $\lambda =$ wavelength of X-ray, $\beta =$ FWHM, $\theta =$ Bragg's angle.

The calculated average crystallite size is 18.4 nm by using Debye Scherrer's Eq. (2). It is observed that the peak intensities increase after the calcination (600 $^{\circ}$ C for 4 h) of the LaFeO₃, which confirms the uniform crystal growth of perovskite phase [21].

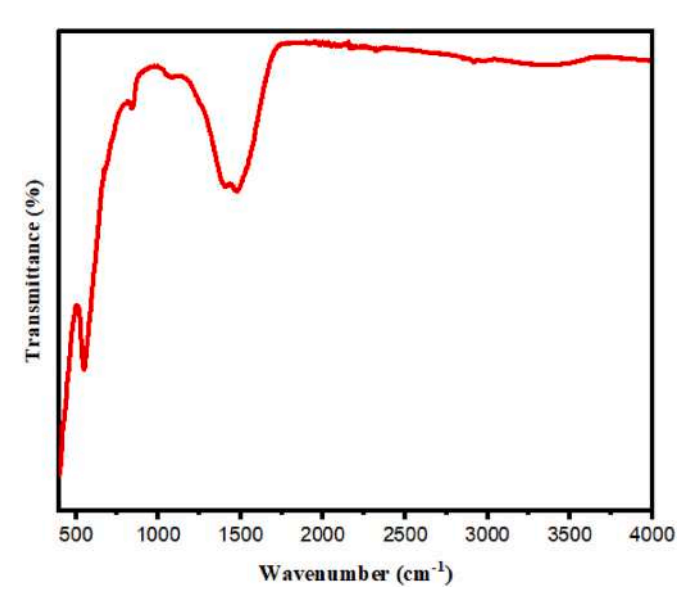


Fig. 8. FT-IR spectrum of LaFeO₃ nanoparticles.

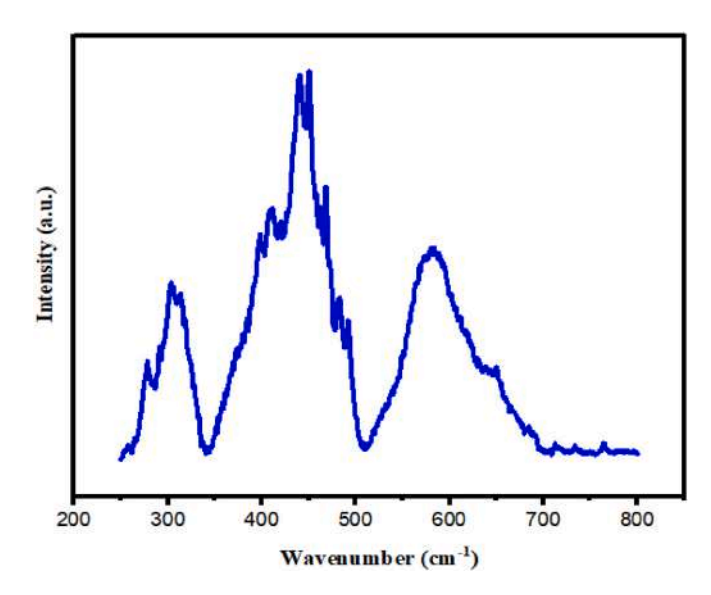


Fig. 9. PL spectrum of LaFeO₃ nanoparticles.

Table 2Input parameters of PSCs.

r · · r · · · · · ·				
Parameter	FTO [29, 30]	TiO ₂ [31, 32]	LaFeO ₃ [20, 33]	Cu ₂ O [29, 33]
Thickness (nm)	500 100		400	50
Eg (eV)	3.5 3.2		2.3	2.17
χ (eV)	4.0 3.9		3.3	3.2
ε	9.0 32		30	7.11
$N_C (cm^{-3})$	$2.2 \times 10^{18} 1$	$\times 10^{19}$	4×10^{18}	2.02×10^{17}
$N_V (cm^{-3})$	$1.8 \times 10^{19} 1$	$\times 10^{19}$	1×10^{19}	1.1×10^{19}
μ_n (cm ² /Vs)	20 20		1.1×10^{-1}	2×10^2
μ_p (cm ² /Vs)	10 10		1.1×10^{-3}	80
N_D (cm ⁻³)	$1 \times 10^{15} 1$	$< 10^{17}$	1×10^{15}	0
N_A (cm ⁻³)	0 0		$1 imes 10^{15}$	1×10^{18}
N_t (cm ⁻³)	$1 \times 10^{15} 1$	$< 10^{13}$	$1\times 10^{13\text{a}}$	1×10^{14}

^a In this work.

Table 3
Input parameters of different ETLs.

Parameter	PCBM	IGZO	In_2O_3	C ₆₀	ZnO	SnO_2	WS_2
	[35]	[20, 36]	[20]	[30]	[37]	[31, 37]	[38]
Thickness (µm)	100 ^a	100	100				
Eg (eV)	2.1	3.05	2.8	1.7	3.3	3.3	1.8
χ (eV)	3.9	4.16	3.7	3.9	4.1	4.0	3.95
ε	3.9	10	8.9	4.2	9.0	9.0	13.6
$N_C (cm^{-3})$	$2.2 \times$	5 ×	$1 \times$	8 ×	$2.2 \times$	$2.2 \times$	$1 \times$
	10^{19}	10^{18}	10^{19}	10^{19}	10^{18}	10^{17}	10^{18}
N_V (cm ⁻³)	$2.2 \times$	5 ×	$1 \times$	8 ×	1.9 ×	$2.2 \times$	2.4 ×
	10^{19}	10^{18}	10^{19}	10^{19}	10^{19}	10^{16}	10^{19}
μ_n (cm ² /	$1 \times$	15	3.4	8 ×	100	200	100
Vs)	10^{-3}			10^{-2}			
μ_p (cm ² /	$2 \times$	0.1	3.4	3.5 ×	25	80	100
Vs)	10^{-3}			10^{-3}			
$N_{\rm D} ({\rm cm}^{-3})$	$1 \times$	$1 \times$	$1 \times$	2.6 ×	$1 \times$	$1 \times$	$1 \times$
	10^{18}	10^{18}	10^{18}	10^{17}	10^{17}	10^{17}	10^{18}
N_A (cm ⁻³)	0	0	0	0	0	0	0
N_t (cm ⁻³)	$1 \times$	$1 \times$	$1 \times$				
	10^{13a}	10^{13a}	10^{13a}	10^{13a}	10^{13a}	10^{13a}	10^{13a}

^a In this work.

Table 4 Input parameters of different HTLs.

Parameter	CuInSe ₂ [39,40]	Spiro-OMeTAD [29,33,39,41]	P3HT [30,42]	D-PBTTT-14 [29]	V ₂ O ₅ [39,43]	CFTS [44]	CBTS [44]
Thickness (µm)	50 ^a	50 ^a	50	50	50 ^a	50 ^a	50 ^a
Eg (eV)	2.17	3.0	1.7	2.16	2.2	1.3	1.9
χ (eV)	3.2	2.45	3.5	3.2	4.0	3.3	3.6
ε	6.6	3.0	3.0	10	10	9.0	5.4
$N_C (cm^{-3})$	2.5×10^{20}	1×10^{19}	2×10^{18}	2.8×10^{19}	9.2×10^{17}	2.2×10^{18}	2.2×10^{18}
$N_V (cm^{-3})$	2.5×10^{20}	1×10^{19}	2×10^{19}	1×10^{19}	5×10^{18}	1.8×10^{19}	1.8×10^{19}
μ_n (cm ² /Vs)	80	1×10^{-4}	1.8×10^{-3}	2.83×10^{-3}	3.2×10^2	21.98	30
$\mu_{\rm p} ({\rm cm}^2/{\rm Vs})$	80	1×10^{-4}	1.8×10^{-2}	2.83×10^{-3}	40	21.98	10
N_D (cm ⁻³)	0	0	0	0	0	0	0
$N_A (cm^{-3})$	1×10^{18}	2×10^{18}	1×10^{18}	1×10^{18}	1×10^{18}	1×10^{18}	1×10^{18}
N_t (cm ⁻³)	1×10^{14a}	1×10^{14}	1×10^{14}	1×10^{14}	1×10^{14}	1×10^{14a}	$1\times 10^{14\text{a}}$

a In this work.

Table 5The PSC performance of CBTS with the different ETLs.

Device architecture	V _{OC} (V)	J _{SC} (mA/cm ²)	FF (%)	PCE (%)
FTO/TiO ₂ /LaFeO ₃ /CBTS/Au	1.82	6.32	68.13	7.87
FTO/PCBM/LaFeO3/CBTS/Au	1.76	7.53	77.49	10.32
FTO/IGZO/LaFeO3/CBTS/Au	1.87	6.41	57.19	6.88
FTO/In ₂ O ₃ /LaFeO ₃ /CBTS/Au	1.82	6.37	81.49	9.46
FTO/C60/LaFeO3/CBTS/Au	1.37	11.36	48.59	7.62
FTO/ZnO/LaFeO ₃ /CBTS/Au	1.82	6.38	61.62	7.17
FTO/SnO ₂ /LaFeO ₃ /CBTS/Au	1.81	6.29	69.20	7.92
FTO/WS ₂ /LaFeO ₃ /CBTS/Au	1.59	10.34	76.11	12.53

4.2. SEM results

The SEM is employed to inspect topography and superficial characteristics of LaFeO $_3$ perovskite material. The nanoparticles of LaFeO $_3$ did not aggregate and have small size depicted in Fig. 5. The nanoparticles are discrete with an average size of ~ 80 nm. The SEM investigation showed that film is not uniform due to there are no surface-protecting layers which lead to agglomeration of the particles. The particle shapes are ambiguous, numerous large and small pores exist in the entire material [15].

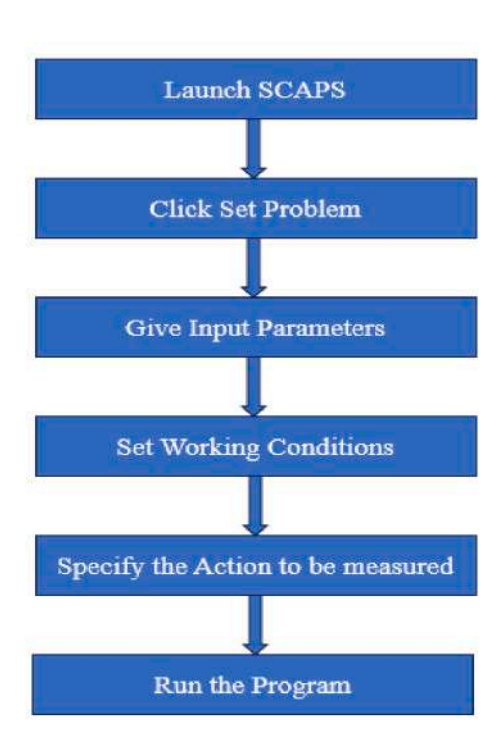


Fig. 10. Simulation procedure.

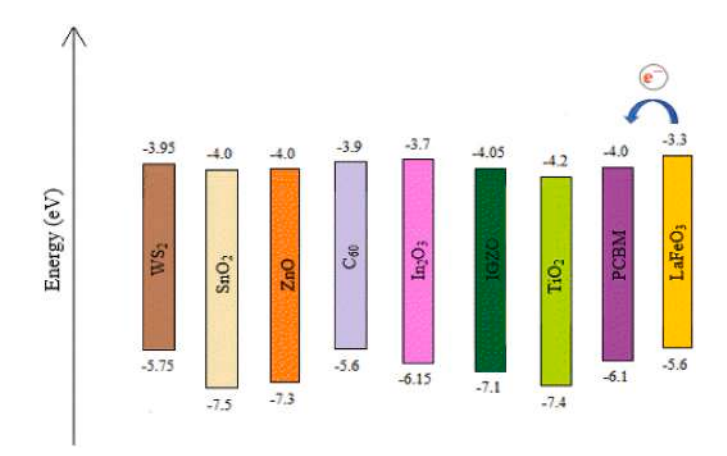


Fig. 11. Band alignment diagram of various ETLs with LaFeO₃ absorber layer.

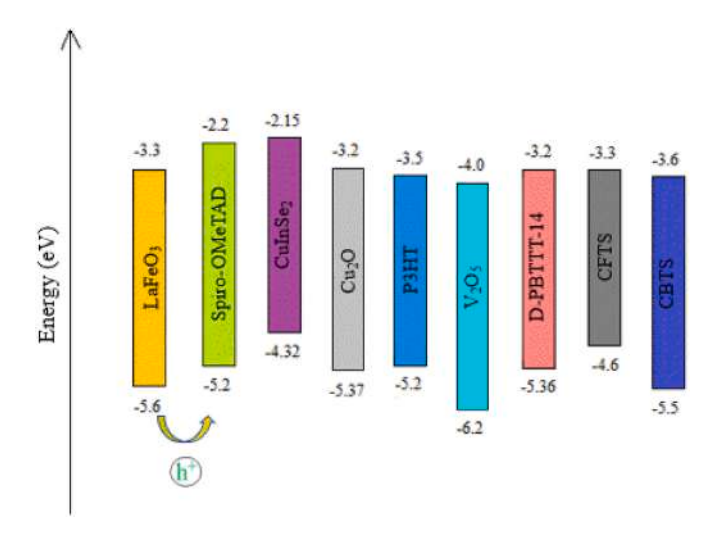


Fig. 12. Band alignment diagram of various HTLs with LaFeO₃ absorber layer.

4.3. EDS spectrum

The composition and chemical purity of elements are investigated using EDS. Fig. 6 demonstrates EDS spectroscopy of LaFeO $_3$. The diagram shows that La, Fe, C and O are observed without no peaks of impurities. The presence of these elements can validate the formation of pure phases. The weight percent of all elements presented in LaFeO $_3$ perovskite were shown below in Table 1.

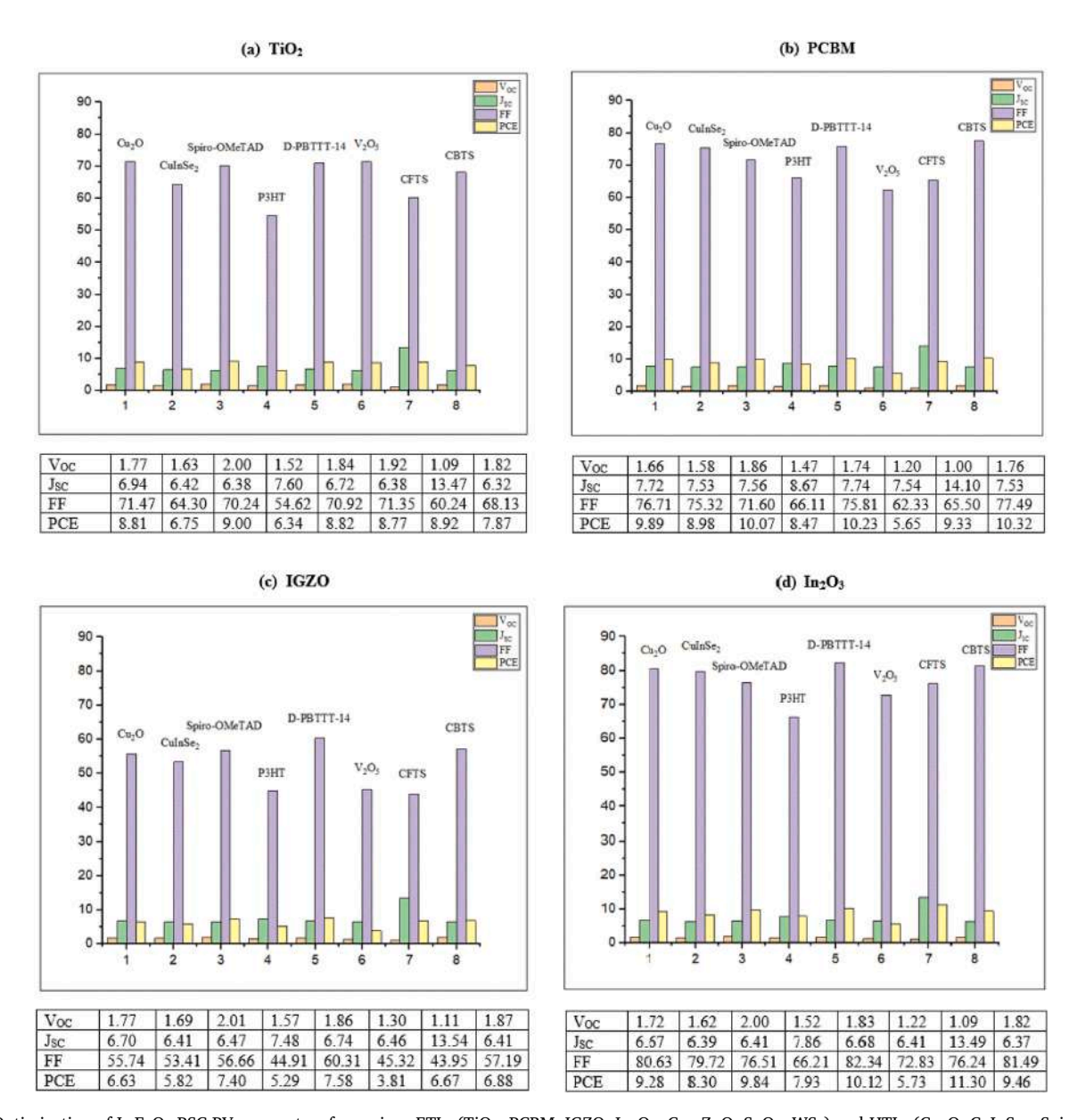


Fig. 13. Optimization of LaFeO $_3$ PSC PV parameters for various ETLs (TiO $_2$, PCBM, IGZO, In $_2$ O $_3$, C $_6$ O $_6$, ZnO, SnO $_2$, WS $_2$) and HTLs (Cu $_2$ O, CuInSe $_2$, Spiro-OMeTAD, P3HT, D-PBTTT-14, V $_2$ O $_5$, CFTS, CBTS) with Au as metal back contact.

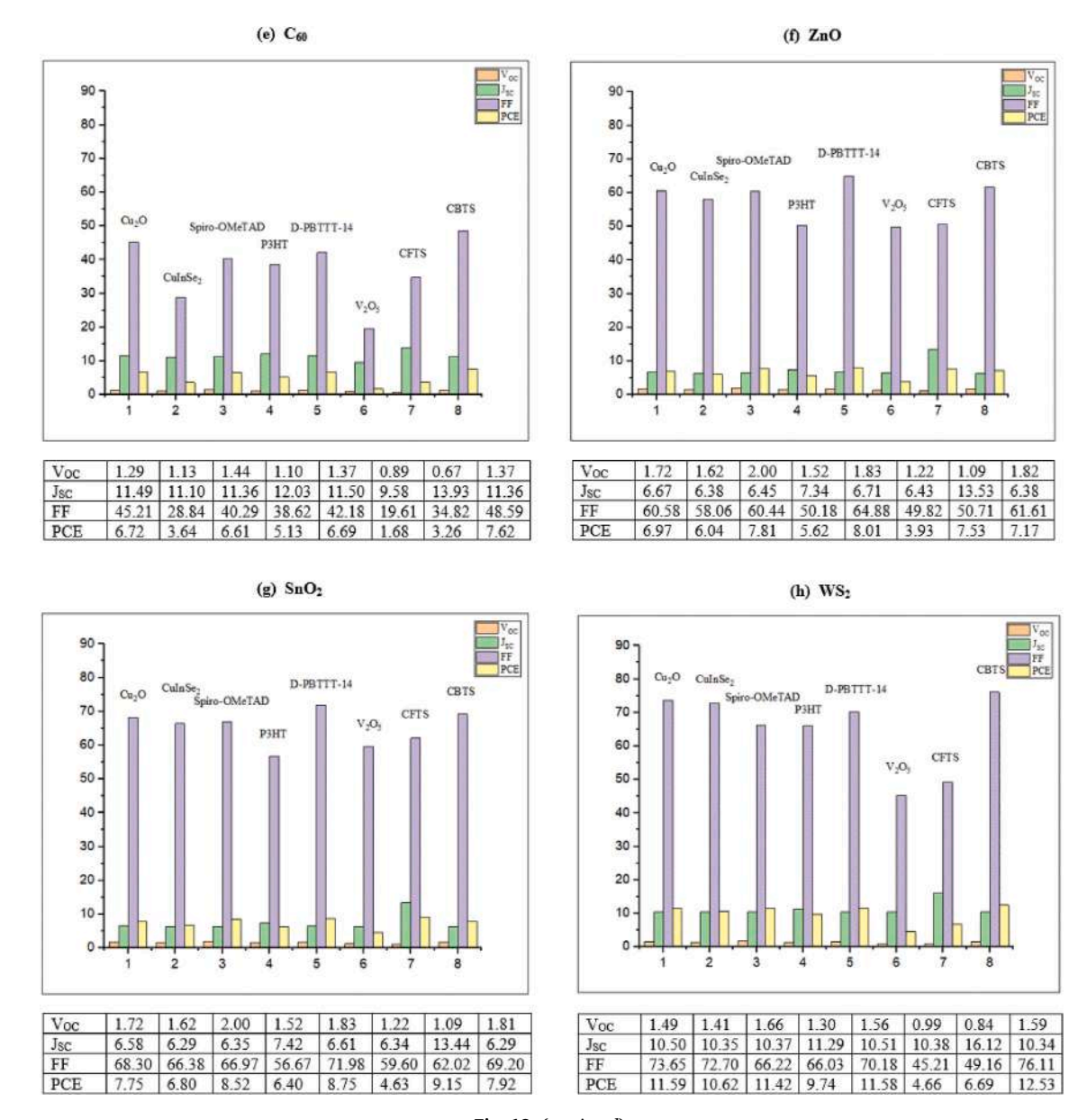


Fig. 13. (continued).

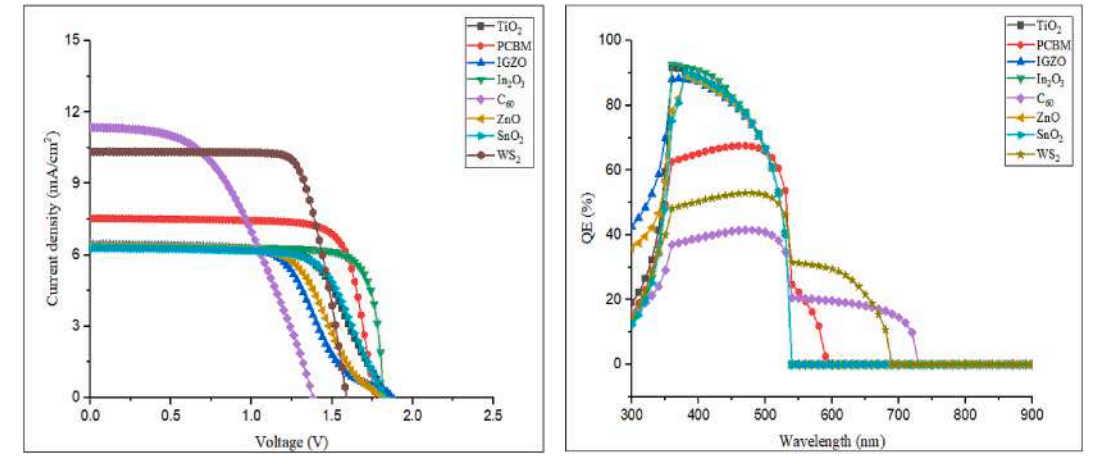


Fig. 14. J-V and QE with distinct ETLs.

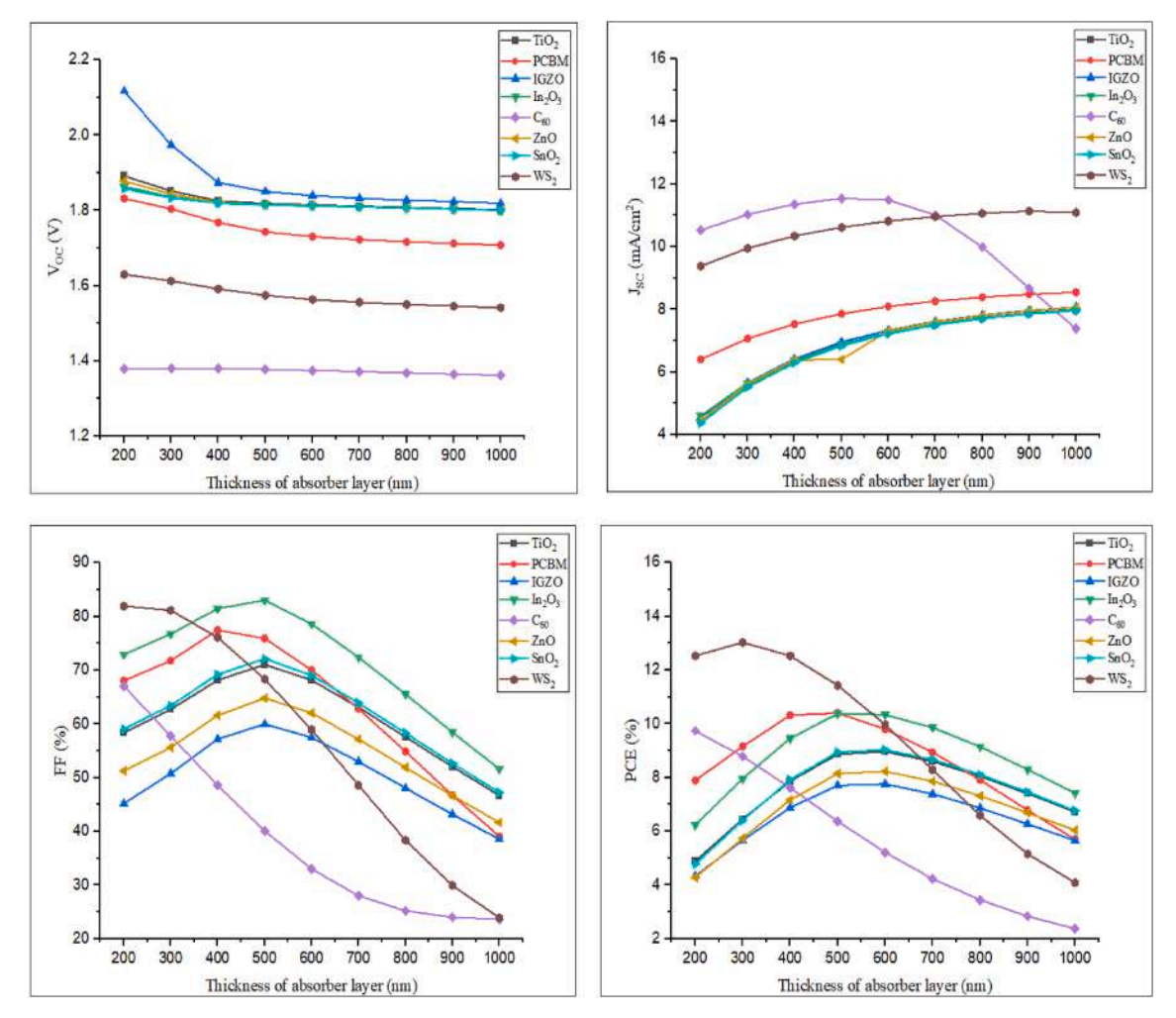


Fig. 15. Impact of thickness on PV parameters of LaFeO₃-based PSCs.

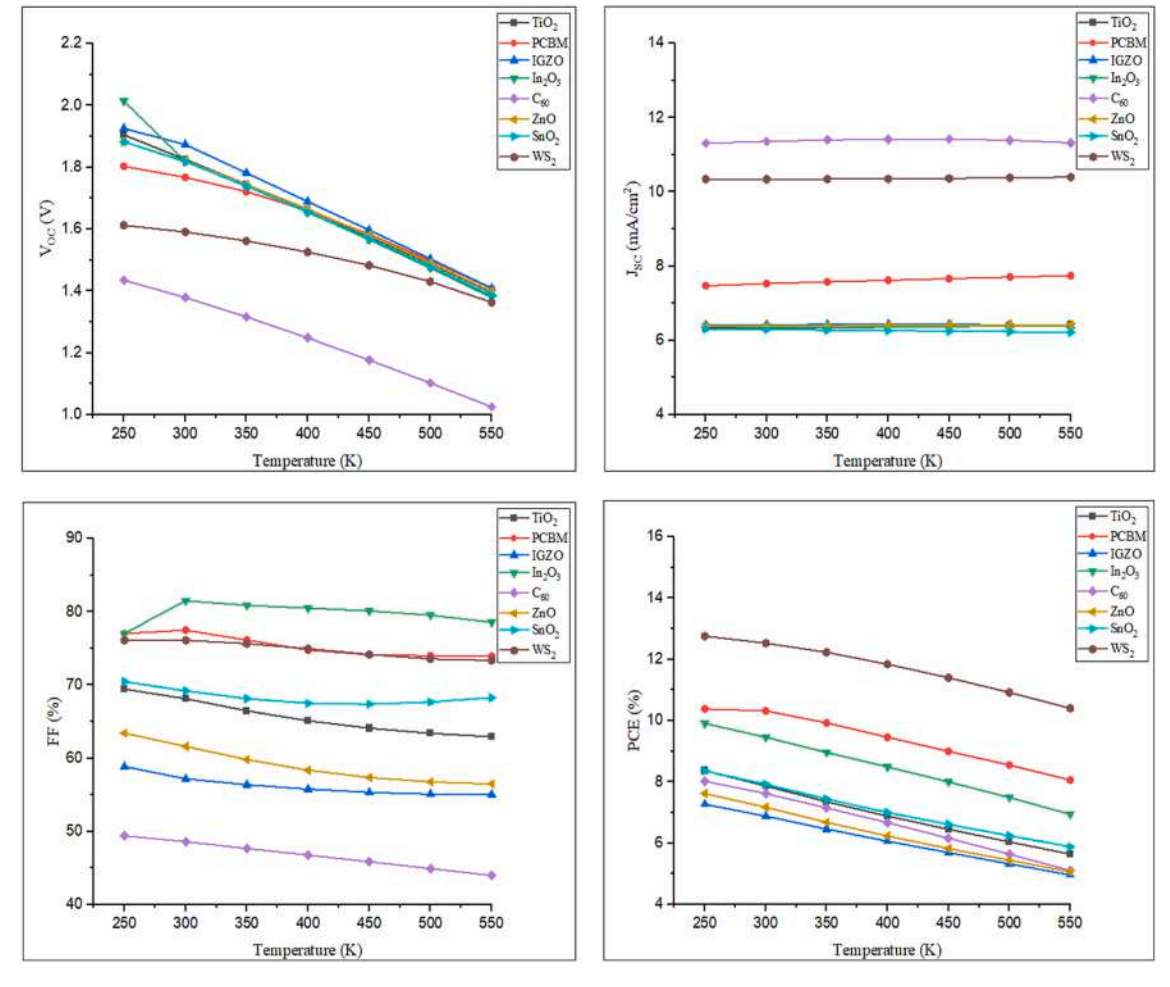


Fig. 16. Change in performance of LaFeO₃-based PSCs with operating temperature.

4.4. UV-vis spectroscopy

UV–Vis spectrum of LaFeO $_3$ perovskite material carried out in order to calculate optical E_g illustrated in Fig. 7. The highest absorption peak of the LaFeO $_3$ sample is observed at 330 nm. The E_g is calculated by equation (3).

$$E_{g} = \frac{hc}{\lambda_{max}} \tag{3}$$

Where, E_g is the band gap energy of the sample, h= Planck's constant, c= speed of light. λ_{max} is the extreme absorption wavelength of the sample. The calculated value of E_g for LaFeO_3 perovskite is approximately 2.3 eV and is in range as reported by Azozi et al. [23].

4.5. FT-IR analysis

FT-IR is employed to distinguish the vibrational modes of LaFeO₃ perovskite material and confirmation of existent functional groups. The FT-IR spectrum of a LaFeO₃ perovskite in the range of 400–4000 cm⁻¹ presented in Fig. 8. The peaks of the LaFeO₃ nanoparticles are near to 552, 838, 1061, 1404, 1480, 2912 and 3359 cm⁻¹. The absorption band is observed at 552 cm⁻¹ which is attributed to Fe–O stretching vibration mode [24,25]. This peak confirms the formation of perovskite phase which commonly exists between 500 and 700 cm⁻¹ [26]. The IR broad peak at 3359 cm⁻¹ arises from H–O bending mode and 2109 cm⁻¹ due to symmetric stretching of the carboxyl group [27].

4.6. Photoluminescence spectrum

To delve deeper into the electronic properties, we conducted room temperature Photoluminescence spectrum (PL) analysis on the synthesized powder. In this investigation, LaFeO $_3$ exhibited a prominent emission peaking around 450 nm, aligning with the band-edge emission observed with excitation wavelength of 330 nm shown below in Fig. 9. The visible emission bands might be associated with oxygen vacancies serving as luminescent sites. These vacancies naturally occur in oxygen-deficient environments and manifest as defects on the surface or within the lattice structures. In this scenario, these oxygen vacancies serve as luminescent centers, capturing both a h $^+$ and an e $^-$ on the nanostructures surface. The recombination of this e $^-$ - h $^+$ pair results in nonradiative emission. The oxygen vacancies found in synthesized perovskites prompt further investigation into their electrical and optical characteristics.

5. Simulation methodology

5.1. SCAPS-1D

The data of different parameters are chosen from previous studies. The simulation was carried out using SCAPS-1D (version 3.3.10). Gent University of Belgium developed SCAPS-1D software, enabling users to model up to seven semiconducting layers under both light and dark conditions. This software can be used for simulations at different input physical conditions. The tool calculation is based on Poisson's and continuity equations for both $e\mbox{'s}$ and $h\mbox{'+}s$ under steady-state conditions

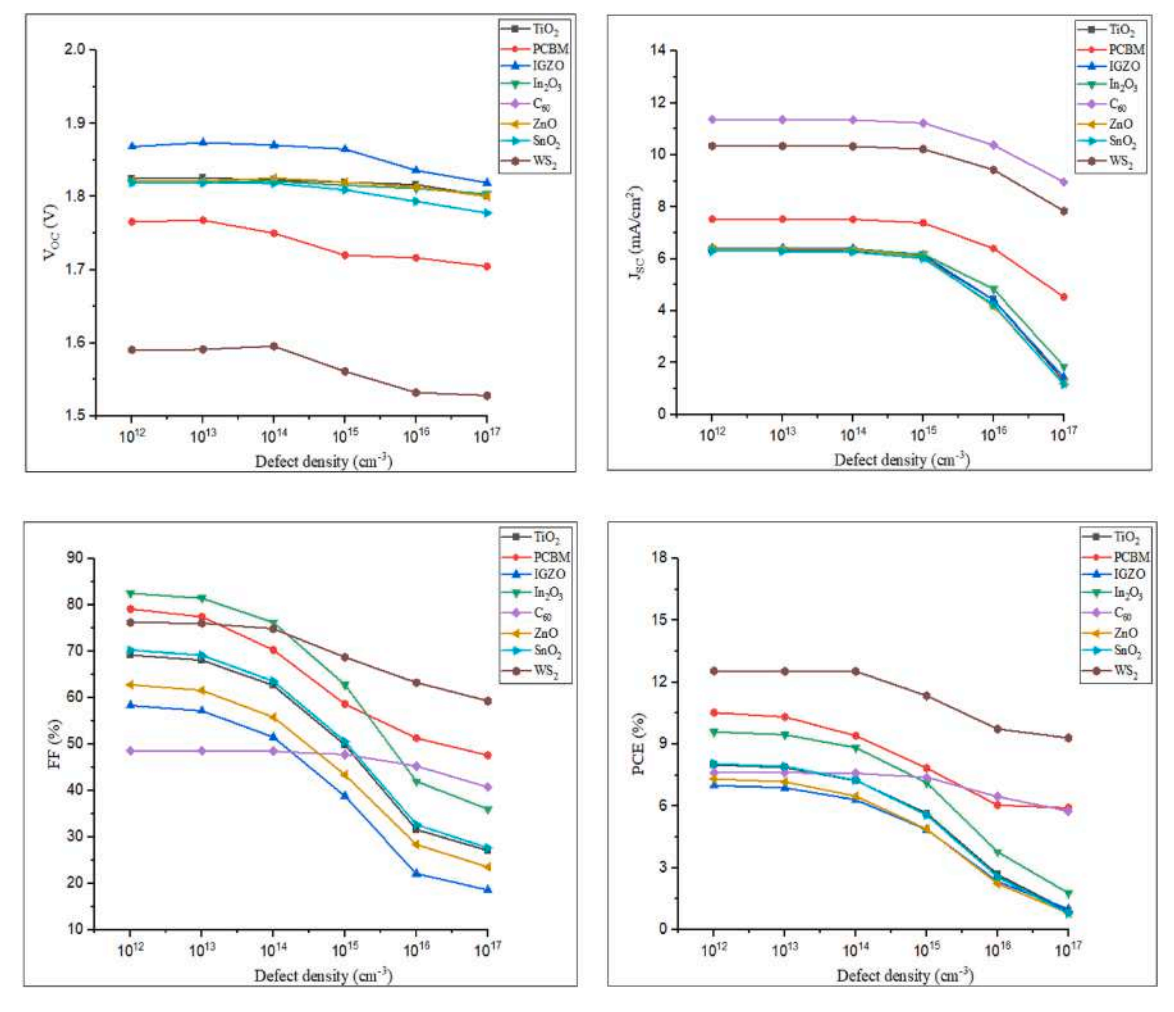


Fig. 17. Impact of N_t on the performance of LaFeO₃-based PSCs.

Table 6 Defect properties of LaFeO $_3$ absorber layer.

Parameters	Values
Density of defect, N _t (cm ⁻³)	$10^{12} – 10^{17}$
Capture cross section electron σ_n (cm ²)	1×10^{-15}
Capture cross section hole σ_h (cm ²)	$1 imes 10^{-15}$
Energetic distribution	Single
Туре	Neutral
Energy level	Midgap

as described below [28].

$$\frac{\partial^2 \psi}{\partial x^2} + \frac{q}{\epsilon} [p(x) - n(x) + N_D - N_A + \rho_p - \rho_n = 0$$
 (4)

$$\frac{1}{q}\frac{dJ_p}{dx} = G_{op}(x) - R(x) \tag{5}$$

$$\frac{1}{q}\frac{dJ_n}{dx} = -G_{op}(x) + R(x) \tag{6}$$

The PSC consists of LaFeO $_3$ perovskite absorber material with layer architecture: glass substrate/FTO/ETL/LaFeO $_3$ /HTL/Back contact depicted in Fig. 1. The input parameters employed in simulation of several layers are enclosed in Tables 2–4. The simulation procedure is shown in Fig. 10Table 5.

6. Simulation results and discussion

6.1. Optimization of suitable ETL and HTL

The various ETLs such as TiO₂, PCBM, IGZO, In₂O₃, C₆₀, ZnO, SnO₂ and WS2 were inserted into the heterostructure to achieve the optimum performance. The band alignment of various ETLs demonstrated in Fig. 11. The input parameters of employed ETLs are demonstrated in Table 3. We have done the simulation by varying the thickness of all ETLs from 50 to 250 nm. We found that the optimized value of ETL thickness is 100 nm for all ETLs. It has been analyzed that there is a negligible change in efficiency of the LaFeO3-based PSC for values greater or less than the optimized value. The different configurations of eight ETLs and eight HTLs are studied to achieve the maximum performance. The band matching is a vital factor. One of the critical issues confronting the PSCs community involves the alignment of energy level between the ETLs and the absorber layer. To tackle this issue, a thorough examination of the ETL/perovskite interface is imperative. Defects arising from lattice mismatching at the ETL/perovskite interface play a vital role in trapping the charge carriers and greatly influence the device efficiency. The conduction band of the WS2 layer is well aligned to the lowest unoccupied molecular orbital (LUMO) of the absorber layer. This can facilitate smooth charge carrier transport, minimizing the impact of defects that may otherwise trap or recombine charges. This band alignment ensures that e's can easily move from the absorber layer to the WS₂ layer and eventually to the contact, contributing to higher overall device efficiency [34]. The conduction band of the ETL is always less than the LUMO of the absorber layer. The gap amid the valence band of

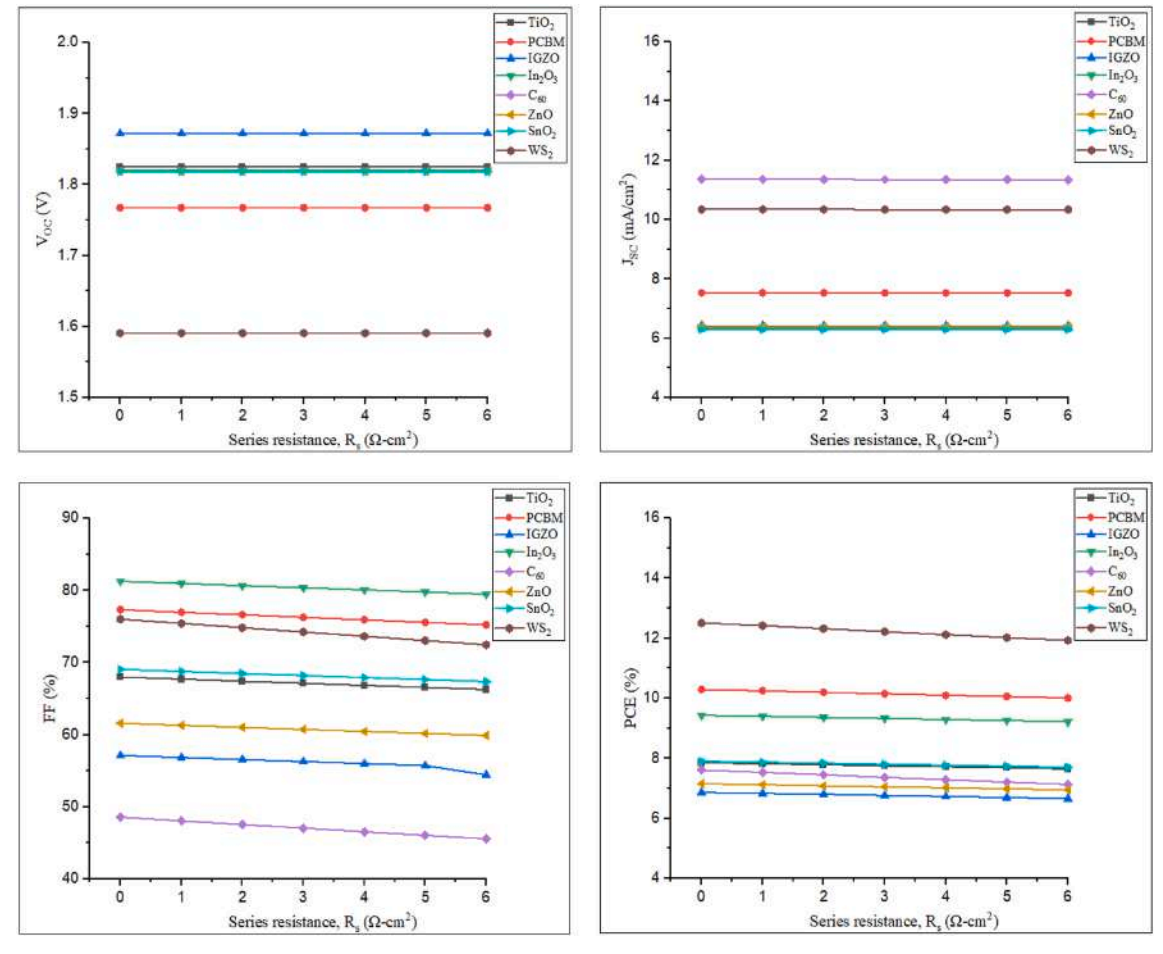


Fig. 18. Impact of R_S on the performance of LaFeO₃-based PSC at $R_{SH}=10^5~\Omega\text{-cm}^2$.

ETL and HOMO level of the absorber layer must always maintain substantial distance, which inhibits the recombination in the absorber layer. The results illustrate that TiO_2 , SnO_2 and ZnO have wide E_g , so that they have exhibited low PCE of around 8 %. ETLs like IGZO, and C_{60} suffering from mismatch in band alignment hence, exhibited low efficiency relatively. In this work WS_2 is most suitable ETL to achieve maximum PCE for LaFeO₃-based PSC. The WS_2 has advantages such as band matching, photoelectrochromic, toughness, high melting point and corrosion resistance. Due to these properties, WS_2 is the promising candidate for optoelectronic application. The maximum efficiency of 13.03 % has been obtained with the heterostructure of VS_2 -LaFeO₃/CBTS/Au.

Impact of distinct HTLs such as Cu_2O , CuInSe_2 , Spiro-OMeTAD, P3HT, D-PBTTT-14, V_2O_5 , CFTS and CBTS with eight different combinations were studied. In contrast, the V_2O_5 , and CFTS achieved less efficiency than other HTLs. The remarkable enhancement in efficiency of a PSC with the inorganic HTL. The inorganic HTL materials are more stable, transparent, and band-aligned, over organic HTL. CBTS is most suitable HTL for LaFeO_3-based PSC due to its diverse properties such as crystalline structure, light absorption, atomic size and an earth-abundant material [22]. The CBTS as HTL offered most suitable band matching as compared to other HTLs shown in Fig. 12, so that it exhibited the highest PCE of 13.03 % for LaFeO_3-based PSCs. The total sixty-four different heterostructures have been simulated to explore appropriate combinations of ETL and HTL for LaFeO_3-based PSC to achieve maximum performance depicted in Fig. 13. The J-V and QE plots of the best eight configurations are illustrated in Fig. 14.

6.2. Impact of thickness of absorber layer

The thickness altered from 200 to 1000 nm at N_t of $1\times 10^{13}~\text{cm}^{-3}$ and temperature of 300 K. It is known to us that as thickness of the layer decreases, absorption rate also lowers. This results in a decrease in photocurrent and therefore PCE of the solar cell also reduces after 300 nm. As an increase in thickness, large numbers of photons are absorbed but simultaneously recombination rate increases and high-rate results in V_{OC} [29,33]. Both V_{OC} and PCE parameters decrease exponentially for increase in thickness from 300 to 1000 nm. It can be seen that WS2 PCE is highest at around 300 nm. Whereas for C₆₀ there is a rapid fall in PCE due to very low value of electron mobility as compared to other ETLs. Hence it can be deduced that the Optimum value of thickness is 300 nm for LaFeO3-based PSC and beyond that PCE falls and decrease in FF is 68.61 %. The maximum efficiency of PSC goes up to 13.03 % together with V_{OC} is 1.61 V, J_{SC} is 9.952 mA/cm² and FF is 81.17 % for the thickness of 300 nm at ETL = 100 nm and HTL = 50 nm. The FF shows a monotonic decrement with the rise in thickness when thickness becomes greater than 300 nm. The change in different PV parameters with thickness of LaFeO₃ layer with CBTS as HTL depicted in Fig. 15.

6.3. Effect of operating temperature

The working temperature range is between 250 and 550 K. Fall in the performance with temperature increase is related to a reduction in diffusion length of charge carriers. Several solar cell architectures show the instability of their overall performance due to deformation among layers at high temperatures. In LaFeO $_3$ -based PSC, fall in efficiency with temperature is 18.11 % for FTO/WS $_2$ /LaFeO $_3$ /CBTS/Au configuration.

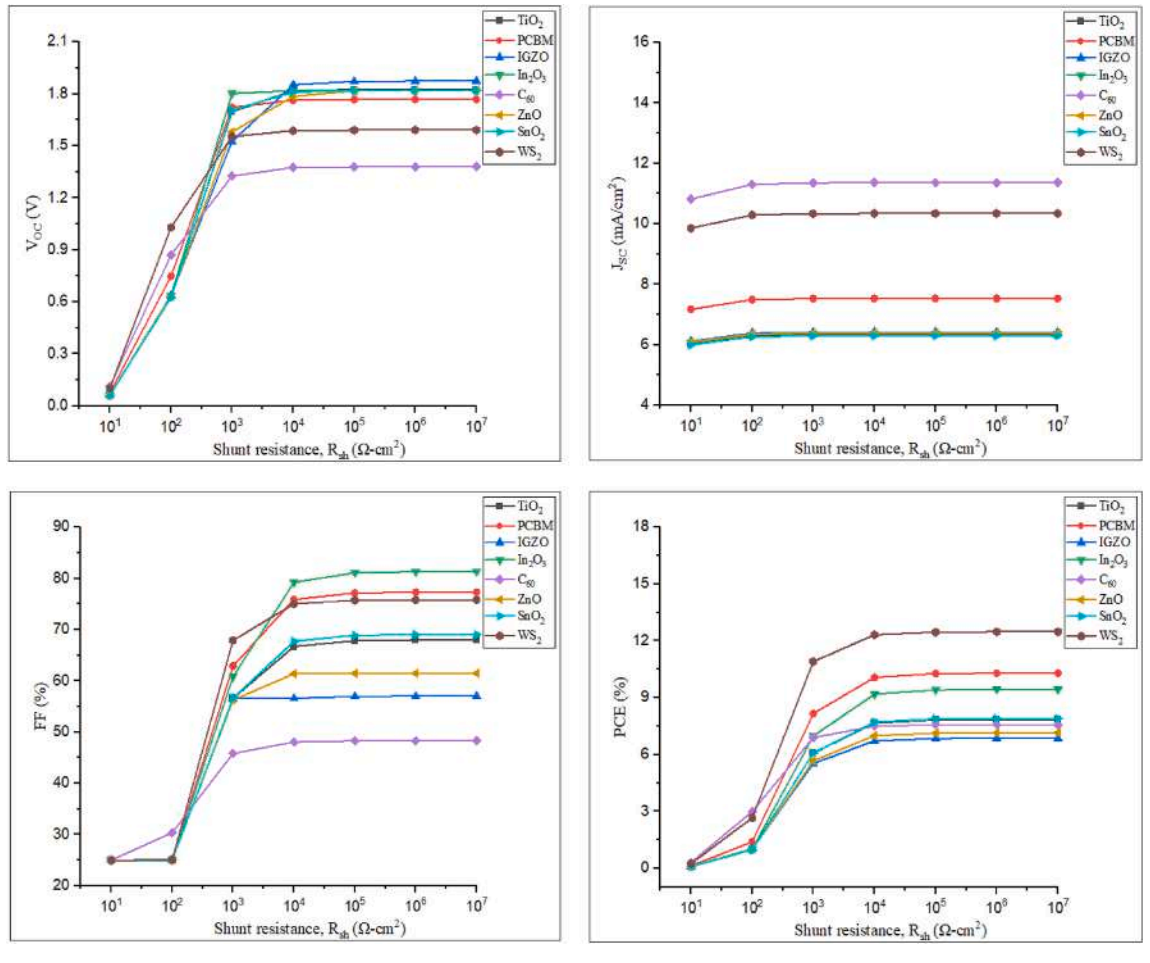


Fig. 19. Impact of R_{sh} on the performance of LaFeO3-based PSC at $R_S=0.5~\Omega\text{-cm}^2$.

When the enhancement of temperature occurs, the PCE drops significantly from 12.70 % to 10.40 % for the given range of temperature. The optimized temperature is 250 K for LaFeO3-based PSC. The value of $V_{\rm OC}$ is decreasing with rise in temperature for all ETLs. The increment in temperature results in reduced the performance of PSC owing to the saturation current and therefore the recombination rate increases [45]. The impact of operating temperature with CBTS as HTL and various ETLs on the PV parameters are shown below in Fig. 16.

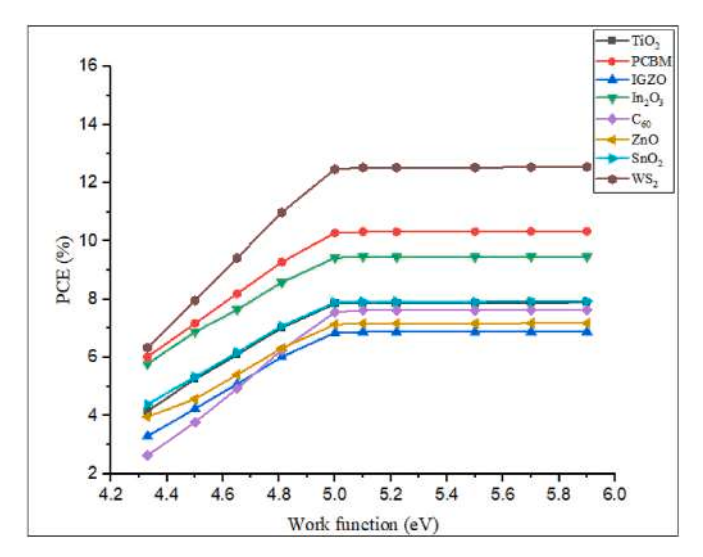


Fig. 20. Impact of various work functions on efficiency.

6.4. Impact of defect density (N_t)

The PSC performance and stability is expressively reduced at a large number of defects [46]. We have analyzed the PV parameters by varying N_t of the absorber layer from 10^{12} to 10^{17} cm⁻³. The optimized value of N_{t} is $1\times10^{13}~\text{cm}^{-3}$ for LaFeO3-based PSC at which it has achieved the maximum PCE of 12.53 %, as illustrated in Fig. 17. The PCE and J_{SC} fall sharply after $10^{15}\,\mathrm{cm}^{-3}$ due to increase in defects hence number of traps of recombination enhances [47,48]. Increase in N_t, results in decrease in short circuit current, which is lastly responsible for fall in FF of the solar devices. The device PCE decreased from 12.53 % to 9.30 % for FTO/WS2/LaFeO3/CBTS/Au heterostructure, when Nt was enhanced from 10^{12} to 10^{17} cm⁻³. Such an increasing amount of recombination resulted in a sharp decrease in PCE. The change in different PV parameters with N_t for LaFeO₃ with CBTS as HTL and different ETLs is depicted in Fig. 17. The fall in PCE is 25.89 % with an increase in value of N_t for optimized structure of LaFeO₃-based PSC. Some defect parameters of LaFeO₃ absorber layer shown below in Table 6.

6.5. Effect of series resistance (R_s)

The R_S has a significant impact on the PCE of the device specially on the FF and short circuit current (I_{SC}). With the increment in R_S , FF reduces which results in decrement in I_{SC} . Hence, devices exhibit poor performance due to large values of R_S . When solar cells are exposed to the environment, thermomechanical fatigue or cracks develop in the solder bonds depending on weather conditions. These cracks lead to an increase in the value of R_S which in turn causes a decline in the PCE [49, 50]. The value of R_S varied from 0 to 6 Ω -cm², at R_{SH} of $10^5 \Omega$ -cm². The

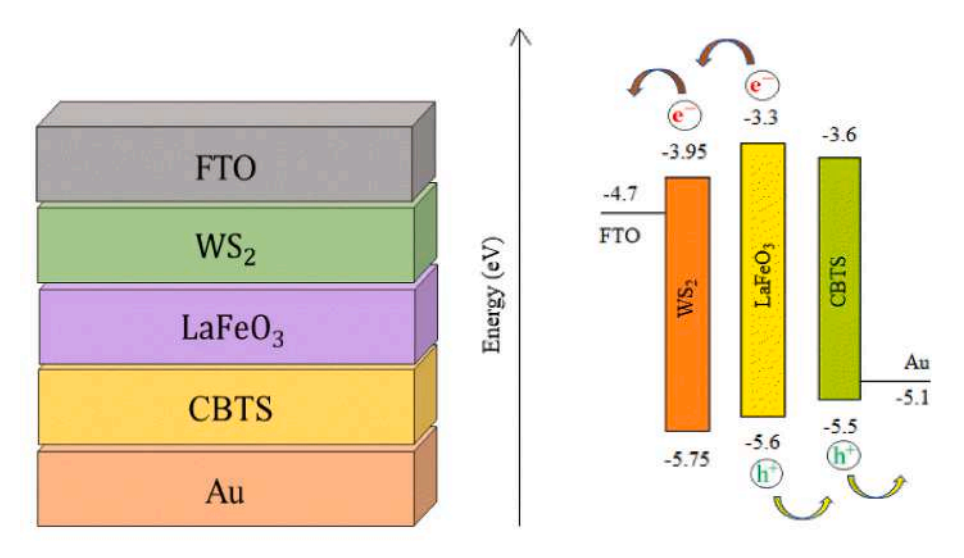
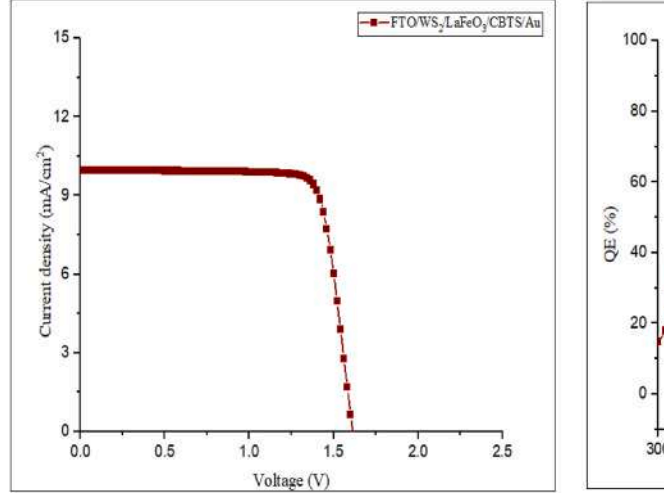


Fig. 21. Structure and band alignment diagram of optimized device.

Table 7Comparison of Experimental, SCAPS-1D and previously reported outcomes.

Parameters	SCAPS-1D	Experimental	Experimental [21]	Simulation [21]	Simulation [20]
V _{OC} (V)	1.61	0.504	0.56	0.90	1.99
J_{SC} (mA/cm ²)	9.95	5.56	0.30	0.097	6.75
FF (%)	81.17	28.31	22	8.55	67.55
PCE (%)	13.03	0.79	0.06	0.01	9.11



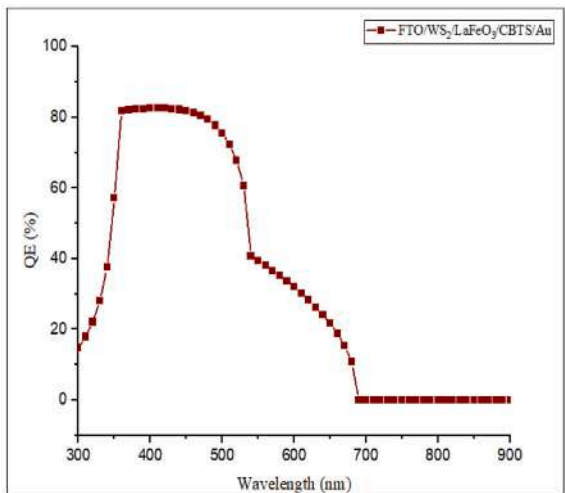


Fig. 22. J-V and QE curve of optimized device.

simulation results of change in value of R_S with PV parameters of PSC shown below in Fig. 18. The FF reduced from 76 to 72 % with an increase in value of R_S while the PCE, V_{OC} and J_{SC} were not affected in every device. The results shown in Fig. 18 are consistent with the previously reported studies [51,52]. The IGZO/LaFeO $_3$ /CBTS and $C_{60}/LaFeO_3/CBTS$ PSC configuration showed the highest V_{OC} and J_{SC} respectively whereas IGZO/LaFeO $_3$ /CBTS PSC configuration showed relatively poor performance [53].

6.6. Effect of shunt resistance (R_{SH})

The R_{SH} varied from 10^1 to $10^7~\Omega\text{-cm}^2$ at constant value of R_S of 0.5 $\Omega\text{-cm}^2$ for FTO/ETL/LaFeO_3/CBTS/Au configuration. The simulated outcome of different PV parameters shown below in Fig. 19. The J_{SC}

varied from 10.82 to 11.36 mA/cm² for FTO/C₆₀/LaFeO₃/CBTS/Au structure whereas $V_{\rm OC}$ and PCE show a significant increment from 0.103 to 1.591 V and 0.25–12.48 % respectively for FTO/WS₂/LaFeO₃/CBTS/Au configuration. The small increase in $J_{\rm SC}$ with $R_{\rm SH}$ is due to decreased currents in the shunt-resisted path. The increment in $V_{\rm OC}$ is due to enhanced value of $R_{\rm SH}$ developing more voltage across the PSC [54]. The relation of the PCE with $R_{\rm SH}$ reported in the literature [55].

6.7. Appropriate back contact

The impact of back contact on PCE of a PSC is studied. We have simulated the different back contacts with a work function (Φ) of 4.3 eV–5.9 eV [56], the range covering the most of the available back contacts. The effect of Φ on the PCE of various PSCs shown below in

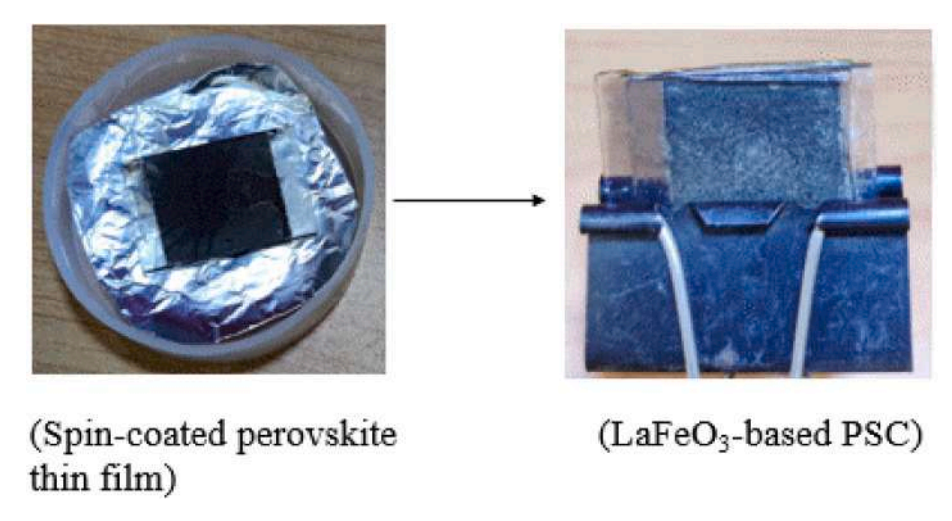


Fig. 23. Fabricated LaFeO₃ PSC.

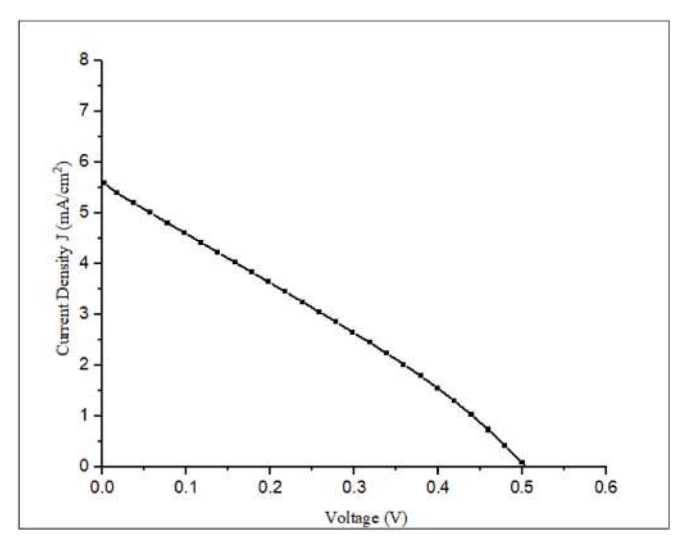


Fig. 24. J-V curve of fabricated LaFeO₃-based PSC.

Fig. 20. For the smaller value of work function, performance decreases gradually due to formation of Schottky junction. The enhancement in the PCE with Φ equal to 5.1 eV (Au) was observed. For the large value of work function, PCE remains constant, there is no chemical reaction amid the absorber layer and metal back contacts. The maximum efficiency of 13.03 % achieved at Φ of 5.1 eV (Au).

7. Experimental results comparison with previously reported results

7.1. Simulation results

The PSC structure and energy band diagram of the optimized device demonstrated below in Fig. 21. The optimum efficiency of 13.03 % with $V_{\rm OC}=1.61$ V, $J_{\rm SC}=9.952$ mA/cm², and FF of 81.17 % has been obtained. The optimized ETL and HTL are WS₂ and CBTS respectively with the Au (gold) as metal back contact. The comparison with the previously reported results illustrated in Table 7. The JV and QE curves of optimized PSC are illustrated in Fig. 22.

7.2. Experimental results

The fabricated LaFeO3 PSC and its J-V characteristics are shown

below in Figs. 23 and 24 respectively. The PV parameters of fabricated PSC is tabulated below in Table 6. One of the possible reasons for low PCE is the spin-coating process which has certain limitations. That is especially low thermal stability of the film, difficulty in fabricating an ideal multilayer structure, substrate size and shape. Typically, less than 5 % of the initial solution effectively deposits onto the substrate to create the thin film, with the remainder lost due to spinner rotation [57]. The LaFeO₃ possesses a bandgap of approximately 2.3 eV [23], which might not be sufficiently wide to prevent rapid recombination of its photogenerated electron-hole pairs which causes low performance of the device. To address this limitation, the preferred approach involves enhancing the Eg through size variation. Decreasing particle size is anticipated to elevate the bandgap, consequently restraining recombination rates. Additionally, optimizing photocatalytic performance involves creating a porous structure to enhance reaction sites. Therefore, augmenting pore density within the particles becomes crucial for maximizing efficiency [23]. LaFeO₃-based PSC still cannot be commercialized due to its weak photocatalytic performance, including issues like larger particle size and smaller surface area, reduced crystallinity from low temperature treatment and rapid charge recombination rate [58]. A 10 % doping of transition metal such as Mn, Co and Cu has potential to enhance the photocurrent of LaFeO3 which results in increase in PCE [59].

8. Conclusions

This work comprises synthesis of LaFeO3 perovskite material and simulation of LaFeO3-based PSC followed by experimental validation. The sol-gel method is employed to synthesize LaFeO₃ perovskite material. The optimization of ETL and HTL has been done to achieve the maximum PCE. The work deduced that WS2 as ETL and CBTS as HTL is most appropriate for LaFeO3 PSC. The simulated and experimentally achieved maximum PCE were 13.03 % (with $V_{OC} = 1.61 \text{ V}$, $J_{SC} = 9.952$ mA/cm^2 , and FF = 81.17 %) and 0.79 % (with $V_{OC} = 0.504 \text{ V}$, $J_{SC} =$ 5.56 mA/cm^2 , and FF = 28.31 %) respectively for the configuration of FTO/WS₂/LaFeO₃/CBTS/Au. This study also includes the optimization of various factors such as thickness of perovskite layer, operating temperature, Nt, metal back contact, series and shunt resistance. The optimized thickness of LaFeO₃ layer is 300 nm and at operating temperature of 300 K. The FTO/WS₂/LaFeO₃/CBTS/Au is the most stable structure. The optimized metal back contact is Gold (Au). These outcomes allude that the study is useful to fabricate the high performance LaFeO3-based

CRediT authorship contribution statement

Rahul Kundara: Writing – original draft, Visualization, Software, Resources, Methodology, Investigation, Formal analysis, Data curation, Conceptualization. **Sarita Baghel:** Writing – review & editing, Validation, Supervision, Project administration.

Declaration of competing interest

The authors declare that they have no known competing financial interests or personal relationships that could have appeared to influence the work reported in this paper.

Data availability

Data will be made available on request.

Acknowledgment

The author, Rahul Kundara is thankful to Delhi Technological University, New Delhi for providing a junior research fellowship. We are also very grateful to Marc Burgelman, the Electronics and Information Systems (ELIS), University of Gent, Belgium, for providing us with SCAPS-1D software.

References

- [1] S.M. Abdulrahim, Z. Ahmad, M.Q. Mehmood, S. Paek, J. Bhadra, N.J. Al-Thani, M. K. Nazeeruddin, A. Belaidi, M. Amani, Effect of illumination and applied potential on the electrochemical impedance spectra in triple cation (FA/MA/Cs) 3D and 2D/3D perovskite solar cells, J. Electroanal. Chem. 902 (2021) 115800, https://doi.org/10.1016/j.jelechem.2021.115800.
- [2] Z. Ahmad, A. Mishra, S.M. Abdulrahim, F. Touati, Electrical equivalent circuit (EEC) based impedance spectroscopy analysis of HTM free perovskite solar cells, J. Electroanal. Chem. 871 (2020) 114294, https://doi.org/10.1016/j. ielechem.2020.114294.
- [3] K. Fu, Y. He, B. Zhang, X. Gao, G. Zou, Enhanced aqueous stability and radiative-charge-transfer of CsPbBr3/Ag2S perovskite nanocrystal hybrids, J. Electroanal. Chem. 858 (2020) 113835, https://doi.org/10.1016/j.jelechem.2020.113835.
- [4] A. Alizadeh, Z. Shariatinia, Unveiling the influence of SmFeO3-TiO2 nanocomposites as high performance photoanodes of dye-sensitized solar cells, J. Mol. Liq. 348 (2022) 118070, https://doi.org/10.1016/j.molliq.2021.118070.
- [5] N. Rai, S. Rai, P.K. Singh, P. Lohia, D.K. Dwivedi, Analysis of various ETL materials for an efficient perovskite solar cell by numerical simulation, J. Mater. Sci. Mater. Electron. 31 (2020) 16269–16280, https://doi.org/10.1007/s10854-020-04175-z.
- [6] F. Moradi, Z. Shariatinia, N. Safari, E. Mohajerani, Boosted performances of mesoscopic perovskite solar cells using LaFeO3 inorganic perovskite nanomaterial, J. Electroanal. Chem. 916 (2022) 116376, https://doi.org/10.1016/j. ielechem.2022.116376.
- [7] X. Fan, Advanced progress in metal halide perovskite solar cells: a review, Mater, Today Sustain. 24 (2023) 100603, https://doi.org/10.1016/j.mtsust.2023.100603.
- [8] K. Domanski, E.A. Alharbi, A. Hagfeldt, M. Grätzel, W. Tress, Systematic investigation of the impact of operation conditions on the degradation behaviour of perovskite solar cells, Nat. Energy 3 (2018) 61–67, https://doi.org/10.1038/ s41560-017-0060-5.
- [9] D. Yang, R. Yang, S. Priya, S. Liu, Recent advances in flexible perovskite solar cells: fabrication and applications, Angew. Chem. Int. Ed. 58 (2019) 4466–4483, https://doi.org/10.1002/anie.201809781.
- [10] R. Kour, S. Arya, S. Verma, J. Gupta, P. Bandhoria, V. Bharti, R. Datt, V. Gupta, Potential substitutes for replacement of lead in perovskite solar cells: a review, Glob, Chall. 3 (2019) 1900050, https://doi.org/10.1002/gch2.201900050.
- [11] N.K. Noel, S.D. Stranks, A. Abate, C. Wehrenfennig, S. Guarnera, A.A. Haghighirad, A. Sadhanala, G.E. Eperon, S.K. Pathak, M.B. Johnston, A. Petrozza, Lead-free organic-inorganic tin halide perovskites for photovoltaic applications, Energy Environ. Sci. 7 (2014) 3061–3068, https://doi.org/10.1039/C4EE01076K.
- [12] M.G. Ju, M. Chen, Y. Zhou, H.F. Garces, J. Dai, L. Ma, N.P. Padture, X.C. Zeng, Earth-abundant nontoxic titanium (IV)-based vacancy-ordered double perovskitch halides with tunable 1.0 to 1.8 eV bandgaps for photovoltaic applications, ACS Energy Lett. 3 (2018) 297–304, https://doi.org/10.1021/acsenergylett.7b01167.
- [13] Z. Zhang, X. Li, X. Xia, Z. Wang, Z. Huang, B. Lei, Y. Gao, High-quality (CH3NH3) 3Bi2I9 film-based solar cells: pushing efficiency up to 1.64, J. Phys. Chem. Lett. 8 (2017) 4300–4307. https://doi.org/10.1021/acs.inclett.7b01952.
- [14] M. Wang, P. Zeng, S. Bai, J. Gu, F. Li, Z. Yang, M. Liu, High-quality sequential-vapor-deposited Cs2AgBiBr6 thin films for lead-free perovskite solar cells, Sol. RRL 2 (2018) 1800217, https://doi.org/10.1002/solr.201800217.
 [15] D. Çoban Özkan, A. Türk, E. Çelik, Synthesis and characterizations of sol–gel
- [15] D. Çoban Ozkan, A. Türk, E. Çelik, Synthesis and characterizations of sol–gel derived LaFeO3 perovskite powders, J. Mater. Sci. Mater. Electron. 31 (2020) 22789–22809, https://doi.org/10.1007/s10854-020-04803-8.

- [16] K.R. Nagavenkatesh, C. Sambathkumar, M. Murugesan, P. Devendran, N. Nallamuthu, P. Lakshmanan, A. Shameem, Review on the recent improvements in lanthanum ferrite perovskites for visible light driven textile dyes degradation and its various hetero-junctions catalysis mechanism, J. Ind. Eng. Chem. (2024), https://doi.org/10.1016/j.jiec.2024.02.024.
- [17] S.L. Yu, M. Wang, E. Ye, S. Lei, J. Liu, G. Liu, G. Qiao, Synergistic enhancement of optical properties in Ca/Ni co-doped LaFeO3 perovskite coatings enabling high-temperature photothermal conversion, Appl. Surf. Sci. 642 (2024) 158595, https://doi.org/10.1016/j.apsusc.2023.158595.
- [18] M. Sabir, N. AlMasoud, M. Ramzan, M. Aamir, S.R. Ejaz, T.S. Alomar, Z.M. El-Bahy, M.A. Salam, S.M. Albukhari, D.F. Baamer, Rare earth and transition metal codoped LaFeO3 perovskite and its CNTs reinforced nanohybrid for environmental remediation application, Ceram. Int. 49 (2023) 20939–20950, https://doi.org/ 10.1016/j.ceramint.2023.03.227.
- [19] S. Bai, B. Shi, L. Ma, P. Yang, Z. Liu, D. Li, A. Chen, Synthesis of LaFeO3 catalytic materials and their sensing properties, Sci. China, Ser. B: Chem. 52 (2009) 2106–2113, https://doi.org/10.1007/s11426-009-0289-3.
- [20] M.K. Das, S. Panda, N. Mohapatra, Power conversion efficiency optimization of LaFeO3 Mott insulator based solar cell with metal oxide transport layers using SCAPS, Mater Today Proc 74 (2023) 756–762, https://doi.org/10.1016/j. matpr.2022.11.031.
- [21] L.N. Moghadam, Z.R. Ranjbar, Cost-efficient solar cells using nanocrystalline perovskite La (Fe and Mn) O3 and candle soot: theory and experiment, J. Alloys Compd. 785 (2019) 117–124, https://doi.org/10.1016/j.jallcom.2019.01.068.
- [22] R. Chakraborty, K.M. Sim, M. Shrivastava, K.V. Adarsh, D.S. Chung, A. Nag, Colloidal synthesis, optical properties, and hole transport layer applications of Cu2BaSnS4 (CBTS) nanocrystals, ACS Appl. Energy Mater. 2 (2019) 3049–3055, https://doi.org/10.1021/acsaem.9b00473.
- [23] W. Azouzi, W. Sigle, H. Labrim, M. Benaissa, Sol-gel synthesis of nanoporous LaFeO3 powders for solar applications, Mater. Sci. Semicond. Process. 104 (2019) 104682, https://doi.org/10.1016/j.mssp.2019.104682.
- [24] W. Zheng, R. Liu, D. Peng, G. Meng, Hydrothermal synthesis of LaFeO3 under carbonate-containing medium, Mater. Lett. 43 (2000) 19–22, https://doi.org/ 10.1016/S0167-577X(99)00223-2.
- [25] M. Romero, R.W. Gómez, V. Marquina, J.L. Pérez-Mazariego, R. Escamilla, Synthesis by molten salt method of the AFeO3 system (A=La, Gd) and its structural, vibrational and internal hyperfine magnetic field characterization, Physica B Condens Matter 443 (2014) 90–94, https://doi.org/10.1016/j. physb.2014.03.024.
- [26] N. Sharma, H.S. Kushwaha, S.K. Sharma, K. Sachdev, Fabrication of LaFeO3 and rGO-LaFeO3 microspheres based gas sensors for detection of NO2 and CO, RSC Adv. 10 (2020) 1297–1308, https://doi.org/10.1039/c9ra09460a.
- [27] X. Ren, H. Yang, S. Gen, J. Zhou, T. Yang, X. Zhang, Z. Cheng, S. Sun, Controlled growth of LaFeO3 nanoparticles on reduced graphene oxide for highly efficient photocatalysis, Nanoscale 8 (2016) 752–756, https://doi.org/10.1039/ c5nr06338h.
- [28] H. Bencherif, L. Dehimi, N. Mahsar, E. Kouriche, F. Pezzimenti, Modeling and optimization of CZTS kesterite solar cells using TiO2 as efficient electron transport layer, Mater. Sci. Eng. B. 276 (2022) 115574, https://doi.org/10.1016/j. mseb 2021 115574
- [29] A.A. Kanoun, M.B. Kanoun, A.E. Merad, S. Goumri-Said, Toward development of high-performance perovskite solar cells based on CH3NH3Gel3 using computational approach, Sol. Energy 182 (2019) 237–244, https://doi.org/ 10.1016/j.solener.2019.02.041.
- [30] K. Deepthi Jayan, V. Sebastian, Comprehensive device modelling and performance analysis of MASnI3 based perovskite solar cells with diverse ETM, HTM and back metal contacts, Sol. Energy 217 (2021) 40–48, https://doi.org/10.1016/j. solener 2021 01 058
- [31] A. Raj, M. Kumar, H. Bherwani, A. Gupta, A. Anshul, Evidence of improved power conversion efficiency in lead-free CsGel 3 based perovskite solar cell heterostructure via scaps simulation, J. Vac. Sci. Technol. B. 39 (2021) 012401, https://doi.org/10.1116/6.0000718.
- [32] A. Husainat, W. Ali, P. Cofie, J. Attia, J. Fuller, Simulation and Analysis of Methylammonium Lead Iodide (CH3NH3PbI3) Perovskite Solar Cell with Au Contact Using SCAPS 1D Simulator, vol. 7, American Journal of Optics and Photonics, 2019, pp. 33–40, https://doi.org/10.11648/j.ajop.20190702.12.
- [33] S. Bhattarai, T.D. Das, Optimization of carrier transport materials for the performance enhancement of the MAGeI3 based perovskite solar cell, Sol. Energy 217 (2021) 200–207, https://doi.org/10.1016/j.solener.2021.02.002.
- [34] H. Bencherif, M.K. Hossain, Design and numerical investigation of efficient (FAPbI3) 1- x (CsSnI3) x perovskite solar cell with optimized performances, Sol. Energy 248 (2022) 137–148, https://doi.org/10.1016/j.solener.2022.11.012.
- [35] U. Mandadapu, Simulation and analysis of lead based perovskite solar cell using SCAPS-1D, Indian J. Sci. Technol. 10 (2017) 1–8, https://doi.org/10.17485/ijst/ 2017/v11i10/110721.
- [36] F. Azri, A. Meftah, N. Sengouga, A. Meftah, Electron and hole transport layers optimization by numerical simulation of a perovskite solar cell, Sol. Energy 181 (2019) 372–378, https://doi.org/10.1016/j.solener.2019.02.017.
- [37] S. Mushtaq, S. Tahir, A. Ashfaq, R. Sebastian Bonilla, M. Haneef, R. Saeed, W. Ahmad, N. Amin, Performance optimization of lead-free MASnBr3 based perovskite solar cells by SCAPS-1D device simulation, Sol. Energy 249 (2023) 401–413, https://doi.org/10.1016/j.solener.2022.11.050.
- [38] M.K. Hossain, G.F.I. Toki, A. Kuddus, M.H.K. Rubel, M.M. Hossain, H. Bencherif, M.F. Rahman, M.R. Islam, M. Mushtaq, An extensive study on multiple ETL and HTL layers to design and simulation of high-performance lead-free CsSnCl3-based

- perovskite solar cells, Sci. Rep. 13 (2023) 2521, https://doi.org/10.1038/s41598-023-28506-2
- [39] N. Lakhdar, A. Hima, Electron transport material effect on performance of perovskite solar cells based on CH3NH3GeI3, Opt. Mater. 99 (2020) 109517, https://doi.org/10.1016/j.optmat.2019.109517.
- [40] M. Singh, R. Singh, V. Kumar, V. Singh, Investigation of CH3NH3PbI3 and CH3NH3SnI3 based perovskite solar cells with CuInSe2 nanocrystals, Optik 246 (2021) 167839, https://doi.org/10.1016/j.ijleo.2021.167839.
- [41] I. Montoya De Los Santos, H.J. Cortina-Marrero, M.A. Ruíz-Sánchez, L. Hechavarría-Difur, F.J. Sánchez-Rodríguez, M. Courel, H. Hu, Optimization of CH3NH3PbI3 perovskite solar cells: a theoretical and experimental study, Sol. Energy 199 (2020) 198–205, https://doi.org/10.1016/j.solener.2020.02.026.
- [42] H. Bencherif, F. Meddour, M.H. Elshorbagy, M.K. Hossain, A. Cuadrado, M.A. Abdi, T. Bendib, S. Kouda, J. Alda, Performance enhancement of (FAPbI3) 1-x (MAPbBr3) x perovskite solar cell with an optimized design, Micro Nanostructures 171 (2022) 207403, https://doi.org/10.1016/j.micrna.2022.207403.
- [43] A. Kuddus, M.F. Rahman, S. Ahmmed, J. Hossain, A.B.M. Ismail, Role of facile synthesized V2O5 as hole transport layer for CdS/CdTe heterojunction solar cell: validation of simulation using experimental data, Superlattices Microstruct 132 (2019) 106168, https://doi.org/10.1016/j.spmi.2019.106168.
- [44] M.K. Hossain, A.A. Arnab, R.C. Das, K.M. Hossain, M.H.K. Rubel, M.F. Rahman, H. Bencherif, M.E. Emetere, M.K.A. Mohammed, R. Pandey, Combined DFT, SCAPS-1D, and wxAMPS frameworks for design optimization of efficient Cs2BiAgl6-based perovskite solar cells with different charge transport layers, RSC Adv. 12 (2022) 35002–35025, https://doi.org/10.1039/d2ra06734j.
- [45] S. Ahmed, F. Jannat, M.A.K. Khan, M.A. Alim, Numerical development of ecofriendly Cs2TiBr6 based perovskite solar cell with all-inorganic charge transport materials via SCAPS-1D, Optik 225 (2021) 165765, https://doi.org/10.1016/j. iileo.2020.165765.
- [46] S. Rai, B.K. Pandey, D.K. Dwivedi, Modeling of highly efficient and low cost CH3NH3Pb(I1-xClx)3 based perovskite solar cell by numerical simulation, Opt. Mater. 100 (2020) 109631, https://doi.org/10.1016/j.optmat.2019.109631.
- [47] M.B. Johnston, L.M. Herz, Hybrid perovskites for photovoltaics: charge-carrier recombination, diffusion, and radiative efficiencies, Acc. Chem. Res. 49 (2016) 146–154, https://doi.org/10.1021/acs.accounts.5b00411.
- [48] H. Bencherif, Towards a high efficient Cd-free double CZTS layers kesterite solar cell using an optimized interface band alignment, Sol. Energy 238 (2022) 114–125, https://doi.org/10.1016/j.solener.2022.04.040.
- [49] M.S. Islam, K. Sobayel, A. Al-Kahtani, M.A. Islam, G. Muhammad, N. Amin, M. Shahiduzzaman, M. Akhtaruzzaman, Defect study and modelling of SnX3-based

- perovskite solar cells with SCAPS-1D, Nanomaterials 11 (2021) 1218, https://doi.org/10.3390/nano11051218.
- [50] K. Poorkazem, D. Liu, T.L. Kelly, Fatigue resistance of a flexible, efficient, and metal oxide-free perovskite solar cell, J Mater Chem A Mater 3 (2015) 9241–9248, https://doi.org/10.1039/c5ta00084j.
- [51] E. Danladi, A.C. Egbugha, R.C. Obasi, N.N. Tasie, C.U. Achem Cu, I.S. Haruna, L. O. Ezeh, Defect and doping concentration study with series and shunt resistance influence on graphene modified perovskite solar cell: a numerical investigation in SCAPS-1D framework, J. Indian Chem. Soc. 100 (2023) 101001, https://doi.org/10.1016/j.jics.2023.101001.
- [52] S. Karthick, S. Velumani, J. Bouclé, Experimental and SCAPS simulated formamidinium perovskite solar cells: a comparison of device performance, Sol. Energy 205 (2020) 349–357, https://doi.org/10.1016/j.solener.2020.05.041.
- [53] H. Heriche, Z. Rouabah, N. Bouarissa, New ultra thin CIGS structure solar cells using SCAPS simulation program, Int. J. Hydrogen Energy 42 (2017) 9524–9532, https://doi.org/10.1016/j.ijhydene.2017.02.099.
- [54] A.K. Sharma, N.K. Chourasia, P.K. Jha, R. Kumar, M. Kumar, R.K. Chourasia, Characteristic features and performance investigations of a PTB7:PC71BM/PFN:Br pure organic solar cell using SCAPS-1D, J. Electron. Mater. 52 (2023) 4302–4311, https://doi.org/10.1007/s11664-022-10202-y.
- [55] P.K. Jha, N.K. Chourasia, A.K. Sharma, R.K. Chourasia, Optimization of electrical properties for performance analysis of p-Si/n-CdS/ITO heterojunction photovoltaic cell, Mater Today Proc 67 (2022) 620–624, https://doi.org/10.1016/j. matpr.2022.05.577.
- [56] G. Pindolia, S.M. Shinde, P.K. Jha, Non-leaded, KSnI3 based perovskite solar cell: a DFT study along with SCAPS simulation, Mater. Chem. Phys. 297 (2023) 127426, https://doi.org/10.1016/j.matchemphys.2023.127426.
- [57] R. Nistico, D. Scalarone, G. Magnacca, Sol-gel chemistry, templating and spin-coating deposition: a combined approach to control in a simple way the porosity of inorganic thin films/coatings, Micropor Mesopor Mat 248 (2017) 18–29, https://doi.org/10.1016/j.micromeso.2017.04.017.
- [58] M. Humayun, H. Ullah, M. Usman, A. Habibi-Yangjeh, A.A. Tahir, C. Wang, W. Luo, Perovskite-type lanthanum ferrite based photocatalysts: preparation, properties, and applications, J. Energy Chem. 66 (2022) 314–338, https://doi.org/ 10.1016/j.jechem.2021.08.023.
- [59] Q. Peng, B. Shan, Y. Wen, R. Chen, Enhanced charge transport of LaFeO3 via transition metal (Mn, Co, Cu) doping for visible light photoelectrochemical water oxidation, Int. J. Hydrog. Energy. 40 (2015) 15423–15431, https://doi.org/ 10.1016/j.ijhvdene.2015.09.072.

ELSEVIER

Contents lists available at ScienceDirect

Materials Science & Engineering B

journal homepage: www.elsevier.com/locate/mseb



Predictive design of KSnI₃-based perovskite solar cells using SCAPS and machine learning model

Rahul Kundara*, Sarita Baghel

Department of Applied Physics, Delhi Technological University, Delhi, India

ARTICLE INFO

Keywords: KSnI₃-based PSC SCAPS-1D Machine learning and HTLs

ABSTRACT

The commercial application of lead (Pb)-based Perovskite Solar Cells (PSCs) are restrained due to its toxicity. In this work, we have investigated potassium tin iodide (KSnI $_3$) which is a potential candidate for non-lead PSC. The SCAPS-1D simulation is employed to examine the effect of several Hole Transport Layers (HTLs) as follow: Spiro-OMeTAD, CuI, CuSCN, Cu $_2$ O, PEDOT: PSS, CdTe, MASnBr $_3$, CFTS on the performance of KSnI $_3$ -based PSCs. The impact of layer thickness, doping density (N $_4$) and defect density (N $_5$) has been analyzed. We have a trained Machine learning model to predict the performance matrices of PSCs. We have obtained a maximum efficiency of 23.08 % at the thickness of the KSnI $_3$ absorber layer of 550 nm and N $_5$ of 10^{13} cm $^{-3}$. The ML model predicts the performance matrices of examined PSC with accuracy of \sim 89 %. Hence, the FTO/WS $_2$ /KSnI $_3$ /PEDOT: PSS/Au configuration is most suitable to manufacture highly efficient PV devices.

1. Introduction

Utilizing solar cells for solar energy harvesting presents a commendable approach mitigating concerns about global warming. The photovoltaic effect converts incident sunlight into electrical energy. In 2009, Perovskite solar cell (PSC) was reported with an efficiency of 3.8 % and has achieved maximum power conversion efficiency (PCE) of greater than 26 % till now [1]. It became popular among the scientific community due to its promising attributes such as tunable bandgap (Eg), high absorption coefficient, high carrier mobility, low manufacturing cost and high PCE or efficiency [2,3]. Perovskite material has an ABX3 structure (where A is an organic or inorganic cation, B is an inorganic metal cation and X is halogen anion) [4]. Despite the high performance of lead (Pb) based PSC, its instability due to rapid oxidation of Pb cation and toxic nature restricted its commercialization [5]. There is a need for alternative perovskite materials that are both less toxic and environmentally friendly while also having the potential to deliver exhibit good photovoltaic (PV) outcomes [6]. Hence there have been various investigations to replace hazardous Pb ions with other alternatives such as Sn [7], Ge [8], Bi [9], Sb [10] and Ag [11]. The tin (Sn) is a suitable choice due to comparable ionic radii and the phenomenal semiconducting properties of APbX₃. The study comprises investigation of KSnI₃ as a perovskite material which is used as an absorber in a PSC. In past reported investigations there is very limited study on KSnI₃ PSC.

Grishma et al. (2023) have reported efficiency of 9.77 % [12]. So there needs to be proper optimization to enhance the efficiency of PSC. Whereas, in this work we have obtained a maximum PCE of 23.08 %. The SCAPS enabled machine learning model is used to optimize and predict the best efficiency [13]. It has been exhibited that ML is helpful in forecasting the design and performance of PSCs [14]. Firstly, we have simulated KSnI₃-based PSC with several HTLs (Spiro-OMeTAD, CuI, CuSCN, Cu₂O, PEDOT: PSS, CdTe, MASnBr₃ and CFTS) and KSnI₃ is employed as a perovskite absorber layer. Secondly, we have optimized the effect of distinct performance parameters of PSCs such as absorber layer thickness, defect density (Nt) and doping density (NA). Ultimately, we trained an ML model to predict the performance parameters of the PSCs with an accuracy of approximately 89 %. The present method serves as a sturdy foundation for subsequent research and investigations driven by artificial intelligence (AI). The efficient PSCs can be designed with application of ML modelling and SCAPS-1D assisted by previous studies.

2. Device architecture and methods

The PSC consists of KSnI $_3$ absorber material with layer architecture: FTO/ETL/Perovskite layer/HTL/Back-contact depicted in Fig. 1. All the input data used in SCAPS simulation obtained from experimental and theoretical work enclosed is in Table 1 for FTO/TiO $_2$ /KSnI $_3$ /Spiro-

E-mail address: rahul_2k20phdap10@dtu.ac.in (R. Kundara).

^{*} Corresponding author.

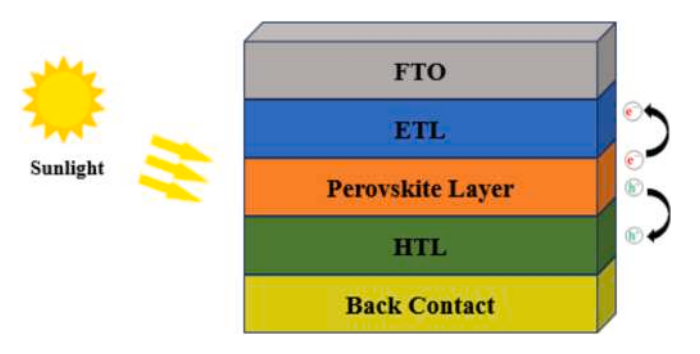


Fig. 1. Architecture of simulated PSCs.

Table 1 Input parameters of simulated PSC.

Parameter	FTO [15,16]	WS ₂ [17]	KSnI ₃ [12]	Spiro-OMeTAD [18,19]
Thickness (nm)	400	100*	300	50
Eg (eV)	3.5	1.8	1.84	3.0
χ (eV)	4.0	3.95	3.44	2.45
ε	9.0	13.6	10.4	3.0
N_C (cm ⁻³)	2.02×10^{18}	1×10^{18}	2.2×10^{18}	1×10^{19}
$N_V (cm^{-3})$	1.8×10^{19}	2.4 ×	1.8×10^{19}	1×10^{19}
μ_n (cm ² /Vs)	20	10 ¹⁹ 100	21.28	1×10^{-4}
μ_p (cm ² /Vs)	10	100	19.46	$1 imes 10^{-4}$
N_D (cm ⁻³)	2×10^{19}	$1 imes 10^{18}$	1×10^{15}	0
N_A (cm ⁻³)	0	0	1×10^{15}	2×10^{18}
$N_t (cm^{-3})$	1×10^{15}	$1\times10^{13^{\ast}}$	1×10^{13}	1×10^{14}

OMeTAD/Au-Metal and HTLs in Table 2.

2.1. SCAPS-1D

The data of different parameters are chosen from previous studies. The SCAPS-1D (version 3.3.10) has been employed for simulation. This software can be used for simulations at different input physical conditions. This tool calculation is dependent on Poisson's and continuity equations. It can calculate Quantum efficiency (QE), J-V curve and carrier lifetime for both electrons (e's) and holes (h⁺s).

$$\frac{\partial^2 \psi}{\partial x^2} + \frac{q}{\epsilon} [p(x) - n(x) + N_D - N_A + \rho_p - \rho_n = 0$$
 (1)

$$\frac{1}{q}\frac{dJ_p}{dx} = G_{op}(x) - R(x) \tag{2}$$

$$\frac{1}{q}\frac{dJ_n}{dx} = -G_{op}(x) + R(x) \tag{3}$$

The simulations were run at 300 K using a "air mass 1.5 global" spectrum and a light power of 1000 W/m^2 . The work is dependent on change in thickness, N_{t} , and N_{A} at which simulation of the proposed PSC has been done. The outcome of the device has been reflected by the I–V characteristics which represent the following PV parameters: J_{SC} , FF, V_{OC} , and PCE. The simulation procedure is depicted in Fig. 2.

2.2. Machine learning

Python was chosen as the programming language for implementing machine learning (ML) due to its widespread use in AI applications [27–29]. To work with the dataset, Numpy and Pandas libraries were utilized. The dataset pertains to solar cell features and was thoroughly cleaned and preprocessed to make it compatible with ML algorithms. Initially, a simple Random Forest algorithm from Scikit-Learn (Sklearn) was employed to determine the significance of each feature for the final model. As a result of this phase, eleven features were selected for further analysis. For feature extraction related to composition of perovskites, Pymatgen and Matminer packages were utilized. The data was then split

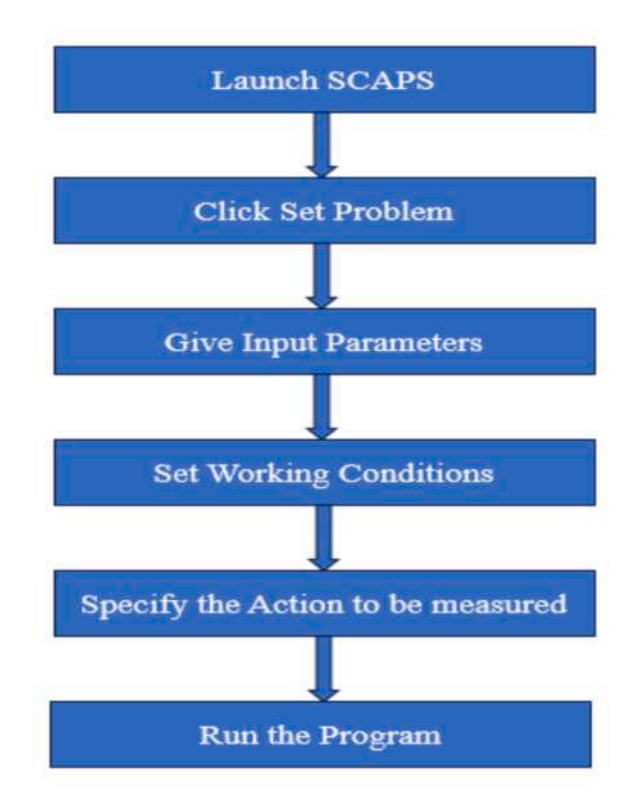


Fig. 2. SCAPS-1D simulation procedure.

Table 2
Input parameters of distinct HTLs.

1 1							
Parameter	CuI [18,19]	CuSCN [19,20]	Cu ₂ O [15,19,21]	PEDOT: PSS [19,22,23]	CdTe [19,24]	MASnBr ₃ [6,19,25]	CFTS [19,26]
Thickness (nm)	50	50	50	50	50	50	50
Eg (eV)	3.1	3.4	2.17	2.2	1.5	2.15	1.3
χ (eV)	2.1	1.9	3.2	2.9	3.9	3.39	3.3
ε	6.5	10	7.11	3.0	9.4	8.2	9.0
N_C (cm ⁻³)	2.8×10^{19}	2.2×10^{19}	2.02×10^{17}	2.2×10^{15}	8.0×10^{17}	1×10^{18}	2.2×10^{18}
$N_V (cm^{-3})$	1×10^{19}	1.8×10^{18}	1.1×10^{19}	1.8×10^{18}	1.8×10^{19}	1×10^{18}	1.8×10^{19}
μ_n (cm ² /Vs)	100	1×10^{-4}	200	1×10^{-2}	3.2×10^2	1.6	21.98
μ_p (cm ² /Vs)	80	1×10^{-2}	80	2×10^{-4}	40	1.6	21.98
$N_D (cm^{-3})$	0	0	0	0	0	0	0
$N_A (cm^{-3})$	1×10^{18}	1×10^{16}	1×10^{18}	1×10^{19}	$2 imes 10^{14}$	1×10^{18}	1×10^{18}
N_t (cm ⁻³)	1×10^{14}	$1\times10^{14^*}$	1×10^{14}	$1 imes 10^{14}$	$1\times10^{14^*}$	$1\times10^{14^{\ast}}$	$1\times10^{14^{*}}$

into training and testing sets for model training. To find the best hyperparameters, two distinct approaches were taken. First a parameter grid (a Python dictionary) inclusive various values for each parameter was prepared. The RandomizedSearchCV and GridSearchCV tools from Scikit-Learn were employed to assess the optimal combination of hyperparameters from this grid. The RandomizedSearchCV randomly selected combinations from the grid and evaluated their performance using cross-validation, while the GridSearchCV evaluated every possible combination of the provided parameters. To ensure the model's performance and consistency, five-fold cross-validation was performed on the final model. Subsequently, a separate test set was used to assess the model's accuracy and overall performance. Random Forest's ability to aggregate the results of individual decision trees helped mitigate overfitting issues and improved the model's predictive performance [30]. Overfitting occurs when a model becomes too tailored to the training data, resulting in high variance and poor predictive performance on the test set. To mitigate overfitting, various techniques can be applied, such as comparing the prediction results between the training and test sets. Several approaches can be used, including increasing the number of decision trees and reducing their maximum depth. The prediction's coefficient of determination acted as the evaluation metric. According to the Sklearn, this metric exhibited as is defined as:

 $R^2 = \left(1 - \frac{u}{v}\right)$ (4).u represent the residual sum of squares ($(y_{pred} - y_{true})^2$). Meanwhile, v stands for the total sum of squares = ($(y_{pred} - mean (y_{true}))^2$. It's worth noting that a constant model that solely predicts the anticipated y, irrespective of input, could obtain a score of R^2 equal to 0.0. The significance of a node j within a single decision tree, the calculation involved as follows [30]:

$$ni_{j} = w_{j}C_{j} - w_{left(j)}Cleft(j) - w_{right(j)}C_{right(j)}$$
(5)

where w_j denotes the weighted number of samples in node j as a fraction of the total weighted number of samples. C_j represents the impurity in node j and left (j) and right (j) corresponds to the child nodes associated with it. The following calculation is used to determine feature's importance [30]:

$$\mathrm{fi_{i}} = \frac{\sum_{j:nodejsplitsonfeaturet} n_{i_{j}}}{\sum_{j\in allnodes} n_{i_{j}}} \tag{6}$$

Ultimately, the feature values were calculated as the mean of every particular decision tree.

3. Results and discussion

3.1. HTL

The HTL exhibits an important role in optimization of PSC performance via two ways such as it transports the light generated holes towards the back contact and HTL hampers the interaction between absorber layer and back contact. Despite the comprehensive application of Spiro-OMeTAD into PSC to increase PCE, low hole mobility (μ_p) , and environment instability confined its commercial application. Consequently, various kinds of HTLs like CuI, CuSCN, Cu2O, PEDOT: PSS, CdTe, MASnBr₃ and CFTS have been analyzed shown in Table 2. To begin the simulation, a PSC architecture of FTO/TiO2/KSnI3/Spiro-OMeTAD/Au was simulated to validate with previously reported results [8]. WS₂ opted as ETL due to its high electron mobility (μ_n), wide range of E_g , and high conductivity of $10^{-3} \Omega^{-1} \text{ cm}^{-1}$ [31]. The validation of the simulated result shown below in Table 3. The highest occupied molecular orbital (HOMO) of HTL should be appropriately aligned with that of the perovskite layer. The proper optimization is required to select appropriate ETL and HTL to maximize the performance of the PSC. The energy bandgap diagram of ETL, absorber layer and various HTLs illustrated below in Fig. 3. The J-V and QE plots of PSC with various HTLs are shown below in Fig. 4. The plotted curve from simulations is

 Table 3

 Comparison with previously reported results.

Cell structure	V _{OC} (V)	J_{SC} (mA/cm ²)	FF (%)	PCE (%)
FTO/TiO ₂ /KSnI ₃ /Spiro- OMeTAD/W	1.70	15.85	36.13	9.77 [8]
FTO/C ₆₀ /KSnI ₃ /PTAA/C	0.76	17.44	80.80	10.83 [32]
$ FTO/TiO_2/KSnI_3/\ Spiro-OMeTAD/Au $	1.48	13.20	79.07	15.55 [This work]

well-fitted with the previously reported outcomes, which validates numerical simulations.

To examine the impact of the several HTLs like Spiro-OMeTAD, CuI, CuSCN, Cu $_2$ O, PEDOT: PSS, CdTe, MASnBr $_3$ and CFTS on the PV parameters of PSC. The thickness of HTLs was 50 nm throughout the simulation. The simulated results are demonstrated in Fig. 4. The PV parameters with several HTLs are presented below in Table 4.

The Spiro-OMeTAD and PEDOT: PSS both are organic materials. The $E_{\mbox{\tiny g}}$ for Spiro-OMeTAD is 3 eV and for PEDOT: PSS is 2.2 eV depicted in table 1 and 2. The PEDOT: PSS has excellent properties such as high electrical conductivity, mechanical flexibility and suitable for thin film formation [33]. The simulation results demonstrated that KSnI₃-based PSC exhibited maximum PCE of 21.08 % (with Voc of 1.59 V, Jsc of 15.08 mA/cm² and FF of 87.43 %) for WS₂ as ETL and PEDOT: PSS employed as HTL. The HOMO level of Spiro-OMeTAD and PEDOT: PSS has good band alignment with KSnI3 therefore with PEDOT: PSS it has achieved maximum PCE but not for Spiro-OMeTAD. This can be attributed to lower hole mobility (μ_p) than PEDOT: PSS [34,35]. Hence, PEDOT: PSS is an appropriate HTL for achieving high PCE. Furthermore, the PEDOT: PSS exhibits good stability in air over Spiro-OMeTAD so that it has wide application in PSCs. Zuo et al. (2017) doped PEDOT: PSS with polymer electrolyte PSS-Na which results in high work function and good band alignment of modified PEDOT: PSS with the absorber layer. Hence, enhanced PCE has been obtained from 12.35 % to 15.56 % [36]. The small amount of 2,3,5,6-tetrafluoro-7,7,8,8-tetracyanoquinodimethane (F4-TCNQ) added to PEDOT: PSS could improve the electrical conductivity and better band matching with the absorber layer. Therefore, the PCE enhanced from 13.30 % to 17.22 % [37,38].

3.2. Optimization of HTL

3.2.1. Impact of thickness

In the preceding section, Table 4 highlighted that PEDOT: PSS emerges as the most promising HTL for KSnI3-based PSC. As the attributes of HTL, such as thickness, doping density (NA), and defect density (N_t), exert a substantial influence on PSC performance and these parameters must be optimized. Notably, HTL thickness exhibits a vital role in facilitating efficacious carrier transport and controlling the recombination rate [39]. Consequently, the thickness of an HTL is optimized to get high PCE. Fig. 5a, b demonstrates the impact of PEDOT: PSS thickness on the J_{SC} and V_{OC} of PSCs. The findings reveal that increasing PEDOT: PSS thickness up to 250 nm enhances both J_{SC} and V_{OC}, beyond which they become constant. According to experimental surveys, thicker HTLs yields smoother film surfaces, reducing interfacial recombination and thus enhancing Voc. The suitable HTL thickness is required to avoid series resistance (R_S) for thicker layers [40,41]. Firstly, a thinner HTL might not accumulate a sufficient number of holes. Secondly, the region among the absorber layer and a thin HTL might not be as potent as in thicker layers, leading to inadequate driving force for carrier partition. The study also indicates that when HTL thickness exceeds 250 nm both V_{OC} and J_{SC} tend to be constant. This is primarily due to carrier travel distance to reach the interface. Consequently, traps promote non-radiative Shockley-Read-Hall (SRH) recombination and enhanced trap-assisted recombination rate [42]. The influence of thickness on PV parameters is depicted in Fig. 5. The initial fall in the

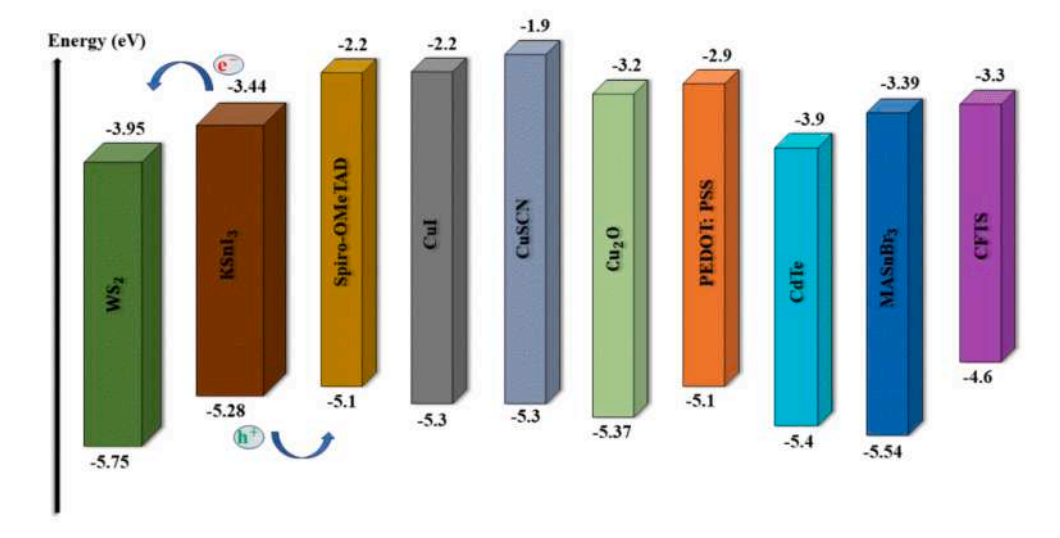


Fig. 3. Energy band diagram of various HTLs.

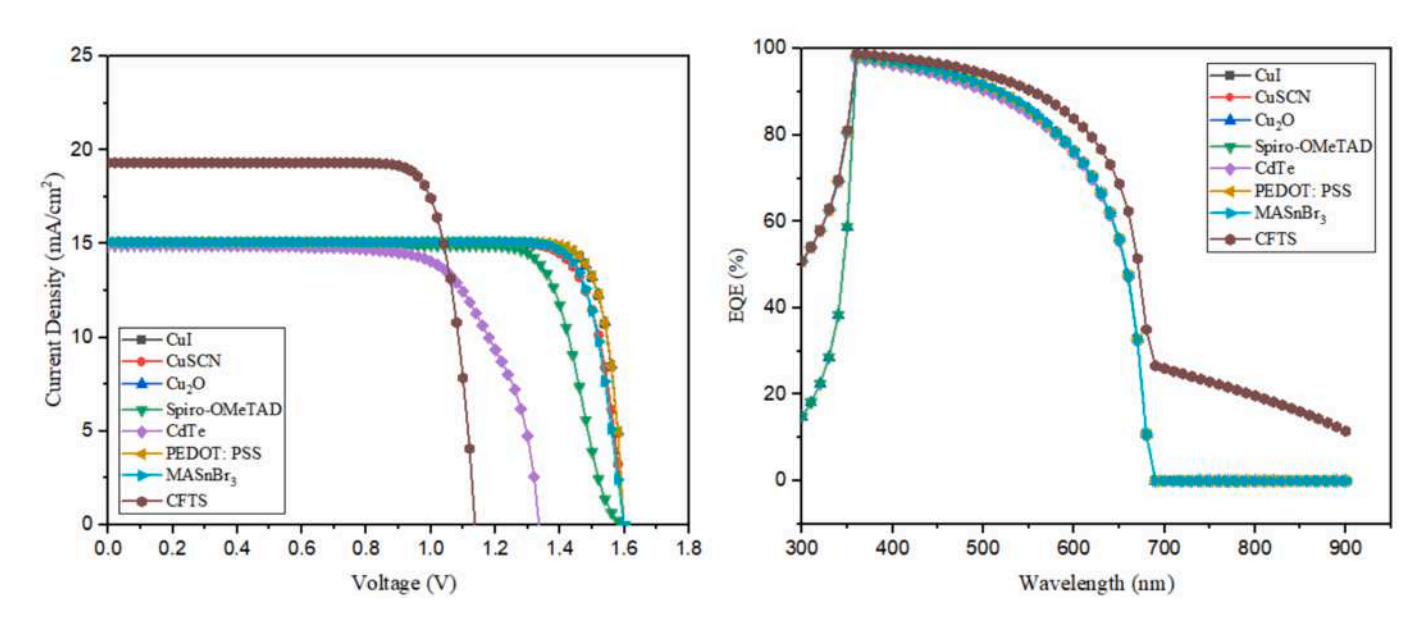


Fig. 4. (a) J-V and (b) QE plots of simulated PSCs with various HTLs.

Table 4
The PV parameters of KSnI₃-based PSC with distinct HTLs.

V _{OC} (V)	J _{SC} (mA/ cm ²)	FF (%)	PCE (%)
1.59	15.01	87.40	20.98
1.59	15.01	84.48	20.27
1.59	14.96	87.63	20.96
1.59	14.89	79.18	18.85
1.59	15.08	87.43	21.08
1.33	14.93	71.06	14.18
1.59	15.09	85.14	20.56
1.13	19.32	81.26	17.85
	(V) 1.59 1.59 1.59 1.59 1.59 1.59 1.59	(V) cm ²) 1.59 15.01 1.59 15.01 1.59 14.96 1.59 14.89 1.59 15.08 1.33 14.93 1.59 15.09	(V) cm ²) 1.59 15.01 87.40 1.59 15.01 84.48 1.59 14.96 87.63 1.59 14.89 79.18 1.59 15.08 87.43 1.33 14.93 71.06 1.59 15.09 85.14

curve is a result of an increase in R_S . The optimized thickness of HTL is 250 nm, yielding a PCE of 21.30 % demonstrated in Fig. 5d.

3.2.2. Impact of NA

The findings from previous studies have shown the significant impact of doping density (N_A) in the HTL vastly affects the PV parameters of

PSCs, including conductivity, recombination rate and V_{OC} [6]. Hence, the solar cell parameters were simulated in the range of N_A values from 10^{14} to $10^{22}\,\mathrm{cm}^{-3}$ at a thickness of 250 nm of HTL. As depicted in Fig. 6a, an enhancement in N_A leads to an increase in V_{OC} . In layered semiconductor architectures, the alignment of the fermi level at the same value results in an equilibrium state, causing band bending and built-in voltage (V_{bi}) [43]. This internal electric field drifts segregated photogenerated e's and h^+s towards the n and p regions respectively, where they gather. Under illumination and open-circuit conditions, the excited carriers induce the separation of quasi-Fermi-levels (EFn and EFp) for e's and h^+s , respectively, within the photoactive semiconductor material. This effectively nullifies V_{bi} , and forms a photo-voltage referred to as V_{OC} [44].

Raising the dopant concentration leads to reduction in the recombination rate, owing to an enhanced internal electric field and accelerated carrier segregation. Simultaneously, there's a slight decrease in J_{SC} within the N_A range of 10^{14} to $10^{18}\ cm^{-3}$. Notably, a pronounced fall in the J_{SC} is observed at $10^{19}\ cm^{-3}$ due to generation of numerous deep Coulomb traps that reduce the μ_p [45]. The Fig. 6a shows that the maximum PCE of 21.32 % is obtained at N_A of $10^{20}\ cm^{-3}$.

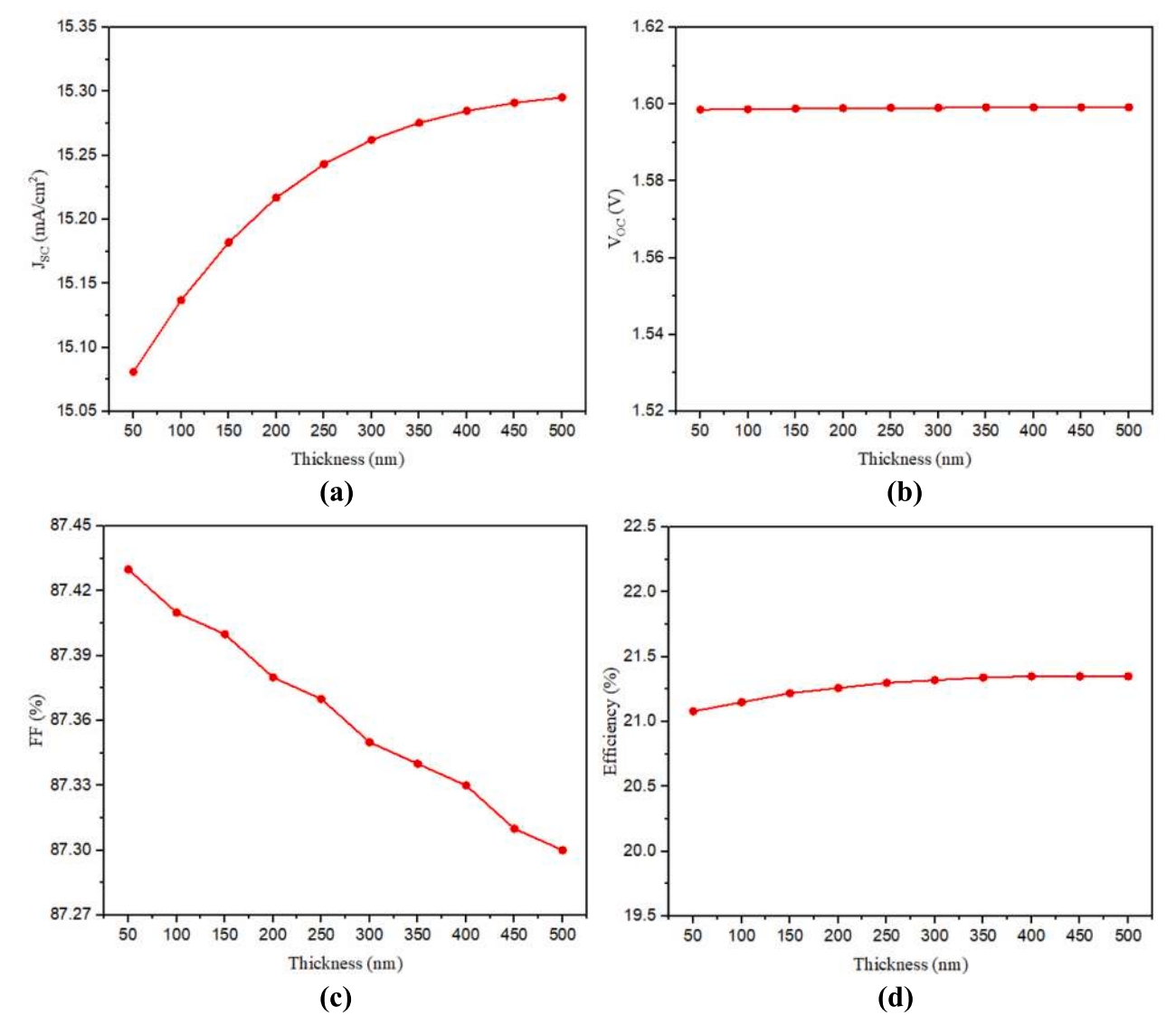


Fig. 5. Impact of the thickness of PEDOT: PSS layer on PV parameters of PSC.

3.2.3. Impact of N_t

In addition to the NA, HTL defect density (Nt) affects the performance of PSCs. The impact on the PSC characteristics demonstrated in Fig. 7. The N_t of 10^{17} to 10^{22} cm⁻³, Fig. 7a, b, c and d reveal no significant changes in PV parameters. However, a pronounced decline in V_{OC} , J_{SC} and PCE surface for change in N_t from $10^{14}~\text{cm}^{-3}$ to $10^{17}~\text{cm}^{-3}$. This precipitous shift is primarily attributed to the rapid emergence of numerous recombination sites in the HTL and at interfaces [46]. A high value of N_t in HTL, arising from diverse sources like undesirable foreign atoms, and native defects, give rise to shallow or deep traps. These traps adversely impact cell performance. Fig. 7d shows that an increase in interface defects leads to reduced efficiency. Beyond a certain Nt, it becomes constant. These interface defects, primarily stemming from the lattice mismatch between absorber layer (AL) and HTL, yield deep traps at the interface. These traps function as SRH recombination centers. Consequently, PCE experiences a decline, reaching about 20.97 % at Nt $=10^{22}$ cm⁻³. In the beginning FF decline is attributed to the abundance of recombination centers and R_S resulting from a significant number of traps (Fig. 7c). Despite the superior outcomes at lower N_t, simulation results diverge from experimental findings. Hence, a value of 1×10^{14} $\,\mathrm{cm}^{-3}$ was selected.

3.3. Optimization of KSnI3 layer

The above outcomes have shown that PEDOT: PSS is the most suitable HTL for KSnI_3-based PSC. The maximum PCE of beyond 21 % has been obtained at 250 nm of thickness of HTL, N_A of $10^{20}~cm^{-3}$ and at N_t of $1\times10^{14}~cm^{-3}$. Therefore, we have opted for this optimized value of thickness, N_A and N_t for the further simulation study to optimize the performance of KSnI_3-based PSC.

3.3.1. Impact of thickness

The characteristics parameters like J_{SC} , V_{OC} , FF and PCE of PSCs are significantly influenced by the thickness of the perovskite absorber layer. In our investigation, we explored the impact of thickness of the absorber layer on the performance of the architecture: FTO/WS₂(100 nm)/KSnI₃/PEDOT: PSS (250 nm)/Au. The thickness of the KSnI₃ layer has exhibited a straight relation with the evaluation of the outcomes of PSC through its effect on the charge carrier's diffusion length. It is known to us that as the thickness of the layer decreases, the absorption rate also lowers. This results in a decrement in photocurrent and therefore PCE of the PSC also reduces from 200 to 1000 nm. The change in PCE is depicted below in Fig. 8a. However, with the thickness increasing up to 550 nm, PCE gradually rises. This phenomenon can be attributed to the generation of large amounts of charge carriers by

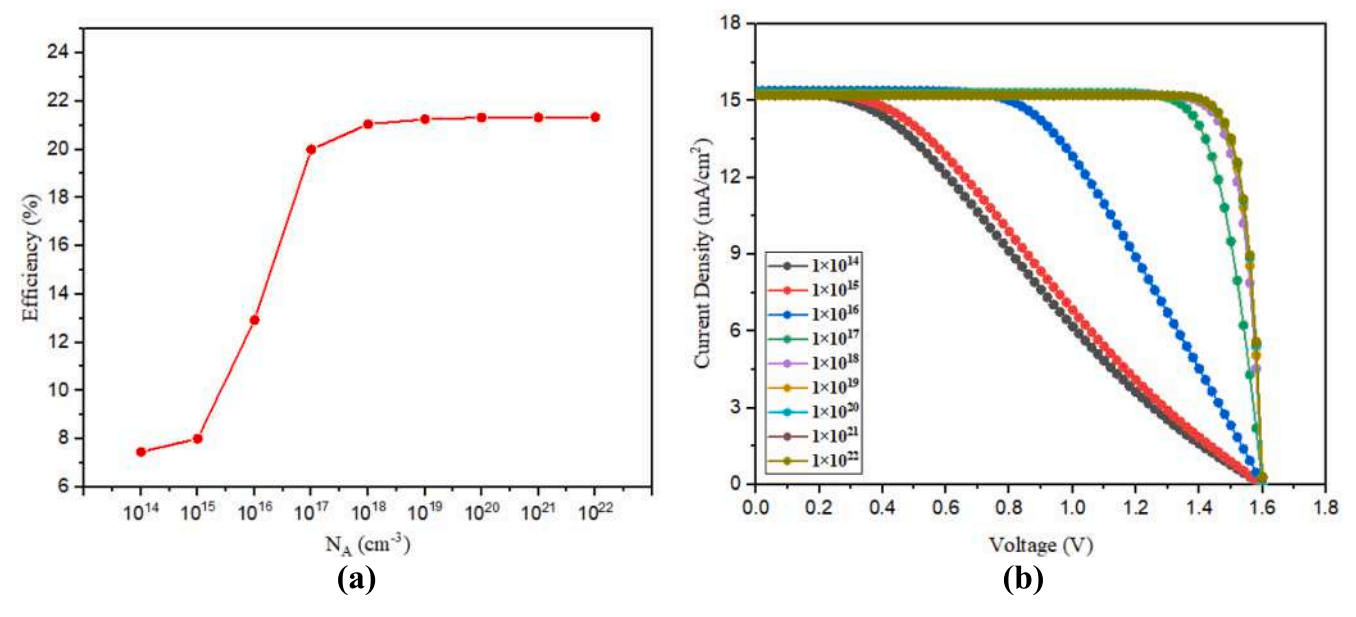


Fig. 6. (a) Efficiency versus N_A of the PEDOT: PSS. (b) J-V curves of HTL depending on its N_A . (c) Efficiency vs thickness of the HTL and (d) Effect of N_t on PCE.

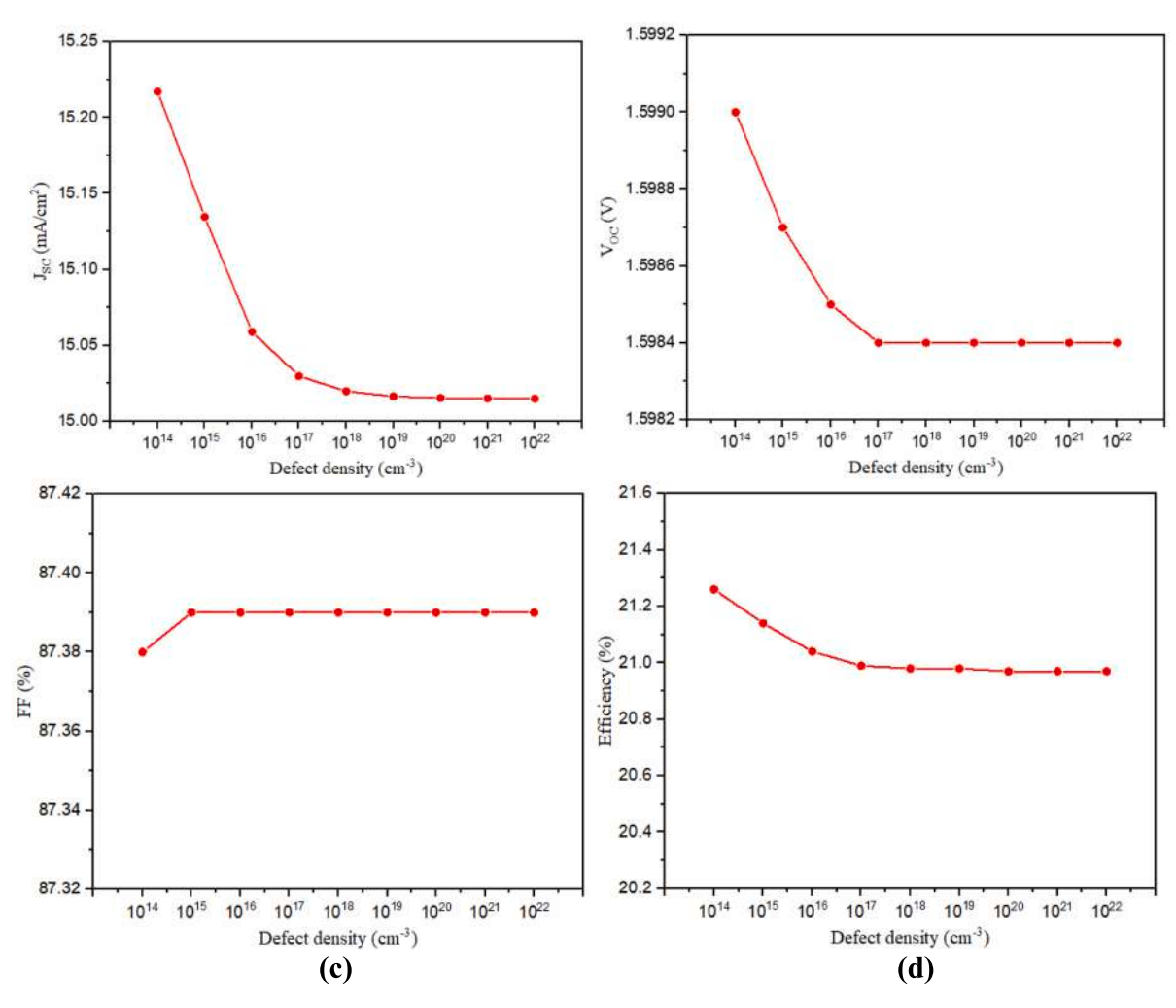


Fig. 7. Impact of N_t of the PEDOT: PSS on PV parameters of $KSnI_3$ -based PSC.

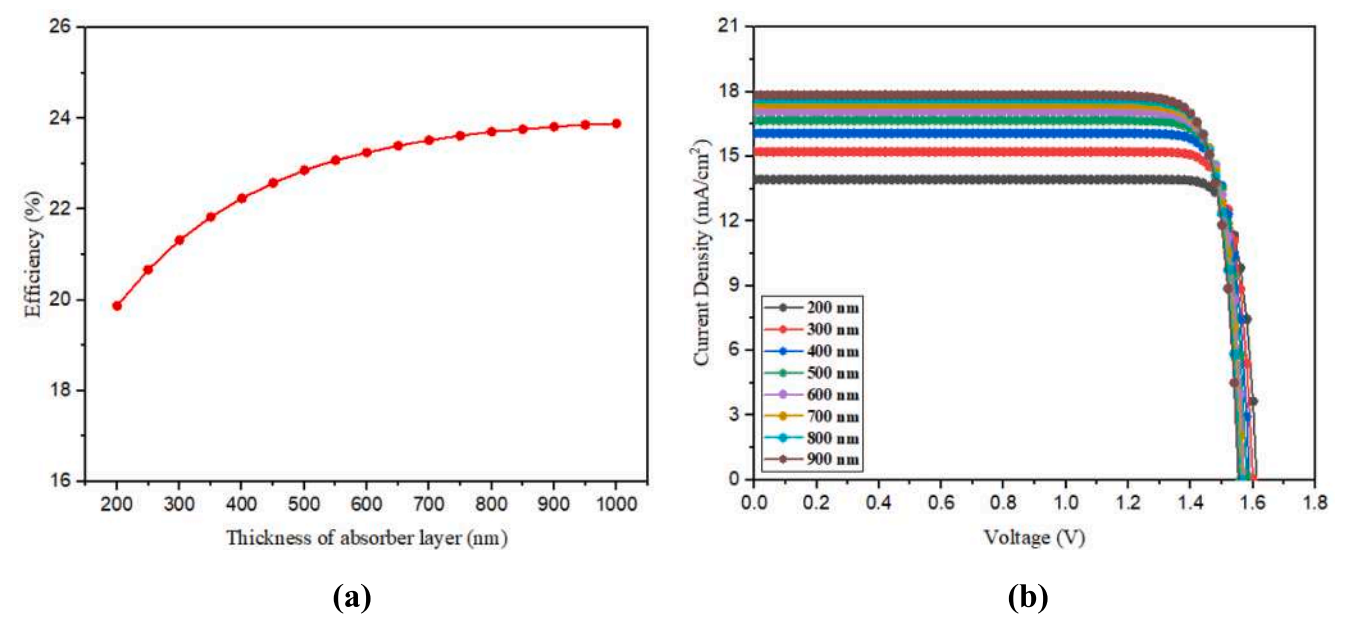


Fig. 8. (a) Efficiency vs thickness of the absorber layer. (b) J-V curves with function of absorber layer thickness.

absorbed photons, leading to higher EQE, J_{SC} , and overall improved performance [47]. This enhancement is also evident in the J-V curves (Fig. 8b). As the absorber layer thickness exceeds 550 nm, both V_{OC} and FF parameters decrease. Optimum thickness value for KSnI₃-based PSC is 550 nm. The maximum efficiency goes up to 23.08 % together with V_{OC} is 1.57 V, J_{SC} is 16.90 mA/cm² and FF is 86.59 % at a thickness of 550 nm.

3.3.2. Impact of N_t

Similarly, with the HTL influence, there is a lack of substantial change in the PV parameters until an N_t value of $10^{13}~\rm cm^{-3}$ is reached. These PV parameters exhibit a decline when a high defect concentration is present. A heightened defect concentration within a low-quality perovskite layer results in an increased number of non-radiative recombination centers, consequently deteriorating PV parameters of PSC. This degradation can be attributed to alterations in the diffusion length of charge carriers and their lifetime. While a low N_t value might contribute to high PCE in simulated PSCs, the elevated fabrication cost is a deterrent. Moreover, a low N_t value does not accurately reflect real-world conditions due to the instability of such perovskites under humid conditions, leading to partial degradation. Therefore, we propose N_t values ranging from 10^{13} to $10^{15}~\rm cm^{-3}$ for the building of high-performance PSCs with reasonable stability. The optimized N_t is $1\times 10^{13}~\rm cm^{-3}$ for KSnI $_3$ perovskite layer at which it has achieved the

maximum PCE of 23.08 %, as demonstrated in Fig. 9a. The J-V plot of KSnI $_3$ PSCs based on the N $_t$ of the absorber layer is simulated and demonstrated in Fig. 9b. For perovskite layers when N $_t$ is increased, the undesirable recombination rate also rises, attributed to the formation of defects that act as dangling bonds, serving as trap state for the charge carriers. This enhancement in recombination leads to fall in J $_{SC}$, which is subsequently responsible for the decrement in FF of solar devices. The device PCE also decreased from 23.08 % to 7.85 %, when N $_t$ was increased from 10^{13} to 10^{20} cm $^{-3}$. Such an increasing amount of recombination resulted in a sharp fall in PCE of PSC.

3.4. Optimized device

The optimized ETL and HTL are WS $_2$ and PEDOT: PSS respectively with the Au (gold) as metal back contact. The optimized parameters such as 1) Thickness: PEDOT: PSS (250 nm), KSnI $_3$ (550 nm), WS $_2$ (100 nm) and FTO (400 nm); 2) NA: PEDOT: PSS ($10^{20}~{\rm cm}^{-3}$) and 3) Nt: PEDOT: PSS ($1\times10^{14}~{\rm cm}^{-3}$), KSnI $_3$ ($1\times10^{13}~{\rm cm}^{-3}$) and WS $_2$ ($1\times10^{13}~{\rm cm}^{-3}$). The PSC structure and energy band diagram of the optimized device demonstrated in Fig. 10. The optimized PCE of 23.08 % with Voc = 1.57 V, JSC = 16.90 mA/cm², and FF of 86.59 % has been obtained. The JV and QE curves of optimized PSC are illustrated in Fig. 11(a-b).

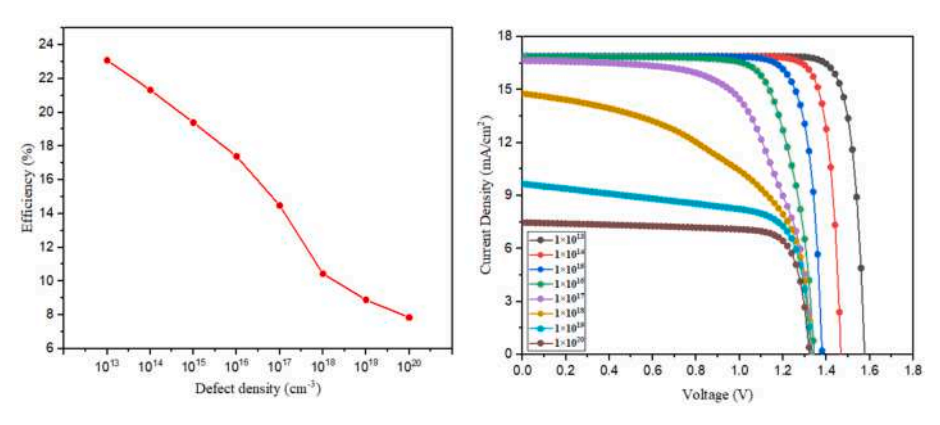


Fig. 9. (a) Efficiency vs N_t of the absorber layer and (b) Effects of N_t on the J-V characteristics of KSnI₃-based PSCs.

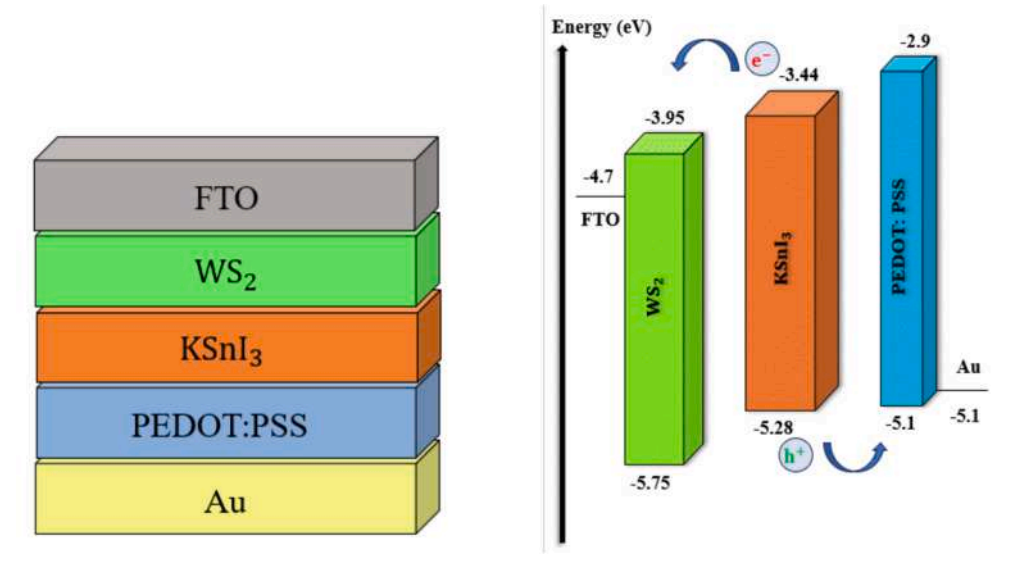


Fig. 10. Architecture and band alignment diagram of optimized PSC.

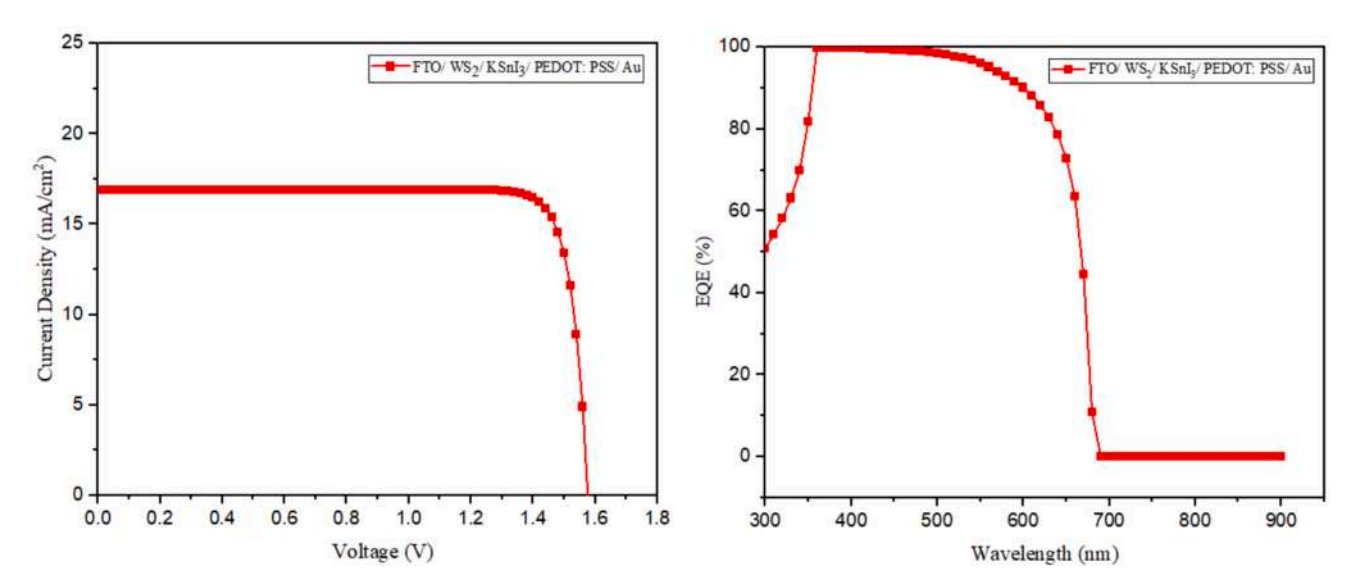


Fig. 11. (a) J-V and (b) QE plot of optimized device.

3.5. Machine learning

In this work, python is employed for the prediction of factors affecting the performance of the PSC. Due to its robustness to overfitting and optimal complexity, the Random Forest algorithm was used for the training and testing [48]. The researchers noted that more powerful rivals, like neural networks and deep neural networks, acquire needless complexity, leading to overfitting and reduced performance [49,50]. Considering the relatively small size of the dataset and its high complexity, compiling a larger set of records would be beneficial. The research focused on reducing the dataset's complexity to improve the model's accuracy. By employing Scikit-Learn, influence of every feature on the entire predictive performance of the ML model was observed. The eleven most important features were identified, and their relative importance was shown in Fig. 12. It has shown that the features such as thickness, Nt, NA, of the HTL were found to be the most responsible in differentiating between the performance of two distinct PSCs. The outcomes guide for the design of new solar cells. Subsequently, a new model was built using the selected important features aiming to achieve a similar level of performance while reducing the model's size due to the

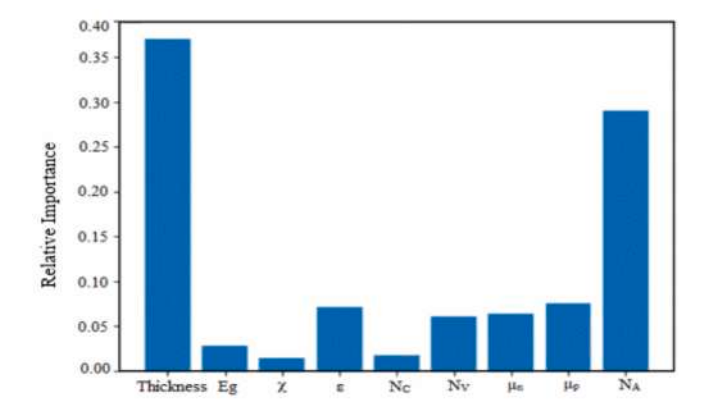


Fig. 12. Different features with relative importance in the ML model.

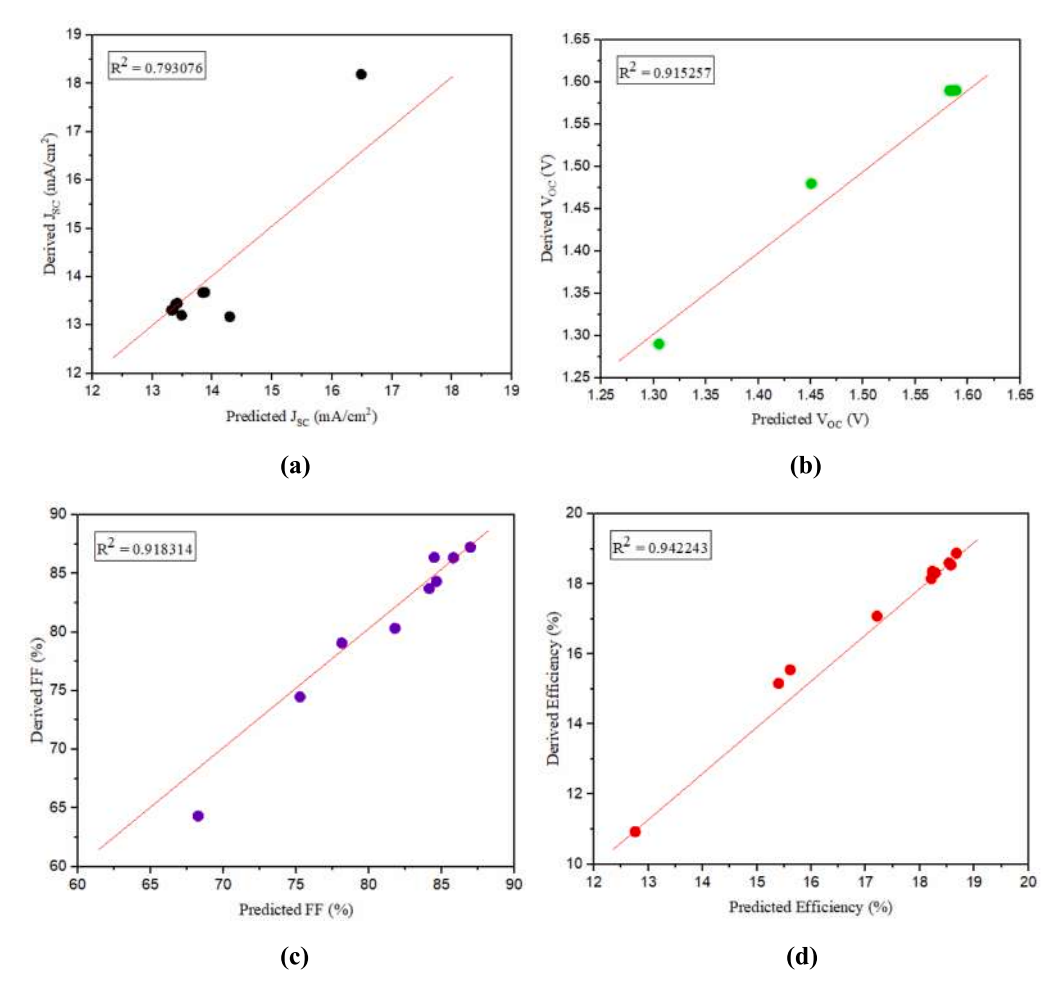


Fig. 13. Derived and predicted values of PV parameters.

fewer features used. The model results were measured and illustrated in Fig. 13 (a-d). Ideally, the slope of plots is near to 1, indicating accurate predictions. The ML model achieved a mean accuracy of 0.89 % and mean $\rm R^2$ of 0.8921 between actual and predicted values for each target feature. While the accuracy might not be extremely high, the results are encouraging for further investigation and bridging the gap between artificial intelligence and materials science. The model trained for large input data which leads to highly efficient and realistic results.

4. Conclusions

This work comprises analysis of KSnI₃-based PSC with the various HTLs. The effect of distinct parameters, including thickness of perovskite absorber layer and HTL, as well as N_A and N_t have been examined using SCAPS-1D. The ML model was used to predict the performance of the PSCs. The study demonstrated PEDOT: PSS as a promising HTL that could replace the expensive and less-conductive Spiro-OMeTAD. The maximum PCE of 23.08 % was obtained for the configuration of FTO/ WS₂/KSnI₃/PEDOT: PSS/Au. The SCAPS-1D outcomes, deduced that the optimized thickness of HTL was 200 nm, with N_t of $1\times 10^{14}\,\text{cm}^{-3}$ and a N_A of 1×10^{20} cm⁻³ results in maximum PCE. The optimized thickness of the KSnI₃ layer is 550 nm and at N_t of 1×10^{13} cm⁻³ for an efficient PSC. The incorporation of the ML approach provided enhanced insight into the critical factors involved in designing and fabricating solar cells. The ML model demonstrated an accuracy score of 89 % in predicting the performance metrics of PSCs. The device PCE improved beyond 23 % by optimizing parameters such as thickness of absorber layer and HTL, N_t and NA. The study focused on proper optimization of perovskite absorber layer and HTL for advanced and efficient architecture of KSnI $_3$ -based PSC. A precise and powerful model can be trained by providing a large number of inputs to ML. With the series of this study, we can study the lead free and other potential material to optimize the performance of PSCs using the ML model.

CRediT authorship contribution statement

Rahul Kundara: Conceptualization, Data curation, Investigation, Methodology, Software, Validation, Writing – original draft. Sarita Baghel: Formal analysis, Project administration, Supervision, Writing – review & editing.

Declaration of competing interest

The authors declare that they have no known competing financial interests or personal relationships that could have appeared to influence the work reported in this paper.

Data availability

Data will be made available on request.

Acknowledgment

The author, Rahul Kundara is thankful to Delhi Technological University, New Delhi for providing a junior research fellowship. We are very grateful to Marc Burgelman, the Electronics and Information

Systems (ELIS), University of Gent, Belgium, for providing us with SCAPS-1D software.

References

- [1] A. Singha, A. Paul, S. Koul, V. Sharma, S. Mallick, K.R. Balasubramaniam, D. Kabra, Stable and efficient large area 4T Si/perovskite tandem photovoltaics with sputtered transparent contact, Solar RRL. 7 (2023) 2300117, https://doi.org/ 10.1002/solr.202300117.
- [2] N. Rai, S. Rai, P.K. Singh, P. Lohia, D.K. Dwivedi, Analysis of various ETL materials for an efficient perovskite solar cell by numerical simulation, J. Mater. Sci. Mater. Electron. 31 (2020) 16269–16280, https://doi.org/10.1007/s10854-020-04175-z.
- [3] I. Elango, M. Selvamani, PC. Ramamurthy, AV. Kesavan, Studying VOC in lead free inorganic perovskite photovoltaics by tuning energy bandgap and defect density, Ceram. Int. 48 (2022) 29414-29420. https://doi. org/10.1016/j. ceramint.2022.06.125.
- [4] M.S. Islam, K. Sobayel, A. Al-Kahtani, M.A. Islam, G. Muhammad, N. Amin, M. Shahiduzzaman, M. Akhtaruzzaman, Defect study and modelling of SnX3-based perovskite solar cells with SCAPS-1D, Nanomaterials 11 (2021), https://doi.org/ 10.3390/nano11051218.
- [5] N. Lakhdar, A. Hima, Electron transport material effect on performance of perovskite solar cells based on CH3NH3Gel3, Opt Mater (AMST). 99 (2020), https://doi.org/10.1016/j.optmat.2019.109517.
- [6] S. Mushtaq, S. Tahir, A. Ashfaq, R. Sebastian Bonilla, M. Haneef, R. Saeed, W. Ahmad, N. Amin, Performance optimization of lead-free MASnBr 3 based perovskite solar cells by SCAPS-1D device simulation, Sol. Energy 249 (2023) 401–413, https://doi.org/10.1016/j.solener.2022.11.050.
- [7] N.K. Noel, S.D. Stranks, A. Abate, C. Wehrenfennig, S. Guarnera, A.A. Haghighirad, A. Sadhanala, G.E. Eperon, S.K. Pathak, M.B. Johnston, A. Petrozza, L.M. Herz, H. J. Snaith, Lead-free organic-inorganic tin halide perovskites for photovoltaic applications, Energy Environ. Sci. 7 (2014) 3061–3068, https://doi.org/10.1039/ c4ee01076k.
- [8] M.G. Ju, M. Chen, Y. Zhou, H.F. Garces, J. Dai, L. Ma, N.P. Padture, X.C. Zeng, Earth-abundant nontoxic titanium(IV)-based vacancy-ordered double perovskite halides with Tunable 1.0 to 1.8 eV bandgaps for photovoltaic applications, ACS Energy Lett. 3 (2018) 297–304, https://doi.org/10.1021/acsenergylett/7b01167.
- [9] Z. Zhang, X. Li, X. Xia, Z. Wang, Z. Huang, B. Lei, Y. Gao, High-quality (CH3NH3) 3Bi2I9 film-based solar cells: pushing efficiency up to 1.64%, J. Phys. Chem. Lett. 8 (2017) 4300–4307, https://doi.org/10.1021/acs.jpclett.7b01952.
- [10] M. Wang, P. Zeng, S. Bai, J. Gu, F. Li, Z. Yang, M. Liu, High-quality sequential-vapor-deposited Cs2AgBiBr 6 thin films for lead-free perovskite solar cells, Solar RRL. 2 (2018), https://doi.org/10.1002/solr.201800217.
- [11] Y. Zong, Y. Zhou, Y. Zhang, Z. Li, L. Zhang, M.G. Ju, M. Chen, S. Pang, X.C. Zeng, N. P. Padture, Continuous grain-boundary functionalization for high-efficiency perovskite solar cells with exceptional stability, Chem 4 (2018) 1404–1415, https://doi.org/10.1016/j.chempr.2018.03.005.
- [12] G. Pindolia, S.M. Shinde, P.K. Jha, Non-leaded, KSnI3 based perovskite solar cell: A DFT study along with SCAPS simulation, Mater. Chem. Phys. 297 (2023), https://doi.org/10.1016/j.matchemphys.2023.127426.
- [13] A. Tara, V. Bharti, S. Sharma, R. Gupta, Device simulation of FASnI3 based perovskite solar cell with Zn(O0.3, S0.7) as electron transport layer using SCAPS-1D, Opt Mater (amst) 119 (2021), https://doi.org/10.1016/j.optmat.2021.111362.
- [14] W. Yan, Y. Liu, Y. Zang, J. Cheng, Y. Wang, L. Chu, X. Tan, L. Liu, P. Zhou, W. Li, Z. Zhong, Machine learning enabled development of unexplored perovskite solar cells with high efficiency, Nano Energy 99 (2022) 107394, https://doi.org/10.1016/j.papog.2022.107394
- [15] S. Rai, B.K. Pandey, D.K. Dwivedi, Modeling of highly efficient and low cost CH3NH3Pb(I1-xClx)3 based perovskite solar cell by numerical simulation, Opt Mater (amst). 100 (2020), https://doi.org/10.1016/j.optmat.2019.109631.
- [16] M. Kumar, A. Raj, A. Kumar, A. Anshul, An optimized lead-free formamidinium Sn-based perovskite solar cell design for high power conversion efficiency by SCAPS simulation, Opt Mater (amst). 108 (2020), https://doi.org/10.1016/j.optmat.2020.110213.
- [17] M.K. Hossain, G.F.I. Toki, A. Kuddus, M.H.K. Rubel, M.M. Hossain, H. Bencherif, M.F. Rahman, M.R. Islam, M. Mushtaq, An extensive study on multiple ETL and HTL layers to design and simulation of high-performance lead-free CsSnCl3-based perovskite solar cells, Sci. Rep. 13 (2023), https://doi.org/10.1038/s41598-023-28506-2
- [18] A.A. Kanoun, M.B. Kanoun, A.E. Merad, S. Goumri-Said, Toward development of high-performance perovskite solar cells based on CH3NH3Gel3 using computational approach, Sol. Energy 182 (2019) 237–244, https://doi.org/ 10.1016/j.solener.2019.02.041.
- [19] S. Bhattarai, T.D. Das, Optimization of carrier transport materials for the performance enhancement of the MAGel3 based perovskite solar cell, Sol. Energy 217 (2021) 200–207, https://doi.org/10.1016/j.solener.2021.02.002.
- [20] S.Z. Haider, H. Anwar, M. Wang, Theoretical device engineering for high-performance perovskite solar cells using CuSCN as hole transport material boost the efficiency above 25%, Physica Status Solidi (A) Applications and Materials Science 216 (2019) https://doi.org/10.1002/pssa.201900102.
- [21] B. Li, H. Di, B. Chang, R. Yin, L. Fu, Y.N. Zhang, L. Yin, Efficient passivation strategy on Sn related defects for high performance all-inorganic CsSnI3 perovskite solar cells, Adv. Funct. Mater. 31 (2021), https://doi.org/10.1002/ adfm.202007447.

- [22] U. Mandadapu, S.V. Vedanayakam, K. Thyagarajan, Simulation and analysis of lead based perovskite solar cell using SCAPS-1D, Indian, J. Sci. Technol. 10 (2017) 1–8, https://doi.org/10.17485/ijst/2017/v10i11/110721.
- [23] K. Deepthi Jayan, V. Sebastian, Comprehensive device modelling and performance analysis of MASnI3 based perovskite solar cells with diverse ETM, HTM and back metal contacts, Sol. Energy 217 (2021) 40–48, https://doi.org/10.1016/j. solaror 2021.01.058
- [24] O. Ahmad, A. Rashid, M.W. Ahmed, M.F. Nasir, I. Qasim, Performance evaluation of Au/p-CdTe/Cs2TiI6/n-TiO2/ITO solar cell using SCAPS-1D, Opt Mater (amst). 117 (2021), https://doi.org/10.1016/j.optmat.2021.111105.
- [25] Y. Gan, X. Bi, Y. Liu, B. Qin, Q. Li, Q. Jiang, P. Mo, Numerical investigation energy conversion performance of tin-based perovskite solar cells using cell capacitance simulator, Energies (basel). 13 (2020), https://doi.org/10.3390/en13225907.
- [26] M.K. Hossain, A.A. Arnab, R.C. Das, K.M. Hossain, M.H.K. Rubel, M.F. Rahman, H. Bencherif, M.E. Emetere, M.K.A. Mohammed, R. Pandey, Combined DFT, SCAPS-1D, and wxAMPS frameworks for design optimization of efficient Cs2BiAgI6-based perovskite solar cells with different charge transport layers, RSC Adv. 12 (2022) 34850–34873, https://doi.org/10.1039/d2ra067341.
- [27] S.P. Ong, W.D. Richards, A. Jain, G. Hautier, M. Kocher, S. Cholia, D. Gunter, V. L. Chevrier, K.A. Persson, G. Ceder, Python Materials genomics (pymatgen): a robust, open-source python library for materials analysis, Comput. Mater. Sci 68 (2013) 314–319, https://doi.org/10.1016/j.commatsci.2012.10.028.
- [28] L. Ward, A. Dunn, A. Faghaninia, N.E.R. Zimmermann, S. Bajaj, Q. Wang, J. Montoya, J. Chen, K. Bystrom, M. Dylla, K. Chard, M. Asta, K.A. Persson, G. J. Snyder, I. Foster, A. Jain, Matminer: An open source toolkit for materials data mining, Comput. Mater. Sci 152 (2018) 60–69, https://doi.org/10.1016/j. commatsci.2018.05.018.
- [29] R.T. Yarlagadda, Novateur publications international journal of innovations in engineering research and technology [IJIERT] python engineering automation to advance artificial intelligence and machine learning systems, 5 (2018). https:// ssrn.com/abstract=3797347.
- [30] Z. Jin, J. Shang, Q. Zhu, C. Ling, W. Xie, B. Qiang, RFRSF: Employee turnover prediction based on random forests and survival analysis. In: Web Information Systems Engineering-WISE 2020: 21st International Conference, Amsterdam, The Netherlands, October 20–24, 2020, Proceedings, Part II 21 2020 (pp. 503-515). Springer International Publishing.
- [31] K. Sobayel, M. Akhtaruzzaman, K.S. Rahman, M.T. Ferdaous, Z.A. Al-Mutairi, H. F. Alharbi, N.H. Alharthi, M.R. Karim, S. Hasmady, N. Amin, A comprehensive defect study of tungsten disulfide (WS2) as electron transport layer in perovskite solar cells by numerical simulation, Results Phys. 12 (2019) 1097–1103, https://doi.org/10.1016/j.rinp.2018.12.049.
- [32] G. Pindolia, S.M. Shinde, Effect of organic charge transport layers on unleaded KSnI3 based perovskite solar cell, Results in Optics. 12 (2023) 100469, https://doi. org/10.1016/j.rio.2023.100469.
- [33] Y. Xia, S. Dai, Review on applications of PEDOTs and PEDOT:PSS in perovskite solar cells, J. Mater. Sci. Mater. Electron. 32 (2021) 12746–12757, https://doi.org/ 10.1007/s10854-020-03473-w.
- [34] L. Zhao, J. Mou, L. Zhu, J. Song, Synergistic effect of NiO and Spiro-OMeTAD for hole transfer in perovskite solar cells, J. Electron. Mater. 50 (2021) 6512–6517, https://doi.org/10.1007/s11664-021-09193-z.
- [35] Q. Du, Z. Shen, C. Chen, F. Li, M. Jin, H. Li, C. Dong, J. Zheng, M. Ji, M. Wang, Spiro-OMeTAD:Sb2S3 hole transport layer with triple functions of overcoming lithium salt aggregation, long-term high conductivity, and defect passivation for perovskite solar cells, Solar RRL. 5 (2021), https://doi.org/10.1002/ solr 202100622
- [36] C. Zuo, L. Ding, Modified PEDOT layer makes a 1.52 V Voc for perovskite/PCBM solar cells, Adv. Energy Mater. 7 (2017), https://doi.org/10.1002/
- [37] D. Liu, Y. Li, J. Yuan, Q. Hong, G. Shi, D. Yuan, J. Wei, C. Huang, J. Tang, M. K. Fung, Improved performance of inverted planar perovskite solar cells with F4-TCNQ doped PEDOT: PSS hole transport layers, J. Mater. Chem. A 5 (2017), https://doi.org/10.1039/C6TA10212C.
- [38] S. Li, Y.L. Cao, W.H. Li, Z.S. Bo, A brief review of hole transporting materials commonly used in perovskite solar cells, Rare Met. 40 (2021) 2712–2729, https://doi.org/10.1007/s12598-020-01691-z.
- [39] H. Sharma, V.K. Verma, R.C. Singh, P.K. Singh, A. Basak, Numerical analysis of high-efficiency CH3NH3PbI3 perovskite solar cell with PEDOT: PSS hole transport material using SCAPS 1D simulator, J. Electron. Mater. 52 (2023) 4338–4350, https://doi.org/10.1007/s11664-023-10257-5.
- [40] M.A. Nalianya, C. Awino, H. Barasa, V. Odari, F. Gaitho, B. Omogo, M. Mageto, Numerical study of lead free CsSn0. 5Ge0. 5I3 perovskite solar cell by SCAPS-1D, Optik 248 (2021) 168060, https://doi.org/10.1016/j.ijleo.2021.168060.
- [41] N. Marinova, W. Tress, R. Humphry-Baker, M.I. Dar, V. Bojinov, S.M. Zakeeruddin, M.K. Nazeeruddin, M. Grätzel, Light harvesting and charge recombination in CH3NH3PbI3 perovskite solar cells studied by hole transport layer thickness variation, ACS Nano 9 (2015) 4200–4209, https://doi.org/10.1021/acsnano.5b00447.
- [42] F. Azri, A. Meftah, N. Sengouga, A. Meftah, Electron and hole transport layers optimization by numerical simulation of a perovskite solar cell, Sol. Energy 181 (2019) 372–378, https://doi.org/10.1016/j.solener.2019.02.017.
- [43] B.L. Williams, V. Zardetto, B. Kniknie, M.A. Verheijen, W.M.M. Kessels, M. Creatore, The competing roles of i-ZnO in Cu(In, Ga)Se2 solar cells, Sol. Energy Mater. Sol. Cells 157 (2016) 798–807, https://doi.org/10.1016/j. solmat.2016.07.049.
- [44] F. Paquin, J. Rivnay, A. Salleo, N. Stingelin, C. Silva-Acuña, Multi-phase microstructures drive exciton dissociation in neat semicrystalline polymeric

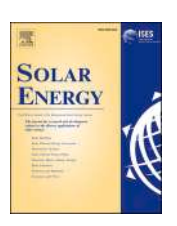
- semiconductors, J Mater Chem C Mater. 3 (2015) 10715–10722, https://doi.org/
- [45] S.J. Yoo, J.H. Lee, J.H. Lee, J.J. Kim, Doping-concentration-dependent hole mobility in a ReO3 doped organic semiconductor of 4,4',4"-tris(N-(2-naphthyl)-Nphenyl-amino) -triphenylamine, Appl. Phys. Lett. 102 (2013), https://doi.org/ 10.1063/1.4804141.
- [46] F. Anwar, R. Mahbub, S.S. Satter, S.M. Ullah, Effect of different HTM layers and electrical parameters on ZnO nanorod-based lead-free perovskite solar cell for high-efficiency performance, Int. J. Photoenergy 2017 (2017), https://doi.org/ 10.1155/2017/9846310.
- [47] L. Hao, T. Li, X. Ma, J. Wu, L. Qiao, X. Wu, G. Hou, H. Pei, X. Wang, X. Zhang, A tin-based perovskite solar cell with an inverted hole-free transport layer to achieve
- high energy conversion efficiency by SCAPS device simulation, Opt. Quant. Electron. 53 (2021), https://doi.org/10.1007/s11082-021-03175-5.
- [48] W. McKinney, Data structures for statistical computing in python, InProceedings of the 9th Python in Science Conference 2010 Jun 28 (Vol. 445, No. 1, pp. 51-56). DOI: 10.25080/Majora-92bf1922-00a.
- [49] J. Schmidhuber, Deep learning in neural networks: an overview, Neural Netw. 61 (2015) 85–117, https://doi.org/10.1016/j.neunet.2014.09.003.
- [50] M. Hasanzadeh Azar, S. Aynehband, H. Abdollahi, H. Alimohammadi, N. Rajabi, S. Angizi, V. Kamraninejad, R. Teimouri, R. Mohammadpour, A. Simchi, SCAPS Empowered Machine Learning Modelling of Perovskite Solar Cells: Predictive Design of Active Layer and Hole Transport Materials, Photonics. 10 (2023). DOI: 10.3390/photonics10030271.

ELSEVIER

Contents lists available at ScienceDirect

Solar Energy

journal homepage: www.elsevier.com/locate/solener



Check for updates

Performance optimization of lead-free KGeCl₃ based perovskite solar cells using SCAPS-1D

Rahul Kundara * O, Sarita Baghel

Department of Applied Physics, Delhi Technological University, Delhi, India

ARTICLE INFO

Handling editor: 'Ranga Pitchumani'

Keywords: KGeCl₃-based PSC SCAPS-1D ETLs and HTLs

ABSTRACT

The commercial application of lead-based Perovskite Solar Cells (PSCs) is restrained by their toxicity. In this work, we have investigated KGeCl $_3$ which is a potential candidate for non-lead PSC. SCAPS-1D software is employed to examine the impact of distinct Hole Transport Layers (HTLs), absorber layer and Electron Transport Layers (ETLs) to maximize the device performance. The effect of absorber layer thickness, its acceptor and donor concentration (NA and ND) have been analyzed. We have obtained a maximum efficiency of 29.82 % with open circuit voltage (VOC) = 1.19 V, short circuit current density (JSC) = 30.08 mA/cm², and fill factor (FF) = 82.74 % for the configuration of FTO/WS2/KGeCl $_3$ /PEDOT: PSS/Au at radiative recombination coefficient of 10^{-12} cm³/sec, operating temperature of 300 K and defect density of 10^{15} cm $_3$. The optimized thickness of the absorber layer is 600 nm. Thus, the investigation suggests that WS $_2$ as ETL and PEDOT: PSS as HTL is most suitable for the Ge-based PSC. Hence, this configuration is most suitable to manufacture highly efficient PSC devices.

1. Introduction

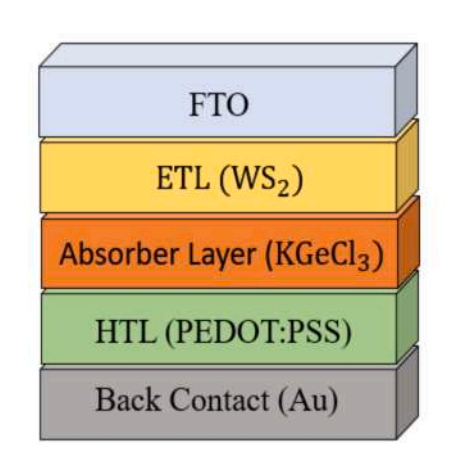
Global warming, rapid industrialization and growing population will drive the demand for renewable sources of energy which should also be environment friendly. In this scenario solar energy devices offer a clean and sustainable solution for the increase in energy demand. Currently Silicon based Photovoltaic (PV) modules dominate the solar cell market due to their stable and efficient performance. But the Silicon technology is not completely environment friendly when analyzed through its complete life cycle assessment. They are difficult to recycle and they have high carbon emission during the production stage. However, perovskite solar cells (PSCs) are the emerging class of photovoltaics due to its promising properties such as tunable bandgap (E_o), high absorption coefficient, low manufacturing cost and low temperature fabrication. Perovskite material has an ABX3 structure (where A is an organic or inorganic cation, B is an inorganic metal cation and X is halogen anion) [1]. In the typical structure of a PSC, the absorber layer is positioned between Electron Transport Layer (ETL) and Hole Transport Layer (HTL). The generation of photocurrent occurs through injection of photoelectrons into the ETL and the transfer holes through the HTL from the absorber layer. Therefore, ensuring appropriate alignment of the energy band levels across the layers is essential for achieving optimal device performance.

In 2009, PSC was reported with an efficiency of 3.8 % and has achieved maximum power conversion efficiency (PCE) approximately 26 % till now for CH(NH₂)₂PbI₃ and CH₃NH₃PbI₃ perovskite materials [2,3,4,5]. Recently various hybrid organic-inorganic perovskite materials have been reported which possess high charge carrier mobilities and also offer low temperature solution-based fabrication techniques [6,7,8]. They possess some challenges related to stability, toxicity and scalability [9]. The inorganic PSCs, particularly those employing materials like cesium lead halides have advantages over hybrid PSCs as follows: improved stability, scalability and non-toxic alternatives [10,11] but they have phase stability issues and complexity in fabrication [12]. It is mostly lead (Pb)-based PSCs [3,4,5] that have demonstrated experimental PCE of 20.17 % for CsPbI₃ [13]. But, despite the high performance of Pb based PSC, its stability is a major challenge. There are many degradation reactions which impact the PV performance and device stability. There is instability due to rapid oxidation of Pb cation, interfacial reactions of Pb with other materials in the device [14]. Apart from this toxicity concerns also need to be addressed. Though Pb is a toxic substance, there are recent studies which indicate that its use in PSC is limited to less than 1 gm/m² which can be easily managed by proper encapsulation and appropriate recycling systems [15]. On the other hand, the effect of toxicity of lead versus non-lead PSCs have also been investigated [16] and the studies show that, due

E-mail address: rahul_2k20phdap10@dtu.ac.in (R. Kundara).

https://doi.org/10.1016/j.solener.2025.113253

 $^{^{\}ast}$ Corresponding author.



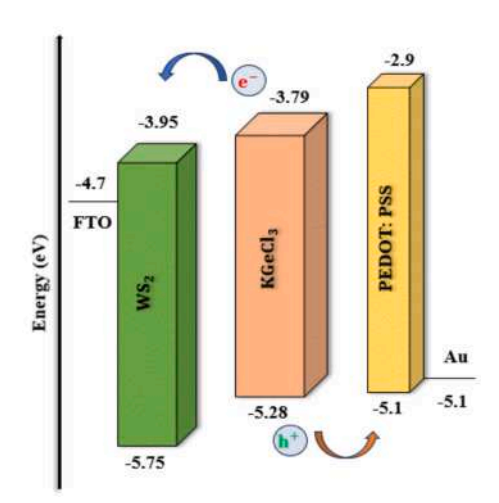


Fig. 1. Architecture and band alignment diagram for KGeCl₃ PSC.

 Table 1

 Input parameters were used in simulation of distinct ETLs.

Parameter	CdS [27]	PCBM [28,29]	C ₆₀ [30]	WS ₂ [31]	KGeCl ₃ [32]
Thickness (μm)	0.050	0.500	0.050	0.100*	0.300
Eg (eV)	2.42	2.1	1.7	1.8	1.49
χ (eV)	4.3	3.9	3.9	3.95	3.52
$\varepsilon_{\rm r}$	9.35	3.9	4.2	13.6	3.52
N_C (cm ⁻³)	$2.2 \times$	2.2×10^{19}	8.0 ×	1×10^{18}	1×10^{18}
	10^{18}		10^{19}		
$N_V (cm^{-3})$	$1.8 \times$	2.2×10^{19}	8.0 ×	2.4 ×	1×10^{19}
	10^{19}		10^{19}	10^{19}	
μ_n (cm ² /Vs)	100	0.001	$8.0 imes 10^{\circ}$	100	20
$\mu_p \; (cm^2/Vs)$	25	0.002	3.5×10^{-3}	100	20
N_D (cm ⁻³)	1.15×10^{17}	1×10^{19}	2.6×10^{17}	1×10^{18}	1×10^{15}
$N_A (cm^{-3})$	0	_	_	0	1×10^{15}
N_t (cm ⁻³)	$1\times10^{15^{\ast}}$	$1 \times 10^{9*}$	1×10^{14}	$1\times10^{13^{\ast}}$	1×10^{13}

^{*}In this work.

to the toxic nature of lead, there is a need to find environmentally friendly substitutes for it. However, before doing so, one has to consider the results of life cycle assessment studies of available alternative materials. There have been various investigations to substitute hazardous Pb ions with other alternatives such as Sn [17], Ge [18], Bi [19], Sb [20] and Ag [21]. But most of the alternatives do not offer substantial advantages in terms of cost, toxicity or environmental safety. Recently reported DFT study shows that KGeCl $_3$ is a promising perovskite material for PV application [Namisi et al. 2023]. There are very few experimental or theoretical investigations on KGeCl $_3$ for solar cell application

so far. The study comprises the application of KGeCl₃ as a perovskite material and simulated the PSC using SCAPS-1D. The recently reported studies demonstrated that KGeCl3-based PSC achieved a PCE of 15.83 % [22] and 19.62 % [23] using SCAPS-1D. Previously germanium-based double PSC has been simulated and obtained a maximum PCE of 22.5 % [24] whereas MAGel3-based PSC has achieved a theoretical PCE of 25.34 % [25]. SnGe-based PSC has been theoretically obtained at an efficiency of 24.20 % [26]. We have simulated the various ETLs (CdS, PCBM, C₆₀ and WS₂) and HTLs (CuI, Spiro-OMeTAD, Cu₂O, PEDOT: PSS and MoS2) and analyzed the effects on the PV parameters of PSC. The optimization of thickness of absorber layer, operating temperature, energy band gap (E_g) and carrier concentration (N_D, N_A) have been done to achieve the maximum PCE. The simulated KGeCl3 device achieved a highest PCE of 29.82 % (with $V_{OC} = 1.19 \text{ V}$, $J_{SC} = 30.08 \text{ mA/cm}^2$, and FF = 82.74 %) at 300 K with WS2 as ETL and PEDOT: PSS as HTL. These photovoltaic outcomes showed that KGeCl3 is promising material to fabricate lead-free low cost and efficient PSCs.

2. Material and Methods

2.1. Device architecture

The Fig. 1 depicts the device architecture and band alignment of the KGeCl $_3$ -based PSC. The PSC structure typically includes distinct layers, an absorber layer situated between ETL and HTL. The gold (Au) is chosen as a back contact electrode with a work function of 5.1 eV. During the simulation of the Ge-based PSC, different ETLs and HTLs are simulated to determine the optimal combination that yields the maximum PCE while also optimizing the thickness of the absorber layer. The thickness of various ETLs (CdS, PCBM, C $_{60}$ and WS $_{20}$) varies from 50 nm to 500 nm shown below in Table 1. The employed KGeCl $_{3}$ absorber

 Table 2

 Input parameters used in simulation of various HTLs.

Parameter	FTO [33,34]	CuI [35]	Spiro-OMeTAD [36,37]	Cu ₂ O [33,35]	PEDOT: PSS [28,30]	MoS ₂ [38]
Thickness (µm)	0.400	0.100	0.213	0.250 0.080		0.200
Eg (eV)	3.5	3.1	3	2.17 2.2		1.29
χ (eV)	4.0	2.1	2.2	3.2 2.9		4.2
$\varepsilon_{\rm r}$	9.0	6.5	3	7.11 3.0		3.0
N_C (cm ⁻³)	2.02×10^{18}	2.8×10^{19}	1×10^{19}	$2.02\times10^{17}~2.2\times$	10^{15}	2.2×10^{18}
$N_V (cm^{-3})$	1.8×10^{19}	1×10^{19}	1×10^{19}	$1.1 \times 10^{19} \ 1.8 \times 1$	1018	1.8×10^{19}
μ_n (cm ² /Vs)	20	100	10 ⁻⁴	$200~1 \times 10^{-2}$		100
$\mu_{\rm D} ({\rm cm}^2/{\rm Vs})$	10	43.9	10-4	80.2×10^{-4}		150
N_D (cm ⁻³)	$2 imes 10^{19}$	_	_			1×10^{15}
$N_A (cm^{-3})$	0	$1 imes 10^{18}$	2×10^{19}	$1\times 10^{18}\ 10^{19}$		1×10^{17}
N_t (cm ⁻³)	$1 imes 10^{15}$	$1 imes 10^{14}$	$1 imes 10^{14}$	$1 \times 10^{14} 1 \times 10^{14}$	1×10^{14}	

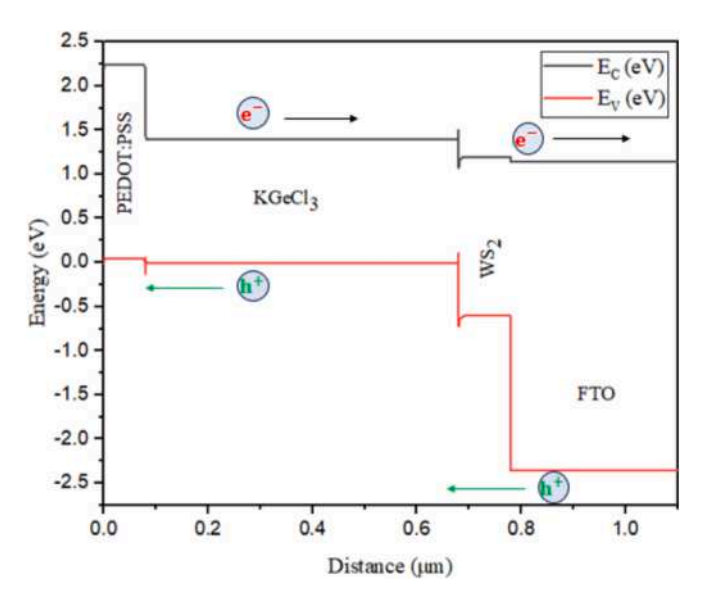


Fig. 2. Energy band diagram of FTO/WS2 /KGeCl3/PEDOT: PSS/Au PSC.

Table 3 KGeCl $_3$ PSC performance before optimization (at thickness of absorber layer =300 nm, $E_g=1.49$ eV, $N_D=N_A=1\times 10^{14}~cm^{-3}$ and $N_t=10^{13}~cm^{-3}$) with different ETLs and HTLs.

Device architecture	V _{OC} (V)	J _{SC} (mA/ cm ²)	FF (%)	PCE (%)
FTO/C ₆₀ /KGeCl ₃ / Spiro- OMeTAD/Au	1.30	22.60	80.39	23.63
FTO/C ₆₀ /KGeCl ₃ / PEDOT: PSS/ Au	1.30	22.67	80.49	23.74
FTO/C ₆₀ /KGeCl ₃ / Cu ₂ O/Au	1.30	22.80	80.56	23.90
FTO/WS ₂ /KGeCl ₃ /MoS ₂ /Au	1.02	23.04	81.11	19.09
FTO/WS ₂ /KGeCl ₃ /CuI/Au	1.31	23.10	84.41	25.57
FTO/WS ₂ /KGeCl ₃ /Spiro- OMeTAD/Au	1.31	23.10	84.22	25.51
FTO/WS ₂ /KGeCl ₃ /PEDOT: PSS/ Au	1.31	23.15	84.36	25.61
FTO/WS ₂ /KGeCl ₃ /CuI/Au	1.31	23.10	84.41	25.57
FTO/CdS/KGeCl ₃ / PEDOT: PSS/ Au	1.30	22.50	74.98	22.05
FTO/WS2/KGeCl3/CBTS/Au	1.31	23.20	83.92	25.52
FTO/WS ₂ /KGeCl ₃ /CFTS/Au	1.12	25.34	87.86	25.01
FTO/PCBM/KGeCl ₃ /Cu ₂ O/Au	1.28	13.61	84.24	14.73

layer with thickness of 300 nm shown below in Table 1. Various HTLs are used to enhance the PCE of the PSC, including CuI, Spiro-OMeTAD, Cu₂O, PEDOT: PSS and MoS₂ with thickness varying from 80 nm to 250 nm shown below in Table 2. The band alignment diagram of the optimized device shown below in Fig. 2 illustrates the transport of charge carriers, specifically the movement of photo-generated electrons (e-s) and holes (h⁺s) across the device. Electrons have propensity to migrate from higher to lower energy levels, transitioning from PEDOT: PSS ($E_C \sim$ 2.2 eV) to KGeCl₃ (with E_C ranging from 0.05 to 1.50 eV), then WS₂ (E_C ~ 1.2 eV), and ultimately to FTO (E_C ~ 1.1 eV). Likewise, hole transport is facilitated by the configuration of valence levels. Holes have ability to migrate freely from FTO ($E_V \sim -2.36$ eV) to WS₂ ($E_V \sim -0.60$ eV), then to KGeCl₃ ($E_V \sim 0$ eV), and finally to PEDOT: PSS ($E_V \sim 0.04$ eV). At the interface of WS2/KGeCl3, a moderate upward cleavage is observed. Instead of being detrimental, this phenomenon acts as a barrier, preventing excessive photo-generated e's and h's from flowing through the conduction and valence bands, respectively. Such regulation is crucial as it helps prevent rapid current saturation. The simulated performance data of KGeCl3 PSC before optimization with distinct ETLs and HTLs demonstrated in Table 3.

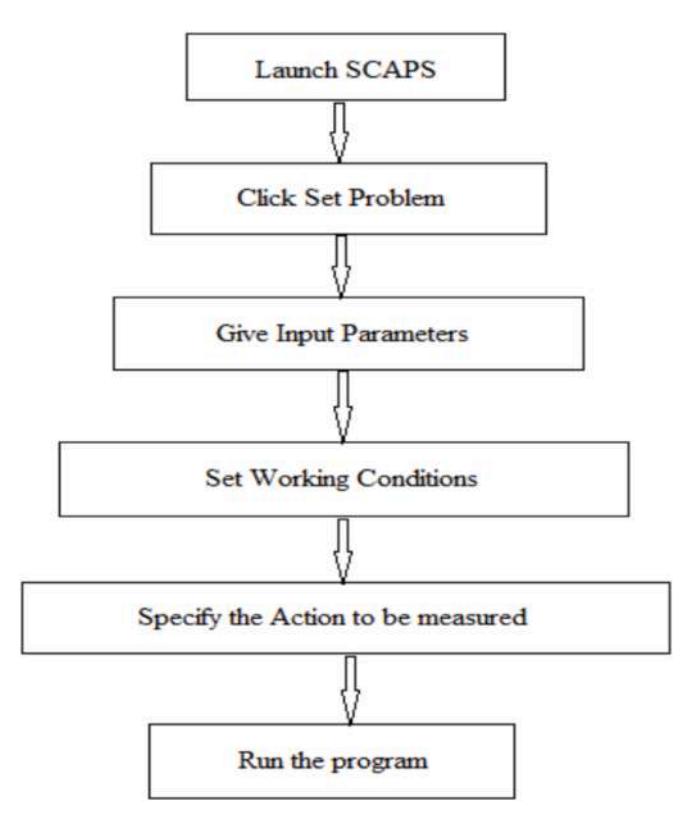


Fig. 3. Flow chart of simulation procedure.

2.2. Simulation Method

The data of different parameters are chosen from previous studies. The SCAPS-1D (version 3.3.10) has been employed for simulation. This software can be used for simulations at different input physical conditions. This tool calculation is dependent on differential equations, including Poisson's and continuity equations. It can calculate Quantum efficiency (QE), J-V curve and carrier lifetime for both e's and h^+s .

$$\frac{\partial^2 \psi}{\partial x^2} + \frac{q}{\epsilon} [p(x) - n(x) + N_D - N_A + \rho_p - \rho_n = 0$$
 (1)

$$\frac{1}{q}\frac{dJ_p}{dx} = G_{op}(x) - R(x) \tag{2}$$

$$\frac{1}{q}\frac{dJ_n}{dx} = -G_{op}(x) + R(x) \tag{3}$$

The simulations were run at 300 K using a "air mass 1.5 global" spectrum and a light power of $1000 \ W/m^2$. The work is dependent on change in thickness, E_g, N_D , and N_A at which simulation of the proposed PSC has been done. The outcome of the device has been reflected by the I–V characteristics which represent the following PV parameters: J_{SC} , FF, V_{OC} , and PCE. The simulation procedure is depicted in Fig. 3.

3. Results and discussion

3.1. Impact of distinct parameters on KGeCl3-based PSC

3.1.1. Effect of bandgap with thickness

This section includes effect of the absorber layer thickness, E_g , donor and acceptor carrier concentration (N_D and N_A) on PV parameters ($V_{\rm OC}$, $J_{\rm SC}$, FF and PCE) of KGeCl₃-based PSC where thickness of absorber layer, bandgap, N_D and N_A are fixed at 0.3 μm , 1.49 eV and 10^{15} cm $^{-3}$ respectively. The contour plot shown below in Fig. 4 demonstrates that change in PV parameters of simulated PSC as a function of thickness of

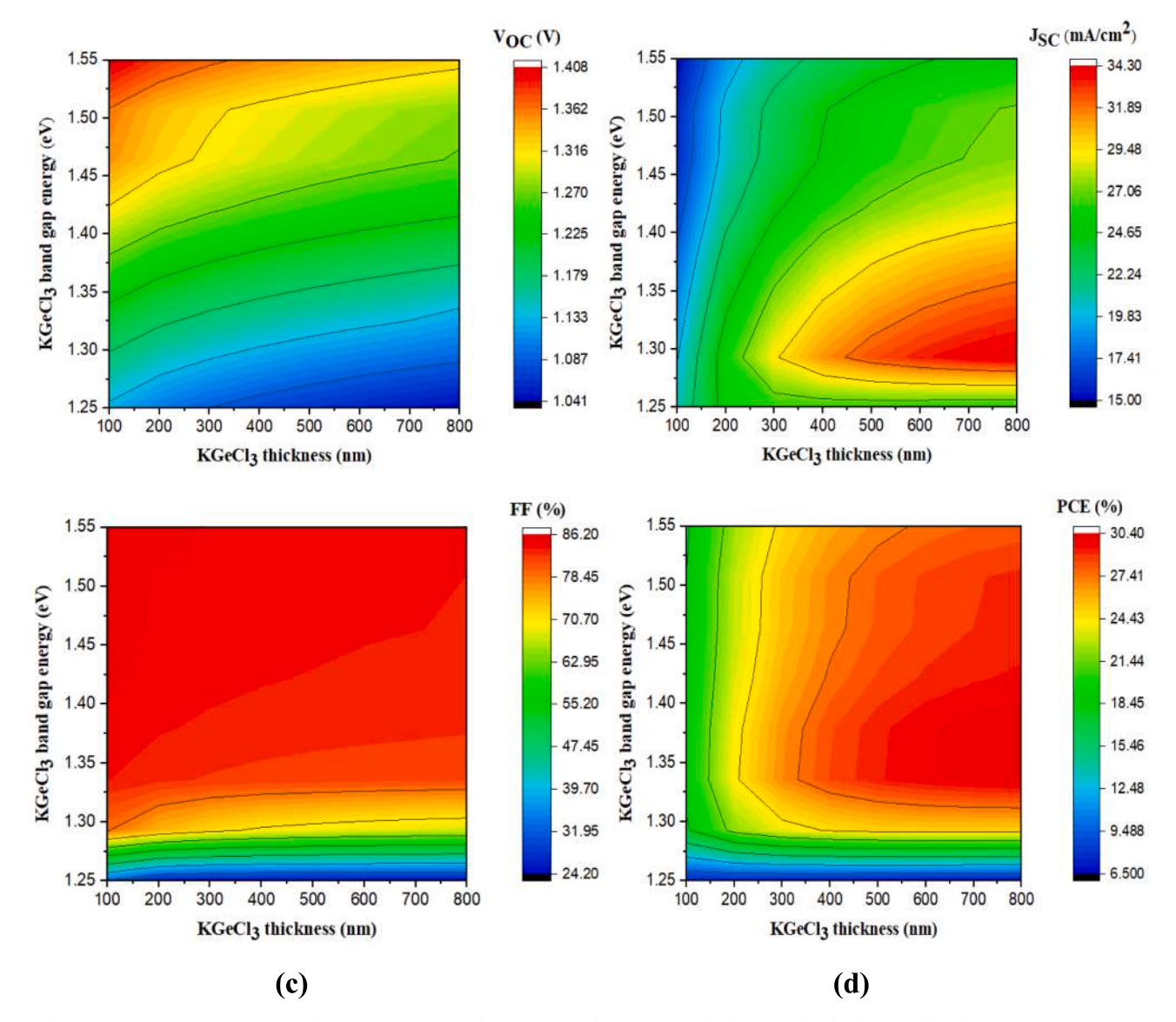


Fig. 4. Change in PV parameters of simulated PSC such as (a) V_{OC} (b) J_{SC} (c) FF and (d) PCE with thickness of absorber layer and bandgap at doping concentration of 10^{15} cm⁻³.

KGeCl₃ and its E_g change from 100 to 800 nm and from 1.25 to 1.55 eV respectively. Fig. 4(a) shows that V_{OC} increases from 1.041 V at E_g of 1.25 eV to about 1.408 V at Eg of 1.55 eV while the change in VOC with thickness rises from 100 to 800 nm. For Fig. 4 (a), a higher Eg leads to a higher V_{OC}, it allows a larger separation between the quasi-fermi levels of electrons and holes. It reduces thermal carrier generation and intrinsic recombination rates. The decrease in V_{OC} with increasing temperature can be attributed to the creation of more interfacial defects, an increase in series resistance, and a reduction in carrier diffusion length [39,40]. The value of J_{SC} falls from 34.30 to 15.09 mA/cm² with an increment in value of 1.25 to 1.55 eV depicted in Fig. 4(b). For Fig. 4 (b), J_{SC} has low values as E_g increases for the thickness between 100 to 300 nm. This is perhaps due to low charge carrier generation due to very small value of thickness. High value of J_{SC} obtained for thickness between 600 to 700 nm and at E_g of 1.30 eV. For the as E_g greater than 1.30 eV causes decreasing the absorption within the layer and hence JSC decreases [41]. The value of J_{SC} increases for each thickness of KGeCl₃, ranging from 100 to 800 nm.

The Fig. 4(c) indicate that the FF was increased from 31.69 to 86.02 % with increment in the value of E_g from 1.25 to 1.55 eV and this with simultaneous increment in KGeCl $_3$ thickness from 100-800 nm with

approximate decrement of 2.59 % in value of FF. The Fig. 4(d) depicted that the value of PCE was 6.89 % at E_g of 1.25 eV with increment in thickness of KGeCl $_3$ from 100-800 nm at various regions. An average PCE of approximately 23.30 % is attained across variations of E_g ranging from 1.25 to 1.55 eV. Additionally, within a thickness range of 500 to 800 nm, a higher performance level of about 28.85 % is achieved. These findings can be elucidated as follows: with an increase in the E_g , there is a concurrent rise in the local collection of light absorption within the KGeCl $_3$ thin film. These outcomes can be clarified by observing that as the E_g increases, the local collection efficiency of light absorption within the absorber layer increases. This enhancement augments the carrier generation rate, consequently leading to a dramatic increase in the $V_{\rm OC}$, as indicated by the equation [42].

$$V_{oc} = \frac{K_B T}{q} \ln(1 + I_{Ph} I_0) \tag{4}$$

Where V_{OC} is open circuit voltage, K_B is Boltzmann constant, T is temperature in K, q is electronic charge, I_{Ph} is Photogenerated current and I_0 is reverse saturation current. The outcomes suggest that to maximize the PCE in PSC, it is optimal to have a KGeCl $_3$ E $_g$ of 1.40 eV and a thickness ranging from 500 to 800 nm. JV plots were simulated for PSCs varying

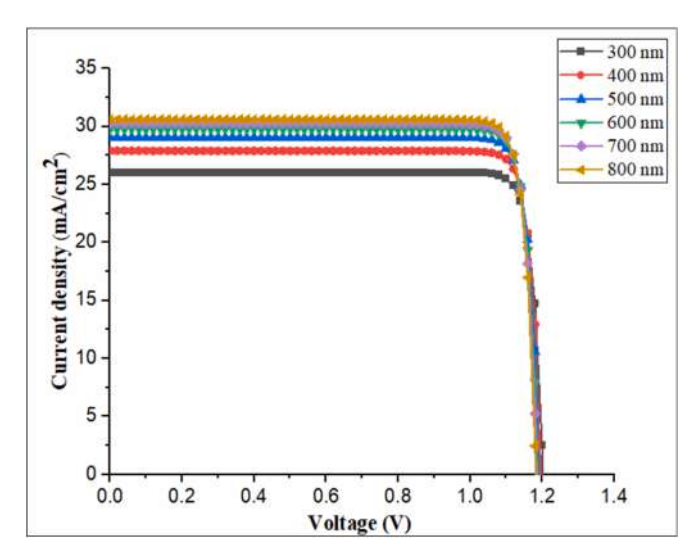


Fig. 5. The JV curves of the PSC with thickness of the absorber layer.

 $KGeCl_3$ thickness ranging from 300 to 800 nm while maintaining a fixed E_g of 1.40 eV, as depicted in Fig. 5. It is suggested that the E_g should be tuned using suitable dopants to get this optimal value of band gap. These results reveal the following trends: V_{OC} ranges between 1.18 V and 1.20 V, the J_{SC} changes from 26.05 to 30.60 mA/cm², FF remains constant at 89 % and PCE ranges from 28.06 to 29.82 % with increase in thickness of KGeCl $_3$ thickness. Notably, the PCE trend closely follows the variations in V_{OC} and FF values.

3.1.2. Effect of donor carrier concentration (ND) with thickness

The Fig. 6 demonstrates the contour plot depicting the PV parameters as functions of the KGeCl $_3$ layer thickness varies 100 to 800 nm (x-axis) and N $_D$ ranging between 1 \times 10 14 to 1 \times 10 21 cm $^{-3}$ (y-axis) respectively. From Fig. 6(a), it is revealed that the V $_{OC}$ increases from approximately 0.96 to 1.41 V as the N $_D$ rises from 1 \times 10 14 to 1 \times 10 21 cm $^{-3}$, with major fluctuations in the V $_{OC}$ values observed with increasing KGeCl $_3$ thickness. According to Fig. 6(b), the J $_{SC}$ value increases approximately 17.72 to 31.06 mA/cm 2 as N $_D$ rises from 1 \times 10 14 to 1 \times 10 19 cm $^{-3}$ and J $_{SC}$ remain constant at about 28.48 mA/cm 2 for KGeCl $_3$ thickness exceeding 400 nm. Conversely, for KGeCl $_3$ thickness below 400 nm, J $_{SC}$ maintains around 21.90 mA/cm 2 below N $_D$ of 1 \times 10 20 cm $^{-3}$. Above N $_D$ of 1 \times 10 21 cm $^{-3}$, the value of J $_{SC}$ falls to 0.37 mA/cm 2 irrespective of the KGeCl $_3$ thickness. Fig. 6(c) suggests that the FF

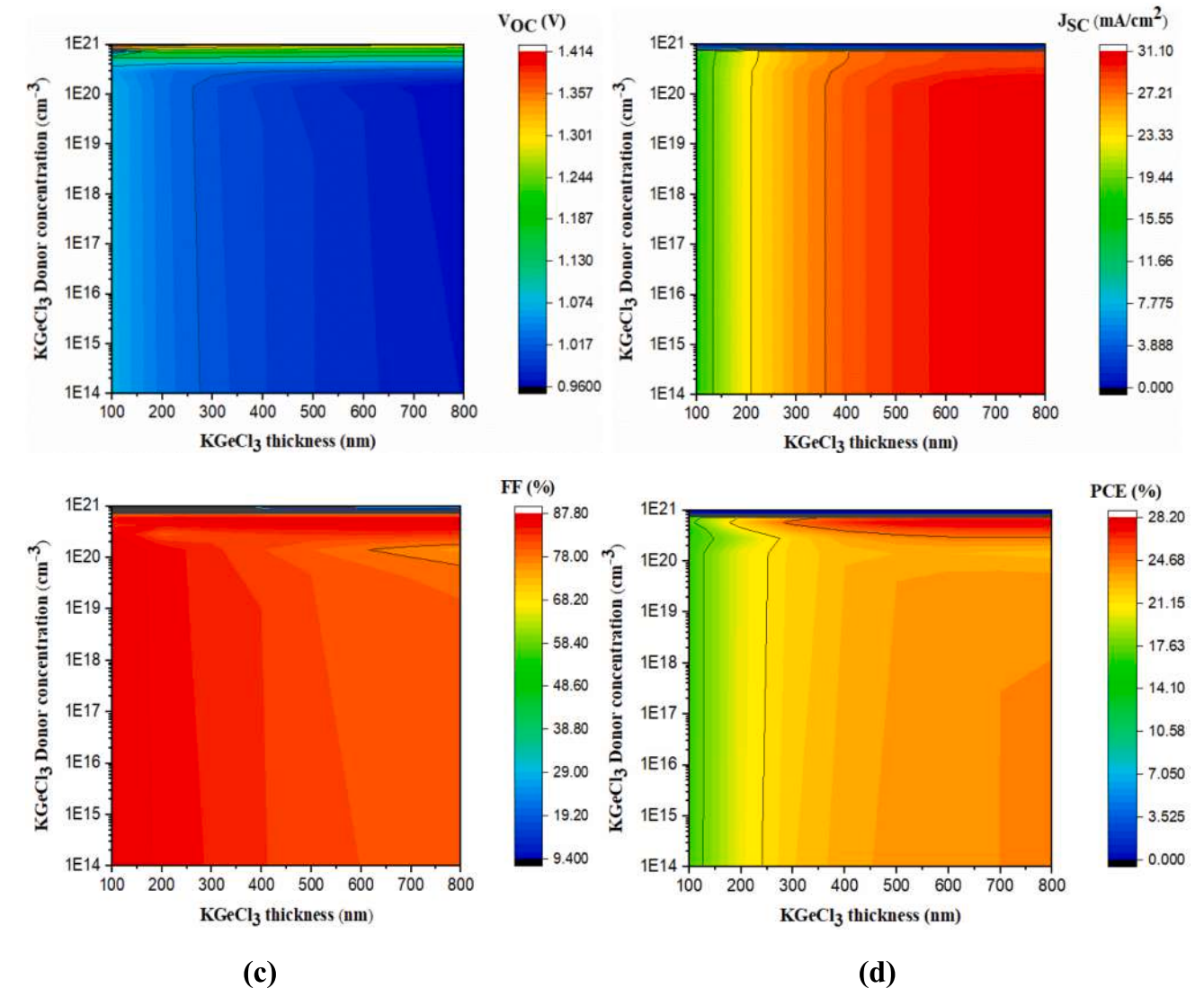
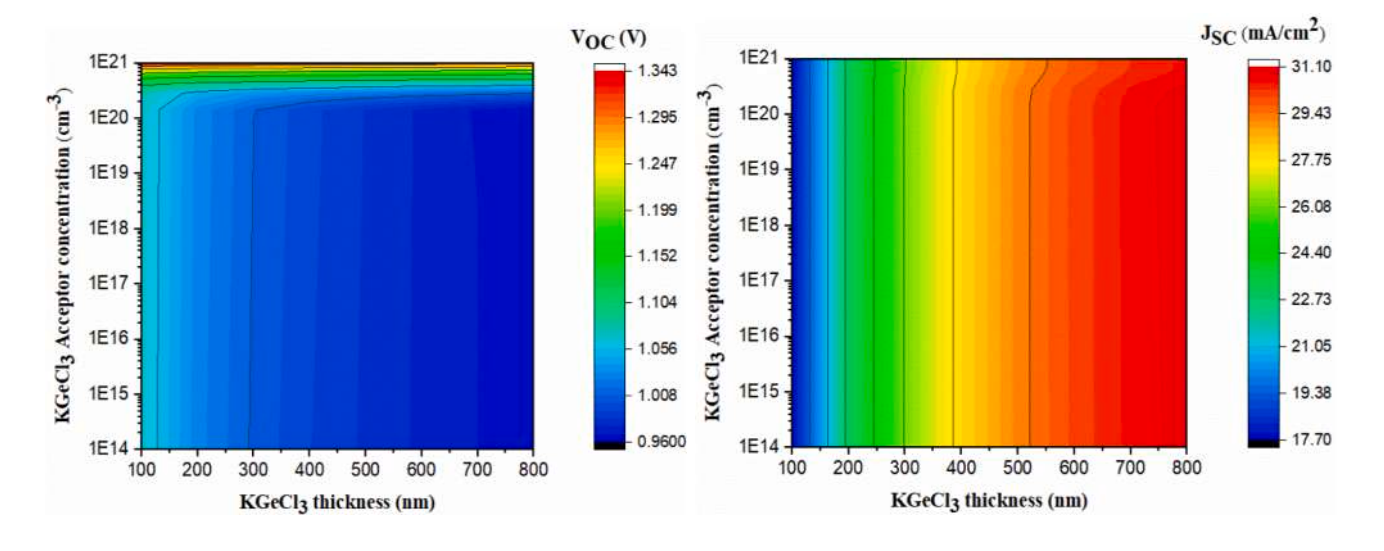


Fig. 6. Variation in PV parameters of simulated PSC such as (a) V_{OC} (b) J_{SC} (c) FF and (d) PCE with thickness of absorber layer and N_D at $E_g=1.40$ eV.



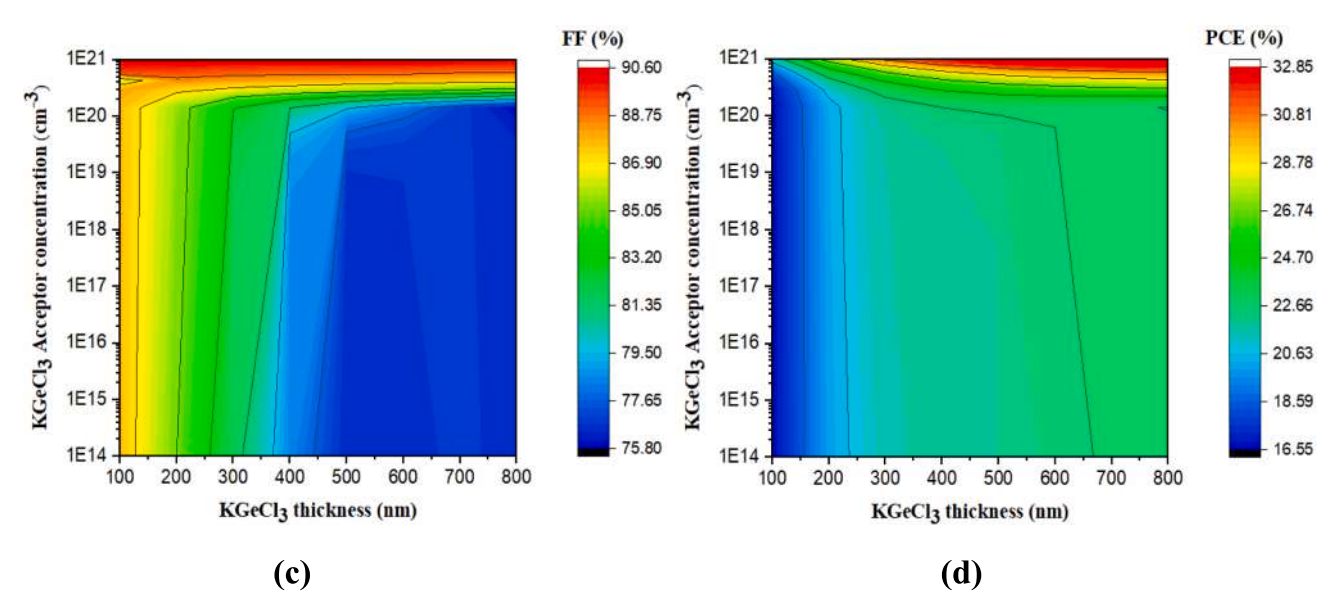


Fig. 7. Variation in PV parameters of simulated PSC such as (a) V_{OC} (b) J_{SC} (c) FF and (d) PCE with thickness of absorber layer and N_A.

maintains a relatively steady value of approximately 82.44 % across various N_D and thickness, except for N_D ranging from 1×10^{19} to 1×10^{19} 10²⁰ cm⁻³. Within a thickness range of 100 to 800 nm, first FF decreases approximately 13.46 % for the range of N_D of 1×10^{14} to 1×10^{16} cm⁻³. The FF shows a slight increase by around 3.27 % for the range of N_D of 1 $\times~10^{17}$ to $1~\times~10^{19}~cm^{-3}$ and further decrease for higher value of N_D . Fig. 6(d) depicts a correlation between N_D and PCE with KGeCl₃ thickness. As N_D increases from 1×10^{14} to 1×10^{19} cm⁻³, PCE increases whereas for N_D greater than the 1×10^{19} cm⁻³ which results in decrease in PCE. Hence, the optimized value of N_D is $1\times10^{18}\ \text{cm}^{-3}$ for KGeCl $_3\text{-}$ based PSC. Specifically, it rises from approximately 16.07 to 28.18 % with initial increment in N_D and thickness of the KGeCl₃ layer. The PCE decreased to 0.01 % with a high value of N_D. The high value of doping results in formation of coulomb traps, which decreases the mobility of charge carriers. So, we need to take the optimal value of ND for simulation [43]. This pattern suggests a direct relationship between N_D and PCE, with a more pronounced effect at higher concentrations. It is evident that increasing N_D of KGeCl₃ absorber layer has no discernible impact on the V_{OC} value, particularly when the concentrations are below $1\times 10^{20}\,\text{cm}^{-3}$, across each individual thickness. This could be attributed to the complete formation of the depletion width, impacting the

generation rate of charge carriers and the diffusion length of minority carrier's holes in ETL and electrons in HTL. Conversely, the $V_{\rm OC}$ value increases with the thickness of KGeCl $_{\rm 3}$ for each value of N $_{\rm A}$. This phenomenon can be ascribed to the prolonged lifetime and enhanced length of charge collection, resulting in greater photogenerated current. Consequently, leakage current and recombination rate decreases as the KGeCl $_{\rm 3}$ thickness grows [44]. The PCE values encapsulate the overall performance of $V_{\rm OC}$, $J_{\rm SC}$ and FF, with its value primarily influenced by $V_{\rm OC}$ and FF shown below in Fig. 6.

3.1.3. Effect of acceptor carrier concentration (N_A) with thickness

Fig. 7 illustrates a contour plot showcasing the change in the photovoltaic parameters with respect to two key factors: thickness of KGeCl $_3$ ranging from 100 to 800 nm and N_A ranging from 1×10^{14} to 1×10^{21} cm $^{-3}$. From Fig. 7(a), it is evident that the V_{OC} shows improvement, increasing from 0.96 to 1.34 V as N_A enhances from 1×10^{14} to 1×10^{21} cm $^{-3}$. Meanwhile, there is only a minor change in the V_{OC} values with increase in KGeCl $_3$ thickness. In Fig. 7(b), it is analyzed that the value of J_{SC} increases from approximately 17.71 to 30.60 mA/cm 2 as N_A rises from 1×10^{14} to 1×10^{21} cm $^{-3}$ for increase in thickness of KGeCl $_3$. However, the value of J_{SC} remains constant around 17.71 mA/cm 2 for

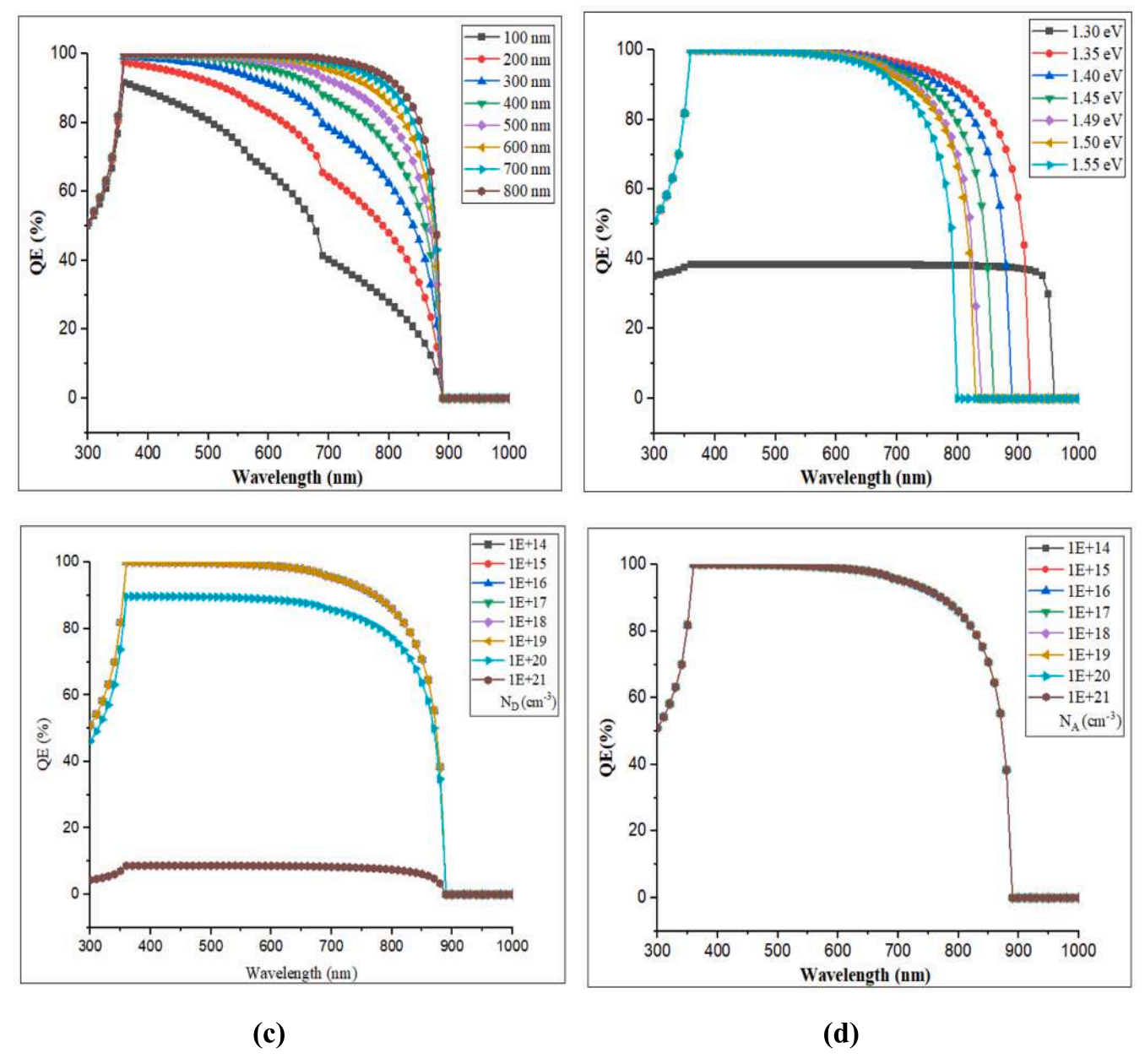


Fig. 8. The QE curves of the simulated PSC as a function of absorber layer (a) thickness, (b) E_o, (c) N_D and (d) N_A.

 N_A ranging from 1×10^{14} to $1\times 10^{21}~\text{cm}^{-3}$ at constant thickness of KGeCl₃. From Fig. 7(c), it can be inferred that the FF values generally remain constant at around 88 % across various NA and thicknesses. However, there is an exception: for N_A ranging from 1×10^{14} to 1×10^{21} cm⁻³ and thickness of the absorber layer between 100 to 500 nm, the FF increases from approximately 76.48 to 90.58 %. Additionally, a higher FF value of about 91 % is achieved for N_A of 1 \times $10^{21}~\text{cm}^{-3}$ and for various thickness ranging from 100 to 800 nm. In Fig. 7(d), it is evident that the PCE increases from 16.56 % to 28.63 % as N_A rises from 1×10^{14} to 1×10^{17} cm⁻³, accompanied by an increase in thickness. Subsequently, as N_A further increases from 1×10^{17} to 1×10^{21} cm⁻³, the value of PCE rises from 17.50 % to 31.10 %. These findings may be rationalized by the increase in carrier concentration leading to heightened electron diffusion from the KGeCl₃ layer to ETL. This elevated electron diffusion subsequently augments the device's built-in voltage (V_{bi}), predominantly formed by the depletion width, consequently resulting in a significant rise in V_{OC} [42,45]. However, the J_{SC} values improve with increasing N_A due to enhancement of photogenerated

charge carriers and the reduction of both leakage current and recombination current, particularly noticeable for KGeCl₃ thickness exceeding 300 nm. These simulation results conclude that the optimized value of N_A is $1\times 10^{19}~cm^{-3}$ for KGeCl₃-based PSC.

In this instance, the shape of PCE closely mirrors J_{SC} , as the N_A predominantly affects the photogenerated current. Consequently, the QE is measured as a function of thickness of absorber layer, E_g and carrier concentration, as illustrated in Fig. 8. It's apparent that QE exhibits a different shape for the different values of thickness, reaching 50 % at 300 nm and 100 % at 800 nm. As the E_g increases from 1.30 to 1.55 eV, the region under the curve representing higher QE shifts downward from 1000 to 800 nm depicted in Fig. 8(b). The Fig. 8(c) showed that the N_D is raised from 1×10^{14} to 1×10^{20} cm⁻³, the QE value enhances from approximately 50 to 98 % across wavelengths from 300 to 640 nm. Conversely, the QE value declines from 98 to 34 % for longer wavelengths from 640 to 880 nm. The QE value falls from 99 to 4 % for all further wavelengths at N_D of 1×10^{21} cm⁻³. Regardless of the N_A value, the QE maintains consistent values and shapes demonstrated in Fig. 8

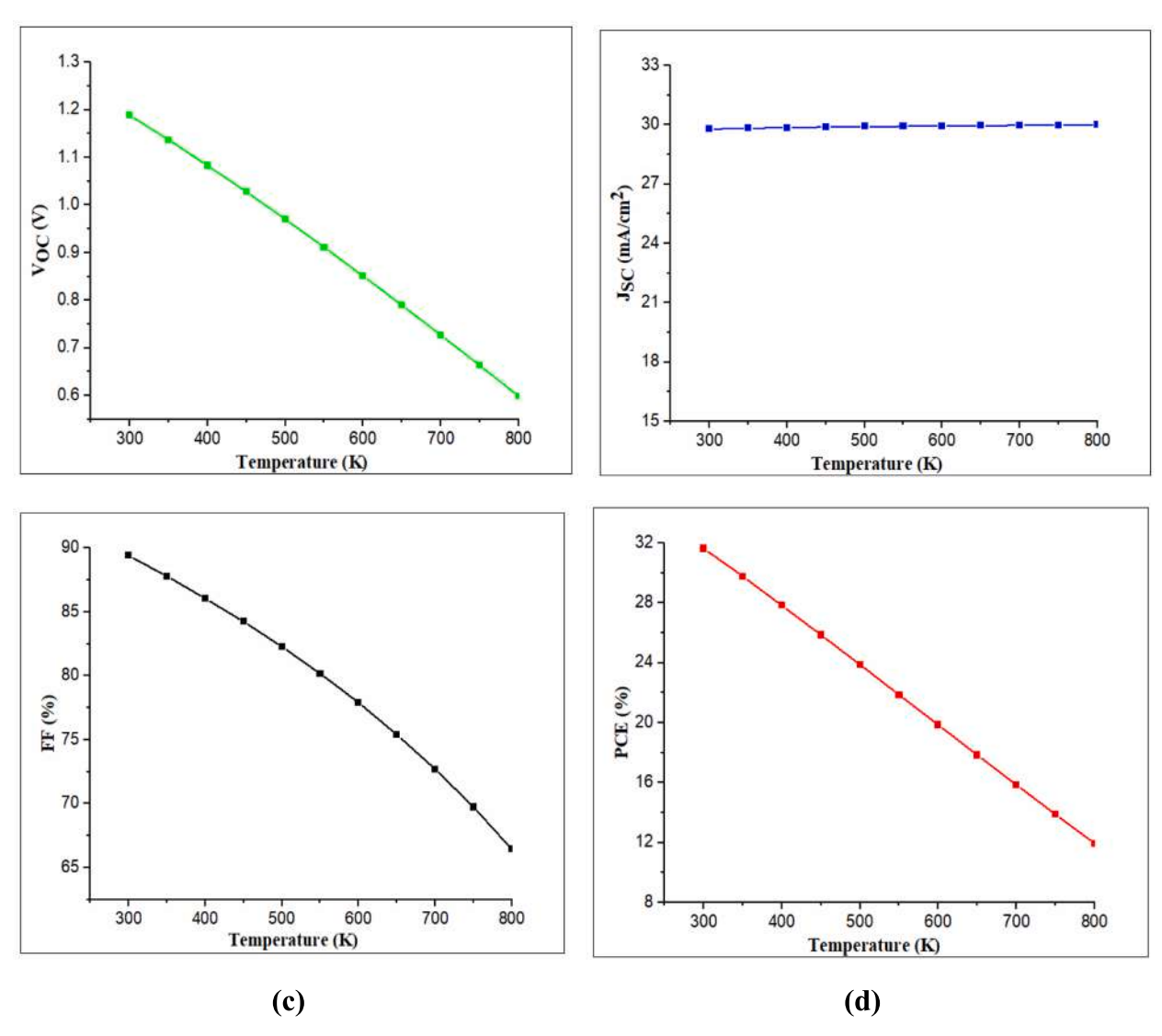


Fig. 9. Impact of temperature on PV parameters of KGeCl₃ PSC.

 Table 4

 Effect of change in temperature on PV parameters.

Temperature	V _{OC} (V)	J_{SC} (mA/cm ²)	FF (%)	PCE (%)
300 K	1.188	29.78	89.39	31.64
350 K	1.136	29.83	87.78	29.78
400 K	1.083	29.86	86.05	27.84
450 K	1.027	29.89	84.23	25.87
500 K	0.970	29.91	82.27	23.88
550 K	0.911	29.93	80.17	21.87
600 K	0.851	29.95	77.91	19.86
650 K	0.789	29.96	75.39	17.84
700 K	0.727	29.98	72.70	15.85
750 K	0.663	29.99	69.74	13.88
800 K	0.598	30.00	66.44	11.93

(d). The findings suggest that the photogenerated current increases with high-energy photons but decreases for lower-energy ones, indicating differing rates of charge generation and recombination that influence J_{SC} . These results confirm and support the notion that PCE is primarily affected by J_{SC} [46]. Based on the simulations, it can be inferred that the KGeCl $_3$ Eg, thickness, N_D and N_A should fall within the ranges of 1.40 eV, 600 nm, 1×10^{18} cm $^{-3}$ and 1×10^{19} cm $^{-3}$, respectively to attain higher PCE.

3.2. Effect of temperature on PSC

To examine the impact of operating temperature on the PV parameters, WS2 is used as ETL and PEDOT: PSS as HTL as illustrated in Fig. 9. The operating temperature at which the PSC operates has been varied between 300 K and 800 K depicted in Table 4. Fall in the performance with temperature increase is related to a decrease in diffusion length of charge carriers [47]. Several solar cell architectures show the instability of their overall performance due to deformation among layers at high temperatures. In KGeCl₃-based PSC, fall in efficiency with temperature is about 63 %, for thickness of ETL and HTL is 100 nm and 80 nm respectively. When the enhancement of temperature occurs, the PCE drops significantly from 31.64 % at 300 K to 11.93 % at 800 K. The sharp fall in PCE shows that the optimized device is highly unstable towards higher values of temperature. The minor rise in J_{SC} with increasing temperature results in reduced E_g and creation of additional e⁻-h⁺ pairs [48]. The value of V_{OC} is decreasing with an increase in the operating temperature with increasing interfacial defects and series resistance. The decrease in diffusion length with increase in temperature, leading to a rise in series resistance, which in turn impacts the FF and overall PCE of the device [49,50]. The increment in temperature results in enhancement in reverse saturation current and recombination rate of charge carriers, therefore the V_{OC}, FF and PCE decreased [51,52]. The simulation outcomes showed that the optimized value of temperature is

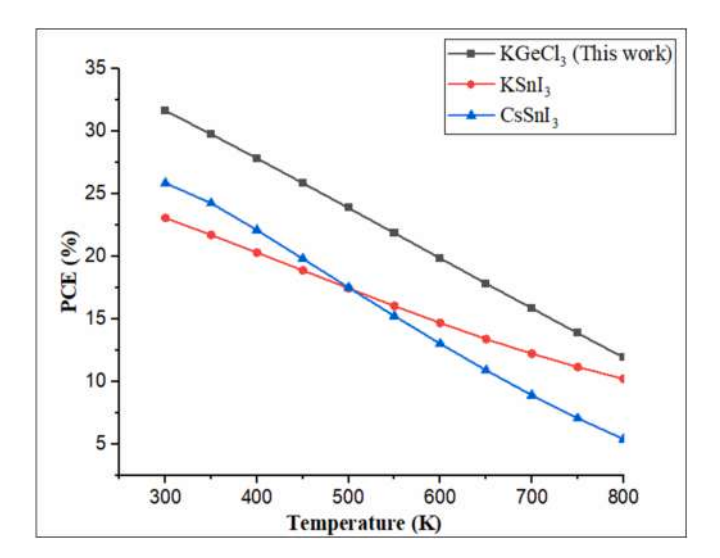


Fig. 10. PCE vs temperature curves of various PSC materials [53,54].

300 K. Comparison of observed temperature dependance with PCE of different PSC materials is shown below in Fig. 10.

3.3. Verification with respect to the ideal cell

The comparison of the obtained PV parameters of KGeCl $_3$ -based PSC as a function of absorber layer E $_g$ with the ideal single junction solar cell parameters has been done. The maximum PCE of 29.82 % with V $_{OC}$ of 1.19 V, J $_{SC}$ of 30.08 mA/cm 2 , and FF of 82.74 % for the optimized configuration of FTO/WS $_2$ /KGeCl $_3$ /PEDOT: PSS/Au has been obtained at E $_g$ of 1.49 eV and radiative recombination coefficient of 10^{-12} cm 3 /sec. The ideal single junction solar cell parameters are as follows: PCE of 31.00 %, V $_{OC}$ of 1.20 V, J $_{SC}$ of 29.80 mA/cm 2 , and FF of 89.80 % at the absorber layer E $_g$ of 1.50 eV [55]. This demonstrated that the work outcomes are within the limit of the ideal single junction solar cell parameters.

4. Conclusions

This work comprises simulation study of KGeCl3-based PSC. The effect of distinct parameters, including thickness of absorber layer, ETLs and HTLs, Eg ND, NA and operating temperature have been examined using SCAPS-1D. The study demonstrated PEDOT: PSS as a promising HTL that could replace the expensive and less-conductive Spiro-OMe-TAD. The maximum PCE of 29.82 % was obtained for the configuration of FTO/WS2/KGeCl3/PEDOT: PSS/Au. The SCAPS-1D outcomes, deduced that the optimized thickness of the absorber layer was 600 nm, with N_D of 1×10^{18} cm⁻³ and a N_A of 1×10^{19} cm⁻³ results in maximum PCE at E_g of 1.40 eV. The optimized PSC is simulated at N_t of 1×10^{15} cm⁻³. The simulation trend demonstrated that photovoltaic performance of a PSC falls with increment in operating temperature hence 300 K is optimized temperature. The device PCE improved beyond 29 % by optimizing thickness, operating temperature, Eg, ND and NA. The proper optimization of suitable ETL and HTL has been done for KGeCl3-based PSC hence, this can be an alternative to Pb-based PSC for the preparation of efficient, low-cost and eco-friendly PSCs.

CRediT authorship contribution statement

Rahul Kundara: Writing – original draft, Visualization, Methodology, Investigation, Formal analysis, Data curation, Conceptualization. **Sarita Baghel:** Writing – review & editing, Validation, Supervision, Resources, Formal analysis.

Declaration of competing interest

The authors declare that they have no known competing financial interests or personal relationships that could have appeared to influence the work reported in this paper.

Acknowledgment

The author, Rahul Kundara is thankful to Delhi Technological University, New Delhi for providing a senior research fellowship. We are very grateful to Marc Burgelman, the Electronics and Information Systems (ELIS), University of Gent, Belgium, for providing us with SCAPS-1D software.

References

- M.S. Islam, K. Sobayel, A. Al-Kahtani, M.A. Islam, G. Muhammad, N. Amin, M. Shahiduzzaman, M. Akhtaruzzaman, Defect study and modelling of SnX3-based perovskite solar cells with SCAPS-1D, Nanomater. 11 (2021), https://doi.org/ 10.3390/nanol1051218
- [2] A. Singha, A. Paul, S. Koul, V. Sharma, S. Mallick, K.R. Balasubramaniam, D. Kabra, Stable and Efficient Large Area 4T Si/perovskite Tandem Photovoltaics with Sputtered Transparent Contact, Sol. RRL. 7 (2023) 2300117, https://doi.org/ 10.1002/solr.202300117.
- [3] J. Jeong, M. Kim, J. Seo, H. Lu, P. Ahlawat, A. Mishra, Y. Yang, M.A. Hope, F. T. Eickemeyer, M. Kim, Y.J. Yoon, Pseudo-halide anion engineering for α-FAPbI3 perovskite solar cells, Nature. 592 (2021) 381–385, https://doi.org/10.1038/s41586-021-03406-5.
- [4] Y. Tang, Z. Gu, C. Fu, Q. Xiao, S. Zhang, Y. Zhang, Y. Song, FAPbl3 Perovskite Solar cells: From Film morphology regulation to device optimization, Sol. RRL. 6 (2022) 2200120, https://doi.org/10.1002/solr.202200120.
- [5] C. Liang, Z. Huang, J. Su, L. Shi, S. Liang, Y. Dong, Study on Performance Optimization of Perovskite Solar Cells Based on MAPbl3, Adv. Theor Simul. 7 (2024) 2301015, https://doi.org/10.1002/adts.202301015.
- [6] Y. Liu, Y. Liu, Y. Guo, Organic-inorganic hybrid perovskite materials and their application in transistors, Mater. Chem. Front. 7 (2023) 5215–5246, https://doi. org/10.1039/D3QM00697B.
- [7] A. Kojima, K. Teshima, Y. Shirai, T. Miyasaka, Organometal halide perovskites as visible-light sensitizers for photovoltaic cells, J. Am. Chem. Soc. 131 (2009) 6050–6051, https://doi.org/10.1021/ja809598r.
- [8] N.G. Park, Perovskite solar cells: an emerging photovoltaic technology, Mater. Today. 18 (2015) 65–72, https://doi.org/10.1016/j.mattod.2014.07.007.
- [9] Y. Zhao, K. Zhu, Organic-inorganic hybrid lead halide perovskites for optoelectronic and electronic applications, Chem. Soc. Rev. 45 (2016) 655–689, https://doi.org/10.1039/C4CS00458B.
- [10] M. Kulbak, D. Cahen, G. Hodes, How important is the organic part of lead halide perovskite photovoltaic cells? Efficient CsPbBr3 cells, J. Phys. Chem. Lett. 6 (2015) 2452–2456, https://doi.org/10.1021/acs.jpclett.5b00968.
- [11] G.E. Eperon, S.D. Stranks, C. Menelaou, M.B. Johnston, L.M. Herz, H.J. Snaith, Formamidinium lead trihalide: a broadly tunable perovskite for efficient planar heterojunction solar cells, Energy Environ. Sci. 7 (2014) 982–988, https://doi.org/ 10.1039/C3FF43822H.
- [12] N.A. Ouedraogo, Y. Chen, Y.Y. Xiao, Q. Meng, C.B. Han, H. Yan, Y. Zhang, Stability of all-inorganic perovskite solar cells, Nano Energy. 67 (2020) 104249, https://doi.org/10.1016/j.nanoen.2019.104249.
- [13] N. Sun, S. Fu, Y. Li, L. Chen, J. Chung, M.M. Saeed, K. Dolia, A. Rahimi, C. Li, Z. Song, Y. Yan, Tailoring Crystallization Dynamics of CsPbI3 for Scalable Production of Efficient Inorganic Perovskite Solar Cells, Adv. Funct. Mater. 34 (2024) 2309894, https://doi.org/10.1002/adfm.202309894.
- [14] J. Zhuang, J. Wang, F. Yan F, Review on chemical stability of lead halide perovskite solar cells, Nano-Micro Letters. 15 (2023) 84. doi: 10.1007/s40820-023-01046-0.
- [15] S. Gressler, F. Part, S. Scherhaufer, G. Obersteiner, M. Huber-Humer, Advanced materials for emerging photovoltaic systems–Environmental hotspots in the production and end-of-life phase of organic, dye-sensitized, perovskite, and quantum dots solar cells, Sustain. Mater. Techno. 34 (2022) e00501. doi: 10.1016/ j.susmat.2022.e00501.
- [16] G. Schileo, G. Grancini, Lead or no lead? Availability, toxicity, sustainability and environmental impact of lead-free perovskite solar cells, J. Mater. Chem. c. 9 (2021) 67–76, https://doi.org/10.1039/D0TC04552G.
- [17] N.K. Noel, S.D. Stranks, A. Abate, C. Wehrenfennig, S. Guarnera, A.A. Haghighirad, A. Sadhanala, G.E. Eperon, S.K. Pathak, M.B. Johnston, A. Petrozza, L.M. Herz, H. J. Snaith, Lead-free organic-inorganic tin halide perovskites for photovoltaic applications, Energy Environ. Sci. 7 (2014) 3061–3068, https://doi.org/10.1039/ c4ee01076k.
- [18] M.G. Ju, M. Chen, Y. Zhou, H.F. Garces, J. Dai, L. Ma, N.P. Padture, X.C. Zeng, Earth-Abundant Nontoxic Titanium(IV)-based Vacancy-Ordered Double Perovskite Halides with Tunable 1.0 to 1.8 eV Bandgaps for Photovoltaic Applications, ACS Energy Lett. 3 (2018) 297–304, https://doi.org/10.1021/acsenergylett.7b01167.

- [19] Z. Zhang, X. Li, X. Xia, Z. Wang, Z. Huang, B. Lei, Y. Gao, High-Quality (CH3NH3) 3Bi2I9 Film-Based Solar Cells: Pushing Efficiency up to 1.64%, J. Phys. Chem. Lett. 8 (2017) 4300–4307, https://doi.org/10.1021/acs.jpclett.7b01952.
- [20] M. Wang, P. Zeng, S. Bai, J. Gu, F. Li, Z. Yang, M. Liu, High-Quality Sequential-Vapor-Deposited Cs2AgBiBr6 Thin Films for Lead-Free Perovskite Solar Cells, Sol. RRL. 2 (2018) 1800217, https://doi.org/10.1002/solr.201800217.
- [21] Y. Zong, Y. Zhou, Y. Zhang, Z. Li, L. Zhang, M.G. Ju, M. Chen, S. Pang, X.C. Zeng, N. P. Padture, Continuous Grain-Boundary Functionalization for High-Efficiency Perovskite Solar Cells with Exceptional Stability, Chem. 4 (2018) 1404–1415, https://doi.org/10.1016/j.chempr.2018.03.005.
- [22] M.A. Siddique, A.S. Rahman, The SCAPS-1D simulation of non-toxic KGeCl3 perovskite from DFT derived properties, Mater. Sci. Eng. b. 303 (2024) 117268, https://doi.org/10.1016/j.mseb.2024.117268.
- [23] N. Shrivastav, M.A. Hamid, J. Madan, R. Pandey, Exploring KGeCl3 material for perovskite solar cell absorber layer through different machine learning models, Sol. Energy. 278 (2024) 112784, https://doi.org/10.1016/j.solener.2024.112784.
- [24] K. Sekar, L. Marasamy, S. Mayarambakam, H. Hawashin, M. Nour, J. Bouclé, Lead-free, formamidinium germanium-antimony halide (FA 4 GeSbCl 12) double perovskite solar cells: the effects of band offsets, RSC Adv. 13 (2023) 25483–25496, https://doi.org/10.1039/D3RA03102K.
- [25] V. Kumar, R. Kumar, F. Chand, Performance analysis of ecofriendly Ge based perovskite solar cell using computational approach, Materials Letters. 361 (2024) 136145, https://doi.org/10.1016/j.matlet.2024.136145.
- [26] M.S. Azizman, A.W. Azhari, D.S. Halin, N. Ibrahim, S. Sepeai, N.A. Ludin, M. N. Nor, L.N. Ho, Progress in tin-germanium perovskite solar cells: A review, Synthetic Metals. 299 (2023) 117475, https://doi.org/10.1016/j.synthmet.2023.117475.
- [27] A. Kuddus, M.F. Rahman, S. Ahmmed, J. Hossain, A.B.M. Ismail, Role of facile synthesized V205 as hole transport layer for CdS/CdTe heterojunction solar cell: Validation of simulation using experimental data, Superlattices Microstruct. 132 (2019) 106168, https://doi.org/10.1016/j.spmi.2019.106168.
- [28] U. Mandadapu, S.V. Vedanayakam, K. Thyagarajan, Simulation and analysis of lead based perovskite solar cell using SCAPS-1D, Indian, Journal of Science and Technology. 10 (2017) 65–72, https://doi.org/10.17485/ijst/2017/v11i10/ 110721
- [29] F. Azri, A. Meftah, N. Sengouga, A. Meftah, Electron and hole transport layers optimization by numerical simulation of a perovskite solar cell, Sol. Energy. 181 (2019) 372–378. https://doi.org/10.1016/j.solener.2019.02.017.
- [30] K.D. Jayan, V. Sebastian, Comprehensive device modelling and performance analysis of MASnI3 based perovskite solar cells with diverse ETM, HTM and back metal contacts, Sol. Energy. 217 (2021) 40–48, https://doi.org/10.1016/j. solener.2021.01.058.
- [31] M.K. Hossain, G.F.I. Toki, A. Kuddus, M.H.K. Rubel, M.M. Hossain, H. Bencherif, M.F. Rahman, M.R. Islam, M. Mushtaq, An extensive study on multiple ETL and HTL layers to design and simulation of high-performance lead-free CsSnCl3-based perovskite solar cells, Sci Rep. 13 (2023) 2521, https://doi.org/10.1038/s41598-023-02506.
- [32] H. Wei, P. Qiu, Y. Li, Y. He, M. Peng, X. Zheng, X. Liu, Challenges and strategies of all-inorganic lead-free halide perovskite solar cells, Ceram. Int. 48 (2022) 5876–5891, https://doi.org/10.1016/j.ceramint.2021.11.184.
- [33] S. Rai, B.K. Pandey, D.K. Dwivedi, Modeling of highly efficient and low cost CH3NH3Pb (I1-xClx) 3 based perovskite solar cell by numerical simulation, Opt. Mater. 100 (2020) 109631, https://doi.org/10.1016/j.optmat.2019.109631.
- [34] S.Z. Haider, H. Anwar, M. Wang, Theoretical device engineering for high-performance perovskite solar cells using CuSCN as hole transport material boost the efficiency above 25%, Phys. Status Solidi (a). 216 (2019) 1900102 https://doi.org/10.1002/pssa.201900102.
- [35] A.A. Kanoun, M.B. Kanoun, A.E. Merad, S. Goumri-Said, Toward development of high-performance perovskite solar cells based on CH3NH3Gel3 using computational approach, Sol. Energy. 182 (2019) 237–244, https://doi.org/ 10.1016/j.solener.2019.02.041.
- [36] S. Bhattarai, T.D. Das, Optimization of carrier transport materials for the performance enhancement of the MAGeI3 based perovskite solar cell, Sol. Energy. 217 (2021) 200–207, https://doi.org/10.1016/j.solener.2021.02.002.
- [37] I.M. De Los Santos, H.J. Cortina-Marrero, M.A. Ruíz-Sánchez, L. Hechavarría-Difur, F.J. Sánchez-Rodríguez, M. Courel, H. Hu, Optimization of CH3NH3PbI3

- perovskite solar cells: A theoretical and experimental study, Sol. Energy. 199 (2020) 198-205. doi: 10.1016/j.solener.2020.02.026.
- [38] S. Kohnehpoushi, P. Nazari, B.A. Nejand, M. Eskandari, MoS2: a two-dimensional hole-transporting material for high-efficiency, low-cost perovskite solar cells, Nanotechnol. 29 (2018) 205201, https://doi.org/10.1088/1361-6528/aab1d4.
- [39] D. Ompong, J. Singh, High open-circuit voltage in perovskite solar cells: The role of hole transport layer, Org. Electron. 63 (2018) 104–108, https://doi.org/10.1016/j. orgel.2018.09.006.
- [40] T. Ouslimane, L. Et-Taya, L. Elmaimouni, A. Benami, Impact of absorber layer thickness, defect density, and operating temperature on the performance of MAPbI3 solar cells based on ZnO electron transporting material, Heliyon. 7(3) (2021) e06379. doi: 10.1016/j.heliyon.2021.e06379.
- [41] M. Asaduzzaman, M. Hasan, A.N. Bahar, An investigation into the effects of band gap and doping concentration on Cu (In, Ga) Se 2 solar cell efficiency, SpringerPlus. 5 (2016) 1–8, https://doi.org/10.1186/s40064-016-2256-8.
- [42] M. Abdelfatah, J. Ledig, A. El-Shaer, A. Wagner, V. Marin-Borras, A. Sharafeev, P. Lemmens, M.M. Mosaad, A. Waag, A. Bakin, Fabrication and characterization of low cost Cu2O/ZnO: Al solar cells for sustainable photovoltaics with earth abundant materials, Sol. Energy Mater. Sol. Cells. 145 (2016) 454–461, https:// doi.org/10.1016/j.solmat.2015.11.015.
- [43] Z. Shang, T. Heumueller, R. Prasanna, G.F. Burkhard, B.D. Naab, Z. Bao, M. D. McGehee, A. Salleo, Trade-off between trap filling, trap creation, and charge recombination results in performance increase at ultralow doping levels in bulk heterojunction solar cells, Adv. Energy Mater. 6 (2016) 1601149, https://doi.org/10.1002/aemm.201601149.
- [44] K.P. Musselman, A. Marin, L. Schmidt-Mende, J.L. MacManus-Driscoll, Incompatible length scales in nanostructured Cu2O solar cells, Adv. Funct. Mater. 22 (2012) 2202–2208, https://doi.org/10.1002/adfm.201102263.
- [45] W.M. Lin, N. Yazdani, O. Yarema, S. Volk, M. Yarema, T. Kirchartz, V. Wood, Simulating nanocrystal-based solar cells: A lead sulfide case study, J. Chem. Phys. 151 (2019) 241104, https://doi.org/10.1063/1.5129159.
- [46] M. Abdelfatah, A.M. El Sayed, W. Ismail, S. Ulrich, V. Sittinger, A. El-Shaer, SCAPS simulation of novel inorganic ZrS2/CuO heterojunction solar cells, Sci. Rep. 13 (2023) 4553, https://doi.org/10.1038/s41598-023-31553-4.
- [47] G. Pindolia, S.M. Shinde, P.K. Jha, Optimization of an inorganic lead free RbGel3 based perovskite solar cell by SCAPS-1D simulation, Sol. Energy. 236 (2022) 802–821, https://doi.org/10.1016/j.solener.2022.03.053.
- [48] V. Deswal, S. Kaushik, R. Kundara, S. Baghel, Numerical simulation of highly efficient Cs2AgInBr6-based double perovskite solar cell using SCAPS 1-D, Mater. Sci. Eng. b. 299 (2024) 117041, https://doi.org/10.1016/j.mseb.2023.117041.
- [49] M.K. Hossain, M.H. Rubel, G.I. Toki, I. Alam, M.F. Rahman, H. Bencherif, Effect of various electron and hole transport layers on the performance of CsPbI3-based perovskite solar cells: A numerical investigation in DFT, SCAPS-1D, and wxAMPS frameworks, ACS Omega. 7 (2022) 43210–43230, https://doi.org/10.1021/ acsomega.2c05912.
- [50] R. Kundara, S. Baghel, Device modelling of lead free (CH3NH3) 2CuX4 based perovskite solar cells using SCAPS simulation, Opt. Quantum Electron. 55 (2023) 968, https://doi.org/10.1007/s11082-023-05244-3.
- [51] S. Áhmed, F. Jannat, M.A.K. Khan, M.A. Alim, Numerical development of ecofriendly Cs2TiBr6 based perovskite solar cell with all-inorganic charge transport materials via SCAPS-1D, Optik. 225 (2021) 165765, https://doi.org/10.1016/j. iileo.2020.165765.
- [52] A. Chen, K. Zhu, Computer simulation of a-Si/c-Si heterojunction solar cell with high conversion efficiency, Sol. Energy. 86 (2012) 393–397, https://doi.org/ 10.1016/j.solener.2011.10.015.
- [53] G. Pindolia, S.M. Shinde, P.K. Jha, Non-leaded, KSnI3 based perovskite solar cell: A DFT study along with SCAPS simulation, Mater Chem Phys. 297 (2023) 127426, https://doi.org/10.1016/j.matchemphys.2023.127426.
- [54] M. Jiang, J. Tang, Simulated development and optimized performance of narrow-bandgap CsSnl3-based all-inorganic perovskite solar cells, J. Phys. d: Appl. Phys. 54 (2021) 465104, https://doi.org/10.1088/1361-6463/ac1e4c.
- [55] A. Morales-Acevedo, Fundamentals of solar cell physics revisited: Common pitfalls when reporting calculated and measured photocurrent density, open-circuit voltage, and efficiency of solar cells, Sol. Energy. 262 (2023) 111774, https://doi. org/10.1016/j.solener.2023.05.051.

RESEARCH ARTICLE



Performance optimization of CsSnI₃-based perovskite solar cells using SCAPS-1D and machine learning analysis

Rahul Kundara¹ · Sarita Baghel¹

Received: 21 September 2024 / Accepted: 13 January 2025 © The Author(s), under exclusive licence to The Optical Society of India 2025

Abstract Tin-based perovskite solar cells (PSCs) can be employed in place of lead-based PSC, delivering equivalent efficiency and stability while eliminating the use of lead. The work comprises simulation of CsSnI₃-based PSC by using the SCAPS-1D software. The device performance with several electron transport layers such as ZnO, TiO₂, WO₃, CdS, IGZO and MoS₂, CuSbS₂, Cu₂O, V₂O₅, CuInS₂ QD as hole transport layers is studied. The several factors such as thickness of the absorber layer, operating temperature, work function and defect density (N_t) are varied. The optimized thickness of the absorber layer is 400 nm. The optimized architecture, FTO/CdS/CSnI₃/MoS₂/Pd has achieved a maximum efficiency of 23.45% at 300 K and N_t of 1×10^{13} cm⁻³. The ML model predicts the effect of distinct parameters on device performance and PCE using SHAP plot, XGB and RF algorithm. XGB model predicts performance with accuracy of 99.93%. The ML model is helpful for the fabrication of efficient CSnI₃ PSCs.

Keywords $SCAPS-1D \cdot CsSnI_3$ -based $PSC \cdot PCE \cdot Machine learning \cdot ETLs$ and HTLs

Introduction

Perovskite solar cells (PSCs) became popular among the researchers in past few years, due to its encouraging characteristics such as tunable energy bandgap (E_g), high optical absorption coefficient, a long diffusion length of charge carriers, high carrier mobility, hybrid nature, less toxicity,

Published online: 01 February 2025

cheap in fabrication, high power conversion efficiency (PCE) or efficiency [1, 2]. Perovskite has many applications in electronic devices viz. photodetectors, light emitting diodes (LEDs), solar cells, counters and photovoltaics (PVs) [3]. Despite various advantages, stability is a major concern for commercialization of PSC devices. To overcome this stability issue, many researchers focused on the inorganic hole transport layer (HTL) and HTL free PSCs [4].

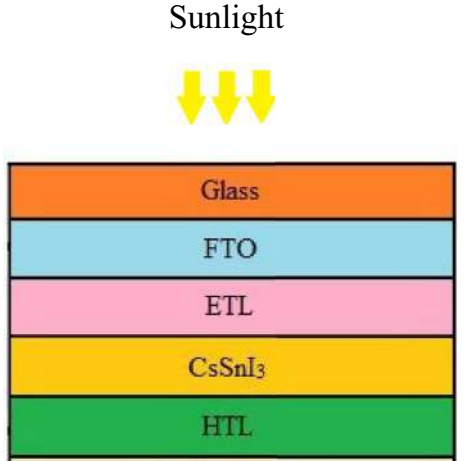
In recent years, the PCE of Sn-based devices has enhanced up to 22% [5]. Elements such as Sn, Bi and Ge are alternatives to Pb in PSCs [6]. A CsSnI₃-based PSC has achieved the highest efficiency of 3.83% [7]. Lead-free inorganic tin-based PSC such as CsSnI₃ has congenial narrow direct bandgap of 1.3 eV with structural stability, long charge-carrier life-time, excellent hole mobility (μ_p) of 585 cm²/V⁻¹ s⁻¹, and high absorption coefficient of 10⁴ cm⁻¹. All these properties are analogous to that of methylammonium lead triiodide (CH₃NH₃PbI₃) [8, 9]. Therefore, it is the widely explored tin-based semiconductor material for photovoltaic (PV) applications. The typical device configuration of PSC is constituted with three layers such as an electron transport layer (ETL), absorber layer and a HTL [10]. ETL's primary roles are preventing holes from passing through it and gathering electrons from the absorber layer [11]. For a suitable HTL in perovskite device, it must have high hole mobility [12], the band matching with the other layers and electrodes [2, 13, 14]. The PSC efficiency is improved by the use of an appropriate ETL and HTL which extracts the photoelectrons and the holes respectively introduced by the perovskite layer. To achieve the maximum efficiency, the proper band matching of the device layers is essential. To choose the best ETL and HTL to increase PSC performance, the suitable bandgap optimization is needed. Till date, the CsSnI₃-based PSC has achieved the maximum efficiency of 12.96% with conventional device structure of ITO/TiO₂/CsSnI₃/Spiro-OMeTAD/Au [15].



Rahul Kundara rahul_2k20phdap10@dtu.ac.in

Delhi Technological University, New Delhi, Delhi, India

We have investigated the impact of several ETLs (ZnO, TiO₂, IGZO, WO₃ and CdS) and HTLs (MoS₂, Cu₂O, CuInS₂ QD, $CuSbS_2$ and V_2O_5) on the performance of PSC. The optimization of thickness of absorber layer, operating temperature, defect density (N_t) and back contact has been done to obtain the optimum performance. Back contact's work function was changed from 4.6 eV to 5.3 eV. The simulated device structure is FTO/ETL/CsSnI₃/HTL/Pd and achieved a maximum PCE of 23.45% for the CsSnI₃-based PSC. The outcome demonstrates that through proper optimization for suitable selection of ETL and HTL, leads to enhanced the performance of PSC. Alongside its substantial influence in multiple fields, machine learning (ML) has become a powerful tool for analyzing and optimizing complex systems. In this work, ML is employed to eliminate the lengthy and tedious calculations usually necessary in simulations. SCAPS-1D produces an extensive dataset by varying the thickness, N_t and operating temperature. XGBoost (XGB) and random forest (RF), ML algorithms have been employed to enhance the accuracy of PCE prediction, aiming to streamline computations and improve precision. Systematic simulations with SCAPS-1D when combined with machine learning have demonstrated the complex interactions between the features such as thickness of absorber layer, defect density and operating temperature. A total of 501 datasets were generated for this study. The XGB outperforms RF with high R² and low mean square error (MSE). The trained XGB model predicts the PCE of PSC with an accuracy of above 99%. SHAP plots generated using ML give the clear comparison of influence, the feature values have on the device efficiency. This approach could facilitate the development of innovative CsSnI₃-based PSCs without the need for tedious and complex simulations. The use of ML algorithms for



Back contact

Fig. 1 Structure of simulated model of PSCs



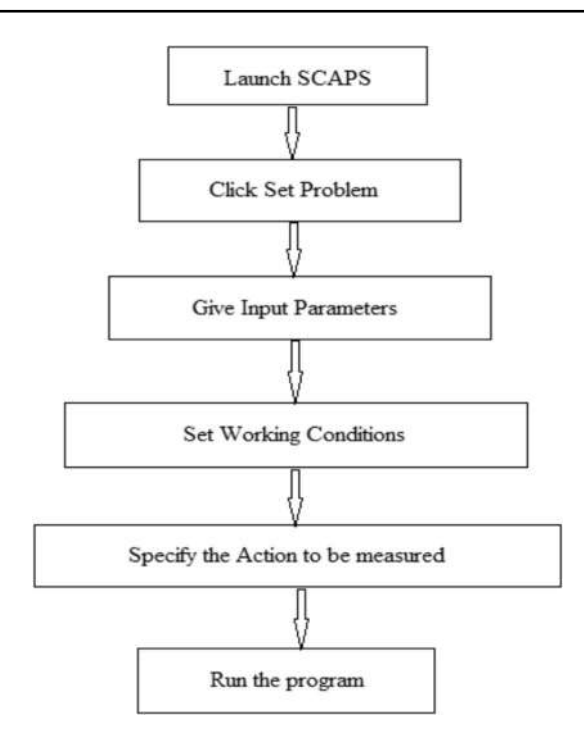


Fig. 2 SCAPS-1D software simulation procedure

PCE prediction in solar cells offers a promising approach to improve accuracy, flexibility, and efficiency. The integration of ML with SCAPS data holds the potential to transform the optimization process and fabrication of the efficient PSCs.

Simulation procedure and device architecture

The data for various parameters have been selected from past studies, and the simulation was performed through SCAPS-1D (version 3.3.10). This software is capable of simulating various input conditions. Its calculations are based on differential equations, including Poisson's and continuity equations.

$$\frac{\partial^2 \psi}{\partial x^2} + \frac{q}{\epsilon} [p(x) - n(x) + N_D - N_A + \rho_p - \rho_n = 0 \tag{1}$$

$$\frac{1}{a}\frac{dJ_p}{dx} = G_{op}(x) - R(x) \tag{2}$$

$$\frac{1}{a}\frac{dJ_n}{dx} = -G_{op}(x) + R(x) \tag{3}$$

The PSC consists of layer structure: glass substrate/FTO/ETL/CsSnI₃/HTL/Back contact as depicted in Fig. 1. The simulations were carried out at 300 K with an "air mass 1.5 global" spectrum and a light intensity of 1000 W/m². This study investigates the effect of varying the absorber layer's

Table 1 Input parameters of PSCs

Parameter	FTO [16, 17]	TiO ₂ [18, 19]	CsSnI ₃ [20]	Spiro- OMeTAD [20–22]
Thickness (µm)	0.400	0.050	0.100	0.200
Eg (eV)	3.5	3.2	1.27	3.0
χ(eV)	4.0	4.0	4.47	2.45
ε	9.0	9	18	3.0
$N_C (cm^{-3})$	2.02×10^{18}	1×10^{21}	1×10^{19}	1×10^{19}
$N_V (cm^{-3})$	1.8×10^{19}	2×10^{20}	1×10^{19}	1×10^{19}
μ_n (cm ² /Vs)	20	20	4.37	1×10^{-4}
$\mu_p (cm^2/Vs)$	10	10	4.37	1×10^{-4}
$N_D (cm^{-3})$	2×10^{19}	1×10^{19}	0	0
$N_A (cm^{-3})$	0	4×10^{15}	1×10^{13}	2×10^{18}
$N_t (cm^{-3})$	1×10^{15}	1×10^{15}	$1 \times 10^{15*}$	1×10^{14}

thickness, N_t, operating temperature, and back contact's work function, all of which were considered in the simulation of the PSC. The device's performance is indicated by the I–V curves, which include key PV parameters. The Random Forest (RF) and XGBoost (XGB) are relatively better when handling the small and complex datasets. Also, the risk of overfitting is lower in these algorithms. The simulation steps are demonstrated in Fig. 2. The input data for simulation taken from previously reported work enclosed is in Table 1, ETLs in Table 2 and HTLs in Table 3.

Verification of the model and comparison of experimental result

The simulated result of PSC shown in Table 2 using previously reported data in Table 1. The thickness of the employed absorber layer, ETL and HTL are 100, 50 and 200 nm respectively. The device obtained PCE of 13.28%, $V_{\rm OC} = 0.90$ V, $J_{\rm SC} = 17.37$ mA/cm² and FF = 84.10%. The low value of open circuit voltage ($V_{\rm OC}$) due to direct charge recombination which results in low PCE. The device with TiO₂ as ETL has low PCE by virtue of small $V_{\rm OC}$ due to the lowest value of electron affinity. The improper band

Table 2 The previously reported experimental and simulation results

Cell structure	$V_{OC}(V)$	J _{SC} (mA/cm ²)	FF (%)	PCE (%)
ITO/TiO ₂ /CsSnI ₃ /spiro-OMeTAD/Au	0.86	23.20	65.00	12.96 [15]
FTO/TiO ₂ /CsSnI ₃ /spiro-OMeTAD/Au	0.86	23.34	64.73	12.96 (wxAMPS-software) [20]
$FTO/TiO_2/CsSnI_3/spiro-OMeTAD/Au$	0.90	17.37	84.10	13.28 [Before Optimization]

Table 3 Input parameters of various ETLs

Parameter	ZnO [21, 26]	IGZO [18]	WO ₃ [20, 21]	CdS [23]
Thickness (µm)	0.050	0.050	0.050	0.050
Eg (eV)	3.2	3.05	2.92	2.42
χ(eV)	4.26	4.16	4.5	4.3
ε	9.0	10	5.76	9.35
$N_C (cm^{-3})$	2.0×10^{18}	5×10^{18}	1.96×10^{19}	2.2×10^{18}
$N_V (cm^{-3})$	5.0×10^{18}	5×10^{18}	1.96×10^{19}	1.8×10^{19}
$\mu_n (cm^2/Vs)$	200	15	10	100
$\mu_p \text{ (cm}^2/\text{Vs)}$	5	0.1	10	25
$N_D (cm^{-3})$	1.5×10^{17}	1×10^{18}	3.68×10^{19}	1.15×10^{17}
$N_A (cm^{-3})$	0	0	0	0
$N_t (cm^{-3})$	1×10^{15}	1×10^{15}	$1 \times 10^{15*}$	$1 \times 10^{15*}$



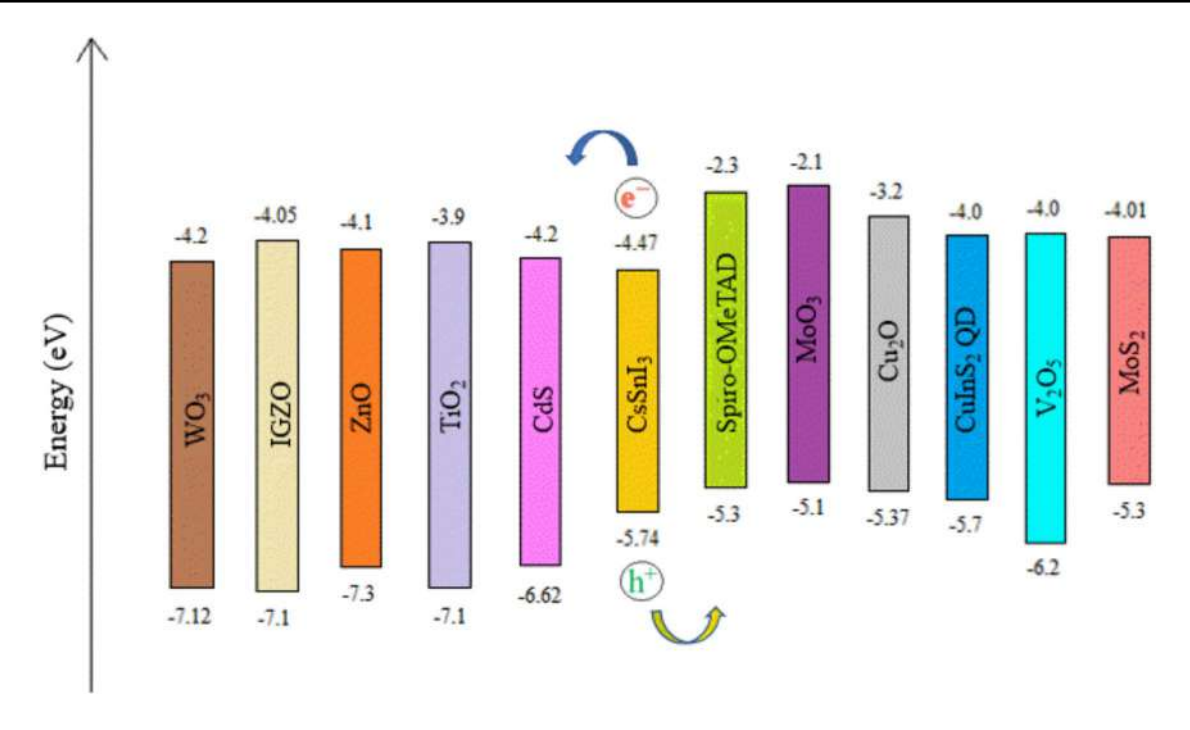


Fig. 3 Band alignment diagram of distinct ETLs, perovskite layer and HTLs

matching of various ETLs, perovskite absorber layer and HTLs is also a reason for low efficiency shown below in Fig. 3. The simulated device PCE is comparable to both the experimental and simulated outcomes demonstrated in Table 2. The quantum efficiency (QE) and J-V plots of PSC are shown in Fig. 4a, b respectively. The obtained PCE is low so there is a need to explore more ETLs and HTLs to improve the performance of PSC.

Fig. 4 a Quantum efficiency and b J-V characteristics plots

$\underline{\underline{\mathscr{D}}}$ Springer

Appropriate ETLs and HTLs to improve performance

To choose a suitable layer, the various ETLs and HTLs simulated for optimization of the PSC performance. The input parameters of simulated different ETLs such as ZnO, TiO₂, IGZO, WO₃ and CdS shown below in Table 3. The employed HTLs in simulation are MoS₂, CuSbS₂, Cu₂O,

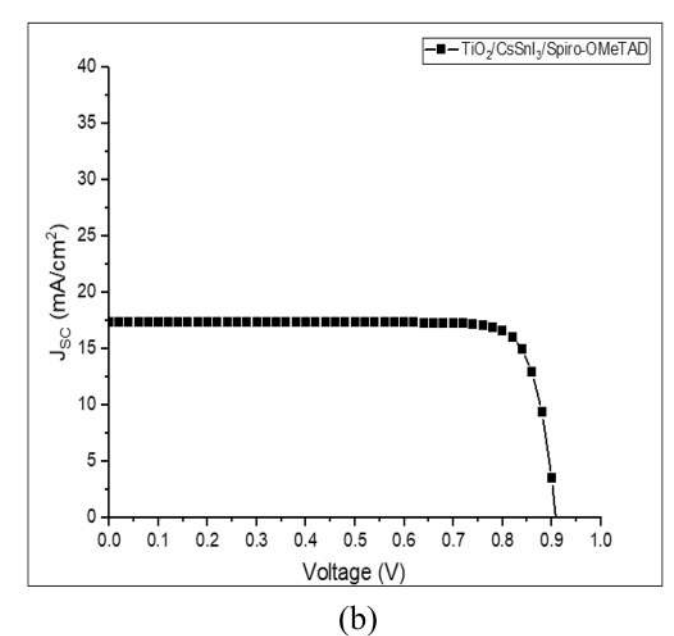


Table 4 Input parameters of distinct HTLs

Parameter	MoO ₃ [27]	Cu ₂ O [9, 16, 20]	CuInS ₂ QD [28]	V ₂ O ₅ [23]	MoS ₂ [29]
Thickness (µm)	0.200	0.200	0.200*	0.200*	0.200*
Eg (eV)	3.0	2.17	1.7	2.2	1.29
χ (eV)	2.3	3.2	4.1	4.0	4.2
ε	5.7	7.11	9.76	10.0	3.0
$N_C (cm^{-3})$	4.386×10^{19}	2.02×10^{17}	2×10^{18}	9.2×10^{17}	2.2×10^{18}
$N_V (cm^{-3})$	4.343×10^{19}	1.1×10^{19}	2×10^{19}	5×10^{18}	1.8×10^{19}
$\mu_n (cm^2/Vs)$	1×10^{-4}	200	100	3.2×10^{2}	100
$\mu_p (cm^2/Vs)$	1×10^{-4}	80	25	4×10^1	150
$N_D (cm^{-3})$	0	0	0	0	1×10^{15}
$N_A (cm^{-3})$	1×10^{18}	1×10^{18}	2×10^{16}	1×10^{18}	1×10^{17}
$N_t (cm^{-3})$	1.5×10^{17}	1×10^{14}	1×10^{14}	$1 \times 10^{14*}$	1×10^{14}

^{*}In this study

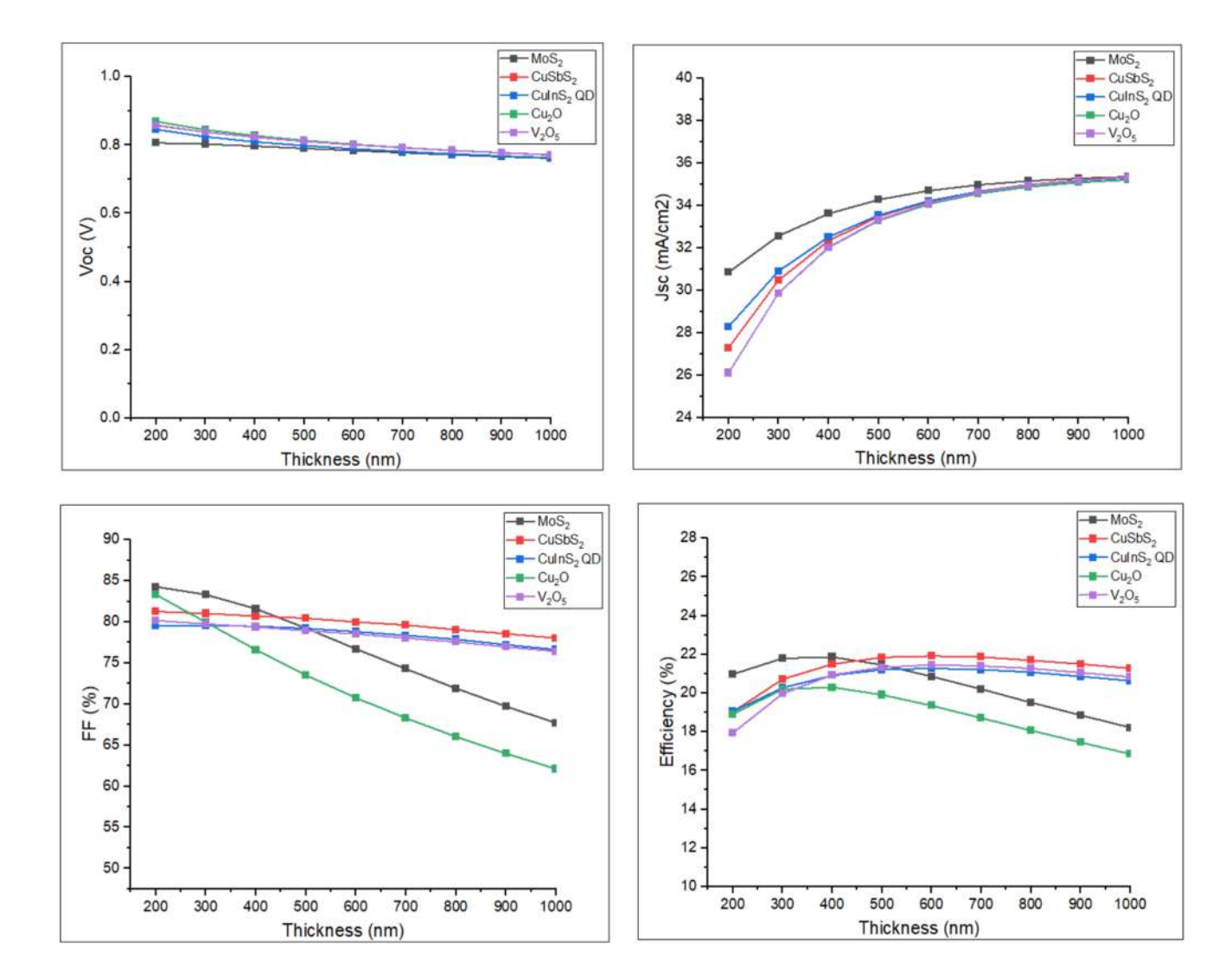
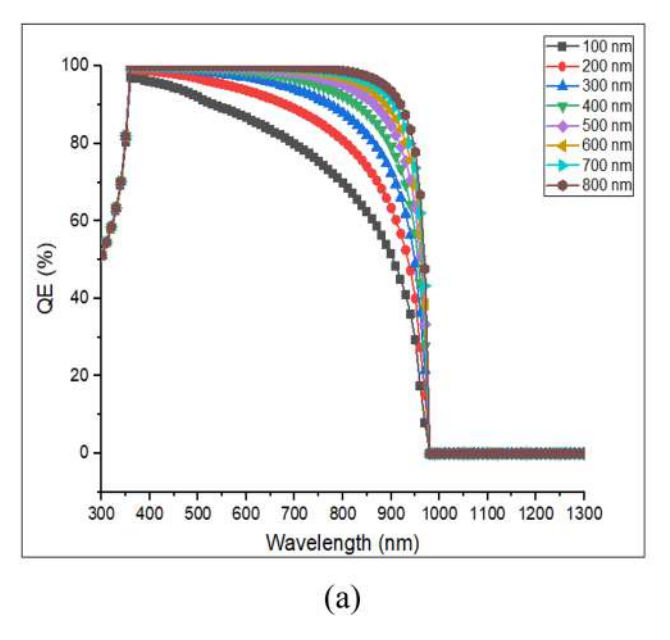


Fig. 5 Change in PV parameters of CsSnI₃-based PSCs with thickness



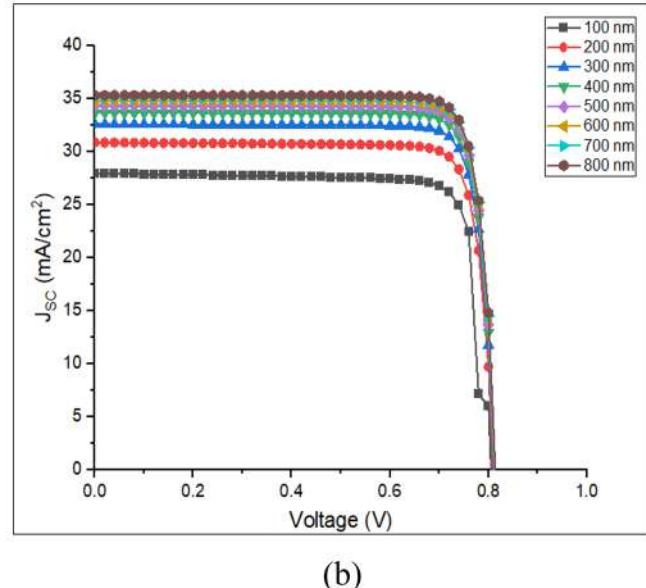


Fig. 6 a QE curve, b J-V plots of optimized CsSnI₃ PSC with thickness

 V_2O_5 and $CuInS_2$ QD demonstrated in Table 4. The value of J_{SC} for the IGZO and TiO_2 offer much nearer value with the congenial mobility of the carriers [21]. The E_g of n-type CdS is 2.4 eV which is an appropriate window material that permits a major portion of the solar spectrum to reach the perovskite layer. CdS has high transmittance and low resistivity due to its wide E_g ; it is appropriate for the fabrication of solar devices [23, 24]. When the MoS_2 is employed as HTL, it gives the highest PCE of 18.82% due to its properties such as profound light-matter interactions, significant carrier mobility and exceptional absorption capacity in visible light wavelengths therefore it has applications in fabrication of PV devices. It has the thermal stability in between the temperature from 300 to 400 K which is efficient for outside installation [25].

Result and discussion

Effect of change in thickness

The thickness of the $CsSnI_3$ layer has a direct impact on PSC performance, influencing the charge carrier's diffusion length. It is well-established that a reduction in thickness leads to a lower absorption rate. This leads to reduction in photocurrent, which consequently lowers the solar cell PCE across the 200–1000 nm range. Both V_{OC} and PCE decline exponentially as the thickness expands from 200 to 1000 nm. Optimum thickness for $CsSnI_3$ -based PSC is 400 nm and beyond that it falls. Fall in FF beyond 400 nm is 17.03%. PCE of the PSC goes up to 21.86% together with V_{OC} is

0.79 V, J_{SC} is 33.62 mA/cm² and FF is 81.60% for 400 nm. The FF decreases consistently as the thickness exceeds 400 nm. The Optimum thickness for $CsSnI_3$ PSC is 400 nm and highest efficiency achieved is 21.86% for ETL = 50 nm and HTL = 200 nm. The variation in various PV parameters with the thickness of the absorber layer, with CdS as ETL, are illustrated in Fig. 5.

The calculated QE illustrates the increment in area of the absorption spectrum with the thickness of $CsSnI_3$ layer, demonstrated in Fig. 6a. This results in high concentration of photo-generated carriers due to the improved light absorption. Hence the performance of solar cells increases. The effect of absorber layer thickness on J-V curves within a range of 100-800 nm is displayed in Fig. 6b. J_{SC} is significantly enhanced from 27.93 to 34.35 mA/cm² for increment in thickness of the $CsSnI_3$ from 100 to 500 nm. For the layer greater than 500 nm, gradual enhancement in J_{SC} attains saturation due to thick layer which could result in increment in the charge carrier recombination rate.

Impact of change in operating temperature

To evaluate the impact of the temperature on the PCE of PSC devices, the operating temperature was changed from 300 to 400 K. Decline in performance with rising temperature is associated with a shorter diffusion length of charge carriers. Many PSCs structures exhibit instability in thorough performance due to layer deformation at high temperatures. For CsSnI₃ PSC, the efficiency drops by 27.90% as the temperature rises, for ETL = 50 nm and HTL = 200 nm. With rising temperature, the PCE drops substantially, from



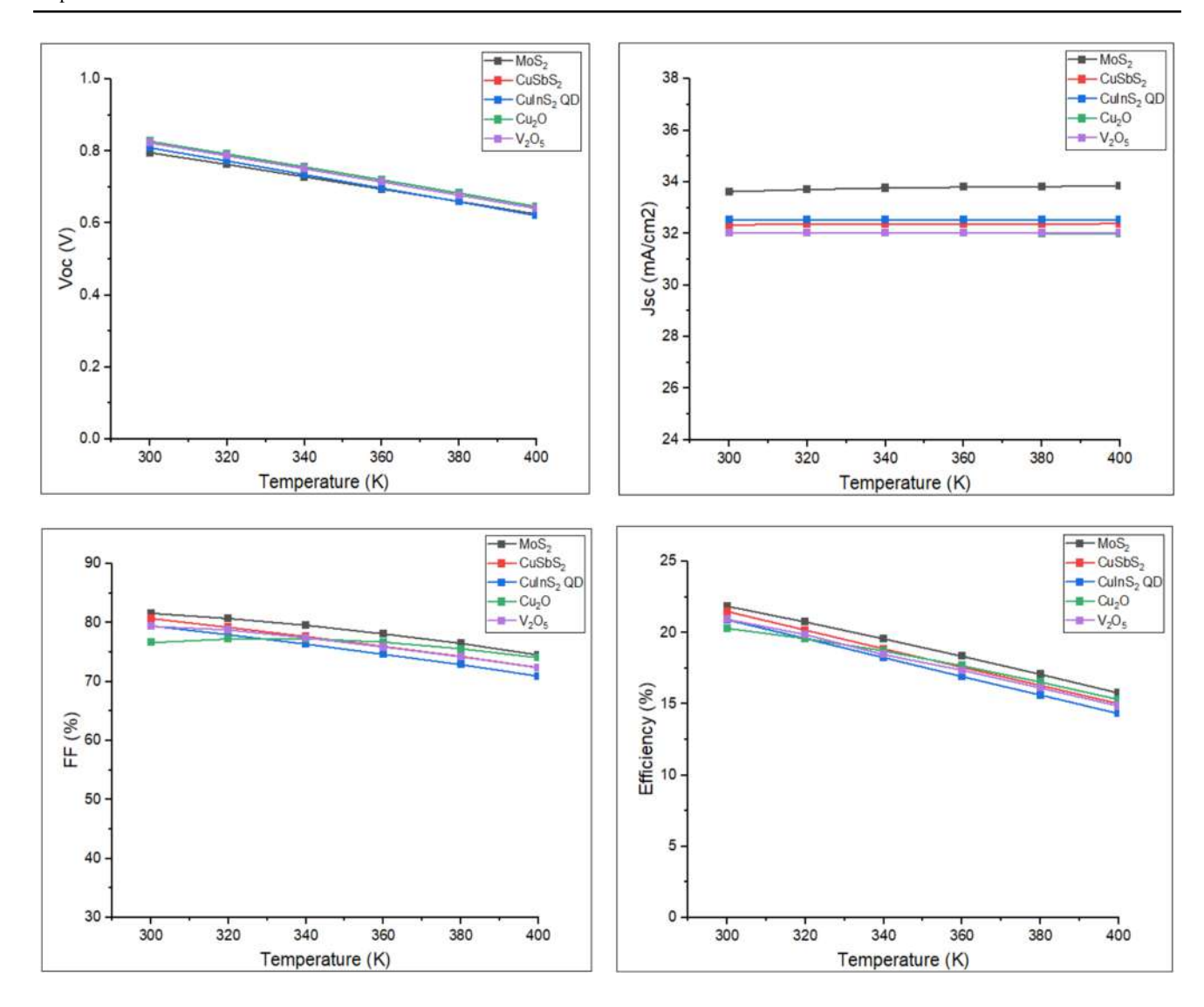


Fig. 7 Change in the PV parameters of CsSnI₃-based PSCs with operating temperature

21.86% at 300 K to 15.76% at 400 K. In simulation of $CsSnI_3$ PSC the optimized value of temperature is 300 K. V_{OC} is reduced with an increase in the operating temperature for all HTLs. The rise in temperature results in decreased performance of PSCs due to an increment in saturation current, which subsequently raises the recombination rate [30]. The effect of temperature with CdS as ETL and different HTLs on other PV parameters together with V_{OC} , J_{SC} , and FF is shown below in Fig. 7.

Impact of change in defect density

The $CsSnI_3$ layer achieves a maximum PCE of 23.45% at an optimized N_t of 1×10^{13} cm⁻³, as illustrated in Fig. 8. For perovskite layers when N_t is increased, the unwanted recombination rate rises as defects create dangling bonds, which function as the trap states for the photo-generated

charge carriers. As a result, the $\rm J_{SC}$ decreased, ultimately leading to a reduction in the FF of the PSCs. The device's PCE dropped from 23.45 to 7.76% as $\rm N_t$ was enhanced from 10^{13} to 10^{17} cm⁻³. This significant rise in recombination led to a steep decline in solar cell efficiency. The change in different PV parameters $\rm V_{OC}$, $\rm J_{SC}$, and FF with defect density for CsSnI₃ with CdS as ETL and different HTLs is demonstrated in Fig. 8. CsSnI₃-based PSC, 66.90% fall in the PCE with increase in $\rm N_t$. The simulated results are comparable to jiang et al. and chen et al. reported outcomes displayed in Table 2.

J-V and QE plots of various ETLs and HTLs

The J-V curves of distinct ETLs and HTLs shown below in Fig. 9 and QE curve demonstrated in Fig. 10. The highest occupied QE is illustrated in Fig. 10a for the CdS layer and



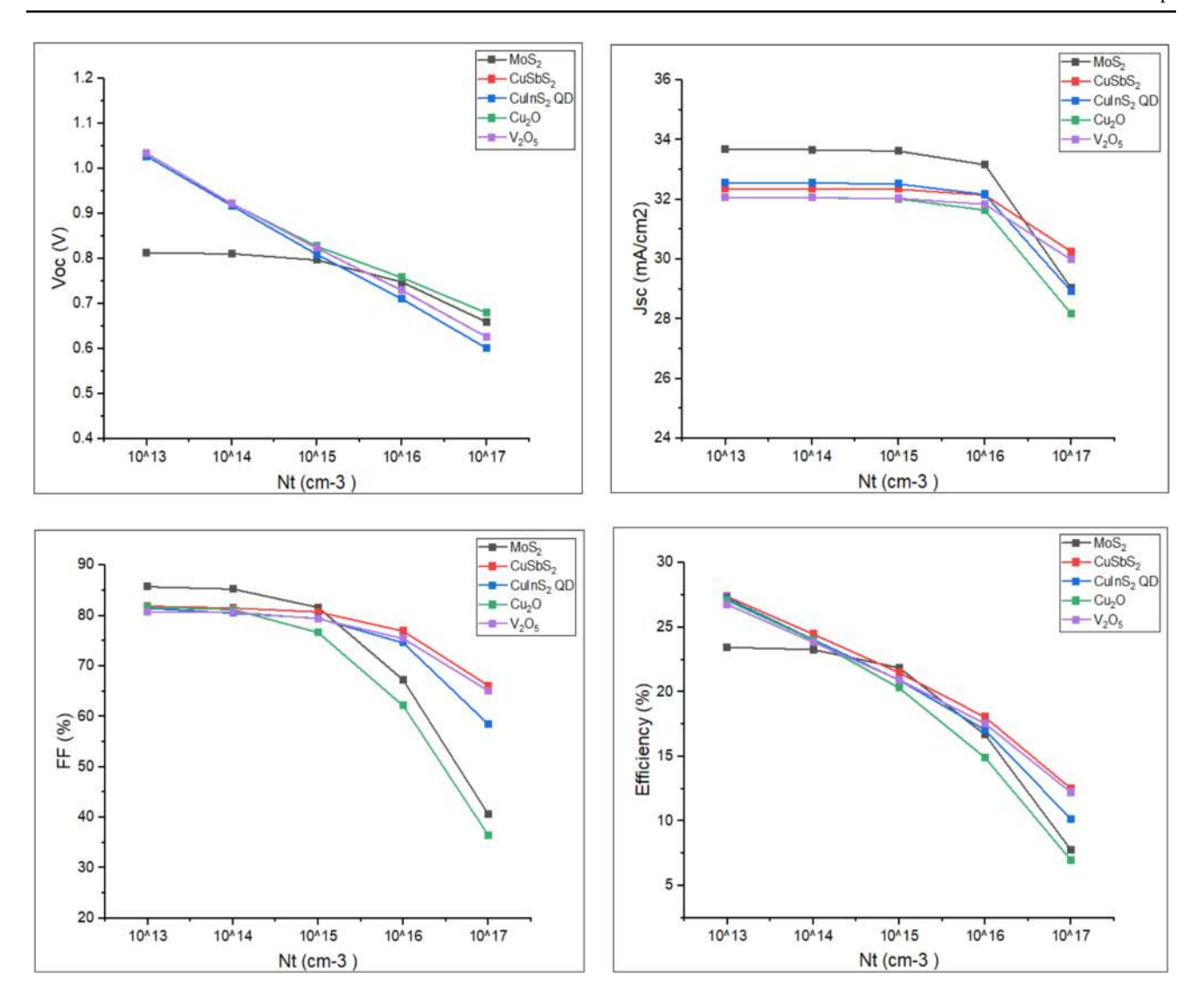


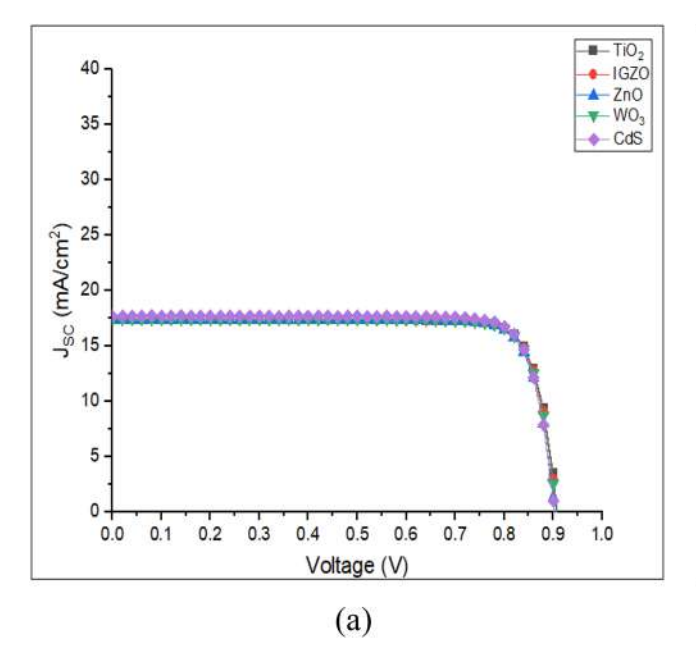
Fig. 8 Impact of N_t on the performance of CsSnI₃ PSCs

in Fig. 10b for the ${\rm MoS_2}$ layer. The device performance with various ETLs and spiro-OMeTAD as HTL in Table 5. The device performance with different HTLs and CdS as ETL tabulated in Table 6. The ${\rm MoS_2}$ HTL has highest hole mobility among the other layers, higher charge mobility is directly proportional to high value ${\rm J_{SC}}$ [31]. We can observe that all ETLs exhibit nearly the same PCE. The cell performance is affected by the band alignment and conductivity of ETLs and HTLs in PSCs [32]. High conductivity decreases ohmic losses of the cell [33]. Result shows that CdS as ETL and ${\rm MoS_2}$ as HTL suitable to achieve high efficiency of PSCs. The energy level diagram of the optimized device shown below in Fig. 11.

The band alignment diagram of the optimized device depicted in Fig. 12 demonstrates the transport of charge

carriers, specifically the movement of photo-generated electrons (e^s) and holes (h^s) across the device. Electrons tends to migrate from higher to lower energy levels, moving from MoS $_2$ ($E_C \sim 1.15~eV$) to CsSnI $_3$ (with E_C ranging from 0.94 to 1.03 eV), then CdS ($E_C \sim 0.80$ to 1.07 eV), and ultimately to FTO ($E_C \sim 0.76~eV$). Likewise, hole transport is facilitated by the configuration of valence levels. Holes have ability to migrate freely from FTO ($E_V \sim -2.73~eV$) to CdS ($E_V \sim -1.60~eV$), then to CsSnI $_3$ ($E_V \sim -0.34~eV$), and finally to MoS $_2$ ($E_V \sim -0.13~eV$). At the interface of CsSnI $_3$ /MoS $_2$, a moderate upward cleavage is observed. Instead of being detrimental, this phenomenon acts as a barrier, preventing excessive photo-generated e^s and h^s from flowing through the conduction and valence bands, respectively. Such regulation is crucial as it helps prevent rapid current saturation.





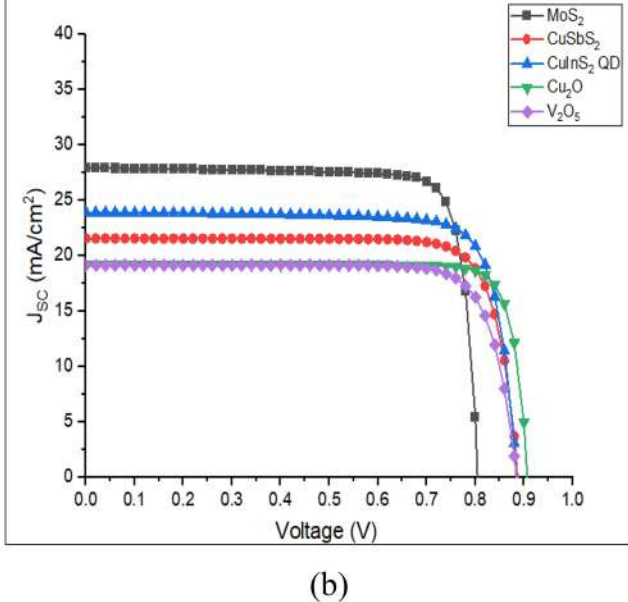
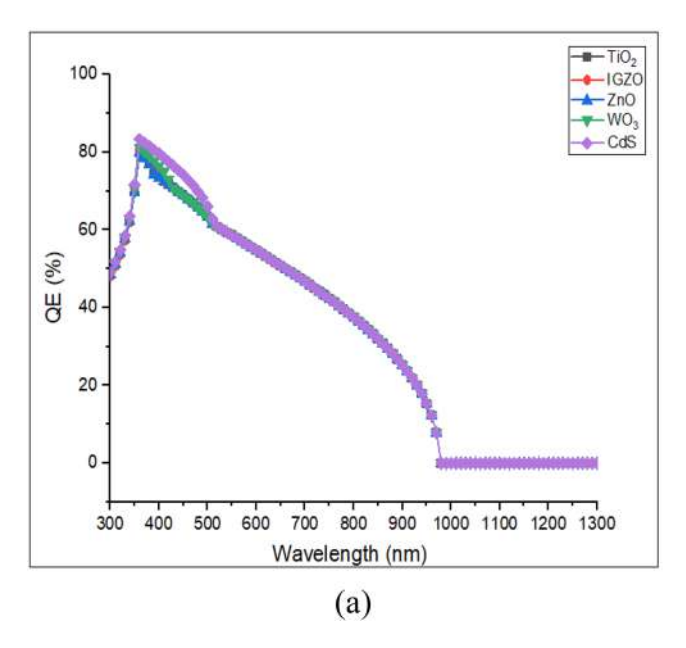


Fig. 9 J-V curve for $CsSnI_3$ PSC with different ETLs and HTLs



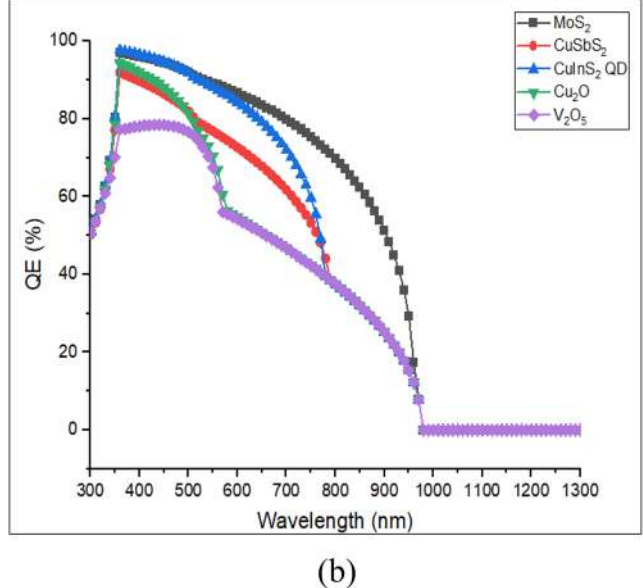


Fig. 10 Quantum efficiency curve for CsSnI₃-based PSC with different ETLs and HTLs

Table 5 Performance of CsSnI₃ PSC with various ETLs

ETLs	$V_{OC}(V)$	J _{SC} (mA/cm ²)	FF (%)	PCE (%)
TiO_2	0.90	17.37	84.10	13.28
IGZO	0.90	17.38	84.11	13.27
ZnO	0.90	17.36	84.04	13.18
WO_3	0.90	17.41	83.98	13.26
CdS	0.90	17.69	84.02	13.41

Table 6 Performance of CsSnI₃ PSC with several HTLs

HTLs	V _{OC} (V)	J _{SC} (mA/cm ²)	FF (%)	PCE (%)
MoS_2	0.80	27.93	83.63	18.82
Cu ₂ O	0.90	19.18	85.94	14.97
CuInS ₂ QD	0.88	23.90	80.71	17.08
CuSbS ₂	0.88	21.55	81.25	15.54
V_2O_5	0.88	19.14	80.59	13.65



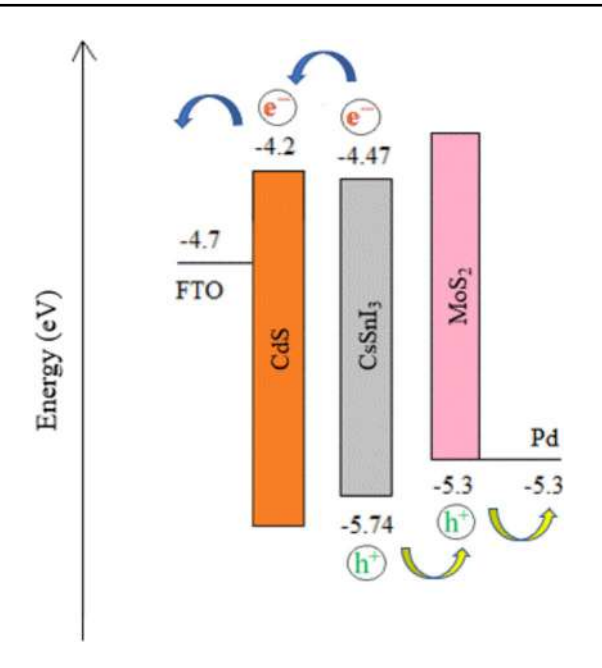


Fig. 11 Energy level diagram of optimized device

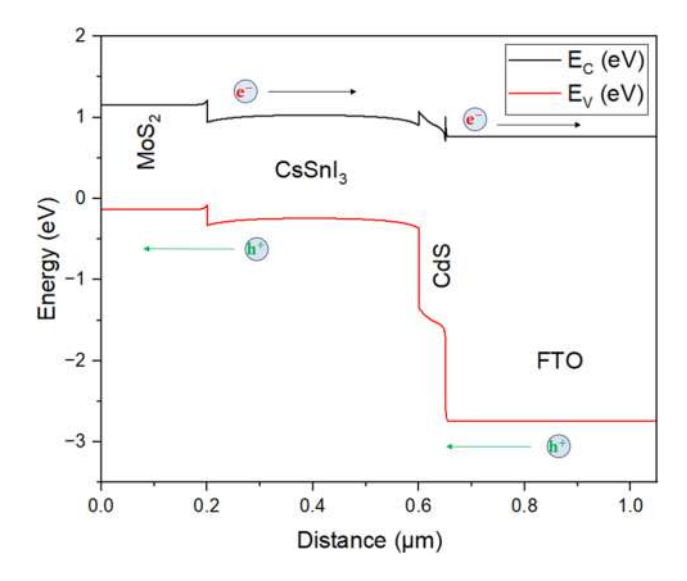
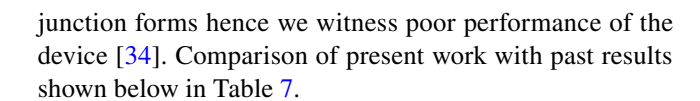


Fig. 12 Energy band diagram of FTO/CdS/CsSnI₃/MoS₂/Pd PSC

Effect of work function

The change in quantum efficiency with the work function of back contact demonstrated in Fig. 13a, b shows the change in J-V characteristics with the back contact work function. It is varied from 4.6 to 5.3 eV to examine its impact on the device performance. The $V_{\rm OC}$ increases from 0.42 to 0.78 V and $J_{\rm SC}$ slightly elevated from 32.87 to 33.62 mA/cm² for the given range of work function shown in Fig. 13b. For the small value of work function (4.6–4.9 eV), a Schottky



Machine learning

The study seeks to investigate the effect of different features such as thickness of absorber layer, defect density and temperature on the performance of a PSC using ML technique [40]. To improve the prediction PCE and minimize simulation complexity in forecasting the PCE of CsSnI₃ PSCs, ML algorithms (RF and XGB) were applied to simulate the data, incorporating variations in thickness of absorber layer, N, and operating temperature. The code was developed on the computing platform. The CSV file containing the SCAPS-1D data was then uploaded for the program to read. The dataset was split into train and test set in the ratio of 80:20. The best hyperparameters were identified using GridSearchCV. For RF regression best hyperparameters were max_depth, min_sample_leaf, n_estimators. While for XGBoost best hyperparameters were learning rate, max depth, min child weight and n estimators. The optimization of CsSnI₃-based PSC includes change in the thickness of from 200 to 2100 nm, with varying N_t of 10^{13} , 10^{16} and 10^{17} cm⁻³ with operating temperature ranging from 300 to 400 K. Python code is utilized to predict PCE using XGB and RF algorithms. Both the algorithms were used for the training and testing [41]. In comparing the XGB and RF models, XGB demonstrated superior performance. The model accuracy metrics showed that RF was less adequate, with a high MSE of 0.272 and a lower R² of 99.53%. In contrast, XGB achieved a much lower MSE of 0.040 and a higher R² of 99.93%. The equations used for computing R² and MSE are shown below [42]:

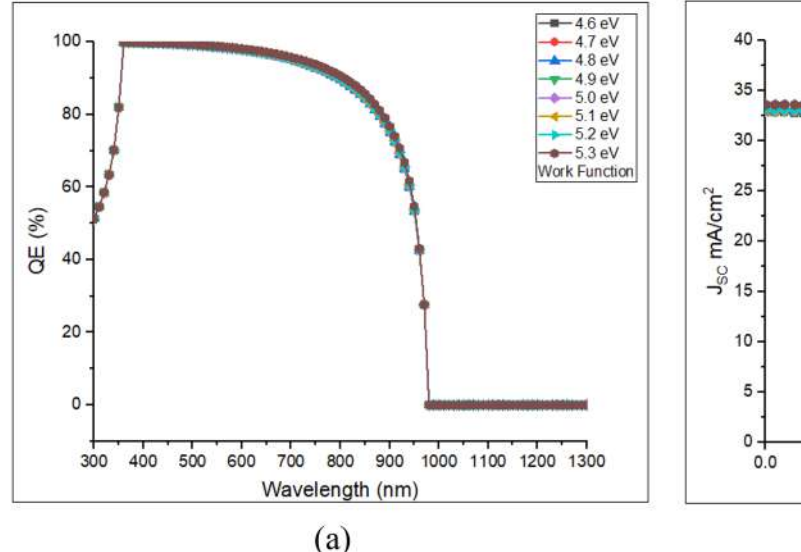
$$MSE = \frac{1}{n} \sum_{i=1}^{n} \left(y_i - \hat{y}_i \right)^2 \tag{4}$$

$$R2 = 1 - \frac{\sum_{i=1}^{n} (y_i - \hat{y}_i)^2}{\sum_{i=1}^{n} (y_i - \bar{y}_i)^2}$$
 (5)

where, y_i = actual value, y = predicted values, y = mean of the actual values and n = total no. of datasets.

The SHAP and actual vs predicted PCE plots for both models are presented in Fig. 14. In Fig. 14b RF model's SHAP plot demonstrated that the SHAP values for defect density are mostly negative. This suggests that higher values of defect density tend to decrease the model's output. The SHAP values for thickness are mostly positive, indicating that higher values of thickness generally lead to an increase in the model's output. The SHAP values for the temperature





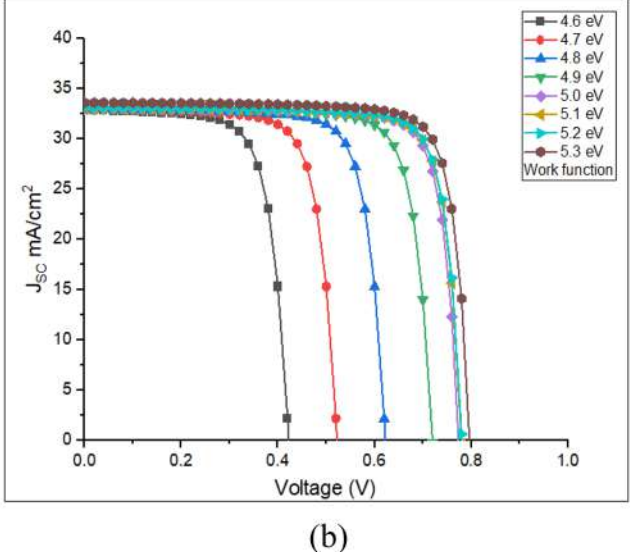


Fig. 13 J-V characteristics and QE curve of optimized CsSnI₃ PSC with various back-contact work functions

Table 7 Comparison with past results

Cell structure	V _{OC} (V)	J _{SC} (mA/cm ²)	FF (%)	PCE (%)
FTO/CdS/CsSnI ₃ /MoS ₂ /Pd	0.81	33.67	85.71	23.45 [This work]
ITO/ZnMgO/CsSnI ₃ /P3HT/Au	0.67	35.61	71.39	17.04 [35]
ITO/PEDOT:PSS/CsSnI ₃ /ICBA/BCP/Ag	0.77	22.68	69.00	12.05 [36]
ITO/c-TiO ₂ /mp-TiO ₂ /CsSnI ₃ -MBAA/P3HT/Au	0.45	24.85	67.00	7.50 [37]
ITO/NiO _x /CsSnI ₃ :CBZ/PCBM/Ag	0.73	21.38	71.99	11.21 [38]
ITO/PCBM/CsSnI ₃ /CuI/Au	0.91	14.24	78.11	10.10 [39]

have a wider distribution, with some values being positive and others negative. This implies that the effect of temperature on the model's output is more complex and depends on its specific value. The model is likely sensitive to changes in defect density and thickness. The Fig. 14d XGB model's SHAP plot shows that defect density seems to have a strong negative impact on the model's output. The red dots (indicating high feature values) are mostly clustered on the left side of the plot, suggesting that higher defect density leads to lower predictions. Thickness appears to have a mixed impact. The are both red and blue dots scattered across the plot, indicating that the effect of thickness on the model's output might not be as straightforward. Temperature also shows a mixed impact, similar to thickness. The red and blue dots are intermingled, suggesting that temperature's influence on the model's output might not be solely positive or negative. This SHAP plot provides insights into how the features contribute to the model's predictions. By understanding the impact of each feature, we can potentially improve the model's performance. The Fig. 14 demonstrated that the XGB method exceeds the performance of RF algorithm, it is clear that the XGB algorithm provides the most accurate PCE anticipation [43]. The models, trained on extensive input data, deliver highly efficient and realistic outcomes. The results provide guidance for designing new PSCs.

Effect of doping density

The absorber layer was doped with p-type, depicted that the acceptor concentration (NA) was there only, and donor concentration $(N_D) = 0$ cm⁻³. The Fig. 15 illustrated that change in the PV parameters such as PCE and FF with absorber layer N_{Δ} ranging from 1×10^{13} to 1×10^{19} cm⁻³ at thickness of 400 nm, temperature of 300 K and N_t of $10^{13}\;\mbox{cm}^{-3}.$ As N_A increases, the FF and PCE of absorber layer increases [44]. For further increase in N_A, the electric field at the CsSnI₃ interface strengthens, resulting is more efficient charge separation. However, this enhanced electric field also leads to increased recombination, which negatively affects performance [33]. The maximum values for FF and PCE are obtained at a N_A is 1×10^{15} cm⁻³, reaching a highest value of 85.73% and 23.46% respectively [45]. These simulation results conclude that the optimized value of N_{Δ} is 1×10^{15} cm⁻³ for CsSnI₃-based PSC.



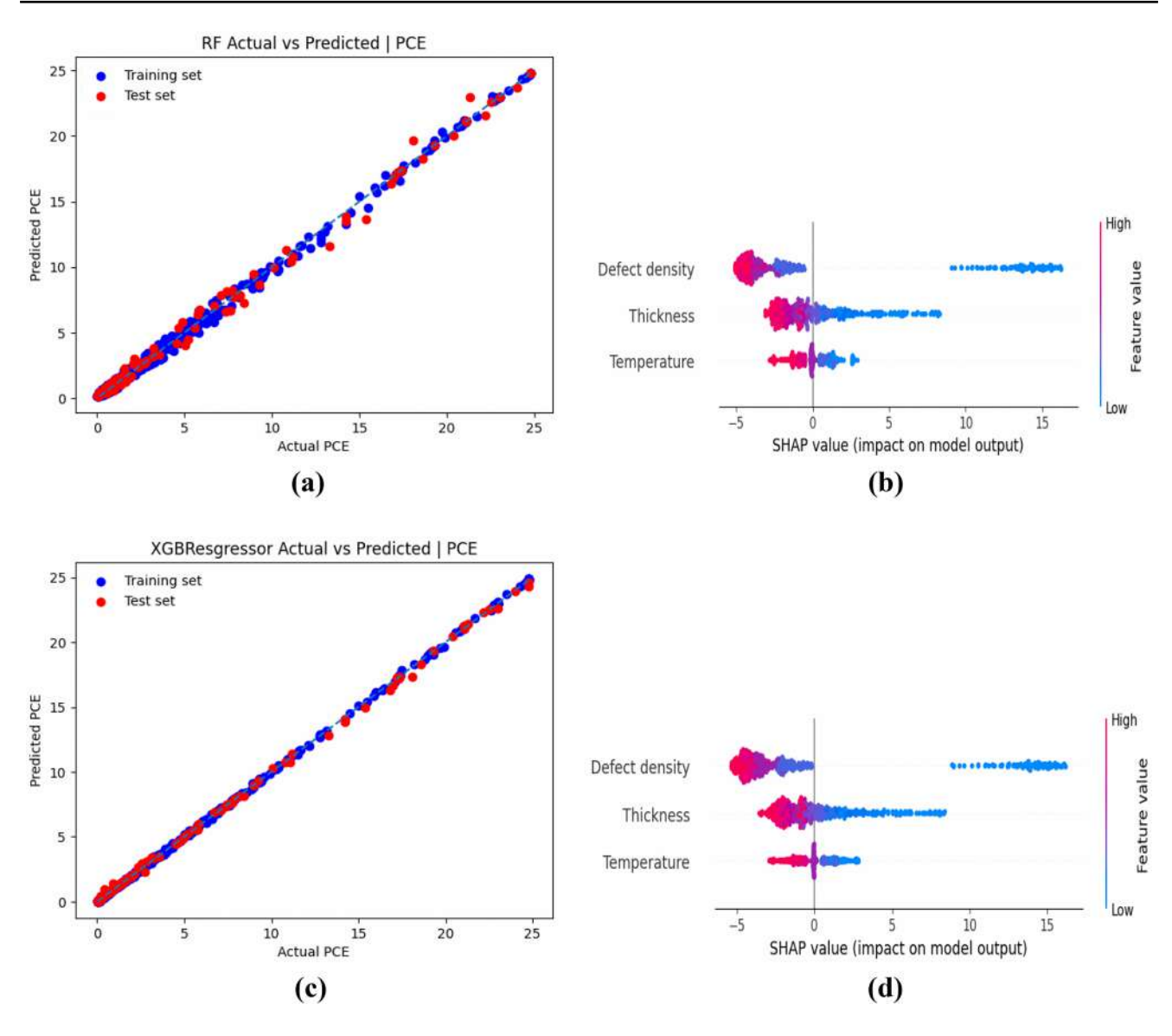


Fig. 14 Actual and predicted value of PCE using, a RF model, c XGB model and SHAP plots, b RF model, d XGB model

Conclusions

The work incorporates comprehensive study of tin-based PSC with the several ETLs and HTLs. The impact of thickness of absorber layer, operating temperature and $N_{\rm t}$ on $CsSnI_3$ PSC were analyzed using SCAPS-1D. The device with maximum efficiency of 23.45% was obtained for the configuration of FTO/CdS/CsSnI_3/MoS_2/Pd. Whereas, suitable HTL must have balanced hole mobility to prepare high PCE devices. The optimized thickness of the CsSnI_3 layer is 400 nm for an efficient PSC. The highest efficiency achieved at a temperature of 300 K and $N_{\rm t}$ of 10^{13} cm $^{-3}$. The simulation trend demonstrated that photovoltaic performance of a PSC falls with increment in operating temperature and defect

density. The device's PCE increased over 23% by optimizing parameters like thickness, work function of back contact, N_t and operating temperature. The proper optimization of suitable ETL and HTL has been completed for CsSnI₃-based PSC. The ML approach is employed to predict the PCE and the parameters which affect the performance of the PSC. Outcomes demonstrated that the XGB algorithm outperforms the RF algorithm with higher R² of 99.93% with low MSE of 0.040. A highly accurate and effective model can be created by providing a substantial amount of data into ML algorithms. Hence, we can optimize the performance of PSCs with the assistance of outcomes of this numerical modeling and ML model.



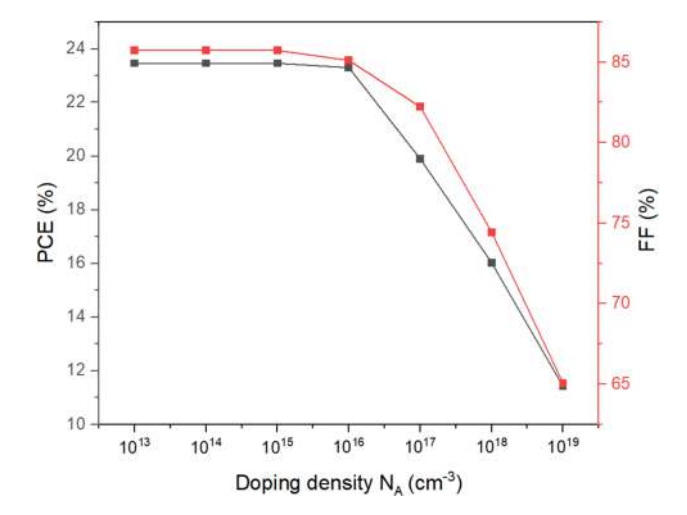


Fig. 15 Impact of N_A on the PCE and FF of CsSnI₃-based PSC

Acknowledgements The author, Rahul Kundara is thankful to Delhi Technological University, New Delhi for providing a senior research fellowship. We are very grateful to Marc Burgelman, the Electronics and Information Systems (ELIS), University of Gent, Belgium, for providing us with SCAPS-1D software.

Data availability Data will be made available on request.

Declarations

Conflict of interest The authors declare that they have no known competing financial interests or personal relationships that could have appeared to influence the work reported in this paper.

References

- N. Rai, S. Rai, P.K. Singh, P. Lohia, D.K. Dwivedi, Analysis of various ETL materials for an efficient perovskite solar cell by numerical simulation. J. Mater. Sci. Mater. Electron. 31, 16269– 16280 (2020). https://doi.org/10.1007/s10854-020-04175-z
- I. Elango, M. Selvamani, P.C. Ramamurthy, A.V. Kesavan, Studying VOC in lead free inorganic perovskite photovoltaics by tuning energy bandgap and defect density. Ceram. Int. 48(19), 29414
 29420 (2022). https://doi.org/10.1016/j.ceramint.2022.06.125
- W. Xiang, S. Liu, W. Tress, A review on the stability of inorganic metal halide perovskites: challenges and opportunities for stable solar cells. Energy Environ. Sci. 14(4), 2090–2113 (2021). https:// doi.org/10.1039/d1ee00157d
- L. Etgar, P. Gao, Z. Xue, Q. Peng, A.K. Chandiran, B. Liu, M.K. Nazeeruddin, M. Grätzel, Mesoscopic CH₃NH₃PbI₃/TiO₂ heterojunction solar cells. J. Am. Chem. Soc. 134(42), 17396–17399 (2012). https://doi.org/10.1021/ja307789s
- Y. Liu, T. Li, M. Shi, J. Zhu, X. Ma, M. Wu, J. Wu, C. Zhang, T. Zhang, Y. Qi, Hole-transport layer-free tin-based perovskite solar cells: improving their performance from a simulation perspective. ECS J. Solid State Sci. Technol. 11(10), 103001 (2022). https://doi.org/10.1149/2162-8777/ac936e
- B. Wu, Y. Zhou, G. Xing, Q. Xu, H.F. Garces, A. Solanki, T.W. Goh, N.P. Padture, T.C. Sum, Long minority-carrier diffusion length and low surface-recombination velocity in inorganic

- lead-free cssni₃ perovskite crystal for solar cells. Adv. Funct. Mater. **27**(7), 1604818 (2017). https://doi.org/10.1002/adfm. 201604818
- T.B. Song, T. Yokoyama, J. Logsdon, M.R. Wasielewski, S. Aramaki, M.G. Kanatzidis, Piperazine suppresses self-doping in CsSnI₃ perovskite solar cells. ACS Appl. Energy Mater. 1(8), 4221–4226 (2018). https://doi.org/10.1021/acsaem.8b00866
- Q. Duan, J. Ji, X. Hong, Y. Fu, C. Wang, K. Zhou, X. Liu, H. Yang, Z.Y. Wang, Design of hole-transport-material free CH₃NH₃PbI₃/ CsSnI₃ all-perovskite heterojunction efficient solar cells by device simulation. Sol. Energy 201, 555–560 (2020). https://doi.org/10. 1016/j.solener.2020.03.037
- B. Li, H. Di, B. Chang, R. Yin, L. Fu, Y.N. Zhang, L. Yin, Efficient passivation strategy on Sn Related defects for high performance all-inorganic CsSnI₃ perovskite solar cells. Adv. Funct. Mater. 31(11), 2007447 (2021). https://doi.org/10.1002/adfm. 202007447
- A.A. Kanoun, M.B. Kanoun, A.E. Merad, S. Goumri-Said, Toward development of high-performance perovskite solar cells based on CH₃NH₃GeI₃ using computational approach. Sol. Energy 182, 237–244 (2019). https://doi.org/10.1016/j.solener.2019.02. 041
- K. Fatema, M.S. Arefin, Enhancing the efficiency of Pb-based and Sn-based perovskite solar cell by applying different ETL and HTL using SCAPS-ID. Opt. Mater. 125, 112036 (2022). https:// doi.org/10.1016/j.optmat.2022.112036
- K. Singh, S. Sonu, V. Chaudhary, P. Raizada, S. Rustagi, P. Singh, P. Thakur, V. Kumar, A. Kaushik, Defect and Heterostructure engineering assisted S-scheme Nb₂O₅ nanosystems-based solutions for environmental pollution and energy conversion. Adv. Colloid Interface Sci. 332, 103273 (2024). https://doi.org/10. 1016/j.cis.2024.103273
- S. Subramanyam, L. Phor, V. Chaudhary, V. Kaushik, P. Kumar, S. Chahal, Progress in MXene synthesis approaches for energy systems: a comprehensive review. J. Energy Storage. 92, 112043 (2024). https://doi.org/10.1016/j.est.2024.112043
- B.A. Taha, A.J. Addie, A.J. Haider, V. Chaudhary, R. Apsari, A. Kaushik, N. Arsad, Exploring trends and opportunities in quantum-enhanced advanced photonic illumination technologies. Adv. Quantum Technol. 7(3), 2300414 (2024). https://doi.org/10.1002/ qute.202300414
- L.J. Chen, C.R. Lee, Y.J. Chuang, Z.H. Wu, C. Chen, Synthesis and optical properties of lead-free cesium tin halide perovskite quantum rods with high-performance solar cell application. J. Phys. Chem. Lett. 7(24), 5028–5035 (2016). https://doi.org/10. 1021/acs.jpclett.6b02344
- S. Rai, B.K. Pandey, D.K. Dwivedi, Modeling of highly efficient and low cost CH₃NH₃Pb(I_{1-x}CI_x)₃ based perovskite solar cell by numerical simulation. Opt. Mater. 100, 109631 (2020). https:// doi.org/10.1016/j.optmat.2019.109631
- S.Z. Haider, H. Anwar, M. Wang, Theoretical device engineering for high-performance perovskite solar cells using CuSCN as hole transport material boost the efficiency above 25%. Phys. Status Sol. (A) Appl. Mater. Sci. 216(11), 1900102 (2019). https://doi. org/10.1002/pssa.201900102
- N. Lakhdar, A. Hima, Electron transport material effect on performance of perovskite solar cells based on CH₃NH₃GeI₃. Opt. Mater. 99, 109517 (2020). https://doi.org/10.1016/j.optmat.2019. 109517
- X. Xu, J. Wang, D. Cao, Y. Zhou, Z. Jiao, Design of all-inorganic hole-transport-material-free CsPbI₃/CsSnI₃ heterojunction solar cells by device simulation. Mater Res Express. 9(2), 025509 (2022). https://doi.org/10.1088/2053-1591/ac5778
- M. Jiang, J. Tang, Simulated development and optimized performance of narrow-bandgap CsSnI₃-based all-inorganic perovskite



- solar cells. J. Phys. D Appl. Phys. **54**(46), 465104 (2021). https://doi.org/10.1088/1361-6463/ac1e4c
- S. Bhattarai, T.D. Das, Optimization of carrier transport materials for the performance enhancement of the MAGeI₃ based perovskite solar cell. Sol. Energy 217, 200–207 (2021). https://doi.org/10. 1016/j.solener.2021.02.002
- I. De Los MontoyaSantos, H.J. Cortina-Marrero, M.A. Ruíz-Sánchez, L. Hechavarría-Difur, F.J. Sánchez-Rodríguez, M. Courel, H. Hu, Optimization of CH3NH3PbI3 perovskite solar cells: a theoretical and experimental study. Sol. Energy. 199, 198–205 (2020). https://doi.org/10.1016/j.solener.2020.02.026
- A. Kuddus, M.F. Rahman, S. Ahmmed, J. Hossain, A.B.M. Ismail, Role of facile synthesized V₂O₅ as hole transport layer for CdS/ CdTe heterojunction solar cell: Validation of simulation using experimental data. Superlattices Microstruct. 132, 106168 (2019). https://doi.org/10.1016/j.spmi.2019.106168
- K.L. Chopra, S.R. Das, *Thin film solar cells* (Springer, Boston, 1983), pp. 1–18
- A.K. Patel, R. Mishra, S.K. Soni, Performance enhancement of CIGS solar cell with two dimensional MoS₂ hole transport layer. Micro Nanostruct. 165, 207195 (2022). https://doi.org/10.1016/j. micrna.2022.207195
- K. Deepthi Jayan, V. Sebastian, Comprehensive device modelling and performance analysis of MASnI₃ based perovskite solar cells with diverse ETM, HTM and back metal contacts. Sol. Energy. 217, 40–48 (2021). https://doi.org/10.1016/j.solener.2021.01.058
- D.K. Maram, M. Haghighi, O. Shekoofa, H. Habibiyan, H. Ghafoorifard, A modeling study on utilizing ultra-thin inorganic HTLs in inverted p–n homojunction perovskite solar cells. Sol. Energy 213, 1–12 (2021). https://doi.org/10.1016/j.solener.2020.11.009
- M. Singh, R. Kumar, V. Singh, S. Srivastava, Theoretical study of highly efficient CH₃NH₃SnI₃ based perovskite solar cell with CuInS₂ quantum dot. Semicond. Sci. Technol. 37(2), 025010 (2021). https://doi.org/10.1088/1361-6641/ac4325
- S. Kohnehpoushi, P. Nazari, B.A. Nejand, M. Eskandari, MoS2: a two-dimensional hole-transporting material for high-efficiency, low-cost perovskite solar cells. Nanotechnology 29(20), 205201 (2018). https://doi.org/10.1088/1361-6528/aab1d4
- S. Ahmed, F. Jannat, M.A.K. Khan, M.A. Alim, Numerical development of eco-friendly Cs₂TiBr₆ based perovskite solar cell with all-inorganic charge transport materials via SCAPS-1D. Optik 225, 165765 (2021). https://doi.org/10.1016/j.ijleo.2020.165765
- Y.F. Gu, H.J. Du, N.N. Li, L. Yang, C.Y. Zhou, Effect of carrier mobility on performance of perovskite solar cells. Chin. Phys. B 28(4), 048802 (2019). https://doi.org/10.1088/1674-1056/28/4/ 048802
- 32. M.A. Nalianya, C. Awino, H. Barasa, V. Odari, F. Gaitho, B. Omogo, M. Mageto, Numerical study of lead free CsSn_{0.5}Ge_{0.5}I₃ perovskite solar cell by SCAPS-1D. Optik. **248**, 168060 (2021). https://doi.org/10.1016/j.ijleo.2021.168060
- S. Abdelaziz, A. Zekry, A. Shaker, M. Abouelatta, Investigating the performance of formamidinium tin-based perovskite solar cell by SCAPS device simulation. Opt. Mater. 101, 109738 (2020). https://doi.org/10.1016/j.optmat.2020.109738
- G. Fang, H. Tian, W. Chang, Z. Wang, Q. He, X. Gao, Optimized analysis of back-contact perovskite solar cells architectures. Optik 207, 164362 (2020). https://doi.org/10.1016/j.ijleo.2020.164362
- M.F. Rahman, M.A. Islam, M. Chowdhury, L.B. Farhat, S. Ezzine, A.S. Islam, Efficiency improvement of CsSnI₃ based heterojunction solar cells with P3HT HTL: A numerical simulation

- approach. Mater. Sci. Eng. B **307**, 117524 (2024). https://doi.org/10.1016/j.mseb.2024.117524
- Z. Zhang, H. Yu, J. Huang, Z. Liu, Q. Sun, X. Li, L. Dai, Y. Shen, M. Wang, Over 12% efficient CsSnI₃ perovskite solar cells enabled by surface post-treatment with bi-functional polar molecules. Chem. Eng. J. 490, 151561 (2024). https://doi.org/10.1016/j.cej. 2024.151561
- T. Ye, K. Wang, Y. Hou, D. Yang, N. Smith, B. Magill, J. Yoon, R.R. Mudiyanselage, G.A. Khodaparast, K. Wang, S. Priya, Ambient-air-stable lead-free CsSnI₃ solar cells with greater than 7.5% efficiency. J. Am. Chem. Soc. 143(11), 4319–28 (2021). https://doi.org/10.1021/jacs.0c13069
- C. Duan, F. Zou, Q. Wen, M. Qin, J. Li, C. Chen, X. Lu, L. Ding, K. Yan, A bifunctional carbazide additive for durable CsSnI₃ perovskite solar cells. Adv. Mater. 35(26), 2300503 (2023). https:// doi.org/10.1002/adma.202300503
- M.K. Hossain, G.I. Toki, D.P. Samajdar, M. Mushtaq, M.H. Rubel, R. Pandey, J. Madan, M.K. Mohammed, M.R. Islam, M.F. Rahman, H. Bencherif, Deep insights into the coupled optoelectronic and photovoltaic analysis of lead-free CsSnI₃ perovskite-based solar cell using DFT calculations and SCAPS-1D simulations. ACS Omega 8(25), 22466–22485 (2023). https://doi.org/10.1021/acsomega.3c00306
- M. Mammeri, L. Dehimi, H. Bencherif, F. Pezzimenti, Paths towards high perovskite solar cells stability using machine learning techniques. Sol. Energy 249, 651–660 (2023). https://doi.org/ 10.1016/j.solener.2022.12.002
- N. Shrivastav, J. Madan, R. Pandey, Maximizing performance in Cs₂CuBiCl₆ perovskite cells through machine learning-driven absorber layer parameter analysis. Mater. Lett. 359, 135929 (2024). https://doi.org/10.1016/j.matlet.2024.135929
- D. Chicco, M.J. Warrens, G. Jurman, The coefficient of determination R-squared is more informative than SMAPE, MAE, MAPE, MSE and RMSE in regression analysis evaluation. PeerJ Comput. Sci. 7, e623 (2021). https://doi.org/10.7717/peerj-cs.623
- N. Shrivastav, J. Madan, R. Pandey, Predicting photovoltaic efficiency in Cs-based perovskite solar cells: a comprehensive study integrating SCAPS simulation and machine learning models. Solid State Commun. 380, 115437 (2024). https://doi.org/10.1016/j.ssc.2024.115437
- 44. H. Bencherif, L. Dehimi, N. Mahsar, E. Kouriche, F. Pezzimenti, Modeling and optimization of CZTS kesterite solar cells using TiO₂ as efficient electron transport layer. Mater. Sci. Eng. B 276, 115574 (2022). https://doi.org/10.1016/j.mseb.2021.115574
- I. Chabri, Y. Benhouria, A. Oubelkacem, A. Kaiba, I. Essaoudi, A. Ainane, SCAPS device simulation study of formamidinium Tin-Based perovskite solar Cells: Investigating the influence of absorber parameters and transport layers on device performance. Sol. Energy 262, 111846 (2023). https://doi.org/10.1016/j.solen er.2023.111846

Publisher's Note Springer Nature remains neutral with regard to jurisdictional claims in published maps and institutional affiliations.

Springer Nature or its licensor (e.g. a society or other partner) holds exclusive rights to this article under a publishing agreement with the author(s) or other rightsholder(s); author self-archiving of the accepted manuscript version of this article is solely governed by the terms of such publishing agreement and applicable law.



Curriculum Vitae



<u>rahul_2k20phdap10@dtu.ac.in</u> rahulkundara1@gmail.com (+91)7011392667 (+91)9873844480

Rahul Kundara

AREA OF INTEREST

Photovoltaic Technology, Solar Energy Material Synthesis and Characterization, Performance Optimization of Solar Devices, Perovskite Solar Cells Simulation and Fabrication.

QUALIFICATIONS

Ph.D. (Physics)	2020-till date	Delhi Technological University, Delhi, India	Thesis submitted
Ph.D. (Physics) Course Work	2021	Delhi Technological University, Delhi, India	SGPA-8.0
M. Tech (Nanoscience & Technology)	2018-2020	Delhi Technological University, Delhi, India	CGPA-7.6
B. Tech (Electronics & Communication)	2011-2015	Northern India engineering College, GGSIP University, Delhi	68.18 %
CBSE (Class XII)	2011	Sarvodaya boys SSS No. I k-BLK Mangolpuri, Delhi	74.8 %
CBSE (Class X)	2009	Govt. Co-ed SSS Pooth Kalan Sec-20 Rohini, Delhi	73.8 %

ACADEMIC PROJECTS

- Synthesis of silver nanoparticles by using extract of different plant leaves
- Solar Power Automatic Street Light Controller

SUMMER INTERNSHIP

- Attended training on study of GaN and its application in military conducted by **DRDO** lab solid state physics laboratory (SSPL), Department of Defence Research and Development in Ministry of Defence, Lucknow Road, Timarpur, Delhi-110054 from 16 June 2014 to 28 July 2014.
- Attended training on telecommunication conducted by Purple Leap a Pearson Educomp company.

ACADEMIC ACHIEVEMENTS AND AWARDS

- Commendable Research Excellence Award by the Delhi Technological University, 2024.
- Awarded the **Senior Research Fellowship** by the Delhi Technological University, 2024.
- University Grants Commission—NET in Electronic Science qualified in 2023.
- Awarded the **Junior Research Fellowship** by the Delhi Technological University, 2020-2023.
- Awarded the scholarship by All India Council for Technical Education (AICTE), 2018-2020.
- Graduate Aptitude Test in Engineering (GATE) qualified in ECE, 2016.
- Reviewer of Multiscale and Multidisciplinary Modeling, Experiments and Design Journal, Springer Nature.

PHD THESIS TITLE: STUDIES ON DESIGN, OPTIMIZATION AND CHARACTERIZATION OF PEROVSKITE SOLAR CELLS

Google Scholar Link: https://scholar.google.com/citations?user=2LvLCvMAAAAJ&hl=en

ATTENTED INTERNATIONAL CONFERENCES

• Presented Paper entitled "Study the various parameters affecting the power conversion efficiency of lead-free Perovskite Solar Cell by SCAPS-1D" in International Conference on Design and Materials (ICDM) Organized by Department of Design, Delhi Technological University (DTU) on 27th-30th January 2022.

- Presented Paper entitled "Efficiency Optimization of Sb₂S₃ Based Solar Cell By SCAPS-1D" in International Conference on Nanotechnology: Opportunities & Challenges (ICNOC-2022) organized by Department of Applied Science & Humanities, Faculty of Engineering & Technology, Jamia Millia Islamia, on 28th 30th November 2022, at New Delhi, India.
- Presented Paper entitled "Optimization Of CH₃NH₃PbI₃ Perovskite Solar Cell: A Statistical And Simulation Based Study" in International Conference on Artificial Intelligence, Advanced Materials, & Mechatronics Systems (AIAMMS-2023) organized by School of Engineering & Technology, JECRC University, on 3rd-4th November 2023, at Jaipur, India.
- Presented Poster entitled "Performance optimization of CsSnI₃-based Perovskite Solar Cells with diverse ETLs and HTLs by using SCAPS-1D" in International Conference on Atomic, Molecular, Material, Nano & Optical Physics with Applications (ICAMNOP-2023) on 20-22nd Dec 2023, organized by Delhi Technological University (DTU), Delhi.

SKILLS

- Characterization Skills: X-ray diffraction, SEM, FTIR, UV-Vis and PL spectroscopy.
- **Technical Skills**: SCAPS-1D Simulation Software, wxAMPS software, Origin Lab Software, ImageJ software, Machine Learning, and MS-Office.
- **Soft skills:** Punctuality, Strong Work ethic, good Oral and Written communication, Flexibility, Fast learner, Multitasking, Team work spirit, Analytic and Problem-solving mindset, Decision making, leadership, Eye for detail

DECLARATION

I hereby declare that the details furnished above are true and correct to the best of my knowledge and belief.

LIST OF PUBLICATIONS

- "Performance optimization of lead-free KGeCl₃ based perovskite solar cells using SCAPS-1D", Rahul Kundara, Sarita Baghel, Solar Energy, Volume 287, 1 February 2025, 113253 (SCIE, IF-6.0).
- 2. "Predictive design of KSnI₃-based perovskite solar cells using SCAPS and machine learning model", Rahul Kundara, Sarita Baghel, Materials Science & Engineering B, Volume 307, 1 September 2024, 117536. (SCIE, IF-3.9)
- 3. "Performance analysis of LaFeO₃ perovskite solar cells: A theoretical and experimental study", Rahul Kundara, Sarita Baghel, Solid State Communications, Volume 389, 12 June 2024, 115590. (SCIE, IF-2.1)
- "Numerical simulation of highly efficient Cs₂AgInBr₆-based double perovskite solar cell using SCAPS-1D", Vishal Deswal, Shubhda Kaushik, Rahul Kundara, Sarita Baghel, Materials Science & Engineering B, Volume 299, 1 January 2024, 117041. (SCIE, IF-3.9)
- 5. "Investigating the Efficiency and Optimization of Germanium-based Perovskite Solar Cell using SCAPS 1D", Anushansha Yadav, Vanshika, Rahul Kundara, Sarita Baghel, Indian Journal of Engineering & Materials Sciences, Volume 30, 1 October 2023, 706-712. (SCI, IF-0.9)
- 6. "Device modelling of lead free (CH₃NH₃)₂CuX₄ based perovskite solar cells using SCAPS simulation", Rahul Kundara, Sarita Baghel, Optical and Quantum Electronics, Volume 55, 02 September 2023, 968. (SCIE, IF-3.3)
- 7. "Study on the Various Parameters Affecting the Power Conversion Efficiency of Lead-Free Perovskite Solar Cell by SCAPS-1D", Rahul Kundara, Sarita Baghel, Journal of Mines, Metals and Fuels 70(9A) (2022) 24–29. (SCOPUS, IF-0.17)
- 8. "Optimization of CH3NH3PbI3 Perovskite Solar Cell: A Statistical and Simulation-Based Study", Rahul Kundara, Sarita Baghel, InTools, Techniques, and Advancements in Engineering Materials Science 2025 (pp. 15-36). IGI Global Scientific Publishing. ISBN13: 9798369355138.
- 9. "Performance optimization of CsSnI₃-based perovskite solar cells using SCAPS-1D and machine learning analysis"; Rahul Kundara, Sarita Baghel, Journal of Optics, (2025). (SCOPUS, IF-1.6)

Citations: 112 h-index: 05

i10-index: 04